transactions of the ASME

journal of heat transfer

Published Quarterly by
The American Society of
Mechanical Engineers
Volume 98 • Series C • Number 1
FEBRUARY 1976

1 1976 Winter Annual Meeting—Call for Papers

2 Journal of Heat Transfer Referees, 1975

4 Information for Authors

5 Behavior of Inert Gas Bubbles in Forced Convective Liquid Metal Circuits (76-HT-X)
W. J. Minkowycz, D. M. France, and R. M. Singer

12 Subcooled Decompression Analysis in PWR LOCA (76-HT-M)
K. Namatame and K. Kobayashi

19 *Asymptotic Analysis of the Average, Steady, Isothermal Flow in Coupled, Parallel Channels* (74-WA/HT-4)
K. O. Lund

26 Experiments on the Transfer Characteristics of a Corrugated Fin and Tube Heat Exchanger Configuration (76-HT-V)
L. Goldstein, Jr. and E. M. Sparrow

35 Theory on Thermal Instability of Binary Gas Mixtures in Porous Media (76-HT-T)
M. L. Lawson, Wen-Jei Yang, and S. Bunditkul

42 Natural Convection in a Porous Medium: Effects of Confinement, Variable Permeability, and Thermal Boundary Conditions (76-HT-Y)
R. J. Ribando and K. E. Torrance

49 Onset of Convection in a Porous Medium With Internal Heat Generation (76-HT-EE)
R. D. Gasser and M. S. Kazimi

55 Natural Convection of a Heat-Generating Fluid Within Closed Vertical Cylinders and Spheres (75-HT-60)
R. J. Kee, C. S. Landram, and J. C. Miles

62 Effect of Thermal Instability on Thermally Developing Laminar Channel Flow (76-HT-R)
Y. Kamotani and S. Ostrach

67 Experimental Investigation of Natural Convection in Inclined Rectangular Regions of Differing Aspect Ratios (75-HT-62)
J. N. Arnold, I. Catton, and D. K. Edwards

72 Laminar and Turbulent Free Convection From Elliptic Cylinders, With a Vertical Plate and Horizontal Circular Cylinder as Special Cases (76-HT-DD)
G. D. Raithby and K. G. T. Hollands

81 On the Calculation of Horizontal, Turbulent, Free Shear Flows Under Gravitational Influence (76-HT-S)
M. M. Gibson and B. E. Launder

88 Convective Instability in a Melt Layer Heated From Below (76-HT-BB)
E. M. Sparrow, L. Lee, and N. Shamsundar

95 Combined Radiation and Developing Laminar Free Convection Between Vertical Flat Plates With Asymmetric Heating (75-HT-19)
J. R. Carpenter, D. G. Briggs, and V. Sernas

101 Molecules Gas Radiation in a Laminar or Turbulent Pipe Flow (76-HT-Q)
A. T. Wassel and D. K. Edwards

108 Laminar Film Condensation on a Vertical Melting Surface (76-HT-AA)
M. Epstein and D. H. Cho

114 Transport-Reaction Mechanism of Mist Formation Based on the Critical Supersaturation Model (76-HT-CC)
Y. Hayashi, A. Takimoto, and M. Kanbe

120 Heat and Mass Transfer From Freely Falling Drops (75–WA/HT-37)
Shi-Chune Yao and V. E. Schrock

127 A Study of Transient Heat Transfer in Long Insulated Wires (76-HT-U)
Y. Jaluria

133 A Continuum Model for Diffusion in Laminated Composite Media (76-HT-Z)
A. Maewal, T. C. Bache, and G. A. Hegemier

139 Correlation of Theoretical Analysis With Experimental Data on the Performance of Charring Ablators (76-HT-P)
K. Mastanaiah

(Contents continued on page 18)

EDITED and PUBLISHED quarterly at the offices of The American Society of Mechanical Engineers, United Engineering Center, 345 E. 47th St., New York, N. Y. 10017. Cable address, "Mechaneer," New York, Second-class postage paid at New York, N. Y., and at additional mailing offices.

CHANGES OF ADDRESS must be received at Society headquarters seven weeks before they are to be effective. Please send old label and new address.

PRICES: To members, $25.00, annually; to nonmembers, $50.00. Single copies, $15.00 each. Add $1.50 for postage to countries outside the United States and Canada.

STATEMENT *from By-Laws.* The Society shall not be responsible for statements or opinions advanced in papers or . . . printed in its publications (B 13, Par. 4).

INDEXED by the Engineering Index, Inc.

CONTENTS (CONTINUED)

TECHNICAL NOTES

144 Free Convection Heat Transfer to Non-Newtonian, Dilatant Fluids From a Horizontal Cylinder
C. B. Kim and D. E. Wollersheim

146 Velocity Measurements for Buoyancy-Induced Flow in Mercury Adjacent to Vertical Single Cylinders
J. R. Welty and D. R. Pelnecke

148 A Closed-Form Solution for the Radiosity at the Edge of a Rectangular Cavity
A. L. Crosbie

150 Critical Thickness of Insulation Accounting for Variable Convection Coefficient and Radiation Loss
L. D. Simmons

ERRATA

34 ERRATUM: K. A. Gardner, "Efficiency of Extended Surface," published in the JOURNAL OF HEAT TRANSFER, TRANS. ASME, Vol. 67, 1945, pp. 621–631.

143 ERRATUM: W. Contreras and R. S. Thorsen, "Transient Melting of a Solid Heated by a Condensing Saturated Vapor—Case 1: Negligible Interface Curvature," Published in the Nov. 1975 issue of the JOURNAL OF HEAT TRANSFER, pp. 570–575.

W. J. Minkowycz[1]
D. M. France
R. M. Singer[2]

Components Technology Division,
Argonne National Laboratory,
Argonne, Ill.

Behavior of Inert Gas Bubbles in Forced Convective Liquid Metal Circuits

Conservation equations are derived for the motion of a small inert gas bubble in a large flowing liquid-gas solution subjected to large thermal gradients. Terms which are of the second order of magnitude under less severe and steady-state conditions are retained, thus resulting in an expanded form of the Rayleigh equation. The bubble dynamics is a function of opposing mechanisms tending to increase or decrease bubble volume while being transported with the solution. Diffusion of inert gas between the bubble and the solution is one of the most important of these mechanisms included in the analysis.

The analytical model is applied to an argon gas bubble flowing in a weak solution of argon gas in liquid sodium. Calculations are performed for these fluids under conditions typical of normal and abnormal operation of a liquid metal fast breeder reactor (LMFBR) core and the resulting bubble radius, internal gas pressure, and mass of inert gas are presented in each case. An important result obtained indicates that inert gas bubbles reaching the core inlet of an LMFBR will always grow as they traverse the core under normal and extreme abnormal conditions and that the rate of growth is quite small in all cases.

Introduction

The existence of inert gas bubbles in forced convective liquid metal systems has become a subject of interest with regard to several engineering problems. Perhaps the most noteworthy of these is the effect of the presence of inert gas bubbles in a liquid metal at the moment of incipient boiling. Henry and Singer [1][3] experimentally demonstrated that entirely misleading interpretation of data can result if the presence of entrained gas bubbles is not considered in the measurement of incipient boiling superheat. Kottowski, et al. [2] showed that the injection of argon bubbles into a flowing liquid sodium stream can prevent the possibility of liquid superheating, and France, et al. [3] demonstrated the same zero superheat condition in a sodium experiment typifying a liquid metal fast breeder reactor (LMFBR) system. In the latter experiments, the condition of zero incipient boiling superheat at LMFBR parametric conditions was attributed to the presence of inert gas bubbles in the hotter (upper) regions of the test section (core). Other engineering problems related to inert gas bubble transport in liquid metal systems include the influence on boiling detection devices, cavitation in system components, and neutron flux as related to changes in heat transfer. The spatial distribution of bubbles in a heated channel has also been shown to be of some interest [4].

One question common to most of these applications is that of survival of an inert gas bubble as it is transported through a liquid metal circuit once it has been established at some location in the system. In a LMFBR it is important to be able to predict the survival of inert gas (usually argon) bubbles generated in the relatively cold region of the primary sodium system (the intermediate heat exchanger) as the bubble is transported through the reactor core to the outlet plenum. As the bubble traverses the core region of increasing sodium temperature, several factors influence its growth or collapse rate. The increasing liquid temperature results in an increased solubility of the inert gas in the liquid sodium outside the bubble, increasing the rate of diffusion out of the bubble, which tends to collapse the bubble. At the same time, this temperature increase raises the sodium vapor pressure and the inert gas pressure inside the bubble which cause bubble growth. The increase in gas pressure also increases the rate of solution of the gas in the liquid. Finally, the growth rate is influenced by such factors as liquid inertia and viscosity, surface tension, and transport of volatile material through the liquid to the bubble surface. All of these effects are interrelated, and in order to quantitatively evaluate the behav-

[1] Also University of Illinois, Department of Energy Engineering, Chicago, Ill.

[2] Presently at EBR-II Division.

[3] Numbers in brackets designate References at end of paper.

Contributed by the Heat Transfer Division for publication in the JOURNAL OF HEAT TRANSFER. Manuscript received by the Heat Transfer Division September 9, 1975. Paper No. 76-HT-X.

ior of a gas bubble in such an environment, it is necessary to analyze the dynamics of such bubbles immersed in a liquid under unsteady conditions of temperature and pressure, taking into account mass, momentum, and energy transport processes.

The diffusion process is the mechanism tending to collapse the inert gas bubble. An order of magnitude calculation reveals that the time constant for this process is generally much larger than the transport time of the bubble through a reactor core under normal conditions. However, when abnormal operating conditions cause the liquid metal to approach saturation, the temperature and concentration gradients may be considerably larger than experienced under steady conditions. In this case, the effect of gas diffusion relative to other mechanisms related to bubble growth is not known a priori. It is the purpose of this study to consider bubble survival under such conditions.

One early study of stability of a gas bubble in a liquid-gas solution was performed by Epstein and Plesset [5]. In their analysis, the pressure and temperature of the solution were held constant and bubble growth and/or collapse occurred only by under- or oversaturated conditions. Numerical results were limited to air bubbles in water. An extension of this analysis was made by Ward [6] in which the presence of vapor in the bubble was included, but consideration was only given to an isothermal liquid solution.

Another analysis is that of Thormeier [7] in which the constant liquid temperature assumption was dropped. However, in that analysis it was assumed that the gas bubble was always in mechanical equilibrium with the liquid and that the equilibrium concentration of the dissolved gas at the bubble-liquid interface was constant. The latter assumption may lead to considerable error when applied to a nonisothermal system.

In this study, the analyses of [5, 7] were extended and generalized to include the effects of mass transfer as well as momentum and thermal variations upon the dynamics of a vapor-gas bubble immersed in a dilute two-component solution of the gas in the liquid. Specific numerical results were obtained for the case of an argon bubble flowing with liquid sodium through a channel with a linear temperature rise and pressure drop, a situation and geometry typical of a LMFBR core.

Physical Model

Fig. 1 represents a schematic of a typical liquid metal experimental loop. The liquid-gas solution leaves the plenum saturated with inert gas. As the liquid-gas solution passes through the heat exchanger, its temperature decreases, which tends to drive the dissolved gas out of solution. This gas will initially fill cavities in the heat exchanger surfaces. Subsequently, bubbles will nucleate from these cavities at the cold end of the exchanger and will be carried along with the flow. It is likely that the inert gas bubbles will pass through the pump and enter the heated channel of length L. As the liquid temperature increases and the pressure decreases through the heated channel, the gas bubbles will either grow, collapse, or possibly remain stable, depending upon the various factors discussed previously. The time available for this process to occur is L/V, the transit time, where V is the liquid velocity. In order to determine the possible bubble sizes that could exist throughout the transit of the heated section, an analysis has been undertaken of the transient heat and mass transfer of a bubble of initial radius R_0 in a liquid-gas solution with a linear temperature increase from T_0 to T_e and linear pressure decrease from p_1 to p_2 in time L/V.

Formulation of the Problem

Mathematical Model and Assumptions. Consider a spherical gas bubble of radius R_0 (containing inert gas and vapor) placed at time $t = 0$ into a liquid-gas solution in which the temperature, pressure, and dissolved gas concentration are uniform and equal to T_0, p_0, and ω_0, respectively. At these conditions, the saturation concentration of gas in the liquid is $\omega_s(0)$, and at time $t > 0$, the liquid temperature and pressure are allowed to vary. (The dissolved gas concentration for a saturated solution at $t > 0$ will be denoted by $\omega_s(t)$.) The variation in temperature and pressure will have a considerable effect on the behavior of the bubble. In order to quantitatively evaluate the possible effects, it is necessary to analyze the dynamics of such a bubble, taking into account the conservation principles of mass, momentum, and energy for the liquid-gas solution. In so doing, the following assumptions were involved:

1 Spherical symmetry exists everywhere in the liquid-gas solution.

2 The convective transport of inert gas caused by bubble expansion or contraction is negligible relative to molecular transport.

3 The concentration of inert gas in the solution is sufficiently small such that the density of the liquid-gas solution, ρ_L, and the diffusion coefficient are constant.

4 There are no spatial gradients in temperature or pressure, so that, with assumption 3, Fick's law of diffusion may be used.

Nomenclature

c_{p_L} = specific heat at constant pressure of liquid-gas solution
D_H = hydraulic diameter of channel
D_{12} = coefficient of diffusivity of gas in liquid-gas solution
f = friction factor
H = total length of channel
$K_H(T)$ = Henry's coefficient
L = length of heated channel
ℓ_1 = length of upstream section
ℓ_2 = length of downstream section
M = molecular weight
$m_{B,g}$ = mass of inert gas in bubble
m_0 = initial mass of inert gas in bubble
p = pressure
p_0 = initial liquid-gas solution pressure
Δp_L = liquid-gas solution pressure drop across heated channel
$\dot{q}''$ = heat flux in the heated channel
R = bubble radius
Re = VD_H/ν_L, Reynolds number
R = gas constant
r = radial coordinate
T = temperature of the liquid-gas solution
t = time = z/V
t_e = transit time for downstream section = $(H - \ell_1 - L)/V$
t_1 = ℓ_1/V, transit time for upstream section
t_2 = L/V, transit time for heated section
V = axial liquid-gas solution velocity
u = radial liquid-gas solution velocity at r
z = axial coordinate in the flow system
δ = mass concentration function of vapor inside the bubble = $\rho_{B,v}/\rho_L$
$\epsilon = 1 - \rho_B/\rho_L$
ν_L = kinematic viscosity of liquid-gas solution
ρ = density
σ = surface tension
ω = mass concentration of inert gas in the solution = $\rho_{L,g}/\rho_L$
ω_s = saturation value of ω at bubble interface
ω_0 = mass concentration of inert gas far away from the bubble

Subscripts

B = in the bubble
B,g = inert gas in the bubble
B,v = saturated vapor in the bubble
e = at exit of heated channel
g = inert gas
g,∞ = inert gas in the plenum
L = in the liquid-gas solution
L,g = inert gas in the liquid-gas solution
L,ℓ = liquid in the liquid-gas solution
L,∞ = liquid-gas solution in the plenum
ℓ = liquid
v = vapor
0 = initial value
∞ = in the plenum or gas blanket
$\dot{()}$, $\ddot{()}$ = indicate time derivatives

5 The boundaries of the liquid-gas solution are sufficiently large relative to the size of the bubble so that no interaction between the bubble and these boundaries occurs.

6 There exists mass and thermal equilibrium at the interface between the bubble and the liquid-gas solution at all times.

7 The heat of solution is negligible.

In addition to the foregoing assumptions, others will be stated as required in subsequent developments.

Continuity Equation for the Liquid-Gas Solution. If the origin of a spherical coordinate system is taken as the center of the gas bubble, the continuity equation for the liquid-gas solution can be written as $\partial/\partial r(r^2u) = 0$, which, when integrated from the bubble interface, $r = R$, to radius r in the liquid, becomes

$$u = u(R)\frac{R^2}{r^2} \tag{1}$$

where $u(R)$ is the solution velocity adjacent to the bubble surface. From a total mass balance on the bubble

$$\frac{d}{dt}\left(\frac{4}{3}\pi R^3\rho_B\right) = 4\pi R^2\rho_L[\dot{R} - u(R)] \tag{2}$$

$u(R)$ can be determined as

$$u(R) = \epsilon\dot{R} + \frac{1}{3}\dot{\epsilon}R \tag{3}$$

where $\dot{R}$ is the velocity of the bubble surface and $\epsilon = 1 - \rho_B/\rho_L$. Substituting equation (3) into equation (1) yields

$$u = \left(\epsilon\dot{R} + \frac{1}{3}\dot{\epsilon}R\right)\frac{R^2}{r^2} \tag{4}$$

which is the global continuity equation for the liquid-gas solution.

Diffusion Equation for the Gas in the Liquid-Gas Solution. The species continuity equation for the gas diffusing through the liquid-gas solution may be written as

$$\frac{\partial\omega}{\partial t} + \frac{R^2}{r^2}\left(\epsilon\dot{R} + \frac{1}{3}\dot{\epsilon}R\right)\frac{\partial\omega}{\partial r} = D_{12}\frac{1}{r^2}\frac{\partial}{\partial r}\left(r^2\frac{\partial\omega}{\partial r}\right) \tag{5}$$

where equation (4) was substituted for the solution velocity and $\omega = \rho_{L,g}/\rho_L$ is the mass fraction of the gas in the liquid-gas solution. The initial and boundary conditions consistent with the assumptions listed earlier and the problem statement are

$$\omega = \omega_0 \text{ at } t = 0,\ \omega = \omega_s(t) \text{ at } r = R,\ \omega \to \omega_0 \text{ as } r \to \infty \tag{6}$$

No closed-form solution of equation (5) is possible with initial and boundary conditions in equation (6). However, neglecting the convective term in equation (5) and making a simple transformation of the coordinate system permits the reduction of the problem to a simple form.

Let $\eta = (r/R) - 1$, $\tau = D_{12}t/R^2$, and $\phi(\eta, \tau) = (r/\omega_0 R)[\omega(r, t) - \omega_0]$. Substituting these variables into equations (5) and (6) yields

$$\frac{\partial\phi}{\partial\tau} = \frac{\partial^2\phi}{\partial\eta^2} \tag{7}$$

$$\phi(\eta, 0) = 0,\ \phi(0, \tau) = \phi_s(\tau),\ \phi(\infty, \tau) = 0 \tag{8}$$

where $\phi_s(\tau) = [\omega_s(t) - \omega_0]/\omega_0$. The solution to this system is readily available from [8] and may be written as

$$\phi(\eta, \tau) = \frac{2}{\sqrt{\pi}}\int_{\eta/2\sqrt{\tau}}^{\infty}\phi_s[\tau - (\eta/2\xi)^2]e^{-\xi^2}d\xi \tag{9}$$

A quantity that will be of importance later is the mass fraction gradient at the bubble surface. By differentiating equation (9) and evaluating the derivative at $\eta = 0$, and then transforming the resulting equation back to its physical variable, one obtains

$$\left(\frac{\partial\omega}{\partial r}\right)_{r=R} = -\left[\frac{\omega_s(t) - \omega_0}{R} + \frac{\omega_s(0) - \omega_0}{\sqrt{\pi D_{12}t}}\right] \tag{10}$$

Equation (9) is a solution of the diffusion problem which is strictly valid only for a fixed bubble size. However, as shown in [5], this is a reasonable approximation for the diffusional process. It is furthermore noted that equation (9) does not by itself specify the concentration field, since the saturation phenomenon is dependent upon the solution temperature and the gas partial pressure in the bubble. Thus, additional relationships must be found to completely specify the problem.

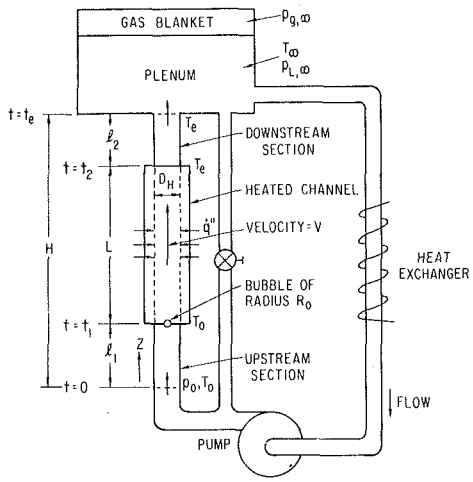

Fig. 1 Typical liquid metal experimental loop

Momentum Equation for the Liquid-Gas Solution. One such relation can be obtained from the conservation of momentum principle for the liquid-gas solution. For an incompressible Newtonian fluid with no external body forces, the motion of the fluid is governed by the one-dimensional equation

$$\frac{\partial u}{\partial t} + u\frac{\partial u}{\partial r} = -\frac{1}{\rho_L}\frac{\partial p}{\partial r} + \nu_L\left[\frac{1}{r^2}\frac{\partial}{\partial r}\left(r^2\frac{\partial u}{\partial r}\right) - \frac{2}{r^2}u\right] \tag{11}$$

Substituting for u from equation (4) and integrating the resulting equation from $r = R$ to $r = \infty$ will yield the momentum equation for the liquid-gas solution in the form

$$\frac{\dot{F}}{R} - \frac{1}{2}\frac{F^2}{R^4} = \frac{1}{\rho_L}[p_L(R) - p_L(\infty)] \tag{12}$$

where

$$F(t) = R^2\left(\epsilon\dot{R} + \frac{1}{3}\dot{\epsilon}R\right) \tag{13}$$

$p_L(R)$ is the pressure in the liquid-gas solution at the bubble boundary and $p_L(\infty)$ is the pressure in the solution at infinity. Assuming thermodynamic equilibrium, the condition of stress continuity across interface implies that

$$p_B + \tau_{rr}(R) - p_L(R) - \frac{2\sigma}{R} = 0 \tag{14}$$

where $p_B = p_{B,v} + p_{B,g}$ is the equilibrium pressure in the bubble, $\tau_{rr}(R) = 2\mu_L(\partial u/\partial r)_{r=R}$ is the radial component of the radial stress at the bubble surface, and σ is the surface tension. Substituting equations (13) and (14) into equation (12), assuming that the inert gas and the vapor behave ideally, rearranging, and letting $\delta = \rho_{B,v}/\rho_L$ yields

$$\ddot{R} + \frac{R}{3\epsilon}\ddot{\epsilon} = F_1(t) \tag{15}$$

where

$$F_1(t) = -\left(\frac{4-\epsilon}{2}\right)\frac{\dot{R}^2}{R} - \left(\frac{6-\epsilon}{3\epsilon}\right)\dot{\epsilon}\dot{R} + \frac{\dot{\epsilon}^2}{18\epsilon}R - \frac{2\sigma}{\rho_L\epsilon}\frac{1}{R^2} - \frac{4\nu_L}{3}\left(\frac{3\dot{R}}{R^2} + \frac{\dot{\epsilon}}{\epsilon}\frac{1}{R}\right) + \frac{T(t)}{\epsilon R}\left[R_g(1-\epsilon) + (R_\ell - R_g)\delta - \frac{p_L(t)}{\rho_L T(t)}\right] \tag{16}$$

This is the momentum equation for the liquid-gas solution and it represents an extended form of the Rayleigh equation. It should be noted that in equation (16) the notation $p_L(\infty)$, which is identically equal to $p_L(\infty, t)$, has been changed to $p_L(t)$.

Equation (15) gives one relationship between the bubble radius R and the gas pressure in the bubble $p_{B,g}$ which is given in terms of the density function ϵ.

Inert-Gas Mass Balance on the Bubble. The second required relation can be obtained from an overall inert-gas mass balance on the bubble. The balance relates the decrease of the mass of inert gas in the bubble to the convection and diffusion of inert gas into the surrounding fluid. Mathematically stated, this balance takes the form

$$-\frac{d}{dt}\left(\frac{4}{3}\pi R^3 \rho_{B,g}\right) = 4\pi R^2 \rho_{L,g}[u(R) - \dot{R}] - 4\pi R^2 \rho_L D_{12}\left(\frac{\partial \omega}{\partial r}\right)_{r=R} \tag{17}$$

Substituting for $u(R)$ and $(\partial\omega/\partial r)_{r=R}$ from equations (3) and (10), respectively, and performing the differentiation, equation (17) becomes

$$[1 - \omega_s(t)]\left[(1-\epsilon)\dot{R} - \frac{1}{3}\dot{\epsilon}R\right] = \frac{1}{3}\dot{\delta}R + \delta\dot{R} - D_{12}\left[\frac{\omega_s(t) - \omega_0}{R} + \frac{\omega_s(0) - \omega_0}{\sqrt{\pi D_{12} t}}\right] \tag{18}$$

after substituting the definitions of ϵ, ω_s, and δ. In the solution of equation (18) it was assumed that $[1 - \omega_s(t)] \equiv 1$, which follows from assumption 3.

A quick reference to equations (15) and (16) indicates that its integration requires an expression for $\ddot{\epsilon}$. This can be obtained by differentiating equation (18) to yield

$$3(1 - \epsilon - \delta)\ddot{R} - R\ddot{\epsilon} = F_2(t) \tag{19}$$

where

$$F_2(t) = 4(\dot{\epsilon} + \dot{\delta})\dot{R} + \ddot{\delta}R + \omega_s(t)[3(1-\epsilon)\dot{R} - \dot{\epsilon}R] - 3D_{12}\left\{\frac{\dot{\omega}_s(t)}{R} - [\omega_s(t) - \omega_0]\frac{\dot{R}}{R^2} - \frac{\omega_s(0) - \omega_0}{2t\sqrt{\pi D_{12} t}}\right\} \tag{20}$$

In equations (19) and (20), $[1 - \omega_s(t)]$ was set equal to one.

Equation (18) gives the second relationship between dependent variables $R(t)$, $\epsilon(t)$, and $\omega_s(t)$. The third relation can be obtained from the assumption of mass equilibrium at the bubble-liquid-gas interface.

Equilibrium Condition From Henry's Law. The saturation concentration of inert gas in the solution can be related to the inert gas partial pressure in the bubble by the assumption that there exists mass equilibrium at the interface between the bubble and the solution. This equilibrium condition, as expressed by Henry's law, states that the saturation mole fraction of the gas is proportional to partial pressure of the gas phase. Mathematically stated, Henry's law may be written as

$$\omega_s(t) = \frac{M_g}{M_\ell} K_H[T(t)] p_{B,g}(t) \tag{21}$$

where the function K_H is Henry's coefficient. Assuming perfect gas behavior, equation (21), in terms of problem variables, may be expressed as

$$\omega_s(t) = \left(\frac{\rho_L M_g R_g}{M_\ell}\right) K_H T(1 - \epsilon - \delta) \tag{22}$$

The derivative of ω_s, which is required in equation (20), becomes

$$\dot{\omega}_s(t) = \left(\frac{\rho_L M_g R_g}{M_\ell}\right) K_H \left[\left(1 + \frac{J \ln 10}{T}\right)(1 - \epsilon - \delta)\dot{T} - (\dot{\epsilon} + \dot{\delta})T\right] \tag{23}$$

where J is a constant in the K_H equation. (For sodium-argon systems, $J = +8175.6$ [9].)

Reference Concentration ω_0. Prior to consideration of initial conditions on variables ϵ, R, and ω_s, the solution of the problem requires the specification of the inert gas concentration far from the bubble surface, i.e., ω_0. It is assumed that this concentration has a constant value throughout the system which is equal to the saturation concentration in the upper plenum. Then, ω_0 may be expressed in terms of the gas partial pressure in the plenum, $p_{g,\infty}$, using Henry's law from (21) as

$$\omega_0 = \frac{M_g}{M_\ell} K_H(T_\infty) p_{g,\infty} \tag{24}$$

where T_∞ is the temperature of the plenum.

Initial Conditions. To complete the statement of the problem, initial conditions on $p_{B,g}$, R, and ω_s must be specified. The most physically realistic assumption concerning the initial state of the bubble is a state of mechanical equilibrium with the liquid-gas solution. This assumption implies that all time derivatives of R and ϵ at $t = 0$ are identically equal to zero. Using this condition, it follows from equations (15) and (16) that

$$\epsilon(0) = 1 + \left(\frac{R_\ell - R_g}{R_g}\right)\delta(T_0) - \frac{p_L(0)}{\rho_L R_g T_0} - \frac{2\sigma(T_0)}{\rho_L R_g T_0 R_0} \tag{25}$$

The initial condition on ω_s can be obtained from equation (22) as

$$\omega_s(0) = \left(\frac{\rho_L M_g R_g}{M_\ell}\right) K_H(T_0) T_0 [1 - \epsilon(0) - \delta(T_0)] \tag{26}$$

where $\epsilon(0)$ is substituted from equation (25). Coupled with the statements that

$$\dot{R}(0) = 0, R(0) = R_0 \tag{27}$$

the problem is completely defined, except for the specification of transients in liquid-gas solution pressure, $p_L(t)$, and temperature, $T_L(t)$.

Application to a Flow in a Heated Channel

In this study the liquid-gas solution pressure and temperature variation associated with the flow of the solution and entrained gas bubble through a uniformly heated channel is considered. By making a one-dimensional approximation to the problem, and, for generality, assuming the possible existence of unheated upstream and downstream sections of the channel, it can be easily shown from momentum and energy balances for a uniform heat flux situation that

$$p_L(t) = p_{L,\infty} + \left[\rho_L H\left(\frac{fV^2}{2D_H} + 1\right)\right]\left(1 - \frac{Vt}{H}\right) \tag{28}$$

and

$$T(t) = T_0 \qquad \text{(upstream channel)} \tag{29}$$

$$= T_0 + \frac{4\dot{q}''}{\rho_L c_{p_L} D_H}(t - t_1) \qquad \text{(heated channel)} \tag{30}$$

$$= T_0 + \frac{4\dot{q}'' L}{\rho_L c_{p_L} D_H V} \equiv T_e \qquad \text{(downstream channel)} \tag{31}$$

where the time t is defined as the channel position z, divided by the liquid-gas solution velocity V, i.e., $t = z/V$, and all other symbols are defined in Fig. 1 and in the Nomenclature. The friction factor f, corresponding to turbulent liquid flow in a channel, has been taken from [10] as

$$f = 0.0032 + 0.221/\mathrm{Re}^{0.237} \tag{32}$$

At this point, the problem is totally defined by equations (15) and (16), (18), (19) and (20), and (22)–(32), with the functions K_H, $\dot{K}_H$, δ, $\dot{\delta}$, $\ddot{\delta}$, σ, and property values obtained or derived from [9, 11] and also available in [12]. The problem was next numerically integrated via a high-speed digital computer.

Before turning to the discussion of results, it should be noted that equations (15) and (19) were solved for $\ddot{R}$ to yield

Table 1 Nominal operating conditions(a)

Parameter	Value
D_H	3.075 mm
D_{12}	3.04 cm²/s
ℓ_1	0.0
ℓ_2	254.0 mm
L	914.4 mm
$p_{g,\infty}$	101.3 kPa
$p_{L,\infty}$	101.3 kPa
T_e	471°C
T_0	316°C
T_∞	471°C
V	5.18 m/s

(a) Valid for all calculations except where noted.

$$\ddot{R} = \frac{1}{(1-\delta)}\left[\epsilon F_1(t) + \frac{1}{3}F_2(t)\right] \tag{33}$$

Equation (33), with functions F_1 and F_2 given by equations (16) and (20), was used in the numerical solution of the problem.

Further, it should be noted that the initial bubble radius, R_0, may be an arbitrary input value to the solution. In a physical system there usually exists a range of bubble radii. Values of R_0 employed in this study were in the range of interest to LMFBR systems.

In addition, it should be also observed that initially there exists mechanical equilibrium between bubble and solution, but not mass equilibrium, since the diffusion equation (18) is not satisfied at time equal to zero. Instead, the mass fraction is taken as constant and equal to ω_0 for $r > R$, and at the interface, $r = R$, the mass fraction is taken as $\omega_s(0)$. This step change in mass fraction at $t = 0$, in addition to the temperature rise and pressure drop in the liquid-gas solution along the heated section of the system, is a forcing function for the problem. Thus, even under isothermal and isobaric conditions, the bubble changes size until an equilibrium condition is reached.

Finally, it is of interest to note that there is a single value of initial radius, R_0, which would satisfy all equations, including (18), at $t = 0$. Such a bubble would initially be in both mechanical and mass equilibrium, where $\omega_s(0) \equiv \omega_0$. However, for LMFBR conditions, this radius is larger than the size range of physical significance. Thus, the mathematical treatment described in the foregoing was employed.

Results and Discussion

Bubble Dynamics Under Steady-State LMFBR Conditions. Since the application of primary interest to this study is the evaluation of the behavior of an inert gas bubble as it passes through an LMFBR operating conditions as summarized in Table 1. During these experiments (as well as those reported in [1]), gas bubbles were observed to enter and completely traverse the heated region; thus, the following calculations all utilize the same conditions listed in Table 1, except where specifically changed and listed in each figure.

LMFBR operating conditions as summarized in Table 1. During these experiments (as well as those reported in [1], gas bubbles were observed to enter and completely traverse the heated region; thus, the following calculations all utilize the same conditions listed in Table 1, except where specifically changed and listed in each figure.

The first study investigated the dynamics of various sized bubbles as they were introduced at the entrance to a heated zone under conditions simulating normal steady-state LMFBR operation. These results are summarized in Figs. 2–4. It is apparent that all bubbles over a large range in initial size survive the transit through such a zone; in fact, a slow growth rate was observed in all cases. The variation of $p_{B,g}$ and mass ratio with time as shown in Figs. 3 and 4 indicate that mass is diffusing into the bubbles, but

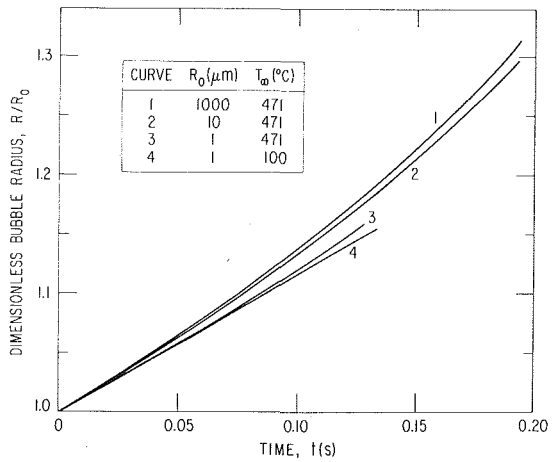

Fig. 2 Results for nominal operating conditions: bubble radius

at a rate sufficiently slow so as not to be able to counteract the decrease in $p_{B,g}$ accompanying the bubble growth.

Under a different system arrangement from that shown in Fig. 1, the plenum temperature, T_∞, can approach the inlet temperature, T_0. This condition may reverse the direction of mass diffusion from the results presented for the normal conditions of Table 1. As an example, a calculation was made setting $T_\infty = 100°C$ which is below T_0 and of course unrealistic for reactor operation. This value was chosen for demonstration purposes and represents the largest potential for mass diffusion out of the bubble. The results shown in Figs. 2–4 for $R_0 = 1\mu m$, indicate that the bubble grows at a rate similar to the normal case even though the mass of argon in the bubble declines drastically, indicating that the liquid sodium pressure and temperature along the channel are controlling the bubble size rather than diffusion. Thus, as expected for the normal cases presented, the bubbles grow as they traverse the channel, and diffusion is a secondary mechanism. In terms of normally operating LMFBR systems, any inert gas bubble reaching the inlet to the core will traverse the core. It is interesting to note, however, that the rate of bubble growth in the core is slow, and nearly independent of plenum temperature (two extremes have been presented) and initial bubble radius, R_0. This independence of R_0 occurs even though the magnitudes of argon pressure and mass in the bubble are quite sensitive to initial radius.

Bubble Dynamics Under Abnormal LMFBR Conditions. The preceding results have indicated that inert gas bubbles will

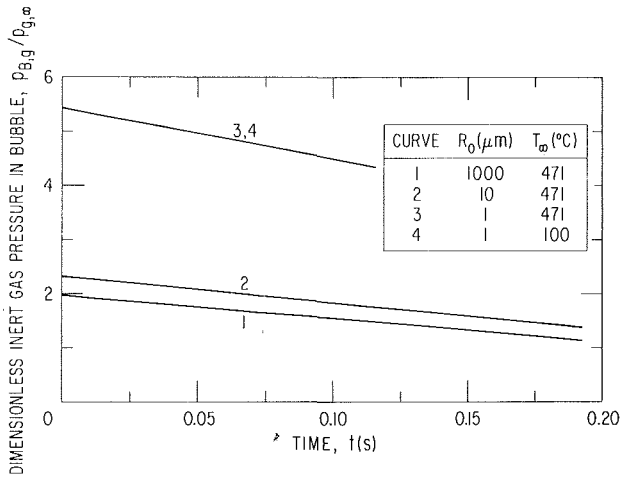

Fig. 3 Results for nominal operating conditions: inert gas partial pressure in bubble

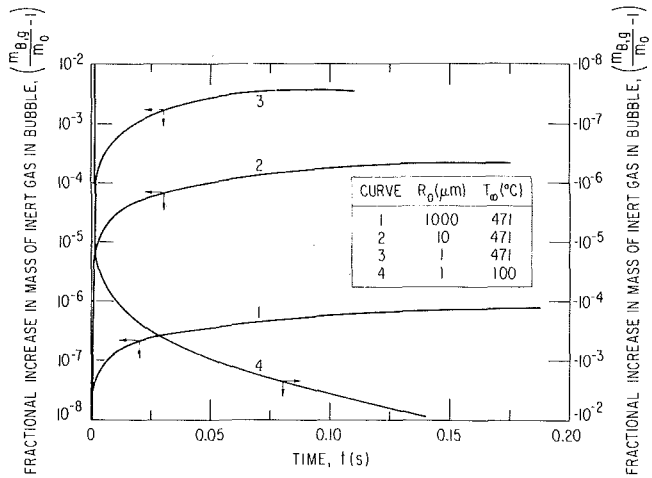

Fig. 4 Results for nominal operating conditions: inert gas mass fraction

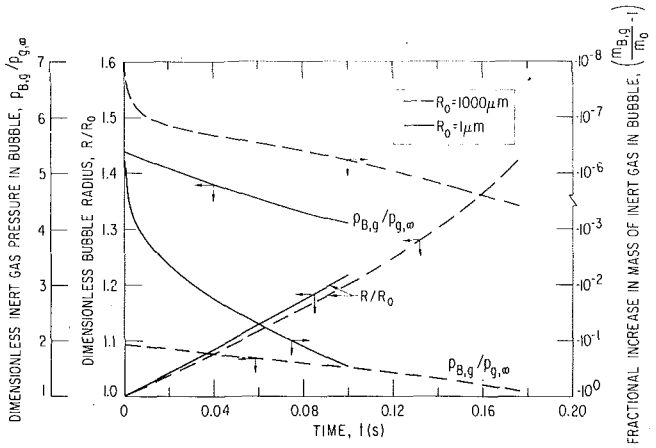

Fig. 5 Results for nominal case with an increased temperature rise

survive the transit of an LMFBR core during normal operating conditions. The behavior of these bubbles under certain abnormal conditions will now be examined in this section, with primary emphasis on situations where large temperature, pressure, and/or mass concentration gradients exist. The types of gradients chosen will be such that mass diffusion is enhanced.

The first such case investigated was that of an over temperature situation where the core exit temperature was 686°C with a plenum temperature of 100°C to further promote diffusion; all other parameters were as listed in Table 1. The results are shown in Fig. 5 and indicate that mass diffusion from the bubbles is increased from the normal case (curve 4 of Fig. 4), but the bubbles still continue to grow as they move through the channel, in fact, at a rate slightly higher than the normal case. In this case, the sodium vapor pressure became important, and although the diffusion of inert gas from the bubble was increased, it was not sufficient to alter the trend of bubble growth. Thus, inert gas bubbles will still survive the transit through a core with a moderate power-to-flow mismatch.

A second case studied was that of a nearly total LMFBR subassembly inlet blockage with continued full power operation. This situation was simulated by reducing the liquid velocity to 0.01 m/s and setting the liquid pressure drop to zero; all other parameters were as per Table 1. In this case, the bubble transit time through the heated channel became 91 s. As shown in Fig. 6, the bubble grew rapidly and approached the channel diameter at 0.423 s corresponding to a position 4.23 mm from the channel inlet. The temperature at this point was 814°C. Inert gas is seen to enter the bubble by diffusion and the rapid growth rate after approximately 0.4 s is due to the large sodium vapor pressure inside the bubble. The inert gas pressure inside the bubble is seen to decrease sharply at this time. Pressure oscillations shown in Fig. 6 were calculated during the early stages of bubble growth, the envelope of which is shown as dashed lines. This observation will be discussed later.

The results presented to this point indicate that under normal and some extreme abnormal LMFBR operating conditions, inert gas bubbles that enter the core will grow as they traverse the core to the plenum. This bubble survival has favorable implications from the standpoint of sodium superheat under conditions of incipient boiling. Nucleation would occur from the gas bubbles; the superheat would then be essentially zero, and available energy for coolant expulsion would be minimized. This result is independent of plenum temperature and initial bubble size of the ranges investigated. Some experimental evidence of this phenomenon was found in the experiments of [1, 3] where bubbles were observed in the heated channel under conditions of a relatively hot plenum temperature as specified in Table 1. (Note that the results of [3] also indicate that for colder plenum temperatures, inert gas bubbles are unlikely to enter the core.) In terms of mass diffusion, the results presented show that under conditions of large temperature gradients which produce large potentials for diffusion, this mechanism is not strong enough to alter the trends of the normal operating case in terms of bubble survival.

Bubble Dynamics Under Constant Pressure and Temperature Conditions. In this section, the response of vapor-gas bubbles in an environment of constant liquid pressure and temperature to changes in the ambient dissolved gas concentration is studied. This is mathematically equivalent to placing an argon bubble into an infinite medium of liquid sodium at constant temperature and pressure with the partial pressure of the gas in the bubble not being in equilibrium with the dissolved gas concentration in the liquid. For the case where the sodium was subsaturated with argon gas compared to bubble conditions of temperature and argon gas pressure, inert gas diffuses out of the bubble, and the bubble must collapse. In this case, diffusion is the only mechanism acting to change the bubble size. However, it is observed from Fig. 7 that the rate of collapse is quite sensitive to initial bubble radius, a result not observed in any of the results presented previously, although both the gas pressure and mass are still very sensitive to R_0. For R_0 = 1μm this case was re-evaluated using a diffusion coefficient larger than the value of Table 1 by a factor of 10^4. The results are shown in Fig. 8 and are not dissimilar to the normal diffusivity case. The process has been significantly accelerated, and large oscillations were found in both the gas pressure and radius for the accelerated

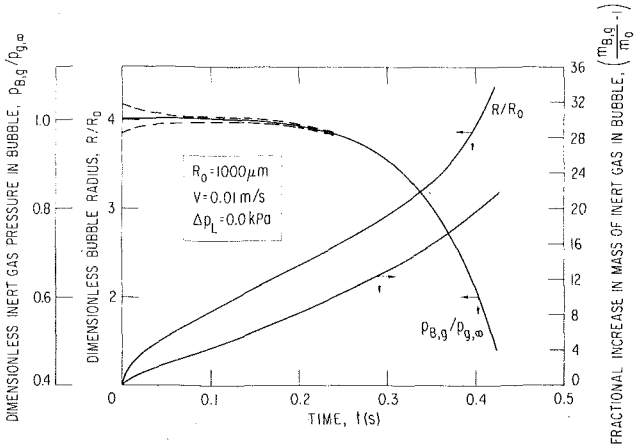

Fig. 6 Results for simulated core blockage case

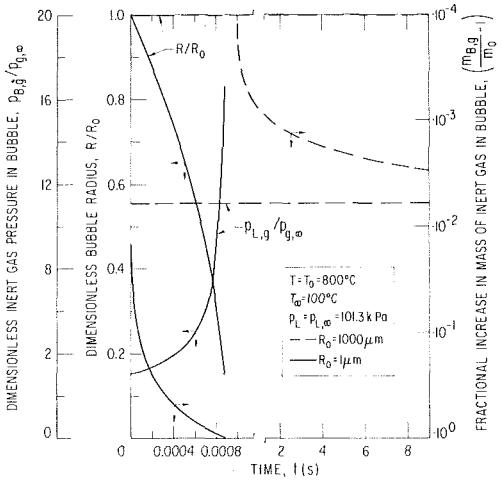

Fig. 7 Results for constant pressure and temperature: subsaturated liquid-gas solution

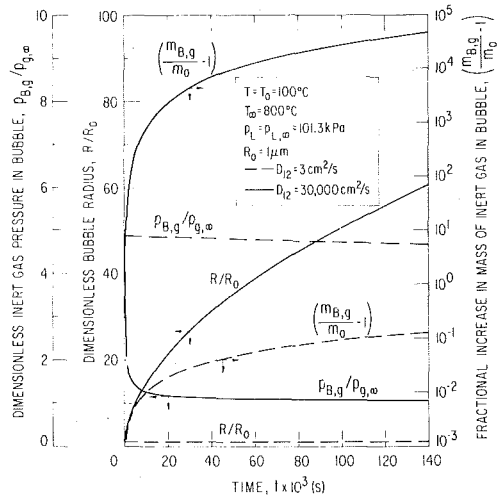

Fig. 9 Results for constant pressure and temperature: supersaturated liquid-gas solution

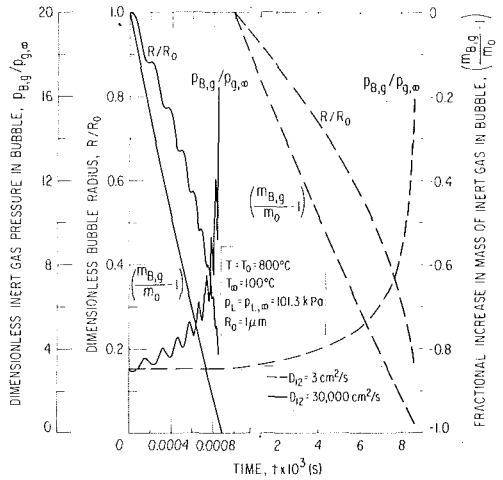

Fig. 8 Results for constant pressure and temperature: subsaturated liquid-gas solution with increased mass diffusivity

case. The steady state solution is of course identical for both values of D_{12}.

A final calculation was made for the isothermal, isobaric system in which the liquid sodium was supersaturated with argon gas based on bubble gas pressure and temperature. In this case, diffusion of gas is from the liquid into the bubble, and the bubble grows as shown in Fig. 9. The results of artificially accelerated growth by increased diffusion coefficient are also presented for this case in Fig. 9.

Oscillations in results have been shown in Figs. 6 and 8. The fact that these instabilities are not a numerical problem within the solution will be apparent from the following description of the computer programs employed. The task of perfecting the computer program used in this study was hampered by the lack of a known solution to use as a test case. To alleviate this problem, a second computer program was written independently as a check on the first. The second program neglected the effect of the time rate of change of ρ_B in equation (4) and solved a simplified set of equations ($\ddot{\epsilon}$ was not required) using a different numerical method. The results of both programs with and without the effect of $\ddot{\epsilon}$ produced the same numerical results to three significant figures for the normal cases of Figs. 2–4. The instabilities of Figs. 6 and 8, apparently an inertia effect, were obtained with both programs and were independent of the time step size over a thousand-fold range.

Conclusions

The primary conclusion of this study is that under both normal and extreme abnormal LMFBR operating conditions, inert gas bubbles (argon) that enter the core will be transported through the core slightly increased in size. This conclusion is valid for initial bubble radii from 1 to 1000 μm and outlet plenum temperatures from 100 to 686°C. Even under conditions of extreme reactor thermal gradients amplifying the potential for diffusion of inert gas out of the bubble, diffusion was found to represent a secondary effect. In one case the bubble was observed to grow as it traversed the core even as mass diffused out of the bubble into the sodium.

The results for isothermal, isobaric systems in which diffusion was the only mechanism influencing bubble size revealed growth or collapse rates highly dependent on initial bubble radius, R_0. These results exhibited similar trends in the case of artificially accelerated diffusion, and in some instances either damped or undamped instabilities were observed.

References

1 Henry, R. E., and Singer, R. M., "Forced Convection Sodium Superheat," *Trans. Amer. Nuc. Soc.*, Vol. 14, No. 2, 1971, p. 723.

2 Kottowski, H., Grass, G., Warnsing, R., and Burke, A., "Reduction of Incipient Boiling Superheating by Argon Bubble Injection," *Proceedings of the Second Meeting of the European Liquid Metal Boiling Working Group*, Casacia (Rome), Italy, Apr. 1970.

3 France, D. M., Carlson, R. D., Rohde, R. R., and Charmoli, G. T., "Experimental Determination of Sodium Superheat Employing LMFBR Simulation Parameters," JOURNAL OF HEAT TRANSFER, TRANS. ASME, Series C, Vol. 96, No. 3, 1974, p. 359.

4 Holland, P. K., "The Radial Distribution of Bubbles in Sodium Flowing Through Heated Channels," C.E.G.B., Berkeley Nuclear Laboratories, Report RD/B/N1630, Mar. 1970.

5 Epstein, P. S., and Plesset, M. S., "On the Stability of Gas Bubbles in Liquid-Gas Solutions," *J. Chem. Phys.*, Vol. 18, No. 11, 1950, p. 1505.

6 Ward, C. A., "On the Stability of Gas-Vapour Bubbles in Liquid-Gas Solutions," University of Toronto, Department of Mechanical Engineering, Technical Publication Series, UT-Mech E-TP7105, May 1971.

7 Thormeier, K., "Solubility of the Noble Gases in Liquid Sodium," *Nuc. Eng. Des.*, Vol. 14, 1970, p. 69.

8 Carslaw, H. S., and Jaeger, J. C., *Conduction of Heat in Solids*, Oxford University Press, 2nd ed., 1959, pp. 63, 305.

9 Reed, E. L., and Troher, J. J., "Solubility and Diffusivity of Inert Gases in Liquid Sodium, Potassium, and NaK," LMEC-69-36, 1969.

10 Kaufman, W., *Fluid Mechanics*, McGraw-Hill, New York, 1963, p. 89.

11 Golden, G. H., and Tokar, J. V., "Thermophysical Properties of Sodium," ANL-7323, Argonne National Laboratory, Aug. 1967.

12 Minkowycz, W. J., France, D. M., and Singer, R. M., "Transport of Inert Gas Bubbles in a LMFBR Core," Technical Memorandum ANL-CT-76-14, Argonne National Laboratory, Aug. 1975.

K. Namatame
K. Kobayashi

Tokai Research Establishment,
Japan Atomic Energy Research Institute,
Tokai-mura, Naka-gun, Ibaraki-ken, Japan

Subcooled Decompression Analysis in PWR LOCA

The thermo-hydraulic behavior of the coolant in the primary system of a nuclear reactor is important in the core heat transfer analysis during a hypothetical loss-of-coolant accident (LOCA). The heat transfer correlations are strongly dependent on local thermo-hydraulic conditions of the coolant. The present work allows to calculate such thermohydraulic behavior of the coolant during subcooled decompression in PWR LOCA by solving the mass, momentum, and energy conservation equations by the method of characteristics. Detailed studies were made on the transient coolant outflow at the pipe rupture and the effect of frictional loss and heat addition to the coolant on the decompression. Based on the studies, a digital computer code, DEPCO-MULTI, has been prepared and numerical results are compared with the ROSA (JAERI) and the LOFT (NRTS) semiscale test data with various coolant pressures, temperatures, pipe break sizes, and omplexity of flow geometry. Good agreement is generally obtained.

Introduction

Subcooled decompression in a primary coolant system of a pressurized water-cooled reactor (PWR) during a hypothetical loss-of-coolant accident (LOCA), a design basis accident, has received much attention in PWR safety assessment by the following reasons: the heat transfer correlations applied to the core heat transfer analysis in LOCA are strongly dependent on local thermo-hydraulic conditions of the coolant, that are changing rapidly; a large oscillatory pressure decrease of short duration is observed in the subcooled water during LOCA, and therefore primary coolant system components such as circulation pumps, steam generators, and reactor vessel internals such as core barrel and fuel assemblies, together with emergency core cooling system (ECCS), must be designed to withstand the pressure load.

Many methods have been developed to predict behavior of subcooled decompression following a LOCA. Among these are the digital computer codes BAM [1],[1] BURST [2], WHAM [3], and BLODWN-2 [4]. These codes have been checked for applicability to subcooled decompression tests for cooling systems of the various degrees of complexity. Considerations have further been extended to the degree of coincidence of the code with the test data, versatility of the computer program, easiness of the data preparation and computation time [5, 6, 7, 8].

In this report, detailed studies are made on the transient coolant outflow at the pipe break location and on the effect of the frictional loss and heat input to coolant on the subcooled decompression by solving the mass, momentum, and energy conservation equations by the method of characteristics. The main interest of the present study is directed to the subcooled water state, but also two-phase state is taken into account by the use of no-slip homogeneous model in the region where the coolant pressure falls below the saturation pressure due to the oscillatory character of the pressure during the subcooled decompression. Based on the studies, the digital computer code DEPCO-MULTI (Subcooled Decompression Process in Loss-of-Coolant Accident-Multiple Pipe Network) has been prepared and numerical results are compared with the ROSA (Rig of Safety Assessment, JAERI) and the LOFT (Loss of Fluid Test, NRTS) semiscale test data.

It should be mentioned that the present analysis is applied only in the subcooled decompression process which precedes the transition and the saturation decompressions.

Fundamental Equations and Solutions

For the analysis of decompression of high enthalpy water in a PWR primary coolant system during LOCA, mass, momentum, and energy conservation equations in a one-dimensional system can be written as shown in the following based on the following assumptions [9]:

[1] Numbers in brackets designate References at end of paper.

Contributed by the Heat Transfer Division for publication in the JOURNAL OF HEAT TRANSFER. Manuscript received by the Heat Transfer Division December 26, 1974. Paper No. 76-HT-M.

1 The radial variation of coolant parameters is disregarded, and the flow is one-dimensional in order to avoid the analytical complexity without losing physical interpretation of the pertinent parameters.

2 The coolant is in thermal equilibrium during any period of rapid perturbation. The degree of this thermal nonequilibrium can be considered small and the quantitative nature of this is not known so far.

3 Heat transfer and buoyancy effects are negligible.

4 The frictional loss is assumed to have the value of steady state.

Continuity Equation.

$$\frac{\partial \rho}{\partial t} + \rho \frac{\partial u}{\partial x} + u \frac{\partial \rho}{\partial x} + \frac{\rho u}{A} \frac{dA}{dx} = 0 \tag{1}$$

Momentum Equation.

$$\frac{\partial u}{\partial t} + u \frac{\partial u}{\partial x} + \frac{1}{\rho} \frac{\partial p}{\partial x} + F = 0 \tag{2}$$

Energy Equation.

$$q + uF = \frac{D}{Dt}(c_v T) + \frac{p}{\rho A} \frac{\partial}{\partial x}(Au) \tag{3}$$

where wall friction in steady state is represented as

$$F = \frac{f_B}{De} \frac{u^2}{2} \frac{u}{|u|} \tag{4}$$

and the factor $u/|u|$ is introduced in order that the frictional force always acts opposite to the direction of motion. Equation (3) can be transformed to (Appendix A)

$$k'(q + uF) = \left(\frac{\partial p}{\partial t} + u \frac{\partial p}{\partial x}\right) - c^2 \left(\frac{\partial \rho}{\partial t} + u \frac{\partial \rho}{\partial x}\right) \tag{5}$$

where the function k' is defined as follows

$$k' = \left(\frac{\partial f}{\partial p}\right)_\rho^{-1} \tag{6}$$

and the function f represents the coolant internal energy as a function of pressure and density, i.e., $c_v T = f(p, \rho)$. The conservation equations (1), (2), and (5) are a set of quasi-linear hyperbolic differential equations and hence the solution can be derived by the method of characteristics as follows [10]:

I—Characteristic

$$\left(\frac{dx}{dt}\right)_{\mathrm{I}} = u + c \tag{7a}$$

$$(du)_{\mathrm{I}} + \frac{1}{\rho c}(dp)_{\mathrm{I}} + \frac{uc}{A} \frac{dA}{dx}(dt)_{\mathrm{I}} + \left[F\left(1 - \frac{k'u}{\rho c}\right) - \frac{k'q}{\rho c}\right](dt)_{\mathrm{I}} = 0 \tag{7b}$$

II—Characteristic

$$\left(\frac{dx}{dt}\right)_{\mathrm{II}} = u - c \tag{8a}$$

$$(du)_{\mathrm{II}} - \frac{1}{\rho c}(dp)_{\mathrm{II}} - \frac{uc}{A} \frac{dA}{dx}(dt)_{\mathrm{II}} + \left[F\left(1 + \frac{k'u}{\rho c}\right) + \frac{k'q}{\rho c}\right](dt)_{\mathrm{II}} = 0 \tag{8b}$$

III—Characteristic

$$\left(\frac{dx}{dt}\right)_{\mathrm{III}} = u \tag{9a}$$

$$(dp)_{\mathrm{III}} - c^2(d\rho)_{\mathrm{III}} = k'(q + uF)(dt)_{\mathrm{III}} \tag{9b}$$

A detailed description of derivation of equations (7), (8), and (9) is given in reference [11].

Equations (7*a*) and (8*a*) represent the propagation of pressure waves, in a one-dimensional system, with sonic velocity in opposite directions within the fluid system. The wave propagation is accompanied by the characteristic values (u, p) whose variation is governed by equations (7*b*) and (8*b*). Equation (9*a*) gives the locus of a coolant particle along which coolant density variation $d\rho$ is integrated. Once the coolant pressure and density are calculated, other property values can readily be determined. The right-hand term $k'(q + uF)(dt)_{\mathrm{III}}$ in equation (9*b*) is proportional to the increase of coolant entropy, as shown in reference [11]. If this value is small compared to the left-hand terms in equation (9*b*), the coolant density will vary along an isentropic process. Equation (9*b*) then becomes a relation defining coolant sonic velocity.

Order-of-Magnitude Estimation and Simplification of the Characteristic Equation

Before proceeding to obtain a numerical solution of equations (7), (8) and (9), an order-of-magnitude analysis of the individual terms is necessary to simplify the characteristic equations so that the computation for a full scale PWR primary coolant system can be made within reasonable computer time with sufficient accuracy.

The order-of-magnitude of the individual terms of equations (7*b*), (8*b*) and (9*b*) is examined in Appendix B by the use of the thermo-hydraulic parameters of typical 1000 MWe PWRs, which are shown in Table 1, and the result is summarized in Table 2. It is assumed by comparing the values in Table 2 that the terms $k'uFdt/(\rho c)$ and $k'qdt/(\rho c)$ are neglected in comparison with the terms du, $dp/(\rho c)$ and Fdt in equations (7*b*) and (8*b*). Similarly the terms dp and $c^2 d\rho$ are considered in equation (9*b*), but the terms $k'uFdt$ and $k'qdt$ are neglected. Then equations (7*b*), (8*b*), and (9*b*) are, respectively, simplified to

$$(du)_{\mathrm{I}} + (dp)_{\mathrm{I}}/(\rho c) + F(dt)_{\mathrm{I}} = 0 \tag{10}$$

$$(du)_{\mathrm{II}} - (dp)_{\mathrm{II}}/(\rho c) + F(dt)_{\mathrm{II}} = 0 \tag{11}$$

$$(dp)_{\mathrm{III}} - c^2(d\rho)_{\mathrm{III}} = 0 \tag{12}$$

where the term of the gradual change of cross-sectional area is not considered but an abrupt change will be used instead. As already mentioned, equation (12) is the relation defining sonic velocity and the decompression follows on the isentropic process.

Method of Computation

In the finite difference solution of equations (7*a*), (8*a*), (10), and

Nomenclature

A = cross-sectional flow area
c = sonic velocity
c_s = sonic velocity in saturated steam
c_v = specific heat at constant volume
c_w = sonic velocity in saturated water
D_e = equivalent diameter
f_B = friction factor
F = wall frictional loss
$k' = (\partial f/\partial p)_\rho^{-1}$, equation (6)
p = pressure
Δp = pressure loss
q = rate of heat transfer per unit time and mass of coolant
R_e = Reynolds number
s = entropy
t = time
Δt = time mesh spacing
T = absolute temperature
u = velocity of flow
x = spatial coordinate
Δx = spatial mesh spacing
α = steam volume fraction
ζ_s = steady pressure loss coefficient at pipe break
ζ_t = transient pressure loss coefficient at pipe break
η = orifice area ratio
ρ = density
ρ_s = saturated steam density
ρ_w = saturated water density

(11), the method of fixed mesh-spacing in the space coordinate and variable mesh-spacing in the time coordinate is used in the first-order accuracy calculation [12]. The effect of higher-order accuracy computation on the computed results is examined, and it is found that the effect is negligibly small.

The coolant pressure, velocity, density, and sonic velocity are known functions of x at time t either from the initial conditions or from the results of the previous calculation step. The values at time $(t + \Delta t)$ must then be determined (Fig. 1). The time step Δt is obtained from

$$\Delta t \approx \frac{\Delta x}{\max_x (u(t,x) + c(t,x))} \tag{13}$$

The characteristic directions I and II crossing at a typical point $(x, t + \Delta t)$ are determined by equations (7a) and (8a) using the coolant velocity and sonic velocity at point 3, shown in Fig. 1. The points 1 and 2, where the characteristic lines I and II intersect the previous time line, can then be obtained. The coolant pressure and velocity at points 1 and 2, i.e., p_1, u_1, p_2, and u_2 are calculated by interpolation using the values of neighboring points $(x - \Delta x, t)$ and 3, and 3 and $(x + \Delta x, t)$, respectively. The pressure and velocity at the typical point, i.e., $p(x, t + \Delta t)$ and $u(x, t + \Delta t)$, can then be derived from the following equations which are, respectively, equations (10) and (11) in a difference form.

$$[u(x, t + \Delta t) - u_1] + [p(x, t + \Delta t) - p_1]/(\rho c)_3 + F\Delta t = 0 \tag{14}$$

$$[u(x, t + \Delta t) - u_2] - [p(x, t + \Delta t) - p_2]/(\rho c)_3 + F\Delta t = 0 \tag{15}$$

where the pressure loss is given by

$$F = \frac{f_B}{D_e}\frac{u_3^2}{2}\frac{u_3}{|u_3|} \tag{16}$$

$$f_B = \begin{cases} \mathrm{R_e}/64 & \mathrm{R_e} < 3000 \\ 0.316\,\mathrm{R_e}^{-0.25} & \mathrm{R_e} \geq 3000 \end{cases} \tag{17}$$

The Martinelli-Nelson multiplier has been used in calculating the two-phase flow pressure loss.

Once the new pressure is determined, the corresponding properties of the coolant can be calculated by integrating from point 3 along an isentropic process.

Boundary Conditions and the Properties of Coolant

As seen in the previous sections, the simplified characteristic equations can treat subcooled decompression in a pipe with uniform cross-sectional area except at its end. Therefore, additional relationships representing the pipe end boundary conditions and also connecting conditions for pipes having different cross-sectional area are needed to apply equations (14) and (15) to a complicated PWR primary coolant system. The end conditions to be considered are "break end," "dead end," "open end," and "constant pressure end." The pipe connecting conditions are given at multiple pipe connection points and coolant flow restrictions in a pipe-network.

End Conditions. At one end of a pipe, depending on whether it is the right-hand or left-hand end in the x coordinate either one of the equations (14) and (15) must be replaced by the relationship representing the end condition.

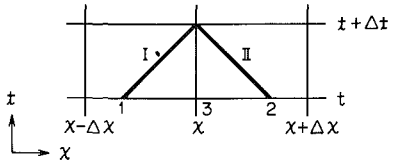

Fig. 1 Method of computation

The pipe break end with and without an orifice plate shows very characteristic behavior due to the highly transient nature of the coolant outflow to the the environment and has a most significant effect on the computed results. It is considered that the coolant outflow at the pipe break end is an inertia dominated flow and that choked flow is not attained during the subcooled decompression due to the low initial velocity of the coolant and the high choking velocity of compressed water. The present analysis employs Daily's work on transient pressure loss in sharp-edged orifice plates and in smooth pipes where variations of flow parameters across the pipe cross section are considered in addition to the axial variation [13]. According to reference [13], the transient pressure loss through the orifice, Δp_0, is calculated by

$$\Delta p_0 = \zeta_t \rho u^2/2 \tag{18}$$

where the transient pressure loss coefficient is given by

$$\zeta_t = \zeta_s + (c_1 + c_2)\frac{2V}{u^2 A}\left(\frac{du}{dt}\right) \tag{19}$$

In equation (19), V represents the coolant volume within control surface and ζ_s is the steady pressure-loss coefficient given by

$$\zeta_s = (1/\eta - 1)(2.75/\eta - 1.56) \tag{20}$$

with an orifice plate (partial break) and

$$\zeta_s = f_B \frac{\Delta x}{D_e} \tag{21}$$

without an orifice plate (full break). The coefficients, c_1 and c_2, are an inertial coefficient and a measure of the deviations of boundary resistance and momentum flux due to unsteadiness. For the partial break, these coefficients are a function of the orifice area ratio only, and they are determined from experiment when $\eta = 0.3$, 0.5, 0.7. For other orifice area ratios than these values, the coefficients are determined by either interpolation or extrapolation from

$$(c_1 + c_2) = 2.63\eta^2 + 9.20\eta - 7.00 \tag{22}$$

For the full break, the value of $(c_1 + c_2) = 1.01$ and 1.62 are used for accelerated and decelerated flows, respectively. It is assumed that the orifice back pressure is kept to the saturation pressure at the coolant temperature at the break location because of the rapid adiabatic expansion of coolant at the downstream of the orifice plate. This assumption is considered to be valid till the time when the pressure difference across the orifice plate becomes zero.

The dead end and the open end conditions have been considered in the same way as reference [9], and discussions on these end conditions and the constant pressure end condition are given in reference [11].

Connecting Conditions. At a connection point of a multiple-piping, the total mass influx to the point is assumed to be zero. In addition, the pressure loss caused by abrupt change in cross-sectional area and flow restrictions such as grid assembly, flow mixer plate and upper and lower core plates are calculated from steady-state relations. The pressure losses at points of connection of more than two pipes are not taken into consideration. Connection up to a maximum of six pipes are considered in the computer code.

The Properties of Coolant. The properties of compressed water for the computation are calculated by the computer code based on the relations of The International Formulation Committee of The Sixth International Conference on The Properties of Steam [14], moreover the properties of saturated water and steam are calculated because the present theory is applied to the two-phase flow with no-slip homogeneous assumption. Sonic velocity in two-phase mixture is determined by the following relation [15]

$$\frac{1}{c^2} = [\alpha\rho_s + (1 - \alpha)\rho_w]\left[\frac{\alpha}{\rho_s c_s^2} + \frac{1 - \alpha}{\rho_w c_w^2}\right] \tag{23}$$

Equation (23) is more pertinent to the homogeneous mixture of noncondensible gas and water rather than the mixture of condensi-

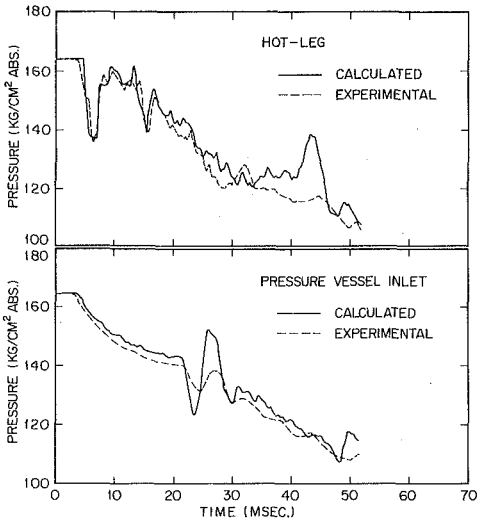

Fig. 2 Comparison of calculated pressure histories with LOFT semiscale test 811 data

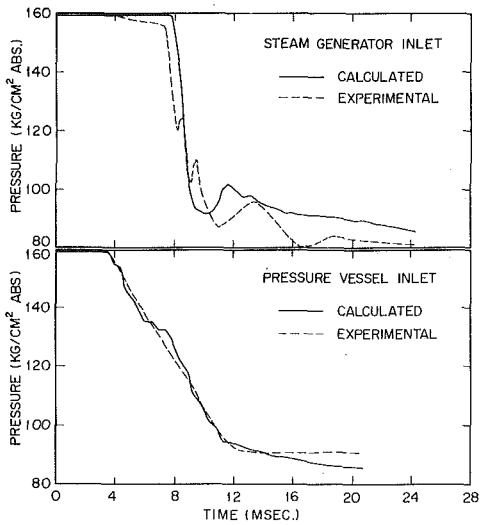

Fig. 3 Comparison of calculated pressure histories with LOFT semiscale test 820-1 data

ble steam and water, but it is used because of the fact that the coolant nonequilibrium effects preclude rapid phase change caused by the pressure change during a short period of computational time interval [15]. The effect of pipe wall elasticity on decompression is considered by the theory shown in reference [16].

Discussion

Based on the considerations given in the previous sections, the computer code DEPCO-MULTI has been prepared for use with the digital computer FACOM 230-60. Numerical results are compared with the test data of the ROSA-I, the ROSA-II and the LOFT semiscale 500, 600, 700, and 800 series tests with various coolant pressures, temperatures, pipe break sizes, and complexity of flow geometry. Good agreement is in general obtained. Moreover the effect of spatial mesh spacing and vessel wall elasticity on the computed results is examined. In what follows, the DEPCO-MULTI results will be compared with the test data in terms of pressure only. The comparison with the other quantities has not been made because these data during subcooled decompression process are not available.

Comparison With The LOFT Semiscale 800 Series Test Data. The LOFT semiscale 800 series test facility and the test results are reported in reference [17]. The testing facility consists of a simulated single-loop reactor coolant system containing a simulated reactor vessel (368 mm ID and 1625 mm height, without vessel internals), a steam generator (43 coolant tubes of 13.5 mm ID and 844 mm long), a coolant circulation pump, control valves and piping (103 mm ID). A pressurizer and auxiliary heaters are equipped. A double-ended blowdown or a single-ended blowdown occurs at the hot-leg of the facility by breaking rupture disks.

Table 1 Major thermo-hydraulic parameters of typical 1000 MWe PWRs

Nominal operating pressure	158 kg/cm² abs
Heat output at full power	3.4×10^6 kW
Coolant hot-leg temperature	325 deg C
Coolant cold-leg temperature	289 deg C
Coolant mean temperature	307 deg C
Total coolant volume	350 m³
Circulation pump developed pressure	6.0 kg/cm²

More detailed information on the test facility and the experimental procedure is written in reference [17].

Fig. 2 shows the calculated pressure histories at the hot-leg and the pressure vessel inlet in comparison with the test data for a 10 percent single-ended break. Major test conditions are listed in Table 3. Fig. 3 is the comparison with the 200 percent double-ended break test data at the steam generator inlet and the pressure vessel inlet. The calculated results of the LOFT semiscale 800 series test are obtained by dividing the test loop into 624 spatial mesh points with the mesh spacing of $\Delta x = 4$ cm. As seen in these figures, the agreement between the calculated and measured pressure histories is generally good.

Comparison With The ROSA-II Test Data. ROSA-II project is going on at JAERI to study the blowdown phenomenon and the effectiveness of ECCS during PWR LOCA. Schematic layout of ROSA-II test facility is shown in Fig. 4. An emergency core cooling system and coolant discharge pipings are equipped, but these are not shown in the figure for the simplicity of illustration. The facility has two primary coolant circulation loops, these are "the unbroken loop" and "the broken loop." Each loop has a steam generator and a coolant circulation pump and moreover the broken loop has two break units and a quick shut valve to simulate single-ended and double-ended breaks. Each break unit has a rupture disk, a rupture initiation needle and a sharp-edged orifice plate which

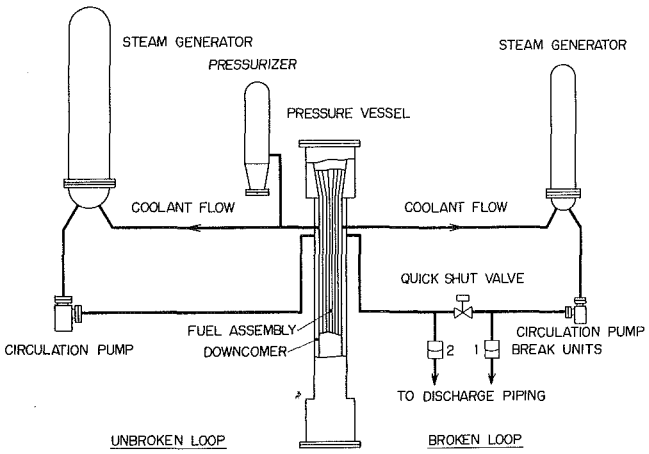

Fig. 4 Schematic layout of ROSA-II facility

Table 2 Order-of-magnitude of the terms of characteristic equations

Characteristic Directions	du	dp	$\frac{dp}{\rho c}$	$c^2 d\rho$	Fdt	k'uFdt	$\frac{k'uFdt}{\rho c}$	k'qdt	$\frac{k'qdt}{\rho c}$
I & II	13	—	13	—	1.6	—	10^{-2}	—	8.6×10^{-1}
III	—	8.3×10^5	—	9.7×10^5	—	6.9×10^2	—	5.8×10^4	—

simulate a break size. The vessel internals such as a simulated core, a core barrel, a flow mixer plate and core plates are inserted in the pressure vessel. Major parameters of the ROSA-II facility are shown in Table 4.

Fig. 5 is the calculated pressure histories at the top of the pressure vessel and the hot-leg of the unbroken-loop in comparison with the test data for 28.3 percent single-ended break (blowdown from the break unit 1) at the cold-leg. Test conditions are listed in Table 3. As seen in the figure, good agreement is also obtained.

Even though the present comparisons are made only with the pressure data, the code is capable of calculating other quantities such as coolant velocity, temperature, density, and sonic velocity. These quantities however can not be measured during the subcooled decompression duration due to the rapid change of these quantities and due to the presence of high pressure and temperature coolant. Thus, only the calculated coolant velocity in the ROSA-II simulated core is shown in Fig. 6. As known from the figure, flow reversal occurs in the core region and coolant velocity approaches to zero at the end of the subcooled decompression.

Conclusions

The digital computer code DEPCO-MULTI has been developed for the calculation of subcooled decompression in a multiple pipe network such as a PWR primary coolant system. The code is capable of calculating coolant velocity, pressure, temperature, density, sonic velocity and kinematic viscosity as functions of space and time, and hence all the necessary parameters for the core heat transfer analysis in PWR LOCA can be determined by the code. The comparison of the calculated results with the ROSA-I, the ROSA-II and the LOFT semiscale 500, 600, 700, and 800 series test data was made and it showed good agreement with the data.

Acknowledgment

The authors wish their thanks to Dr. S. Suguri and Mr. H. Shimamune for their encouragement in the course of the present work, and to the members of ROSA project group who prepared valuable test data. Acknowledgement is also extended to Dr. K. Sanokawa for furnishing the steam table computer code.

References

1 Berta, V. T., "Subcooled Pressure Gradient Calculations in PWR Systems Following Primary Coolant Loop Breaks," IDO-17243, Phillips Petroleum, Idaho, Mar. 1968.

2 Rose, R. P., Hanson, G. H., and Jayne, G. A., "Hydrodynamics Describing Acoustic Phenomena During Reactor Coolant System Blowdown," IDO-17254, Phillips Petroleum, Idaho, July 1967.

3 Fabic, S., "Computer Program WHAM for Calculation of Pressure, Velocity, and Force Transients in Liquid Filled Piping Network," Kaiser Engineers Report No. 67-49-R, Kaiser Industries, Ill., Nov. 1967.

4 Fabic, S., "Westinghouse APD Computer Program for Calculation of Fluid Pressure, Flow, and Density Transients During a Loss-of-Coolant Accident," *Transactions of The American Nuclear Society Fifteenth Annual Meeting,* American Nuclear Society.

5 Hanson, G. H., "Subcooled-Blowdown Forces on Reactor-System Components: Calculational Method and Experimental Confirmation," IN-1354, Idaho Nuclear Corp., Idaho, June 1970.

6 Gruen, G. E., "WHAM Prediction of Semiscale Test Results," IN-1431, Idaho Nuclear Corp., Idaho, Oct. 1970.

7 Hanson, G. H., and Anderson, J. E., "Subcooled Blowdown Forces on Reactor System Components," *Trans. ANS,* Vol. 12 No. 2, 1969, p. 881.

8 Shinoda, W., et al., "Analysis of Pressure Wave Propagation in Pipe Rupture Accidents of Light-Water Cooled Reactors by Use of The BURST Code," JAERI-M 4473, Japan Atomic Energy Research Institute, Japan, June 1971.

9 Shapiro, A. H., "Unsteady, One-Dimensional, Continuous Flow," *The Dynamics and Thermodynamics of Compressible Fluid Flow,* Vol. 2, Ronald, New York, 1954, pp. 930–991.

10 Forsythe, G. E., and Wasow, W. R., "Systems of Hyperbolic Differential Equations and Their Characteristics," *Finite-Difference Methods for Partial Differential Equations,* Wiley, New York, Section 6, 1960, pp. 38–49.

11 Namatame, K., and Kobayashi, K., "Digital Computer Code DEPCO-MULTI for Calculating the Subcooled Decompression in PWR LOCA," JAERI-M 5623, Japan Atomic Energy Research Institute, Japan, Feb. 1974.

12 Lister, M., "The Numerical Solution of Hyperbolic Partial Differential Equations by The Method of Characteristics," *Mathematical Methods for Digital Computers,* Wiley, New York, Part IV, 1960, pp. 165–179.

13 Daily, J. W., Hankey, W. L., Olive, R. W., and Jordaan, M. M., "Resistance Coefficients for Accelerated and Decelerated Flows Through Smooth Tubes and Orifices," TRANS. ASME, Vol. 78, July 1956, pp. 1071–1077.

14 "Formulations and Equations," *JSME Steam Tables,* JSME, Tokyo, Third ed., Sept. 1968, pp. 99–116.

Table 3 Conditions of the ROSA-II and the LOFT semiscale blowdown tests

Tests	Pressure	Temperature	Flow Rate	Break Per Cent
ROSA-II 301	157 kg/cm² abs	308 deg C	29.6 ℓ/s	28.3 single-ended
LOFT 811	164	307	22.2	10 single-ended
LOFT 820-1	159	309	0	200 double-ended

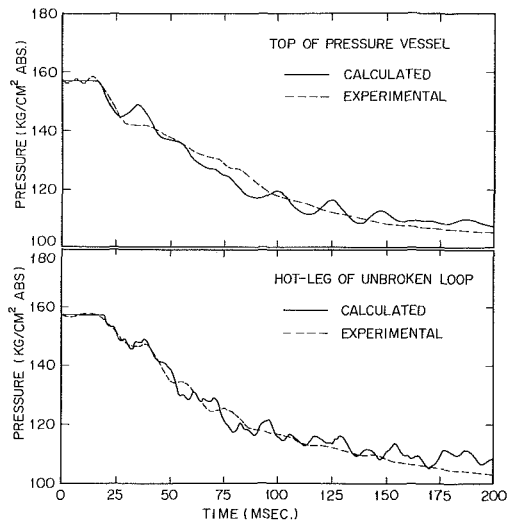

Fig. 5 Comparison of calculated pressure histories with ROSA-II test 301 data

Table 4 Major parameters of ROSA-II test facility

			Unbroken loop	Broken loop
Coolant pressure, kg/(cm²abs)	160	Primary coolant loops		
Coolant temperature, deg C	325	Hot leg piping I.D., mm	87.3/108	43.1
Total coolant volume, m³	0.854	Hot leg length, mm	4,665	4,543
Pressure vessel		Cold leg piping I.D., mm	87.3	43.1/57.3
Core section I.D., mm	280	Cold leg length, mm	4,263	7,884
Upper plenum I.D., mm	380	S.G.-pump piping I.D., mm	87.3	57.3
Lower plenum I.D., mm	340	S.G.-pump piping length, mm	754	1,296
Core barrel O.D., mm	238	Coolant volume, m³	0.097	0.034
Axial length, mm	4,855	Steam generators		
Coolant volume, m³	0.292	Number of U-tubes	123	51
Simulated core		U-tube I.D., mm	14.4	14.4
Number of fuel rods	96	Mean U-tube length, mm	6,450	4,970
Number of tie rods	13	Primary coolant volume, m³	0.225	0.073
Fuel rod O.D., mm	10.7	Circulation pumps (canned type)		
Pitch (square array), mm	14.3	Circulation rate, m³/min.	1.4	0.46
Heated length, mm	1,500	Developed head, kg/cm²	1.1	1.1
Number of spacers	3			
Total heating power, MW	2.24			
Pressurizer (electric heating)				
Shell I.D., mm	280			
Axial length, mm	2,550			
Volume, m³	0.133			

15 Wallis, G. B., "Homogeneous Flow," *One-Dimensional Two-Phase Flow*, McGraw-Hill, New York, 1969, pp. 18–26.

16 Streeter, V. L., and Wyle, E. B., *Hydraulic Transients*, McGraw-Hill, New York, 1967, p. 17.

17 Heiselmann, H. W., Olson, D. J., and Whitbeck, J. F., "Semiscale Blowdown and Emergency Core Cooling (ECC) Project Test Report—Tests 803 Through 820," IN-1404, Idaho Nuclear Corporation, Idaho, Oct. 1970.

APPENDIX A

Equation (1) is transformed to

$$\frac{p}{\rho A}\frac{\partial}{\partial x}(Au) = -\frac{p}{\rho 2}\left(\frac{\partial \rho}{\partial t} + u\frac{\partial \rho}{\partial x}\right) \tag{A1}$$

On the other hand, the internal energy term in equation (3) can be represented as follows

$$\frac{D}{Dt}(c_v T) = \left(\frac{\partial f}{\partial p}\right)_\rho \left(\frac{\partial p}{\partial t} + u\frac{\partial p}{\partial x}\right) + \left(\frac{\partial f}{\partial \rho}\right)_p \left(\frac{\partial \rho}{\partial t} + u\frac{\partial \rho}{\partial x}\right) \tag{A2}$$

where the function f represents the internal energy as a function of pressure and density, i.e., $c_v T = f(p, \rho)$. By substituting equations (A1) and (A2) into the right-hand terms of equation (3) and rearranging the terms, equation (3) can be transformed to

$$\frac{q + uF}{(\partial f/\partial p)_\rho} = \left(\frac{\partial p}{\partial t} + u\frac{\partial p}{\partial x}\right) + \frac{(\partial f/\partial \rho)_p - p/\rho 2}{(\partial f/\partial p)\rho}\left(\frac{\partial \rho}{\partial t} + u\frac{\partial \rho}{\partial x}\right) \tag{A3}$$

The following equation is derived from the well-known thermodynamic relationship, i.e., $Tds = df + pd(1/\rho)$

$$Tds = \left(\frac{\partial f}{\partial p}\right)_\rho dp + \left[\left(\frac{\partial f}{\partial \rho}\right)_p - \frac{p}{\rho^2}\right] d\rho \tag{A4}$$

Equation (A4) can be transformed as follows by the isentropic condition

$$\frac{(\partial f/\partial \rho)_p - p/\rho^2}{(\partial f/\partial p)_\rho} = -\left(\frac{dp}{d\rho}\right)_s \equiv -c^2 \tag{A5}$$

Equation (A3) is then represented as follows by substituting relation (A5) into the right-hand term of equation (A3)

$$k'(q + uF) = \left(\frac{\partial p}{\partial t} + u\frac{\partial p}{\partial x}\right) - c^2\left(\frac{\partial \rho}{\partial t} + u\frac{\partial \rho}{\partial x}\right) \tag{5}$$

where the function k' is defined by equation (6).

APPENDIX B

The order-of-magnitude of the terms of equations (7*b*), (8*b*), and (9*b*) is examined in a case of the cold-leg break which is the most severe LOCA for subcooled decompression, by the use of the thermo-hydraulic parameters of typical 1000 MWe PWRs, shown in Table 1.

The coolant pressure decreases from the reactor operating value

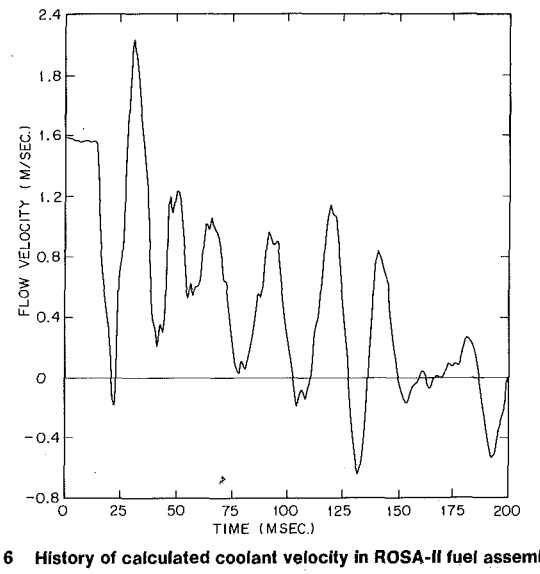

Fig. 6 History of calculated coolant velocity in ROSA-II fuel assembly

(158 kg/(cm^2 abs.)) to the saturation pressure ($\simeq$75 kg/(cm^2 abs.)), which corresponds to the cold-leg temperature, within few hundred milliseconds depending on the break size. The terms proportional to the pressure change in equations (7b), (8b), and (9b) are thus approximated by $dp \simeq 0.83 \times 10^6$ kg/m^2 and $dp/(\rho c) \simeq 13$ m/s with the values of $\rho \simeq 74$ kg s^2/m^4 and $c \simeq 900$ m/s which are the coolant specific density and the sonic velocity at the reactor operating pressure and temperature. The corresponding change in coolant velocity is then determined as $du \simeq 13$ m/s by using the relation $du = dp/(\rho c)$ which is derived from equation (8b) by neglecting the terms of wall friction, heat input and cross-sectional area change as the first approximation. The term $c^2 d\rho$ in equation (9b) has the value of 9.7×10^5 kg/m^2 because coolant specific masses have the values of 74 and 72.8 kg s^2/m^4 before LOCA and after the saturation state at the end of the subcooled decompression, respectively.

The terms proportional to the heat input in equations (7b), (8b), and (9b) are $k'qdt \simeq 5.8 \times 10^4$ kg/m^2 and $k'qdt/(\rho c) \simeq 0.86$ m/s since the value of k' is derived from the steam table as 1.8×10^5 kg^2/(m^2-kcal) and the heat input is calculated from Table 1 as $q \simeq$ 3.2 kcal/(kg-s).

The mean frictional loss in a coolant system is determined from the circulation pump developing pressure Δp_p in Table 1 by the relation $F = \Delta p_P/(\rho L) \simeq 16$ m/s^2 when the length of coolant system, L, is approximately 50 m in each of coolant loops. With this value for the terms proportional to the frictional loss, $Fdt \simeq 1.6$ m/s, $k'uFdt \simeq 6.9 \times 10^2$ kg/m^2 and $k'uFdt/(\rho c) \simeq 1.0 \times 10^{-2}$ m/s are calculated. These values are summarized in Table 2.

K. O. Lund

General Atomic Co.,
San Diego, Calif.

Asymptotic Analysis of the Average, Steady, Isothermal Flow in Coupled, Parallel Channels

The conservation equations of mass and momentum are derived for the average flow of gases in coupled, parallel channels, or rod bundles. In the case of gas-cooled rod bundles the pitch of the rods is relatively large so the flows in the channels are strongly coupled. From this observation a perturbation parameter, ϵ, is derived and the descriptive equations are scaled using this parameter, which represents the ratio of the axial flow area to the transverse flow area, and which is of the order of 10^{-3} in current gas-cooled fast breeder reactor designs. By expanding the velocities into perturbation series in ϵ the equations for two channels are solved as an initial value problem, and the results compared to a finite difference solution of the same problem. Then, the N-channel, problem is solved to the lowest order as a two-point boundary value problem with the pressures specified at the inlet and the outlet. It is concluded from the study that asymptotic methods are effective in solving the flow problems of rod bundles; however, further work is required to evaluate the possible computational advantages of the methods.

Introduction

Parallel, coupled flow channels arise in the rod-bundle geometry of nuclear reactor cores, and of many heat exchangers where heat is generated inside the rods and removed from the outside of the rods by a fluid flowing predominantly in the axial direction. This geometry has been in use for many years in water-cooled thermal reactors, but now it is also being applied in the design of liquid-metal-cooled and gas-cooled fast breeder reactors. A typical rod bundle is shown in Fig. 1, which is the cross-sectional view of a fuel element design for a gas-cooled breeder reactor [1].[1]

To assure high thermal efficiency and safety of these reactors, it is necessary to accurately predict the turbulent flow and heat transport processes in the rod bundles. This is an exceedingly difficult problem viewed from basic principles, not only because of the complicated geometry, but also because the equations of motion of turbulent flow are neither completely defined nor easily solved, even for simpler geometries. Therefore, various approximations in conjunction with experiments are required to model this flow and heat transfer problem.

Recent experiments and analyses of rod bundles have dealt with detailed, fully developed flow distributions, as reported by Kjellström [2], Nijsing and Eifler [3], Rowe [4], Ramm and Johannsen [5], and Trupp and Azad [6]. However, because of varying degrees of heating in the rods and of various rod spacing devices the flow in the bundles is generally not fully developed; thus, it is necessary to solve for an axially changing flow field. To approximate this flow field it is commonly divided into subchannels, as shown in Fig. 1, and the descriptive equations are derived from balances over axially differential subchannel volumes. In each subchannel we consider the average velocity to be sufficiently developed so that the average surface shear stress of the subchannel can be related to the velocity in terms of a friction factor; however, the average subchannel velocity can change slowly in the axial direction due to entrance conditions and fluid property variations. This approximation results in a system of differential equations in the axial coordinate which will be quite large for rod bundles such as the one in Fig. 1. The equations of the system are coupled because of the occurrence of Reynolds stresses at the subchannel interfaces and because of net, transverse flows between the subchannels. Although

[1] Numbers in brackets designate References at end of paper.

Contributed by the Heat Transfer Division and presented at the Winter Annual Meeting, New York, N.Y., November 17–22, 1974, of THE AMERICAN SOCIETY OF MECHANICAL ENGINEERS. Revised manuscript received by the Heat Transfer Division, April 4, 1975. Paper No. 74-WA/HT-4.

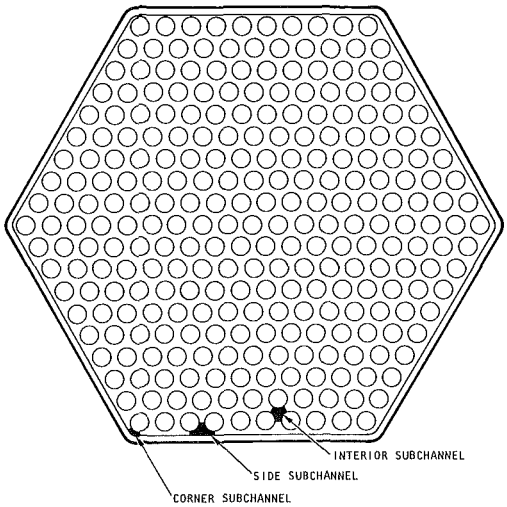

Fig. 1

the subchannel approach gives only a limited description of the flow field as discussed by Lewis and Buettiker [7], it appears to be the only practical approach for large rod-bundles.

The axial integration of the equations is usually performed by finite difference methods, such as in the COBRA computer program [8]; however, for large systems such as the one in Fig. 1 this method can be costly and tax the storage limitations of present day computers. For incompressible liquids, Nijsing and Eifler [9] used an eigenvalue method to solve for developing temperatures in a fully developed flow field; but for gases it is necessary to consider an axially changing flow field as well. Therefore, it is of interest to seek alternative approaches to the integration of the equations. Subchannel analyses have also been extended to transient flows by Rowe [10], and to flows in bundles with blockages by Gosman, et al. [11] and by Eifler and Nijsing [12]. In this analysis, only mildly perturbed, steady flows are considered.

The ultimate goal of the asymptotic analysis of large rod-bundles is to determine the temperature field within the bundles by an efficient computational method and to gain a better understanding of the transport processes. For simplicity, only the averaged isothermal flow equations are solved in this work. However, the complete problem of flow of gases with heat addition can be similarly solved by asymptotic expansions.

Problem Statement

Descriptive differential equations for flow in parallel, coupled channels, or rod bundles, can be found in many references (cf. Rowe [10]). But, for completeness, a brief derivation of the relevant equations is presented here.

To derive the axial momentum equations, we consider the momentum fluxes in and out of the differential control volume for the ith subchannel, as shown in Fig. 2 (a). If the ith subchannel is connected only to the jth subchannel as shown, then the net change of momentum per length dx is given by

$$\frac{d}{dx}(\rho A u^2)_i + \rho s w u_i + \rho s w_t (u_i - u_j)$$

where the cross-flow velocity, w, represents a net transport of mass and momentum from the ith to the jth subchannel, and where w_t denotes a turbulent, fluctuating velocity, that causes a transport of momentum but not of mass. In Fig. 2 (a), w was assumed positive as shown; however, for negative w when the crossflow is from j to i, ρu_j would be transported by w instead of ρu_i. Therefore, to account for this dependence on the direction of w, the second term in the foregoing equation is written as

$$\rho s w \bar{u} + 0.5\, \rho s |w| \Delta u$$

where

$$\bar{u} \equiv 0.5\,(u_i + u_j)$$

$$\Delta u \equiv u_i - u_j$$

The third term in the foregoing equation contains the "mixing velocity," w_t, which must be related to the average velocities. For simplicity, w_t is taken as proportional to the average axial velocity as follows,

$$w_t = \beta \bar{u}$$

where β is an experimentally determined constant (cf. Castellana, et al. [13]). More complicated turbulent interchange models are possible (cf. Ramm and Johannsen [5]), but the foregoing model is adequate for the objective of this work, which is to illustrate the

Nomenclature

A_c = characteristic area
A_i = area of ith subchannel
C = subchannel connection matrix
C^T = transpose of connection matrix C
C_D = cross flow drag coefficient, equation (3)
C_L = cross flow drag coefficient, equation (28)
K = pressure loss coefficient
L = length of the bundle or flow channels
M = number of branches
N = number of subchannels
P_i = friction perimeter in ith subchannel
U = characteristic velocity
b = number of a branch
b_i, b_j = constants in equation (11)
f = Darcy friction factor
g = gravitational acceleration
k_i = friction and mixing parameter
m = number of a source node
n = number of a sink node
p_i = pressure in ith subchannel
r = ratio of outer velocities
s_c = characteristic gap width
t = ratio of outer velocities
u_i = average axial velocity of ith subchannel
w_k = cross flow velocity of kth branch
w_t = turbulent mixing velocity
x = axial coordinate
α = eigenvalue
β = turbulent mixing parameter
δ = Dirac delta function
δ_{ij} = Kronecker delta
ϵ, η, ν, ω = perturbation parameters
ξ = stretched axial coordinate
ℓ = dimensionless flow development length
τ_0 = surface shear stress

Subscripts

i, j = subchannel i, j
k = branch or subchannel connection k
0 = zeroth order variable
1 = first order variable

Special Symbols

Δ = difference between variables in two subchannels
$-$ = the average value of variables in two subchannels
$\sim$ = boundary layer correction function

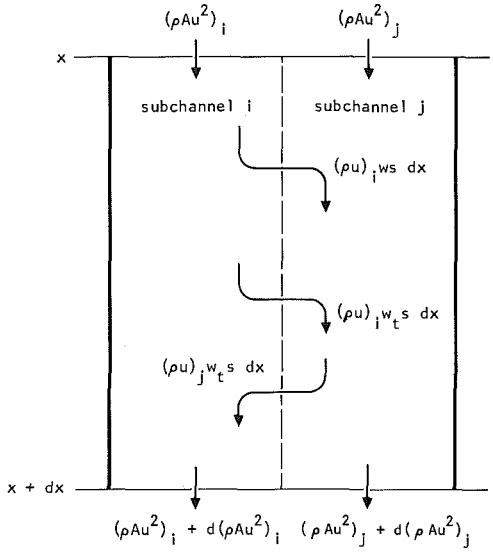

Fig. 2(*a*)

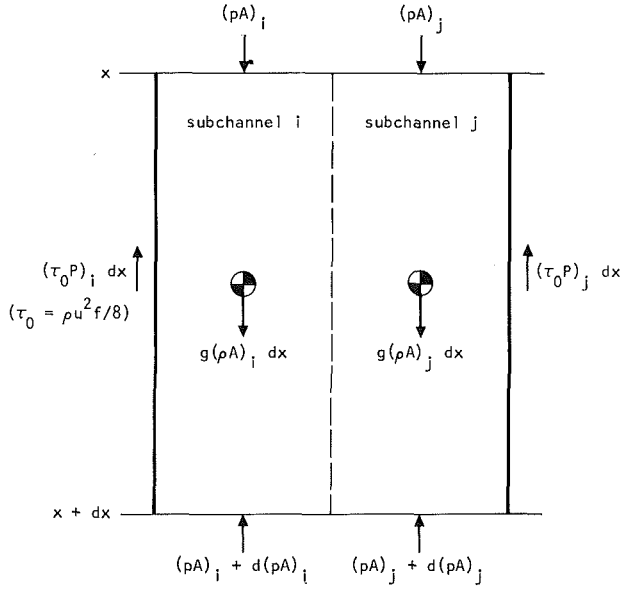

Fig. 2(*b*)

application of asymptotic expansions to calculate flow distributions in rod bundles. This method of solution is general and not limited to the simple model in the foregoing.

In the foregoing derivation, crossflow and mixing were considered only between two subchannels, but in a rod bundle, any one subchannel will be connected to several adjoining subchannels. To account for this in the describing equations, it is convenient to introduce a subchannel connection matrix which relates a particular subchannel (node) and subchannel connection (branch) to a number scheme of the whole rod bundle, similarly as done by Rowe [10]. For any branch or pair of nodes, we define a triplet of numbers *b, m, n;* where b is the branch number, m is the source-node number, and n is the sink-node number, as shown:

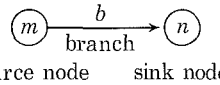

Thus, the interconnected subchannels take on the form of a directed graph. Now, the element of the connection matrix C associated with the ith subchannel, or node, and the kth subchannel connection, or branch, can be defined in terms of the Kronecker delta:

$$C_{ik} = \delta_{kb}(\delta_{im} - \delta_{in})$$

That is, C_{ik} is zero for all branches except b, is $+1$ if i is the source-node of branch b, and is -1 if i is the sink-node of branch b.

With this description, the rate of change of momentum of the ith subchannel is now equated to the summation of forces acting on the control volume, shown in Fig. 2 (*b*). Thus, the momentum equation for the ith subchannel is as follows:

$$\frac{d}{dx}(\rho Au^2)_i + C_{ik}(\rho sw\bar{u} + \rho s(\beta\bar{u} + 0.5|w|)\Delta u)_k = -\frac{d}{dx}(\rho A)_i - \frac{1}{8}(\rho Pu^2 f)_i + \rho gA_i, \quad i = 1, 2, \ldots, N \quad (1)$$

where the repeated subscript, k, implies summation over the M branches in the network of subchannels (or matrix multiplication), where the variables in the brackets are associated with the particular subscript of the bracket, and where the friction factors, f_i, were defined in terms of the subchannel-average wall shear stresses: $\tau_{0i} = (\rho u^2 f/8)_i$.

The mass equations are derived similarly as the momentum equations in the foregoing. In isothermal and incompressible flow it is clear that the axial rate of change of the volumetric flow in a subchannel i must be balanced by the summation of transverse flows out of the subchannel. Thus, the equations of conservation of mass can be written as follows:

$$\frac{d}{dx}(uA)_i + C_{ik}(ws)_k = 0, \quad i = 1, 2, \ldots, N \quad (2)$$

The system of equations to be solved is completed by the M transverse momentum equations. These are written simply with the use of an empirical drag coefficient (cf. Rowe [10]):

$$C_{ki}{}^T p_i = \Delta p_k = 0.5\rho C_D(|w|w)_k, \quad k = 1, 2, \ldots, M \quad (3)$$

There are indications that inertia terms are equally important (cf. Eifler and Nijsing [12]), but here we will consider only the frictional forces in equation (3).

Equations (1)–(3) are now $2N + M$ equations to solve for the N u_i's and p_i's, and the M w_k's. The boundary conditions associated with these equations depend on the type of problem. In the case of some experimental rod bundles the flow distribution can be controlled at the inlet, and the u_i's and p_i's have initial data; in the case of reactor rod bundles, the subchannels are connected to common inlet and outlet plena, and the required $2N$ boundary conditions are provided by the $p_i(0)$'s and $p_i(L)$'s. No boundary conditions can be placed on the w_k's in the previous formulation because they occur only algebraically in the equations.

Method of Solution

The approach to the solution of the above boundary value problem is by asymptotic expansions, which often find application in problems having very different length scales in different coordinate directions. In this case, a small parameter, ϵ, can always be identified as the ratio of the length scales and used as the perturbation parameter in constructing asymptotic series. A number of methods are available for constructing asymptotic series. For example, in the method of matched asymptotic expansions a function, $f(x)$, is expanded into an asymptotic series, $\nu_0(\epsilon)f_0(x) + \nu_1(\epsilon)f_1(x) + \ldots$, and the outer solutions, $f_0(x)$, $f_1(x)$, ..., are obtained successively for large x by repeated application of the limit $\epsilon \to 0$. Then, defining an inner variable, $\xi = x/\phi(\epsilon)$, another series is constructed for small x, $\tilde{\nu}_0(\epsilon)\tilde{f}_0(\xi) + \tilde{\nu}_1(\epsilon)\tilde{f}_1(\xi) + \ldots$, and the inner solutions are obtained, $\tilde{f}_0, \tilde{f}_1, \ldots$. If all goes well an intermediate region will exist where both series are valid and can be matched together to form a composite series, valid in the whole domain of x. In the method of composite asymptotic expansions the above two series are combined prior to the analysis:

$$f(x;\epsilon) \sim \nu_0(\epsilon)f_0(x) + \tilde{\nu}_0(\epsilon)\tilde{f}_0(\xi) + \nu_1(\epsilon)f_1(x) + \tilde{\nu}_1(\epsilon)\tilde{f}_1(\xi) + \ldots \quad (4)$$

then, the matching condition is that the inner variables, $\tilde{f}_0, \tilde{f}_1 \ldots$, vanish in the limit as $\xi \to \infty$ (i.e., as $\epsilon \to 0$ for fixed x). For further details the reader is referred to several excellent texts on the subject [14–18]. For the present analysis, we will use composite expansions with a slight modification to be discussed.

In the case of rod bundles, the characteristic axial dimension, L, is the length of the bundle. With the subchannel approximation the variables associated with the cross-sectional geometry are the subchannel areas, A_i, the gap widths, s_k, and the friction perimeters, P_i. Therefore, a characteristic gap, s_c, and area, A_c, are introduced for scaling the cross-sectional lengths and areas. For example, s_c and A_c could be the average gap and area associated with a whole rod bundle, as in Fig. 1. For convenience, the factor $8s_c$ is used to scale the friction perimeters. Let A_c/s_c be the transverse length scale, then the perturbation parameter arising from the equations, $\epsilon = A_c/Ls_c$, will be of the order of 10^{-3} or 10^{-2} if s_c is not too small, leading to closely approximating series. In gas-cooled rod bundles, s_c is comparatively large to provide adequate heat removal, so ϵ will be small. Thus, we characterize rod bundles as having strongly coupled subchannels if the parameter $\epsilon \equiv A_c/Ls_c$ is much less than 1. The limit $\epsilon \to 0$ corresponds to infinitely long bundles, or $L \to \infty$ for fixed A_c/s_c. The outer solutions thus reflect the system behavior far from the inlet of the rod bundle.

To introduce the perturbation parameter into equations (1)–(3) the variables are scaled according to the boundary conditions and the lengths of the rod bundle. Thus, the dimensionless, scaled variables are as follows:

$$x' = x/L, \quad s_k' = s_k/s_c,$$

$$A_i' = A_i/A_c, \quad P_i' = P_i/8s_c,$$

$$u_i' = u_i/U, \quad w_k' = w_k/\omega U,$$

$$g' = gA_c/s_cU^2, \quad p_i' = (p_i - p_i(0))/p_c$$

The characteristic pressure and velocity are related by $p_c = \rho U^2/\epsilon$, and either U or $p_c = p(0) - p(L)$ may be specified depending on the problem under consideration. The crossflows, w_k, are scaled relative to U by introducing an unknown parameter, ω. Substitution of the scaled variables into equations (1)–(3), and dropping immediately the primes from the scaled variables, the perturbation equations are as follows:

$$\epsilon\frac{d}{dx}(Au)_i + \omega C_{ik}(sw)_k = 0, \quad i = 1, 2, \ldots, N \quad (5)$$

$$\epsilon\frac{d}{dx}(Au^2)_i + \omega C_{ik}(sw\bar{u} + s(\beta\bar{u} + 0.5|w|)\Delta u)_k$$

$$= -\frac{d}{dx}(pA)_i - (Pu^2f)_i + gA_i, \quad i = 1, 2, \ldots, N \quad (6)$$

$$\Delta p_k = 0.5\epsilon\omega^2 C_D(|w|w)_k, \quad k = 1, 2, \ldots, M \quad (7)$$

Equations (5) and (6) are singular in the perturbation parameter, ϵ, because in the limit as ϵ approaches zero the differential equations are reduced in order from first-order equations to algebraic equations. This singular perturbation problem can be solved by asymptotic expansions, as shown in the following examples.

Case I: Initial Value Problem for Two Channels

As the first example of the solution of equations (5)–(7), we consider the isothermal flow in two coupled channels, i and j, where the scaled velocities are specified at the inlet. This problem is of interest for comparison with finite difference solutions. The pressure does not enter into this problem directly, so it can be eliminated from the equations; hence, the initial value problem with a constant friction factor can be stated as follows:

$$\epsilon\frac{du_i}{dx} + \omega sw/A_i = 0, \quad \epsilon\frac{du_j}{dx} - \omega sw/A_j = 0 \quad (8)$$

$$\epsilon\frac{d}{dx}(u_i^2 - u_j^2 - 0.5\omega^2 C_D w|w|) + k_i u_i^2 - k_j u_j^2$$

$$+ \omega s\bar{A}(2w\bar{u} + |w|\Delta u)/A_iA_j = 0 \quad (9)$$

$$u_i(0) = u_i^*, \quad u_j(0) = u_j^* \quad (10)$$

where

$$k_i = fP_i/A_i + s\beta\bar{A}/A_iA_j, \quad k_j = fP_j/A_j + s\beta\bar{A}/A_iA_j$$

$$\bar{A} = 0.5(A_i + A_j)$$

and where w is positive for flow from i to j. In equation (9) w is differentiated, but later we shall neglect terms of the order of magnitude of ω^2 so no initial condition on w is required.

We now restrict the analysis to a mildly perturbed flow in which the initial conditions, u_i^* *and* u_j^*, do not differ greatly from the outer velocities (i.e., the first term in an expansion similar to equation (4)). That is, if b_i and b_j are numbers of 0(1), where 0 means "the order of magnitude of," and η is a small parameter, then the following equations define b_i and b_j:

$$u_{0i}(0) + \eta b_i = u_i^* \quad (11)$$

$$u_{0j}(0) + \eta b_j = u_j^*$$

The parameter η can be taken as any small number less than one to make the b's of the order of magnitude of 1. The result will be a linearization of equation (9) when the terms of $0(\eta^2)$ are neglected. With the above type of initial conditions we form the following expansions:

$$u_i(x;\eta;\epsilon) \sim u_{0i}(x) + \eta\tilde{u}_{0i}(\xi) + \nu_1(\eta,\epsilon)u_{1i}(x) + \tilde{\nu}_1(\eta,\epsilon)\tilde{u}_{1i}(\xi) + \ldots$$

$$u_j(x;\eta;\epsilon) \sim u_{0j}(x) + \eta\tilde{u}_{0j}(\xi) + \nu_1(\eta,\epsilon)u_{1j}(x)$$

$$+ \tilde{\nu}_1(\eta,\epsilon)\tilde{u}_{1j}(\xi) + \ldots \quad (12)$$

$$w(x;\eta;\epsilon) \sim w_0(x) + \tilde{w}_0(\xi) + \omega_1(\eta,\epsilon)w_1(x) + \tilde{\omega}_1(\eta,\epsilon)\tilde{w}_1(\xi) + \ldots$$

where the inner variable is $\xi \equiv x/\epsilon$.

First, we seek the fundamental, or reduced, solution to equations (8)–(10) in the limit as $\epsilon \to 0$. This solution will be the functions $u_{0i}(x)$, $u_{0j}(x)$, and $w_0(x)$ in equations (12) because $\tilde{u}_{0i}(x/\epsilon)$, $\tilde{u}_{0j}(x/\epsilon)$, and $\tilde{w}_0(w/\epsilon)$ vanish as $\epsilon \to 0$ for all $x > 0$. From equations (8) the fundamental solution evidently is $w_0 = 0$, and from equation (9)

$$u_{0j}/u_{0i} = r \equiv \sqrt{k_i/k_j} \quad (13)$$

The constant velocities u_{0i} and u_{0j} are the first terms in the outer expansion; these terms incorporate all aspects of the flow far from the inlet, so the higher-order, outer terms are identically zero. In the case where β is negligible it is observed that the velocities are in the ratio of the square root of their respective hydraulic diameters. Only the ratios of the velocities are determined because there are no far-field boundary conditions. The loss of the initial conditions occurred because the derivative terms in equations (8) and (9) vanish for $\epsilon = 0$. However, eliminating w between equations (8) we find that for all x

$$A_iu_i(x) + A_ju_j(x) = A_iu_i^* + A_ju_j^*$$

so that with equation (13) the fundamental solution is as follows:

$$u_{0i} = \frac{A_iu_i^* + A_ju_j^*}{A_i + rA_j}, \quad u_{0j} = ru_{0i}, \quad w_0 = 0 \quad (14)$$

This solution is valid far from the inlet, and because it was obtained from algebraic equations it cannot satisfy any initial conditions. To satisfy equations (10) or (11) we introduce the stretched coordinate $\xi = x/\epsilon$ into equations (8) and (9) so that $\epsilon d/dx$ becomes $d/d\xi$, and we include from equations (12) the zeroth order "boundary layer corrections," $\tilde{u}_{0i}$, $\tilde{u}_{0j}$, and $\tilde{w}_0$. Neglecting terms of $0(\eta^2)$ and $0(\epsilon)$ we then obtain the equations,

$$\eta \frac{d\tilde{u}_{0i}}{d\xi} + \omega \frac{s}{A_i}\tilde{w}_0 = 0, \quad \eta \frac{d\tilde{u}_{0j}}{d\xi} - \omega \frac{s}{A_j}\tilde{w}_0 = 0$$

$$\frac{d}{d\xi}(2\eta u_{0i}\tilde{u}_{0i} - 2\eta u_{0j}\tilde{u}_{0j} - 0.5\omega^2 C_D|\tilde{w}_0|\tilde{w}_0) + 2\eta k_i u_{0i}\tilde{u}_{0i}$$

$$- 2\eta k_j u_{0j}\tilde{u}_{0j} + \omega s\bar{A}(2\bar{u}_0\tilde{w}_0 + \Delta u_0|\tilde{w}_0|)/A_iA_j = 0 \quad (15a, b, c)$$

In the inner region near the inlet all terms in the continuity equations, equations (15a and 15b), should be retained; therefore, we select the scale for the crossflow as $\omega = \eta$. Since terms of $0(\eta^2)$ are neglected to the lowest order, and with equation (13), equations (15) become the linear system,

$$\frac{d\tilde{u}_{0i}}{d\xi} + \frac{s}{A_i}\tilde{w}_0 = 0, \quad \frac{d\tilde{u}_{0j}}{d\xi} - \frac{s}{A_j}\tilde{w}_0 = 0$$

$$D(\tilde{u}_{0i}, \tilde{u}_{0j}, \tilde{w}_0) \equiv \frac{d\tilde{u}_{0i}}{d\xi} + k_i\tilde{u}_{0i} - r\left(\frac{d\tilde{u}_{0j}}{d\xi} + k_j\tilde{u}_{0j}\right)$$

$$+ \frac{1}{2}\left((1+r)\tilde{w}_0 + (1-r)|\tilde{w}_0|\right)s\bar{A}/A_iA_j = 0 \quad (16a, b, c)$$

with the initial conditions from equations (11),

$$\tilde{u}_{0i}(0) = b_i, \quad \tilde{u}_{0j}(0) = b_j$$

The solution to these equations is easily obtained by taking $\tilde{u}_{0i} = a_0e^{-\alpha\xi}$, $\tilde{u}_{0j} = b_0e^{-\alpha\xi}$, $\tilde{w}_0 = c_0e^{-\alpha\xi}$, where a_0, b_0, and c_0 are undetermined constants; then, substitution into equations (16) yields the eigenvalue

$$\alpha = 2\frac{k_iA_j + rk_jA_j}{A_j + (2r-1)A_i}, \quad \tilde{w}_0 > 0 \qquad (17)$$

$$\alpha = 2\frac{k_jA_i + tk_iA_i}{A_i + (2t-1)A_j}, \quad \tilde{w}_0 < 0, \quad t \equiv 1/r$$

Satisfying the initial conditions we have the boundary layer correction functions (cf. O'Malley's terminology [18]) as follows:

$$\tilde{u}_{0i}(\xi) = b_ie^{-\alpha\xi}, \quad \tilde{u}_{0j}(\xi) = b_je^{-\alpha\xi}, \quad \tilde{w}_0(\xi) = \alpha\frac{A_i}{s}b_ie^{-\alpha\xi}$$

We note that these functions have the correct asymptotic behavior of approaching zero as $\xi \to \infty$. Now, combining equations (11) and (14) with the above functions, as per equations (12), we have the solution to equations (8)–(10) to the lowest order of approximation:

$$u_i(x;\epsilon) \sim u_{0i} + (u_i^* - u_{0i})e^{-\alpha x/\epsilon}$$

$$u_j(x;\epsilon) \sim u_{0j} + (u_j^* - u_{0j})e^{-\alpha x/\epsilon}$$

$$w(x;\epsilon) \sim \alpha\frac{A_i}{s}(u_i^* - u_{0i})e^{-\alpha x/\epsilon} \qquad (18)$$

It should be noted that equations (18) do not depend on the value of $\eta = \omega$. These parameters were introduced only formally to achieve a linearization of the equations by neglecting terms of $0(\eta^2) = 0((u_i^* - u_{0i})^2)$. The solution is, of course, accurate only to the extent that max $\{(u_i^* - u_{0i})^2\}$ is negligible for given numerical data.

In equations (18) we see that there is a dimensionless entrance length, $\ell = \epsilon/\alpha$, which is characteristic of the bundle geometry and the mixing and friction factors. Thus, the flow would be fully distributed in about five ℓ's, and all blockage effects or disturbances to the flow at the inlet would be dissipated downstream of this distance from the inlet in this particular example. As can be seen from the form of the eigenvalue, ℓ decreases (flow develops faster) with increasing mixing and friction factors, as would be expected.

As an example, the flow development was calculated with equations (18) for two channels, such as the adjoining side and corner subchannels in Fig. 1, with different areas and friction perimeters. Comparison of the results in Fig. 3 with a finite difference solution using COBRA [8] shows there is good agreement of the axial velocities, even when the higher-order terms involving the cross-flow drag coefficient are neglected. For illustration, in Fig. 3 we have

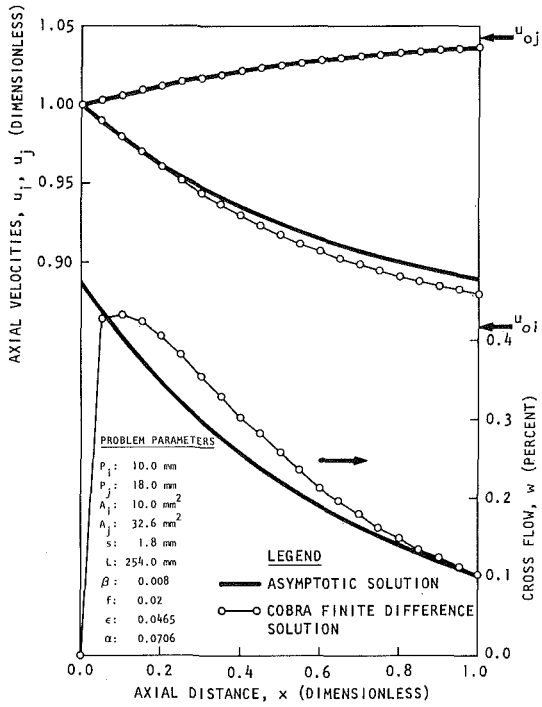

Fig. 3

taken $u_i^* = u_j^* = 1$, and $\omega = 1$ with the other data given in the figure. Although the cross-flow velocity in the lower part of Fig. 3 is much smaller than the axial velocities, it is nevertheless important to consider its variation because the cross-flow area over the length of the subchannels is much larger than the axial flow area for a subchannel; thus, a significant amount of fluid can be diverted between subchannels even though the transporting velocity is small.

In Fig. 4, the same problem as in Fig. 3 is solved, except that the friction factor is larger. As can be seen, this flow is nearly fully developed at $x = 1$, and there is excellent agreement between the asymptotic velocities indicated by the arrows and the numerical calculations.

It is possible to include the cross-flow drag coefficient in the solution by considering the higher-order terms in the expansions, equations (12). The outer solutions, $u_{1i}(x)$, $u_{1j}(x)$, and $w_1(x)$, are zero because u_{0i}, u_{0j}, and w_0 satisfy equations (8) and (9) identically for any ϵ. The higher-order inner equations are obtained by collecting terms of $0(\tilde{\nu}_1)$ and $0(\tilde{\omega}_1)$. Substituting the expansions into equations (8) and selecting $\tilde{\nu}_1 = \eta\tilde{\omega}_1$, we obtain the mass conservation equations

$$\frac{d\tilde{u}_{1i}}{d\xi} + \frac{s}{A_i}\tilde{w}_1 = 0, \quad \frac{d\tilde{u}_{1j}}{d\xi} - \frac{s}{A_j}\tilde{w}_1 = 0 \qquad (19)$$

From the momentum equation, equation (9), we select $\tilde{\nu}_1 = \eta^2$, so $\tilde{\omega}_1 = \eta$, and we obtain

$$D(\tilde{u}_{1i}, \tilde{u}_{1j}, \tilde{w}_1) = \frac{-F(\xi)}{2u_{0i}} \qquad (20)$$

where D is the same differential operator as in equation (16c), and where the forcing function is given by

$$F(\xi) \equiv \frac{d}{d\xi}(\tilde{u}_{0i}^2 - \tilde{u}_{0j}^2 - C_D|\tilde{w}_0|\tilde{w}_0/2) + k_i\tilde{u}_{0i}^2$$

$$- k_j\tilde{u}_{0j}^2 + (2\tilde{w}_0\bar{\tilde{u}}_0 + |\tilde{w}_0|\Delta\tilde{u}_0)s\bar{A}/A_iA_j$$

This function is known because $\tilde{u}_{0i}$, $\tilde{u}_{0j}$, and $\tilde{w}_0$ have already been determined; it is obviously of the form $e^{-2\alpha\xi}$. Since the initial conditions have already been met, $\tilde{u}_{1i}$ etc., satisfy homogeneous initial conditions, and since the differential operator in equation (20) is

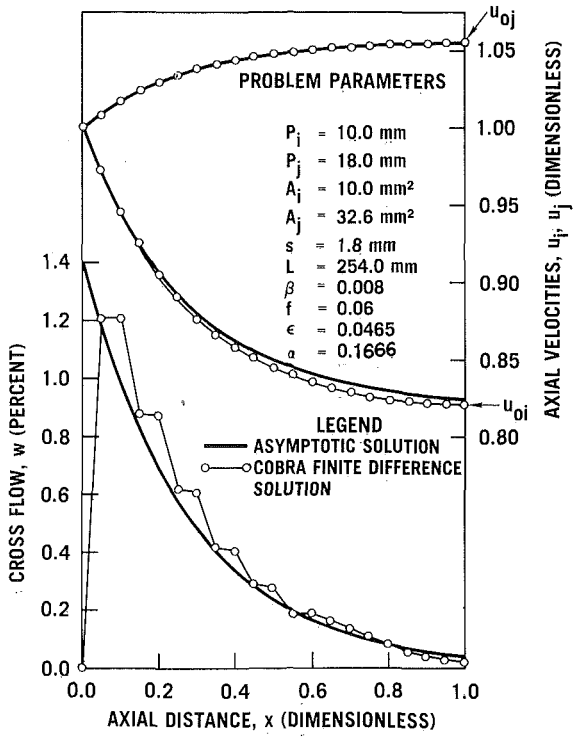

Fig. 4

the same as previously, the homogeneous solutions are of the form $e^{-\alpha\xi}$. The particular solution has the same form as the forcing function, so including the higher-order terms, the solutions are as follows:

$$u_i(\xi) \sim u_{0i} + (u_i^* - u_{0i})e^{-\alpha\xi} + \eta^2 B_i(e^{-\alpha\xi} - e^{-2\alpha\xi})$$

$$u_j(\xi) \sim u_{0j} + (u_j^* - u_{0j})e^{-\alpha\xi} + \eta^2 B_j(e^{-\alpha\xi} - e^{-2\alpha\xi})$$

$$w(\xi) \sim \alpha\frac{A_i}{s}(u_i^* - u_{0i} + \eta^2 B_i)e^{-\alpha\xi} - 2\alpha\eta^2\frac{A_i}{s}B_i e^{-2\alpha\xi}$$

where B_i and B_j are complicated algebraic expressions containing the drag coefficient, C_D. It can be shown that the constants B_i and B_j are proportional to $1/\eta^2$ times functions of $(u_i^* - u_{0i})^2$ and $(u_j^* - u_{0j})^2$ so that the solution is independent of η as previously. In the present examples, the terms of $0((u_i^* - u_{0i})^2)$ are too small to affect the solution significantly and were, therefore, not included in the figures.

Case II: Two-Point Boundary Value Problem For N Channels

In this problem the reduced solution is obtained from equations (5–7) in the limit as $\epsilon \to 0$. This implies that the cross-flow velocities, w_k, are zero (equation (5)) and, consistently, that the pressure differences between subchannels vanish (equation (7)). The boundary conditions are that

$$p_i(0) = 0, \quad p_i(1) = -1, \quad i = 1, 2, \ldots, N \tag{21}$$

which can be met by the reduced pressure function

$$p_0(x) = -x$$

With this function, the outer pressure gradient is $dp_0/dx = -1$; thus, as $\epsilon \to 0$, equation (6) becomes

$$(\rho u_0^2 f_0)_i + C_{ik}(s\beta\bar{u}_0\Delta u_0)_k = A_i(1 + g)$$

Or, in matrix notation,

$$[F_0]\{u_0^2\} = 2(1 + g)\{A\} \tag{22}$$

where F_0 is an $N \times N$ matrix involving the friction and mixing factors. In the case of two subchannels i and j the equation is written as

$$\begin{bmatrix} 2P_i f_{0i} + s\beta & -s\beta \\ -s\beta & 2P_j f_{0j} + s\beta \end{bmatrix} \begin{Bmatrix} u_{0i}^2 \\ u_{0j}^2 \end{Bmatrix} = 2(1 + g) \begin{Bmatrix} A_i \\ A_j \end{Bmatrix}$$

Equation (22) is sufficient to determine the u^2's directly when the friction factors are constants. If velocity dependence is included then equation (22) must be solved iteratively; this can be done effectively because, as can be seen, the matrix F_0 is diagonally dominant. In this example p_0, and the constant u_{0i}'s determined from equation (22), are not only the outer solutions of the problem, but the complete solution to equations (5)–(7), as can be verified by substitution. That is, for isothermal flow in coupled channels connected to common inlet and outlet plena and having only distributed frictional losses (f can be $f(u)$, but not $f(x, u)$), the velocities in the channels are constant from inlet to outlet, as calculated from equation (22). From the physical aspects of the problem, this is almost a foregone conclusion when one considers the special boundary conditions of equations (21).

Equation (22) provides the fundamental solution to the flow in an idealized rod bundle. In a real rod bundle, there are disturbances to the flow caused by rod support fixtures at the ends of the bundle, and by rod spacers at intermediate locations. Also, when there is heat generation in the bundle, the flow is perturbed due to density and viscosity changes. Normally, all these disturbances to the flow are sufficiently small so they occur as higher-order perturbations to the fundamental flow distribution of equation (22), which is the same as the outer flow distribution of the CASE-I initial value problem with the appropriate total flow rate. The effect of disturbances at the inlet of the rod bundle can be modeled by including loss coefficients, K_i, with the friction factors in equation (6). For a single channel the pressure loss from the inlet to position x is given, in dimensional variables by

$$p(0-) - p(x) = q\left(f\frac{x}{D_H} + K\right)$$

where q is the velocity head, D_H is the hydraulic diameter, and K represents all inlet and flow-development losses. In terms of the Dirac delta function this can also be written as

$$-\frac{dp}{dx} = q\left(\frac{f}{D_H} + K\delta(x)\right)$$

or, in scaled variables for subchannel i,

$$-\frac{d(pA)_i}{dx} = (u^2(Pf + \tfrac{1}{2}\epsilon AK\delta(x)))_i$$

It is clear that the entrance loss should be of order ϵ since for long channels where $\epsilon \to 0$, the K-losses are negligible. With the foregoing modification to f, equation (6) thus accounts for entrance effects. Losses for spacers at location $x = x_\ell$ can be modeled similarly by introducing the delta function $\delta(x - x_\ell)$, and a stretched coordinate $\xi = (x - x_\ell)/\epsilon$.

The effect of the delta function is to determine the boundary conditions for the terms with the highest derivatives. The acceleration term in equation (6) is of higher order than the pressure gradient; therefore, we can write

$$-\int_{0-}^{0+} dp_i = \tfrac{1}{2}\int_{0-}^{0+} (u^2\epsilon K\delta(x))_i dx$$

or, since $p_i(0-) = 0$,

$$p_i(0^+) = \frac{-\epsilon}{2}(u^2(0)K)_i \tag{23}$$

so that for loss coefficients of order 1, the scaled inlet pressures differ from zero only by order ϵ. With the foregoing boundary conditions on the pressures equations (5)–(7) again describe the boundary value problem to be solved by asymptotic series.

For the problem with entrance losses we can formally obtain an asymptotic approximation to the solution of equations (5)–(7), using the method of composite expansions. Accordingly, to the

lowest order, we assume the expansions,

$$u_i \sim u_{0i} + \tilde{u}_i(\xi)$$

$$p_i \sim p_0(x) + \epsilon\tilde{p}_i(\xi)$$

$$w_k \sim 0 + \tilde{w}_k(\xi)$$

such that with $\omega = 1$ in equations (5)–(7), and with $\tilde{u}_i(\xi) \ll u_{0i}$, we obtain the following system of equations for the boundary layer corrections:

$$A_{(i)}\frac{d\tilde{u}_i}{d\xi} + C_{ik}(s\tilde{w})_k = 0 \tag{24}$$

$$2(Au_0)_{(i)}\frac{d\tilde{u}_i}{d\xi} + C_{ik}[s\beta(\bar{u}_0\Delta\tilde{u} + \bar{\tilde{u}}\Delta u_0) + s(\bar{u}_0\tilde{w} + \Delta u_0|\tilde{w}|/2)]_k$$

$$= -A_{(i)}\frac{d}{d\xi}\tilde{p}_i - 2(Pfu_0\tilde{u})_i \tag{25}$$

$$C_{ki}{}^T\tilde{p}_i = \tfrac{1}{2}C_D(|\tilde{w}|\tilde{w})_k \tag{26}$$

with the boundary conditions

$$\tilde{p}_i(0) = -\tfrac{1}{2}(Ku_0{}^2)_i \tag{27}$$

If we replace equation (26) with the linear resistance law, similarly as in [10],

$$C_{ki}{}^T\tilde{p}_i = (C_L\tilde{w})_k \tag{28}$$

then the foregoing system can be solved formally as follows. A pressure function which satisfies the initial conditions and which has the appropriate asymptotic limit can be written as

$$\tilde{p}_i(\xi) = \tilde{p}_i(0)e^{-\alpha\xi}$$

then, from equation (28) we obtain

$$\tilde{w}_k(\xi) = \tilde{w}_k(0)e^{-\alpha\xi}$$

where

$$\tilde{w}_k(0) = C_{ki}{}^T\tilde{p}_i(0)/C_{L(k)}$$

We assume the solution

$$\tilde{u}_i(\xi) = \frac{1}{\alpha}a_ie^{-\alpha\xi}$$

so that with $\tilde{w}_k(0)$ known, the a_i's can be determined from equation (24). Substitution of these solutions into equation (25) then results in a linear homogeneous system from which an α can be determined.

With all boundary conditions and equations satisfied, we have obtained a formal solution of the N-channel two-point boundary-value problem to the lowest order. Higher order corrections can similarly be constructed, but these will be small as illustrated in Case I.

Conclusions

It has been demonstrated that the method of asymptotic expansions is applicable to the calculation of flow distributions in rod bundles or coupled, parallel channels, and that the solutions thus obtained agree well with the traditional finite difference solutions of this problem. In the case of N-coupled channels connected to common inlet and outlet plena the isothermal velocity distributions are obtained from solving the Nth order linear, or weakly nonlinear, algebraic system (equation (22)), and a numerical eigenvalue problem if entrance effects are considered. This may lead to significant computational savings in large rod bundles. Further analysis is required to solve the problem with heat addition to the subchannels, but investigations in progress indicate that this problem can also be solved by asymptotic methods.

An important point to note is that the outer solutions of the initial value problem, CASE I, are identical to those of the two point boundary value problems, CASE II. Thus, the only difference between these problems is in the higher-order disturbances. Therefore, in slender rod bundles where the asymptotic approximation is valid, the two-point boundary value problem is obtained correctly as the outer solutions.

Acknowledgments

The author wishes to express his thanks to Prof. Forman Williams of the Applied Mechanics and Engineering Science Department of the University of California, San Diego, for his guidance and helpful comments, to Prof. D. R. Smith of the Mathematics Department for reviewing the manuscript, and to Mr. H. J. Snyder and Dr. A. F. Weinberg of General Atomic Company for their interest in this work.

References

1 Melese-d'Hospital, G. B., and Dee, J. B., "Gas-Cooled Fast Breeder Reactor Designs," *Mech. Engr.*, Vol. 18, Jan.–Feb. 1972.

2 Kjellström, B., "Studies of Turbulent Flow Parallel to a Rod Bundle of Triangular Array," AB Atomenergi, Studsvik, Sweden, Report No. AE-487, 1974.

3 Nijsing, R., and Eifler, W., "Temperature Fields in Liquid-Metal-Cooled Rod Assemblies," *Progress in Heat and Mass Transfer*, **Vol. 7**, O. E. Dwyer, ed., Pergamon Press, New York, 1973.

4 Rowe, D. S., "Measurement of Turbulent Velocity, Intensity and Scale in Rod Bundle Flow Channels," USAEC, Report BNWL-1736, Battelle Pacific Northwest Laboratory, May 1973.

5 Ramm, H., and Johannsen, K., "Prediction of Local and Integral Turbulent Transport Properties for Liquid-Metal Heat Transfer in Equilateral Triangular Rod Arrays," JOURNAL OF HEAT TRANSFER, TRANS. ASME, Series C, Vol. 26, May 1975.

6 Trupp, A. C., and Azad, R. S., "The Structure of Turbulent Flow in Triangular Array Rod Bundles," *Nuclear Engineering and Design*, Vol. 32, 1975, pp. 47–84.

7 Lewis, M. J., and Buettiker, P., "Momentum Losses and Convection Heat Transfer in Rod Bundles—An Overview," *Nuclear Engineering and Design*, Vol. 31, 1974, pp. 351–362.

8 Rowe, D. S., "COBRA-II: A Digital Computer Program for the Thermal-Hydraulic Subchannel Analysis of Rod Bundle Nuclear Fuel Elements," USAEC, Report BNWL-1229, Battelle Pacific Northwest Laboratory, Feb. 1970.

9 Nijsing, R., and Eifler, W., "A Computation Method for the Steady-State Thermohydraulic Analysis of Fuel Rod Bundles With Single Phase Cooling," *Nuclear Engineering and Design*, Vol. 30, 1974, pp. 145–185.

10 Rowe, D. S., "A Mathematical Model for Transient Subchannel Analysis of Rod-Bundle Nuclear Fuel Elements," JOURNAL OF HEAT TRANSFER, TRANS. ASME, Series C, Vol. 74, May 1973.

11 Gosman, A. D., et al., "The SABRE Code for Prediction of Coolant Flows and Temperatures in Pin Bundles Containing Blockages," Atomic Energy Establishment, Winfrith, England, Report AEEW-R-905, 1973.

12 Eifler W., and Nijsing, R., "The Decay of Disturbances of the Velocity Fields in Rod-Bundles," *Atomwirtschaft*, Apr. 1975, pp. 177–179 (in German).

13 Castellana, F. S., et al., "Single-Phase Subchannel Mixing in a Simulated Nuclear Fuel Assembly," *Nuclear Engineering and Design*, Vol. 26, 1974, pp. 242–249.

14 Van Dyke, M., *Perturbation Methods in Fluid Mechanics*, Academic Press, New York, 1964.

15 Cole, J. D., *Perturbation Methods in Applied Mathematics*, Blaisdell Publishing Co., Waltham, Mass., 1968.

16 Kumar, I. J., "Recent Mathematical Methods in Heat Transfer," in *Advances in Heat Transfer*, Vol. 8, J. P. Hartnett and T. F. Irvine, Jr., eds., Academic Press, New York, 1972.

17 Nayfeh, A. H., *Perturbation Methods*, Wiley, New York, 1973.

18 O'Malley, R. E., Jr., *Introduction to Singular Perturbations*, Academic Press, New York, 1974.

Leonardo Goldstein, Jr.
E. M. Sparrow

Department of Mechanical Engineering,
University of Minnesota,
Minneapolis, Minn.

Experiments on the Transfer Characteristics of a Corrugated Fin and Tube Heat Exchanger Configuration

Local and average air-side transfer coefficients have been measured for a one-row corrugated fin and tube heat exchanger configuration. The measurements were accomplished via the heat-mass transfer analogy in conjunction with the naphthalene sublimation technique. The local transfer coefficients revealed the presence of several vortex systems which are activated and strengthened with increasing Reynolds number. The vortices serve to augment the transfer coefficients. The windward or leeward orientation of the facets of the corrugated wall was found to have a decisive effect on the transfer characteristics, with appreciably higher transfer rates prevailing on the windward facets. The average transfer coefficients were compared with those for a corresponding plane-walled heat exchanger configuration. The comparison showed that the augmentation due to the corrugated fin surface increased with Reynolds number. At a Reynolds number of 1000, the average coefficient for the corrugated fin system was about 45 percent greater than that for the plane fin system.

Introduction

In recent years, considerable interest has been focused on techniques for increasing (i.e., augmenting) convective transfer coefficients in heat transfer devices, as is evidenced by the surveys reported in [1, 2].[1] In particular, augmentation techniques have been employed to improve the heat transfer performance of plate fin and tube heat exchangers. Such a heat exchanger consists of a set of equally spaced parallel plates and an array of tubes which pass perpendicularly through the plates. Among numerous other applications, plate fin and tube heat exchangers are most widely employed in air-conditioning equipment.

The most common augmentation technique for plate fin and tube heat exchangers is the use of corrugated fins instead of plane fins. The corrugated fins are, in essence, plates that have been fabricated with a periodic waviness in the streamwise direction. In view of the widespread use of corrugated fin and tube heat exchangers, it is remarkable that the authors were unable to find any information in the open literature about their convective transfer characteristics.

The present research was undertaken to investigate and report on the transfer characteristics of corrugated fin and tube heat exchangers. The objectives of the work were to determine local air-side transfer coefficients from which transport mechanisms can be deduced and also to obtain average air-side transfer coefficients as a guide to design. The difficulties of making local temperature and/or heat transfer measurements on thin (~0.15 mm), closely spaced (~1.5 mm) corrugated fins motivated consideration of the analogy between heat and mass transfer. Among a number of mass transfer approaches that were examined, the naphthalene sublimation technique appeared most suitable for the fulfillment of the objectives of the research.

The apparatus that was designed and constructed was a mass transfer model of a one-row corrugated fin and tube heat exchanger configuration. The corrugated fins were modeled by naphthalene plates. The amplitude and wavelength of the naphthalene surface corrugations were patterned after one of the corrugated fin designs employed in air-conditioning applications. The naphthalene plates were cast in specially designed molds which, together

[1] Numbers in brackets designate References at end of paper.

Contributed by the Heat Transfer Division for publication in the JOURNAL OF HEAT TRANSFER. Manuscript received by the Heat Transfer Division August 20, 1975. Paper No. 76-HT-V.

with the casting technique, ensured that the plate surfaces possessed the desired shape and smoothness. A pair of such plates, together with an array of disks which served both to model the tubes and as separators between the plates, constituted the test section.

Local mass transfer rates (and mass transfer coefficients) were determined from measurements of the surface contour of the naphthalene plates before and after a data run. Results for the average transfer rate and the average transfer coefficient were obtained by weighing the naphthalene plates before and after a run. Mass balances were closed by comparing the surface integral of the local transfer rates with the overall transfer rate determined from the weighings.

The local and average transfer coefficients will be presented in dimensionless form in terms of the Sherwood number, which is the mass transfer analogue of the Nusselt number. In addition, mass transfer ratios were evaluated which will facilitate a comparison of the contributions of different portions of the corrugated fin to the overall mass transfer rate. The results will be parameterized by the Reynolds number. The Schmidt number (analogous to the Prandtl number) was 2.5.

Experimental Apparatus and Procedure

The description of the experimental apparatus is facilitated by reference to Figs. 1 and 2. The first of these figures is a schematic side view of the test section, and the second is a plan view of the corrugated fin and tube heat exchanger configuration.

The corrugated-walled flow passage, as seen in Fig. 1, is bounded by the naphthalene plates. Each of the corrugated bounding surfaces consists of four facets. The successive facets on each surface will be designated as 1, 2, 3, and 4, with facet number 1 situated adjacent to the inlet and facet number 4 situated adjacent to the exit. The slope α of the facets relative to the horizontal was approximately 21 deg (more precisely, α was 21 deg 9 min). The traces of the peaks and valleys of the corrugations are indicated in Fig. 2.

The channel height H was set by a row of spacers which served to model the tubes of the heat exchanger. These spacers were specially fabricated aluminum disks with top and bottom surfaces precisely contoured to mate with the respective peak and valley of the lower and upper corrugated plates. The spanwise spacing between the disks is S. Although the disks served to faithfully model the fluid mechanics of the tubes in a fin and tube heat exchanger, they did not participate directly in the mass transfer process. The lateral area of the tubes in the present experiments was about seven percent of the total fin and tube transfer area.

To provide a well defined hydrodynamic inlet condition, the upstream end of the test section was set into a slot in a baffle plate as shown in Fig. 1. The upstream edges of the naphthalene plates were flush with the upstream face of the baffle. To guard against extraneous mass transfer during a data run, all faces and edges of each naphthalene plate were covered with pressure-sensitive tape, except for the corrugated surface which bounded the flow channel.

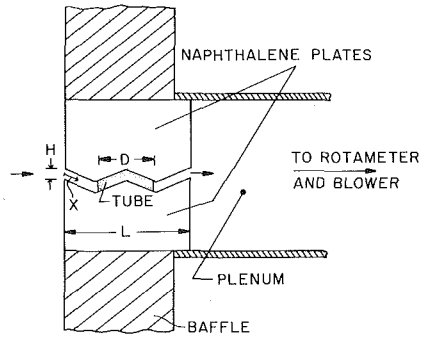

Fig. 1 Schematic side view of the test section

During a data run, air from the laboratory room was drawn through the test section by a blower situated at a downstream location. After passing through the test section and an adjacent downstream plenum, the flow was metered by a rotameter from where it passed into an exhaust system which vented to the outdoors at the roof of the building. The outside exhaust ensured that the laboratory room was always free of naphthalene vapor. The room was temperature controlled at about 20°C. The rotameter used for flow metering had been calibrated by using a volume displacement method and is believed to be accurate to well within 1 percent over its entire range.

The fabrication of the corrugated-surfaced naphthalene plates is an ingredient that is essential to the execution of the research. The plates were cast in especially designed molds. Two molds were employed, respectively, for the upper and lower bounding walls of the flow channel. The walls of each mold enclosed a rectangular cavity whose top was left open for pouring of the molten naphthalene. Corrugations were cut into one of the surfaces of the mold by means of a horizontal-end milling machine and a special form cutter. All of the active mold surfaces were of aluminum and were hand polished and lapped to a high degree of smoothness. The molds were fitted with auxiliary parts which ensured correct alignment. Once poured, the molten naphthalene was allowed to solidify under air cooling conditions, with additional molten material being added to compensate for contraction. The removal of a cast plate from its mold was accomplished without the use of lubricants.

Prior to a data run, the naphthalene plates, sealed and wrapped to prevent sublimation, were left overnight in the laboratory room to attain thermal equilibrium. Immediately before a run, surface contour measurements were made and the plates were weighed. The test section was then assembled and the air flow initiated. The

Nomenclature

D = tube diameter
D_h = hydraulic diameter, equation (7)
$\mathcal{D}$ = diffusion coefficient
G = mass velocity at minimum flow area
H = channel height
K = local mass transfer coefficient, equation (6)
$\overline{K}$ = average mass transfer coefficient, equation (8)
L = projected length of channel, Figs. 1 and 2
L^* = length measured along sloping facets, $L/\cos\alpha$
$\dot{M}'(x)$ = spanwise-integrated mass transfer rate at axial station x
$\dot{M}(x)$ = surface-integrated mass transfer rate between $x = 0$ and $x = x$
$\dot{M}_j$ = mass transfer rate for facet j
$\dot{m}$ = local mass transfer rate/area
Re = Reynolds number, D_hG/ν
S = spacing between tube centers
Sc = Schmidt number
$\overline{\mathrm{Sh}}$ = local Sherwood number, $\overline{K}D_h/\mathcal{D}$
Sh = average Sherwood number, $KD_h/\mathcal{D}$
x = streamwise coordinate, Figs. 1 and 2
y = spanwise coordinate, Fig. 2
α = slope angle of facets
ν = kinematic viscosity
ρ_n = concentration of naphthalene vapor

Subscripts

be = exit bulk
bi = inlet bulk
bx = local bulk
lo = lower wall
up = upper wall
w = at the wall

duration time of a run ranged from about 2200 to 6500 s, depending on the Reynolds number. The duration time was limited so as to avoid excessive sublimation which might have caused excessive changes in the channel dimensions (the average sublimation from each plate was limited to about 0.035 mm). Immediately after the conclusion of a run, the plates were weighed and surface contour measurements were performed.

The measurements of surface contour were carried out with the aid of a sensitive dial gage having a smallest scale division of 0.00005 in. (~0.001 mm). The dial gage was mounted on a fixed strut that overhung a movable coordinate table which could be traversed in two directions in the horizontal plane. To accommodate the dial gage to the sloping facets of the corrugated-walled naphthalene plates, the coordinate table was fitted with a sloping ramp which served to position pairs of facets in a horizontal plane (i.e., facets 1 and 3 or facets 2 and 4 were simultaneously in a horizontal plane).

The surface contour traverses were made in the typical section outlined by the dashed lines in Fig. 2. This is one of the symmetry regions that are distributed across the span of the test section. The measurement sequence was such that the stylus of the dial gage was traversed in the spanwise direction (i.e., y-direction) at each of a succession of fixed streamwise stations characterized by x. Separate measurements were made on the upper and lower bounding surfaces of the channel. Measurements were made at as many as 1000 surface locations.

The change in the mass of each naphthalene plate which occurred during a data run was measured by a precision balance capable of detecting 0.05 mg. Typically, the mass transfer from each plate was about 75 mg.

Other quantities measured during the experiments were the duration time of a data run (using a digital timer) and the temperature of the air flow (using a calibrated copper constantan thermocouple and a digital millivoltmeter). Detailed information about the apparatus, about the design, fabrication, and use of the molds, and about the experimental procedure is available in [3].

The dimensions H, L, S, and D were chosen to be equal to those of a one-row *plane* fin and tube heat exchanger configuration that was investigated in [4] by means of the naphthalene sublimation technique. This equality of dimensions enables an assessment to be made of the augmentation characteristics of the corrugations.

It is common practice to characterize fin and tube heat exchangers by the number of fins per inch, by the physical dimensions of the fins and tubes, and by the face velocity. On the other hand, the present authors prefer to employ dimensionless quantities to achieve greater generality. The dimensionless parameters characterizing the present experiments are as follows:

$$\frac{H}{D} = 0.193, \quad \frac{S}{D} = 2.50, \quad \frac{L}{D} = 2.17$$

$$135 \leq \text{Reynolds number} \leq 1200$$

The actual physical dimensions are: H = 1.65 mm (0.065 in.), S = 21.3 mm (0.840 in.), L = 18.5 mm (0.727 in.), and D = 8.53 mm (0.336 in.).

Experimental Data and Evaluation of Results

The data reduction procedures will now be briefly outlined. Additional details can be found in [3].

The local differences between the surface contour measurements before and after a data run were employed, after correction, as the basis for the local mass transfer rates and transfer coefficients. Three corrections were carefully applied. The first and second were for natural convection mass transfer that occurred during the time when surface contour measurements were being made and when the test section was being assembled. These natural convection corrections were determined from auxiliary in situ experiments. The third correction was for changes in surface elevation inherent in removing and subsequent repositioning of the naphthalene plate on the coordinate table. This positioning correction was made by employing surface contour measurements under the spacer disks. Inasmuch as these surface locations are shielded from mass transfer during a data run, any measured changes in their elevation can be ascribed either to natural convection or to positioning. Once the natural convection correction is applied, the residue can be identified as the positioning correction.

The accuracy of the corrections is supported by the closure of the mass balances. As noted earlier, mass balances were evaluated by comparing the overall mass transfer obtained from weighing with that obtained by numerical integration of the local mass transfer distribution. The closure of the mass balances ranged from about 0.5 to 8.5 percent. In view of the complex local mass transfer distributions that had to be integrated, the aforementioned closure is believed to be highly satisfactory.

From a knowledge of the local change in surface elevation $\delta(x, y)$ and duration time t_0 of the data run, the local rate of mass transfer $\dot{m}(x, y)$ per unit area was evaluated from

$$\dot{m}(x, y) = \delta(x, y)\rho_s/t_0 \tag{1}$$

where ρ_s is the density of solid naphthalene. Next, the spanwise-integrated mass transfer rate $\dot{M}'(x)$ at a given axial station x was obtained by evaluating

$$\dot{M}'(x) = \int_0^{S/2} \dot{m}(x, y)dy \tag{2}$$

The integral is extended over the span of the typical element delineated by the dashed lines in Fig. 2. At surface locations beneath the tubes, $\dot{m}(x, y)$ was set equal to zero. The integration was separately performed for the upper and lower bounding surfaces. Then, the rate of mass transfer $\dot{M}(x)$ from each fin surface between $x = 0$ and $x = x$ was found by integration of the corresponding $\dot{M}'(x)$ values

$$\dot{M}(x) = \int_0^x \dot{M}'(x)dx \tag{3}$$

The local mass transfer is driven by the difference between the local concentrations of naphthalene vapor at the wall and in the bulk. These quantities are, respectively, denoted by $\rho_{n,w}$ and $\rho_{n,\text{bx}}$. The former is a constant at all positions on the wall, inasmuch as the wall temperature is constant. It was evaluated from the Sogin [5] vapor pressure-temperature relation for naphthalene in conjunction with the perfect gas law. The local bulk concentration was determined from a mass balance.

$$\rho_{n,\text{bx}} = \rho_{n,\text{bi}} + [\dot{M}_{\text{up}}(x) + \dot{M}_{\text{lo}}(x)]/\dot{Q} \tag{4}$$

The subscripts *up* and *lo* refer, respectively, to the upper and lower bounding walls. $\dot{Q}$ is the volume flow passing through the typical element, and $\rho_{n,\text{bi}}$ is the inlet bulk concentration (= 0 in these experiments). The log-mean concentration difference between the inlet (i) and exit (e) was calculated from

$$(\Delta\rho_n)_m = \frac{(\rho_{n,w} - \rho_{n,\text{bi}}) - (\rho_{n,w} - \rho_{n,\text{be}})}{\ln((\rho_{n,w} - \rho_{n,\text{bi}})/(\rho_{n,w} - \rho_{n,\text{be}}))} \tag{5}$$

Local mass transfer coefficients K and Sherwood numbers Sh for surface locations on each plate were obtained from the definitions

$$K = \frac{\dot{m}}{\rho_{n,\text{w}} - \rho_{n,\text{bx}}}, \quad \text{Sh} = \frac{KD_h}{\mathcal{D}} \tag{6}$$

in which $\mathcal{D}$ is the naphthalene-air diffusion coefficient and D_h is the hydraulic diameter. The former was evaluated via the Schmidt number Sc = $\nu/\mathcal{D}$, where Sc = 2.5 [5] and ν is the kinematic viscosity of air. For the hydraulic diameter, the Kays and London [6] definition was used

$$D_h = \frac{4\ (\text{minimum flow area})\ (\text{streamwise length})}{\text{transfer surface area}} \tag{7}$$

where the denominator was evaluated using both the fin and tube surface areas.

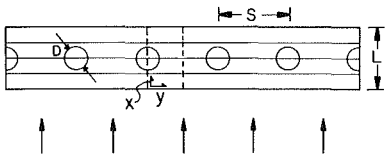

Fig. 2 Plan view schematic of the test section

Average transfer coefficients $\overline{K}$ and Sherwood numbers $\overline{\mathrm{Sh}}$ were also evaluated

$$\overline{K} = \frac{\dot{M}_{\text{total}}/A_{\text{total}}}{(\Delta\rho_n)_m}, \qquad \overline{\mathrm{Sh}} = \frac{\overline{K}D_h}{\mathcal{D}} \tag{8}$$

in which $\dot{M}_{\text{total}}$ is the total mass transfer rate from both surfaces and A_{total} is the total transfer surface area of the fins.

In the presentation of results, the Reynolds number will be used as a primary parameter. It was evaluated from the Kays-London definition [6]

$$\mathrm{Re} = D_h G/\mu \tag{9}$$

where G is the mass velocity at the minimum flow area and D_h is from equation (7). For purposes of reference, it may be noted that the channel Reynolds number (with $D_h = 2H$ and G corresponding to the channel cross section) is

$$\mathrm{Re}_{\text{channel}} = 0.91\ \mathrm{Re} \tag{10}$$

There is, therefore, only a small difference between the channel Reynolds number and the Kays-London Reynolds number.

In addition to the quantities discussed here, the mass transfer rate for each facet as a whole was also evaluated. Let $\dot{M}_j$ denote the facet mass transfer rate, where j = 1,2,3, 4 is the facet number. Then,

$$\dot{M}_j = \int_j \dot{m}(x, y)dxdy \tag{11}$$

Results and Discussion

The presentation of results will begin with the local transfer coefficients, followed by the spanwise-integrated mass transfer results, the facet-integrated mass transfer results and, finally, the average transfer coefficients for the entire exchanger.

Local Results. The local mass transfer coefficients, expressed in terms of the local Sherwood number, are presented in Figs. 3, 4, and 5, respectively, for Reynolds numbers of 989, 606, and 209. Each figure has an (*a*) and a (*b*) part. The (*a*) part contains results for the lower bounding wall and the (*b*) part contains results for the upper bounding wall. In turn, each part is made up of a succession of graphs, each of which corresponds to a given axial station x/L^*. In each graph, the spanwise distribution of the local Sher-

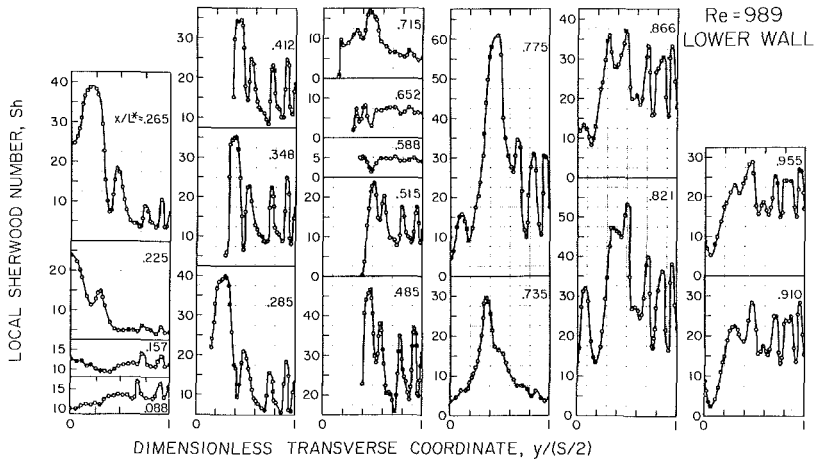

Fig. 3(*a*) Distributions of local Sherwood number on the lower wall for Re = 989, Sc = 2.5

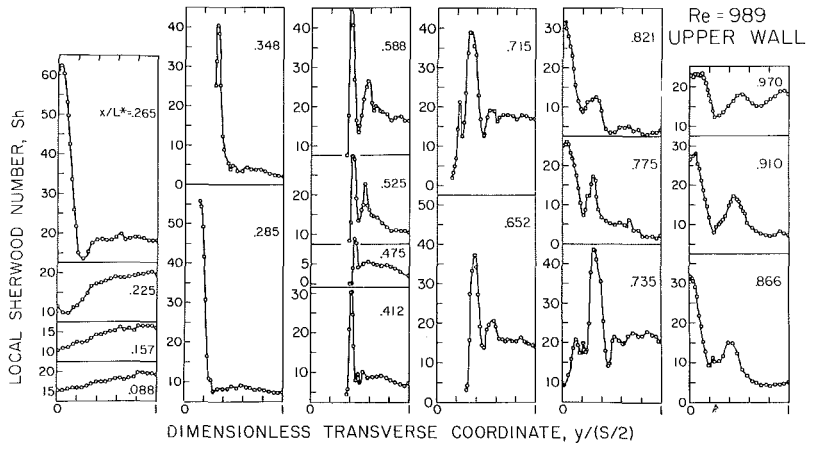

Fig. 3(b) Distributions of local Sherwood number on the upper wall for Re = 989, Sc = 2.5

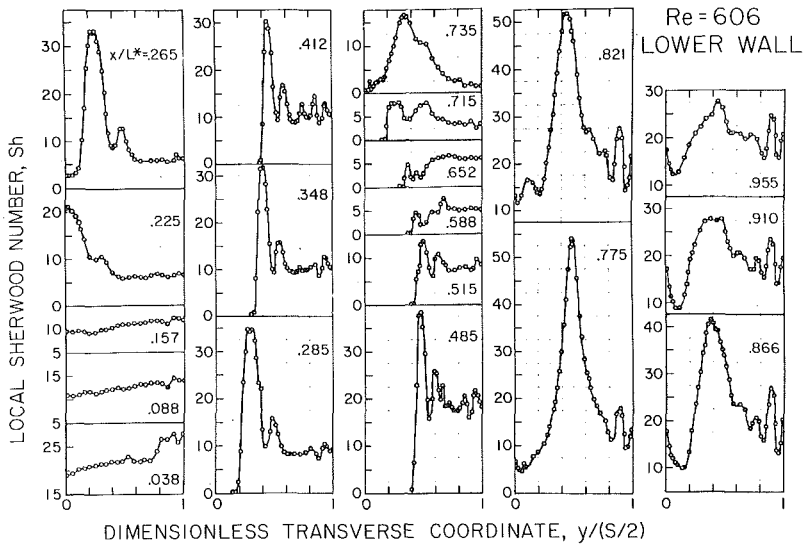

Fig. 4(*a*) Distributions of local Sherwood number on the lower wall for Re = 606, Sc = 2.5

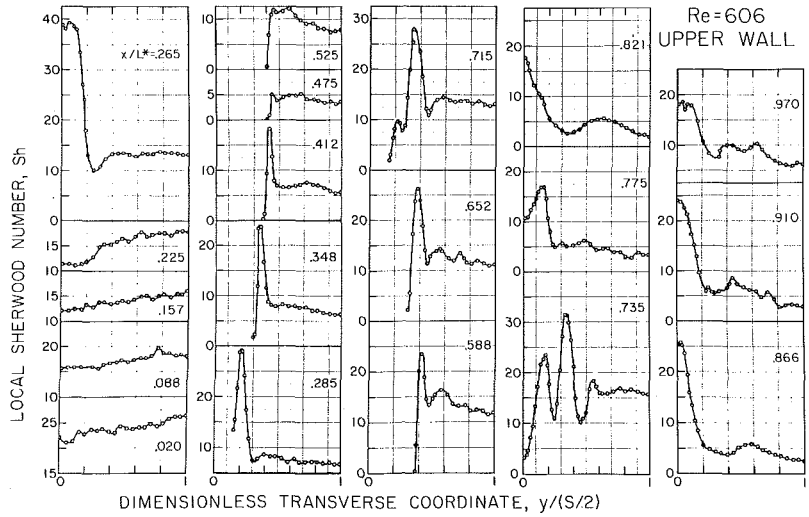

Fig. 4(*b*) Distributions of local Sherwood number on the upper wall for Re = 606, Sc = 2.5

wood number is plotted as a function of the dimensionless spanwise coordinate $y/(S/2)$. The quantity L^* is the overall streamwise length of the fin surface measured along the sloping surfaces of the facets. Therefore, in terms of the length L depicted in Figs. 1 and 2

$$L^* = L/\cos\alpha \tag{12}$$

Surface locations on the first facet are characterized by x/L^* values between 0 and 0.25, those on the second facet by x/L^* between 0.25 and 0.5, etc. At axial stations situated at the side of the tube, the distribution curves do not extend all the way to $y = 0$ owing to the fact that a part of the fin is blocked out by the tube. Each graph has its own ordinate range to accommodate the local values of the Sherwood number.

Attention will first be turned to Fig. 3, which corresponds to the highest Reynolds numbers (~1000) for which local measurements were made. As will be seen later, some of the phenomena in evidence at this Reynolds number are muted at lower Reynolds numbers. Examination of Figs. 3(a) and 3(b) reveals a highly complex set of distribution curves which require lengthy and thoughtful study for their understanding. These curves contain some of the same features that were previously identified in [4] for the plane fin and tube heat exchanger, but there are a number of additional features in evidence in Figs. 3(a) and 3(b) that are suggestive of new phenomena.

In common with the plane fin case, the initial portion of the first facet lies within the regime of developing boundary layers. Just upstream of the tube, a vortex is formed which gives rise to high mass transfer rates as evidenced by the peak in the distribution curves which first appears at stations near $x/L^* = 0.25$. It is interesting to note that the first facet of the upper wall is shielded from the effect of the vortex by the ridge which is formed by the corrugation. On the lower wall, there is evidence of a secondary vortex which causes a lower peak than that of the primary vortex.

The results for positions on the second facet ($0.25 < x/L^* < 0.50$) are markedly affected by the corrugated nature of the channel walls. From the standpoint of the airflow, the second facet of the upper surface appears to be the leeward side of a ridge, whereas the second facet of the lower surface appears to be the wind-

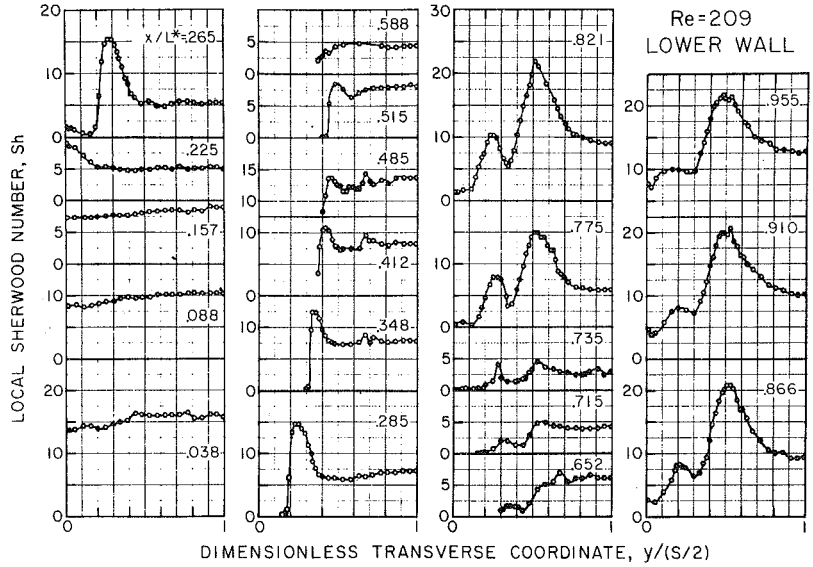

Fig. 5(*a*) Distributions of local Sherwood number on the lower wall for Re = 289, Sc = 2.5

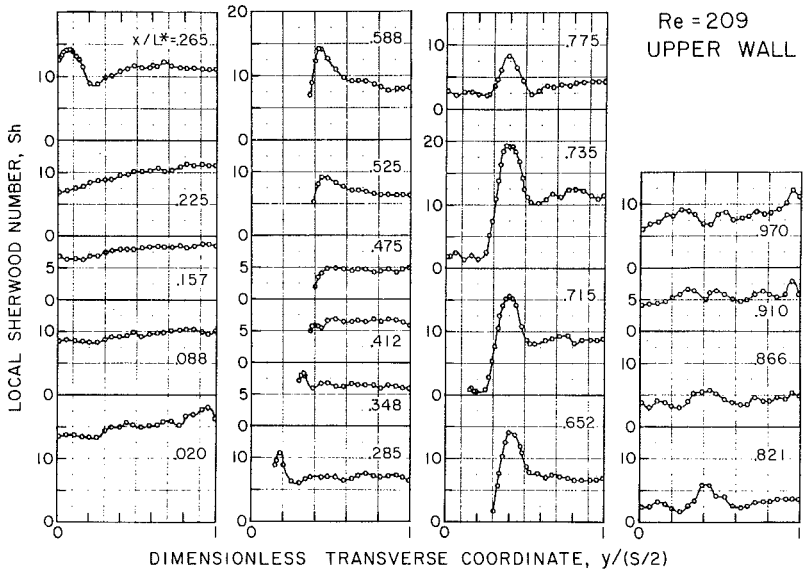

Fig. 5(*b*) Distributions of local Sherwood number on the upper wall for Re = 289, Sc = 2.5

ward side of a ridge (see Fig. 1). This distinction has a profound effect on the mass transfer. On the upper surface, the transfer coefficients are quite low, except for the tall peak which is caused by the vortex that is swept from the front of the tube around the side. On the other hand, the distribution curves for the lower surface show a series of peaks and valleys. The tallest of the peaks and, perhaps, its neighbor are caused by the aforementioned vortices from the front of the tube. The other peaks and valleys are due to Görtler vortices, the origin of which will now be briefly discussed.

Whenever a flow passes over a surface which has concave curvature in the flow direction, a centrifugal force is developed which tends to lift the fluid off the surface. The lift-off occurs selectively at discrete spanwise locations. To satisfy mass conservation, there are fluid inflows toward the surface at spanwise locations between those at which lift-off occurs. The just-mentioned lift-offs and inflows, when superimposed on the streamwise flow, give rise to a corkscrew-like pattern which is well portrayed in Fig. 17.32(b) of Schlichting [7].

The third facet ($0.5 < x/L^* < 0.75$) is a leeward surface on the lower wall and a windward surface on the upper wall. On the former, the transfer coefficients are substantially reduced, except near its trailing edge (i.e., near $x/L^* \sim 0.75$) where the vortex from the front of the tube appears to have reattached and causes a distinct peak. The transfer coefficients on the upper surface are higher, and the peaks due to the vortices from the front of the tube are in evidence. There are only traces of the Görtler vortices.

The transfer coefficients on the fourth facet ($0.75 < x/L^* \leq 1$) are affected by the wake of the tube, as well as by the other phenomena already discussed. There is a strong vortex situated directly behind the tube which, evidently, impinges on the upper wall and causes a peak at $y/(S/2) = 0$. Laterally displaced from this vortex is another vortex system in the wake, as evidenced by the

innermost peaks on the lower wall at $x/L^* = 0.821$ and 0.866. The vortex from the front of the tube continues to augment the transfer coefficients on both walls, but to a greater extent on the lower wall. This vortex may also interact with vortices shed from the side of the tube. The Görtler vortices are very active on the lower wall.

The foregoing description of the causal phenomena which contribute to shaping the local results is based both on a detailed study of the distribution curves and on careful examination of the naphthalene plates. Such inspections revealed clear evidence of the cited phenomena.

The local transfer coefficients for Re = 606, as presented in Figs. 4(*a*) and 4(*b*), are qualitatively similar to those already discussed for Re = 989. There is, however, a definite muting of the action of the vortices owing to the strengthened role of viscosity. As the Reynolds number is further reduced, the manifestations of certain phenomena disappear altogether. This can be seen in Figs. 5(*a*) and 5(*b*), which pertain to Re = 209. In these figures, the Görtler vortices no longer appear, and some of the wake effects are no longer in evidence.

Integrated and Average Results. It is of interest to inquire about the contributions of different parts of the fin to the overall mass transfer rate. This question will be examined from several viewpoints. First, consideration is given to the rate of mass transfer at different axial stations. To present this information, we form the ratio

$$\frac{\text{mass transfer rate at axial station } x}{\text{average of the transfer rates at all axial stations}} \tag{13}$$

The numerator is the quantity $\dot{M}'(x)$ that is defined by equation (2), whereas the denominator is the average value of $\dot{M}'(x)$; that is

$$\frac{1}{L^*}\int_0^{L^*} \dot{M}'(x)dx \tag{14}$$

Equation (13) was separately evaluated for the lower and upper bounding walls, and the results are plotted in Figs. 6(*a*) and 6(*b*), respectively. The figures show that the boundary layer regime that prevails on the first facet is an important factor in bringing about high rates of mass transfer, as is the intense vortex action on the fourth facet of the lower wall. Axial stations on the second and third facets show relatively low mass transfer rates, and this is in part due to the diminished fin area caused by the presence of the tubes.

Particular insights are gained by comparing Figs. 6(*a*) and 6(*b*). From such a comparison, it is seen that for any given facet, the relative transfer rates are higher on either the upper wall or the lower wall depending on whether the respective surfaces are windward or leeward. For instance, on facet number one, the upper wall is windward and the lower wall is leeward, and the former exhibits higher transfer rates. This distinction between windward and leeward is especially important on the fourth facet. In fact, it is the high transfer rates on the windward fourth facet which contribute a major portion of the augmentation provided by the corrugated fin relative to the plane fin, as can be seen by comparing Fig. 6 with Fig. 6 of [4].

Table 1 Fractional mass transfer contributions of each facet

		Facet Number			
Re	Wall	1	2	3	4
989	Lower	0.292	0.239	0.101	0.368
	Upper	.406	.138	.241	.215
	Two-Sided	.346	.191	.167	.296
606	Lower	0.314	0.204	0.082	0.400
	Upper	.460	.154	.217	.169
	Two-Sided	.381	.181	.145	.293
209	Lower	0.393	0.208	0.094	0.306
	Upper	.439	.186	.211	.164
	Two-Sided	.415	.197	.150	.238

As a final remark about Fig. 6, it is interesting to note that when the results are plotted in the ratio defined by equation (13), the axial distributions are not very sensitive to the Reynolds number.

Further insights may be gained by considering the contribution of each facet to the overall rate of mass transfer. This information is contained in the ratios

$$(\dot{M}_j/\dot{M}_{\text{total}})_{\text{up}} \text{ and } (\dot{M}_j/\dot{M}_{\text{total}})_{\text{lo}} \tag{15}$$

where j is the facet number and $\dot{M}_{\text{total}}$, as used in equation (15), are the respective overall transfer rates for the upper and lower walls. These ratios give the fractional contribution of each facet.

Since, in practice, a given facet would have both upper and lower surfaces that bound adjacent channels, the average performance of such a two-sided facet is of practical interest. The fractional contribution of such a two-sided facet is given by

$$(\dot{M}_{\text{up}} + \dot{M}_{\text{lo}})_j/\dot{M}_{\text{total}} \tag{16}$$

where now $\dot{M}_{\text{total}}$ represents the sum for both the upper and lower walls.

The fractional mass transfer contributions defined by equations (15) and (16) are listed in Table 1 for Reynolds numbers of 989, 606, and 209. Inspection of the table shows that the subdivision of the overall mass transfer rate amongst the component facets changes with Reynolds number. The first facet always makes the major contribution, but to a lesser extent at the highest Reynolds number than at the lowest Reynolds number. An opposite trend prevails for the fourth facet. The windward facets are always more effective transfer surfaces than are the leeward facets, especially at

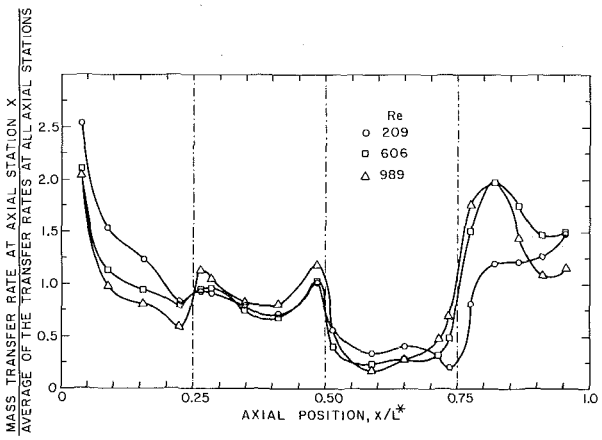

Fig. 6(*a*) Variation of the spanwise-integrated mass transfer rate along the lower wall

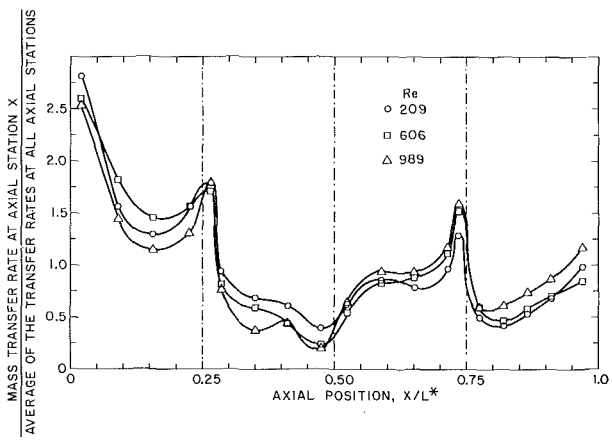

Fig. 6(*b*) Variation of the spanwise-integrated mass transfer rate along the upper wall

Table 2 Relative mass transfer rates per unit area

Re	Wall	Facet Number 1	2	3	4
989	Lower	0.998	1.152	0.485	1.259
	Upper	1.389	0.666	1.162	0.734
	Two-Sided	1.194	0.909	0.824	0.997
606	Lower	1.072	0.985	0.393	1.369
	Upper	1.573	0.741	1.048	0.577
	Two-Sided	1.323	0.863	0.721	0.969
209	Lower	1.344	1.000	0.453	1.044
	Upper	1.499	0.897	1.017	0.562
	Two-Sided	1.422	0.949	0.735	0.803

the higher Reynolds numbers. For the two-sided wall, there is a clear tendency for a more uniform mass transfer distribution among the facets as the Reynolds number increases.

Table 1 indicates relatively low transfer rates on facets 2 and 3. This is due, in part, to the fact that a portion of each of these facets is blocked out by the tube. To provide information on the relative rate of mass transfer *per unit transfer area* on each facet, Table 2 has been prepared. The table contains the ratio

$$\frac{(\dot{M}_j/A_j)}{(\dot{M}/A)_{\text{total}}} \tag{17}$$

where the numerator pertains to facet j and the denominator corresponds to the wall (i.e., lower, upper, or two-sided) of which that facet is a part. A table entry of 1.0 for a particular facet would indicate that the mass transfer per unit area for that facet is equal to the average for the lower, upper, or two-sided walls, whichever is relevant. Entries that are greater or less than one indicate transfers per unit area that are, respectively, greater or less than the relevant average.

From an examination of the table, it can be seen that on a unit area basis, the windward sides of facets 2 and 3 transfer mass at or near the average rate, but that the leeward sides are substantially below average, especially at the higher Reynolds numbers. In fact, on this basis, the windward sides of facets 2 and 3 perform very much better than does the leeward side of the fourth facet.

Another assessment of the performance of the individual facets is provided by a comparison of average Sherwood numbers for the various facets. This information is available in [3].

The overall performance of the entire fin surface is represented by the average mass transfer coefficient or by its dimensionless counterpart, the average Sherwood number $\overline{\text{Sh}}$. Results for the average Sherwood number are plotted as a function of Reynolds number in Fig. 7. The results for the upper wall, the lower wall, and the two-sided wall are presented separately. At any given Reynolds number, the data point for the latter is the average of the data points for the former. The logarithmic ordinate scale tends to slightly distort this relationship between the three sets of data. Also included in the figure for purposes of comparison are the data

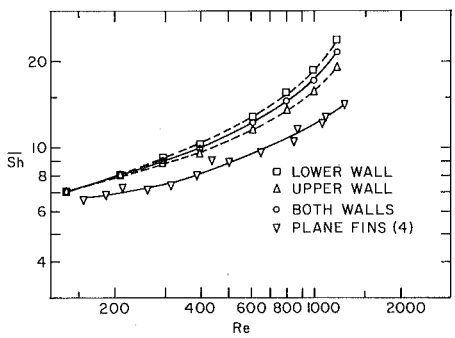

Fig. 7 Average Sherwood number results

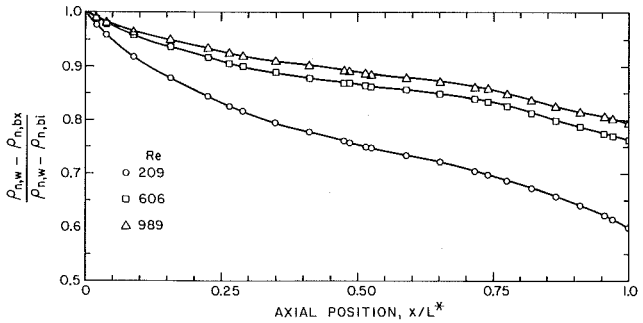

Fig. 8 Variation of the bulk concentration of the naphthalene vapor along the channel

of [4] for the plane fin and tube heat exchanger configuration.

From the figure, it is seen that the average Sherwood number increases smoothly and continuously as the Reynolds number increases. A significant part of the increase may be attributed to the activation and strengthening of the various vortex systems discussed in connection with Figs. 3, 4, and 5. The average coefficients for the lower wall are higher than those for the upper wall, partly because of the windward/leeward difference of the respective fourth facets. The spread between the results for the lower and upper walls is more marked at higher Reynolds numbers.

The augmentation effect of the corrugated fin surface may be gauged by comparing the average Sherwood number results for the two-sided corrugated fin with those for the plane fin. The figure shows that the degree of augmentation increases with the Reynolds number. At Re = 500, the average coefficient for the corrugated fin system is about 24 percent greater than that for the plane fin system, whereas at Re = 1000 the extent of the augmentation is about 45 percent. An additional factor which further increases the transfer rate for the corrugated system is its larger fin surface area.

As a final result, information is presented in Fig. 8 on the variation of the bulk vapor concentration $\rho_{n,\text{bx}}$ along the length of the flow channel. This variation is analogous to that of the bulk temperature in a heat exchanger. The ordinate is the ratio of the local wall-to-bulk concentration difference to the corresponding concentration difference at the inlet to the channel. With increasing distance from the inlet, the bulk concentration increases and the wall-to-bulk concentration decreases. Therefore, the curves drop off as x/L^* increases. The greatest drop-off occurs at the smallest Reynolds number.

Concluding Remarks

The experiments reported herein have documented the presence of a set of complex flow phenomena in the channels of a corrugated fin and tube heat exchanger configuration. Of particular interest from the standpoint of heat or mass transfer is the effect of the windward or leeward orientation of the facets which comprise the corrugated wall. The windward facets are primarily responsible for the augmentation in the transfer coefficients which is provided by the corrugated-wall exchanger relative to the plane-wall exchanger. The transfer characteristics of the leeward facets are believed to be strongly affected by flow separation. If additional augmentation is desired it would appear that efforts should be concentrated on the leeward facets.

The Sherwood number results presented here can be converted to Nusselt numbers and thereby made applicable to heat transfer situations by multiplying by the ratio $(\text{Pr}/2.5)^n$. The exponent n can be selected as 1/3 or 0.4. Furthermore, by the analogy, the present results correspond to isothermal heat transfer fins, that is, to fins having an efficiency of unity.

The results of Fig. 8 at $x/L^* = 1$, in conjunction with the heat-mass transfer analogy, enables the evaluation of the exchanger heat transfer effectiveness ϵ. For an isothermal-walled heat ex-

changer, ϵ can be expressed as

$$\epsilon = (T_{be} - T_{bi})/(T_w - T_{bi}) \tag{18}$$

Then, as shown in [3],

$$\epsilon = 1 - (\text{ordinate of Fig. 8 at } x/L^* = 1)^{\beta} \tag{19}$$

where $\beta = (\text{Pr/Sc})^{n-1}$.

Acknowledgment

Scholarship support from the Brazilian National Council of Research (CNPq) and from Pontificia Universidade Católica do Rio de Janeiro extended to Leonardo Goldstein, Jr. is gratefully appreciated. The research was supported by the National Science Foundation under grant ENG-7503221.

References

1 Bergles, A. E., "Survey and Evaluation of Techniques to Augment Convective Heat and Mass Transfer," in *Progress in Heat and Mass Transfer*, Vol. 1, Pergamon Press, 1969, pp. 331–424.

2 Bergles, A. E., "Recent Developments in Convective Heat Transfer Augmentation," *Applied Mechanics Reviews*, Vol. 26, 1973, pp. 675–682.

3 Goldstein, L., Jr., "Local Mass Transfer in Corrugated-Walled Ducts and Heat Exchanger Configurations," PhD thesis, Department of Mechanical Engineering, University of Minnesota, Minneapolis, Minn., 1975.

4 Saboya, F. E. M., and Sparrow, E. M., "Local and Average Transfer Coefficients for One-Row Plate Fin and Tube Heat Exchanger Configurations," JOURNAL OF HEAT TRANSFER, TRANS. ASME, Series C, Vol. 96, 1974, pp. 265–272.

5 Sogin, H. H., "Sublimation From Disks to Air Streams Flowing Normal to Their Surfaces," TRANS. ASME, Vol. 80, 1958, pp. 61–71.

6 Kays, W. M., and London, A. L., *Compact Heat Exchangers*, Second ed., McGraw-Hill, New York, 1964.

7 Schlichting, H., *Boundary Layer Theory*, Sixth ed., McGraw-Hill, New York, 1968.

ERRATUM

Erratum: K. A. Gardner, "Efficiency of Extended Surface," published in the JOURNAL OF HEAT TRANSFER, TRANS. ASME, Vol. 67, 1945, pp. 621–631.

Page 623, equation (7) should read: $(x/p)\sqrt{\ }$ instead of $x\sqrt{\ }$. Since this was typographical, no subsequent equations in the text are affected.

Page 624, Fig. 4, Sketch (B), equation for u_b should read: $2\sqrt{2}\ldots$ instead of $2\sqrt{2/3}\ldots$. The curve for this case ($n = -1$) is correctly drawn, however.

Page 626, equation (23): the numerator should contain tanh, not tan h. This error also is typographical and has no other effect on text or graphs.

By way of clarification, it should be added that the captions $X_e/X_b = 1$ in Figs. 5 and 6 are to be interpreted as the limiting value of X_e/X_b when the radial length of the fin $(X_e - X_b)$ becomes very small in relation to the inner radius of the fin X_b, i.e., $(X_e - X_b)/X_b \to 0$ which corresponds to $X_e/X_b \to 1$.

These errors were first pointed out to the author by Kraus of the University of South Florida in the fifties while he was writing a book on extended surfaces. No action seemed necessary to me at the time, and none was taken. In early 1975 they were rediscovered by Suryanarayana of Michigan Technological University, who prepared a Technical Note on the subject and submitted it to the JOURNAL OF HEAT TRANSFER. Subsequent correspondence led to preparation of this Erratum.

M. L. Lawson
Mechanical Engineering Department,
Ahmadu Bello University,
Zaria, Nigeria

Wen-Jei Yang
S. Bunditkul

Department of Mechanical Engineering,
The University of Michigan,
Ann Arbor, Mich.

Theory on Thermal Instability of Binary Gas Mixtures in Porous Media

A theory is developed which predicts the instability of a horizontal layer of porous medium saturated with a binary gas mixture. The lower boundary of the system is maintained at a higher temperature and the upper one at low temperature. The transport equations and coefficients are developed on the basis of kinetic theory. A linear perturbation technique is employed to reduce the governing equations for momentum, heat, and mass transfer to eigenvalue differential equations which are solved by the Finlayson method, the combination of the Galerkin method and the Routh-Hurwitz stability criterion. Only neutral stationary stability is found to occur in the system. Its criterion can be predicted by a simple algebraic equation. Both the critical Rayleigh and wave numbers for the onset of convection are governed by five independent dimensionless parameters, two of which are most influential. The critical Rayleigh number may be lower or greater than that for pure fluid layer depending upon whether thermal diffusion induces the heavier component of the mixture to move toward the cold or hot boundary, respectively. The theory compares well with the experimental results.

Introduction

Theoretical study has been performed on the Benard problem in a binary mixture of dilute gases in which an imposed vertical temperature gradient induces a concentration gradient owing to thermal diffusion or the Soret effect [1].[1] The transport equations and coefficients are developed on the basis of kinetic theory. These equations are then solved by first-order perturbation method, which leads to instability criteria. It is disclosed that instability can set in only as stationary convection in a layer of binary mixture of dilute gases owing to the action of thermal diffusion effect. This is in sharp contrast to the finding of Hurle and Jakeman [2] that the Soret effect can give rise to oscillatory instability in liquids and concentrated gases. In the mixtures of dilute gases, thermal diffusion is a destabilizing force which aids the temperature gradient to promote the occurrence of stationary instability at a critical Rayleigh number lower than 1717, the value for a pure gas layer. The destabilization of the layer due to the thermal diffusion effect is enhanced as the thermal diffusion ratio and/or the molecular weight ratio increase.

Several studies, both theoretical and experimental, have been conducted on the stability of pure fluid-saturated porous media [3–6]. The critical Rayleigh number for stationary stability in the porous medium was found to be 39.5.

Recently, an experimental study was conducted to investigate the onset of convective motion in binary gas mixtures in a thin layer of porous medium heated from below [7]. The binary gas mixtures consisted of nitrogen and helium gases at various composition, while a packed bed of tiny steel balls 0.101 cm in diameter constituted the porous medium. The Schmidt-Milverton principle [8] was employed for detecting the onset of convective currents. It was disclosed that the critical Rayleigh number for pure gas is lowered by the presence of another species of different molecular weight and has a minimum value at a certain composition of the binary mixture.

This paper extends the theory of reference [1] to the onset of convective motion in binary gas mixtures in porous media. The effect of thermal diffusion is taken into account. The perturbation technique is employed to solve the modified Darcy's equations and heat and mass transfer equations. Through the separation of vari-

[1] Numbers in brackets designate References at end of paper.

Contributed by the Heat Transfer Division for publication in the JOURNAL OF HEAT TRANSFER. Manuscript received by the Heat Transfer Division April 29, 1975. Paper No. 76-HT-T.

ables, these equations and the appropriate boundary conditions are reduced to those of an eigenvalue problem which are solved approximately by the Finlayson's method [9]. Analytical results are compared with experiments on the helium-nitrogen mixtures of different composition [7].

Analysis

Consider a large horizontal layer of porous material of thickness h saturated with a binary gas mixture. The porous medium-gas mixture system is confined between two large horizontal plates both at temperature T_b. The molecular concentration fraction (also called relative number density) of the heavier species is uniform at C_0 throughout the layer. C is defined as $n_1/(n_1 + n_2)$ where n is the number density (number of molecules-per-unit volume). The subscripts 1 and 2 denote the heavier and lighter species, respectively. The cylindrical coordinates (r, θ, z) are employed in the analysis with the origin fixed at the center of the layer and z measuring the distance normal to the plates. This coordinate system is selected for convenience in comparing theoretical results with the available test data [7], without suffering undue hardship in mathematical manipulation.

Now, the lower plate is heated to a higher temperature T_a, while the temperature of the upper plate is held at T_b. When the temperature difference $(T_a - T_b)$ is small, the gas mixture remains motionless because the buoyancy forces cannot overcome the viscous dissipation. Heat transfer in the layer occurs only by conduction. Then, the steady temperature distribution $T_B(z)$ is given by

$$T_B(z) = T_0 - az \tag{1}$$

where $T_0 = (T_a + T_b)/2$ and $a = (T_b - T_a)/h$. The subscripts B and 0 refer to the base state and average value, respectively. It is known that the temperature gradient in a binary fluid mixture induces a redistribution of concentration due to the thermal diffusion or Soret effect. If the confining plates are impermeable so that the mass flux vanishes, then the mechanical driving potential associated with ordinary (concentration) diffusion is counterbalanced by the thermal driving potential associated with thermal diffusion (or mass):

$$\frac{\partial C_B}{\partial z} = -\frac{k_T \partial T_B}{T_B \partial z} \tag{2}$$

in which k_T is the thermal diffusion ratio. Equation (2) is integrated with the aid of equation (1). The resulting expression is then expanded in terms of z and approximated by retaining only the first two terms, as

$$C_B = C_0 + ak_T z/T_0 \tag{3}$$

Here, C_0 is the initially uniform concentration prior to the application of the temperature gradient a and also represents the average of $C_B(z)$ over the entire layer.

With the aid of the thermodynamic equation of state for an ideal gas

$$P = n\mu T \tag{4}$$

the density of the mixture

$$\rho = n_1 m_1 + n_2 m_2$$

can be expressed as

$$\rho = \frac{P}{\mu T}[m_2 + (m_1 - m_2)C] = \frac{P}{\bar{R}T}[M_2 + (M_1 - M_2)C] \tag{5}$$

Here, P is the total pressure, μ the Boltzmann constant, m the molecular mass, n the total number density of the mixture ($n = n_1 + n_2$), $\bar{R}$ the universal gas constant, and M the molecular weight.

Since the mixture density is a function of both temperature and concentration, one can write a first-order Taylor-series expansion for ρ with respect to its mean value $\rho_0(T_0, C_0)$ in the form

$$\rho = \rho_0 + (\partial\rho/\partial T)_0(T - T_0) + (\partial\rho/\partial C)_0(C - C_0) \tag{6}$$

where the subscript 0 refers to the uniform state (P, T_0, C_0). With the aid of equations (4) and (5), equation (6) can be written as

$$\rho = \rho_0[1 - \beta_T(T - T_0) + \beta_c(C - C_0)] \tag{7}$$

in which β_T denotes the thermal cubical expansion coefficient and β_c relates density increases to increases in solute concentration:

$$\beta_T = 1/T_0,\ \beta_c = (m_2 n/\rho)_0(M_1/M_2 - 1) \tag{8}$$

In view of equations (1), (3), and (7), the density distribution at the base state (P, T_B, C_B) may be expressed as

$$\rho_B = \rho_0[1 + az(1 + \phi)/T_0]$$

$$\text{or } (\rho_B - \rho_0)/\rho_0 = (T_b - T_a)(1 + \phi)\frac{z}{hT_0} \tag{9}$$

where $\phi = k_T\beta_c$. The quantity ϕ is called the thermal diffusion pa-

Nomenclature

A_{ij} = parameter as defined by equation (34c)
$a = (T_b - T_a)/h$
$b = \xi/(h^2\epsilon)$
C = concentration of heavier gas, n_1/n; C_B, at steady state as defined by equation (3); C_0, initial value; C', unsteady component
C_p = specific heat at constant pressure; C_{pf}, of gas mixture; C_{pm}, of fluid-porous medium combination
$D = d/dR$
D_1 = mass diffusivity of the heavier gas
D_i = Hurwitz determinants
D_x = effective mass diffusivity, $= \epsilon D_1/1.4$
d = diameter of spherical porous material (steel balls used in experiment)
e_i = coefficients of the characteristic equation of the system of equations (33)
f = function as defined by equation (25)
g = gravitational acceleration
H' = function as defined by equation (16); $H^* = H'/k_T$; $H = H^*/f$
H_i = function as defined by equation (32c)
h = thickness of horizontal layer of porous medium
i = integer
j = integer
K = thermal conductivity; K_f, of gas mixture; K_m, of fluid-porous medium combination
k_T = thermal diffusion ratio
M = molecular weight; M_1, of heavier gas; M_2, of lighter gas
N, n = integers
m = molecular mass: m_1, of heavier gas; m_2, of lighter gas
n = number density, $= n_1 + n_2$; n_1, of heavier gas
P = total pressure; P', of pressure perturbation
Q = wave number of the disturbance; Q_c, critical wave number
$R = r/h$
$\bar{R}$ = universal gas constant
Ra = Rayleigh number; R_{ac}, critical Rayleigh number
r = radial variable in the cylindrical coordinate (r, θ, z)
Sc = schmidt number, $= \nu/D_x$
T = temperature; T_a and T_b, of the upper and lower boundaries, respectively, of the layer at steady state; T_B, steady temperature distribution in the layer; $T_0 = (T_a + T_b)/2$; T', temperature perturbation; $T^* = T'/T_0$

(Continued on next page)

rameter whose magnitude depends on concentration. However, in the present analysis it is treated as a constant corresponding to a specified concentration. The parameter is a measure of the contribution of thermal diffusion.

As the temperature difference across the layer ($T_a - T_b$) is increased, the buoyancy forces are increased. A point is reached in which the buoyancy forces counterbalance the viscous and thermal dissipation and fluid motion occurs. The onset of instability can be predicted by the solution to an eigenvalue problem derived from the continuity, modified Darcy's, energy and mass equations as follows.

Let u', v' and w' denote the velocity components in the perturbed state in the r-, θ-, and z- direction, respectively. T', C' and P' represent corresponding perturbation in temperature, concentration and pressure, respectively. The continuity equation reads

$$\frac{1}{r}\frac{\partial}{\partial r}(ru') + \frac{1}{r}\frac{\partial v'}{\partial \theta} + \frac{\partial w'}{\partial z} = 0 \tag{10}$$

Equations describing the motion of Newtonian fluid in porous media were deived by Irmay [10] and Whitaker [11] by averaging the Navier-Stokes equations over a small control volume. For low velocity, the equations reduce to modified Darcy's equations which for this analysis become

$$r\text{-component}\ \frac{1}{\epsilon}\frac{\partial u'}{\partial t} + \frac{\nu}{\xi}u' = -\frac{1}{\rho_0}\frac{\partial P'}{\partial r} \tag{11}$$

$$\theta\text{-component}\ \frac{1}{\epsilon}\frac{\partial v'}{\partial t} + \frac{\nu}{\xi}v' = -\frac{1}{\rho_0 r}\frac{\partial P'}{\partial \theta} \tag{12}$$

$$z\text{-component}\ \frac{1}{\epsilon}\frac{\partial w'}{\partial t} + \frac{\nu}{\xi}w' = -\frac{1}{\rho_0}\frac{\partial P'}{\partial z} + g(\beta_T T' - \beta_c C') \tag{13}$$

According to reference [1], the energy and mass equations can be written as

$$(\rho C_P)_m \frac{\partial T'}{\partial t} - a(\rho C_P)_f w' = K_m \nabla^2 T' - (\rho C_P)_f T_0 \frac{n}{\rho}(m_1 - m_2) D_x \nabla^2 H' \tag{14}$$

and

$$\frac{\partial C'}{\partial t} + a k_T \frac{w'}{T_0} = D_x \nabla^2 H' \tag{15}$$

respectively, in which

$$H' = C' + k_T T'/T_0 \tag{16}$$

Here, t is the time; ν, the kinematic viscosity; g, the gravitational acceleration; ϵ and ξ, the porosity and permeability of the porous medium, respectively; D_x, the effective mass diffusivity equal to $\epsilon D_1/1.4$ [11]; D_1, the mass diffusivity of the heavier species; C_p, the specific heat; and K, the thermal conductivity. The subscripts m and f refer to the porous medium-fluid combination and fluid, respectively. The second term on the R.H.S. of equation (14) accounts for the portion of the heat flux incidental to mass diffusion. To be complete, it would contain the base temperature T_B measured in absolute units and hence, for small variation from the mean temperature, the approximation of $T_B = T_0$ made within this term is not expected to lead to serious error.

Taking the divergence of equations (11), (12), and (13) and making use of the continuity equation (10), it yields

$$-\frac{1}{\rho_0}\nabla^2 P' + g\left(\beta_T \frac{\partial T'}{\partial z} - \beta_c \frac{\partial C'}{\partial z}\right) = 0 \tag{17}$$

By taking the Laplacian of equation (13), one gets

$$\frac{1}{\epsilon}\frac{\partial(\nabla^2 w')}{\partial t} + \frac{\nu}{\xi}\nabla^2 w' = -\frac{1}{\rho_0}\frac{\partial}{\partial z}(\nabla^2 P') + g(\beta_T \nabla^2 T' - \beta_c \nabla^2 C') \tag{18}$$

Equations (17) and (18) are then combined to eliminate P'. It yields

$$\left(\frac{1}{\epsilon}\frac{\partial}{\partial t} + \frac{\nu}{\xi}\right)\nabla^2 w' = g\beta_T\left(\nabla^2 T' - \frac{\partial^2 T'}{\partial z^2}\right) - g\beta_c\left(\nabla^2 C' - \frac{\partial^2 C'}{\partial z^2}\right) \tag{19}$$

Equations (14), (15), and (19) are to be solved subject to the boundary conditions

$$W' = T' = \frac{\partial H'}{\partial z} = 0 \tag{20}$$

at $z = \pm h/2$, which describe two rigid, impervious, and perfect-conducting boundaries.

The following dimensionless quantities are defined

$$Z = \frac{z}{h},\ R = \frac{r}{h},\ \tau = \frac{\nu t}{h^2}$$

$$W^* = \frac{a(\rho C_P)_f h^2}{K_m T_0} w',\ T^* = \frac{T'}{T_0},\ H^* = \frac{H'}{k_T}$$

$$b = \frac{\xi}{h^2 \epsilon},\ R_a = \frac{a\beta_T g(\rho C_P)_f \xi h^2}{\nu K_m}$$

Nomenclature

T_i = function as defined by equation (32b)
t = time
u' = velocity component in the r-direction at perturbated state
v' = velocity component in the θ-direction at perturbed state
$W^* = a(\rho C_p)_f h^2 w'/(K_m T_0)$; $W = W^*/f$
W_i = function as defined by equation (32a)
w' = velocity component in the z-direction at perturbed state
$Z = z/h$
z = axial variable in the cylindrical coordinate
β_c = solutal expansion coefficient as defined by equation (8)
β_T = thermal expansion coefficient as defined by equation (8)
$\gamma = \nu(\rho C_p)_f/K_m$
ϵ = porosity of the porous medium
θ = variable in the cylindrical coordinate
Λ_i = function as defined by equation (34a)
μ = Boltzmann constant
ν = fluid kinematic viscosity
ξ = permeability of the porous medium, $\epsilon^3 d^2/[150(1-\epsilon)^2]$
Ω_i = function as defined by equation (34b)
π_1, π_2, π_3 = parameters as defined by equation (36)
ρ = fluid density; ρ_0, at T_0; ρ_B, at T_B; ρ_f, of gas mixture; ρ_m, of fluid-porous medium combination
$\sigma = (\rho C_p)_m/(\rho C_p)_f$
$\tau = \nu t/h^2$
ϕ = thermal diffusion parameter, $= k_T \beta_c$

Superscripts

$'$ = at perturbed state
$-$ = matrix, universal constant, or complex number

Subscripts

a = lower plate
B = at base state (i.e., initial steady state)
b = upper plate
f = of the fluid (i.e., binary gas mixture)
m = of the fluid-porous medium combination*
0 = average value (i.e., evaluated at T_0)
1 = of heavier gas
2 = of lighter gas

$$Sc = \frac{\nu}{D_x},\ \gamma = \frac{\nu(\rho C_P)_f}{K_m},\ \sigma = \frac{(\rho C_P)_m}{(\rho C_P)_f} \tag{21}$$

W^*, T^*, and H^* are functions of R, θ, Z, and τ. b describes the nature of the porous medium; Ra, the equivalent Rayleigh number; Sc, the Schmidt number for the binery mixture; and γ, the product of the Prandtl number of the binary mixture and the ratio of thermal conductivities K_f/K_m. Utilizing the definition, the governing equations (14), (15), and (19) can be rewritten in dimensionless form as

$$\sigma\gamma \frac{\partial I^*}{\partial \tau} - W^* = \nabla^2 T^* - \frac{\phi\gamma}{\mathrm{Sc}} \nabla^2 H^* \tag{22}$$

$$\gamma \left(\frac{\partial H^*}{\partial \tau} - \frac{\partial I^*}{\partial \tau} \right) + W^* = \frac{\gamma}{\mathrm{Sc}} \nabla^2 H^* \tag{23}$$

and

$$\left(b \frac{\partial}{\partial \tau} + 1 \right) \nabla^2 W^* = R_a(1 + \phi) \left[\frac{1}{R} \frac{\partial}{\partial R} \left(R \frac{\partial T^*}{\partial R} \right) + \frac{1}{R^2} \frac{\partial^2 T^*}{\partial \theta^2} \right] - \phi R_a \left[\frac{1}{R} \frac{\partial}{\partial R} \left(R \frac{\partial H^*}{\partial R} \right) + \frac{1}{R^2} \frac{\partial^2 H^*}{\partial \theta^2} \right] \tag{24}$$

respectively. The parameter ϕ eliminates the solutal Rayleigh number from this problem.

Let us assume

$$W^* = W(Z, \tau) f(R, \theta)$$
$$T^* = T(Z, \tau) f(R, \theta)$$
$$H^* = H(Z, \tau) f(R, \theta) \tag{25}$$

Then, equations (22), (23), and (24) become

$$\sigma\gamma \frac{\partial T}{\partial \tau} - W = (D^2 - Q^2)T - \frac{\phi\gamma}{\mathrm{Sc}} (D^2 - Q^2)H \tag{26}$$

$$\gamma \left(\frac{\partial H}{\partial \tau} - \frac{\partial T}{\partial \tau} \right) + W = \frac{\gamma}{\mathrm{Sc}} (D^2 - Q^2)H \tag{27}$$

and

$$b \frac{\partial}{\partial \tau} (D^2 - Q^2)W + (D^2 - Q^2)W = -Q^2 R_a(1 + \phi)T + \phi Q^2 R_a H \tag{28}$$

respectively, only if the function $f(R, \theta)$ satisfies the equation

$$\frac{1}{R} \frac{\partial}{\partial R} \left(R \frac{\partial f}{\partial R} \right) + \frac{1}{R^2} \frac{\partial^2 f}{\partial \theta^2} + Q^2 f = 0 \tag{29}$$

Here, Q is the wave number of the disturbance and D denotes d/dz. Multiplying equation (27) by σ and then adding the result to equation (26), it yields

$$\sigma\gamma \frac{\partial H}{\partial \tau} = (D^2 - Q^2)T + (1 - \sigma)W + \frac{\gamma}{\mathrm{Sc}} (\sigma - \phi)(D^2 - Q^2)H \tag{30}$$

The appropriate boundary conditions are

$$W = T = DH \approx 0 \text{ at } Z = \pm \tfrac{1}{2} \tag{31}$$

These linearized perturbation equations (26), (28), and (30) govern the onset of instability. After the disturbance grows, the full nonlinear equations must be used. For Ra less than R_{ac}, the critical Rayleigh number, the system is stable. When Ra is equal to R_{ac}, the amplitude of the fluid motion can remain at a constant value, called neutral stationary instability, or can oscillate about an average value, termed neutral oscillatory instability.

The eigenvalue problem described by equations (26), (28), (30), and (31) can be solved through the use of the Finlayson method [9], which is the combination of the Galerkin method and the Routh-Hurwitz stability criterion. In the Galerkin method, the solutions are expressed in terms of a series with unknown time-dependent coefficients:

$$W(Z, \tau) = \sum_{i=1}^{N} W_i(\tau) \cos [(2i - 1)\pi Z] \tag{32a}$$

$$T(Z, \tau) = \sum_{i=1}^{N} T_i(\tau) \cos [(2i - 1)\pi Z] \tag{32b}$$

$$H(Z, \tau) = \sum_{i=1}^{N} H_i(\tau) \cos (2i\pi Z) \tag{32c}$$

for $i = 1, \ldots, N$. These solutions are orthogonal and satisfy the boundary conditions (31). The trial functions in equations (32) for $i = 0$ have been tried as the first approximation but produce the critical Rayleigh number only for neutral oscillatory instability and none for neutral stationary instability. Employing these results as an initial guess, the second approximation yields no critical Rayleigh number for instabilities. Hence, the series in equations (32) begin with $i = 1$ as the first approximation. Equations (32) are substituted into equations (26), (28), and (30) followed by orthogonizing the resulting equations with respect to Z to the appropriate residuals in the interval $(-\frac{1}{2}, \frac{1}{2})$ using $\cos [(2j - 1)\pi z]$ and $\cos (2j\pi z)$ as the weighting functions where $j = 1, 2, \ldots, N$. It yields

$$\frac{dT_i}{d\tau} = \frac{1}{\sigma\gamma} \left[-\Lambda_i T_i + W_i + \frac{2\phi\gamma}{\mathrm{Sc}} \Omega_i A_{ij} H_i \right] \tag{33a}$$

$$\frac{dW_i}{d\tau} = \frac{1}{b\Lambda_i} [Q^2 R_a(1 + \phi)T_i - \Lambda_i W_i - 2\phi Q^2 R_a A_{ij} H_i] \tag{33b}$$

$$\frac{dH_i}{d\tau} = \frac{2}{\sigma\gamma} \left[-\Lambda_i A_{ji} T_i + (1 - \sigma) A_{ji} W_i - \frac{\gamma(\sigma - \phi)}{2\mathrm{Sc}} \Omega_i H_i \right] \tag{33c}$$

where

$$\Lambda_i = (2i - 1)^2 \pi^2 + Q^2 \tag{34a}$$

$$\Omega_i = (2i\pi)^2 + Q^2 \tag{34b}$$

$$A_{ij} = \frac{\sin[(i + j - \frac{1}{2})\pi]}{[2(i + j) - 1]\pi} + \frac{\sin[(i - j + \frac{1}{2})\pi]}{[2(i - j) + 1]\pi} \tag{34c}$$

The stability of the system approximated by the solution to the set of equations (33) can be determined by the Routh-Hurwitz criterion [9]: the neutral oscillatory instability is characterized by $D_{n-1} = 0$, while $e_n = 0$ corresponds to neutral stationary instability, where D is the Hurwitz determinant and e and $n(= 3N)$ are, respectively, the coefficient and order of the characteristic equation for the system of equations (33). Whichever condition $e_n = 0$ or $D_{n-1} = 0$ occurs first determines the type of instability.

Since equations (33) are merely an approximation to the system of partial differential equations (26), (28), and (30), the convergence of successive approximations must be examined to insure the approximation is a good one. As will be discussed in the succeeding section, computer results indicate that the first approximation is adequate for the present system since the results of the first three approximations converge very rapidly. For the first approximation, corresponding to $N = 1$ ($n = 3$), the conditions for instability are found as

$$R_a \left(\frac{Q}{\Lambda_1} \right)^2 = \frac{[\pi_1 + \pi_2(\sigma - \phi + \pi_3)/\pi_1 + \sigma - \phi + \pi_2][1 + (\sigma - \phi)/\pi_2]}{(\pi_1 + \pi_2)(1 + \phi) + \pi_3[(\sigma - 1)\pi_1 - \pi_2 + \sigma^2 - 1]} \tag{35a}$$

for neutral oscillatory instability and

$$R_a \left(\frac{Q}{\Lambda_1} \right)^2 = \frac{1 + (\sigma - \phi)/\pi_3}{(1 + \phi([1 - \sigma + \sigma\pi_2/(1 + \phi) + (\sigma - \phi)/\pi_3]} \tag{35b}$$

for neutral stationary instability. Here, Q_c is the critical wave number and

$$\pi_1 = \frac{\sigma \mathrm{Sc}}{b\Omega_1},\ \pi_2 = \frac{\Lambda_1 \mathrm{Sc}}{\gamma\Omega_1},\ \pi_3 = \left(\frac{4}{3\pi} \right)^2 \phi \tag{36}$$

In case all time derivations in equations (26), (27), and (28) are equated to zero, one obtains the first approximation for neutral

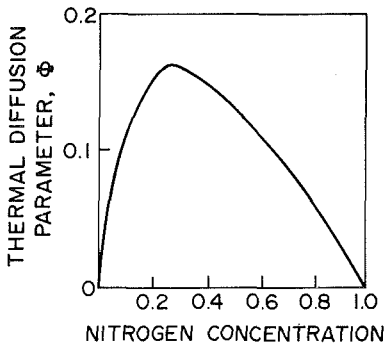

Fig. 1 Thermal diffusion parameter versus nitrogen concentration in N_2–He mixtures

stationary instability

$$R_a \left(\frac{Q}{\Lambda_1}\right)^2 = \frac{1}{(1+\phi)(1-\pi_3)+\pi_2\pi_3} \qquad (35c)$$

which is identical to equation (35*b*) for $\sigma = \infty$, corresponding to the system with $(\rho C_P)_m \gg (\rho C_P)_f$. Computer results indicate that the values of Ra obtained from equations (35*b*) and (35*c*) are different by less than 0.2 percent for σ ranging from 5 to 10^6. In other words, equations (35*b*) and (35*c*) give practically the same Ra for any large value of σ. It is important to note that small values of σ are not reasonable since this parameter signifies the ratio of heat capacity of the solid-gas mixture to the heat capacity of the gas.

Theoretical Results and Discussion

As indicated in equation (6), the density of binary gas mixture depends on temperature as well as concentration and in the base state the concentration effect features through the thermal diffusion parameter ϕ. By applying the definition and equation (8), the variation of ϕ with concentration is illustrated in Fig. 1 for *N_2-He* mixtures. Its value is zero at both zero and hundred percent concentrations signifying the absence of thermal diffusion effect in pure gases. It has a maximum at a concentration of approximately 27.5 percent. Equation (9) shows that under the temperature gradient, the density gradient increases with ϕ. This is in accord with the fact that thermal diffusion induces the heavier component of the gas mixture to move down the temperature gradient and the lighter component to move in the opposite direction. Equation (9) also indicates that for a given value of $(\rho - \rho_0)/\rho_0$, the base temperature gradient a must decrease when ϕ increases. This means that when the thermal diffusion effect increases, lower temperature gradient is required to give rise to a desired buoyancy force.

In a gas mixture having positive ϕ, the heavier component tends to move down the temperature gradient during the thermal diffusion process. On the other hand, in a mixture having negative value of ϕ, the heavier molecules tend to move up the temperature gradient. ϕ can take a negative value in a gas mixture having negative thermal diffusion ratio. Under equal proportion, i.e., C = 0.5, the values of ϕ are 0.135, 0.65, and 0.00235 for the binary mixtures of nitrogen-helium, helium-argon, and nitrogen-oxygen, respectively. The neon-ammonia mixture is known to take negative value of ϕ in some concentration ranges.

An examination of equations (33) or (35) reveals that the conditions for the onset of oscillatory and stationary convection as indicated by the magnitude of the critical Rayleigh and wave number are governed by five independent dimensionless parameters b, ϕ, γ, Sc, and σ and by four parameters b, ϕ, γ and Sc, respectively. Numerical computations were performed to determine the conditions for the onset of instability using a digital computer. Successive approximations were carried out up to the third order. The first approximations for $N = 1$ case have the analytical solutions in closed form, equations (35). These results were then employed as an initial guess in the second approximations. Iterative procedure was adopted to obtain the numerical solutions to the second approximations. The third approximations were solved in a similar manner. Numerical investigation was conducted for the values of ϕ between −1.0 and 1.0, γ between $\frac{1}{3}$ and 1 and Sc and σ between 5 and 10^6. The value of b is 5.144×10^{-4}, corresponding the porous medium employed in the experimental study [7]: a 1.143 cm-thick layer of steel balls of 0.101 cm in diameter (randomly spaced in a space 10.16 cm in diameter). Physical properties of nitrogen and helium under high pressure were obtained from references [13, 14]. Only a few representative results were presented graphically in Figs. 2–4. It is important to note that the results of the first and second approximations differ by less than ± 0.2 percent, while those of the second and third approximation differ even less. This indicates a very good convergence of the series, equations (32). One may then conclude that the first approximation would give the solutions which are accurate enough for most applications. The nature of the porous medium affects thermal instability insignifi-

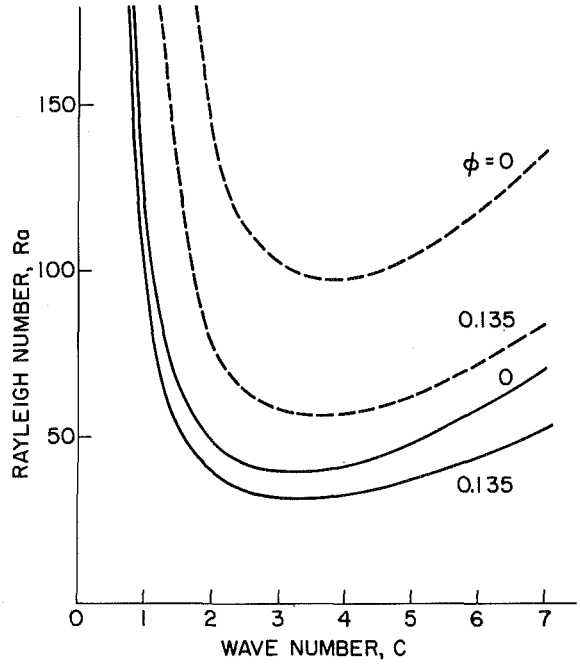

Fig. 2 Conditions for stationary instability (solid lines) and oscillatory instability (broken lines) for $\phi = 0$ (100 percent N_2) and $\phi = 0.135$ (50 percent N_2–50 percent He mixture)

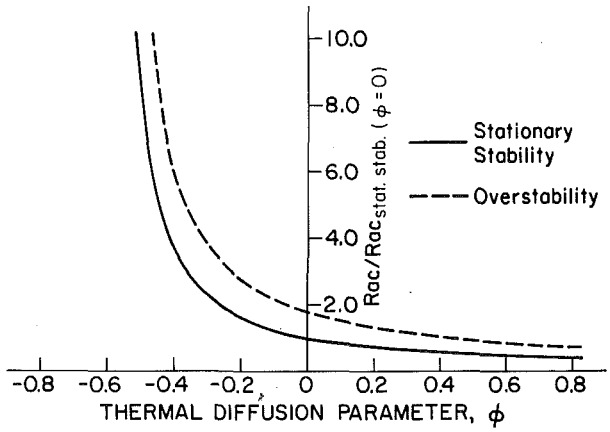

Fig. 3(*a*) Critical Rayleigh number versus thermal diffusion parameter for $Ra_{c_{stat.stab.(\phi=0)}} = 39.5$, $\sigma = 5$, SC = 5 and $\gamma = \frac{1}{3}$

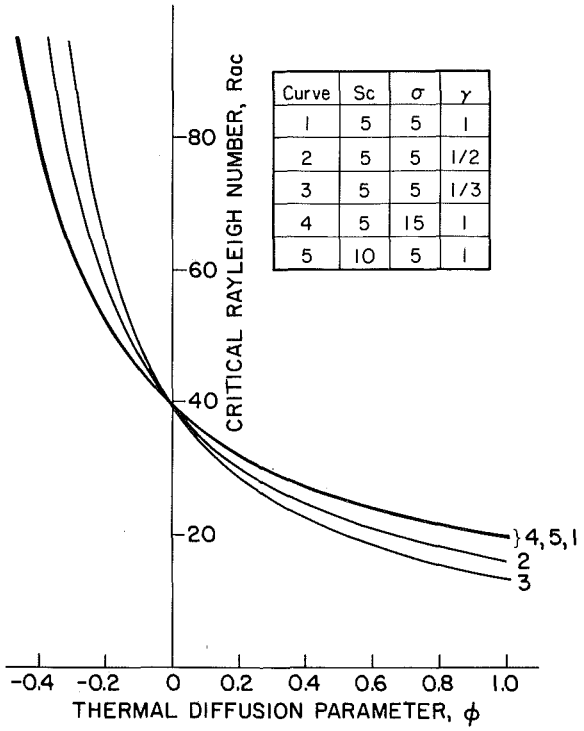

Fig. 3(*b*) Critical Rayleigh number for neutral stationary instability versus thermal diffusion parameter for various values of Sc and γ

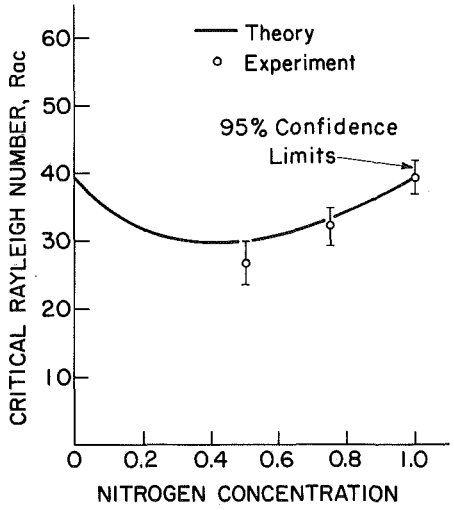

Fig. 5 Comparison of theory with experimental results in steel ball layer saturated with N_2–He mixtures (Sc = 5.0)

cantly since the parameter b fails to appear in equation (35b) or (35c).

Fig. 2 illustrates the variation of the Rayleigh number with wave number for $\phi = 0$ and 0.135 cases, which correspond to pure nitrogen gas and 50 percent nitrogen-50 percent helium mixture, respectively. In a pure nitrogen system, the solid line for $e_n = 0$ exhibits a minimum at a wave number of 3.16 and a Rayleigh number of 39.5. These critical numbers for neutral stationary instability agree with those obtained in references [3, 6]. In a nitrogen-helium mixture of equal proportion, the thermal diffusion effect gives rise to stationary instability at the critical wave and Rayleigh numbers of 3.26 and 31.39, respectively. Since the broken lines for $D_{n-1} = 0$ lie high above the corresponding solid lines for $e_n = 0$, therefore, thermal instability will always set in as stationary convection.

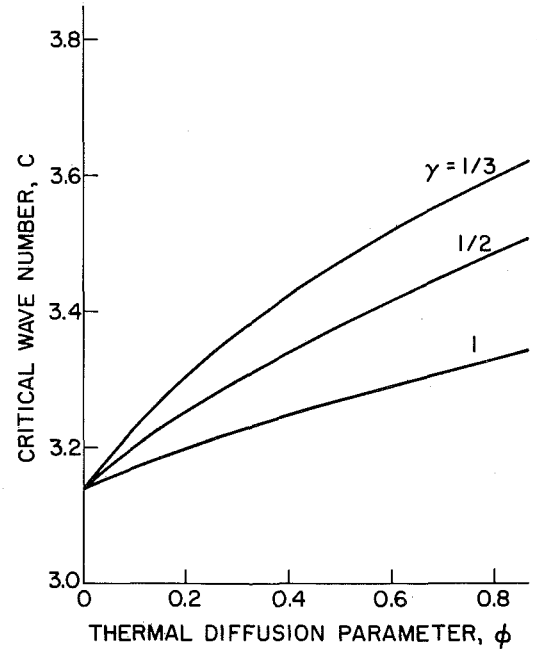

Fig. 4 Critical wave number for neutral stationary instability versus thermal diffusion parameter for Sc = 5.0

Figs. 3(a) and 3(b) demonstrate the effect of thermal diffusion on the onset of instability in binary gas mixtures in porous media. Take the systems with $\sigma = 5$, Sc = 5 and $\gamma = 1/3$ for example. The results of successive approximations up to the third order yield a pair of hyperbolic curves for each instability. Only one of the pair is shown in the figure, while the other lies in the third quadrant. The latter is ruled out as a solution since its value diverges with successive approximations. Since the broken line for $D_{n-1} = 0$ lies above the solid line for $e_n = 0$, it is a solid evidence that indeed there is no oscillatory instability in the porous medium-gas mixture system. The solid curve in Fig. 3(a) shows that thermal diffusion is destabilizing for positive ϕ (since R_{ac} decreases as ϕ increases), while it tends to inhibit the onset of convection for negative ϕ (since R_{ac} increases as $|\phi|$ increases). This is an expected trend since positive ϕ augments the adverse density gradient induced by the temperature gradient. The critical Rayleigh number asymptotically approaches infinity at ϕ of about -0.55. Fig. 3(b) indicates the effects of the parameters Sc and γ on the critical Rayleigh number for stationary instability. It is seen that γ plays the most important role on the onset of stationary convection. As the value of γ increases, the critical Rayleigh number increases for positive ϕ but decreases for negative ϕ. The parameter Sc exerts negligible influence on stationary instability, as seen by comparing curve 4 with curve 1.

The critical wave number is also strongly influenced by the parameters ϕ and γ as seen in Fig. 4. It increases with an increase in ϕ and a decrease in γ for a given value of Sc. If plotted, the curve for $\gamma = 1$ and Sc = 10 would have coincided with the curve for $\gamma = 1$ and Sc = 5 in Fig. 4. This indicates the minor role of the parameter Sc on the critical wave number.

Theoretical results are compared with the test data [7] in Fig. 5. For the mixture of nitrogen and helium at the nitrogen concentrations of 0.5, 0.75, and 1.0, theoretical prediction falls within the 95 percent confidence limit of the test results.

Conclusions

The convective instability of a binary gas mixture saturating a layer of porous medium is analyzed. Instability is found to set in

only as stationary motion, the criterion of which can be predicted by equation (35*b*) or (35*c*). The Rayleigh number and wave number are strongly dependent on the parameters γ and ϕ. The parameter γ is a modified Prandtl number with the thermal conductivity of the fluid being replaced by that of the fluid-porous medium combination. The parameter ϕ is a measure of the influence of thermal diffusion and depends on the molecular weights, concentration, and the thermal diffusion factor of the pair of gases. For a given γ, the critical Rayleigh number decreases with an increase in ϕ. For mixtures with very low value of ϕ, the effect of thermal diffusion is hardly noticeable. Thus, instability experiment on such mixture will give results as if it were a one-component fluid. The nature of the porous medium exerts practically no influence on thermal instability so long as the system is one-dimensional.

Theoretical results agree well with experimental data for the nitrogen-helium gas mixtures of 100, 75, and 50 percent nitrogen compositions. It is thus confirmed that theory based on linear perturbation predicts satisfactorily the influence of thermal diffusion on the onset of convective instability of binary gas mixtures in a horizontal layer of porous medium.

References

1 Lawson, M. L., and Yang, Wen-Jei, "The Stability of a Layer of Binary Gas Mixtures Heated From Below," *Journal of Fluid Mechanics*, Vol. 57, Part 1, 1973, pp. 103–110.

2 Hurle, D. T. J., and Jakeman, E., "Soret-Driven Thermosolutal Convection," *Journal of Fluid Mechanics*, Vol. 47, Part 4, 1971, pp. 667–687.

3 Lapwood, E. R., "Convection of a Fluid in a Porous Medium," *Proceedings of Cambridge Philosophical Society*, Vol. 44, 1948, pp. 508–521.

4 Morrison, H. L., Roggers, F. T., and Horton, C. W., "Convection Currents in Porous Media, II: Observation of Conditions at Onset of Convection," *Journal of Applied Physics*, Vol. 20, 1949, pp. 1027–1029.

5 Elder, J. W., "Steady Free Convection in a Porous Medium Heated From Below," *Journal of Fluid Mechanics*, Vol. 27, 1967, pp. 29–48.

6 Katto, Y., and Masuoka, T., "Criterion for the Onset of Convective Flow in a Fluid in a Porous Medium," *International Journal of Heat and Mass Transfer*, Vol. 10, 1967, pp. 297–309.

7 Lawson, M. L., and Yang, Wen-Jei, "Thermal Stability of Binary Gas Mixtures in a Porous Medium," JOURNAL OF HEAT TRANSFER, TRANS. ASME, Series C, Vol. 97, 1975, pp. 378–381.

8 Chandrasekhar, S., *Hydrodynamic and Hydromagnetic Stability*, Oxford University Press, England, 1961.

9 Finlayson, B. A., *The Method of Weighted Residuals and Variational Principles*, Academic Press, New York, Chapter 6, 1972.

10 Irmay, S., "On the Theoretical Derivation of Darcy and Forchheimer Formulas," *Transactions American Geophysics Union*, Vol. 39, 1958, pp. 702–707.

11 Whitaker, S., "Advances in Theory of Fluid Motion in Porous Media," in *Flow Through Porous Media*, ACS Publications, 1970.

12 Carman, P. C., *Flow of Gases through Porous Media*, Academic Press, New York, 1965.

13 Lenoir, J. M., and Cumings, E. W., "Thermal Conductivity of Gases," *Chemical Engineering Progress*, Vol. 47, No. 5, 1951, pp. 223–231.

14 Chelton, D. B., and Mann, D. B., "Cryogenic Data Book," Wright Air Development Center Technical Report 59-8, AD No. 208155, Wright-Patterson Air Force Base, Ohio, 1959.

R. J. Ribando
K. E. Torrance
Mem. ASME

Sibley School of Mechanical and Aerospace Engineering,
Cornell University,
Ithaca, N. Y.

Natural Convection in a Porous Medium: Effects of Confinement, Variable Permeability, and Thermal Boundary Conditions

Two-dimensional numerical calculations are reported for natural convection of a fluid in a porous, horizontal layer heated from below. Effects of the following parameters are examined: rigid (impermeable) and constant-pressure (permeable) upper boundaries; isothermal and uniform heat flux at the lower boundary; and permeabilities which are constant, or which vary with depth to simulate compaction of a porous medium or property variations of real fluids within the medium. Steady-state results are presented for the heat flux distribution on the upper surface, as well as for flow and temperature fields in the interior.

Introduction

Natural convection in a porous medium is important in many technological applications, and is increasing in importance with the growth of interest in geothermal energy. Indeed, it has been estimated that geothermal resources in the United States could supply 395,000 MW of electric power by the year 2000 [1].[1] Clearly, development to such a scale will require optimizing the draw-off rates and operating pressures of reservoirs. To achieve this, a detailed understanding of flow processes in reservoirs, and in porous media in particular, will be required. The present study considers natural convection in an idealized porous layer, and determines the effects of different modes of heating from below, of confined and open upper boundaries, and of variable permeability.

The literature on natural convection in a porous medium heated from below includes early work by Lapwood [2] to determine conditions for the onset of convection. Critical Rayleigh numbers of Ra = 39.5 and 27.1 were obtained for a horizontal layer with isothermal boundaries and with impermeable and permeable upper surfaces, respectively. Similar results for a layer with a uniform heat flux from below are derived in the Appendix and are Ra = 27.1 and 17.7 for impermeable and permeable upper boundaries, respectively. More recent work on the structure of convection at above-critical Rayleigh numbers has emphasized layers with impermeable, isothermal boundaries. For example, Straus [3] applied a Galerkin (Fourier) technique and determined both the structure and stability of finite-amplitude, two-dimensional convection. Holst and Aziz [4] have numerically treated the three-dimensional case. An approximate solution for a layer with a permeable top and isothermal boundaries was given by Lapwood [2]. Later, Donaldson [5] reconsidered the problem and arbitrarily imposed a recharge-discharge profile for mass flow across the upper boundary. The resulting solutions correspond to mixed (free and forced) convection.

From the foregoing literature survey, it is apparent that very little is known about finite-amplitude convection in a porous layer when the upper surface permits throughflow, or when the lower surface is changed from isothermal to one of uniform heat flux. In addition, the effects of a spatially varying permeability on flow structure have not been determined. The present paper examines these effects using numerical solutions of the governing equations. Quantitative information is presented on surface heat fluxes and on the flow and temperature fields.

Problem Formulation

Consider a horizontal, heat-conducting porous medium confined between two horizontal boundaries a distance h apart with the acceleration of gravity g directed downward. The upper boundary at $z = 0$ is maintained at a temperature T_0; the lower boundary at $z = -h$ is maintained at $T = T_h$, with $T_h > T_0$. In the absence of fluid motion temperature varies linearly across the layer. The porous medium has scalar permeability k and is saturated with a fluid of density ρ_f and viscosity μ. Fluid motion is assumed to be two-dimensional roll convection. As shown by the work of Straus [3] for the case of impermeable, isothermal boundaries, stable two-di-

[1] Numbers in brackets designate References at end of paper.

Contributed by the Heat Transfer Division for publication in the JOURNAL OF HEAT TRANSFER. Manuscript received by the Heat Transfer Division September 2, 1975. Paper No. 76-HT-Y.

mensional rolls are expected for a finite band of horizontal wavenumbers. Thermal conductivities and specific heats of both fluid and matrix are taken as constant, as is the thermal expansion coefficient, α, of the fluid. However, the ratio of fluid viscosity to matrix permeability, μ/k, is allowed to vary with the vertical coordinate z.

The governing equations for steady, natural convection may be written with the Boussinesq, Darcy flow, and negligible inertia approximations as [2, 6, 7]:

$$0 = -\nabla p' - \frac{\mu}{k}\mathbf{v}' - \rho_f g \mathbf{e}_z \tag{1}$$

$$\nabla \cdot (\mathbf{v}'\theta') = \kappa_m \nabla^2 \theta' \tag{2}$$

$$\nabla \cdot \mathbf{v}' = 0 \tag{3}$$

$$\rho_f = \rho_0(1 - \alpha\theta') \tag{4}$$

Primes denote quantities which will later be made dimensionless; θ' denotes a temperature difference relative to the upper boundary, $\theta' = T' - T_0'$. The form used for the energy equation (2) implies that thermal equilibrium is achieved locally between fluid and porous medium.

Fluid viscosity μ and matrix permeability k appear only through the ratio μ/k in equation (1). Later, it will be convenient to attribute variations of the ratio to variations of either μ or k. The ratio is modeled by the exponential form:

$$\frac{\mu}{k} = \left(\frac{\mu}{k}\right)_0 e^{-z'/z_0'} \tag{5}$$

where the reference amplitude $(\mu/k)_0$ is evaluated at the upper boundary. A positive value of the e-folding distance z_0' corresponds to μ/k increasing with depth; a negative value corresponds to μ/k decreasing with depth. Setting $z_0' = \pm\infty$ corresponds to a medium with constant viscosity and constant permeability, or to a constant ratio of the two.

The foregoing equations may be combined and simplified by introducing the Stokes stream function, and by taking the curl of equation (1). It is also convenient to introduce $L, L^2/\kappa_m$ and ΔT as reference values for length, time, and temperature. For a layer of constant μ/k ratio, L is taken as the layer depth h and $\Delta T \equiv T_h' - T_0'$. For a layer with variable μ/k ratio, the length L is the e-folding distance $|z_0'|$ and ΔT is taken as the temperature difference between the e-folding depth and the surface in the absence of convection. The governing equations in nondimensional form become

$$u = -\frac{\partial\psi}{\partial z},\ w = \frac{\partial\psi}{\partial x} \tag{6}$$

$$\frac{\partial}{\partial x}\left(e^{-z/z_0}\frac{\partial\psi}{\partial x}\right) + \frac{\partial}{\partial z}\left(e^{-z/z_0}\frac{\partial\psi}{\partial z}\right) = \mathrm{Ra}_t\frac{\partial\theta}{\partial x} \tag{7}$$

$$\nabla \cdot (\mathbf{v}\theta) = \nabla^2\theta \tag{8}$$

A numerical solution of equations (6)–(8) will be obtained using ψ and θ as dependent variables. The form of the solution depends upon z_0 and the Rayleigh number based on temperature difference

$$\mathrm{Ra}_t = \left(\frac{k}{\mu}\right)_0 \frac{\rho_0 g \alpha \Delta T L}{\kappa_m} \tag{9}$$

The foregoing nondimensional equations also apply for a prescribed, uniform heat flux $\dot{q}''$ at the lower boundary. In that case, the reference temperature difference is defined as $\Delta T = \dot{q}''L/\lambda_m$, with L identified as either h or $|z_0'|$ for layers of constant or variable μ/k ratio, respectively. In addition, a Rayleigh number based on heat flux appears in equation (7)

$$\mathrm{Ra}_f = \left(\frac{k}{\mu}\right)_0 \frac{\rho_0 g \alpha \dot{q}'' L^2}{\kappa_m \lambda_m} \tag{10}$$

Boundary conditions must be specified to complete the problem formulation. The porous medium was introduced previously as a layer of infinite horizontal extent. For a numerical solution, however, we will restrict the horizontal extent to a region of width ℓ. That is, we will consider the physical region $0 \le x' \le \ell$ and $-h \le z' \le 0$. The domain and boundary conditions simulate either of two physical geometries: a finite porous region of aspect ratio h/ℓ; or a half-wavelength interval of a horizontally periodic flow of wavelength 2ℓ, each wave consisting of two mirror-image flows of width ℓ. The aspect ratio h/ℓ thus enters as a geometric parameter.

The hydrodynamic boundary condition for an impermeable surface (i.e., the bottom and sides in all cases, and the top in about half the cases) is the Dirichlet condition $\psi = 0$. Note that the governing equations for flow in a porous medium do not permit the additional hydrodynamic constraint of no-slip or no shear. Flow or recharge through a permeable upper boundary may occur when either a standing liquid or a second porous medium (with a much larger permeability) overlies the porous layer of interest. For such cases, the least restrictive boundary condition at the permeable surface is one of constant pressure [2]. The constant pressure assumption implies no viscous interaction between an overlying liquid and the porous layer. From the horizontal momentum balance and the stream function definitions, a constant pressure surface is represented by the Neumann condition $u = -\partial\psi/\partial z = 0$.

Thermal boundary conditions consist of an isothermal upper surface ($\theta = 0$), adiabatic vertical boundaries ($\partial\theta/\partial x = 0$), and either prescribed temperature ($\theta = h/L$) or prescribed flux ($\partial\theta/\partial z = 1$) at the lower boundary.

Numerical Method

Finite differences are used to approximate equations (6)–(8). Three-point central differences are used for linear space derivatives, and conserving, upwind differences for the nonlinear transport term $\nabla\cdot(\mathbf{v}\theta)$ in the energy equation [8]. Starting from initial data, stream function is advanced first by iteratively solving a dif-

Nomenclature

$\mathbf{e}_z$ = unit vector in z-direction
g = acceleration of gravity
h = height of layer
k = permeability
L = significant length scale
ℓ = width of layer
Nu = average value of Nu_x
Nu_x = local Nusselt number
p = total static pressure
p_m = motion pressure = $p + \rho_0 g z + \rho_0 g \alpha \Delta T z^2/2L$
$\dot{q}''$ = heat flux
Ra_f = Rayleigh number based on heat flux
Ra_t = Rayleigh number based on temperature difference
T = temperature
T_h = temperature of lower boundary
T_0 = temperature of upper boundary
u = horizontal velocity
$\mathbf{v}$ = vector velocity
w = vertical velocity
x = horizontal coordinate
z = vertical coordinate
z_0 = e-folding distance of permeability
α = coefficient of thermal expansion of the fluid
ΔT = temperature difference between $z = -L$ and $z = 0$
θ = dimensionless temperature = $(T - T_0)/\Delta T$
θ' = temperature difference = $T - T_0$
Θ = deviation from the linear equilibrium temperature profile
κ_m = modified thermal diffusivity = $\lambda_m/(\rho c_p)_f$
λ_m = thermal conductivity of the mixture of fluid and solid
μ = viscosity
ρ_f = density of fluid
ρ_0 = reference density of fluid
$(\rho c_p)_f$ = heat capacity of fluid
ψ = stream function

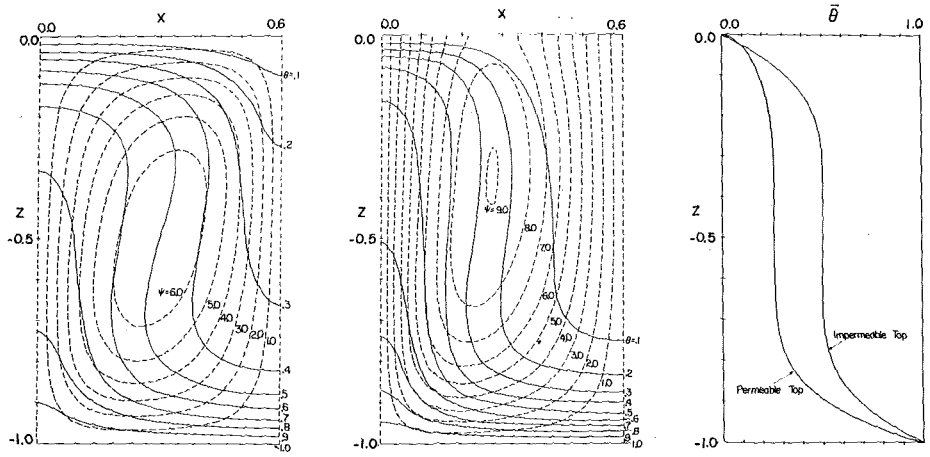

Fig. 1. Constant permeability, constant bottom temperature, Ra_t = 200: (*a*) impermeable top, Nu = 4.07, ψ_{max} = 6.87; (*b*) permeable top, Nu = 6.38, ψ_{max} = 9.06; (*c*) horizontally averaged temperature

ference approximation of equation (7). One Gauss-Seidel iteration is used, followed by several optimized, successive-over-relaxation iterations. Up to ten sweeps, with alternating direction, are used. The velocity field is obtained from equation (6) and the temperature field explicitly advanced with one Jacobi iteration of equation (8). The procedure may then be repeated. The foregoing procedure avoids the numerical instability noted by Elder [9] for Ra > 100. The reason lies in the present treatment of the energy equation, which does not separately advance the convection and conduction terms.

The foregoing double iteration procedure is analogous to solving the system of equations (6)–(8) with a time derivative $\partial\theta/\partial t$ added to equation (8), and with the largest stable time step used at each grid point. In this view, the iteration transient is similar to a true transient. During the iteration the field always evolved smoothly from arbitrary initial data to final, steady flows. No unusual oscillations, suggestive of real-time oscillations, were ever observed. Iteration was terminated when a global energy balance on the region closed to 0.5 percent. The resulting steady-state flows are presented in the next section.

All Dirichlet boundary conditions are treated as known boundary data during the iteration procedure. At boundaries with Neumann conditions special forms of either the energy equation or the stream function equation are required. For boundaries with adiabatic or prescribed heat fluxes, a finite-difference energy balance is constructed for the volume element adjacent to the boundary. The same energy balance is used to obtain the heat flux and Nusselt number at an isothermal boundary. For the permeable upper surface, boundary conditions require that the following difference form be satisfied for each grid point (i, j) along the boundary:

$$\frac{\psi_{i+1,j} - 2\psi_{i,j} + \psi_{i-1,j}}{(\Delta x)^2} - 2\frac{\psi_{i,j} - \psi_{i,j-1}}{(\Delta z)^2} = 0 \qquad (11)$$

The i and j indices denote grid locations in the (x, z) coordinate system. Equation (11) applies for a porous medium with constant μ/k ratio; slight modifications are required for the case of a variable ratio.

For calculations with constant μ/k ratio, the (x, z) region was covered by a uniform 16 × 16 grid. For the variable μ/k ratios a 15 × 20 grid was applied with a nonuniform grid spacing in the z-direction. Convergence with mesh size was verified by employing coarser and finer grids on selected test problems. Results in the next section (at Ra = 200) are believed correct to about 5 percent for global quantities.

Results and Discussion

Steady-state results are presented for both constant and variable μ/k ratios. In all cases, the effects of both isothermal and uniform-flux lower boundaries, and of permeable and impermeable upper boundaries, are considered and discussed.

Constant μ/k Ratio. Consider the case of a layer with constant properties. An aspect ratio of $h/\ell \approx 1.67$ is assumed. This value is in the center of the region of stable two-dimensional flows at Ra_t = 200 [3] and yields the maximum heat flux for the isothermal bottom boundary, impermeable top case [3, 10]. Guidance as to aspect ratio for the other boundary conditions considered in this study was not available. To facilitate comparison, an aspect ratio of 1.67 was used for all constant μ/k cases, although a detailed stability analysis of the flows has not been carried out. Aspect ratio was not varied as a parameter in this study.

The case of isothermal boundaries at Ra_t = 200 is considered first to permit comparison with previous work. Fig. 1 illustrates computed streamlines and isotherms and includes a graph of horizontally averaged temperature as a function of height. The form of Fig. 1 is used for presentation of results throughout this paper. Isotherms are shown with solid lines, streamlines with dashed lines, and magnitudes of θ and ψ are indicated. The Nusselt number for the layer and the maximum value of ψ are given in the caption. In all cases, fluid circulates in a clockwise direction.

Figs. 1(a) and 1(b), respectively, illustrate flows with impermeable and permeable upper boundaries. In Fig. 1(a), the ascending and descending plumes are symmetric since the thermal and hydrodynamic boundary conditions are symmetric. The Nusselt number is 4.07, which is within 1.5 percent of data interpolated from Straus [3]. The pressure field for this case was found diagnostically from the temperature field (using $\nabla^2 p_m = Ra_t(\partial\Theta/\partial z)$, where Θ is the deviation from the linear conduction solution) and is illustrated in Fig. 2.

When the upper boundary is changed from a rigid-lid to a constant pressure surface, flow through the boundary develops as shown in Fig. 1(b). Removal of the lid leads to enhanced convective motion (compared to Fig. 1(a)) as shown by increases in both the Nusselt number and the maximum value of stream function. The plumes are no longer symmetric. With the hot plume free to leave the system, its velocity is higher and its width narrower. Furthermore, in the confined case the cold plume emerges from a thermal boundary layer along the top surface. As such, descending fluid is generally warmer than in the case of a permeable top, where all fluid entering the porous medium is at the temperature of the cold upper surface. Note that in our treatment of the upper boundary condition, equation (11), flow through the boundary is

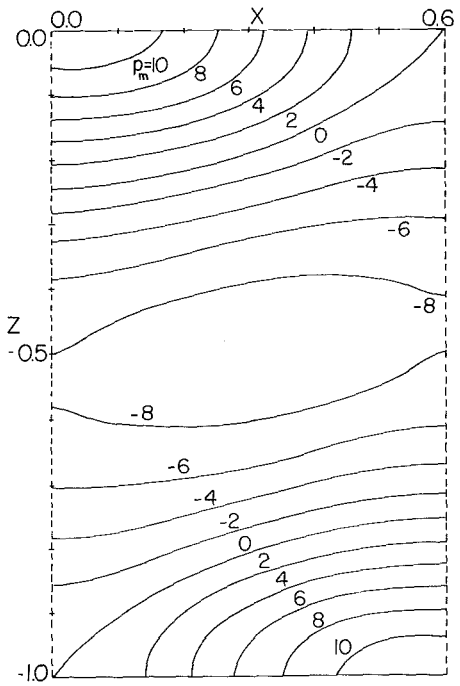

Fig. 2. Motion pressure field for conditions of Fig. 1(*a*)

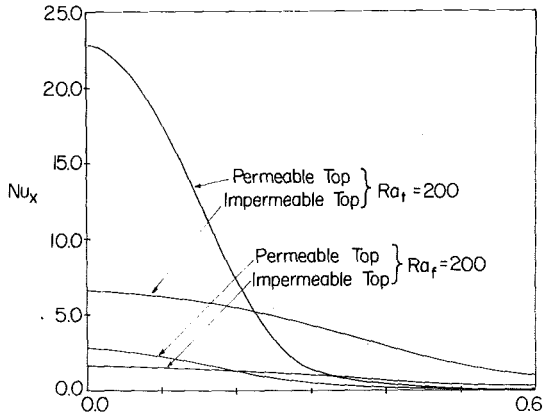

Fig. 4. Local Nusselt number versus position along surface, constant permeability cases

determined by the buoyancy-driven flow within the porous layer. Our results thus differ from those of Donaldson [5] whose upper boundary condition was one of forced flow.

The vertical profile of horizontally averaged temperature is shown in Fig. 1(*c*). As expected, the impermeable top case shows symmetry and a well-defined, isothermal core. The permeable top case shows lower overall temperatures, mainly due to the widening of the cold plume. Also, the thermal boundary layer at the top, where the vertical velocity is not forced to go to zero, is appreciably thinner than at the bottom.

The case of a prescribed, uniform heat flux at the lower boundary is illustrated in Fig. 3 for a Rayleigh number based on flux of $Ra_f = 200$. Such heating is a good approximation when the bottom heat flux is limited by conduction through thick, impermeable layers at depth. The effects of changing from isothermal to uniform-flux heating conditions are illustrated by comparing Figs. 1 and 3. Graphs (*a*) and (*b*), respectively, illustrate impermeable and permeable upper boundaries. It is apparent that convective motion in the case of uniform bottom heating is less intense, in terms of both isotherm distortion and the maximum value of stream function. From the definitions given by equations (9) and (10), it is clear that a flux Rayleigh number can be constructed for the results in Fig. 1 by multiplying Ra_t by Nu. Similarly, an approximate Ra_t for Fig. 3 can be obtained by multiplying Ra_f by a suitable mean $\Delta\theta$ across the layer. In either case the computed temperatures would also have to be rescaled. However, it should be noted that a constant bottom-temperature run for $Ra_t = 200$ yielding a Nu of 4.07 would not be entirely equivalent to a constant bottom flux run for $Ra_f = 814$, since in the former case the flux into the bottom is not uniform. Nevertheless, the underlying reason for the difference between the $Ra_f = 200$ and $Ra_t = 200$ flows is apparent. As in Fig. 1, the effect of a permeable top is to enhance and narrow the hot plume, and to widen the cold plume.

For many technological and geophysical applications, the surface heat flux is an important quantity. Fig. 4 shows the variation of local Nusselt number across the surface for the four cases discussed so far. The average Nusselt number is equal to unity for the constant flux cases, and to $\int Nu_x dx$ for the constant temperature cases. The moderating influence of an impermeable top is readily apparent. Note that in all cases, both permeable and impermeable,

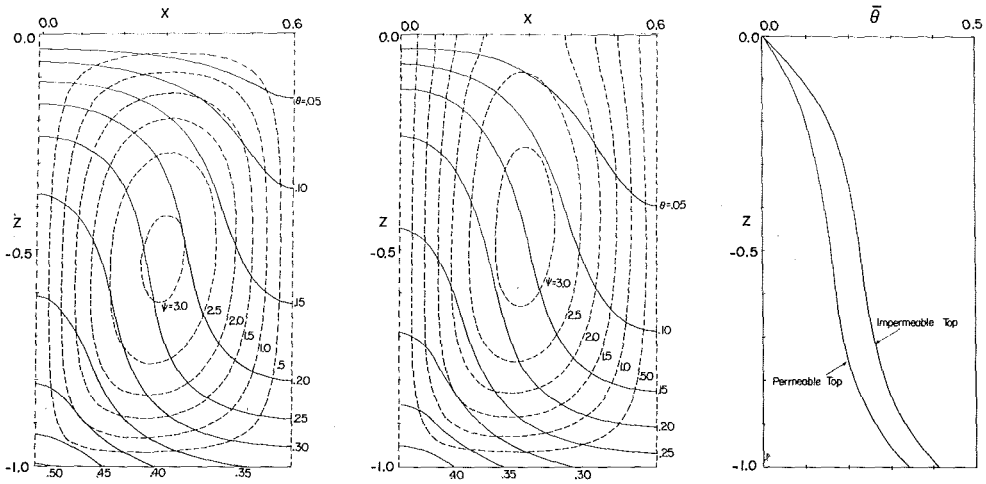

Fig. 3. Constant permeability, constant bottom flux, $Ra_f = 200$: (*a*) impermeable top, $\psi_{max} = 3.1$; (*b*) permeable top, $\psi_{max} = 3.21$; (*c*) horizontally averaged temperature

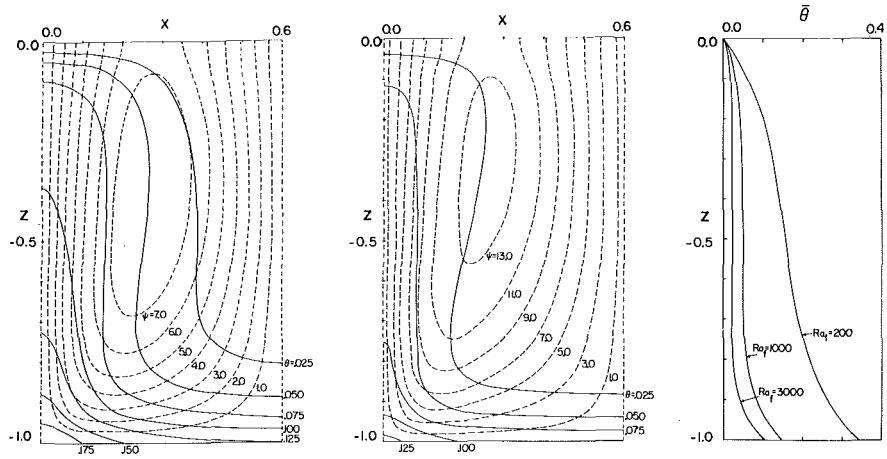

Fig. 5. Constant permeability, constant bottom flux, permeable top: (*a*) $Ra_f = 1000$, $\psi_{max} = 7.98$; (*b*) $Ra_f = 3000$, $\psi_{max} = 13.85$; (*c*) horizontally averaged temperature

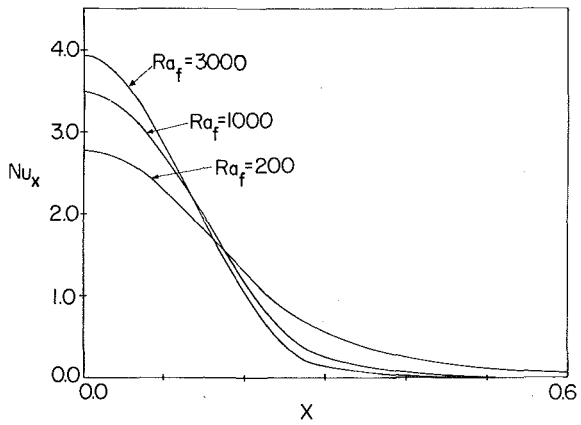

Fig. 6. Local Nusselt number versus position along surface, constant permeability, constant bottom flux, permeable top cases

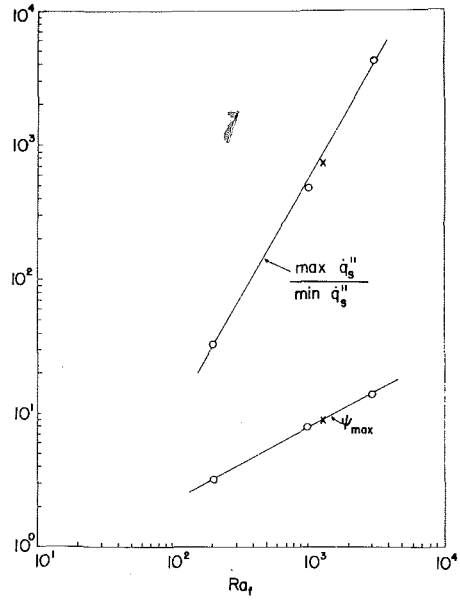

Fig. 7. Ratio-maximum surface heat flow to minimum surface heat flow and maximum value of streamfunction, constant permeability, constant bottom flux, permeable top cases (point designated by *x* represents flow shown in Fig. 1(*b*) plotted in terms of an equivalent Ra_f)

there is no convective transport of heat across the upper boundary and Nu_x is attributable to heat conduction. This is a consequence of using the isothermal, top boundary temperature as a reference in the nondimensionalization.

The uniform heat flux, permeable top conditions are relevant to many water-saturated crustal regions. Since the heat flux at depth may be fixed by the underlying rock structure, it is of interest to examine the effects of changing the uniform permeability of the porous layer. Fig. 5 illustrates results for a permeable top for Ra_f = 1000 and 3000. Straus [3] gives $Ra_t = 380$ as the upper limit for stable, two-dimensional flows with an impermeable top. Recalling that a given value of Ra_f corresponds to a significantly lower value of Ra_t, it is reasonable to expect that our solutions correspond to physically realizable flows. The most obvious effect of increasing Ra_f in Figs. 3(*b*), 5(*a*), and 5(*b*) is to increase flow velocities and the size of the cold plume. The reduced temperatures and development of an isothermal core are apparent in Fig. 5(*c*). Fig. 6 illustrates the effects of Ra_f on surface heat flow. A geophysically useful correlation is shown in Fig. 7 for the ratio of surface heat flow at the center of the hot plume to that at the center of the cold plume. The maximum value of stream function is also indicated.

Variable μ/k Ratio. The effects of allowing μ/k to vary using the exponential form (5) are now examined. Two cases are considered: μ/k increasing with depth, and μ/k decreasing with depth. Physically, the first case is interpreted as a decrease in permeability with depth due to compaction of the porous medium by overburden pressure. Alternatively, a decrease of permeability with depth could result from thermal stress cracking in a cooling material; for example, at a lithospheric spreading center where new crust is being formed. The second case models a fluid whose viscosity decreases with increasing temperature.[2] At low Rayleigh numbers, temperature is to a good approximation a linear function of depth. Thus, the temperature dependence may be taken as a simple depth dependence. Although this approximation breaks down at higher Rayleigh numbers, and the exponential form (5) only

[2] We are grateful to Prof. David R. Kassoy of the University of Colorado for pointing out the importance, geophysically, of this case.

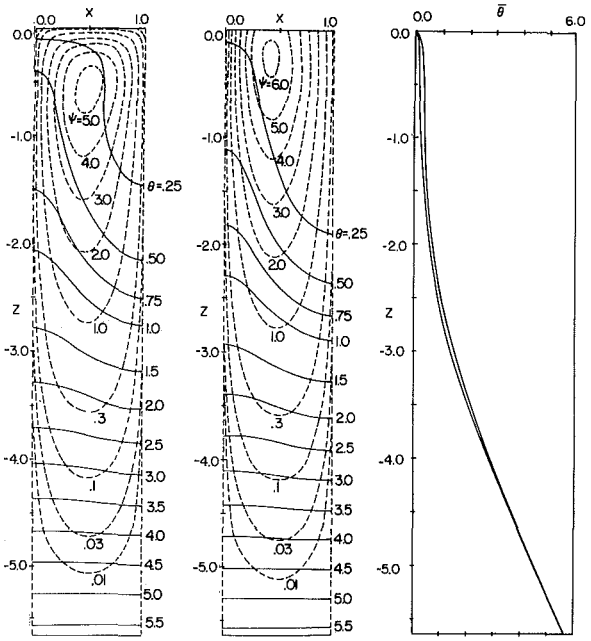

Fig. 8. Exponentially decreasing permeability, constant bottom temperature, $Ra_f = 200$: (*a*) impermeable top, Nu = 1.76, $\psi_{max} = 5.36$; (*b*) permeable top, Nu = 1.82, $\psi_{max} = 6.32$; (*c*) horizontally averaged temperature

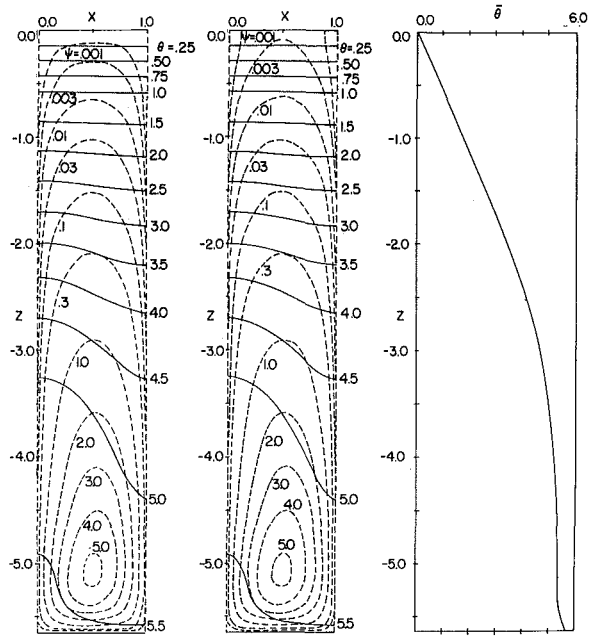

Fig. 9. Exponentially increasing permeability (exp. dec. vis.), constant bottom temperature, $Ra_f = 0.071$: (*a*) impermeable top, Nu = 1.73, $\psi_{max} = 5.14$; (*b*) permeable top, Nu = 1.73, $\psi_{max} = 5.14$; (*c*) horizontally averaged temperature

roughly approximates the viscosity-temperature relation of real fluids, our results should illustrate the qualitative effects of a temperature dependent viscosity. An aspect ratio of $|z_0|/\ell = 1$, based on e-folding distance, is assumed; the aspect ratio based on layer depth is $h/\ell = 5.64$. The μ/k ratio varies by a factor of about 280 between top and bottom.

The case of μ/k ratio increasing with depth is shown in Fig. 8. An isothermal lower boundary is used with $Ra_t = 200$. Results for impermeable and permeable upper boundaries are shown in Figs. 8(a) and 8(b). The region of vigorous flow corresponds to the region of high permeability. However, small but significant amounts of fluid do penetrate to the bottom despite the extremely small values of local Rayleigh number in that region. (To the best of our knowledge, the critical Rayleigh number for a layer of variable permeability has not been determined.) As in the constant permeability case, the unconfined flow in Fig. 8(b) is more vigorous and results in greater heat transfer and a wider cold plume than the confined flow in Fig. 8(a). The vertical profiles of horizontally averaged temperatures in Fig. 8(c) are convectively controlled near the top and are nearly linear conduction profiles at the bottom.

Cases with μ/k increasing with depth and with a prescribed, uniform heat flux at the lower boundary were also run. The results are not displayed here because they are, when scaled properly, essentially identical to runs with an isothermal lower boundary. The reason is, of course, that conduction is the dominant mode of heat transfer near the bottom of the porous medium. Consequently, with isotherms horizontal and the heat flux vector vertical (and uniform in x), isothermal and uniform flux lower boundary conditions are interchangeable. For example, results in Figs. 8(a) and 8(b) are equivalent to cases with a uniform bottom heat flux at $Ra_f = 352 (= 1.76 \times 200)$ and $Ra_f = 364 (= 1.82 \times 200)$, respectively. Temperatures must be scaled down by the same factor.

Although results for uniform heat flux and isothermal lower boundaries can be interchanged when permeability decreases with depth, there are advantages to using one formulation over the other. For example, the isothermal lower boundary condition (Dirichlet) leads to much faster numerical convergence than does the heat flux boundary condition (Neumann). On the other hand, it is frequently desirable to treat heat flux as an independent variable, using the constant flux formulation in which Ra_f and aspect ratio h/ℓ emerge as the only parameters. In the limit $h/\ell \to \infty$, for fixed Ra_f, the near-surface convective flows become independent of h/ℓ. Near-surface convective flows, by comparison, remain dependent on h/ℓ in the isothermal boundary formulation.

The case of μ/k ratio decreasing with depth is shown in Fig. 9 for isothermal lower boundaries. The Rayleigh number used was less by a factor of $e^{5.64}$ than that used in the runs depicted in Fig. 8. Thus, based on the minimum μ/k ratio in the fields, the flows should be comparable. Greatly increased flows in areas of low viscosity are apparent. It can be seen that Fig. 9(a) is almost identical to Fig. 8(a) when turned upside down. The slight differences are ascribed to grid spacing differences. A comparison of Figs. 9(a) and 9(b) shows that the flows are not dependent upon the top hydrodynamic boundary condition. In the permeable case only streamlines with $\psi \leq 0.0029$ penetrate the top and the computed maximum stream function value and the Nusselt number are virtually identical with the impermeable top results. Surface heat fluxes are essentially uniform with x for both cases. The effect of a prescribed, uniform heat flux at the lower boundary was not investigated as it is expected to have only a minor effect on the physical region of most interest, i.e., near the top.

Concluding Remarks

A relatively simple model has been used to examine the effects of bottom heating, of upper boundary confinement, and of a variable μ/k ratio on convection in a porous layer. Factors such as nonisotropy and nonhomogeneity of permeability, aspect ratio, and realistic morphology of the porous layer have not been studied. Present knowledge of in situ values of these factors precludes their consideration at this time. For eventual understanding of geothermal reservoirs additional factors need to be considered, such as different forms of withdrawal and replenishment, and the effects of phase changes. Nevertheless, computer simultations in conjunction with experimental work in the laboratory and in the field will continue to be effective tools for developing a basic understanding of flow processes in porous media.

Acknowledgment

This research has been supported by the Division of Engineering of the National Science Foundation under Grant ENG 75-14596.

References

1 Hickel, W. J., Chairman, Denton, J. C., Editor, "Geothermal Energy," Sept. 1972, National Technical Information Service Publication No. PB-222 326.

2 Lapwood, E. R., "Convection of a Fluid in a Porous Medium," *Proceedings of the Cambridge Philosophical Society,* Vol. 44, 1948, pp. 508–521.

3 Straus, J. M., "Large Amplitude Convection in Porous Media," *Journal of Fluid Mechanics,* Vol. 64, Part 1, 1974, pp. 51–63.

4 Holst, P. H., and Aziz, K., "Transient Three-Dimensional Natural Convection in Confined Porous Media," *International Journal of Heat and Mass Transfer,* Vol. 15, 1972, pp. 73–90.

5 Donaldson, I. G., "Temperature Gradients in the Upper Layers of the Earth's Crust Due to Convective Water Flows," *Journal of Geophysical Research,* Vol. 67, No. 9, Aug. 1962, pp. 3449–3459.

6 Katto, Y., and Masuoka, T., "Criterion for the Onset of Convective Flow in a Fluid in a Porous Medium," *International Journal of Heat and Mass Transfer,* Vol. 10, 1967, pp. 297–309.

7 Bear, J., *Dynamics of Fluids in Porous Media,* American Elsevier, 1972.

8 Torrance, K. E., "Comparison of Finite Difference Computations of Natural Convection," *Journal of Research of the National Bureau of Standards—B. Mathematical Sciences,* Vol. 72B, No. 4, Oct.–Dec. 1968, pp. 281–301.

9 Elder, J. W., "Steady Free Convection in a Porous Medium Heated From Below," *Journal of Fluid Mechanics,* Vol. 27, Part 1, 1967, pp. 29–48.

10 Combarnous, M. A., and Bories, S. A., "Hydrothermal Convection in Saturated Porous Media," *Advances in Hydroscience,* Ven Te Chow, ed., Academic Press, Vol. 10, 1975, pp. 231–307.

11 Nield, D. A., "Onset of Thermohaline Convection in a Porous Medium," *Water Resources Research,* Vol. 4, No. 3, June 1968, pp. 553–560.

APPENDIX

The critical Rayleigh number for the onset of convection in a porous medium was determined by Lapwood [2] for a constant permeability layer with isothermal boundaries and an impermeable bottom. For impermeable and permeable tops, he found $\mathrm{Ra}_{cr} = 39.4$ and 27.1, respectively. Following his procedure this Appendix extends his analysis to a layer with isothermal upper boundary and a prescribed, uniform heat flux at an impermeable, lower boundary. Permeable and impermeable tops are considered.[3] With a slight change of notation for the constant flux case, we obtain the equation for marginal stability:

$$\nabla^4\Theta = -\frac{k\rho g\alpha\dot{q}''}{\mu\kappa_m\lambda_m}\left[\frac{\partial^2\Theta}{\partial x^2}+\frac{\partial^2\Theta}{\partial y^2}\right]$$

Assuming a solution of the form $\Theta = Z \sin \ell x \sin my$ where Z is a function of z only, we obtain: $(D^2 - a^2)^2 Z = \lambda^2 a^2 Z$, where $a^2 = h^2(\ell^2 + m^2)$, $z = h\xi$, $\partial/\partial\xi = D$, and $\lambda^2 = \mathrm{Ra}_f$. The general solution is: $Z = A_1 e^{\gamma\xi} + A_2 e^{-\gamma\xi} + A_3 e^{\delta\xi} + A_4 e^{-\delta\xi}$ where $\gamma^2 = a^2 + a\lambda$ and $\delta^2 = a^2 - a\lambda$.

For constant bottom flux, the bottom thermal condition becomes $D\Theta = 0$ instead of Lapwood's $\Theta = 0$. The imposed boundary conditions for the permeable top case are $DZ = (D^2 - a^2)Z = 0$ at $\xi = 0$ and $Z = D(D^2 - a^2)Z = 0$ at $\xi = 1$. (In this Appendix, $\xi = 0$ and 1, respectively, correspond to the bottom and top of the layer, to be consistent with Lapwood's choice of origin.) The resulting system of four linear equations for A_1, A_2, A_3, and A_4 has a nontrivial solution if the determinant of coefficients is zero:

$$\begin{vmatrix} \gamma & -\gamma & \delta & -\delta \\ 1 & 1 & -1 & -1 \\ e^{\gamma} & e^{-\gamma} & e^{\delta} & e^{-\delta} \\ \gamma e^{\gamma} & -\gamma e^{-\gamma} & -\delta e^{\delta} & \delta e^{-\delta} \end{vmatrix} = 0$$

This determinant yields:

$$2\gamma\delta + \delta^2 \sinh\gamma \sinh\delta + 2\gamma\delta \cosh\gamma \cosh\delta + \gamma^2 \sinh\gamma \sinh\delta = 0$$

No solution exists for δ,γ real. Taking the imaginary root $\delta = i\eta$ we obtain:

$$2\gamma\eta + (\gamma^2 - \eta^2) \sinh\gamma \sin\eta + 2\gamma\eta \cosh\gamma \cos\eta = 0$$

The solution is $\eta = 2.07$ and $\gamma = 3.2$. Thus, we obtain $a = 1.75$, $\lambda^2 = \mathrm{Ra}_{cr} = 17.7$.

For the case of constant bottom flux, impermeable top and bottom, the boundary conditions are $DZ = (D^2 - a^2)Z = 0$ at $\xi = 0$ and $Z = (D^2 - a^2)Z = 0$ at $\xi = 1$. The resulting consistency requirement is:

$$\begin{vmatrix} \gamma & -\gamma & \delta & -\delta \\ 1 & 1 & -1 & -1 \\ e^{\gamma} & e^{-\gamma} & e^{\delta} & e^{-\delta} \\ e^{\gamma} & e^{-\gamma} & -e^{\delta} & -e^{-\delta} \end{vmatrix} = 0$$

The determinant when expanded yields:

$$\delta \sinh\gamma \cosh\delta + \gamma \cosh\gamma \sinh\delta = 0$$

which again has no roots for δ and γ both real. Taking δ imaginary $(= i\eta)$ we obtain:

$$\eta \sinh\gamma \cos\eta + \gamma \cosh\gamma \sin\eta = 0$$

This relationship is exactly what Lapwood found for the constant bottom temperature, permeable upper boundary case and yields $\mathrm{Ra}_{cr} = 27.1$.

A table of critical Rayleigh numbers for the four constant permeability cases considered may now be set up:

	Ra	Impermeable top	Permeable top
Constant bottom temperature (Lapwood)	$\dfrac{k\rho g\alpha\Delta Th}{\mu\kappa_m}$	39.5	27.1
Constant bottom flux	$\dfrac{k\rho g\alpha\dot{q}''h^2}{\mu\kappa_m\lambda_m}$	27.1	17.7

Even though different definitions for Ra are used, they are equivalent at subcritical values of Ra and may be compared. As expected, the case involving two Neumann conditions is the least stable, and the case with no Neumann conditions the most stable. Curiously enough, the two cases involving one Neumann condition show exactly the same critical Rayleigh number, which is midway between the other two values.

[3] Subsequent to the acceptance of this paper, it was discovered by the authors that the permeable top case had been considered previously by Nield [11].

R. D. Gasser
M. S. Kazimi

Fast Reactor Safety Division,
Department of Applied Science,
Brookhaven National Laboratory,
Upton, N. Y.

Onset of Convection in a Porous Medium With Internal Heat Generation[1]

The conditions leading to onset of thermal convection in a horizontal porous layer are determined analytically using the method of linear stability of small disturbances. The lower boundary is treated as a rigid surface and the upper boundary as a free surface. The critical internal and external Rayleigh numbers are determined for both stabilizing and destabilizing boundary temperatures. The predicted critical external Rayleigh number in the limit of no heat generation is in agreement with the critical number predicted for a porous medium heated from below.

Introduction

The occurrence of natural convection in a fluid-saturated porous medium with internal heat generation is of interest in the evaluation of the capability of heat-removal from particulate nuclear fuel debris that may result from a hypothetical accident in a nuclear reactor [1],[2] and in examinations of subterranean porous layers when radioactive heating may be expected either naturally or due to proximity of nuclear wastes. The problem is similar to the occurrence of natural convection in a porous medium heated from below, which has been investigated more extensively in literature [2–6]. However, with the presence of internal heat generation, the temperature gradient of the fluid is nonlinear, and hence thermal convection may occur whether the top boundary temperature is lower or higher than the bottom boundary temperature, as long as a negative temperature gradient of sufficient magnitude occurs somewhere within the layer. The conditions which lead to onset of convection in the otherwise quiescent fluid depend on the porous medium thickness and permeability, fluid and porous medium physical properties, and the rate of internal heat generation. These parameters may be grouped in terms of two pertinent nondimensional numbers:

1 the external Rayleigh number, defined here as

$$R_E = \frac{K_f}{K_m} \cdot \frac{g\beta\Delta TLP}{\nu_f \alpha_f} \tag{1}$$

and

2 the internal Rayleigh number, defined here as

$$R_I = \frac{K_f}{K_m} \cdot \frac{g\beta Q_v L^3 P}{\nu_f \alpha_f K_m} \tag{2}$$

The purpose of this paper is to predict the critical values of R_E and R_I, i.e., the values below which convection does not occur.

Many investigators have considered the conditions for instability in a porous layer heated from below, which was primarily motivated by geophysical considerations [2–4]. Horton and Rogers [2] and Lapwood [3], seem to have been the first to establish analytically the critical Rayleigh number for onset of convection in a fluid-saturated porous layer heated from below (only the external Rayleigh number is of interest in this case). Katto and Masuoka [5] resolved some of the apparent divergence between theoretical predictions and experimental results on convective critical conditions for bottom-heated porous media by introducing the effective thermal diffusivity $\alpha_m = K_m/(\rho C_p)_f$ to replace $\alpha_f = K_f/(\rho C_p)_f$ in the more conventional external Rayleigh number. More recently, Gupta and Joseph's [6] numerical treatment showed excellent agreement with experimental results on the heat transport across a bottom heated porous layer.

Sparrow, Goldstein, and Jonsson [7] studied analytically the thermal instability of an internally heated fluid layer as well as a layer heated from below, with various boundary conditions. They showed that with increasing heat generation rate the fluid becomes more prone to instability, that is, the critical external Rayleigh number decreases. Thirlby [8] conducted a numerical study of

[1] Work carried out under the auspices of the United States Nuclear Regulatory Commission.

[2] Numbers in brackets designate References at end of paper.

Contributed by the Heat Transfer Division for publication in the JOURNAL OF HEAT TRANSFER. Manuscript received by the Heat Transfer Division August 11, 1975. Paper No. 76-HT-EE.

laminar convection in an infinite fluid layer, with particular attention to the dependence of the critical conditions on the Prandtl number. More recently, Suo-Anttila and Catton [9] reported numerical results for the heat transfer upward and downward in a horizontal layer for a destabilizing temperature difference at the upper and lower boundaries. Their results show some agreement with the observations of Kulacki and Goldstein [10], who measured the heat flux and maximum temperature in a fluid layer with equal temperatures at the boundaries. Jahn and Reineke [11] reported measurements that agreed well with those of Kulacki and Goldstein.

Thermal stability of a fluid in an internally heated porous medium has been given only limited attention. Buretta [12] and Sun [13] conducted limited experimental investigations involving electric-current heating of water-saturated bead-filled beds, for the case of no heat flux at the lower boundary. These results, however, are reported only in terms of a Nu number versus R_I with no attention given to the simultaneous effect of R_E on the heat transport. As will be discussed later, simultaneous consideration of the values of R_I and R_E is required for internally heated porous beds. Hwang [16] employed the small parameter method of Poincare to investigate the stability of thermal convection patterns in an internally heated porous medium.

Mathematical Formulation

A schematic diagram for a fluid-saturated bead-filled layer is shown in Fig. 1.

The governing equations for fluid motion in a porous bed are the usual continuity, energy, and momentum equations. These three equations are:

Continuity.

$$\frac{D\rho}{Dt} + \rho\nabla\cdot\bar{v} = 0 \tag{3}$$

Momentum.

$$\rho\frac{D\bar{v}}{Dt} = (0, 0, \rho g) - \nabla p - \frac{\mu}{P}\bar{v} + \mu\nabla^2\bar{v} \tag{4}$$

Energy.

$$\rho C_p\frac{DT}{Dt} = K_m\nabla^2 T + Q_v \tag{5}$$

The third term on the right-hand side of equation (4) results from application of Darcy's law which relates the component of the pressure gradient due to flow resistance in a porous medium to the fluid velocity:

$$\frac{\mu}{P}\bar{v} = -\nabla p \tag{6}$$

When the permeability, P, is large, the resistance to flow becomes effectively controlled by the ordinary viscous resistance, $\mu\nabla^2\bar{v}$. In this case, the convection phenomenon is similar to that in a fluid layer. In early investigations of thermal convection in porous media, the viscous resistance to flow has usually been ignored. This is an appropriate assumption as long as the size of a pore is relatively small compared to the dimensions of the layer.

Determination of the onset of convection is achieved by assuming that instability occurs by way of a perturbation to an existing steady-state or equilibrium condition. In the absence of convection, an equilibrium state is achieved such that heat is removed from the layer by conduction only. This equilibrium state may be expressed mathematically in the following manner (see Fig. 1):

$$\bar{v} = 0, \quad \text{and} \quad K_m\nabla^2 T_0 = -Q_v \tag{7}$$

so that

$$T_0 = \frac{-Q_v z^2}{2K_m} + \left[\frac{Q_v L}{2K_m} - \frac{T_D - T_U}{L}\right] z + T_D \tag{8}$$

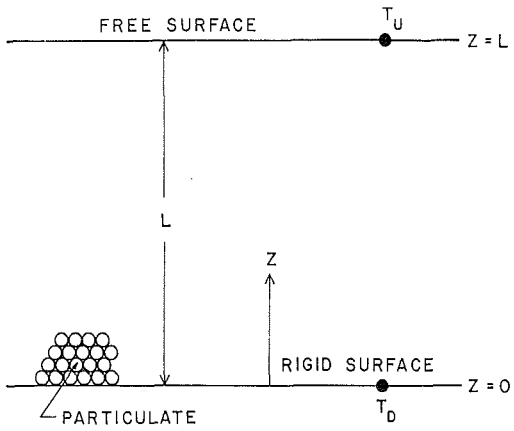

Fig. 1 Schematic illustration of a porous layer

Nomenclature

A_m = constant in the sine series solution
a = wave number
B_m = arbitrary constant in equation (32)
C_m = arbitrary constant in equation (34)
C_p = heat capacity
D_m = arbitrary constant in equation (34)
E_m = arbitrary constant in equation (34)
F_m = arbitrary constant in equation (34)
g = acceleration of gravity
$I_i^{(nm)}$ = ith integral in equation (36) (see Appendix)
K = thermal conductivity
L = layer depth
P = permeability
p = pressure
Q_v = volumetric heat source strength
R_E = external Rayleigh number
$\tilde{R}_E$ = critical external Rayleigh number
R_I = internal Rayleigh number
$\tilde{R}_I$ = critical internal Rayleigh number
T = temperature
ΔT = temperature differential between upper and lower surface (absolute value)
t = time
u = x-component of velocity
v = y-component of velocity
$\bar{v}$ = vector velocity
W = component of w which is a function of z only
w = z-component of velocity
x = direction orthogonal to z
y = direction orthogonal to x and z
y = direction orthogonal to x and z
z = distance in the particle bed measured upward from the bottom surface
α = thermal diffusivity
β = bulk thermal expansion coefficient
β_1,β_2 = constants which satisfy the homogeneous equation (31)
η = dimensionless heat source strength
θ = perturbed temperature
μ = viscosity
ν = kinematic viscosity
ξ = dimensionless length
φ = parameter grouping (equation (32b))
ψ = parameter grouping (equation (32a))
ρ = density

Subscripts and Superscripts

f = fluid properties
m = composite properties of particle bed
U = upper surface
D = lower surface
0 = equilibrium or stable condition
m = incremental integer in sine series solution (equation (30))
n = incremental integer in sine series solution

Equation (8) gives the equilibrium temperature distribution as a function of the vertical distance, z, above the bottom of the porous layer.

The fluid density may be expressed by

$$\rho = \rho_c(1 - \beta T) \tag{9}$$

where ρ_c is the density at $T = 0$.

In a well established procedure (see reference [3 or 14]), we now consider a small departure from equilibrium conditions. Then, the velocity and temperature in the disturbed medium are given by

$$\bar{v} = u\vec{i} + v\vec{j} + w\vec{k} \tag{10}$$

$$T = T_0 + \theta \tag{11}$$

The conservation equations (3)–(5) then take the form

$$\frac{\partial}{\partial t}(u, v, w) = (0, 0, g\beta\theta) - \frac{1}{\rho}\left(\frac{\partial}{\partial x}, \frac{\partial}{\partial y}, \frac{\partial}{\partial z}\right) p - \frac{\nu}{P}(u, v, w) + \nu\nabla^2(u, v, w) \tag{12}$$

$$\frac{\partial u}{\partial x} + \frac{\partial v}{\partial y} + \frac{\partial w}{\partial z} = 0 \tag{13}$$

$$(\rho C_p)_m \frac{\partial \theta}{\partial t} + (\rho C_p)_f \left(u\frac{\partial T}{\partial x} + v\frac{\partial T}{\partial y} + w\frac{\partial T}{\partial z}\right) = K_m \nabla^2\theta \tag{14}$$

The primary assumptions involved in these approximations are: (1) that density changes are negligible except insofar as they modify gravity (in the third of equations (4)); and (2) second order terms are insignificant and, therefore, can be neglected. The first of these two assumptions involves the so called Boussinesq approximation in which physical properties are assumed to be constant with temperature, including density except where it affects the acceleration term in the momentum equation. As demonstrated by Jeffreys [15], the onset of convective currents takes place at the condition of marginal stability in which $\partial/\partial t = 0$.

When substituting the temperature gradient obtained by differentiating equation (8) into equation (14) and applying the condition of marginal stability, we obtain:

$$\frac{(\rho C_p)_f}{K_m} w\left\{\frac{Q_v}{K_m}\left(\frac{L}{2} - z\right) - \frac{T_D - T_U}{L}\right\} = \nabla^2\theta \tag{15}$$

Equation (15) is cast into dimensionless form by using L, $\alpha\nu/g\beta L^3$, and α/L as units of length, temperature, and velocity, with the result:

$$\left[\mathrm{R}'_I\left(\frac{1}{2} - \xi\right) - \mathrm{R}'_E\right] w' = \nabla^2\theta' \tag{16}$$

Here, R_I' and R_E' are the modified internal and external Rayleigh numbers defined as follows:

$$\mathrm{R}'_I = \left(\frac{K_f}{K_m}\right)\frac{g\beta Q_v L^5}{\nu_f \alpha_f k_m} \tag{16a}$$

$$\mathrm{R}'_E = \left(\frac{K_f}{K_m}\right)\frac{g\beta\Delta T L^3}{\nu_f \alpha_f} \tag{16b}$$

Turning attention now to the continuity and momentum equations, we take the divergence of the first and second of equations (12), which yields:

$$\nabla\left(\frac{\partial u}{\partial t} + \frac{\partial v}{\partial t}\right) = -\frac{1}{\rho}\left(\frac{\partial^2 p}{\partial x^2} + \frac{\partial^2 p}{\partial y^2}\right) + \nu\nabla\left(\frac{\partial^2 u}{\partial x^2} + \frac{\partial^2 v}{\partial y^2}\right) - \frac{\nu}{P}\left(\frac{\partial u}{\partial x} + \frac{\partial v}{\partial y}\right) \tag{17}$$

Using equation (13) we can eliminate the u and v components in equation (17) and, thereby, obtain:

$$\left(\frac{\partial}{\partial t} - \nu\nabla^2 + \frac{\nu}{P}\right)\frac{\partial w}{\partial z} = \frac{1}{\rho}\nabla_1{}^2 p \tag{18}$$

where

$$\nabla_1{}^2 = \frac{\partial^2}{\partial x^2} + \frac{\partial^2}{\partial y^2} \tag{19}$$

By applying the operator $\nabla_1{}^2$ to both sides of the third of equations (12), we obtain:

$$\frac{1}{\rho}\frac{\partial}{\partial z}(\nabla_1{}^2 p) = g\beta\nabla_1{}^2\theta \tag{20}$$

Eliminating $\nabla_1{}^2 P$ between (18) and (20) and again assuming a state of marginal stability, we obtain:

$$\left(\nabla^2 - \frac{1}{P}\right)\nabla^2 w = -\frac{g\beta}{\nu}\nabla_1{}^2\theta \tag{21}$$

Nondimensionalizing as before, we arrive at the second equation that relates w' and θ':

$$\left(\nabla^2 - \frac{L^2}{P}\right)\nabla^2 w' = -\nabla_1{}^2\theta' \tag{22}$$

Assuming, at the onset of instability, the velocity and temperature distribution are given by a normal wave function (14), such that:

$$\nabla_1{}^2\theta' = -a^2\theta' \tag{23}$$

and

$$\nabla_1{}^2 w' = -a^2 w' \tag{24}$$

then, equations (22) and (16) may be written as:

$$\left(D^2 - a^2 - \frac{L^2}{P}\right)(D^2 - a^2)W(\xi) = a^2\theta(\xi) \tag{25}$$

$$(D^2 - a^2)\theta(\xi) = \left[\mathrm{R}'_I\left(\frac{1}{2} - \xi\right) - \mathrm{R}'_E\right] W(\xi) \tag{26}$$

Solution

In the present paper, we consider a fluid-saturated porous bed with a free surface as an upper boundary condition and a rigid surface as a lower boundary condition. Mathematically, these boundary conditions are expressed by the following equations:

$$W = DW = 0 \qquad \text{at } \xi = 0 \tag{27}$$

$$W = D^2W = 0 \qquad \text{at } \xi = 1 \tag{28}$$

$$\theta = 0 \qquad \text{at } \xi = 0, 1 \tag{29}$$

Employing a Fourier sine series solution, we have

$$\theta = \frac{1}{a^2}\sum_m A_m \sin(m\pi\xi) \tag{30}$$

and, from equation (25):

$$\left(D^2 - a^2 - \frac{L^2}{P}\right)(D^2 - a^2)W = \sum_m A_m \sin(m\pi\xi) \tag{31}$$

This form of the solution satisfies the boundary conditions in equation (29), and only four additional conditions need to be met.

The particular solution for equation (31) is given by;

$$W_p = \sum_m B_m \sin(m\pi\xi)$$

where

$$B_m = \frac{A_m}{(m\pi)^4 + \psi(m\pi)^2 + \varphi} \tag{32}$$

$$\psi = 2a^2 + \frac{L^2}{P} \tag{32a}$$

$$\varphi = a^2\left(a^2 + \frac{L^2}{P}\right) \tag{32b}$$

The homogeneous solution for equation (31) is of the form:

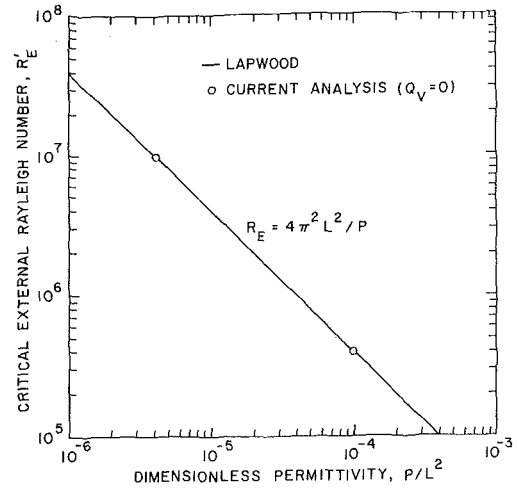

Fig. 2 First three eigenvalues for critical internal Rayleigh number as a function of wave number

$$W_h = C \sinh(\beta_1\xi) + D \sinh(\beta_2\xi) + E \cosh(\beta_1\xi) + F \cosh(\beta_2\xi) \quad (33)$$

where

$$\beta_1^2 = a^2 \quad (33a)$$

and

$$\beta_2^2 = a^2 + \frac{L^2}{P} \quad (33b)$$

Then, the general solution is

$$W = \sum_m B_m \{\sin(m\pi\xi) + C_m \sinh(\beta_1\xi) + D_m \sinh(\beta_2\xi) + E_m \cosh(\beta_1\xi) + F_m \cosh(\beta_2\xi)\} \quad (34)$$

By applying the boundary conditions (27) and (28), the constants C_m through F_m can be evaluated (see Appendix).

The mathematical form of the solution is completed by substituting the expression for the velocity, W (equation (34)), back into equation (26) to obtain:

$$(D^2 - a^2) \sum_m A_m \sin(m\pi\xi) = a^2 \left[R'_I\left(\frac{1}{2} - \xi\right) - R'_E\right] \times \sum_m B_m \{\sin(m\pi\xi) + C_m \sinh(\beta_1\xi) + D_m \sinh(\beta_2\xi) + E_m \cosh(\beta_1\xi) + F_m \cosh(\beta_2\xi)\} \quad (35)$$

When equation (35) is multiplied by $\sin(n\pi z)$ and integrated between $\xi = 0$ and 1, a set of n equations result:

$$\sum_m \frac{[(m\pi)^2 + a^2]}{a^2} A_m I_0^{nm} = \sum_m B_m \left\{\left[R'_E - \frac{R'_I}{2}\right] \times [I_0^{nm} + C_m I_1^{(n)} + D_m I_2^{(n)} + E_m I_3^{(n)} + F_m I_4^{(n)}] + R_I'[I_5^{nm} + C_m I_6^{(n)} + D_m I_7^{(n)} + E_m I_8^{(n)} + F_m I_9^{(n)}]\right\} \quad (36)$$

(see Appendix for the I's.)

Results—Stability Criteria

In this analysis, a sixth order ($n = 6$) approximation was used. This being the case, equation (36) yielded a 6×6 matrix of coefficients of the A_m terms. In order that the A_m be nontrivial, it is required that the determinant obtained from the matrix of the coefficients of A_m vanish. These coefficients are functions of the Rayleigh numbers, R'_I and R'_E, and the wave number, a.

A numerical method was employed to obtain the values of one of the Rayleigh numbers that cause the determinant to vanish when the wave number and the alternate Rayleigh number are specified. For example, if the wave number and the external Rayleigh number, R'_E, are specified, calculations of the eigenvalues yield the first six critical internal Rayleigh numbers, R'_I. If these calculations are performed for various values of the wave number, a relation between the internal Rayleigh number and the wave number is obtained. Fig. 2 shows the variation of R'_I with the wave number for the lowest three harmonics when $R'_E = 0$ and $L^2/P = 2.45 \times 10^5$. The critical value of R'_I for a specified R'_E is the minimum value of R'_I which corresponds to the lowest harmonic. For the case shown in Fig. 2, the critical internal Rayleigh number corresponding to $R'_E = 0$ is $R'_I = 1.15 \times 10^8$.

It was found that if both Rayleigh numbers are multiplied by the dimensionless permeability, P/L^2, all the calculated critical modified Rayleigh numbers fall on a single curve. Fig. 3 shows the critical internal Rayleigh number, $\tilde{R}_I$, as a function of R_E for both stabilizing and destabilizing temperatures at the boundaries. In fact, the graph in Fig. 3 can also be viewed as showing the critical external Rayleigh number, $\tilde{R}_E$, as a function of R_I. It is clear that for a destabilizing temperature condition in the absence of an internal heat source, a definite $\tilde{R}_E$ exists above which convective currents will occur. Increasing the internal heat source will decrease the $\tilde{R}_E$, and this is shown in Fig. 3.

For stabilizing boundary temperatures, the inclusion of a heat source of sufficient magnitude has the effect of moving the position of maximum temperature from the top surface to a position within the layer. This results in a situation in which denser fluid overlies less dense fluid and the conditions for potential fluid motion are established. Since increasing the temperature difference at the boundaries in this case increases the degree of stability in the layer, an increased volumetric heat source will be required in order to establish an unstable condition. This is demonstrated in the upper curve of Fig. 3.

Lapwood [3] established a stability criterion for a porous medium heated from below for the case of two impervious conducting boundaries with a linear destabilizing temperature gradient. His analytical result has been verified by a number of investigators [4]. Writing his results in terms of the external Rayleigh number we have:

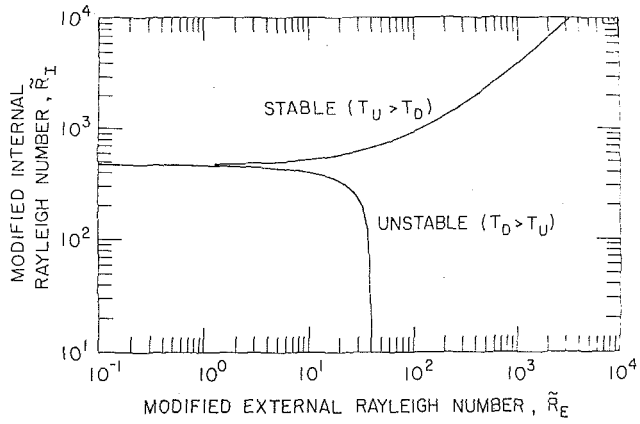

Fig. 3 Critical internal Rayleigh number versus external Rayleigh number for stabilizing and destabilizing temperature differences

$$\tilde{R}_E = 4\pi^2 \tag{37}$$

Extending his analysis to include various combinations of boundary conditions at the upper and lower surfaces, Lapwood established that equation (37) also applied to the case of a rigid lower surface and free upper surface. Although this is a surprising result in view of the fact that the rigid-rigid and the rigid-free boundary conditions produce different results in the analysis of a nonporous liquid layer [7], Lapwood suggests that the difference between the two cases in the case of a porous medium is a second order effect. Fig. 4 shows Lapwood's criterion compared to that established in this analysis for the case of no internal heat source. The circles correspond to calculated points from this analysis. It is seen from Fig. 4 that the results of this work agree quite well with the Lapwood criterion for the case of no internal heat source.

Katto and Masuoka [5] suggest that, due to the effects of heterogeneity, anisotropy, and various other factors including the possible inaccuracy of the Darcy law, theoretical results may deviate from experimental results for P/L^2 higher than some critical number (of the order of 5×10^{-3}). As the permeability increases, the Darcy law resistance decreases and the critical Rayleigh number should approach that of a simple nonporous liquid layer. Katto and Masuoka suggest that the analytical approach using Darcy's law is accurate so long as $d/L < 0.1 \rightarrow 0.2$, where d is the particle diameter and L is the bed depth. Having stated this, however, they proceed to indicate that the theoretical predictions with Darcy's law seem to show relatively small deviation from their experimental results for values of d/L which approach 1.0. However, the scatter of their data make such a conclusion questionable [12].

Direct experimental verification of the present work does not appear to be currently available. Buretta [12] and Sun [13], who experimentally determined the critical internal Rayleigh number for an internally heated porous medium, both quote a critical Rayleigh number of approximately 33. However, their experiments were performed with isothermal rigid upper surface and an adiabatic rigid lower surface. The present analysis employs a rigid lower surface with a free upper surface and isothermal conditions at the upper and lower surfaces. The combination of critical Rayleigh numbers presented here is expected to hold true for a bed with a rigid isothermal upper boundary as well as a free isothermal surface upper boundary. However, due to the adiabatic heat flux condition at the lower boundary in Sun's and Buretta's experiments, it is not possible to compare the present results with the data from those experiments. Hwang [16], who employed the small parameter method of Poincare, supplies a list of critical external Rayleigh numbers as a function of the dimensionless heat source, $\eta = Q_v L^2/K_m \Delta T$. The critical internal Rayleigh number can be calculated directly, since $\eta = \tilde{R}_I/\tilde{R}_E$. A list of Hwang's results is found in Table 1. Hwang did not solve the problem for a stabilizing temperature difference, but his results for the destabilizing case agree remarkably well with the present results shown in Fig. 3.

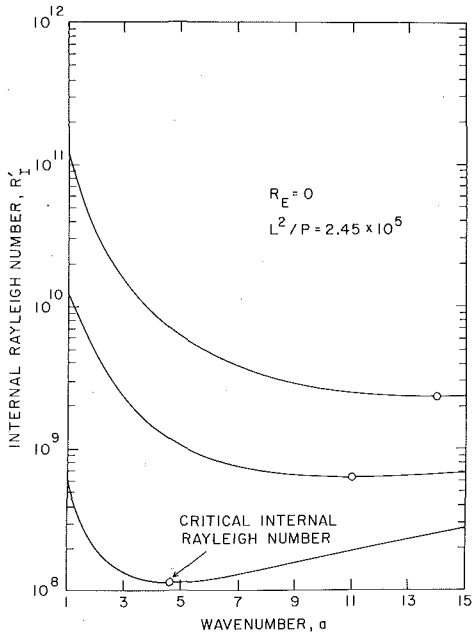

Fig. 4 Comparison between present results and Lapwood's results for no internal heat generation

Table 1 Hwang's results

$\eta = \frac{Q\dot{L}^2}{K_m \Delta T}$	$\tilde{R}_E$	$\tilde{R}_I$
0	39.48	0
5	34.59	173.0
10	27.02	270.2
15	21.45	321.7
20	17.63	352.5
25	14.92	372.9
30	12.91	387.4
40	10.16	406.4
50	8.37	418.4
60	7.11	426.7
80	5.47	437.4
100	4.44	443.9

Results of this analysis may be applied in the field of nuclear reactor safety where the problem of containing the debris which may result from a hypothetical reactor core disruptive accident is of primary concern. Current analysis of hypothetical accidents in the liquid-sodium-cooled fast breeder reactor, for example, predicts the formation of sodium flooded fuel particulate beds at various locations outside the original core region. The heat generated by radioactive decay of fission products in such a debris bed remains appreciable (about 1 percent of the full nominal operating-power level) for an hour after termination of the neutronic chain reaction. Heat transfer rates within the debris bed determine the maximum bed depth and thus the amount of fuel which can be retained in the bed.

Although the present results can be used to predict the conditions for which convective heat transfer can be expected to occur, actual heat transfer rates have not been calculated. Further work in this direction should, therefore, include determination of local Nusselt numbers and perhaps inclusion of various additional boundary conditions. In particular, in a reactor debris case, a coolant layer may overlay the debris bed and, hence, a pervious boundary for the porous bed will be of interest.

In summary, an analytical approach has been used to predict the conditions for the onset of instability in a liquified porous layer with an internal heat source and both stabilizing and destabilizing boundary temperature conditions. The results agree very well with earlier, existing analyses in the limit of no internal heat source. The results of this analysis also agree well with a previous analysis [16] employing a different approach for the case of a destabilizing boundary temperature condition. This analysis, while agreeing well with existing analytical solutions, nevertheless remains to be substantiated by an adequate experimental investigation.

References

1 Kazimi, M. S., and Chen, J. C. "A Condensed Review of the Technology of Post-Accident Heat Removal for the LMFBR," BNL 19856, Brookhaven National Laboratory, Nov. 1974.

2 Horton, C. W., and Rogers, F. T., Jr., "Convective Currents in a Porous Medium," *J. App. Phys.*, Vol. 16, 1945, pp. 367–370.

3 Lapwood, E. R., "Convection of a Fluid in a Porous Medium," *Proc. Camb. Phl. Soc.*, Vol. 44, 1948 pp. 508–521.
4 Shneider, K. J., "Investigation of the Influence of Free Thermal Convection on Heat Transfer Through Granular Material," 11th Int. Cong. of Refrigeration, Paper 11-4, Munich, 1964.
5 Katto, Y., and Masuoka, T., "Criterion for the Onset of Convective Flow in a Fluid in a Porous Medium," *International Journal of Heat and Mass Transfer*, Vol. 10, 1967 pp. 297–309.
6 Gupta, V. P., and Joseph, D. H., "Bounds for Heat Transport in a Porous Layer," *J. Fluid Mech.*, Vol. 57, 1973 pp. 491–514.
7 Sparrow, E. M., Goldstein, R. J., and Jonsson, V. K., "Thermal Instability in a Horizontal Fluid Layer: Effect of Boundary Conditions and Non-Linear Temperature Profile," *J. Fluid Mech.*, Vol. 18, 1964 pp. 513–528.
8 Thirlby, R. "Convection in an Internally Heated Layer," *J. Fluid Mech.*, Vol. 44, 1970 p. 673.
9 Suo-Anttila, A. J., and Catton, I., "The Effect of a Stabilizing Temperature Gradient on Heat Transfer From a Molten Fuel Layer With Volumetric Heating," Presented at the ASME 1974 Winter Meeting in New York, ASME Paper No. 74-WA/HT-45, 1974.
10 Kulacki, F. A., and Goldstein, R. J., "Thermal Convection in a Horizontal Fluid Layer With Uniform Volumetric Energy Source," *J. Fluid Mech.*, Vol. 55, 1972 pp. 271–280.
11 Jahn, M., and Reineke, H., "Free Convection Heat Transfer With Internal Heat Sources—Calculations and Measurements," *Proc. 5th Int. Conf. on Heat Transfer*, Tokyo, 1974.
12 Buretta, R., "Thermal Convection in a Fluid Filled Porous Layer With Internal Heat Generation," PhD thesis, University of Minnesota, 1972.
13 Sun, W. J., "Convective Instability in Superposed Porous and Free Layers," PhD thesis, University of Minnesota, 1973.
14 Chandrasekhar, S., *Hydrodynamic and Hydromagnetic Stability*, Oxford Press, 1961, p. 9.
15 Jeffreys, H., "The Stability of a Layer of Fluid Heated Below," *Phil. Mag.*, Vol. 2, 1926 pp. 833–844.
16 Hwang, I., "Finite Amplitude Thermal Convection in Porous Media With Heat Source and Variable Viscosity," PhD thesis, University of Minnesota, 1971.

APPENDIX

The following system of equations results from applying the boundary conditions in equations (28)–(30) to equation (33):

$$\begin{bmatrix} 0 & 0 & 1 & 1 \\ \beta_1 & \beta_2 & 0 & 0 \\ \sinh(\beta_1) & \sinh(\beta_2) & \cosh(\beta_1) & \cosh(\beta_2) \\ \beta_1^2 \sinh(\beta_1) & \beta_2^2 \sinh(\beta_2) & \beta_1^2 \cosh\beta_1) & \beta_2^2 \cosh(\beta_2) \end{bmatrix} \begin{bmatrix} C_m \\ D_m \\ E_m \\ F_m \end{bmatrix} = \begin{bmatrix} 0 \\ -m\pi \\ 0 \\ 0 \end{bmatrix}$$

Using Cramer's rule to evaluate C_m through F_m yields:

$$C_m = \frac{-m\pi \cosh(\beta_1) \sinh(\beta_2)}{[\beta_1 \cosh(\beta_1) \sinh(\beta_2) - \beta_2 \cosh(\beta_2) \sinh(\beta_1)]}$$

$$D_m = \frac{m\pi \cosh\beta_2) \sinh(\beta_1)}{[\beta_1 \cosh(\beta_1) \sinh(\beta_2) - \beta_2 \cosh(\beta_2) \sinh(\beta_1)]}$$

$$E_m = \frac{m\pi \sinh(\beta_1) \sinh(\beta_2)}{[\beta_1 \cosh(\beta_1) \sinh(\beta_2) - \beta_2 \cosh(\beta_2) \sinh(\beta_1)]}$$

$$F_m = \frac{-m\pi \sinh(\beta_1) \sinh(\beta_2)}{[\beta_1 \cosh(\beta_1) \sinh(\beta_2) - \beta_2 \cosh(\beta_2) \sinh(\beta_1)]}$$

The integrals in equation (35) are defined in the following manner:

$$I_0^{nm} = \int_0^1 \sin(n\pi\xi) \sin(m\pi\xi) d\xi$$

$$I_1^{(n)} = \int_0^1 \sin(n\pi\xi) \sinh(\beta_1\xi) d\xi$$

$$I_2^{(n)} = \int_0^1 \sin(n\pi\xi) \sinh(\beta_2\xi) d\xi$$

$$I_3^{(n)} = \int_0^1 \sin(n\pi\xi) \cosh(\beta_1\xi) d\xi$$

$$I_4^{(n)} = \int_0^1 \sin(n\pi\xi) \cosh(\beta_2\xi) d\xi$$

$$I_5^{nm} = \int_0^1 \xi \sin(n\pi\xi) \sin(m\pi\xi) d\xi$$

$$I_6^{(n)} = \int_0^1 \xi \sin(n\pi\xi) \sinh(\beta_1\xi) d\xi$$

$$I_7^{(n)} = \int_0^1 \xi \sin(n\pi\xi) \sinh(\beta_2\xi) d\xi$$

$$I_8^{(n)} = \int_0^1 \xi \sin(n\pi\xi) \cosh(\beta_1\xi) d\xi$$

$$I_9^{(n)} = \int_0^1 \xi \sin(n\pi\xi) \cosh(\beta_2\xi) d\xi$$

Evaluation of these integrals yields:

$$I_0^{(nm)} = \frac{\delta_{nm}}{2}$$

$$I_1^{(n)} = \frac{-n\pi \sinh(\beta_1) \cos(n\pi)}{\beta_1^2 + (n\pi)^2}$$

$$I_2^{(n)} = \frac{-n\pi \sinh(\beta_2) \cos(n\pi)}{\beta_2^2 + (n\pi)^2}$$

$$I_3^{(n)} = \frac{-n\pi[\cosh(\beta_1) \cos(n\pi) - 1]}{\beta_1^2 + (n\pi)^2}$$

$$I_4^{(n)} = \frac{-n\pi[\cosh(\beta_2) \cos(n\pi) - 1]}{\beta_2^2 + (n\pi)^2}$$

$$I_5^{nm} = \begin{cases} \frac{1}{4}\delta_{nm} \text{ if } n = m \\ \frac{-4nm}{\pi^2[n^2 - m^2]^2} \text{ if } (n - m) \text{ is odd} \end{cases}$$

$$I_6^{(n)} = \frac{2n\pi\beta_1[\cosh(\beta_1) \cos(n\pi) - 1]}{[(n\pi)^2 + \beta_1^2]^2} - \frac{n\pi \sinh(\beta_1) \cos(n\pi)}{(n\pi)^2 + \beta_1^2}$$

$$I_7^{(n)} = \frac{2n\pi\beta_2[\cosh(\beta_2) \cos(n\pi) - 1]}{[(n\pi)^2 + \beta_2^2]^2} - \frac{n\pi \sinh(\beta_2) \cos(n\pi)}{(n\pi)^2 + \beta_2^2}$$

$$I_8^{(n)} = \frac{2n\pi\beta_1 \sinh(\beta_1) \cos(n\pi)}{[(n\pi)^2 + \beta_1^2]^2} - \frac{n\pi \cosh(\beta_1) \cos(n\pi)}{(n\pi)^2 + \beta_1^2}$$

$$I_9^{(n)} = \frac{2n\pi\beta_2 \sinh(\beta_2) \cos(n\pi)}{[(n\pi)^2 + \beta_2^2]^2} - \frac{n\pi \cosh(\beta_2) \cos(n\pi)}{(n\pi)^2 + \beta_2^2}$$

R. J. Kee
Mem. ASME

C. S. Landram[1]
Mem. ASME

Aerothermodynamics Division 8111,
Sandia Laboratories,
Livermore

J. C. Miles
Monsanto Research Corp.,
Mound Laboratory,
Miamisburg, Ohio

Natural Convection of a Heat-Generating Fluid Within Closed Vertical Cylinders and Spheres

Steady natural convective flow fields were numerically and experimentally characterized for 0.7 Prandtl number fluids having constant, uniformly distributed, internal heat sources. The bounding isothermal walls containing the fluid were considered to be either a sphere or a cylinder of finite height. An instrumented cylinder containing radioactive tritium gas was used to demonstrate experimental and analytical agreement for local temperatures over a range of Grashof numbers. For the spherical geometry, a generalized correlation was obtained for the surface-averaged Nusselt number as a function of a modified Grashof number.

Introduction

The natural convection of enclosed, heat-generating fluids has received limited attention. The few specialized cases reported in the literature have consisted of either long, vertical tubes resembling nuclear reactor liquid fuel elements [1, 2],[2] or, in one recent case [3], a long horizontal tube filled with a reacting gaseous mixture obeying Arrhenius's law for the reaction rate dependency on temperature.

For certain processes such as fermentation, liquid radioactive-waste heat removal, or certain chemical reactions possessing reaction rates nearly independent of temperature, the enclosed fluid may be modeled as having a constant, uniformly distributed heat source. Usually, there exists for such systems a quasi-steady state wherein the eventual attenuation of the heat generated within the fluid is slow compared with the time needed for the convective flow and temperature fields to develop from any given change in the heat-generation rate.

When a heat-generating fluid is contained in a vessel, there exist temperature gradients throughout the fluid. The temperature-induced density differences cause a circulatory motion in which the lighter, warmer fluid in the interior regions of the vessel is generally buoyed upward and the heavier, cooler fluid near the walls flows downward. The motion persists in such a way as to conserve the mass, momentum, and thermal energy of the contained fluid. In the steady state, the heat extracted at the walls must equal the total amount of heat generated by the fluid.

For a Prandtl number of 0.7, the convective flow fields which occur in both spherical and vertical cylindrical vessels were obtained numerically using a computationally efficient combination of previously used numerical procedures [3–5]. Local temperatures were measured within a vertical cylinder containing the radioactive (hydrogen) isotope, tritium, and were compared to computed values over a range of Grashof numbers. So as to exclude dependency on cylinder aspect ratio, the numerical procedure was extended to a spherical case so that the apparent shift from a global type flow to a boundary layer flow could be generally characterized solely by a modified Grashof number (Prandtl number fixed at 0.7).

Analysis

Flow Field Relationships. Although only the steady flow and temperature fields are sought, the transient computational process used to obtain them is allowed to progress until a steady state is achieved. Therefore, in deriving the governing equations, we retain time dependencies and treat the fluid as initially quiescent and isothermal until a step in heat generation rate is applied uniformly.

The analysis is based on the assumptions of laminar incompressible flow, and, because of the small temperature differences in the experimental work, the use of constant transport properties is justified. The numerical procedure, however, is not necessarily limit-

[1] Presently at General Electric Vallecitos Nuclear Center, Pleasanton, Calif.

[2] Numbers in brackets designate References at end of paper.

Contribution by the Heat Transfer Division of THE AMERICAN SOCIETY OF MECHANICAL ENGINEERS and presented at the AIChE-ASME Heat Transfer Conference, San Francisco, Calif., August 10-13, 1975. Revised manuscript received by the Heat Transfer Division October 21, 1975. Paper No. 75-HT-60.

ed to the constant property assumption. Viscous dissipation is ignored because the local velocities are small. Even though the flow is taken to be incompressible, the Boussinesq approximation will be used to allow for the temperature dependent buoyancy forces caused by local density differences.

The flow field can be described by the continuity, momentum, and thermal energy equations. In dimensionless vector form the thermal energy equation is written as

$$\frac{\partial \phi}{\partial \tau} + \vec{u} \cdot \text{grad } \phi = \frac{1}{\text{Pr}} (\text{div grad } \phi + 1) \tag{1}$$

where the last term is the contribution of the internal heat source. Use of the Boussinesq approximation introduces the temperature into the momentum equation through the body force term

$$\vec{f} = -\frac{L^3}{\nu^2} \left(1 - \frac{A_0 \beta L^2}{k} \phi\right) \vec{g} \tag{2}$$

For the numerical work, it is convenient to introduce the momentum and continuity equations in terms of stream function and vorticity. Vorticity is defined as the curl of the velocity, and a vorticity transport equation is obtained by taking the curl of the momentum equation. The vorticity equation is derived as

$$\frac{\partial \vec{\omega}}{\partial \tau} + \vec{u} \text{ grad } \vec{\omega} = \text{div grad } \vec{\omega} + \text{Gr}^* \text{ curl } \left(\phi \frac{\vec{g}}{g}\right) + \vec{\omega} \text{ grad } \vec{u} \tag{3}$$

The modified Grashof number $\text{Gr}^* = A_0 g \beta L^5 / k \nu^2$ is a dimensionless parameter group that emerges from the nondimensionalization of the vorticity equation. Unlike the standard Grashof number, Gr^* does not use a characteristic temperature difference, and the length scale appears to the fifth power rather than the third power.

A solution to equations (1) and (3) is possible after the vorticity and velocity vectors are related to a common variable, namely the stream function. It is this additional relationship which limits the type of geometry which can be considered by the present numerical technique. The fundamental restricting requirement allowing for the explicit relationship of vorticity to stream function is that the vorticity vector be unidirectional and normal to the plane of the velocity field. For the sphere and cylinder, this requirement is satisfied when the axis of the enclosure is parallel to the gravitational vector and when there are no circumferential variations in the wall temperature distribution. In such cases, and after equation (3) has been expanded to a coordinate system, only the magnitude of the vorticity must be considered, and the vorticity transport equation may be treated as a scalar equation. Also, the last term of equation (3) will be zero.

The stream function is defined in terms of the local velocity components so as to identically satisfy the continuity equation. These relationships cannot be written in a general vector form; they must be referred to a specific coordinate system. When the definitions of stream function are substituted into the definition of vorticity a second-order elliptic equation relating stream function to vorticity emerges. The relationships for the geometries considered here are:

Cylinder.

$$u_r = -\frac{1}{r}\frac{\partial \psi}{\partial x}; \; u_x = \frac{1}{r}\frac{\partial \psi}{\partial r} \tag{4}$$

and

$$\omega = \frac{\partial}{\partial r}\left(\frac{1}{r}\frac{\partial \psi}{\partial r}\right) + \frac{\partial}{\partial x}\left(\frac{1}{r}\frac{\partial \psi}{\partial x}\right) \tag{5}$$

Sphere.

$$u_r = \frac{1}{r^2 \sin\theta}\frac{\partial \psi}{\partial \theta}; \; u_\theta = -\frac{1}{r \sin\theta}\frac{\partial \psi}{\partial r} \tag{6}$$

and

$$\omega = \frac{1}{r \sin\theta}\left[\frac{\partial^2 \psi}{\partial r^2} + \frac{\sin\theta}{r^2}\frac{\partial}{\partial \theta}\left(\frac{1}{\sin\theta}\frac{\partial \psi}{\partial \theta}\right)\right] \tag{7}$$

Equation (1), (3), and either (4) and (5) or (6) and (7) form a closed set of nonlinear second-order partial differential equations. The solutions to the finite-difference analogs of these equations may be obtained numerically once initial and boundary conditions are specified.

Although the numerical solution will accommodate any wall-temperature specification without curcumferential variations, we consider here the case of an isothermal wall. For that case, the nondimensional temperature must vanish at the wall. Though a boundary condition at the walls requires that the velocity $\vec{u}$ vanish there, in the present formulation, this condition must be cast in terms of boundary values for the vorticity and stream function equations. The vorticity boundary condition is obtained by evaluating the stream function equation on the boundaries according to the velocity boundary condition. For a transient solution, the vorticity boundary conditions continually change as the stream func-

Nomenclature

A_0 = volumetric internal heat source $\frac{\text{cal}}{\text{cm}^3\text{s}}$ [1.907 × 10⁻⁵ × P] [3]

c_p = specific heat evaluated at constant pressure, $\frac{\text{cal}}{\text{gm K}}$ [1.168]

D = diameter, cm

f = term in momentum equation owing to body force, equation (2)

g = gravitational acceleration, cm/s²

Gr^* = modified Grashof number, $\frac{A_0 g \beta L^5}{k \nu^2}$

H = height of cylinder, cm

k = thermal conductivity of the fluid, $\frac{\text{cal}}{\text{s cm K}}$ [2.558 × 10⁻⁴]

L = characteristic length, taken here to be the diameter for both the cylinder and the sphere, cm

Nu = Nusselt number, equation (11)

$\overline{\text{Nu}}_\infty$ = steady surface-averaged Nusselt number, equation (12)

P = pressure, atm

Pr = Prandtl number, ν/α

q_w = heat flux at walls, $\frac{\text{cal}}{\text{cm}^2}$

r = nondimensional radius (dimensional radius divided by characteristic length)

s = surface area of either vessel, cm²

t = time, s

T = local fluid temperature, K

T_m = mean fluid temperature, equation (10), K

T_w = wall temperature, K

u = dimensionless velocity, UL/ν

V = volume of vessel, cm³

x = nondimensional axial coordinate (dimensional coordinate divided by characteristic length)

α = thermal diffusivity of fluid, cm²/s [8.888 × 10⁻¹/P]

β = coefficient of cubic expansion, K⁻¹ [3.555 × 10⁻³]

ρ = fluid density, gm/cc [2.4616 × 10⁻⁴ × P]

ν = kinematic viscosity of fluid, cm²/s [6.222 × 10⁻¹/P]

θ = polar coordinate (the line along which θ = 0 and π is coincident with the gravity vector)

ϕ = dimensionless temperature, $\frac{T - T_w}{A_0 L^2/k}$

τ = dimensionless time, $t\nu/L^2$

$\vec{\omega}$ = vorticity ≡ curl $\vec{u}$

ψ = stream function

[3] The quantities in brackets are the properties of tritium gas (at 25°C) that are used in subsequent cylinder calculations.

tion field varies. The stream function values on the boundaries are obtained by evaluating the stream function definitions at the walls; on a solid boundary the stream function is a constant.

In the nondimensionalization of the equations for both the cylinder and the sphere, we have chosen the diameter as the characteristic length scale by which the coordinates are normalized. Therefore, for the vertical cylinder an additional parameter—the height-to-diameter ratio—must be introduced in order to apply the boundary conditions. Such a parameter does not occur in the spherical geometry since the polar coordinate is inherently dimensionless.

Transport properties used for tritium in comparing experimental results to the numerical solution are given in the nomenclature. The viscosity and thermal conductivity were determined from hydrogen data by means of a kinetic-theory correction for the molecular weight of tritium (see, for example, reference [6]). The density and specific heat capacity were determined by means of the ideal-gas equation of state since the pressures were low enough to justify its use. The Prandtl number was calculated as 0.7. The internal heat generated by the beta emission process during radioactive tritium decay results from the beta particles giving up their kinetic energy by collisions with the surrounding gas. This heating has been accurately measured by calorimetry, and its value was taken to be 0.3240 W/gm [7], from which A_0 was calculated. The range of the average energy (5.65 kev) betas is 0.4 and 4 cm for gas pressure of 1 and 0.1 atm, respectively. Therefore, some energy released by the decay can be absorbed in the vessel walls instead of the gas. However, because the ranges are relatively small with respect to the vessel dimensions, and because some of the betas will be reflected back into the gas from the wall, it is felt that the assumption of uniform heating is a good one for the present experiments. The half-life of tritium is 12.43 yr [7], so the convective flow field is essentially steady for the purposes of this study.

Nusselt Number and Mean Temperature. In addition to the local temperatures and velocities, it is often useful to know the mean fluid temperature and the wall heat transfer. In terms of the dimensionless variables used, the local wall heat flux is given by

$$q_w = -A_0 L(\text{grad } \phi)_{\text{wall}} \tag{8}$$

In the steady state, the spatial integral of q_w must equal the total amount of heat generated by the fluid; thus,

$$\lim_{\tau\to\infty} \int_s (\text{grad } \phi)_{\text{wall}}\, ds = -\frac{V}{L} \tag{9}$$

Since constant fluid properties have been taken, the mean fluid temperature T_m is given by a volumetric average of the local temperatures

$$T_m = T_w + \frac{A_0 L^2}{k}\frac{1}{V}\int_V \phi dV \tag{10}$$

The integral appearing in equation (10) can be written in terms of the Nusselt number; thus if the Nusselt number is known, the mean temperature can then be determined. The local Nusselt number is defined by

$$\text{Nu} = \left(\frac{q_w}{T_m - T_w}\right)\frac{L}{K} = \frac{-V(\text{grad } \phi)_{\text{wall}}}{\int_V \phi dV} \tag{11}$$

At steady state the surface averaged Nusselt number is given by

$$\overline{\text{Nu}}_\infty = \lim_{\tau\to\infty}\frac{1}{S}\int_s \text{Nu}\, ds = \frac{V}{SL}\left(\frac{1}{V}\int_v \phi\, \text{dv}\right)^{-1} \tag{12}$$

which is a function of Gr* and Pr, and for the finite vertical cylinder, is also a function of height-to-diameter ratio. The minimum value of $\overline{\text{Nu}}_\infty$ is given by the pure conduction solution (i.e., Gr* = 0) and is, of course, independent of the Prandtl number. For the sphere, this minimum value for $\overline{\text{Nu}}_\infty$ is 10.

Numerical Solution

The finite-difference analogs to the governing equations were solved for each discrete point on a grid network.[4] Special consideration was given in writing the finite-difference equations at $r = 0$ where the equations become singular (see, for example, reference [8]). Although only the steady solutions were of concern, the transient solutions for an initial step in A_0 (constant T_w) were obtained. This procedure allows the retention of the parabolic or marching character of the transport equations.

The numerical technique used is a modification of an alternating-direction-implicit (ADI) method [9]. This modification increases the computational efficiency by treating the advective and source terms in the transport equations in an explicit way [8]. The procedure requires fewer computations per timestep than does an ADI method, and permits taking larger, but nonetheless stable, timesteps than does the explicit method. If the advective terms are treated implicitly in the ADI scheme, the coefficient matrices of the tridiagonal sets of equations must be evaluated at each timestep. However, when only the diffusion terms are evaluated implicitly, and when the transport properties are constant, the coefficient matrices are functions of the grid geometry alone and not the flow field. Therefore, it is necessary to evaluate the tridiagonal coefficients only once at the beginning of the solution instead of at each timestep, and the computational procedure is more efficient than the normal ADI method. For the Gr* of interest here the stabilizing influence of the implicit treatment of the diffusion terms allows timesteps comparable to those of the full ADI method. The diffusion and source terms are differenced with second-order central differences and the advective terms are differenced with first-order conservative windward differences. Although other approximations could be made for the advective terms, it is felt that the physical nature of advection is best described by the windward difference formulation [10].

The numerical procedure, which is developed in detail in reference [8] is outlined as follows. Begin by setting the initial and boundary conditions. The velocities, which are used in the advective terms, are then calculated from the stream function field using central-difference approximations to equations (4) or (6). Next, the transport equations [temperature, equation (1); and vorticity, equation (3)] are advanced one timestep in an ADI procedure; in the present formulation, the advective terms are evaluated entirely explicitly (at the previous timestep) and can be thought of as source terms in a diffusion equation. With the new vorticity field, the new stream function field can be found by solving the stream function equation [equation (5) or (7)]. To do so, these elliptic equations are solved using an iterative successive over-relaxation technique. The new values of the vorticity boundary condition are then computed from the stream function field and the velocity boundary conditions. The entire procedure, beginning with the velocity evaluation, is repeated until the steady-state solution results.

For the low-Grashof-number computations, a few hundred seconds of CDC 6600 time were required, while several thousand seconds of computation were needed for the high-Grashof-number calculations in the sphere. Since most of the computer time is spent in solving the stream function equation, the computational efficiency could be increased by using a faster Poisson solver. As Gr* becomes large the overall accuracy of solution can be enhanced by concentrating grid points near the boundaries. However, for the Gr* of interest here it is felt that a uniform grid spacing provides sufficient accuracy.

Experimental Method

Numerical results for the cylinder were compared with experimentally determined temperatures at three axial and two radial locations over a range of internal gas pressures (0.1, 0.5, 1.0 atm) to

[4] For the vertical cylinder an equally spaced grid network of 19 radial by 39 axial divisions was used. For the sphere the grid was composed of 40 radial by 39 polar divisions.

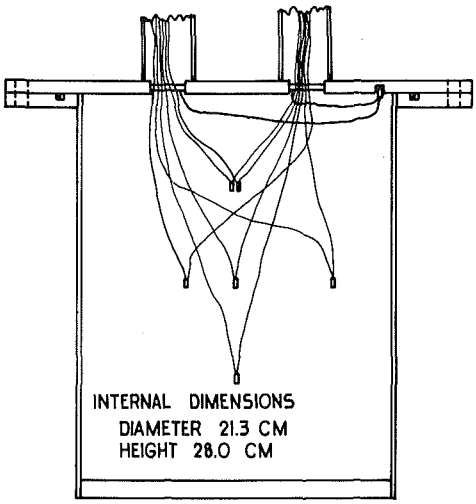

Fig. 1 Cross section of the 10-l cylindrical vessel, including locations of thermistor thermometers

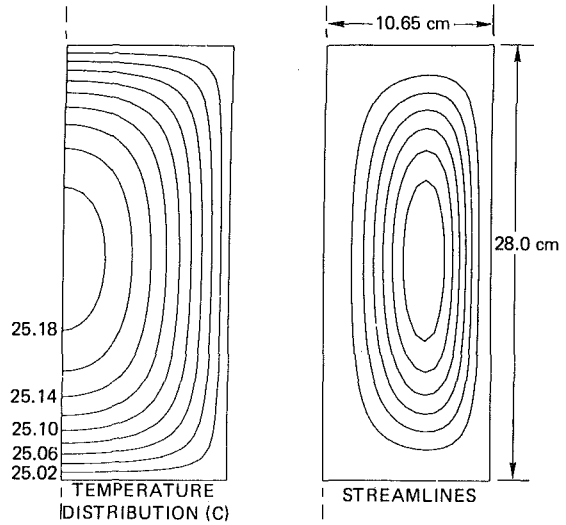

Fig. 2 Calculated isotherms and streamlines for the 10-l vessel filled with tritium gas at 0.1 atm ($Gr^*_D = 2.78 \times 10^3$)

simulate a range of modified Grashof numbers. Relatively pure (99 percent) tritium contained in the cylinder provided a uniformly distributed heat source. The cylinder was placed in a well-stirred constant-temperature (298.0 ± 0.003 K) water bath to ensure isothermal boundaries. The cylinder volume was 10 l, and its height and diameter were 28 and 21.3 cm, respectively (Fig. 1).

The temperature measurements were obtained with small (2.5 mm dia by 6 mm long) resistance thermometers (thermistor) placed at each of five positions. The sensors were suspended on thin but stiff lead wires, and their positions were checked before and after the tests to make sure that no movement had occurred. The sensors consisted of a semiconductor metallic oxide sensing element encapsulated and hermetically sealed in glass. Sensors were calibrated by comparison with a calibrated platinum resistance thermometer in the bath and with a non-heat-generating gas (air or hydrogen) in the cylinder. Using small increments in the bath temperature, the sensors were calibrated over the range of tritium-induced temperature rises. The calibration procedure was repeated after each series of temperature measurements to verify the stability of the sensors after exposure to tritium nuclear radiation. Their integrity during the test was verified by measuring the wall temperature (which is equal to the bath temperature) with a sensor that is in contact with the tritium environment. Resistive heating in the sensors was reduced to negligible levels by systematically lowering sensor electrical current until the measured resistances were constant at a given temperature. The limited number of sensors and the smallness of the sensor wires minimized interference with the thermal and convective flow fields inside the cylinder.

The overall measurement uncertainty is estimated to be ±0.06 K at a pressure of 1 atm and ±0.04 K at the lower pressures. These estimated measurement errors represent the sum of reasonable bias estimates plus two standard deviations of the random variability of the measurements.

Results

The experimental and calculated temperature fields are compared here for the vertical cylinder filled with tritium gas at pressures of 0.1, 0.5, and 1.0 atms. These pressures correspond to Gr* values (based on cylinder diameter) of 2.8 (10^3), 3.5 (10^5), and 2.8 (10^6), respectively. The numerical solutions are shown in Figs. 2, 3, and 4 as steady-state isotherms and streamlines. Also, the calculated axial velocity profiles at the cylinder midheight (14 cm from the cylinder base) are plotted in Fig. 5. Very small velocities occur at the low pressures while velocities as large as 3.2 cm/s occur at a pressure of 1 atm. As would be expected, the wall boundary layer becomes thinner and shifts nearer the wall for higher Gr*.

At the lowest pressure, the absence of significant convection is revealed both by the negligibly small velocities and by the symmetry of the isotherms. Thus, the solution approaches the conduction solution (i.e., no fluid velocity) as a lower limit of small Gr*. For the pure conduction solution, which can be obtained analytically [11], the isotherms would be perfectly symmetric about a horizontal plane at the cylinder midheight. For a pressure of 0.1 atm, the peak conduction temperature is 25.198°C, and the peak temperature computed in the convective field is 25.192°C. At a pressure of 1 atm, the conduction peak temperature is 26.918°C, and it still occurs at the cylinder center. However, at this higher pressure, the convective effects become important, the peak temperature is reduced to 25.97°C, and its location is shifted to one well above the cylinder center (Fig. 4). In the limit of infinite Gr*, the temperature field will become almost isothermal, with all the temperature gradients occurring in a very narrow boundary layer near the wall.

Experimental temperature measurements were taken at five

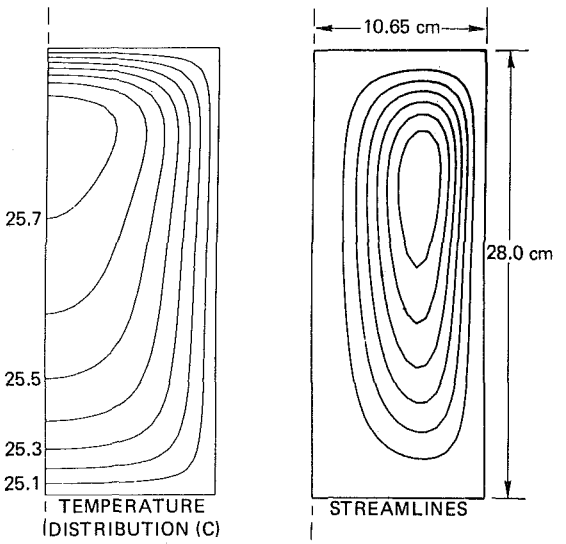

Fig. 3 Calculated isotherms and streamlines for the 10-l vessel filled with tritium gas at 0.5 atm ($Gr^*_D = 3.5 \times 10^5$)

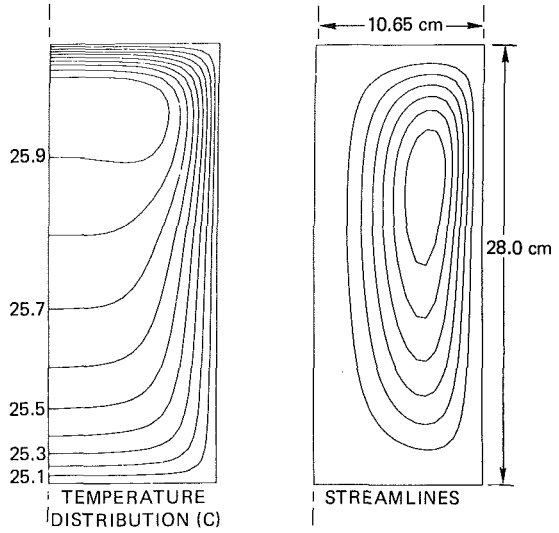

Fig. 4 Calculated isotherms and streamlines for the 10-l vessel filled with tritium gas at 1.0 atm ($Gr^*_D = 2.78 \times 10^6$)

points within the cylinder: three along the cylinder axis and two at the cylinder midheight. These data are plotted for the three pressure levels in Figs. 6 and 7 along with the corresponding calculated temperature profiles. Since the estimated uncertainty in the measurements is ±0.06 K, the calculations are well within the limits of experimental error. The fact that the measured temperatures are below those calculated for the $Gr^* = 2.78(10^3)$ case may be caused by the deposition of some of the energy in the cylinder walls and not in the gas.

Because the height-to-diameter ratio is eliminated, the sphere is the more suitable geometry for illustrating the dependency of the flow on Grashof number. Moreover, the conduction solution, which is a lower bound for $Gr^* = 0$, is unidimensional and thus provides a convenient basis for comparison with the higher-Gr^* results. The steady-state conduction solution is given analytically by

$$T(r) = \frac{A_0 D^2}{6k}\left(\frac{1}{4} - r^2\right)$$

Three representative solutions are given in Figs. 8–10 for successively increasing values of Gr^*_D. These figures show plots of isotherms, streamlines, and normalized[5] temperatures, each as a function of radius. The dashed line on each plot is the conduction solution; the solid lines are the convection solution on rays of angles, 0, 45, 90, 135, and 180 deg from the top; and the line defined by asterisks is the computed mean temperature.

For $Gr^* = 10^5$ (Fig. 8), the velocities are low and the convection results are not too far from the conduction solution; thus, the peak temperature has shifted only slightly above the center. The flow field may be characterized as global because no particularly steep gradients exist.

As the modified Grashof number increases, however, steeper gradients begin to form near the walls. Around Gr^* of 10^7, a boundary-layer type of flow is apparent near the walls. The increased velocities cause the peak temperature to shift closer to the top of the sphere, and there is a significant departure from the conduction solution. The crescent shape in the isotherms (Fig. 9) is caused by the updraft of warm fluid in the interior regions accompanied by a downflow within the boundary layer on the cooler wall. The increased fluid velocities are responsible for mixing the fluid and reducing the temperatures well below the values for conduction alone.

At $Gr^* = 10^{10}$, the velocities are still larger and there is significant fluid mixing; thus the internal temperatures are nearly uniform, and most of the temperature drop occurs close to the walls. In contrast with that of the pure conduction problem, the temperatures for high Gr^* are small. Fig. 10 reveals a thin, high-velocity boundary layer and a bowing of the streamlines in the interior regions, phenomena which may imply a vortex separation there. At these high-Gr^* values, instabilities in the flow are likely to develop. Some evidence of the possibility of turbulence is apparent in the kidney shape of the vortex patterns at $Gr^* = 10^{10}$ and in the large gradients near the wall. Therefore, the very-high-Gr^* solu-

[5] All temperatures are normalized to the peak conduction temperature.

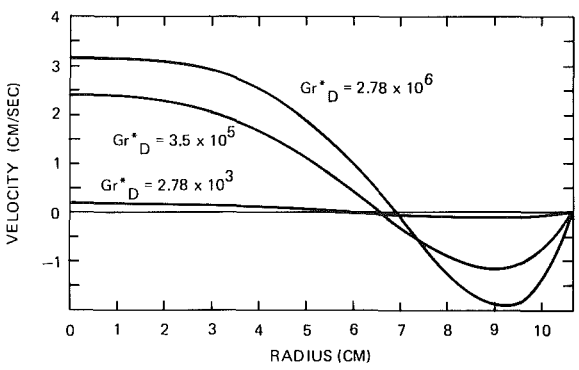

Fig. 5 Calculated axial velocity profiles at cylinder midheight for three values of Gr^*_D

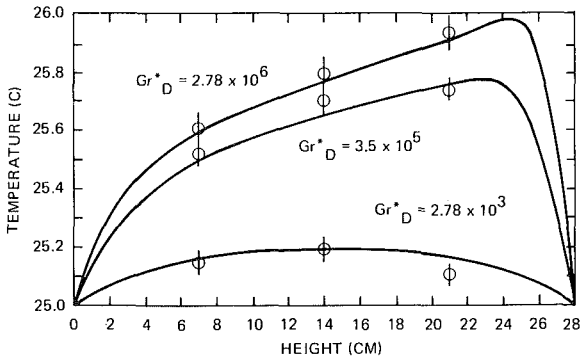

Fig. 6 Comparison of measured (points) and calculated (solid lines) axial temperature profiles in a 10-l cylindrical vessel filled with tritium gas at various values of Gr^*_D

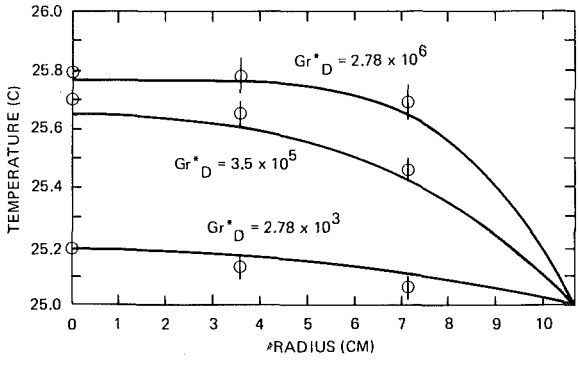

Fig. 7 Comparison of measured (points) and calculated (solid lines) radial temperature profiles at the midheight of a 10-l cylindrical vessel filled with tritium gas at various values of Gr^*_D

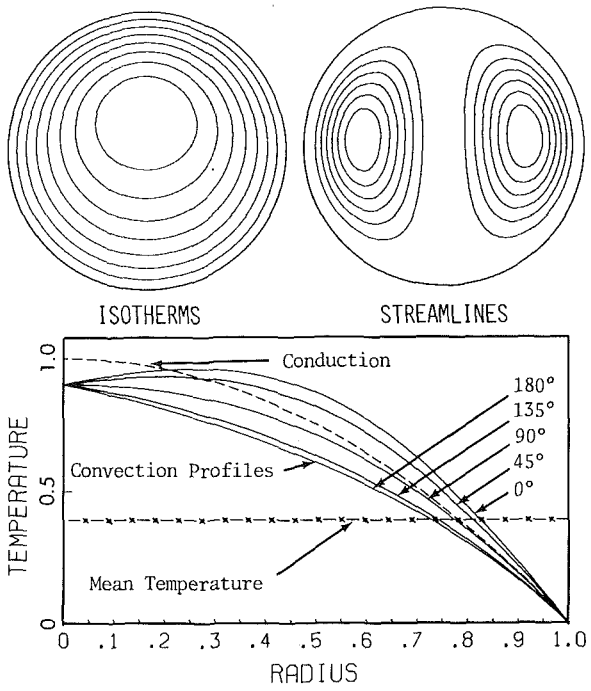

Fig. 8 Computed isotherms, streamlines, and radial temperature profiles in a sphere of fluid having $Gr^* = 10^5$

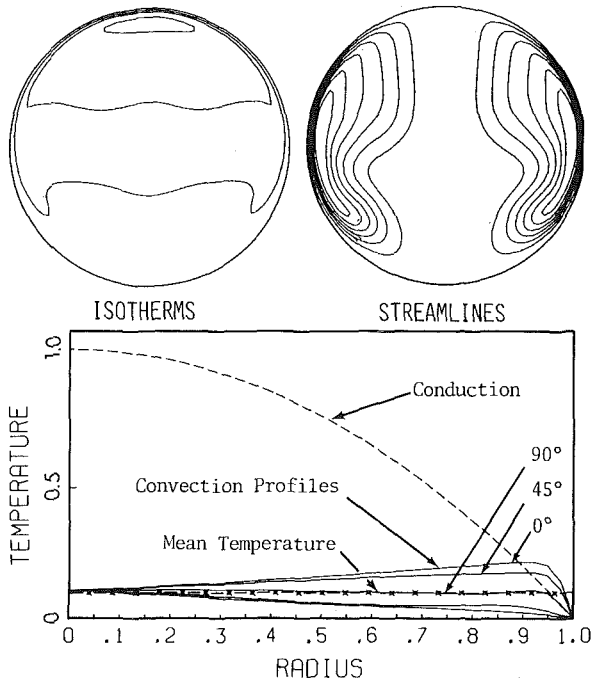

Fig. 10 Computed isotherms, streamlines, and radial temperature profiles in a sphere of fluid having $Gr^* = 10^{10}$

tions do have more inaccuracies associated with them than do the lower. It is for this reason that results are not presented at higher Gr* even though the numerical calculations can be made.

The convective contribution to the surface-averaged Nusselt number, $\overline{Nu}_\infty - 10$, is plotted as a function of Gr^*_D for a 0.7 Prandtl number fluid in Fig. 11. The shift from a global to a boundary-layer type of flow is responsible for the gradual change in slope of the Nusselt number curve in the range $10^5 < Gr^* < 10^7$.

For a particular vessel and fluid, the correlation shown in Fig. 11 allows the prediction of the Nusselt number from which the steady mean fluid temperature can be determined.

Acknowledgments

The authors wish to acknowledge the experimental assistance of A. F. Ciramella. This work was supported under U. S. Energy Research and Development Administration contract numbers AT-(29-1)-789 and AT-33-1-GEN-53.

References

1 Murgatroyd, W., and Watson, A., "An Experimental Investigation of the Natural Convection of a Heat Generating Fluid Within a Closed Vertical Cylinder," *Journal Mechanical Engineering Science*, Vol. 12, No. 5, 1970, pp. 354–363.

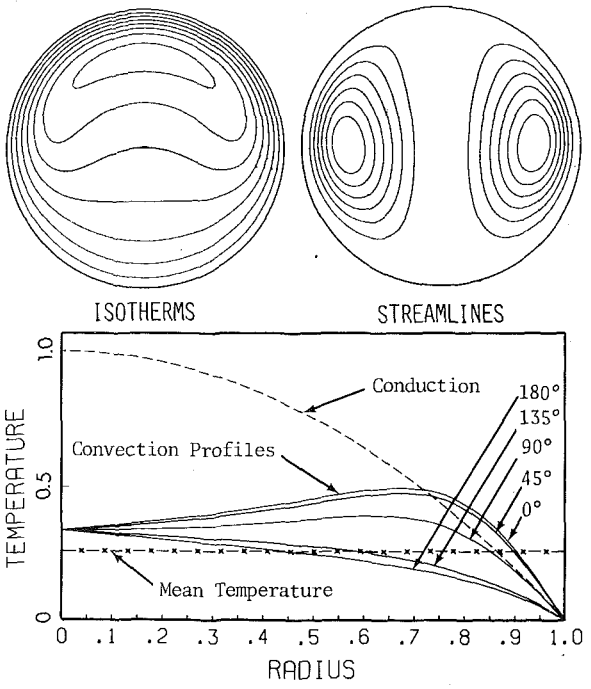

Fig. 9 Computed isotherms, streamlines, and radial temperature profiles in a sphere of fluid having $Gr^* = 10^7$

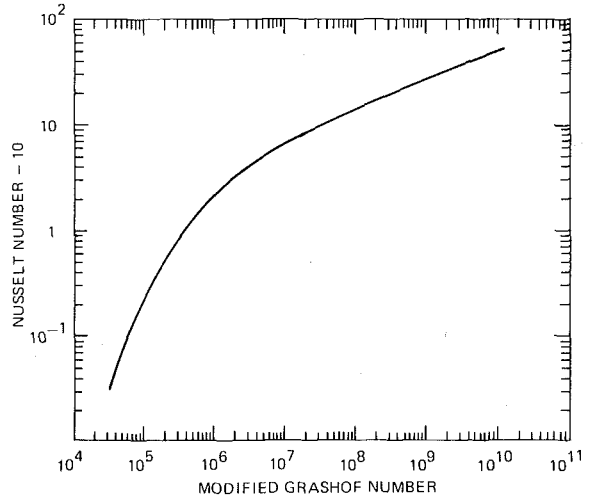

Fig. 11 General correlation between the surface-averaged Nusselt number and the modified Grashof number for a sphere of heat-generating fluid

2 Martin, B. W., "Free Convection in a Vertical Cylinder With Internal Heat Generation," *Proc. Roy. Soc.*, Series A, Vol. 301, 1967, pp. 327–341.

3 Jones, D. R., "Convective Effects in Enclosed, Exothermically Reacting Gases," *International Journal of Heat and Mass Transfer*, Vol. 17, 1974, pp. 11–21.

4 Torrance, K. E., "Comparison of Finite-Difference Computations of Natural Convection," *Journal of Research of the National Bureau of Standards*, Vol. 72, Series B, No. 4, 1968, pp. 281–301.

5 Wilkes, J. O., and Churchill, S. W., "The Finite-Difference Computation of Natural Convection in a Rectangular Enclosure," *American Inst. of Chemical Eng. Journal*, Vol. 12, No. 1, 1966, pp. 161–166.

6 Michels, A., Schipper, A. C. J., and Rintoul, W. H., "The Viscosity of Hydrogen and Deuterium," *Physica*, Vol. XIX, 1953, pp. 1011–1028.

7 Pillinger, W. L., Hentges, J. J., and Blair, J. A., "Tritium Decay Energy," *Physical Review*, Vol. 121, No. 1, Jan. 1961, pp. 232–233.

8 Kee, R. J., "A Numerical Study of Natural Convection Inside a Horizontal Cylinder With Asymmetric Boundary Conditions," PhD thesis, University of California, Davis, Calif., May 1974, pp. 87–118.

9 Peaceman, D. W., and Rachford, H. H., Jr., "The Numerical Solution of Parabolic and Elliptic Differential Equations," *Journal Society of Indust. Appl. Math.*, Vol. 3, 1955, p. 28.

10 Roache, P. J., *Computational Fluid Dynamics*, Hermosa Publishers, Albuquerque, N. Mex., 1972, p. 73.

11 Carslaw, H. S., and Jaeger, J. C., *Conduction of Heat in Solids*, Oxford University Press, Second ed., 1959, pp. 223, 232.

Y. Kamotani
Research Associate.

S. Ostrach
Professor. Mem. ASME

Department of Fluid, Thermal, and Aerospace Sciences, Case Western Reserve University, Cleveland, Ohio

Effect of Thermal Instability on Thermally Developing Laminar Channel Flow

Results are reported of an experimental investigation in the thermal entrance region of a horizontal parallel-plate channel when the lower plate is heated and the upper one is cooled. The experiments covered a range of Rayleigh numbers between 10^3 and 3.1×10^4 and Reynolds numbers between 30 and 1100 using air. Measurements of Nusselt numbers and temperature distributions indicate much higher critical Rayleigh numbers than the theoretically predicted values. Beyond critical Rayleigh numbers second-type vortex rolls are predominant and the local Nusselt number increases gradually with the Rayleigh number. The thermal-entrance length as determined from temperature profiles does not show appreciable change with the Rayleigh number.

Introduction

The effects of a thermal instability on a fully developed laminar flow between two horizontal flat plates where the lower plate is heated and the upper is cooled have been studied theoretically, as well as experimentally, by several investigators (e.g., Ostrach and Kamotani [1][1] and Hwang and Cheng [2]). Beyond a critical temperature difference longitudinal vortex rolls appear in the passage and appreciable heat transfer augmentation is obtained.

In practice fully developed conditions are usually not met because of the limited length of the flow passage. Thus, the study of thermal instability in the entrance region is very useful. However, very little work has been done on this problem. Hwang and Cheng [3] determined theoretically the conditions marking the onset of thermal instability in a hydrodynamically fully developed but thermally developing region. They found that for $Pr \geq 0.7$, the flow is more stable in the thermal entrance region than in the fully developed region, but the opposite is true for $Pr \leq 0.2$. They calculated critical Rayleigh numbers at different locations in the thermal boundary layer.

In the present experiments the heat transfer rate was measured in the thermal entrance region in the range $Ra = 10^3$–3.1×10^4 and $Re = 30$–1100. The onset of thermal instability was determined experimentally and was compared to the theoretical prediction of Hwang and Cheng. In addition, temperature distributions were investigated to study the effects of longitudinal vortex rolls on the temperature field in the thermal entrance region and, hence, on the augmentation of the heat transfer.

Experimental Apparatus and Procedure

A sketch of the test apparatus and the coordinate system adopted herein is shown in Fig. 1. The test section was 31.8 cm wide and 26.7 cm long. The lower plate of the test section was made of a 6.35 mm thick aluminum plate. Electrical heating mats were bonded to the back of the aluminum plate. Six heaters of various sizes were arranged as shown in Fig. 2. Four guard heaters were used to compensate for the heat loss to both sides of the plate. The input to each heater was regulated individually by a voltage controller. The upper plate of the test section was made of a 6.35-mm plexiglas plate and it was cooled by water flowing over it. The cooling water was maintained by a constant temperature circulator which controlled the temperature of the water within ± 0.01°C. The surface temperatures of the lower and upper plates were measured by several copper-constantan thermocouples embedded in both plates. The surface temperatures of both plates were kept very uniform (within ± 1 percent) throughout the experiments. The temperature of the upper plate was kept at the main stream temperature to eliminate a thermal boundary layer on the upper wall.

The side walls of the test section were made of 3.2 mm thick insulating boards. The height of the test section was adjusted by the

[1] Numbers in brackets designate References at end of paper.

Contributed by the Heat Transfer Division for publication in the JOURNAL OF HEAT TRANSFER. Manuscript received by the Heat Transfer Division July 14, 1975. Paper No. 76-HT-R.

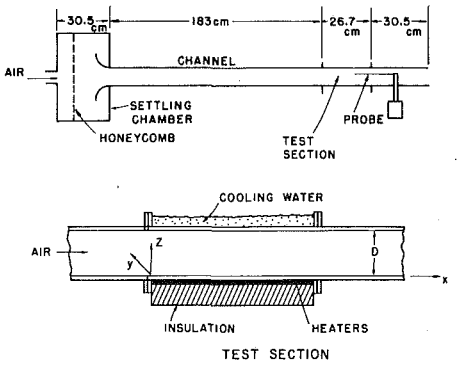

Fig. 1 Sketch of test apparatus

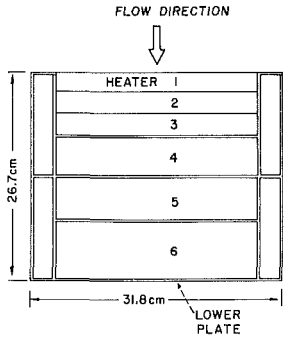

HEATER SIZE

HEATER NUMBER	W cm	L cm
1	2.54	25.4
2	2.54	25.4
3	2.54	25.4
4	5.08	25.4
5	5.08	25.4
6	7.62	25.4
GUARD HEATERS	2.54	12.7

Fig. 2 Heater arrangement

height of the side walls. The height was varied between 12.70 and 19.05 mm in the present experiments.

Air from a compressor passed through a settling chamber and a 183 cm long rectangular channel before entering into the test section. The volume flow rate of air was measured by a flowmeter. The mean speed at the test section was calculated from the total flow rate.

The heat transfer rate was calculated from the net heat input to the air in the test section. The calculation of the net heat input is explained in detail in Ostrach and Kamotani [1]. The heat transfer coefficient and Nusselt number are defined as

$$\frac{Q_{\text{NET}}}{\text{area}} = h(T_1 - T_0)$$

$$\text{Nu} = \frac{hD}{k}$$

The experimental error in the value of Nu was estimated to be ±10 percent.

To measure velocity and temperature distributions in the test section a probe was inserted from the downstream end of the test section. The probe was supported by a three-way traversing device. Temperature was measured by a copper-constantan thermocouple probe. Velocity was measured by a hot-wire probe which was operated by a constant current anemometer.

Experimental Results

Preliminary Investigation of Flow Field. In order to confirm the fully developed laminar velocity profile at the test section, cross-sectional velocity distributions were measured near the entrance of the test section using a hot wire. Fig. 3 shows that in the range of Reynolds numbers covered in the present experiments the velocity profile is fully developed at the test section. The turbulence level of the main stream was small but increased with the Reynolds number. Since most of the present data were taken for Re < 200, the effect of the free stream turbulence was considered to be negligible. To check the two-dimensionality of the main stream, spanwise velocity distributions were measured at the mid-height. One example is shown in Fig. 4 for Re = 200. The profile was very flat over most of the test section, and the side wall boundary layers did not extend to the region covered by the main heaters so that their effect on the heat transfer measurements was considered to be small. The low turbulence level is also indicated on the figure.

Temperature distributions were measured at various axial locations in the boundary layer for subcritical temperature differences. The results are shown in Fig. 5. The axial distance from the start of the heated section was nondimensionalized as $x' = x/D\text{Pe}$ where Pe = Pr Re. The present data agree very well with the theoretical results given by Hwang and Cheng [3]. It is noted that the temperature field becomes fully developed at around $x' = 0.4$. The same degree of two-dimensionality was observed for the temperature distribution as for the velocity distribution.

Heat Transfer Rate and Temperature Distribution. Fig. 6 shows the variation of mean (over a given length) Nusselt number with x' for $10^3 < \text{Ra} < 3.0 \times 10^4$ and $30 < \text{Re} < 1100$. The solid line is the theoretical curve given by Hatton and Turton [4] for the subcritical temperature difference. When Ra < 1700 (the critical Rayleigh number for the fully developed region) the mean Nusselt number variation with x' agrees very well with the theoretical result. For fully developed flow and temperature fields it was shown in Ostrach and Kamotani [1] that there is a sharp increase in the Nusselt number when the Rayleigh number exceeds 1700. Although the same qualitative trend can be observed in Fig. 6 for cases with a thermal boundary layer, the situation is more complex. The enhanced heat transfer now occurs at different axial locations depending on the Rayleigh number. Furthermore, for a fixed Rayleigh number (in the range studied herein) the heat transfer augmentation is less in the thermal boundary layer region (x' less than approximately 0.4) than in the fully developed region. Nevertheless, by increasing the Rayleigh number (beyond the critical) conventional thermal boundary layer heat transfer can be sig-

Nomenclature

D = height of test section
Gr = Grashoff number, $g\beta\Delta TD^3/\nu^2$
g = acceleration of gravity
h = heat transfer coefficient
Nu = Nusselt number, hD/k
Pe = Peclet number, PrRe
Q_{NET} = net energy input
Ra = Rayleigh number, $g\beta\Delta TD^3/\nu\kappa$
Re = Reynolds number, $\bar{U}D/\nu$
T = temperature
T_1 = surface temperature of the heated plate
T_0 = temperature of main stream and the cooled plate
ΔT = temperature difference, $T_1 - T_0$
$\bar{T}$ = average temperature
$\bar{U}$ = volume averaged speed of the main flow
u = velocity fluctuation
x = coordinate parallel to the main flow direction measured from the leading edge
x' = dimensionless axial distance, $x/D\text{Pe}$
y = coordinate in spanwise direction
z = coordinate normal to horizontal plates
β = coefficient of volumetric expansion
κ = thermal diffusivity of air evaluated at $\frac{1}{2}(T_1 + T_0)$
ν = kinematic viscosity of air evaluated at $\frac{1}{2}(T_1 + T_0)$

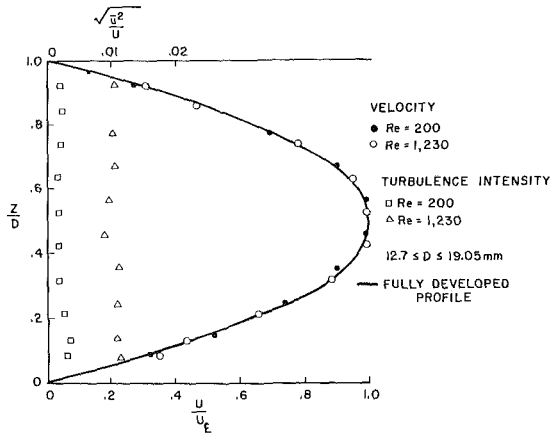

Fig. 3 Fully developed velocity distribution

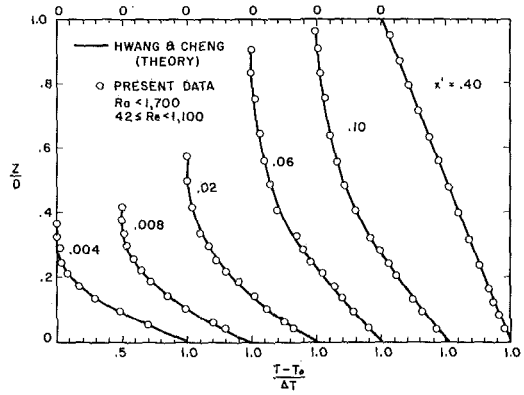

Fig. 5 Sub-critical temperature distribution

nificantly increased as will be discussed shortly. As can be seen in Fig. 6 even at a large Rayleigh number of 3×10^4 the mean Nusselt number does not differ from the subcritical values up to $x' = 0.7$. The location where the mean Nusselt number deviates from the subcritical value moves upstream as the Rayleigh number increases.

In order to see the effect of Rayleigh number on Nusselt number locally the average Nusselt number over each heater was calculated. The variation of the locally averaged Nu with Ra is shown in Fig. 7. Nu $[a \leq x' \leq b]$ means Nusselt number averaged over $a \leq x' \leq b$. In the region of small x' (Nu $[0.011 \leq x' \leq 0.023]$ in Fig. 7) Nu is constant within the experimental error up to Ra = 3.1×10^4 which is the maximum Ra studied herein. In the region $0.080 \leq x' \leq 0.113$, Nu increases gradually with Ra starting from Ra $\doteq 10^4$. A similar trend occurs for the region $0.035 \leq x' \leq 0.054$. Although the heat transfer increase is gradual with Ra the overall effect can be considerable for large Ra and, furthermore, it appears as if Nu above that for the fully developed case can also be obtained. In the fully developed region (Nu $[0.457 \leq x' \leq 0.649]$ in Fig. 7) Nu shows a sharp increase across Ra = 1700. Since the increase of Nu is due to thermal instability, the thermal boundary layer is more stable in the developing than in the fully developed region.

Using linear stability theory Hwang and Cheng [3] calculated the critical Rayleigh numbers in the thermal boundary layer. Their results are shown in Fig. 8 for Pr = 0.7 and Pe = ∞. According to Hwang and Cheng the curve for Pe = ∞ is very close to ones for Pe ≥ 100. The present Nu measurements show much higher critical Rayleigh numbers than given by Hwang and Cheng. To verify this

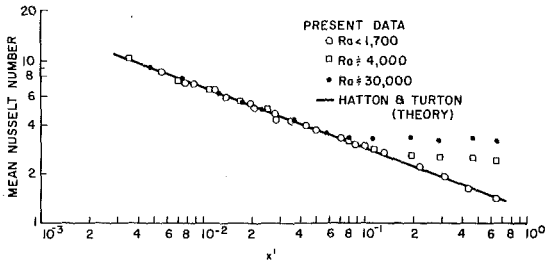

Fig. 6 Mean Nusselt number

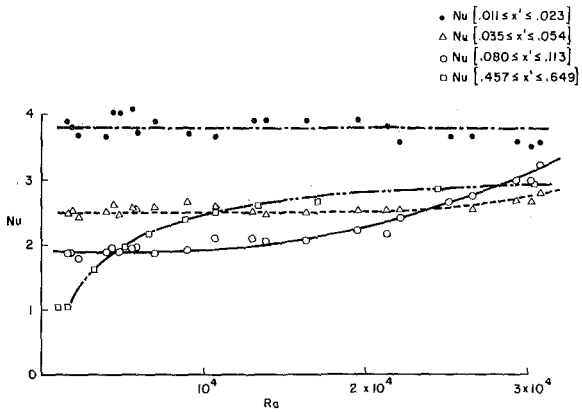

Fig. 7 Locally averaged Nusselt number

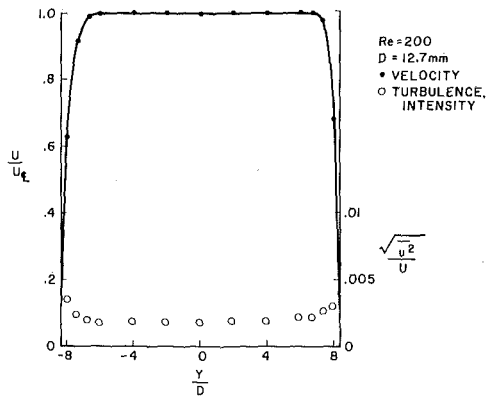

Fig. 4 Spanwise velocity distribution

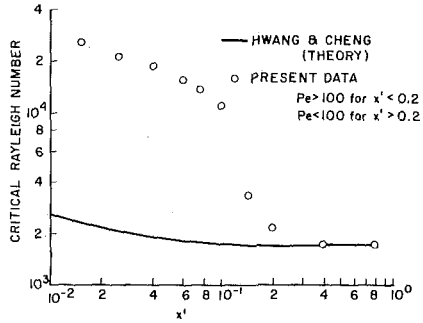

Fig. 8 Critical Rayleigh number

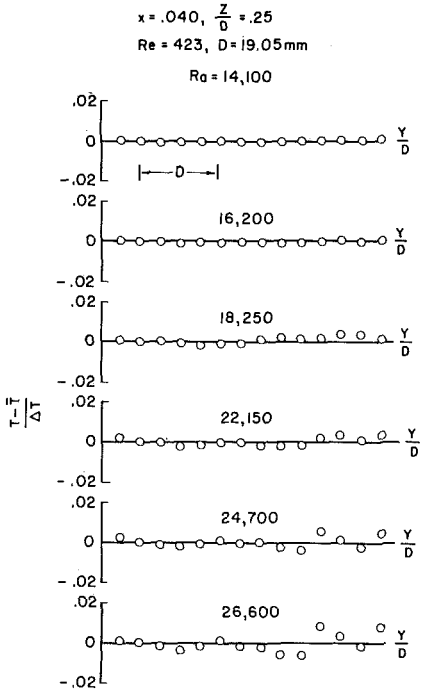

Fig. 9 Spanwise temperature distribution near critical Rayleigh number

the onset of thermal instability was checked by measuring the spanwise temperature distributions. According to Akiyama, et al. [5] and Ostrach and Kamotani [1] the spanwise temperature distribution starts to show small irregularities near the critical Ra. One set of data taken at $x' = 0.040$ and $Z/D = 0.25$ is given in Fig. 9. The temperature distribution starts to show an increase of the fluctuation level around $Ra = 1.8 \times 10^4$. To see the increase of the fluctuation level objectively the standard deviation around the mean temperature was calculated for each temperature distribution. The results are shown in Fig. 10. As observed in the foregoing, the standard deviation shows sharp increase at $Ra = 1.8 \times 10^4$ which is considered to be the critical Rayleigh number at $x' = 0.040$. In this way critical Rayleigh numbers at several locations were measured and presented in Fig. 8. Although the Nusselt numbers in Fig. 7 are averaged over a length, qualitative agreement with the results of Fig. 8 can be observed. Comparison with the theoretical result by Hwang and Cheng shows that the critical Rayleigh numbers are almost one order of magnitude higher than the theoretical values in the thermal boundary layer, which agrees with the finding from the heat transfer measurements.

In the analysis of Hwang and Cheng, the gap D was used as the

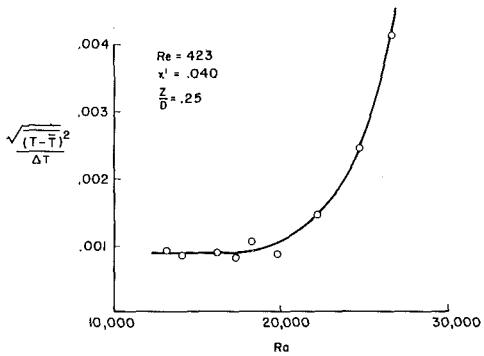

Fig. 10 Standard deviation of spanwise temperature fluctuation

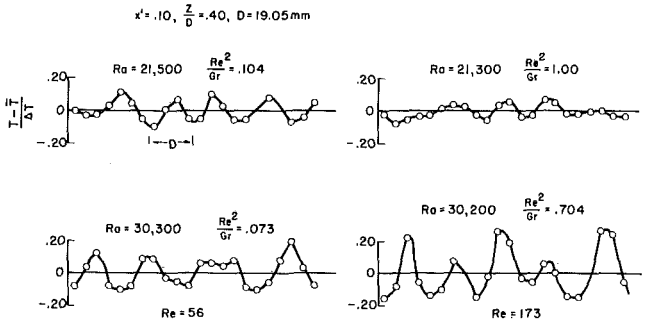

Fig. 11 Spanwise temperature distribution

vertical length scale. However, since the temperature difference ΔT exists only in the thermal boundary layer, the boundary-layer thickness is the more appropriate scale. Thus, the theoretical critical Rayleigh numbers should be interpreted as being based on that length. Since the boundary layer thickness is always smaller than D, this leads to higher critical Rayleigh numbers based on D than given by Hwang and Cheng.

Well above the critical Rayleigh numbers spanwise temperature distributions are expected to be periodic due to the convective motion of longitudinal vortex rolls. Fig. 11 shows spanwise temperature distributions at $x' = 0.10$ measured under various experimental conditions. A nearly periodic variation becomes apparent above $Ra = 2 \times 10^4$. It is interesting to note that the pitch of vortex rolls is close to D instead of $2D$ which was observed in the fully developed region in the range $1700 < Ra < 8000$ (Ostrach and Kamotani [1]). As discussed by Ostrach and Kamotani, in the fully developed region regular vortex rolls are destroyed beyond $Ra = 8000$ because of the appearance of a second type of vortex rolls which has half the size of the regular rolls. However, as evidenced by the results in Fig. 11, second type vortex rolls persist in the boundary layer, which gives the periodicity equal to D.

The flow structure in the thermal boundary layer was found to be influenced not only by Ra but also by the Froude number (Re^2/Gr) which shows the relative importance of inertia forces (forced convection) to buoyancy. In the present experiments the effect of Froude number on the flow structure was studied by measuring temperature distributions for various Re at fixed Ra. Comparison of spanwise temperature distributions for two different Reynolds numbers at $Ra \doteqdot 2.1 \times 10^4$ in Fig. 11 shows that the temperature distribution becomes more orderly as Fr decreases because of the increasing importance of the thermal instability. However, at higher Ra ($Ra \doteqdot 3 \times 10^4$ in Fig. 11) stronger effects of the thermal instability leads to destruction of vortex rolls and eventually to a turbulent flow.

In addition to spanwise temperature distributions, vertical temperature distributions were also measured. Fig. 12 shows the distributions of the mean temperature $\bar{T}(x,z)$ which is defined as

$$\bar{T}(x,z) = \frac{1}{L}\int_{y_0}^{y_0+L} T(x,y,z)dy$$

where L covers several wavelengths.

At $Ra = 2 \times 10^4$ even though one observes well-defined vortex rolls as explained in the foregoing, the mean vertical temperature distribution is not much different from the subcritical temperature distribution at the same axial location. The vertical temperature distribution is modified gradually with increasing Ra. As a result, the local Nu increases gradually with Ra as can be seen in Fig. 7, which is quite a contrast to a sharp increase of Nu across the critical Ra in the fully developed region. The vortex motion does not reach the upper wall at $Ra \doteqdot 2 \times 10^4$, but its influence reaches further from the lower wall as Re^2/Gr decreases (Fig. 12). At $Ra = 3 \times 10^4$ the vortex motion reaches the upper wall and substantial heat

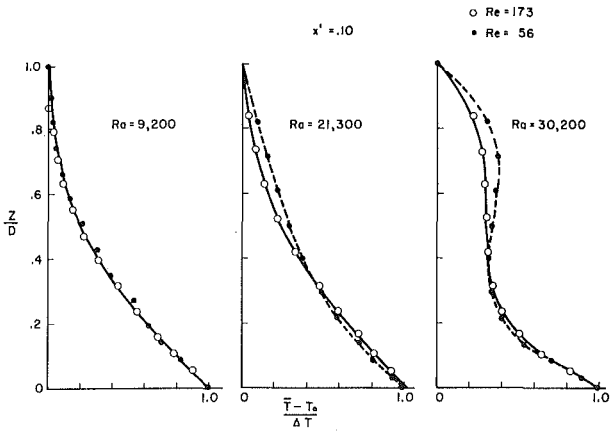

Fig. 12 Mean vertical temperature distribution

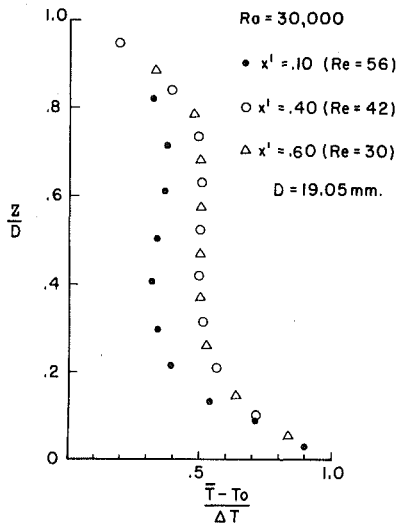

Fig. 13 Mean vertical temperature distribution

transfer takes place at the upper wall surface. The heat transfer rate at the upper wall increases as Re^2/Gr decreases.

The effect of Froude number on the heat transfer rate at the lower plate surface was not clear because of the limited range of Fr number covered by the present experiments. However, it appears that the Nusselt number is not very sensitive to Fr, because even though Fr was changed as much as a factor of 50 (for a fixed Ra) in the present experiments, no appreciable change of the mean temperature gradient at the lower plate surface was observed (see Fig. 12).

It was found that the vertical temperature distribution profile for $Ra = 3 \times 10^4$ becomes independent of the axial distance at about $x' = 0.40$ (Fig. 13). Since this is almost the same as the entrance length of the subcritical flow, Rayleigh number does not seem to affect the entrance length at least in the range of Ra studied herein.

Conclusions

Experiments were carried out to investigate the effects of thermal instability in the hydrodynamically fully developed but thermally developing region of a channel flow of air on the heat transfer rate and the temperature field. The following conclusions were obtained from the experiments:

1 The flow is more stable in the thermal entrance region than in the fully developed region. The critical Rayleigh numbers are much higher than the theoretically predicted values.

2 Beyond critical Rayleigh numbers the heat transfer rate increases gradually with increasing Rayleigh number. The heat transfer augmentation was lower than that for fully developed flow and temperature fields in the Rayleigh number range studied herein. However, there is evidence that this is different for larger Rayleigh numbers.

3 Spanwise temperature distributions start to show irregularities across critical Rayleigh numbers, and eventually become spatially periodic, the dominant wavelength being close to the gap width between two places.

4 The entrance length as determined from the temperature profiles does not change appreciably with the Rayleigh numbers in the range of Ra studied herein.

Acknowledgment

This research was supported by the U.S. Air Force Office of Scientific Research under Grant AFOSR-72-2342C.

References

1 Ostrach, S., and Kamotani, Y., "Heat Transfer Augmentation in a Laminar Fully-Developed Channel Flow by Means of Heating from Below," JOURNAL OF HEAT TRANSFER, TRANS. ASME, Series C, Vol. 97, No. 2, May 1975, pp. 220–225.

2 Hwang, G. J., and Cheng, K. C., "A Boundary Vorticity Method for Finite Amplitude Convection in Plane Poiseuille Flow," *Developments in Mechanics, Proceedings of the 12th Midwestern Mechanics Conference,* Vol. 6, 1971, pp. 207–220.

3 Hwang, G. J., and Cheng, K. C., "Convective Instability in the Thermal Entrance Region of a Horizontal Parallel-Plate Channel Heated From Below," JOURNAL OF HEAT TRANSFER, TRANS. ASME, Series C, Vol. 95, No. 1, 1973, pp. 72–77.

4 Hatton, A. P., and Turton, J. S., "Heat Transfer in the Thermal Entry Length With Laminar Flow Between Parallel Walls at Unequal Temperatures," *International Journal of Heat and Mass Transfer,* Vol. 5, 1962, pp. 673–679.

5 Akiyama, M., Hwang, G. J., and Cheng, K. C., "Experiments on the Onset of Longitudinal Vortices in Laminar Forced Convection between Horizontal Plates," JOURNAL OF HEAT TRANSFER, TRANS. ASME, Series C, Vol. 93, No. 4, pp. 335–341.

J. N. Arnold
I. Catton
D. K. Edwards

University of California,
Los Angeles, Calif.

Experimental Investigation of Natural Convection in Inclined Rectangular Regions of Differing Aspect Ratios

An experimental investigation of steady natural convection heat transfer was carried out for finite rectangular regions. The effect of angle of inclination on heat transfer across rectangular regions of several aspect ratios was measured for Rayleigh numbers between 10^3 and 10^6. The angle of inclination varied from 0 deg (heated from above) to 180 deg (heated from below) with aspect ratios of one, three, six, and twelve. Comparison is made with past theoretical work, and a simple scaling law is derived which is valid for angles of inclination from 0 to 90 deg (vertical).

Introduction

Since the time of Rayleigh [1],[1] steady state natural convection in an enclosed rectangular geometry has been extensively studied, but only for vertical and horizontal (heated from below) orientations. Comprehensive reviews of both experimental and theoretical studies have been given by Ayyaswamy [2] and Hart [3]. As indicated by them, there is a serious lack of information regarding the heat transfer rates for natural convection in inclined geometries. The first systematic theoretical and experimental analysis of the effect of sloping boundaries was that of Hart [3]. Dropkin and Somerscales [4] have presented some experimental data and heat transfer correlations. They limited their experimentation to very high Rayleigh number and angles of inclination such that the bottom plate was hotter than the top one (90 deg $< \theta <$ 180 deg in the notation used here; see Fig. 1 for an explanation of the notation). In their experiments aspect ratios (see Fig. 1) were 18, 6, and 4.5. Their correlations indicated no aspect ratio dependency.

Hart investigated aspect ratios of 25 and 37, and likewise did not report any dependence upon aspect ratios. Hollands and Konicek [5] made similar measurements using aspect ratios of 25, 37, and 43. Both of these papers were concerned with values of the critical Rayleigh number at which the flow deviates from unicellular and not with angle dependence of heat transfer at higher Rayleigh numbers.

Catton, Ayyaswamy, and Clever [6] used the Galerkin method to investigate, theoretically, natural convection in an inclined rectangular region, and their results indicate a pronounced aspect ratio dependency. Their solutions were two-dimensional and limited to 0 deg $< \theta <$ 120 deg. For this range they present predictions for aspect ratios from 0.2 to 20 up to Rayleigh number of 10^6. Ayyaswamy and Catton [7] investigated the boundary layer regime and were able to show that, when the Rayleigh number is sufficiently high, a simple rescaling of the results for θ = 90 deg can be accomplished. They found that

$$\mathrm{Nu}(\theta) = \mathrm{Nu}(\theta = 90\ \mathrm{deg})\sin^{1/4}\theta \qquad 0\ \mathrm{deg} < \theta < 110\ \mathrm{deg} \qquad (1)$$

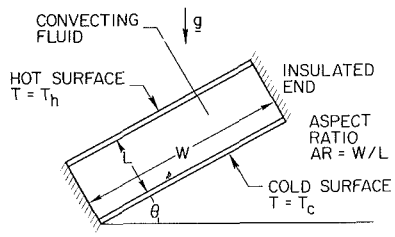

Fig. 1 Schematic of rectangular region

[1] Numbers in brackets designate References at end of paper.

Contributed by the Heat Transfer Division of THE AMERICAN SOCIETY OF MECHANICAL ENGINEERS and presented at the AIChE–ASME Heat Transfer Conference, San Francisco, Calif. August 11–13, 1975. Revised manuscript received by the Heat Transfer Division September 25, 1975. Paper No. 75-HT-62.

This rescaling allows one to reinterpret the results for the well-understood vertical cavity problem.

Clever [8] investigated, theoretically, the heated-from-below geometry, 90 deg $< \theta \leq$ 180 deg. He found that, at least for high Prandtl number fluids and very high aspect ratios, the heat transfer resulting from thermal instabilities overwhelmed the heat transfer due to the slow creeping motion resulting from the tilting of the rectangular region. The Rayleigh number required to induce thermal instabilities is 1707/cos(180 deg $- \theta$). Hence, as long as the Rayleigh number is somewhat in excess of this value, there holds the relation

$$\frac{\text{Nu}}{\text{Nu}(\theta = 180 \text{ deg})} = f(\cos(180 \text{ deg} - \theta)) \tag{2}$$

Of course, as the vertical configuration is approached, hydrodynamic instabilities (transverse rolls) begin to interfere with the motion induced by the thermal instabilities (longitudinal rolls), and the heat transfer is affected.

Ozoe, et al. [9, 10] have reported theoretical work on low aspect ratio rectangular regions up to Ra = 10^4 with some experimental confirmation. They were concerned with aspect ratios 1–4. Arnold, et al. [11] have reported experimental work for aspect ratio 6.

In this work, the effect of angle of inclination is investigated over the range 0 deg $\leq \theta \leq$ 180 deg, for aspect ratios of 1, 3, 6, and 12. The experimental Rayleigh numbers ranged from 10^3 to 10^6 or from 5×10^4 to 10^7 depending upon the aspect ratios and fluid. The theoretical predictions of reference [6] are substantiated, and the circumstances under which one or the other of the simple scaling laws given in reference [7] or [8] is applicable are established.

Experimental Apparatus and Procedure

The experimental apparatus used was that described by Sun and Edwards [12], see Fig. 2. The fluid is contained between two sets of heat meters which are of rectangular cross section (125 × 152 mm). The heat meter is a calibrated layer of insulation between a copper face plate and copper back-up plate. The face plate is 0.176 mm thick, and the layer of insulation is 1.42 mm of phenolic-filled cloth. On the top of each heat meter is fastened a 19-mm brass block in which heating and cooling water is circulated and upon which a massive bakelite block (38 mm thick) was placed to reduce heat losses. The fluid is contained laterally by 22-mm thick walls of insulating polyurethane foam. Chromel-constantan thermocouples, embedded in the copper plates, were connected in such a way that the temperature differences across the fluid ($T_3 - T_2$) and the temperature difference across the heat meters ($T_4 - T_3$) and ($T_2 - T_1$) are recorded.

The heat meter assemblies are attached to steel bars which are held by sleeve-clamp guides to a rectangular yoke (see Fig. 2). The yoke is free to turn clockwise or counterclockwise around its horizontal pivots. A modified sealing system was employed which allowed angles of tilt from 0 deg (heated from above) to 180 deg (heated from below).

The 152-mm tilted length W was used to obtain AR = 12. Paperboard was used to divide the length into two in order to obtain aspect ratio 6. Filled phenolic 0.176 mm thick was used to obtain the lower aspect ratios.

Two parameters are desired from the raw data taken; an experimental Nusselt number and an experimental Rayleigh number.

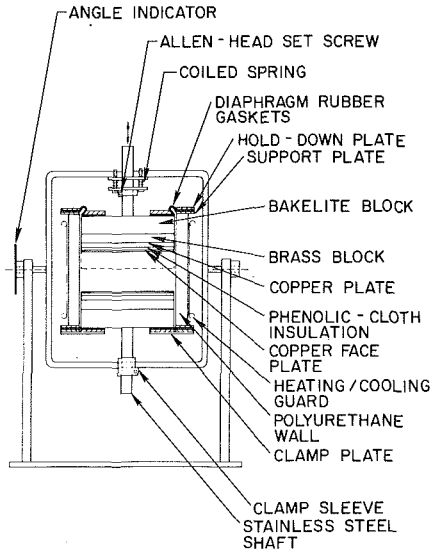

Fig. 2 Experimental apparatus (schematic cross section)

The Nusselt number is defined as the ratio of heat convected to heat conducted through the fluid between the meters. This can be written as

$$\text{Nu} = \frac{q_w}{\frac{k}{L}\Delta T} \tag{3}$$

where q_w can be expressed as

$$q_w = \frac{k_{\text{eff}}}{L}\Delta T \tag{4}$$

thus making

$$\text{Nu} = \frac{k_{\text{eff}}}{k} \tag{5}$$

Sun [13], using a lumped-capacitance model, derived an expression for Nu,

$$\text{Nu} = (1 + X)\frac{R}{R_0} - X \tag{6}$$

where

$$R = \frac{\{(T_2 - T_1) + (T_4 - T_3) - \tau(\dot{T}_3 - \dot{T}_2)\}}{(T_3 - T_2)} \tag{7}$$

and X is a wall conduction correction $k_w A_w / kA$ which is negligible in the present work [12, 13]. The dot represents a time derivative, and τ, the time constant, is found by conducting two runs with different decay rates. The time constant was on the order of 0.009 hr for all runs. The quantity R_0 is found by a steady-state run heated from above. The Rayleigh number is defined as

$$\text{Ra} = \frac{g\beta\Delta T L^3}{\nu\kappa} \tag{8}$$

Nomenclature

AR = aspect ratio W/L; see Fig. 1
g = gravitational acceleration
k = thermal conductivity
L = height of core
Nu = Nusselt number
q_w = heat flux through a wall
R = experimental temperature ratio
Ra = Rayleigh number based on height
T = temperature
T_c = temperature on cold side
T_h = temperature on hot side
W = width of a rectangle
X = X factor
β = volumetric expansion coefficient
θ = azimuthal angle from X axis
κ = thermal diffusivity
τ = time constant
ν = kinematic viscosity

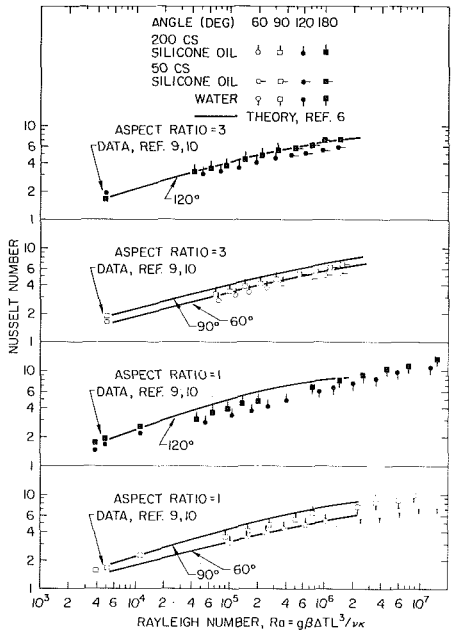

Fig. 3 Nusselt number versus Rayleigh number for $AR = 1, 3$

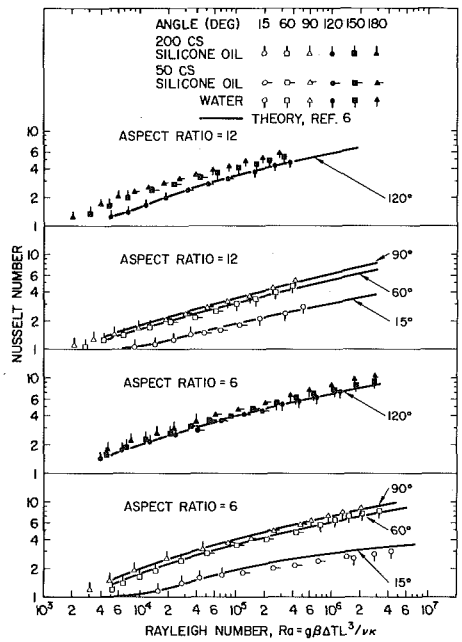

Fig. 4 Nusselt number versus Rayleigh number for $AR = 6, 12$

where ΔT in this case is $(T_3 - T_2)$.

Results and Discussion

Fig. 3 and 4 present the Nusselt number, which measures the effective thermal conductivity of the fluid, as a function of the Rayleigh number, Ra, which may be viewed as a nondimensional temperature difference, and angle of inclination, θ. Fig. 3 presents experimental results for $AR = 1$ and 3 for angles of inclination $\theta = 0$ deg (heated from above) to $\theta = 180$ deg (heated from below). Fig. 4 presents similar results for $AR = 6$ and 12. The experimental results for $AR = 6$ were previously reported by Arnold, et al. [11]. The solid lines in the figures are theoretical predictions made by Catton, Ayyaswamy, and Clever [6] for an infinite Prandtl number fluid and for perfectly insulating end walls. Agreement is seen to be good for the higher aspect ratios. In the case of the lower aspect ratios 1 and 3 the theory tends to be high. In the worst case, Fig. 3, for $AR = 1$ and $\theta = 120$ deg, the discrepancy is as large as 50 percent. If one compares the data for this case with the theoretical predictions [6] for perfectly conducting end walls, about the same discrepancy occurs, but the data fall *above* the prediction.

One way to judge whether the end wall should be regarded as insulating or conducting is to evaluate its fin effectiveness. If the effectiveness is low, it is insulating, and if it is high (approaching unity), the end wall is to be regarded as conducting. Such an evaluation for the cells used to obtain aspect ratios 1 and 3 indicates a fin effectiveness (based upon a fin of $L/2$ and $h = k/L$) on the order of 50 percent. The fact that the theoretical results for perfectly insulating and perfectly conducting end walls bracket the present experimental data thus lends strong support to the theoretical predictions of Catton, et al. [6]. In the case of the higher aspect ratios the end wall conduction effect is not large.

In the main, the measured results are as one would expect from theoretical analyses [6]. As the angle of inclination increases, the heat flux increases. The fluids used in this work covered a range of Prandtl number from Pr = 4.5 (water) to Pr = 2000 (200 Cs silicon oil). No effect of Prandtl number on the measured heat transfer could be found. This lack of dependency and the good comparison with infinite Prandtl number predictions leads one to infer that a fluid with $Pr \geq 4.5$ behaves like a fluid with $Pr = \infty$ at least for $Ra \leq 10^7$.

The highest heat transfer at a given ΔT (maximum convection) occurs at $\theta = 180$ deg. As the angle of inclination is decreased, the Nusselt number first decreases, and then as $\theta = 90$ deg is approached, it increases to a local maximum. With further decrease in θ, the Nusselt number again decreases. Results for some angles have been deleted due to excess crowding of the graphs. Measurements at $\theta = 180$ deg compare well with those of Silveston [14]. Dropkin and Somerscales [4] did not report the aspect ratios they used. For this reason, no comparison with their work is shown.

A better view of the effect of angle of inclination is found in Fig. 5 where the Nusselt number is plotted as a function of angle for several values of the Rayleigh number. For any Rayleigh number, the heat transfer increases as the angle of inclination increases until it reaches 90 deg. As mentioned in the foregoing, a local maximum exists at $\theta = 90$ deg, and between $\theta = 90$ deg and $\theta = 180$ deg the heat transfer reaches a local minimum which is less than the value at either $\theta = 90$ deg or $\theta = 180$ deg. For the larger aspect ratios, 6 and 12, it seems that as the Rayleigh number increases, the minimum gradually disappears. For the lower aspect ratios, 1 and 3, the minimum is more pronounced, and it does not disappear as the Rayleigh number increases. These minima are presumably caused by a transition between two different flow patterns. The "transverse" or unicellular pattern which would prevail if Benard type instabilities did not exist, would cause the convection to be symmetric about $\theta = 90$ deg and zero at $\theta = 0,180$ deg. The fluid in the rectangular region would circulate up the heated plate and down the cooled plate about an axis perpendicular to the W by L rectangle in Fig. 1. The form of the motion caused by thermal instability is somewhat arbitrary at $\theta = 180$ deg, but will have a preferred form and direction when $\theta < 180$ deg. This preferred thermal-instability-induced motion is in the form of "longitudinal" rolls [8].

The experimental results seem to indicate that the transition between the two motions changes for differing aspect ratios. Fig. 6 shows these changes. For large aspect ratio, $AR \geq 12$, the angle of minimum heat transfer reaches an asymptote at 110 deg. As aspect ratio is decreased, the angle at which the minimum occurs increases toward 180 deg. The occurrence of a minimum shows that the two forms of motion do not superpose; rather one or the other seems to prevail.

Ozoe, Sayama, and Churchill [9] have reported experimental measurements for angles from $\theta = 90$ to 180 deg (in our notation)

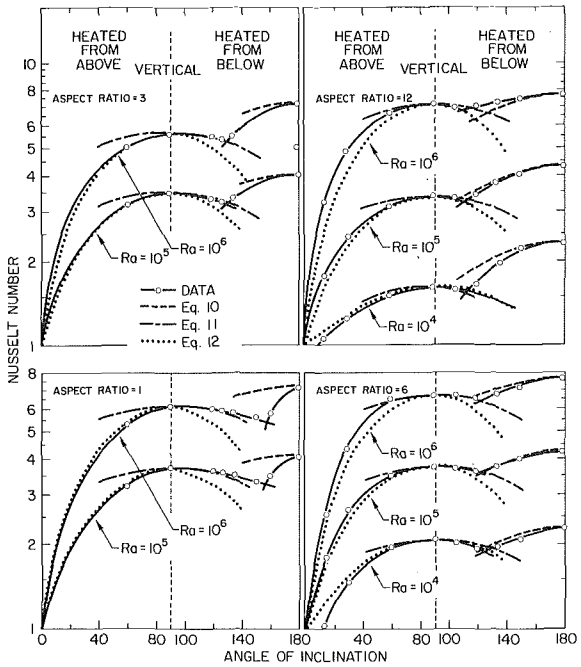

Fig. 5 The effect of angle of inclination on Nusselt number

for an aspect ratio of unity at Rayleigh numbers of 3800, 4950, and 11000. They too show a minimum in Nusselt number as a function of θ at a fixed Rayleigh number, but their minimum lies at 175 deg, somewhat greater than the 155 deg found here. In the present investigation Rayleigh number ranged from 5×10^4 to 10^7 so that no direct overlap exists. Fig. 3 shows how their data fall in relation to the present results.

In a second paper, Ozoe, et al. [10] report measurements for θ = 0 to 180 deg for an aspect ratio of 3 at a single Rayleigh number of 4770. Their minimum in Nu versus θ occurs in the neighborhood of 175 deg in contrast to the present values near 135 deg. These findings suggest that the angle of the minimum Nusselt number shifts toward the horizontal as the Rayleigh number falls. The present results for aspect ratio 3 cover the Rayleigh number range from 5×10^4 to 10^6 so that again no direct overlap exists. Fig. 3 shows their low Rayleigh number data points.

Another difference in the behavior observed by Ozoe, et al. [9, 10] at low Rayleigh numbers and that reported here for moderate and high Rayleigh numbers is in the absolute maximum Nusselt number as a function of θ. At a high Rayleigh number the maximum occurs at 180 deg (horizontal, heated from below), and Nu decreases faster than $[\cos(\theta - 180 \text{ deg})]^{0.29}$ as θ deviates from 180 deg. In contrast, at a Rayleigh number near the critical value for θ = 180 deg, a change in θ causes an increase in Nu, particularly for a low aspect ratio, because the transverse mode of convection grows rapidly with tilt under these circumstances.

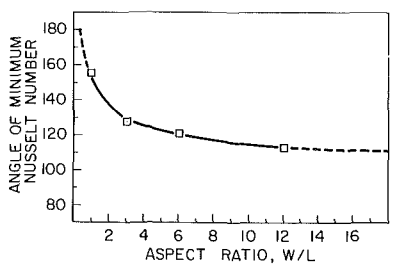

Fig. 6 Effect of aspect ratio on the angle of minimum Nusselt number

Assuming that the convection resulting from thermal instabilities dominates, Clever [8] scaled the relevant governing equations and indicated that replacing g with $g \cdot \cos(\theta - 180 \text{ deg})$ or Ra with $\text{Ra} \cdot \cos(\theta - 180 \text{ deg})$ would allow one to rescale $\theta = 180$ deg data to $\theta < 180$ deg. As can be seen from Figs. 3 and 4, all of the results obey a power law when Ra is sufficiently large, and the power law is roughly the same for all angles of inclination. A power law of the form

$$\text{Nu} = C_1 \text{Ra}^{0.29} \qquad \text{Ra} > 10^4 \tag{9}$$

is adequate for $\theta = 180$ deg. If one follows Clever's reasoning,

$$\text{Nu}(\theta) = \text{Nu}(\theta = 180 \text{ deg})(\cos(\theta - 180 \text{ deg}))^{0.29} \tag{10}$$

Comparisons of the expression given by equation (10) are shown in Fig. 5. The agreement is seen to be good at high aspect ratio, high Rayleigh number, and θ above the transition value. The power law form given by equation (10) is only applicable for $\text{Ra} \cdot \cos(\theta - 180 \text{ deg}) > 10^5$. Below that value one would want to scale according to Clever directly from Silveston's data [14].

When $\theta < 90$ deg and Ra is high enough, a boundary layer flow should result. Ayyaswamy and Catton [7] investigated the possibility of rescaling results for $\theta = 0$ deg to $\theta = 90$ deg when the boundary layer regime existed. They found that

$$\text{Nu}(\theta) = \text{Nu}(\theta = 90 \text{ deg}) \sin^{1/4}\theta \tag{11}$$

A comparison of equation (11) with measured results are shown in Fig. 5. As can be seen, the rescaling yields reasonable approximations for 60 deg $< \theta <$ 120 deg. It is believed that for these aspect ratios, the boundary layer regime has not been reached, and the *convective* contribution to the heat transfer should follow the simple scaling law

$$\text{Nu}(\theta) = 1 + (\text{Nu}(\theta = 90 \text{ deg}) - 1)\sin\theta \tag{12}$$

as indicated by Arnold et al. [11]. Predictions based on equation (12) are also shown in Fig. 5 and are seen to be excellent for $\theta < 90$ deg.

Summary and Conclusions

Heat transfer due to natural convection in four different rectangular regions inclined at various angles from 0 to 180 deg has been measured. Comparison with the work of Catton, Ayyaswamy, and Clever [6] shows that their predictions are good. It seems that the scaling suggested by Clever [8] is good for high aspect ratios but not for those less than or equal to 3. On the other hand, the scaling by Ayyaswamy and Catton does not seem to be good for $\theta < 90$ deg. The simple scaling of the convective part of the heat transfer done by Arnold, et al. [11] is shown to yield excellent results for $\theta < 90$ deg and all aspect ratios. The complexities of the flow in the $\theta > 90$ deg cases preclude use of any simple scaling law. This regime needs further theoretical study. The present experimental study was made for aspect ratios greater than or equal to 1; more work is needed for aspect ratios less than 1. Ozoe, et al. [9, 10] have done some preliminary work in this area, but as of yet have not shown how the minimum is affected.

Acknowledgment

The work reported here was supported by National Science Foundation Grant GK 35892.

References

1 Lord Rayleigh, "On Convection Currents in a Horizontal Layer When the Higher Temperature is on the Underside," *Phil. Mag.*, Series 6, Vol. 32, 1916, pp. 529–546.

2 Ayyaswamy, P. S., "Natural Convection Flows in Tilted Configurations," PhD dissertation, University of California, Los Angeles, 1971.

3 Hart, J. E., "Stability of the Flow in a Differentially Heated Inclined Box," *J. Fluid Mech.*, Vol. 47, 1971, pp. 547–576.

4 Dropkin, E., and Somerscales, E., "Heat Transfer by Natural Convection in Liquids Confined by Two Parallel Plates Which are Inclined at

Various Angles With Respect to the Horizontal," JOURNAL OF HEAT TRANSFER, TRANS. ASME, Series C, Vol. 87, 1965, pp. 77–84.

5 Hollands, K. G. T., and Konicek, L., "Experimental Study of the Stability of Differentially Heated Inclined Air Layers," *International Journal of Heat and Mass Transfer*, Vol. 16, 1973, pp. 1467–1476.

6 Catton, Ivan, Ayyaswamy, P. S., and Clever, R. M., "Natural Convection Flow in a Finite Rectangular Slot Arbitrarily Oriented with Respect to the Gravity Vector," *International Journal of Heat and Mass Transfer*, Vol. 17, 1974, pp. 173–184.

7 Ayyaswamy, P. S., and Catton, Ivan, "The Boundary Layer Regime for Natural Convection in a Differentially Heated, Tilted Rectangular Cavity," JOURNAL OF HEAT TRANSFER, TRANS. ASME, Series C, Vol. 95, 1973, pp. 543–545.

8 Clever, R. M., "Finite Amplitude Longitudinal Convection Rolls in an Inclined Layer," JOURNAL OF HEAT TRANSFER, TRANS. ASME, Series C, Vol. 95, 1973, pp. 407–408.

9 Ozoe, H., Sayama, H., and Churchill, S. W., "Natural Convection in an Inclined Square Channel, *International Journal of Heat and Mass Transfer*, Vol. 17, 1974, pp. 401–406.

10 Ozoe, H., Yamamoto, K., Sayama, H., and Churchill, S. W., "Natural Convection in an Inclined Rectangular Channel Heated on One Side and Cooled on the Opposing Side," *International Journal of Heat and Mass Transfer*, Vol. 17, 1974, pp. 1209–1217.

11 Arnold, J. N., Bonaparte, P. N., Catton, I., and Edwards, D. K., "Experimental Investigation of Natural Convection in a Finite Rectangular Region Inclined at Various Angles from 0° to 180°," *Proceedings of the 1974 Heat Transfer and Fluid Mechanics Institute*, June 1974, Stanford University Press, Stanford, Calif.

12 Sun, W. M., and Edwards, D. K., "Natural Convection in Cells With Finite Conducting Side Walls Heated From Below," *Heat Transfer 1970, Proceedings of the 4th International Heat Transfer Conference*, Versailles, Sept. 1970, Elsevier Publishing Company, Amsterdam, 1971.

13 Sun, W. M., "Effect of Arbitrary Wall Conduction and Radiation on Free Convection in a Cylinder," PhD dissertation, University of California, Los Angeles, 1970.

14 Silveston, P. L., "Warmedurchgang in Waagerechter Flussigkeitsschichten," *Forsch. Ing. Wes.*, Vol. 24, 1958, pp. 29–32, 59–69.

G. D. Raithby
Assoc. Professor.
Mem. ASME

K. G. T. Hollands
Assoc. Professor.
Mem. ASME

Thermal Engineering Group, Department of Mechanical Engineering, University of Waterloo, Waterloo, Ontario, Canada

Laminar and Turbulent Free Convection From Elliptic Cylinders, With a Vertical Plate and Horizontal Circular Cylinder as Special Cases

Heat transfer by free convection from thin elliptic cylinders is predicted, accounting for both the effect of thick boundary layers at low Rayleigh numbers and the influence of turbulence at higher Rayleigh numbers. Isothermal and constant heat flux boundary conditions are treated. The results are compared with experimental data, which are available for the limiting cases of large eccentricity (vertical plate) and small eccentricity (horizontal circular cylinder); the agreement is excellent. Accurate correlation equations, from which the average heat transfer can be calculated, are given.

1 Introduction

Particularly in the last decade, a large effort has been directed toward predicting the heat transfer by free convection from the external surfaces of bodies of various contours. In view of this, it might be expected that good agreement between the predicted and measured *average* or *total* heat transfer rates would have been obtained, at least for "simple" geometries. Such is not the case. Even for the classic problem of heat transfer from a vertical flat plate, there may be large discrepancies between experiment and analysis, depending on the Rayleigh number range.

There are two basic reasons for these discrepancies. At low Rayleigh numbers, the boundary layers become thick, resulting in the failure of the boundary-layer equations (in the form that they are usually applied) to accurately represent the physical process. On the other hand, at high Rayleigh numbers turbulent heat transfer occurs on part of the surface, and analyses do not account for this. Although there may be regions on the surfaces where good agreement between analysis and experiment can be demonstrated, the existence of other regions of poor agreement causes the predicted *average* heat transfer to be in error.

Several investigations have been directed at extending the range of validity of the analytical results to lower Rayleigh numbers; a discussion of these, as they apply to the present problem, is deferred to a later section. Only limited success has been reported.

The analysis reported herein was undertaken: (1) to predict the average heat transfer from slender elliptic cylinders over a large Rayleigh number range (thus including both turbulence and thick boundary layer effects), (2) to evaluate the accuracy and practicality of the present approximate method relative to earlier analyses, (3) to obtain simple yet accurate correlation equations, and (4) to attempt to explain some apparently conflicting results of some earlier investigations. The prediction of local velocity profiles, temperature profiles, or heat transfer rates was not of direct concern, except as they were needed to achieve the stated goals. The elliptic cylinder contour was chosen because the limiting cases of large eccentricity (vertical plate) and small eccentricity (horizontal cylinder) have been the subjects of several experimental studies, thereby permitting the present method of analysis to be validated.

In many analyses great attention is given to precisely solving equations which themselves only crudely describe the real physical process. A conscious effort has been made in this investigation to focus on the major causes of disagreement between analysis and experiment, and to keep the degree of complexity of solutions to a level consistent with the approximations inherent in the underlying equations.

2 Problem Statement and Coordinate System

An elliptic cylinder, oriented as shown in Fig. 1, transfers heat from its surface at temperature T_w to a quiescent fluid at temperature T_∞. The ellipse is generated by choosing a given value of η =

Contributed by the Heat Transfer Division for publication in the JOURNAL OF HEAT TRANSFER. Manuscript received by the Heat Transfer Division January 15, 1975. Paper No. 76-HT-DD.

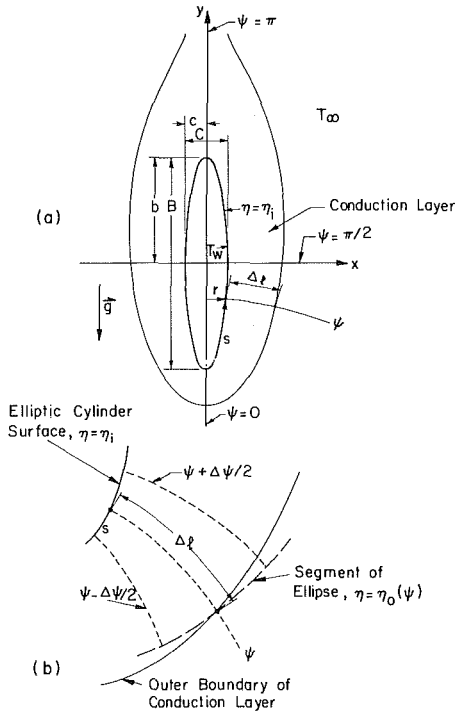

Fig. 1 Schematic showing thin elliptic cylinder, and nomenclature

η_i in the coordinate transformation

$$y = -a \cosh \eta \cos \psi, \quad x = a \sinh \eta \sin \psi \tag{1}$$

where ψ is varied over the range $0 < \psi < 2\pi$. Varying η over the range $0 < \eta < \infty$ generates a family of confocal ellipses, one ellipse for each value of η. In the x, y plane, curves of constant ψ are hyperbolas, orthogonal to the ellipses. The differential distance in the η, ψ, and z coordinate directions are, respectively, $\sqrt{g_\eta}\, d\eta$, $\sqrt{g_\psi}\, d\psi$ and $\sqrt{g_z}\, dz$, where the metric coefficients (see Yovanovich [1][1]) g_η, g_ψ, and g_z are

$$g_\eta = g_\psi = a^2 (\cosh^2 \eta - \cos^2 \psi); \quad g_z = 1 \tag{2}$$

Focusing attention on the $\eta = \eta_i$ elliptic cylinder in Fig. 1, it is seen from equation (1) that

$$b = a \cosh \eta_i, \; c = a \sinh \eta_i, \; r = c \sin \psi \tag{3a}$$

It follows that

$$a = \sqrt{b^2 - c^2}, \quad \eta_i = 0.5 \ln \{(b + c)/(b - c)\} \tag{3b}$$

For $\eta_i = 0$ the ellipse becomes a vertical plate of zero thickness; for $\eta_i \to \infty$, $c \to b$ and the elliptic cylinder becomes circular.

Along the η_i surface, the length ds is

$$ds = (\sqrt{g_\psi})_{\eta=\eta_i}\, d\psi = b\, [\sin^2 \psi + (c/b)^2 \cos^2 \psi]^{1/2}\, d\psi = b\, \chi(\psi, c/b)\, d\psi \tag{4}$$

The half-perimeter of the surface, S, (between $\psi = 0$ and $\psi = \pi$) is, therefore,

$$S = b \int_0^\pi \chi(\psi, c/b)\, d\psi = b f_1 \tag{5}$$

f_1 is tabulated in Table 1 for various c/b.

Table 1 Values of f_1 and f_2

c/b	f_1	f_2	$2^{1/4} f_2^{3/4}/f_1$
0.0	2.000	2.000	1.000
0.1	2.032	2.019	0.991
0.2	2.101	2.059	0.973
0.4	2.301	2.169	0.924
0.6	2.553	2.300	0.870
0.8	2.836	2.441	0.819
0.9	2.987	2.514	0.795
1.0	3.142	2.587	0.772

3 Thin-Layer Analysis and Results

Definition. In the vicinity of the solid boundary (and extending almost to the location of the velocity maximum in the boundary layer) the transport of heat normal to the surface is almost entirely by conduction. When the boundary layers are everywhere much thinner than the local radius of curvature, the area available to this conductive heat flow along its path remains almost constant—that is, if y is defined as distance normal to the wall, the y-conduction term in the energy equation can be approximated by $k\partial^2 T/\partial y^2$. Equations containing this approximation will be called thin-layer equations and their solutions thin-layer solutions. Thick-layer solutions or corrections, on the other hand, are defined here as those which account for the altered resistance to heat

Nomenclature

a: see equation (3)
$A(\phi)$: see equation (17)
b, B, c, C: see Fig. 1
C_ℓ: see equation (7)
$\bar{C}_\ell = (4/3)C_\ell$
C_t: see equation (18)
f_1, f_2 = definite integrals, see Table 1
g, g_s = gravitational acceleration, and component of g parallel to surface at s
$h = (q/A)/\overline{\Delta T}$
$\bar{h} = (\overline{q/A})/\overline{\Delta T}$
k = thermal conductivity
K = constant, equation (30)
m = constant, equation (32)
Nu_ζ = local Nusselt number, $h\zeta/k$, ζ is any length scale
$\overline{\mathrm{Nu}}_B$ = average Nusselt number, $\bar{h}B/k$
$(\overline{\mathrm{Nu}}_\zeta)^P$ = predictor (or thin-layer) value of the Nusselt number
q/A, $\overline{q/A}$ = local and average heat flow per unit area and time
r = local half-width of body, see Fig. 1
$\mathrm{Ra}_\zeta = g\beta\zeta^3 \Delta T/\kappa\nu$, ζ is any length scale
$\overline{\mathrm{Ra}}_\zeta = g\beta\zeta^3 \overline{\Delta T}/\kappa\nu$, ζ is any length scale
$\mathrm{Ra}_\zeta^* = g\beta\zeta^3 ((q/A)b/k)/\kappa\nu$, ζ is any length scale
$\mathrm{Ra}_{\zeta,r} = g\beta\zeta^3 \Delta T_r/\kappa\nu$, ζ is any length scale
s = distance along the surface measured from stagnation point in flow direction
S = one-half perimeter
T_c = temperature at $s = S/2$
T_w = surface temperature
$\bar{T}_w$ = average surface temperature
T_∞ = temperature far from body
ΔT = local value of $T_w - T_\infty$
$\Delta T_c = T_c - T_\infty$
$\overline{\Delta T} = \bar{T}_w - T_\infty$
ΔT_r = arbitrary reference temperature difference
$\Delta T^* = \Delta T/\Delta T_r$
y = distance normal to wall
β = thermal expansion coefficient
η = elliptic coordinate, equation (1)
κ = thermal diffusivity
ν = kinematic viscosity
ϕ: see equation (17)
$\chi = [\sin^2 \psi + (c/b)^2 \cos^2 \psi]^{1/2}$, equation (4)
ψ = elliptic coordinate, equation (1)

Subscripts

ℓ = laminar heat transfer from entire surface
t = turbulent heat transfer from entire surface

Operator

$[A_1, A_2]^\bullet = A_1$ if $A_1 \le A_2$
$= A_2$ if $A_1 > A_2$

transfer from the wall associated with the change in heat flow area.

It would be more compact (but less elucidating of the underlying problem with thin-layer solutions) to define thin-layer equations as boundary-layer equations written in local cartesian coordinates. Thick-layer solutions would then account for some or all of the curvature effects which are thereby implicitly neglected. As an example, the classical vertical flat plate solution is also the thin-layer solution for a vertical circular cylinder. Sparrow and Gregg [2] and Minkowycz and Sparrow [3] have presented solutions which account for some of the curvature effects, and would, therefore, be classified here as thick-layer solutions.

Thin-layer solutions are available for bodies of fairly arbitrary contour. Chaing and Kaye [4], Saville and Churchill [5], and Lin and Chao [6] begin by applying different transformations to the thin-layer equations before extracting a series solution. The present authors [7] have developed an *approximate* thin-layer solution which is much easier to apply and evaluate. This latter solution is now applied to the present problem and the results compared: (1) with other thin-layer solutions and (2) with experiment.

A Thin-Layer Analysis for Laminar Heat Transfer.

Local Heat Transfer. The general solution of reference [7] for a two-dimensional body predicts the following *local* Nusselt number for heat transfer from a surface of constant or varying temperature to an isothermal, quiescent fluid:

$$\frac{hs}{k} = C_\ell \, \mathrm{Ra}_{s,r}^{1/4} \left[\frac{g_s}{g} \Delta T^*\right]^{1/3} \Bigg/ \left[\frac{1}{s\Delta T^{*\,4/3}} \int_0^s \left(\frac{g_s}{g}\right)^{1/3} \Delta T^{*\,5/3}\, ds\right]^{1/4} \quad (6)$$

where ΔT^* is the local temperature difference $(T_w - T_\infty)$ relative to an arbitrary reference temperature difference, ΔT_r, upon which $\mathrm{Ra}_{s,r}$ is based. The present recommended equation (see discussion in following section) for C_ℓ is

$$C_\ell = 0.50/[1 + (0.49/\mathrm{Pr})^{9/16}]^{4/9} \quad (7)$$

and g_s is the component of g along the surface, i.e.,

$$g_s/g = [1 - (dr/ds)^2]^{1/2} \quad (8)$$

Combining the relation for r in equation (3) for an elliptic cylinder with equations (4) and (8) one obtains

$$g_s/g = |\sin\psi|/\chi \quad (9)$$

The following integral is of importance:

$$\int_0^S (g_s/g)^{1/3}\, ds = b \int_0^\pi \sin^{1/3}\psi\, \chi^{2/3}\, d\psi = bf_2 \quad (10)$$

Numerical values f_2 are tabulated in Table 1.

Using these equations, equation (6) can be rewritten in the elliptic coordinate ψ as follows:

$$\frac{hb}{k} = C_\ell \, \mathrm{Ra}_{b,r}^{1/4} \frac{(\sin\psi)^{1/3}\, \Delta T^{*\,2/3}}{\chi^{1/3}} \Bigg/ \left[\int_0^\psi (\sin\psi)^{1/3}\, \chi^{2/3}\, \Delta T^{*\,5/3}\, d\psi\right]^{1/4} \quad (11)$$

The local Nusselt number is easily obtained by evaluating this equation. At the lower stagnation point ($\psi = 0$) and at the thickest part of the cylinder ($\psi = \pi/2$) the following simple equations are obtained for an isothermal surface ($\Delta T^* = 1$):

$$\mathrm{Nu}_B = (8/3)^{1/4}\, C_\ell\, (B/C)^{1/2}\, \mathrm{Ra}_B^{1/4} \quad \text{at } \psi = 0 \text{ (isothermal)} \quad (12a)$$

$$\mathrm{Nu}_B = (4/f_2)^{1/4}\, C_\ell\, \mathrm{Ra}_B^{1/4} \quad \text{at } \psi = \pi/2 \text{ (isothermal)} \quad (12b)$$

For the vertical flat plate limit ($g_s/g = 1$) with a temperature difference which varies as s^n:

$$\mathrm{Nu}_s = (5n/3 + 1)^{1/4}\, C_\ell\, \mathrm{Ra}_s^{1/4} \quad (\Delta T^* \propto s^n, \text{ flat plate}) \quad (12c)$$

The analysis here also yields the well known result that when $n = 1/5$ the surface heat flux is uniform.

Average Heat Transfer. The local heat transfer predicted from equation (6) can be integrated around the surface of the elliptic cylinder to obtain the following average Nusselt number, valid when the boundary layer is everywhere thin and laminar:

$$\overline{\mathrm{Nu}}_S = \frac{\bar{h}S}{k} = \bar{C}_\ell\, \mathrm{Ra}_{S,r}^{1/4} \left[\frac{1}{S}\int_0^S \Delta T^{*\,5/3} \left(\frac{g_s}{g}\right)^{1/3} ds\right]^{3/4} \quad (13)$$

where

$$\bar{C}_\ell = 4C_\ell/3 \quad (14)$$

For an isothermal elliptic cylinder, $\Delta T^* = 1$, and equation (13), using equations (5) and (10), becomes

$$\overline{\mathrm{Nu}}_B = (2^{1/4} f_2^{3/4}/f_1)\, \bar{C}_\ell\, \mathrm{Ra}_B^{1/4} \quad \text{(isothermal)} \quad (15a)$$

Numerical values of the coefficient are tabulated in Table 1 for various C/B. As $C/B \to 0$, the cylinder degenerates into a vertical plate of height B; in this case $f_2 \to 2$ and $f_1 \to 2$ so that

$$\overline{\mathrm{Nu}}_B = \bar{C}_\ell\, \mathrm{Ra}_B^{1/4} \quad \text{(vertical isothermal plate)} \quad (15b)$$

As $C \to B$, the elliptic cylinder becomes circular so that

$$\overline{\mathrm{Nu}}_B = 0.77\, \bar{C}_\ell\, \mathrm{Ra}_B^{1/4} \quad \text{(isothermal horizontal circular cylinder)} \quad (15c)$$

The average Nusselt numbers for elliptic cylinders of intermediate eccentricity fall between these two extremes.

It is interesting to note that the coefficient in equation (15*a*) changes by less than 1 percent between $C/B = 0.1$ and $C/B = 0$. Therefore, the average heat transfer is very insensitive to the thickness of the cylinder and the "sharpness" of its leading edge near the flat-plate limit.

Comparison of Present Thin-Layer Results With Previous Analyses. The foregoing results arise from the application of a general but approximate solution to the particular problem at hand. To demonstrate the accuracy of this rather simple solution, several comparisons with earlier analyses are made, first for the limiting case of the vertical flat plate, second for the horizontal cylinder, and last for elliptic cylinders of intermediate eccentricity.

Vertical Plate. The expression for C_ℓ *derived* in [7] was not convenient for calculations, but it did suggest a dependence on Pr alone (i.e., no geometrical dependence). A more convenient equation was recommended in reference [7], and an expression which is still convenient, but more accurate at small Prandtl numbers, is recommended in the foregoing. This is equation (7), proposed by Churchill and Usagi [8] for isothermal vertical plates. For completeness, Table 2 is presented to compare the resulting $\bar{C}_\ell$ values with those reported by Ostrach (see [9]) and (for $\mathrm{Pr} = 0.01$) by Sparrow and Gregg [10]. The agreement is excellent, as Churchill and Usagi have already suggested.

It needs to be emphasized here that the particular choice of the equation for C_ℓ is not a key point in the proposed method. The key point is rather the hypotheses that the parameters grouped in the coefficient called C_ℓ are functions of the Prandtl number alone. Once this hypothesis is made, one must find a convenient expression. This could have been derived to fit the cumbersome equation

[1] Numbers in brackets designate References at end of paper.

Table 2 Values of $\overline{\mathrm{Nu}}_B/\mathrm{Ra}_B{}^{1/4}$ for isothermal vertical plate

Pr	0.01	0.1	0.72	10	10^2	10^3
Sparrow and Gregg [8]	0.242	0.389	0.516	0.620	0.652	0.664
Result using equation (15*b*)	0.240	0.385	0.513	0.619	0.652	0.662

Table 3 $Nu_s/Ra_s^{1/4}$ for vertical flat plate, uniform heating

Pr	10^{-2}	10^{-1}	1.0	10	10^2	10^3	∞
Churchill and Ozoe [11]	0.21	0.34	0.46	0.52	0.55	0.56	0.56
$(4/3)^{1/4} C_1$, equation (12c)	0.19	0.31	0.43	0.50	0.53	0.53	0.54
percent error	8.9%	7.7%	6.1%	4.8%	4.5%	4.6%	4.6%

Table 4 $\overline{Nu}_b/Ra_b^{1/4}$ for a horizontal isothermal, circular, cylinder

Pr	0.01	0.7	1000
Saville and Churchill [5]	0.15	0.33	0.44
Present result, (15c)	0.14	0.34	0.41

in [7], it could have been obtained from analysis for any shape of body, or it could have been determined experimentally. The flat-plate equation for C_ℓ is used because it is simple, yet accurate. This equation having been chosen, the remainder of the comparisons with earlier analyses can be made testing (1) the ability of the analysis to generate the correct form of solution, and (2) the underlying hypothesis that C_ℓ is indeed a universal function of Pr.

The first of these tests compares the predictions of the present method for a vertical flat plate with uniform surface heat flux with the solutions of Churchill and Ozoe [11]. Numerical values, and percentage errors in the present predictions, are given in Table 3. The errors are approximately 5 percent for $Pr \gtrsim 1$, increasing to 9 percent at Pr = 0.01. The reason that the present coefficients are in greater error at low Pr has been discussed in [7]. These errors would be acceptable for most practical problems; indeed they are within the normal experimental uncertainty.

Circular Cylinders. The testing of the present analysis continues by focusing attention of heat transfer from circular cylinders first with uniform wall temperature, and second with uniform heat flux. The prediction for the isothermal cylinder, (equation (15c)) has the same form as the solution obtained by Saville and Churchill [5] but the coefficients are different. Table 4 compares these coefficients for various Prandtl numbers. The results are in excellent agreement.

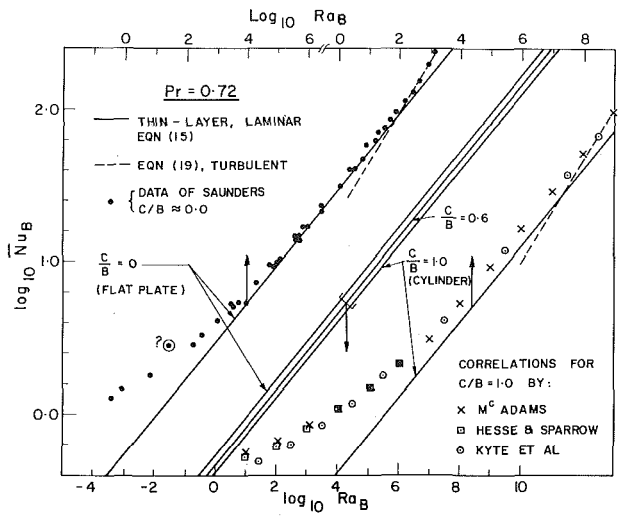

Fig. 2 Thin-layer results compared to experimental data—$C/B \to 0$ is the vertical flat-plate limit

For the uniform heat flux cylinder, Wilks [12] has extended the Saville-Churchill method and obtained $\overline{Nu}_B/\overline{Ra}_B^{1/4} = 0.37$ for Pr = 0.7. The application of the present method, equation (13), yields a value of 0.34 for this constant. The method of performing the integration to obtain this result will be described in a later section. Koh [13] has also addressed this problem.

Elliptic Cylinders (Isothermal). The local heat transfer from isothermal elliptic cylinders has been recently reported by Lin and Chao [6]. Equation (12a) predicts that the Nusselt number at the upstream stagnation point increases with $(B/C)^{1/2}$ for a given Rayleigh number; this agrees well with the Lin-Chao calculations. For Pr = 10 and ∞, the present predictions agree to within 1 percent for all angles and for all C/B reported in their graphs. For Pr = 0.72 the agreement on the upstream half of the cylinders is also within 1 percent, but becomes slightly worse on the rear half for $C/B = 1$ (up to 5 percent) and $C/B = 0.5$ (up to 3 percent).

Conclusions Concerning Accuracy of Present Thin-Layer Analysis. From the foregoing comparison with more complex, but more accurate analyses, the following conclusions emerge. For the constant wall temperature the predictions of $\overline{Nu}$ are accurate to within about 1 percent for $Pr \gtrsim 0.7$ for the wide variety of body contours tested. Comparisons have not been made for very low Pr, but somewhat larger errors would be expected since C_ℓ changes more rapidly with Pr (see [7]). For uniform heat flux, the predictions are normally low by between 5 and 8 percent for $Pr \gtrsim 0.7$, with the difference becoming somewhat larger at lower Pr. When the wall temperature varies more sharply, the errors also increase (up to nearly 20 percent in some extreme cases tested, see [7]); the loss in accuracy of the method under extreme conditions was anticipated in the original formulation of the method in [7]. The results are not intended to apply to problems where the ambient fluid is thermally stratified.

In view of the failure of the underlying thin-layer assumptions demonstrated in the next section, the accuracy of the present predictions would normally be satisfactory.

Comparison of Thin-Layer Predictions With Experiment. The average Nusselt number, $\overline{Nu}_B$, according to equation (15a) is plotted in Fig. 2 for $C/B \to 0$, $C/B = 0.6$, and $C/B \to 1.0$. The curves for the two limiting cases are also replotted in the same figure (note the different scales) to facilitate comparison with experimental data.

For $C/B = 0$ (vertical flat plate) the prediction is compared with the data of Saunders [14] for nearly isothermal vertical plates. The agreement is good in the restricted range $10^5 \lesssim Ra_B \lesssim 10^8$, but outside this range the data lie consistently above the prediction. (A comparison with the plotted results of Saunders suggests that a data-tabulation error has been made in the case of the circled point in Fig. 2.)

For $C/B \to 1.0$, the recommendation of McAdams [15] based on early measurements of the heat transfer from horizontal cylinders, and recommendations of Hesse and Sparrow [16], Kyte, et al. [17], and Collis, et al. [18] based on more recent experiments, have been plotted for comparison with the prediction. The predicted $\overline{Nu}_B$ values are about 25 percent too low in the range $10^4 < Ra_B < 10^8$ with the differences becoming larger outside this range. (Morgan [19] has published a thorough review of experiments related to circular cylinders.)

Discussion of the Applicability of Thin Layer Analyses. The discrepancies between experiment and analysis evident in Fig. 2 are very much larger than the difference between the present approximate solution and more exact solutions of the basic thin-layer, laminar equations. The discrepancies therefore must represent the failure of the basic equations themselves—the same equations on which *all* of the analyses (Chaing-Kaye, Saville-Churchill, Lin-Chao, and the present method) are based. For small Ra_B this failure is thought to be caused by the presence of thick-layer effects while at higher Ra_B the heat transfer is affected by turbulent heat transfer from part of the surface. It is particularly disturbing that for $C/B \to 1.0$, there is *no* Rayleigh-number range for which the thin-layer results are adequate. The same conclusion would be

expected to apply to most blunt bodies.

If the objective of an analysis were to determine local heat transfer rates, there is a region on the surface (whose extent depends on the Rayleigh number) where the series solutions of Saville and Churchill, Lin and Chao, and Chaing and Kaye would be nearly valid. In these regions, the numerical effort required to obtain the solutions may be justified. However, from the evidence just presented, if the *average* Nusselt number is the objective of the analysis (and it normally would be for engineering applications) highly refined solutions of the thin-layer equations do not appear to be justified; even the numerical effort required to evaluate the leading term in their series solutions would appear difficult to justify.

For these purposes, it is felt that the present approximate solution keeps the level of complexity consistent with the accuracy of the underlying equations. Rather than attempting to increase the accuracy of this solution to the thin-layer equations, it is more fruitful to improve it by accounting for the (more important) influences of turbulence and thick boundary layers.

4 Modifying the Thin-Layer Analysis

Turbulent Heat Transfer. In the turbulent regime, the heat transfer becomes dependent on local conditions and "forgets" what has happened upstream. Based on this, and an analogy with equation (6), it was proposed in reference [7] that fully turbulent heat transfer is described locally by the equation

$$\frac{hs}{k} = C_t A(\phi)\ \mathrm{Ra}_s^{1/3} \tag{16}$$

where ϕ is the local angle of the surface from the vertical (positive when the heated surface is upward-facing), $\phi = \sin^{-1}(-dr/ds)$. The proposed relations for A and C_t are

$$A(\phi) = \begin{cases} 0.71\cos^{1/3}\phi & \text{for } -90 \text{ deg} \leqslant \phi \leqslant 19.7 \text{ deg} \\ \sin^{1/3}\phi & \text{for } 90 \text{ deg} \geqslant \phi \geqslant 19.7 \end{cases} \tag{17}$$

and

$$C_t = [0.14\ \mathrm{Pr}^{0.084}, 0.15]^* \tag{18}$$

where $[\ ,\ ]^*$ is defined such that $[A, B]^* = A$ if $A \leq B$ and $[A, B]^* = B$ if $A < B$. These proposals have been made based on available experimental data. Additional confirmation is needed, particularly for $\mathrm{Pr} \gg 1$ and $\mathrm{Pr} \ll 1$.

If the Rayleigh number is so large that turbulent heat transfer occurs from nearly all regions on the surface, these equations can be integrated to determine the average Nusselt number. For the isothermal flat plate and horizontal circular cylinder respectively, the following equations are obtained:

$$\overline{\mathrm{Nu}}_B = 0.71\ C_t\ \mathrm{Ra}_B^{1/3} \text{ (vertical plate)} \tag{19a}$$

$$\overline{\mathrm{Nu}}_B = 0.72\ C_t\ \mathrm{Ra}_B^{1/3} \text{ (horizontal cylinder)} \tag{19b}$$

It is of interest that these asymptotic results are nearly identical; Kutataladze [20] made a similar observation.

These equations are plotted in Fig. 2 for $\mathrm{Pr} = 0.72$. For the vertical flat plate, the data of Saunders [14] closely approaches the result given. There is also excellent agreement with Warner's [21] data and with the experiments of Pirovano, et al. [22] which gave $\overline{\mathrm{Nu}}_B/\mathrm{Ra}_B^{1/3} = 0.104$ for $\mathrm{Pr} \approx 0.7$ compared to 0.096 from equation (19*a*). For circular cylinders, equation (19*b*) is seen to be in very close agreement with the recommendations of McAdams [15] and Kyte, et al. [17] at high Ra_B.

Criterion for Transition. For the range of Rayleigh number of interest, it is necessary to predict average Nusselt numbers when part of the surface is subjected to laminar heat transfer and the remainder to transition and turbulent heat transfer. Since it is the *average* value which is of interest, the problem can be simplified by defining a transition location (rather than region) at which a sudden transition from fully laminar to fully turbulent flow is presumed to occur. Equation (11) would be used on the laminar side of this location and equation (16) on the other. The location should be chosen somewhere in the middle of the actual transition zone such that the integrated local flux across the zone is correct. A criterion for determining this location is required.

The authors have proposed a criterion which requires the introduction of two length scales; these will also prove useful for other purposes in the following sections. The local resistance to heat transfer can be imagined to arise from a fictitious *stationary* layer of fluid enveloping the surface and across which the total temperature drop occurs. Because the local resistance varies with position on the surface, the thickness of this layer also depends on position. The heat transfer across the layer is entirely by conduction. If the layer is very thin, the local Nusselt number based on this layer thickness will be unity. Therefore, for thin layers, the local thickness for laminar and turbulent heat transfer are, respectively,

$$\Delta_\ell = k/h \tag{20}$$

where h in this equation is defined by equation (11), and

$$\Delta_t = s/(C_t\ A(\phi)\ \mathrm{Ra}_s^{1/3}) \tag{21}$$

These length scales are related to the actual thickness of the thermal boundary layer in the moving fluid. They also bear some resemblance to Langmuir's [23] average conduction-layer thickness.

The required transition criterion is based on a comparison of Δ_ℓ and Δ_t at each location on the surface. If $\Delta_\ell \leqslant \frac{4}{3}\ \Delta_t$, the laminar equations are used; if $\Delta_\ell > \frac{4}{3}\ \Delta_t$, the fully turbulent result is used. For transition on an isothermal, inclined plate transferring heat to air or water, this criterion has been checked [7] and found to work well. For other boundary conditions and for Prandtl numbers well removed from unity, experimental data are not yet available, and the tentative nature of the proposal must be stressed. However, the results to be described give a posteriori justification for its use even for $\mathrm{Pr} \gg 1$.

Thick-Layer Effects. Suppose the local value of Δ_ℓ is large, as shown in Fig. 1(*b*). If the area available to heat transfer by conduction away from the surface changes along its path, then the resistance to heat transfer from the surface is affected. This will cause the given thin-layer results to be in error since the use of $\partial^2 T/\partial y^2$ in the conduction term in the basic equation is no longer valid, as described earlier. One remedy would be to replace this term in the differential equation by the appropriate term in elliptic-cylinder coordinates. This would require beginning the solution anew. Another method would be to use the local value of q/A or Nu_B already obtained from the thin-layer solution as the predictor in a predictor-corrector type of approach. The corrector portion would contain information on how quickly the area available to heat transfer is actually changing. The latter strategy is adopted here. The advantages are the general applicability of the method to almost any surface shape and the guidance it provides in choosing correlation equations.

Therefore, in the remainder of this paper, the local (thin-layer) Nusselt numbers described in the foregoing for both laminar and turbulent flow will be considered as predictor values. Where confusion can arise, a superscript p is added (e.g., $(\mathrm{Nu}_B)^p$) to denote this.

Supposing either that $\Delta_\ell < 4\ \Delta_t/3$ (or that laminar flow everywhere has been *assumed*), the length Δ_ℓ along the ψ curve falling through location s on the surface has been shown in Fig. 1(*b*). The corrected value of (q/A) from the area between $\psi - \Delta\psi/2$ and $\psi + \Delta\psi/2$ is obtained by equating it to the *local* heat flux between confocal ellipses distance Δ_ℓ apart along this ψ curve. This outer ellipse is specified by the single parameter η_0. Note that since Δ_ℓ changes with ψ, so will η_0. Using the equation for resistance to heat transfer between confocal ellipses developed by Yovanovich [1], the corrected (q/A) is

$$q/A = k\Delta T^*\ \Delta T_r/b(\eta_0 - \eta_i)\ \chi \tag{22}$$

or

$$\mathrm{Nu}_b = 1/(\eta_0 - \eta_i)\ \chi \tag{23}$$

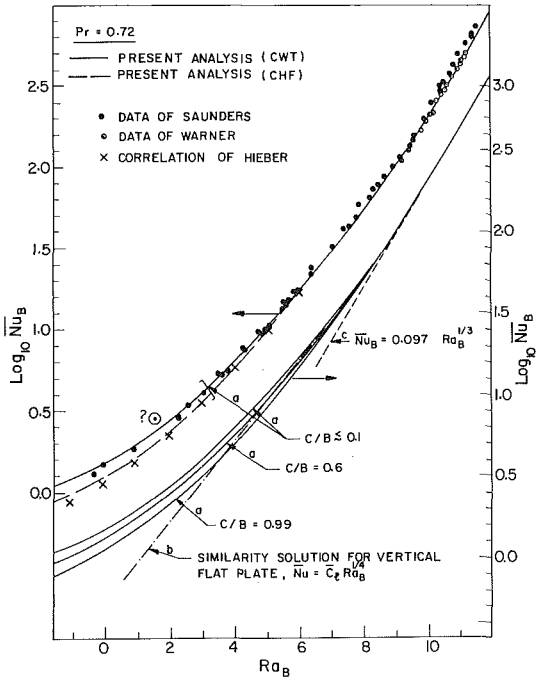

Fig. 3 Analytical results corrected for turbulence and thick-layer effects

η_0 is defined such that

$$a \int_{\eta_i}^{\eta_0(\psi)} (\cosh^2 \eta - \cos^2 \psi)^{1/2} \, d\eta = \Delta_\ell(\psi) \tag{24}$$

η_0 can be simply found by integrating equation (24) numerically (at any required value of ψ) until a value of $\eta = \eta_0$ is found for which the equality is satisfied. This is substituted into (23) to give the corrected Nusselt number. If $\Delta_\ell > 4\Delta_t/3$, and if one wishes to account for turbulence, Δ_t is the appropriate distance to be used in equation (24) in place of Δ_ℓ.

The average Nusselt number based on $\overline{\Delta T}$ is, therefore,

$$\overline{\mathrm{Nu}}_b = \int_0^\pi \frac{\Delta T^*}{(\eta_0 - \eta_i)} \, d\psi/(f_1 \, \overline{\Delta T^*}) \tag{25}$$

where, by definition of average temperature,

$$\overline{\Delta T^*} = \int_0^\pi \Delta T^* \, \chi \, d\psi/f_1 \tag{26}$$

If ΔT^* is specified on the surface, the interval $0 \leq \psi \leq \pi$ is divided into N equal intervals, the value of η_0 found at the middle of each interval, and the integration for $\overline{\mathrm{Nu}}_b$ carried out in a straightforward way. For an isothermal surface, $\Delta T^* = \overline{\Delta T^*} = 1$ and the application is particularly easy.

When the heat flux is specified, the ΔT^* distribution must first be found. For a given local (q/A), a local value of ΔT^* is guessed from which Δ_ℓ and Δ_t can be calculated from equation (20) and (21), respectively. The corresponding value of η_0 is then computed from (24) and substituted into (22) to obtain an improved value of ΔT^*. This is used as the next "guessed" value of ΔT^* in an iteration scheme which terminates when values of ΔT^* and η_0 of sufficient accuracy are known. The process is repeated at required locations around the surface until ΔT^* and η_0 are known at the center of each of the N intervals. $\overline{\mathrm{Nu}}_b$ is then found from equation (25). The reference temperature in this calculation is entirely arbitrary. However, if the heat flux is constant around the surface it is convenient to choose $\Delta T_r = (q/A)b/k$ so that $\overline{\mathrm{Nu}}_b = 1/\overline{\Delta T^*}$.

5 Predictions, Accounting for Turbulence and Thick-Layer Effects

The improved $\overline{\mathrm{Nu}}_B$ values for $C/B \to 0$, 0.6, and $\to 1.0$ (corresponding to the curves plotted in Fig. 2) are shown in Fig. 3 (curves a). The line b shows, for comparison, the thin-layer results obtained in Section 3 for $C/B \to 0$, and the line c is the prediction for turbulent heat transfer everywhere on the surfaces. The thick-layer correction results in a much larger heat transfer at low values of Ra_B and the turbulence correction causes the $\overline{\mathrm{Nu}}_B$ results for all C/B to gradually converge onto almost the same curve. The latter behavior is not surprising since equations (19a) and (19b) must be asymptotically approached.

Vertical Plate, Isothermal. A comparison with experimental data indicates that these corrections bring analysis and experiment into close agreement over a much wider range of Rayleigh numbers. For vertical plates, the $C/B \approx 0$ curve has been replotted in the upper portion of the figure on an offset scale, along with experimental data of Saunders [14] and Warner, et al. [21]. Good agreement is now obtained for the entire experimental range of Ra_B. Some discrepancy between the present results and Saunders' data might be expected because his vertical surface was not perfectly isothermal. Calculations both by Saunders and the present authors indicate, however, that they were nearly isothermal at low Ra_B. The analytical results for constant heat flux (CHF), to be described in the next section, are plotted for comparison with the data in Fig. 3. For $\mathrm{Ra}_B \gtrsim 10^5$ the CWT and CHF predictions are almost identical. For smaller Ra_B (based on the *mean* temperature difference) lower $\overline{\mathrm{Nu}}_B$ are obtained for CHF and the data fall between the CWT and CHF curves, closer to the CWT side, as expected.

Some previous investigations have evaluated higher-order boundary-layer effects for this (CWT) problem and Hieber [24] has been able to give a first-order correction to classical (thin-layer) theory for the global heat transfer. His corrected correlation, plotted in Fig. 3, brings the classical analysis into improved agreement with experiment, but the results are not as satisfactory as those obtained by the present method.

There was almost no dependence of $\overline{\mathrm{Nu}}_B$ on C/B near the flat plate limit ($C/B \lesssim 0.1$) in the thin-layer results. The same result was found to apply to these improved predictions.

Horizontal Circular Cylinders, Isothermal. A comparison between the present analysis and former empirical correlations for isothermal circular cylinders is shown in Fig. 4. Curve (a) is the laminar thin-layer result, curve (b) is for turbulent heat transfer everywhere, curve (c) corrects for thick-layer effects but assumes the heat transfer is laminar everywhere, while curve (d) is the result accounting for both thick-layer and turbulence effects. Shown for comparison are the recommended correlations of several au-

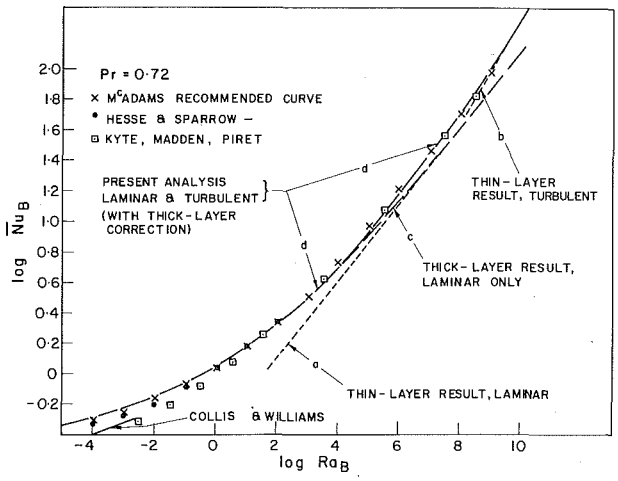

Fig. 4 A comparison of analysis and experiment for horizontal circular cylinders

thors (McAdams [15], Hesse and Sparrow [16], Kyte, et al. [17], Collis and Williams [18]). It is seen that the analysis has been brought into very close agreement with experiment for $Ra_B \gtrsim 10^{-2}$. Below this value there is disagreement between different investigators, but the present results do appear to predict a $\overline{Nu}_B$ which is too large.

Kim, et al. [25] have recently reported *local* heat transfer rates from an isothermal cylinder to a high Prandtl number oil. The results for their lowest temperature difference (where property values change the least) have been plotted in Fig. 5 for comparison with the present predicted local values. The gradual transition is, of course, not predicted but the trends are correct and the average Nusselt number is predicted to within about 4 percent of the experimental value.

Peterka and Richardson [26] have evaluated the leading term in a series solution of the complete equations of motion for laminar flow around a horizontal, isothermal, circular cylinder. Table 5 records their ratio of $(\overline{Nu}_B)/(\overline{Nu}_B)^p$ for Pr = 0.72, where $\overline{Nu}_B$ accounts for thick-layer effects, and $(\overline{Nu}_B)^p$ is the thin-layer Nusselt number. The corresponding "present results," assuming laminar flow everywhere on the cylinder, are tabulated for comparison. The corrections agree to within 1 percent.

Constant Heat Flux (CHF) Results. Values of Nu_b have also been measured by Kim, et al. [21] for a CHF horizontal cylinder. These are compared, for their lowest heat flux, with the present prediction in Fig. 5. The trends are again correctly predicted and the average Nusselt number is predicted to within 5 percent.

For a CHF vertical plate, the *local* Nusselt number is plotted versus the local Rayleigh number, Ra_s, in Fig. 6. For Pr = 7 (water) the thick-layer effects cause the heat transfer to increase for $Ra_s \lesssim 10$ above that predicted by the thin-layer equations. The upper portion of Fig. 6 shows that the temperature distribution deviates from the $s^{1/5}$ variation near the leading edge to an extent which depends on the value of $Ra_b{}^*$.

The predicted Nu_B results are in good agreement with the measurements of Goldstein and Eckert [27] and others. Their measured temperature variation along the plate for $Ra_b{}^* \approx 10^8$ is plotted in the upper portion of the figure. The good agreement with the present corrected results indicates that their observed departure from the 1/5-power curve was at least partly due to thick-layer effects.

To conserve space the average Nusselt number results are not shown. However, correlations will be presented in a later section which closely represent these results.

General Conclusions. The present predictions, accounting for thick-layer and turbulence effects are, therefore, seen to be in excellent agreement with experiment in the two limiting cases of $C/B \to 0$ and $C/B \to 1$. It would appear that these limiting geometries would be most demanding of the analysis (because the sharp leading-edge effect is most severe for the vertical plate, and the area exposed to turbulence is maximum for the circular cylinder). Therefore, even though experimental data are not available for intermediate eccentricities, good agreement with experiment would be expected.

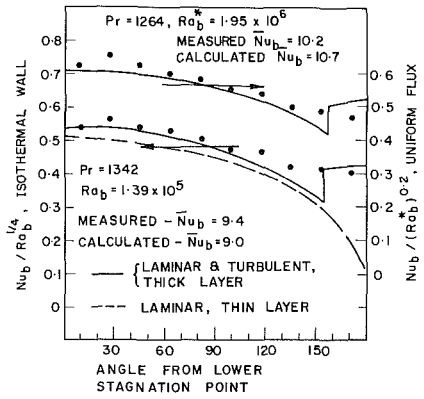

Fig. 5 A comparison of measured and predicted local Nusselt numbers for isothermal and constant heat flux circular cylinders

6 Some Comments on Previous Work

Based on the present analysis, it is possible to explain some conflicting results which have appeared in the literature.

Recently Suriano and Yang [28] published the results of a numerical solution which indicated that, for a vertical isothermal plate, $\overline{Nu}_B \to 1.078$ as $Ra_B \to 0$. In this solution, the T_∞ boundary condition was applied on a rectangular boundary $7.5B$ above and below the center of the plate and $9.0B$ away from the plate in the lateral direction. The heat transfer by conduction between the plate and this boundary would be approximately the same as between the plate and an elliptic cylinder with a semimajor axis of about $7.5B$. This corresponds to a value of η_0 in equation (23) of 3.4 (since $7.5B = b \cosh \eta_0$ defines the value of the η_0 ellipse passing through this point). The corresponding Nusselt number, arising from the conductive heat transfer alone, is therefore $Nu_B \approx \pi/\eta_0 = 0.92$. This is close to the limiting value obtained by Suriano and Yang. It is therefore quite clear that their $\overline{Nu}_B$ asymptotically approached a limiting value as $Ra_B \to 0$ because the boundary condition at "infinity" was applied much too close to the plate.

Gryzagoridis [29] has published measurements of $\overline{Nu}_B$ versus Ra_B for an isothermal wall boundary condition which indicate that the classical solution for a vertical plate holds down to $Ra_B \approx 10$. The disagreement of his results with the present analysis and with earlier results is therefore great. It is here speculated that the chambers containing his plates were so small that the heat transfer behavior was more like that for an enclosure. The decrease in heat transfer due to enclosure effects can be seen from the work of Powe [30]. It is the enclosure effect which is likely also responsible for the dependence of the local Nusselt number on both Ra *and* ΔT in his later experiments [31].

7 Correlation Equations

Isothermal Surfaces. The average Nusselt number for laminar, thin-layer heat transfer can be simply found from equation (15*a*) (for an isothermal surface). However, these are usually not directly useful because of the presence of thick-layer effects and turbulence. When these effects are accounted for, the foregoing method involves numerical integrations and the simple, explicit equation for $\overline{Nu}_B$ is lost. Although it is elementary to write a computer program to solve the integrals (less than 100 statements in Fortran), it would be more convenient if the analytical results could be adequately represented by equations.

It is not clear what form of equation should be forced to fit the final predictions. Therefore, the simpler problem of finding equations which are, respectively, correct in the limits of laminar heat transfer everywhere on the surface, and turbulent heat transfer everywhere, is addressed. Once these are known they are combined to give the final equation.

The appropriate equation in the limit as the entire surface is subjected to *turbulent* heat transfer is given by equations (19*a*) and (19*b*). Since the coefficients in these equations are so nearly equal the same equation can be used for all eccentricities. For the purposes of this section, this *turbulent* Nusselt number is designated as $\overline{Nu}_{Bt}$.

Table 5 $\overline{Nu}_B/(\overline{Nu}_B)^p$ for horizontal, isothermal cylinders

(Ra_b/Pr) for Pr = 0.72 →	10^5	10^4	6×10^3	3×10^3	1.38×10^3	10^3
Peterka and Richardson	1.09	1.15	1.17	1.20	1.25	1.26
Present result	1.08	1.14	1.16	1.19	1.23	1.24

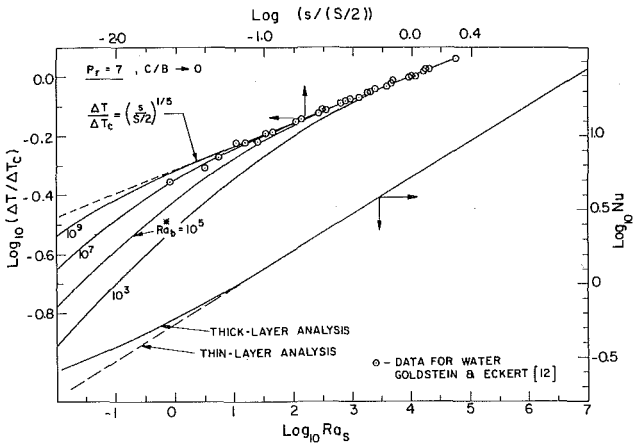

Fig. 6 Distribution of local Nusselt number (lower) and temperature difference along a vertical, constant-heat-flux vertical plate

Table 6 k^* and q^* for use in equation (33)

	$\overline{Ra}_B$ presentation		$Ra_B{}^*$ presentation	
C/B	k^*	q^*	k^*	q^*
1.0	2.00	$0.76\,\bar{C}_\ell\,\overline{Ra}_B{}^{1/4}$	1.64	$1.05\,\bar{C}_\ell\,Ra_B{}^{*1/5}$
$\lesssim 0.1$	1.83	$\bar{C}_\ell\,\overline{Ra}_B{}^{1/4}$	1.49	$1.30\,\bar{C}_\ell\,Ra_B{}^{*1/5}$

The average Nusselt numbers for *laminar* heat transfer from the entire surface can be obtained by rerunning the analysis with the turbulent heat transfer "turned off." Let these Nusselt numbers be designated by $\overline{Nu}_{B\ell}$. Guided by an examination of the equations in the limiting cases as $C/B \to 0$ and $C/B \to 1$ (the *latter* case was examined in [7]) the following equation for $\overline{Nu}_{B\ell}$ was obtained:

$$\overline{Nu}_{B\ell} = \frac{(2\pi K/f_1)}{\ln(1 + 2^{3/4}\,\pi K/(f_2{}^{3/4}\,\bar{C}_\ell\,Ra_B{}^{1/4}))} \tag{29}$$

where K is a constant depending on C/B which is fit well with the equation

$$K = [0.91,\ (C/B)^{0.041}]_{MAX} \tag{30}$$

The maximum value of the two quantities in brackets is used.

Now that the equations for $\overline{Nu}_{B\ell}$ and $\overline{Nu}_{Bt}$ are known, they must be combined to fit the analytical results. This is done, following the suggestion of Churchill and Usagi [8], using

$$(\overline{Nu}_B)^m = \{Nu_B\}^m + \{\overline{Nu}_{Bt}\}^m \tag{31}$$

where m is some constant.

Inserting the appropriate equations one obtains

$$(\overline{Nu}_B)^m = \left\{\frac{2\pi K/f_1}{\ln[1 + 2^{3/4}\,\pi K/(f_2{}^{3/4}\,\bar{C}_\ell\,Ra_B{}^{1/4})]}\right\}^m + \{0.72\,C_t\,Ra_B{}^{1/3}\}^m \tag{32}$$

where f_1 and f_2 are tabulated in Table 1, K is given by equation (30) and m may be adequately found from

$$m = 3.5/\sqrt{(C/B) + 0.1} \tag{32a}$$

While this is a cumbersome equation, it fits the results of the analysis for all $Ra_B \gtrsim 10^{-2}$, for all C/B, and all Prandtl numbers to within about 5 percent. For any C/B and Pr all the constants can be computed and the equation becomes much simpler.

Constant Heat Flux Surfaces. An equation of the form of (31) can also be used for the CHF surfaces. The presentation of appropriate equations for $\overline{Nu}_{B\ell}$ and $\overline{Nu}_{Bt}$ is, however, complicated by the availability of several possible choices for the reference temperature. In the following, the average temperature difference, $\overline{\Delta T}$, is used in defining $\overline{Nu}_B$; the correlations are given either in terms of $\overline{Ra}_B$ (which uses $\overline{\Delta T}$) or $Ra_B{}^*$ (which uses $(q/A)\,b/k$ as the reference temperature).

For calculating $\overline{Nu}_{B\ell}$ in equation (31), the following equation can be used:

$$\overline{Nu}_{B\ell} = k^*/\ln\,(1 + k^*/q^*) \tag{33}$$

where k^* and g^* are given separately for each of the two cases in Table 6.

The equations for $\overline{Nu}_{Bt}$ are

$$\overline{Nu}_{Bt} = 0.72\,C_t\,\overline{Ra}_B{}^{1/3} \quad (\overline{Ra}_B \text{ presentation}) \tag{34a}$$

$$= [0.21\,Pr^{0.063},\ 0.22]\cdot Ra_B{}^{*\,1/4} \quad (Ra_B{}^* \text{ presentation}) \tag{34b}$$

Equations (33) and (34) are inserted into (31) and, using (32a) for m, $\overline{Nu}_B$ is calculated. The results are accurate for $Ra_B{}^* \gtrsim 0.1$.

Comparison With Previous Correlations. The equations just presented appear to be the first proposals for elliptic cylinders. However, for the limiting cases of $C/B \to 0$ and $C/B \to 1$, previous equations have been suggested, the most competitive proposals being those by Churchill and Chu [32–34] (which appeared while the present paper was under review). Their equations are plotted in Fig. 7, along with equation (32), and the data from Figs. 3 and 4 (using the same symbols). For both geometries, the Churchill-Chu equations fall substantially below the data, and equation (32), for Ra_B near 10^2. For very large Ra_B, their $\overline{Nu}_B$ values are higher than ours by about 5 percent, but both lie within experimental scatter. For $Ra_B \lesssim 10^{-2}$, there are large discrepancies between experiments. The present equation appears to fall slightly above the data (this could be changed by decreasing K in equation (32)) near 10^{-2} but has the correct conduction limit as $Ra_B \to 0$; the Churchill-Chu equations yield a constant Nusselt number in the conduction limit. This limiting behavior would be correct only if conduction directly to the enclosure walls, or end effects (finite length of cylinder or width of plate), became dominant. However, since the limiting value in $\overline{Nu}_B$ is then experiment-dependent, it does not seem appropriate to represent it by a single constant value.

Their equations are simpler to evaluate, requiring (after all coefficients have been evaluated) four operations compared to 11 for equation (32); if the equations are used in a computer program, this difference does not seem important.

8 Summary

A general (but approximate) method of obtaining solutions to free-convection heat transfer problems, accounting for thick-boundary-layer effects and turbulent transport, has been used in this paper to predict the heat transfer from thin elliptic cylinders over a very large range of Rayleigh numbers. The following summarizes the contributions of the analysis.

1 It was shown to be very important to account for thick layer effects and turbulent heat transfer when predicting the average Nusselt number for elliptic cylinders. The same conclusion probably applies to all two-dimensional bodies.

2 In the limiting case of large eccentricity the elliptic cylinder degenerates to a vertical flat plate. New solutions to this (classic) problem have been obtained for both constant wall temperature (CWT) and constant heat flux (CHF) boundary conditions. The present analysis is more successful than any previous analysis (known to the authors) in bringing predictions and experiment together over a large range of Rayleigh number. The effect of small but finite plate thickness, and of a finite radius on the leading edge, was found to be negligible. It is essential in this analysis that the flat plate be treated as the limiting case of an elliptic cylinder.

3 In the limiting case of small eccentricity, the cylinder becomes circular. A new solution to this problem is reported for CHF boundary conditions. The predictions for both CWT and CHF conditions are compared to experiment, and excellent agreement is found over a very wide range of Rayleigh number.

4 New CWT and CHF solutions are presented for local and average heat transfer from elliptic cylinders of intermediate eccentricity. No experimental data are known to exist for this case, but

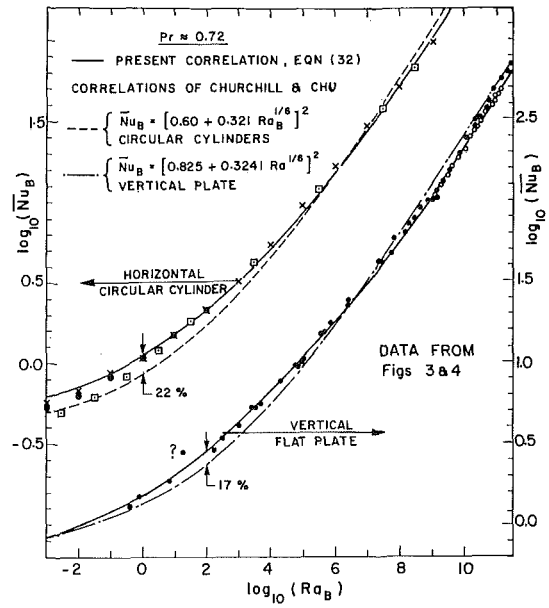

Fig. 7 Comparison of equation (32) with correlating equations proposed by Churchill and Chu and with experiment for vertical plates and horizontal circular cylinders

the excellent agreement for the limiting cases in 2 and 3 lends confidence to the accuracy of these predictions.

5 Correlation equations are presented which fit the results of the analysis closely for $10^{-2} \lesssim Ra_B \lesssim 10^{12}$ for all eccentricities for CWT boundary conditions. Similar equations, but with a slightly reduced range of validity in Rayleigh number, are also given for CHF conditions. The CWT equation is compared with data and the recent proposals of Churchill and Chu.

Acknowledgments

The authors wish to thank Profs. Goldstein, Warner, and Wollersheim for access to their data. We are grateful also to Prof. M. M. Yovanovich for helpful discussions, and to Profs. B. T. Chao and E. M. Sparrow for making accurate graphs of the Lin-Chao predictions available. This work was supported by Operating Grants from the National Research Council of Canada.

References

1 Yovanovich, M. M., "A General Expression for Predicting Conduction Shape Factors," *Progress in Astronautics and Aeronautics,* Vol. 35, Thermophysics and Spacecraft Thermal Control, 1974, pp. 265–291.

2 Sparrow, E. M., and Gregg, J. L., "Laminar-Free-Convection Heat Transfer From the Outer Surface of a Vertical Circular Cylinder," TRANS. ASME, 1956, pp. 1823–1829.

3 Minkowycz, W. J., Sparrow, E. M., "Local Non-Similar Solutions for Natural Convection on a Vertical Cylinder," JOURNAL OF HEAT TRANSFER, TRANS. ASME, Series C, Vol. 96, 1974, pp. 178–183.

4 Chiang, T., and Kaye, J., "On Laminar Free Convection From a Horizontal Cylinder," *Proceedings of 4th National Congress of Applied Mechanics,* 1962, pp. 1213–1219.

5 Saville, D. A., and Churchill, S. W., "Laminar Free Convection in Boundary Layers Near Horizontal Cylinders and Vertical Axisymmetric Bodies," *Journal of Fluid Mechanics,* Vol. 29, 1967, pp. 391–399.

6 Lin, F. N., and Chao, B. T., "Laminar Free Convection Over Two-Dimensional and Axisymmetric Bodies of Arbitrary Contour," JOURNAL OF HEAT TRANSFER, TRANS. ASME, Series C, Vol. 96, 1974, pp. 435–442.

7 Raithby, G. D., and Hollands, K. G. T., "A General Method of Obtaining Approximate Solutions to Laminar and Turbulent Free Convection Problems," *Advances in Heat Transfer,* Academic Press, Vol. 11, 1975, see also *Internation Journal of Heat and Mass Transfer,* Vol. 17, 1974, pp. 1620–1622.

8 Churchill, S. W., and Usagi, R., "A General Expression for the Correlation of Rates of Transfer and Other Phenomena," *AIChE Journal,* Vol. 18, 1972, pp. 1121–1128.

9 Bird, R., Stewart, W. E., and Lightfoot, E. N., *Transport Phenomena,* Wiley, New York, 1960.

10 Sparrow, E. M., and Gregg, J. L., "Laminar Free Convection From a Vertical Plate With Uniform Surface Heat Flux," TRANS. ASME, Vol. 78, 1956, pp. 435–440.

11 Churchill, S. W., and Ozoe, H., "A Correlation for Laminar Free Convection From a Vertical Plate," JOURNAL OF HEAT TRANSFER, TRANS. ASME, Series C, Vol. 95, 1973, pp. 540–541.

12 Wilks, G., "External Natural Convection About Two-Dimensional Bodies With Constant Heat Flux," *International Journal of Heat and Mass Transfer,* Vol. 15, 1972, pp. 351–354.

13 Koh, J. C. Y., "Laminar Free Convection From a Horizontal Cylinder With Prescribed Surface Heat Flux" *International Journal of Heat and Mass Transfer,* Vol. 7, 1964, pp. 811–813.

14 Saunders, O. A., "The Effect of Pressure on Natural Convection in Air," *Proceedings Royal Society* (London), Series A, Vol. 157, 1936, pp. 278–291.

15 McAdams, W. H., *Heat Transmission,* McGraw-Hill, New York, 1954.

16 Hesse, G., and Sparrow, E. M., "Low Rayleigh Number Natural Convection Heat Transfer From High-Temperature Horizontal Wires to Gases," *International Journal of Heat and Mass Transfer,* Vol. 17, 1974, pp. 796–798.

17 Kyte, J. R., Madden, A. J., and Piret, E. L., "Natural Convection Heat Transfer at Reduced Pressure," *Chem. Eng. Prog.,* Vol. 49, 1953, pp. 653–662.

18 Collis, D. C., and Williams, M. J., "Free Convection of Heat From Fine Wires," Aeronautical Research Laboratories, Australia, Note 140, 1954.

19 Morgan, V. T., "The Overall Convective Heat Transfer From Smooth Circular Cylinders," *Advances in Heat Transfer,* Vol. 11, Academic Press, 1975.

20 Kutateladze, S. S., *Fundamentals of Heat Transfer,* Academic Press, New York, 1963, p. 293.

21 Warner, C. Y., and Arpaci, V. S., "An Experimental Investigation of Turbulent Natural Convection in Air at Low Pressure on a Vertical Heated Flat Plate," *International Journal of Heat and Mass Transfer,* Vol. 11, 1968, pp. 397–406.

22 Pirovano, A., Viannay, S., and Jannot, M., "Convection naturelle en regime turbulent le long d'une plaque plane verticale," 4th International Heat Transfer Conference, Paris, Paper NC1.8, 1970.

23 Langmuir, I., "Convection and Conduction of Heat in Gases, *Physical Review,* Vol. 34, 1912, pp. 401–422.

24 Hieber, C. A., "Natural Convection Around Semi-Infinite Vertical Plate: Higher Order Effects," *International Journal of Heat and Mass Transfer,* Vol. 17, 1974, pp. 785–791.

25 Kim, C. B., Pontikes, T. J., and Wollersheim, D. E., "Free Convection From a Horizontal Cylinder With Isothermal and Constant Heat Flux Surface Conditions," JOURNAL OF HEAT TRANSFER, TRANS. ASME, Series C, Vol. 97, 1975, pp. 129–130.

26 Peterka, J. A., and Richardson, P. D., "Natural Convection From a Horizontal Cylinder at Moderate Grashof Numbers," *International Journal of Heat and Mass Transfer,* TRANS. ASME, Series C, Vol. 12, 1969, pp. 749–752.

27 Goldstein, R. J., and Eckert, E. R. G., "The Steady and Transient Free Convection Boundary Layer on a Uniformly Heated Vertical Plate," *International Journal of Heat and Mass Transfer,* TRANS. ASME, Series C, Vol. 1, 1960, pp. 208–218.

28 Suriano, F. J., and Yang, K. T., "Laminar Free Convection About Vertical and Horizontal Plates at Small and Moderate Grashof Numbers," *International Journal of Heat and Mass Transfer,* TRANS. ASME, Series C, Vol. 11, 1968, pp. 473–490.

29 Gryzagoridis, J., "Natural Convection From a Vertical Flat Plate in the Low Grashof Number Range," *International Journal of Heat and Mass Transfer,* TRANS. ASME, Series C, Vol. 14, 1971, pp. 162–165.

30 Powe, R. E., "Bounding Effects on the Heat Loss by Free Convection From Spheres and Cylinders," JOURNAL OF HEAT TRANSFER, TRANS. ASME, Series C, Vol. 96, 1974, pp. 558–560.

31 Gryzagoridis, J., "Leading Edge Effects on the Nusselt Number for a Vertical Plate in Free Convection," *International Journal of Heat and Mass Transfer,* Vol. 16, 1973, pp. 517–520.

32 Churchill, S. W., and Chu, H. H. S., "Correlating Equations for Laminar and Turbulent Free Convection From a Horizontal Cylinder," *International Journal of Heat and Mass Transfer,* Vol. 18, 1975, pp. 1049–1053.

33 Churchill, S. W., and Chu, H. H. S., "Correlating Equations for Laminar and Turbulent Free Convection From a Vertical Plate," *International Journal of Heat and Mass Transfer,* Vol. 18, 1975, pp. 1323–1329.

34 Churchill, S. W., and Churchill, R. U., "A Comprehensive Correlating Equation for Heat and Component Transfer by Free Convection," *AIChE Journal,* Vol. 21, No. 3, 1975, pp. 604–606.

M. M. Gibson
B. E. Launder

Imperial College of Science and Technology,
Department of Mechanical Engineering,
London SW7, England

On the Calculation of Horizontal, Turbulent, Free Shear Flows Under Gravitational Influence

1 Introduction

The transport of heat, mass, and momentum in the environment is usually complicated by the important effect exerted by the earth's gravitational field. Gravitational forces acting on the mean flow will cause hot gaseous exhausts to rise on discharge to the atmosphere; and a submerged jet of warm water will tend to spread out over the top surface of a lake or estuary. A buoyant shear flow may display markedly different characteristics from an isothermal shear flow subject to the same boundary conditions due to the influence of buoyant forces on the internal structure of the *turbulent* motion. The present contribution provides proposals for modeling these effects and shows the outcome of calculations of some non-equilibrium free shear flows.

Available models for buoyancy-affected turbulence tend to be oversimplified or of such complexity that their use for practical calculations is unattractively expensive. Models of the former kind predict collapse of the turbulence at a critical value of the flux collapse of the turbulence at a critical value of the flux Richardson number, R_f, defined by:

$$R_f \equiv \frac{\text{Rate of turbulent energy removal by buoyant forces}}{\text{Rate of turbulent energy creation by mean shear}}$$

Towsend [1][1] and Ellison [2] give widely different values for $R_{f\text{crit}}$ of 0.5 and 0.15, respectively. Moreover, these simple theories do not allow the turbulence stresses and heat fluxes to be determined.

More elaborate models based on the solution of approximate transport equations for the turbulent stress and heat-flux components have been proposed by Lumley [3] and Donaldson, Sullivan, and Rosenbaum [4]. In the most general circumstances the latter model entails the solution of ten coupled, highly nonlinear differential equations for turbulence correlations, and the former twelve. This is a formidable task, even for two-dimensional thin shear flows.

Neither the simple nor the elaborate models mentioned in the foregoing distinguish between turbulent flow near a wall and free shear flows. It is now recognized, however, that the presence of a rigid surface substantially alters the character of the pressure fluctuations in its vicinity [5, 6] which in turn affect the level of stress and heat flux. Gravitational forces too have been shown to affect the turbulent pressure fluctuations [7] and their influence likewise remains to be included in any complete "second-order" closure. In our view, models of this kind, while providing the best medium-term prospect for a generally valid treatment of turbulence, are at present too expensive for most practical applications, particularly as the models themselves are still the subject of rapid development and change.

The present contribution provides a model intermediate in complexity between the two kinds of closures discussed in the foregoing. The turbulent fluxes are calculated from the local values of just two scalar turbulence properties: the turbulence kinetic energy (k) and its dissipation rate (ϵ). The approach does not entail a priori acceptance of the effective-viscosity concept on which earlier k-ϵ models are based [8, 9]. Instead, algebraic formulas are derived connecting the turbulent stresses and heat fluxes with the local values of k and ϵ and with the mean velocity and/or temperature fields.[2]

The basic physical model has been developed by Launder [7] for the restricted case where turbulence-energy production and dissipation rates were equal throughout the flow. The present work extends the treatment to more realistic flow situations in which the production : dissipation ratio varies from point to point.

Predictions are presented for the horizontal buoyant mixing layer and the surface jet, both of which exhibit the correct character of progressive collapse as the mean Richardson number increases. Comparisons are also drawn with recently published data of the thermal fields of the turbulent wake and plane jet.

[1] Numbers in brackets designate References at end of paper.

Contributed by the Heat Transfer Division for publication in the JOURNAL OF HEAT TRANSFER. Manuscript received by the Heat Transfer Division December 2, 1974. Paper No. 76-HT-S.

[2] The method used here was proposed by Rodi [10] for momentum transport in nonbuoyant flows. Similar though, we believe, less satisfactory simplification schemes, have been suggested by Launder [11] and by Mellor and Yamada [12].

2 Analysis

Reference [7] has proposed the following pair of equations for determining the turbulent stresses and heat fluxes in buoyancy-affected free shear flows:

$$\frac{D\overline{u_iu_j}}{Dt} = \mathfrak{D}(\overline{u_iu_j}) + P_{ij} - \frac{2}{3}\delta_{ij}\epsilon - c_1\frac{\epsilon}{k}(\overline{u_iu_j} - \frac{2}{3}\delta_{ij}k) - c_2(P_{ij} - \frac{2}{3}\delta_{ij}P) \quad (1)$$

$$\frac{D\overline{u_iT'}}{Dt} = \mathfrak{D}(\overline{u_iT'}) - \overline{u_iu_k}\frac{\partial T}{\partial x_k} - c_{1T}\frac{\epsilon}{k}\overline{u_iT'} + P_{iT}(1 - c_{2T}) \quad (2)$$

where the operator $\mathfrak{D}(\ )$ denotes the rate of diffusive transport of the quantity within parentheses. The quantities P, P_{ij}, and P_{iT} represent, respectively, the production rates of turbulence energy, of $\overline{u_iu_j}$, and of that part of $\overline{u_iT'}$ attributable to mean shear and effects of buoyancy.

$$P \equiv -\left\{\overline{u_iu_k}\frac{\partial U_i}{\partial x_k} + \frac{\alpha g_i}{T}\overline{u_iT'}\right\}$$

$$P_{ij} \equiv -\left\{\overline{u_iu_k}\frac{\partial U_j}{\partial x_k} + \overline{u_ju_k}\frac{\partial U_i}{\partial x_k}\right\} - \frac{\alpha}{T}\left\{g_j\overline{u_iT'} + g_i\overline{u_jT'}\right\}$$

$$P_{iT} \equiv -\left\{\overline{u_kT'}\frac{\partial U_i}{\partial x_K} + \frac{\alpha g_i}{T}\overline{T'^2}\right\} \quad (3)$$

A detailed derivation of equations (1) and (2) from the exact equations for $\overline{u_iu_j}$ and $\overline{u_iT'}$ is given in reference [7]. The fine-scale turbulent motion is assumed to be isotropic and the pressure-strain (ϕ_{ij}) and pressure-temperature-gradient (ϕ_{iT}) correlations, which appear as unknowns in the exact equations, are approximated by:

$$\phi_{ij} = -c_1\frac{\epsilon}{k}\left(\overline{u_iu_j} - \frac{2}{3}\delta_{ij}k\right) - c_2\left(P_{ij} - \frac{2}{3}\delta_{ij}P\right) \quad (4)$$

$$\phi_{iT} = -c_{1T}\frac{\epsilon}{k}\overline{u_iT'} - c_{2T}P_{iT} \quad (5)$$

Reference [7] considered only the case of equilibrium buoyant flows, i.e., where the production and dissipation rates of turbulence energy are in balance. The convective and diffusive transport terms in equations (1) and (2) were then zero. Since these are the only terms containing derivatives of the turbulent stresses and heat fluxes, the equations are thus reduced from a differential to an algebraic set for $\overline{u_iu_j}$ and $\overline{u_iT'}$.

Here, for the case of nonequilibrium shear flows, we approximate the transport terms in equations (1) and (2) in such a way that again algebraic formulas emerge for the turbulent stresses and heat fluxes. Following Rodi [10], it is assumed that:

$$\frac{D\overline{u_iu_j}}{Dt} - \mathfrak{D}(\overline{u_iu_j}) = \frac{\overline{u_iu_j}}{k}\left\{\frac{Dk}{Dt} - \mathfrak{D}(k)\right\} \quad (6)$$

That is, the nett transport of stress component $\overline{u_iu_j}$ is assumed to be proportional to the transport of kinetic energy times the factor $\overline{u_iu_j}/k$. The assumption is reasonably correct in thin shear flows except in the vicinity of an axis of symmetry.

Now, the transport equation for turbulence energy (see equation (19)) expresses the fact that the nett transport of k at any point equals the excess of the local production rate over the dissipation rate of k. Equation (6) may thus be rewritten as:

$$\left[\frac{D\overline{u_iu_j}}{Dt} - \mathfrak{D}(\overline{u_iu_j})\right] = \frac{\overline{u_iu_j}}{k}(P - \epsilon) \quad (7)$$

Equations (1) and (7) may then be combined to yield the following formula for the Reynolds stresses:

$$\frac{\overline{u_iu_j} - \frac{2}{3}\delta_{ij}k}{k} = \phi\frac{P_{ij} - \frac{2}{3}\delta_{ij}P}{\epsilon} \quad (8)$$

in which:

$$\phi \equiv (1 - c_2)/(c_1 - 1 + P/\epsilon) \quad (9)$$

Equation (8) is identical with the formula obtained by Launder [7] except that in the definition of ϕ the denominator $(c_1 - 1 + P/\epsilon)$ now replaces c_1.

The values of the empirical coefficients adopted in [7] here: $c_1 = 2.2$; $c_2 = 0.55$ are consistent with the proposals of [7] for non-buoyant flows.

The transport terms in equation (2) are approximated in a precisely parallel way. It is assumed that:

$$\frac{D}{Dt}\overline{u_iT'} - \mathfrak{D}(\overline{u_iT'}) \simeq \frac{\overline{u_iT'}}{k^{1/2}\sqrt{T'^2}}\left\{\frac{D}{Dt}\left(k^{1/2}\sqrt{T'^2}\right)\right.$$

Nomenclature

B = function defined by equation (28)
b_u = characteristic width of velocity field: $b_u = x_3(0.5)$ for jet or wake; $b_u = x_3(0.9) - x_3(0.1)$ for mixing layer
b_T = characteristic width for temperature field equivalent to b_u
k = turbulence energy $\frac{1}{2}\overline{u_i^2}$
P = rate of production of turbulence energy, equation (3)
P_{ij} = rate of production of $\overline{u_iu_j}$, equation (3)
P_{iT} = rate of production of $\overline{u_iT'}$, equation (3)
P_T = rate of production of $\overline{T'^2}$
R_f = flux Richardson number, equation (25)
Ri_1, Ri_2 = gradient Richardson numbers, equation (39)
T = mean temperature
T' = fluctuating temperature
$\hat{T}$ = mean temperature normalized with respect to maximum and minimum values
U_i = mean velocity component in i-direction
$\hat{U}_1$ = mean velocity normalized with respect to maximum and minimum values
u_i = fluctuating velocity component in i-direction
x = coordinate
$x_3(0.5)$ = cross-stream coordinate of "half-velocity" point
$x_3(0.1)$ = cross-stream coordinate of 10 percent velocity point
$x_3(0.9)$ = cross-stream coordinate of 90 percent velocity point
α = dimensionless volumetric coefficient of expansion
δ_1 = displacement thickness
δ_2 = momentum thickness
ϵ = rate of dissipation of turbulence energy
ϵ_T = rate of dissipation of $\overline{T'^2}$
η = dimensionless cross-stream coordinate $\{x_3 - x_3(0.5)\}/b_u$
η_T = dimensionless cross-stream coordinate based on temperature field
λ = thermal diffusivity
ν_t = "turbulent" viscosity
σ_t, σ_k, σ_ϵ = turbulent Prandtl-Schmidt numbers for T, k, and ϵ
ϕ = function defined by equation (9)
ϕ_T, ϕ'_T = functions defined by equations (14) and (15)
ΔT = mean temperature difference
ΔU = mean velocity difference

Subscripts

i, j, k = Cartesian coordinates, direction i, j, k
1, 3 = horizontal and vertical directions in two-dimensional plane flow
0 = initial or nonbuoyant conditions

$$-\mathcal{D}\left(k^{1/2}\sqrt{\overline{T'^2}}\right)\Big\} = \frac{\overline{u_i T'}}{2\overline{T'^2}}(P_T - \epsilon_T) + \frac{\overline{u_i T'}}{2k}(P - \epsilon) \quad (10)$$

where P_T and ϵ_T denote, respectively, the rates of production and destruction of the temperature fluctuations:

$$P_T \equiv -2\,\overline{u_k T'}\,\frac{\partial T}{\partial x_k} \quad (11)$$

$$\epsilon_T \equiv 2\lambda\left(\overline{\frac{\partial T'}{\partial x_k}}\right)^2 \quad (12)$$

Substitution of equation (10) into (2) results in the following expression for $\overline{u_i T'}$:

$$-\overline{u_i T'} = \phi_T \frac{k}{\epsilon}\overline{u_i u_k}\frac{\partial T}{\partial x_k} - \phi'_T \frac{k}{\epsilon} P_{iT} \quad (13)$$

where:

$$\phi_T \equiv \left[c_{1T} + \tfrac{1}{2}(P/\epsilon - 1) + \tfrac{1}{2}\frac{k}{\epsilon}\frac{\epsilon_T}{\overline{T'^2}}(P_T/\epsilon_T - 1)\right]^{-1} \quad (14)$$

$$\phi'_T \equiv \phi_T(1 - c_{2T}) \quad (15)$$

This equation is again the same as obtained in [7] except for the presence of the groups containing $(P/\epsilon - 1)$ and $(P_T/\epsilon_T - 1)$ in equation (14). Following [7] the quantities c_{1T} and c_{2T} are assigned the values: $c_{1T} = 3.2$; $c_{2T} = 0.50$.

Let us note at this point the degree of completeness achieved so far in the turbulence-model specification. We have a set of algebraic equations for the turbulent stress components, equation (8), and the heat fluxes, equation (13). These contain four scalar properties of turbulence as unknowns: k, ϵ, $\overline{T'^2}$ and ϵ_T. In general, the value of these quantities will be quite substantially affected by the levels prevailing in neighboring regions; that is to say, transport effects are significant. To provide an entirely consistent level of closure, therefore, all four quantities should be found from approximated transport equations. This is quite a manageable computing task. However, for the present it has seemed preferable to adopt the following simpler practice. The dissipation rate of $\overline{T'^2}$ is assumed to be related to ϵ, k, and $\overline{T'^2}$ by:

$$\epsilon_T = \frac{2}{c_{T'}}\left(\frac{\epsilon}{k}\right)\overline{T'^2} \quad (16)$$

and, moreover, the dissipation and production rates of T'^2 are assumed nearly in balance. Thus, equation (14) simplifies to:

$$\phi_T = [c_{1T} + \tfrac{1}{2}(P/\epsilon - 1)]^{-1} \quad (17)$$

and $\overline{T'^2}$ which appears in the buoyancy contribution to P_{iT} is approximated as

$$\overline{T'^2} = -c'_T \frac{k}{\epsilon}\overline{u_k T'}\frac{\partial T}{\partial x_k} \quad (18)$$

Following [7], the coefficient c'_T is taken as 1.6 to give the correct rate of decay of temperature fluctuations in grid turbulence. This rudimentary treatment of the temperature fluctuation seems justified because $\overline{T'^2}$ appears in a less prominent position in the model than do k or ϵ, while ϵ_T is still less influential. Moreover, when the fluctuating motions principally responsible for the level of k are the same as those responsible for $\overline{T'^2}$, the time and length scales associated with the velocity and thermal turbulence fields should be closely similar.

The transport effects are thus contained solely in the treatment of k and ϵ. Their values are found from the conservation equations for k and ϵ used in the $k \sim \epsilon$ viscosity model [8, 9]:

$$\frac{Dk}{Dt} = \frac{\partial}{\partial x_j}\left(\frac{\nu_t}{\sigma_k}\cdot\frac{\partial k}{\partial x_j}\right) + P - \epsilon \quad (19)$$

$$\frac{D\epsilon}{Dt} = \frac{\partial}{\partial x_j}\left(\frac{\nu_t}{\sigma_\epsilon}\cdot\frac{\partial \epsilon}{\partial x_j}\right) - c_{\epsilon 1}\frac{\epsilon}{k}\overline{u_i u_j}\frac{\partial U_i}{\partial x_j} - c_{\epsilon 2}\frac{\epsilon^2}{k} \quad (20)$$

It is noted however that now buoyancy generation is included (in P) in the turbulence energy equation. There is strictly a corresponding buoyancy term in the ϵ equation, but it appears its effect should be negligible (see Lumley [3]) provided the fine-scale motion remains isotropic. The quantity ν_t is to be thought of as a scalar diffusion coefficient whose magnitude is determined as described in the following. As proposed in [9], the coefficients σ_ϵ, $c_{\epsilon 1}$, and $c_{\epsilon 2}$ take the values 1.3, 1.45, and 1.90.

3 Expressions for Horizontal Flows

We now limit further attention to predominantly horizontal thin shear flows remote from walls.[3] By convention, the stream-wise direction is x_1 and x_3 is vertically upward. Equations (8) and (13) then yield the following formulas for the relevant stress and heat-flux components:

$$-\overline{u_1 u_3} = \frac{k}{\epsilon}\phi\left\{\overline{u_3^2}\frac{\partial U_1}{\partial x_3} - \frac{\alpha g}{T}\overline{u_1 T'}\right\} \quad (21)$$

$$\frac{\overline{u_3^2}}{k} = \frac{2}{3}\left(1 - \frac{P}{\epsilon}\phi\right) - \frac{2}{3}\frac{P}{\epsilon}\phi\frac{R_f}{1 - R_f} \quad (22)$$

$$-\overline{u_1 T'} = \phi_T \frac{k}{\epsilon}\overline{u_1 u_3}\frac{\partial T}{\partial x_3} + \phi'_T \frac{k}{\epsilon}\overline{u_3 T'}\frac{\partial U_1}{\partial x_3} \quad (23)$$

$$-\overline{u_3 T'} = \phi_T \frac{k}{\epsilon}\overline{u_3^2}\frac{\partial T}{\partial x_3} + \phi'_T c'_T \frac{k^2}{\epsilon^2}\frac{\alpha g}{T}\overline{u_3 T'}\frac{\partial T}{\partial x_3} \quad (24)$$

A verbal definition of the flux Richardson number has been given in the foregoing; in symbolic form it may be written:

$$R_f \equiv \frac{\overline{u_3 T'}\,\dfrac{\alpha g}{T}}{\overline{u_1 u_3}\,\partial U_1/\partial x_3} \quad (25)$$

The flux $\overline{u_3 T'}$ is obtained directly from equation (24) as:

$$-\overline{u_3 T'} \equiv \gamma\frac{\overline{k u_3^2}}{\epsilon}\frac{\partial T}{\partial x_3} \quad (26)$$

with

$$\gamma \equiv \phi_T[1 + \phi'_T c'_T B]^{-1} \quad (27)$$

$$B \equiv \frac{\alpha g}{T}\frac{k^2}{\epsilon^2}\frac{\partial T}{\partial x_3} \quad (28)$$

A parallel expression for $\overline{u_1 u_3}$ is obtained by combining equations (21), (23), and (24):

$$-\overline{u_1 u_3} = \beta\frac{k\overline{u_3^2}}{\epsilon}\frac{\partial U_1}{\partial x_3} \quad (29)$$

where:

$$\beta \equiv \frac{\phi}{1 + \phi(\phi_T + \phi'_T/\sigma_t)B} \quad (30)$$

and σ_t is the turbulent Prandtl number, β/γ, which may be found by dividing equation (30) by (27):

$$\sigma_t = \sigma_{t0}\frac{1 + \phi'_T(c'_T - \phi_T)B}{1 + \phi\phi_T B} \quad (31)$$

σ_{t0} is the limiting value, ϕ/ϕ_T of σ_t as B tends to zero, i.e., in non-stratified flow. An expression for the "turbulent viscosity," ν_t, may now be obtained by combining equations (22) and (30) with the definition implied in equation (29):

$$\nu_t \equiv \beta\frac{k u_3^2}{\epsilon} = \frac{\frac{2}{3}\phi(1 - P/\epsilon\cdot\phi) - \frac{2}{3}P/\epsilon\,\phi^2\dfrac{R_f}{1 - R_f}}{1 + \phi(\phi_T + \phi'_T/\sigma_t)B}\cdot\frac{k^2}{\epsilon} \quad (32)$$

[3] The presence of a nearby wall produces changes in the neighboring fluctuating pressure field that were not accounted for in equations (1) and (2). Further discussion of the effect is provided in reference [6].

Finally, the transport equations (19) and (20), for k and ϵ, reduce to the following parabolic forms:

$$\frac{Dk}{Dt} = \frac{\partial}{\partial x_3}\left(\frac{\nu_t}{\sigma_k}\frac{\partial k}{\partial x_3}\right) + \nu_t\left(\frac{\partial U_1}{\partial x_3}\right)^2(1 - R_f) - \epsilon \tag{33}$$

$$\frac{D\epsilon}{Dt} = \frac{\partial}{\partial x_3}\left(\frac{\nu_t}{\sigma_\epsilon}\cdot\frac{\partial \epsilon}{\partial x_3}\right) + c_{\epsilon 1}\,\nu_t\frac{\epsilon}{k}\left(\frac{\partial U_1}{\partial x_3}\right)^2 - c_{\epsilon 2}\frac{\epsilon^2}{k} \tag{34}$$

These equations together with the auxiliary equations (31) and (32) provide a closed set for determining the shear stress and heat flux in buoyant flows. Equations (33) and (34) are solved simultaneously with the mean-flow momentum and energy equations:

$$\frac{DU_1}{Dt} = \frac{\partial}{\partial x_3}\left(\nu_t\frac{\partial U_1}{\partial x_3}\right) - \frac{1}{\rho}\frac{\partial p}{\partial x_3} \tag{35}$$

$$\frac{DT}{Dt} = \frac{\partial}{\partial x_3}\left(\frac{\nu_t}{\sigma_t}\frac{\partial T}{\partial x_3}\right) \tag{36}$$

This set of four transport equations has been solved by means of the Patankar-Spalding [13] procedure using a CDC 6600 computer. Twenty-two cross-stream nodes were used with a forward step of approximately 2 percent of the shear-layer width; computing times were typically 60 s per run.

To begin computations, what we judged to be plausible initial profiles of velocity, temperature, k and ϵ were prescribed; at the edges of the shear flow a quiescent free stream was assumed. Only for the plane wake did the initial conditions have a significant effect in the region of interest; these are discussed in more detail in the following when the results for this flow are considered.

4 Comparison With Experimental Data

Before considering buoyant flows we examine briefly how well the model performs for neutral conditions. The plane jet in stagnant surroundings and the plane mixing layer (with or without a stationary stream) provide important examples of self preserving free shear flows. Table 1 summarizes the predicted and measured rates of spread for the jet and for two types of mixing layer. It is seen that the predicted behavior accords satisfactorily with the consensus of measured values. The predicted mean temperature and velocity profiles for the plane jet are compared with the experimental data [14] in Fig. 1. A similar measure of agreement was also obtained for the mixing layer.

A feature of the present model is the appearance of the production:dissipation ratio as a parameter in the transport coefficients. On putting the Richardson number to zero and inserting the appropriate numerical values for the coefficients, equations (31) and (32) become:

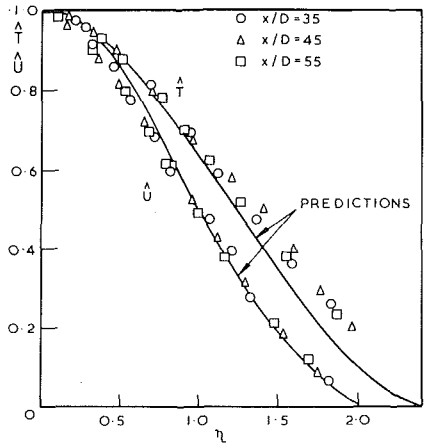

Fig. 1 Mean velocity and temperature profiles in a self-preserving plane jet in stagnant surroundings; data from [14]

$$\nu_{t0} = \frac{0.36 + 0.165\,P/\epsilon}{(1.2 + P/\epsilon)^2}\cdot\frac{k^2}{\epsilon} \tag{37}$$

$$\sigma_{t0} = \frac{0.225\,(5.4 + P/\epsilon)}{(1.2 + P/\epsilon)} \tag{38}$$

This dependence on P/ϵ contrasts with the conventional $k \sim \epsilon$ model reviewed in [9] which takes the transport coefficients as directly proportional to k^2/ϵ. Rodi [10] (see also [8]) seems to have been the first to recognize the importance of P/ϵ in determining the level of effective viscosity in free shear flows. His empirical correlation of $\nu_{t0}\epsilon/k^2$ (normalized by its value at $P/\epsilon = 1$) is shown in Fig. 2. It exhibits the same trends as equation (37) above though it possesses rather greater sensitivity to the level of P/ϵ for values of this parameter less than about 0.7. To our knowledge, the present work provides the first proposals for the dependence of the turbulent Prandtl number on P/ϵ. It is extremely difficult to measure reliable local values of this parameter because of the large amount of data processing involved. Nevertheless, Watt's [15] mixing-layer data do imply a rise in σ_{t0} toward the edges of the layer (as P/ϵ falls to zero) of about the same magnitude as equation (38)

Table 1

Flow	Growth rate	Calculated	Data	Data Sources
Plane jet	$\frac{db_u}{dx}$	0.112	0.096, 0.120, 0.096	Data from sources quoted by Jenkins and Goldschmidt [14]
	$\frac{db_T}{dx}$	0.138	0.137, 0.170, 0.141	
Plane mixing layer velocity ratio 0	$\frac{db_u}{dx}$	0.147	0.130, 0.150, 0.160, 0.20, 0.165	Data from sources quoted by Rodi [10]
velocity ratio 0.51	$\frac{db_u}{dx}$	0.044	0.046	Watt [15]
	$\frac{db_T}{dx}$	0.047	0.051	

Growth rates of velocity and thermal fields of self-preserving, free, shear flows.

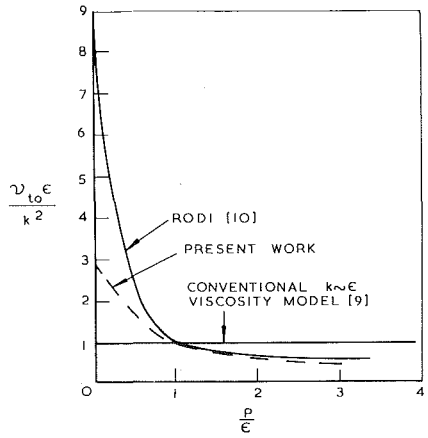

Fig. 2 Dependence of turbulent viscosity coefficient on P/ϵ, equation (37)

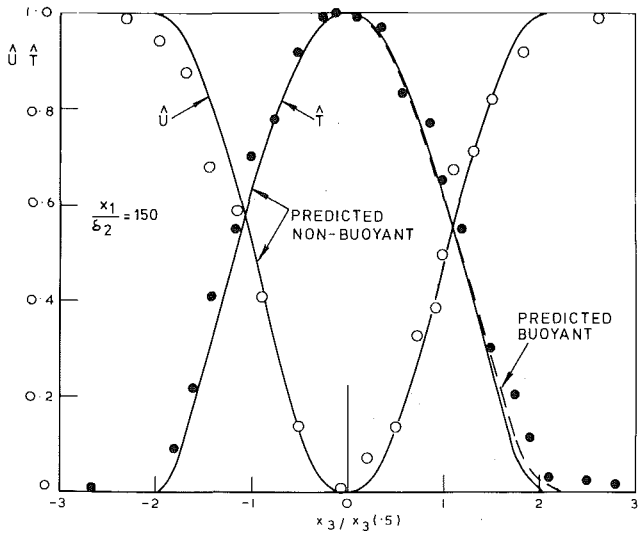

Fig. 4 Mean velocity and temperature profiles in a plane turbulent wake; data from [16]

suggests. It also appears that in conformity with equation (38), the average level of turbulent Prandtl number in a wake is somewhat higher than in a jet (the average level of P/ϵ being about 0.85 in the former and about 1.05 in the latter).

The computed behavior of extensive nonequilibrium free shear flows (jets in a moving stream, large velocity-deficit wakes, etc.) has been reported in the *Proceedings of the Langley Free Shear Flow Conference*. The most successful of the six models reported in [8] for predicting these flows was a version of the $k \sim \epsilon$ viscosity model which used Rodi's [10] correlation for the dependence of the viscosity coefficient on P/ϵ. Because the present model implies a dependence on this parameter very similar to Rodi's over the range of P/ϵ encountered in these flows we may expect that very similar predictions would result from the present closure. As an example of a nonequilibrium flow, predictions are provided in Figs. 3–4 of the development of the wake behind a heated flat plate. The measured behavior is that reported by Kovasznay and Ali [16] though a more extensive investigation of the velocity field (with the plate unheated) is available in Chevray and Kovasznay [17]. Here the initial conditions leave an effect on the flow development throughout the region of interest. The predictions adopted initial profiles for velocity and k from [17] (assuming for the latter that the lateral fluctuations—which were not measured—equalled the mean of the streamwise and transverse components). The value of ϵ was set equal to the local value of $0.3\, k\partial U_1/\partial x_3$ in the absence of more precise information and the normalized mean temperature and velocity profiles were assumed to be coincident.

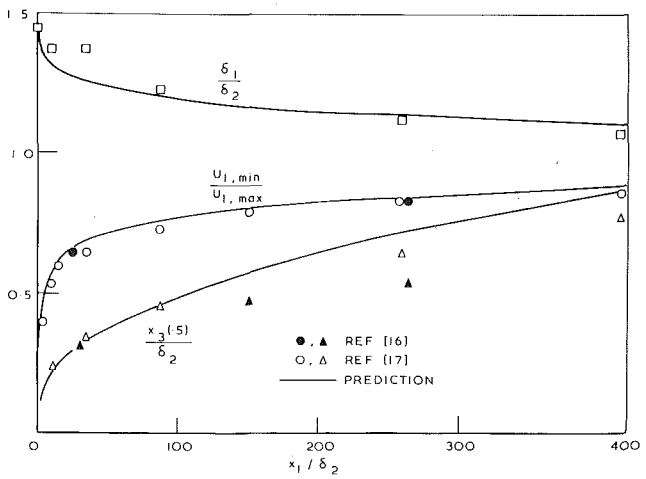

Fig. 3 Development of a plane turbulent wake

Fig. 3 shows the calculated development of the wake compared with the measurements reported in [16, 17]. The width of the heated wake [16] grew less rapidly than that of the isothermal flow and both are overpredicted slightly by the present calculations. The agreement between measured and calculated values of the minimum mean velocity and the shape factor appears to be satisfactory. The asymmetrical profiles of turbulence quantities plotted in [16] suggest that buoyancy effects may not be wholly negligible in this flow. At the station where the bulk of the profile measurements were made, 150 momentum thicknesses from the trailing edge of the heated plate, the average Richardson number defined by:

$$\mathrm{Ri}_1 = \frac{\alpha g \Delta T}{T\, \Delta U_1 \left(\dfrac{\partial U_1}{\partial x_3}\right)_{\max}} \tag{39}$$

had a value of approximately 0.035. The mean velocity profile at this station, shown in Fig. 4, is unaffected by buoyant interactions and the mean temperature profile only very slightly so. The computed profiles show the result of including the gravitational terms in the equations compared with calculations which took the wake centerline as an axis of symmetry and neglected these terms. On the stably stratified side of the flow ($\eta < 0$) the difference is insignificant and it is slight for $\eta > 0$.

By contrast, the measured profiles of turbulent heat flux and shear stress exhibit considerable asymmetry which is quite well predicted by the present model, as is shown in Fig. 5. The results suggest that the turbulence structure is significantly influenced by buoyancy interactions although the mean-flow quantities remain unaffected. The evidence of Fig. 5 is that the model tends to underestimate these effects although the agreement is considered to be surprisingly good.

Turning now to flows in which buoyancy plays a more dominant role, Fig. 6 shows the variation with P/ϵ of the critical flux Richardson number, i.e., the value of R_f at which the transport coefficients collapse to zero. $R_{f\mathrm{crit}}$ is approximately 0.3 when P/ϵ is unity and rises to unity as P/ϵ tends to zero, though it is probably unwise to place much reliance on these values for values of P/ϵ below about 0.5. If $R_{f\mathrm{crit}}$ is multiplied by P/ϵ the resultant parameter (denoted in Fig. 6 as R^*_{crit}) is rather less sensitive to variations in turbulence generation rates. Thus, one can more usefully speak of α

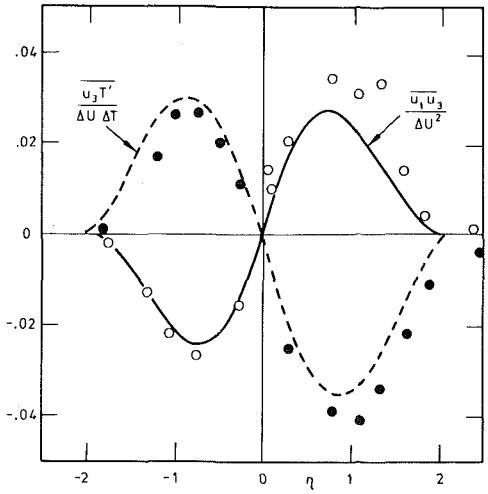

Fig. 5 Profiles of turbulent shear stress and heat flux in a plane heated wake: $x_1/\delta_2 = 150$; $Ri_1 = 0.035$ (data from [16])

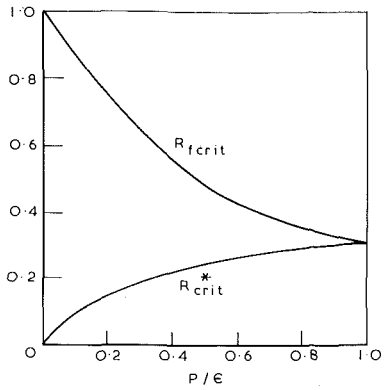

Fig. 6 Dependence of critical Richardson number on P/ϵ $R^*_{crit} = R_{fcrit}$ P/ϵ

critical value of R* rather than R_f. The behavior shown in Fig. 6 is consistent with Webster's [18] measurements in a horizontal shear flow where the velocity and temperature increases linearly with height. In that flow P/ϵ appeared to be about 0.7 and the reported value of R_{fcrit} was 0.35. We shall see later that the results are also consistent with Ellison and Turner's [19] measurements of entrainment rates in surface jets. A number of other workers have reported measured values of R_{fcrit} between 0.07 and 0.2. In almost every case, however, these results relate to experiments in wall-affected turbulence. As we have noted in the foregoing, the presence of a horizontal wall tends to diminish vertical fluctuations and hence the critical Richardson number in such flows is smaller than in a truly free shear flow.

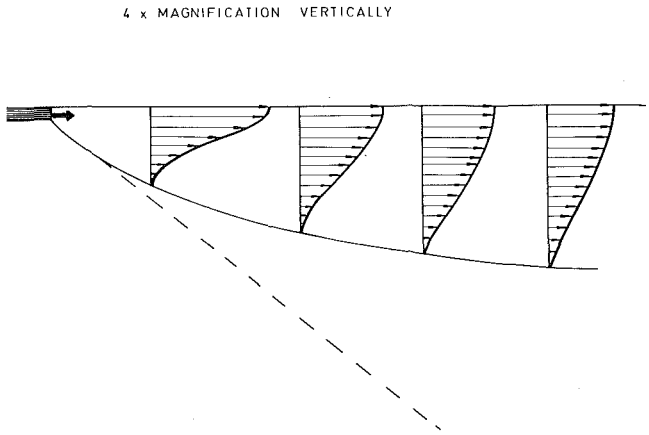

Fig. 7 Calculated development of mean velocity profiles in a plane surface jet

Figs. 7 and 8 show the development of the mean velocity profiles in a plane two-dimensional surface jet and in a buoyant plane mixing layer. In each case the initial behavior is the same as in a nonbuoyant jet with a linear rate of increase in shear layer width with distance. There is however significant departure from this nonbuoyant growth pattern by the time the average Richardson number at any section, Ri_1, has built up to about 0.1. With further progress downstream the shear flows then approach what seems to be an asymptotic thickness with the turbulence gradually dying away. Well-documented measurements of mean velocity profiles of either flow do not seem to be available for comparison with predictions.

Fig. 9 shows the effect of buoyancy on the rate of entrainment of nonturbulent fluid into the plane surface jet. The comparison is made with Ellison and Turner's data [19] which have been used as empirical input to several integral-profile calculations of buoyant flow [20]. The functions plotted are those devised by Ellison and Turner. Ri_2 is an overall Richardson number based on a characteristic layer width and velocity obtained by cross-stream integration of the mean velocity and temperature profiles. The function $E(Ri)_2$ represents the entrainment rate divided by the characteristic velocity.

Predicted entrainment rates in neutral flow, E_0, are 0.078 and 0.11 for the surface jet and for the mixing layer with velocity ratio of 2.1:1, respectively; the former agrees well with the measured

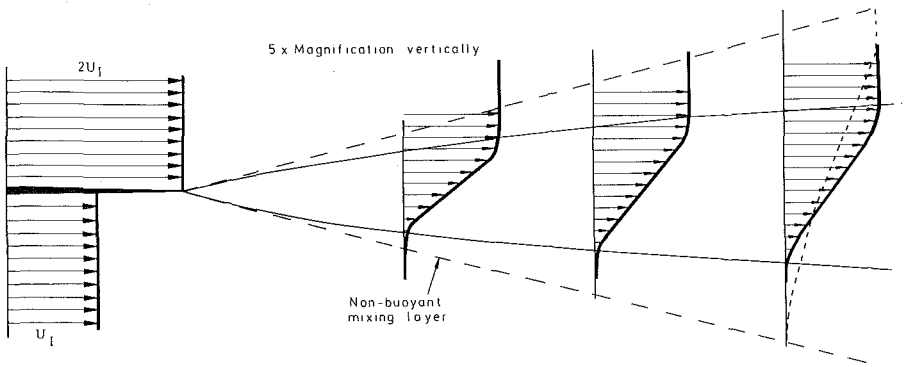

Fig. 8 Calculated development of mean velocity profiles in a plane mixing layer

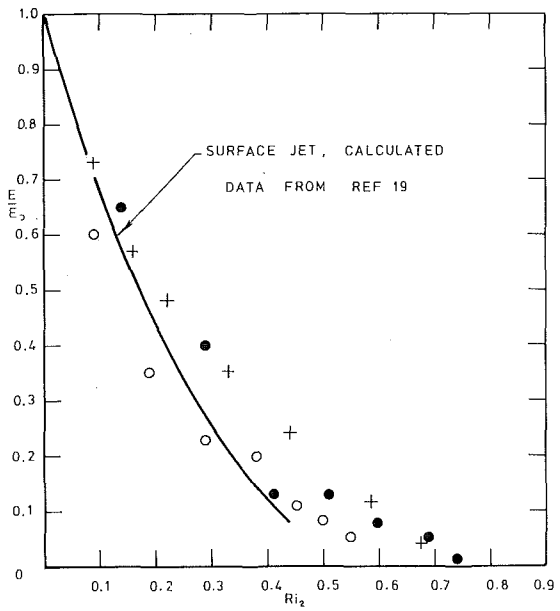

Fig. 9 Entrainment in plane surface jet

value of 0.075 quoted by Ellison and Turner. Predictions of E/E_0 versus Ri_2, plotted in Fig. 9, are in excellent agreement with the Ellison and Turner experiments considering the scatter in the data. There appears to be no meaningful counterpart of Ri_2 for the plane mixing layer. If, however, Ri_1 had been used instead, the predicted entrainment decay for the mixing layer would have displayed nearly the same form as for the surface jet. This perhaps helps to explain why workers who have used the Ellison-Turner data as an empirical input to momentum-integral procedures have achieved tolerable success at predicting flows other than those from which the correlation was obtained.

5 Concluding Remarks

The present proposals extend the range of applicability of the k-ϵ effective-viscosity model [9] by taking into account the dependence of the turbulent transport coefficients on the P/ϵ ratio. Although special attention has been given to buoyancy-affected turbulence the empirical coefficients appearing in the model have been deduced from nonbuoyant flow data.

Predictions for horizontal, thin, buoyant, shear flows exhibit qualitatively the correct behavior of turbulence collapse at a critical Richardson number although few definitive experimental data are available with which to make a searching comparison. However, the closeness with which the model predicts the "entrainment law" of Ellison and Turner [19], and the asymmetry of heat and momentum fluxes in the slightly-buoyant wake [16], is highly encouraging. The predicted dependence of the turbulent Prandtl number of P/ϵ also seems to be reasonably in accordance with what the available experimental data suggest.

It should perhaps be re-emphasized that the current proposals relate only to free shear flows. They should be reasonably successful in predicting buoyant influences for flows such as a jet discharged into a lake but they will almost certainly underestimate buoyant effect in the atmospheric boundary layer or in strongly heated flow in ducts.

Acknowledgement

We are grateful to Dr. W. Rodi for drawing our attention to an error in an earlier version of Fig. 9.

References

1 Townsend, A. A., "Turbulent Flow in a Stably Stratified Atmosphere," *J. Fluid Mech.*, Vol. 3, 1957.

2 Ellison, T. H., "Turbulent Transport of Heat and Momentum From an Infinite Rough Plane," *J. Fluid Mech.*, Vol. 2, 1957.

3 Lumley, J. L., "A Model for Computation of Stratified Turbulent Flows," International Symposium on Stratified Flow, Novisibirsk, 1972.

4 Donaldson, C. du P., Sullivan, R. D., and Rosenbaum, H., "A Theoretical Study of the Generation of Atmospheric Clear Air Turbulence," *AIAA Journal*, Vol. 10, 1972.

5 Bradshaw, P., "The Strategy of Calculation Methods for Complex Flows," Imperial College Aero Report 73-05, 1973.

6 Launder, B. E., Reece, G. J., and Rodi, W. R., "Progress in the Development of a Reynolds Stress Turbulence Closure," *J. Fluid Mech.*, Vol. 68, 1975.

7 Launder, B. E., "On the Effects of a gravitational Field on the Turbulent Transport of Heat and Momentum," *J. Fluid Mech.*, Vol. 67, 1975.

8 Launder, B. E., Morse, A., Spalding, D. B., and Rodi, W. R., "The Prediction of Free Shear Flows—a Comparison of the Performance of Six Turbulence Models," *Proceedings NASA Conference on Free Turbulent Shear Flows*, Vol. 1 NASA—SP321, 1973.

9 Launder, B. E., and Spalding, D. B., "The Numerical Calculation of Turbulent Flow," *Comp. Methods in Appl. Math and Eng.*, Vol. 3, 1974, p. 269.

10 Rodi, W. "The Prediction of Free Turbulent Boundary Layers by Use of a 2-Equation Model of Turbulence," PhD thesis, University of London, 1972.

11 Launder, B. E., "An Improved Algebraic Modeling of the Reynolds Stresses," Imperial College, Mechanical Engineering Department Rep TM/TN/A/9, 1971.

12 Mellor, G. L., and Yamada, T., "A Hierarchy of Turbulence Closure Models for Planetary Boundary Layers," *J. Atmos. Sci.*, Vol. 31, 1974, p. 10.

13 Patankar, S. V., and Spalding, D. B., "Heat and Mass Transfer in Boundary Layers," *Intertext Books*, Second ed., 1970.

14 Jenkins, P. E., and Goldschmidt, V. W., "Mean Temperature and Velocity in a Plane Turbulent Jet," *Journal of Fluids Engineering*, TRANS ASME, Dec. 1973.

15 Watt, W. E., "The Velocity-Temperature Mixing Layer," University of Toronto, Department of Mechanical Engineering, Report TP6705, 1967.

16 Kovasznay, L. S. G., and Ali, S. F., "Structure of the Turbulence in the Wake of a Heated Flat Plate," *Proceedings 5th International Heat Transfer Conference*, Vol. IV, Tokyo, 1975.

17 Chevray, R., and Kovasznay, L. S. G., "Turbulence Measurements in the Wake of a Thin Flate Plate," *AIAA Journal*, Vol. 7, 1969, p. 8.

18 Webster, C. A. G., "An Experimental Study of Turbulence in a Density Stratified Shear Flow," *J. Fluid Mech.*, Vol. 19, 1964.

19 Ellison, T. H., and Turner, J. S., "Turbulent Entrainment in Stratified Flows," *J. Fluid Mech.*, Vol. 6, 1959.

20 Stolzenbach, K. D., and Harlemann, D. R. F., "An Analytical and Experimental Investigation of Surface Discharges of Heated Water," Environmental Protection Agency, Water Pollution Control Research Series 16130 DJU 02/71, 1971.

E. M. Sparrow
L. Lee[1]
N. Shamsundar

Department of Mechanical Engineering
University of Minnesota,
Minneapolis, Minn.

Convective Instability in a Melt Layer Heated From Below

Consideration is given to the onset of convective motions in a horizontal melt layer created by solid-to-liquid phase change. The melt layer is heated at its lower bounding surface either due to convective transfer from an adjacent fluid medium or to a step change in wall temperature. The analysis is carried out for liquid melts whose densities decrease with increasing temperature. Linear stability theory is employed to determine the conditions marking the onset of motion. The results of the analysis are expressed in terms of two Rayleigh numbers. One of these, the internal Rayleigh number, is based on the instantaneous thickness and instantaneous temperature difference across the layer. The other, the external Rayleigh number, is more convenient to use in applications problems since it contains quantities which are constant and a priori prescribable. For a melting problem where the external Rayleigh number is large, instability occurs soon after the start of heating. At smaller external Rayleigh numbers, the duration time of the regime of no motion increases markedly. At large times, the stability results for convective heating coincide with those for stepped wall temperature. In addition to the results for the stability problem, results for conduction phase change (in the absence of motion) are also presented for the surface convection boundary condition.

Introduction

This paper is concerned with the conditions marking the onset of convective motions in a horizontal, liquid melt layer. The melt layer is created when a solid, initially at its saturation temperature, is heated from below. As the heating continues, more and more solid is transformed into liquid, so that the thickness of the melt layer increases with time. Owing to the fact that the hottest, least-dense liquid is situated adjacent to the heating surface and the coolest, most-dense liquid is next to the solid-liquid interface, the state of rest which initially prevails in the melt layer is prone to instability. The determination of the conditions marking the onset of instability is a problem of linear stability theory.

Evidently, the variation of density with height plays a key role in the instability phenomenon. In turn, the density variation is closely related to the temperature distribution. In melt layers, the rest-state temperature distribution is not a straight line as in conventional liquid or gas layers that are heated from below. Rather, the temperature distribution is nonlinear, and it changes with time as the thickness of the melt layer increases. Furthermore, the temperature distribution is influenced by the manner in which heat is added at the lower bounding surface and by the relative importance of the heat sinks associated with phase change (latent heat) and liquid-phase energy storage.

The determination of the instability characteristics was carried out for two types of heat addition. In one case, the temperature of the lower bounding wall is increased in a stepwise manner and maintained constant thereafter. The conduction phase change problem for this heating condition is the well-known Stefan problem, a description of which is available in various text books. The Stefan problem yields a closed-form solution for the temperature distribution in terms of the error function.

For the other case, the heating is initiated when the lower bounding wall is exposed to a fluid whose temperature and heat transfer coefficient are spatially and temporally uniform. The corresponding conduction phase change problem does not yield an exact solution, and a variety of approximate solution methods have been employed in the literature. These include, for example, polynomial approximations for the temperature distribution, with the

[1] On leave from the University of Maine, Orono, Me.

Contributed by the Heat Transfer Division for publication in the JOURNAL OF HEAT TRANSFER. Manuscript received by the Heat Transfer Division August 15, 1975. Paper No. 76-HT-BB.

coefficients of the polynomial determined either by an overall energy balance [1][2] or by collocation [2]. Solutions of this type do not provide input information of sufficient accuracy for the stability problem, especially in that temperature gradients are needed rather than the temperature distribution itself. Finite-difference solutions, limited to relatively thin melt layers, have been carried out [3] and, for these, only the time history of the position of the solid-liquid interface is reported. In order to approach the stability problem, it is necessary to obtain the heightwise distribution of the temperature gradient for the relevant range of the governing parameters. This has been accomplished here via a fully implicit difference scheme.[3]

The stability problem is formulated using an approach similar to that for the classical Bénard problem and its variants. Small disturbances are superposed on the rest-state temperature and velocity fields, and the conditions are determined under which these disturbances do not decay and, thereby, terminate the existence of the rest state. The dimensionless group which serves to characterize the onset of instability is the Rayleigh number. The critical value of the Rayleigh number (i.e., the value at instability) depends upon the parameters of the problem. These include the Stefan number (ratio of heat capacity to latent heat) and, for the case of convective heating, the Biot number.

The present problem differs from other convective instability problems in that there are two distinctly different Rayleigh numbers that can be used to characterize the results. These may, respectively, be termed the internal Rayleigh number and the external Rayleigh number. The internal Rayleigh number contains the thickness of the melt layer and the temperature difference between the lower bounding wall and the solid-liquid interface; that is, it contain quantities which directly characterize the geometric and thermal state of the layer. This Rayleigh number is useful as a means for comparing the present results with those for other convective instability problems.

From the standpoint of application, the internal Rayleigh number is inconvenient to use in that the melt layer thickness is not an a priori prescribable quantity and is, in fact, a function of time. Furthermore, in the case of convective heating, the temperature of the lower bounding wall is also time dependent and not prescribable. In view of these considerations, it is appropriate to define and evaluate another Rayleigh number, the external Rayleigh number, which contains quantities that are a priori prescribable. The specific makeup of the external Rayleigh number will be discussed later.

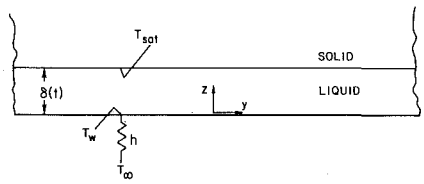

Fig. 1 Schematic diagram of the physical problem

It may be noted that the Biot number, which enters the analysis in the case of convective heating, contains the melt layer thickness as its length dimension. Therefore, as is the case with the internal Rayleigh number, the Biot number is not a convenient parameter for use in applications.

Analysis

The physical situation to be analyzed here is depicted schematically in Fig. 1. A solid of sufficient lateral extent to preclude edge effects is initially at its saturation temperature T_{sat}. At time $t = 0$, heating is initiated at the lower bounding surface ($z = 0$), either as a step increase in the wall temperature to a value T_w or as a convective heat transfer from an adjacent fluid with temperature T_∞ and transfer coefficient h. Subsequent to $t = 0$, T_w is constant and spatially uniform in the former case, whereas in the latter, T_∞ and h are constant and spatially uniform but the wall temperature varies with time. As a result of the heating, a melt layer is formed as solid is transformed into liquid.

If density changes associated with the solid-liquid phase change are neglected, as is standard practice in conduction phase change analyses, there are no fluid motions within the melt layer until the onset of natural convection. In particular, although the solid-liquid interface moves as more and more solid is transformed into liquid, the adjacent liquid is stationary. In the rest state, heat is transferred across the melt layer to the interface by conduction alone. The rest-state temperature distribution T_{rs} is a function of z and t, and the layer thickness δ varies with time.

To investigate the conditions under which the rest state is unstable, small disturbances are superposed on the rest-state temperature, velocity, and pressure fields. In general, the disturbances will depend on all three coordinates and time, so that the resultant quantities (rest state plus disturbance) will have a similar dependence. Therefore,

$$T(x, y, z, t) = T_{rs}(z, t) + T^*(x, y, z, t),$$

[2] Numbers in brackets designate References at end of paper.

[3] This is in contrast to [3], where a Crank-Nicolson scheme was employed. In addition, the interface energy balance was differently implemented.

Nomenclature

a = wave number of disturbance
Bi = Biot number, $h\delta/k$
c = specific heat
Fo = Fourier number, $\alpha t/(k/h)^2$ for convection, $\alpha t/L^2$ for stepped T_w
F, G = disturbance amplitudes, equation (7)
g = acceleration of gravity
h = heat transfer coefficient
$h_{s\ell}$ = latent heat for solid-liquid phase change
k = thermal conductivity
L = arbitrary length
p = static pressure
Ra_e = external Rayleigh number, $g\beta(T_\infty - T_{sat})(k/h)^3/\alpha\nu$ for convection, $g\beta(T_w - T_{sat})L^3/\alpha\nu$ for stepped T_w
Ra_i = internal Rayleigh number, $g\beta(T_w - T_{sat})\delta^3/\alpha\nu$
Ste_w = Stefan number, $c(T_w - T_{sat})/h_{s\ell}$
Ste_∞ = Stefan number, $c(T_\infty - T_{sat})/h_{s\ell}$
T = temperature
T_{sat} = saturation temperature
T_w = temperature of lower wall
T_∞ = temperature of heating medium
t = time
u, v, w = velocity components
X, Y, Z = dimensionless coordinates, x/δ, y/δ, z/δ
x, y = coordinates in horizontal plane
z = vertical coordinate
α = thermal diffusivity
β = thermal expansion coefficient
δ = thickness of melt layer
ζ = dimensionless coordinate, hz/k
θ = dimensionless temperature, $(T - T_{sat})/(T_\infty - T_{sat})$
μ = viscosity
ν = kinematic viscosity
ρ = density
Ω = function of Ste_w, equation (17)

Subscript

rs = rest state

Superscript

* = disturbance quantity

$$p(x, y, z, t) = p_{rs}(z, t) + p^*(x, y, z, t), \quad u = u^*(x, y, z, t),$$
$$v = v^*(x, y, z, t), \quad w = w^*(x, y, z, t) \quad (1)$$

The Disturbance Equations. As a starting point for the analysis, the Navier-Stokes equations are written for all three coordinate directions. Constant fluid properties are assumed, except for the density which appears in the body force. For the z- (i.e., vertical) direction, with quadratic disturbance terms neglected

$$\rho(\partial w^*/\partial t) = -(\partial p/\partial z) - \rho g + \mu\nabla^2 w^* \quad (2)$$

If p is replaced by $(p_{rs} + p^*)$ from equation (1) and note is taken of the fact that $(\partial p_{rs}/\partial z) = -\rho_{rs}g$, then with the Boussinesq equation of state

$$-\partial p/\partial z - \rho g + \partial p^*/\partial z = g(\rho_{rs} - \rho) = g\beta\rho\,(T - T_{rs}) = g\beta\rho T^* \quad (3)$$

which may be substituted back into equation (2). Next, after the x- and y- momentum equations are, respectively, differentiated with respect to $\partial/\partial x$ and $\partial/\partial y$, they are added and the resulting equation is combined with the z-momentum equation, which gives

$$(\partial/\partial t - \nu\nabla^2)\nabla^2 w^* = g\beta\nabla_{xy}{}^2 T^* \quad (4)$$

where $\nabla_{xy}{}^2 = (\partial^2/\partial x^2 + \partial^2/\partial y^2)$.

The energy equation is then written, and it is noted that the rest-state temperature distribution obeys $\partial T_{rs}/\partial t = \alpha(\partial^2 T_{rs}/\partial z^2)$ and that quantities such as $u^*(\partial T^*/\partial x)$, etc., are quadratically small. Therefore,

$$(\partial/\partial t - \alpha\nabla^2)T^* = -w^*(\partial T_{rs}/\partial z) \quad (5)$$

The elimination of T^* from equations (4) and (5) gives rise to

$$(\partial/\partial t - \alpha\nabla^2)(\partial/\partial t - \nu\nabla^2)\nabla^2 w^* = -g\beta(\partial T_{rs}/\partial z)\nabla_{xy}{}^2 w^* \quad (6)$$

which contains the disturbance velocity w^* as the only unknown. The rest-state temperature gradient $\partial T_{rs}/\partial z$, which appears in equation (6), is not independent of z as is the case in the classical Bénard problem.

In accordance with linear stability theory, the w^* and T^* disturbances are written as [4]

$$w^* = F(z)G(x, y)e^{\sigma t}, \; T^* = H(z)G(x, y)e^{\sigma t} \quad (7)$$

In order that these functional forms be compatible with the energy equation (5), it is necessary that

$$\nabla_{xy}{}^2 G/G = \text{constant} \quad (8)$$

where the constant has to be negative to yield a disturbance field that is periodic in the x, y plane.

Next, dimensionless coordinates are introduced such that X, Y, Z are defined as x/δ, y/δ, and z/δ and the dimensionless constant appearing on the right-hand side of equation (8) is denoted by $-a^2$. Then, w^* from (7) is introduced into the disturbance equation (6), and (8) is employed to simplify the manipulations. Furthermore, since the threshold of instability is being sought, σ is set equal to zero [4]. The end result of these operations is

$$F^{\mathrm{VI}} - 3a^2F^{\mathrm{IV}} + 3a^4F'' - a^6F - a^2\mathrm{Ra}_i\{T_{rs}'/(T_w - T_{\mathrm{sat}})\}F = 0 \quad (9)$$

where the primes denote derivatives with respect to Z, and Ra_i is the internal Rayleigh number defined as

$$\mathrm{Ra}_i = g\beta(T_w - T_{\mathrm{sat}})\delta^3/\alpha\nu \quad (10)$$

The thickness δ of the melt layer, which appears in Ra_i, can be found by solving the conduction phase change problem, but it is not an a priori prescribable quantity. The same is true for $(T_w - T_{\mathrm{sat}})$ in the case of the convective boundary condition.

The rest-state input grouping $\{T_{rs}'/(T_w - T_{\mathrm{sat}})\}$ depends on Z. As will be demonstrated shortly, it does not depend explicitly on time for the case of the step-change wall temperature boundary condition (Stefan problem). On the other hand, it is time dependent for the convective boundary condition and, in this case, equation (9) is solved repeatedly at a succession of times.

The boundary conditions will now be discussed. Both the lower bounding wall and the solid-liquid interface do not admit velocity slip, so that $u^* = v^* = 0$ or $\partial u^*/\partial X = \partial v^*/\partial Y = 0$. From the equation of continuity, it then follows that $\partial w^*/\partial Z = 0$. The lower wall is impermeable, so that $w^* = 0$. Furthermore, $w^* = 0$ at the solid-liquid interface when density differences due to phase change are neglected. This is because the moving interface is only a demarcation between phases and is not attached to material particles. In terms of the variables of the analysis, the velocity boundary conditions are

$$F = F' = 0 \text{ at } Z = 0 \text{ and } Z = 1 \quad (11)$$

With respect to the temperature boundary conditions, it may be noted that $T = T_{rs} = T_{\mathrm{sat}}$ at the solid-liquid interface, so that $T^* = 0$. When the lower bounding surface is held at a constant temperature T_w, then $T = T_{rs} = T_w$ and, again, $T^* = 0$. For the case of convection at the lower bounding surface

$$-k(\partial T/\partial z) = h(T_\infty - T_w), \quad -k(\partial T_{rs}/\partial z) = h(T_\infty - T_{w,rs}) \quad (12)$$

Upon substitution of $T = (T_{rs} + T^*)$, there is obtained

$$k(\partial T^*/\partial z) = hT^* \quad (13)$$

The transformation of the boundary conditions on T^* to equivalent boundary conditions on w^* is accomplished by employing equation (4) (with $\partial/\partial t$ deleted since only the $\sigma = 0$ case is being considered). For fixed surface temperature, the outcome of the transformation is

$$F^{\mathrm{IV}} - 2a^2F'' + a^4F = 0 \quad (14)$$

whereas for convection at the lower bounding surface

$$F^{\mathrm{V}} - 2a^2F''' + a^4F' = (h\delta/k)(F^{\mathrm{IV}} - 2a^2F'' + a^4F) \quad (15)$$

The quantity $h\delta/k$ is a Biot number. It contains the layer thickness δ which is a function of time. For the stability calculations, the Biot number will be treated as a prescribable parameter. Later, in the presentation of results, the δ versus t relationship will be employed to recast the results in terms of quantities that are truly prescribable.

Solutions for the Rest-State Problem. As was demonstrated in the prior section, information on the distribution of $\partial T_{rs}/\partial Z$ is a necessary prerequisite for the solution of the stability problem. This information can be obtained from the solutions of the relevant conduction phase change problems. For the case of a step jump in the temperature of the lower bounding surface (the Stefan problem), the solution is available in various texts and may be stated as

$$T_{rs} - T_{\mathrm{sat}} = (T_w - T_{\mathrm{sat}})\{1 - (\mathrm{erf}\Omega Z)/\mathrm{erf}\Omega\} \quad (16)$$

where Ω is a constant whose magnitude, which depends on the Stefan number, is obtained from the following transcendental equation

$$\Omega(\mathrm{erf}\Omega)e^{\Omega^2} = \mathrm{Ste}_w/\sqrt{\pi} \quad (17)$$

with the Stefan number defined as

$$\mathrm{Ste}_w = c(T_w - T_{\mathrm{sat}})/h_{s\ell} \quad (18)$$

The solution also gives the thickness versus time relatjon

$$\delta = 2\Omega\sqrt{\alpha t} \quad (19)$$

The input information needed for the stability problem is readily derived from equation (16) as

$$T_{rs}'/(T_w - T_{\mathrm{sat}}) = -(2\Omega/\sqrt{\pi}\mathrm{erf}\Omega)e^{-\Omega^2 Z^2} \quad (20)$$

The right-hand side of equation (20) is independent of time. It depends parametrically on the Stefan number. For sufficiently small values of the Stefan number, it is easily shown from equation (17) that $\Omega^2 \sim \mathrm{Ste}_w$. Therefore, according to (20), T_{rs}' is nearly inde-

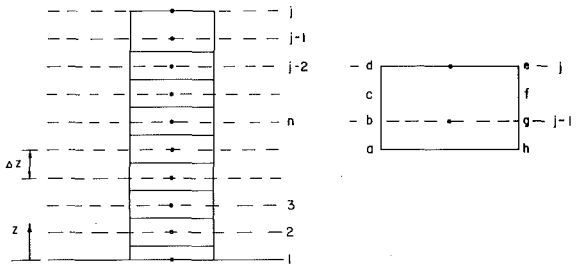

Fig. 2 Grid layout for the finite difference solution of the conduction phase change problem for the case of convective heating

pendent of Z for small Ste_w, so that the rest-state temperature distribution is very nearly a straight line.

For the case of convective heating at the lower bounding surface, an exact closed form solution of the conduction phase change problem cannot be obtained. The need to obtain highly accurate values of the temperature gradient $\partial T_{rs}/\partial Z$ precludes the use of approximate analytical solutions. On the other hand, a numerical method, when properly employed, can yield results possessing the desired accuracy.

In considering various finite-difference formulations, cognizance must be taken of the fact that the size of the melt layer is continuously changing. One way of coping with this is to superpose a finite difference grid (i.e., lines of z = constant) on the melt layer and on the adjacent solid and then to require that the moving interface coincide with a grid line at the end of each time interval. This can be accomplished by regarding each successive time interval as an unknown, with its value being found to bring about the desired coincidence. An implicit finite-difference formulation can be used effectively to implement this procedure.

The grid layout is depicted in the left-hand diagram of Fig. 2. The horizontal lines denoted by 1, 2, . . . , j represent the successive positions of the interface at times $t_1(=0)$, t_2, . . . , t_j. These lines also represent the finite-difference grid and are spaced a distance Δz apart. At any node n, excluding 1, $(j-1)$, and j, the standard implicit formulation gives

$$k(T_{n-1}{}^j - T_n{}^j)/\Delta z + k(T_{n+1}{}^j - T_n{}^j)/\Delta z = \rho c \Delta z (T_n{}^j - T_n{}^{j-1})/\Delta t_j \quad (21)$$

where the superscripts denote the time and $\Delta t_j = (t_j - t_{j-1})$. For node 1, one has

$$h(T_\infty - T_1{}^j) + k(T_2{}^j - T_1{}^j)/\Delta z = \rho c(\Delta z/2)(T_1{}^j - T_1{}^{j-1})/\Delta t_j \quad (22)$$

The more interesting difference equations are those at nodes $(j-1)$ and j. Consider the enlarged control volume shown at the right of Fig. 2. Heat that is conducted across the boundary ah during the time interval Δt_j increases the temperature of the mass within $abcfgh$ from $T_{j-1}{}^{-1}$ to $T_{j-1}{}^j$ and changes the phase of the mass within $bcdefg$. Therefore,

$$k(T_{j-2}{}^j - T_{j-1}{}^j)/\Delta z = h_{s\ell}\rho \Delta z/\Delta t_j + \rho c \Delta z (T_{j-1}{}^j - T_{j-1}{}^{j-1})/\Delta t_j \quad (23)$$

At node j, the boundary condition

$$h_{s\ell}\rho(\partial\delta/\partial t) = -k(\partial T/\partial z) \quad (24)$$

is discretized as

$$h_{s\ell}\rho \Delta z/\Delta t_j = -k(T_{\mathrm{sat}} - T_{j-1}{}^j)/\Delta z \quad (25)$$

If the temperatures at time t_{j-1} are regarded as known, the foregoing difference equations contain $(j-1)$ unknown temperatures corresponding to time t_j. In addition, the time interval Δt_j is unknown. To solve for the unknowns, a trial value of Δt_j is selected, and the $(j-1)$ linear algebraic equations for nodes 1 through $(j-1)$ are solved for the temperatures. Then, a new value of Δt_j is obtained from equation (25). This procedure is continued until convergence is attained. For the present calculations, convergence was defined by a fractional change of 10^{-7} in Δt_j between successive iterations.

To minimize the number of parameters in the numerical calculations, dimensionless variables were employed as follows

$$\zeta = hz/k, \qquad \theta = (T - T_{\mathrm{sat}})/(T_\infty - T_{\mathrm{sat}}) \quad (26)$$

With these, only the Stefan number, Ste_∞, remains as a parameter where

$$\mathrm{Ste}_\infty = c(T_\infty - T_{\mathrm{sat}})/h_{s\ell} \quad (27)$$

In addition, it was found that the computations were facilitated when the latent heat term was eliminated from equation (23) with the aid of equation (25).

Once the temperature distributions were obtained, the desired z derivatives, in the form $\partial\theta/\partial\zeta$, were evaluated by the use of cubic splines [5]. These derivatives were converted into input values for the stability problem by the transformation

$$T_{rs}'/(T_w - T_{\mathrm{sat}}) = (\partial\theta/\partial\zeta)(h\delta/k)/\theta(0) \quad (28)$$

in which $\theta(0)$ represents $(T_w - T_{\mathrm{sat}})/(T_\infty - T_{\mathrm{sat}})$.

Solution of the Stability Problem. Now that the input information required by the stability problem has been established, attention may be turned to its solution. It may be noted that the governing equation (9) for the disturbance amplitude is homogeneous. In addition, all of the boundary conditions (11), (14), and (15) are also homogeneous. Therefore, the solution of the system consisting of equations (9), (11), (14), and (for surface convection) (15) involves an eigenvalue problem. The eigenvalue problems for the cases of stepped wall temperature and of convective heating are slightly different, and they will be discussed successively.

For the step change in wall temperature, it is readily verified by examination of equations (9), (11), (14), and (20) that there are three parameters Ra_i, $\underline{a}$, and Ste_w. The approach adopted here is to select a value of Ste_w and seek the conditions marking the onset of instability by solving the eigenvalue problem involving Ra_i and $\underline{a}$. To deal with the eigenvalue problem, a value of $\underline{a}$ is chosen and the corresponding value of Ra_i is determined as an eigenvalue of the system of equations. The method used to find the eigenvalue is conceptually identical to that of [6], but with certain differences in numerical procedure. Then, a second $\underline{a}$ value is chosen and the corresponding eigenvalue Ra_i is determined.

Additional $\underline{a}$ values are assigned and each yields an Ra_i. If a listing or a graph of Ra_i versus $\underline{a}$ is examined, it is seen that there is a minimum value of Ra_i. This Ra_i is the critical value of the Rayleigh number marking the onset of convection at the given Stefan number. Then, a new Stefan number is assigned and the procedure repeated.

In the case of surface convection, the eigenvalue problem involves equations (9), (11), (14), (15), and (28). These equations contain Bi $(= h\delta/k)$ as an additional parameter besides those that were encountered in the equations for the step change in wall temperature. For the solution of the eigenvalue problem, Ste_∞ and Bi were assigned, and the critical Rayleigh number was determined from the minimum of the Ra_i versus $\underline{a}$ relation. For each Ste_∞, Bi was varied parametrically. Owing to the presence of the Bi parameter, the stability computations for the convective heating case were much more extensive than those for the case of stepped wall temperature.

Results and Discussion

Stability Results: Ra_i. The values of Ra_i marking the onset of instability are presented in Fig. 3 as a function of the Biot number. The curves are parameterized by the Stefan number Ste_∞ over the range from 0.001 to 10, which encompasses present and foreseeable

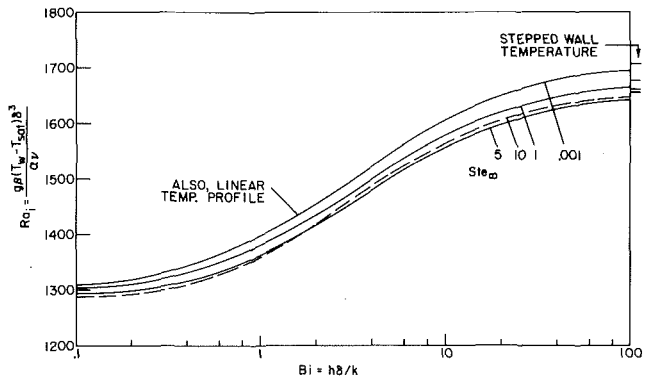

Fig. 3 Results for the internal Rayleigh number marking the onset of instability

applications. The Stefan number of 0.001 represents the situation where the heat capacity of the melt layer, as measured by $c(T_\infty - T_{sat})$, is negligible compared with the latent heat $h_{s\ell}$. Increasing values of the Stefan number correspond to relatively larger heat capacities.

Inspection of the figure indicates that the critical Rayleigh number is significantly affected by the Biot number, but that the Stefan number effect is small. For any given Stefan number, the critical Rayleigh number increases monotonically with the Biot number. The variation is most rapid in the midrange of Biot numbers but is slight at the extremes. The tendency toward increased stability with increasing Biot number is plausible because larger h values provide a tighter tie-in between T_w and T_∞, and the constancy of the latter tends to constrain the disturbance amplitude of the former.

The right margin of the figure contains line segments which represent the results for the stepped wall temperature. These segments are parameterized by Ste_w values of 0.001, 1, 10, and 5, respectively, from top to bottom. It appears that the segments play the role of asymptotes for the results of the convective heating case. In this connection, it may be noted that T_w approaches T_∞ at large Biot numbers (as will be demonstrated later), so that Ste_w and Ste_∞ approach each other.

The $Ste_\infty = 0.001$ curve of Fig. 3 coincides with that for a layer of single phase fluid with convective heating from below and a constant temperature at its upper bounding surface. Similarly, the uppermost line segment in the right margin is coincident with the critical Rayleigh number for the classical Bénard problem. The rest-state temperature profiles in these single phase problems is a straight line.

Another interesting feature of the results of Fig. 3 is the crossing of the curves for $Ste_\infty = 5$ and 10. To facilitate the clear identification of these curves, the latter has been plotted as a dashed line. The crossing of the curves indicates a nonmonotonic variation of the critical Rayleigh number with the Stefan number. This behavior is examined in greater detail in Fig. 4.

In this figure, the critical Rayleigh number is plotted as a function of Ste_w or Ste_∞, respectively, for the cases of stepped wall temperature and of convective heating with Bi = 1. In both cases, the critical Rayleigh number at first decreases, reaches a minimum, and then increases. The value of the Stefan number at which the minimum occurs depends on the boundary conditions and on the value of Bi. This dependence is also reflected in Fig. 3 by the fact that the $Ste_\infty = 10$ curve lies below that for $Ste_\infty = 5$ for one range of Bi and above in another range.

The occurrence of the aforementioned nonmonotonic behavior of Ra_i with Ste can be made plausible by examining the temperature profiles of the rest state. Representative profiles for the case of stepped wall temperature are presented in Fig. 5. The figure shows that the profiles depart more and more from a straight line as the Stefan number increases. In particular, the slope becomes steeper near the lower bounding wall (smaller z/δ) and more gradual near the solid-liquid interface (larger z/δ). It is known that the tendency toward instability is increased as the slope becomes steeper. On the other hand, the instability-prone portion of the layer becomes thinner as the region of gradual slope occupies a larger part of the overall thickness, and this tends to enhance stability. These two opposing tendencies are more and more in evidence as Ste increases, and their conflict affords the possibility of an extremum.

Fig. 5 also contains a set of curves to illustrate the sensitivity of the rest-state temperature profiles to the Biot number. Clearly, the profiles are quite insensitive. Therefore, the variation of the critical Rayleigh number with Biot number, as evidenced in Fig. 3, may be attributed to the convective boundary condition for the disturbance equation rather than to the rest-state temperature profile.

Stability Results: Ra_e. Thus far, the stability results have been presented in terms of the internal Rayleigh number Ra_i. However, as was noted earlier, it is not convenient to use Ra_i for applications since it contains quantities such as δ and, for convective heating, $(T_w - T_{sat})$ which are not prescribable a priori. These quantities vary with time. For the same reason, the Biot number, which contains δ, is also not a convenient parameter. It is, therefore, appropriate to recast the stability results in terms of quantities which are externally prescribable.

For the case of convective heating, (k/h) and $(T_\infty - T_{sat})$ are, respectively, a naturally occurring length scale and temperature dif-

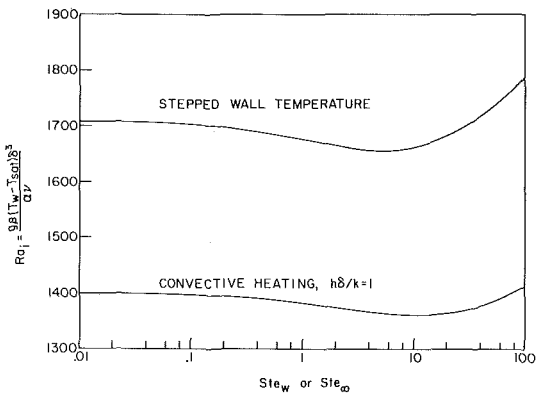

Fig. 4 Variation of the internal Rayleigh number with the Stefan number

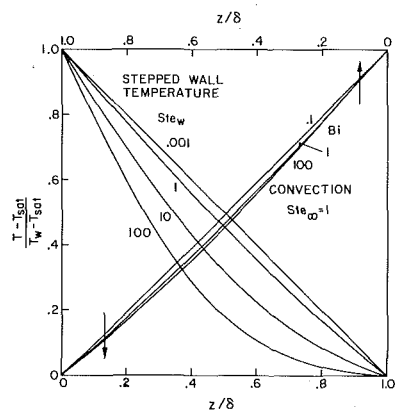

Fig. 5 Representative rest state temperature profiles

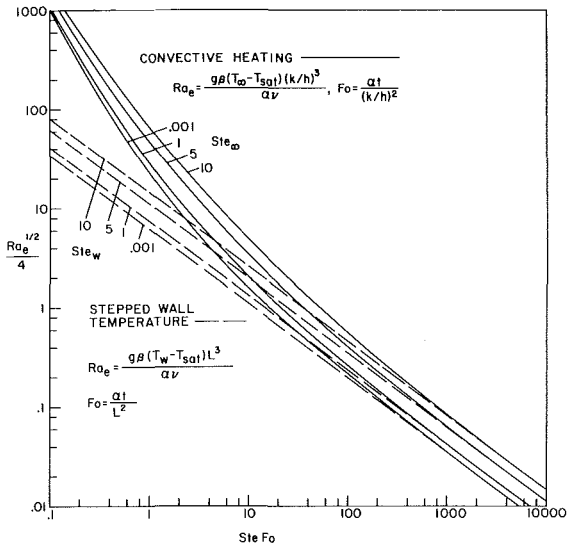

Fig. 6 Results for the external Rayleigh number marking the onset of instability

ference. Both of these quantities are known a priori. With them, an external Rayleigh number Ra_e may be defined and then tied in with other quantities that have appeared in the analysis.

$$Ra_e = g\beta(T_\infty - T_{sat})(k/h)^3/\alpha\nu = Ra_i/Bi^3\theta(0) \tag{29}$$

For given values of Ste_∞ and Bi, the corresponding values of the critical Rayleigh number Ra_i and of the dimensionless rest-state wall temperature $\theta(0)$ have already been determined, so that Ra_e can be evaluated from equation (29). Furthermore, the thickness versus time relationship was also obtained as one of the results of the rest-state solution. In dimensionless terms, this yields a relation between the Biot number and the Fourier number Fo, where

$$Fo = \alpha t/(k/h)^2 \tag{30}$$

If the Fourier number is assigned, then there is a corresponding Biot number and, in addition, a corresponding critical Rayleigh number Ra_e via equation (29).

In this way, a graph of Ra_e versus Fo can be constructed for parametric values of the Stefan number. If the value of Ra_e that characterizes an applications problem is evaluated from the known physical quantities g, β, $(T_\infty - T_{sat})$, k, h, α, and ν, then the Fourier number marking the onset of instability can be read from the graph.

A graphical presentation of this type is made in Fig. 6. To achieve a more compact presentation, $Ra_e^{1/2}/4$ is plotted on the ordinate in lieu of Ra_e, and SteFo is used as the abscissa variable

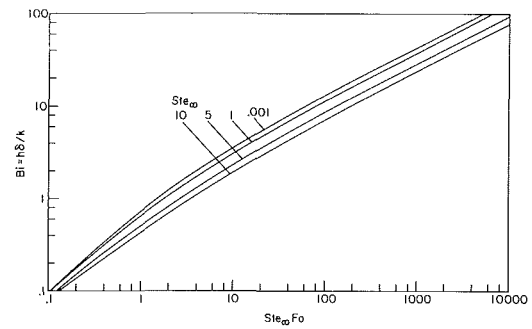

Fig. 7 Melt layer thickness versus time for conduction phase change with convective heating

rather than Fo. The results for convective heating are represented by solid lines that are parameterized by Ste_∞.

The figure shows that if a melting problem is characterized by a large value of Ra_e, instability occurs at a small value of the Fourier number. That is, the quiescent regime of no motion breaks down soon after the start of heating. For smaller values of Ra_e, the duration time of the quiescent regime increases markedly. If it is desired to maintain the quiescent regime during the entire melting period, an upper limit on the Rayleigh number can be found such that instability will not occur for any smaller value of Rayleigh number. The determination of the limiting Rayleigh number will be discussed shortly.

From the figure, it is seen that the use of SteFo is quite effective in minimizing the separate dependence of the stability results on the Stefan number. Had the results been plotted versus Fo alone, the curves for the various Stefan numbers would have been widely separated.

The results for the stepped wall temperature case are also presented in Fig. 6 as dashed lines. These are straight lines whose equation is readily deduced from (10) and (19) as

$$Ra_e^{1/2}/4 = \chi(Ste_w Fo)^{-3/4} \tag{31}$$

where χ is a constant whose value depends only on Ste_w

$$\chi = \{Ra_i(Ste_w)^{3/2}/128\Omega^3\}^{1/2} \tag{32}$$

There is not a naturally occurring characteristic length for the stepped wall temperature problem, and none is needed. This is because there is complete cancellation of the lengths that appear on the left- and right-hand sides of equation (31). Therefore, any length L may be selected provided that the same one is used in Ra_e and Fo.

The stability results for the stepped wall temperature case show the same qualitative behavior as that for the convective heating case. That is, the lower the value of Ra_e that characterizes a melting problem, the longer is the duration time of the quiescent regime prior to onset of instability. The fact that the dashed lines lie below the solid lines at small and intermediate values of SteFo is of no particular significance since Ra_e, Ste, and Fo have different definitions for the two cases.

On the other hand, it is highly significant that the solid and dashed lines merge at the larger values of SteFo. Under these conditions, $Ste_\infty \sim Ste_w$ (since $T_\infty \sim T_w$) and the lengths appearing in $Ra_e^{1/2}$ and $Fo^{-3/4}$ cancel, as was explained in connection with equation (31). The merging of the two sets of curves indicates that the stability characteristics of the two modes of heating become common for sufficiently large SteFo (~1000). Furthermore, it provides support for the validity of the analysis and the computational procedure, inasmuch as many aspects of the treatment of the two cases are different.

Layer Thickness and Surface Temperature Results. In this section, results obtained from the conduction phase-change solutions (i.e., rest state solutions) for convective heating will be presented. This information is not now available in the literature except for the thickness versus time results of [3, 7], which are limited to thin melt layers. Furthermore, the rest state results are useful in interpreting the results of the stability analysis.

In Fig. 7, the dimensionless thickness—time relation for the melt layer is plotted in terms of Bi versus Ste_∞ Fo, with Ste_∞ as the curve parameter. The thickness is seen to increase steadily with time. Only at relatively large times do the curves become straight lines that correspond to the δ versus $\sqrt{t}$ dependence that characterizes the stepped wall temperature case. The separate dependence of the results on Ste is muted by the use of SteFo as the dimensionless time variable.

The conditions under which instability will not occur during the entire melting period can be found with the aid of Figs. 6 and 7. If δ is the final thickness of the melt layer, then $h\delta/k$ can be evaluated and the corresponding $Ste_\infty Fo$ read from Fig. 7. With this as

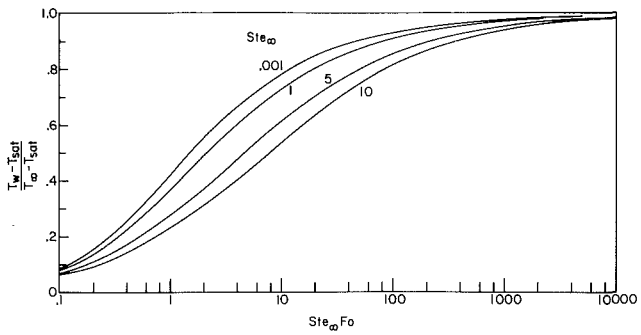

Fig. 8 Variation of surface temperature with time for conduction phase change with convective heating

input to Fig. 6, the value Ra_e given by the figure provides an upper bound such that stability is insured for all smaller values of Ra_e.

The history of the temperature T_w at the lower bounding surface of the melt layer is presented in Fig. 8. As can be seen in the figure, T_w is very much less than the temperature T_∞ of the fluid heating medium at small times. The wall temperature rises as time passes and, for sufficiently large times, it approaches T_∞. As a consequence, Ste_∞ and Ste_w are nearly equal at large times.

Concluding Remarks

Linear stability theory has been applied to determine the conditions marking the onset of convective motions in a melt layer that is heated from below. Heating conditions corresponding to a step change in wall temperature and to convection were considered. In connection with the latter case, it was necessary to solve the conduction phase change problem for the quiescent regime of no motion in order to obtain the distribution of the vertical temperature gradient.

It was found that the critical Rayleigh number based on quantities internal to the melt layer is significantly affected by the convective boundary condition (i.e., by the value of the Biot number). At large Biot numbers, the results for the convective heating case appear to be asymptotic to those for the case of stepped wall temperature. The effect of the Stefan number, although small, is interesting in that there is a nonmonotonic variation of the Rayleigh number with the Stefan number. This is attributed to changes in the shape of the rest-state temperature distribution as the Stefan number is varied.

To facilitate their use in applications problems, the stability results were recast in terms of parameters which are a priori prescribable (i.e., external parameters). For a melting problem where the external Rayleigh number is large, instability occurs soon after the start of heating. At smaller external Rayleigh numbers, the duration time of the quiescent regime of no motion increases markedly. At large times, the stability results for convective heating and stepped wall temperature coincide.

As a final remark, it may be noted that the stability analysis and results presented here are for liquid melts whose densities decrease with increasing temperature. Most liquids exhibit this type of behavior, with water being a notable exception.

References

1 Goodman, T. R., "Application of Integral Methods to Transient Nonlinear Heat Transfer," *Advances in Heat Transfer*, Vol. I, Academic Press, New York, 1964.

2 Megerlin, F., "Geometrisch eindimensionale Wärmeleitung beim Schmelzen und Erstarren," *Forsch Ing.-Wes.*, Vol. 34, 1968, pp. 40–46.

3 Stephen, K., and Holzknecht, B., "Heat Conduction in Solidification of Geometrically Simple Bodies" *Wärme- und Stoffübertragung*, Vol. 7, 1974, pp. 200–207.

4 Pellew, A. R., and Southwell, R. V., "On Maintained Convective Motion in a Fluid Heated From Below," *Proceedings of the Royal Society of London*, Vol. A176, 1940, pp. 312–343.

5 Ahlberg, J. H., Nilson, E. N., and Walsh, J. L., *The Theory of Splines and Their Applications*, Academic Press, New York, 1967.

6 Sparrow, E. M., Munro, W. D., and Jonsson, V. K., "Instability of the Flow Between Rotating Cylinders: The Wide Gap Problem," *Journal of Fluid Mechanics*, Vol. 20, 1964, pp. 35–46.

7 Lin, S., "An Analytical Method for Solving Geometric One-Dimensional Freezing or Melting Problems," ASME Paper No. 73-WA/HT-33, 1973.

J. R. Carpenter
Member of the Technical Staff,
Bell Telephone Laboratories,
Holmdel, N. J.

D. G. Briggs
V. Sernas

Department of Mechanical and Aerospace Engineering,
Rutgers University,
New Brunswick, N. J.
Mem. ASME

Combined Radiation and Developing Laminar Free Convection Between Vertical Flat Plates With Asymmetric Heating

A numerical investigation of the interaction of radiation with developing laminar free convective heat transfer in vertical parallel plate channels with asymmetric heating is presented. A unique iterative-marching technique is developed to solve the resulting nonlinear partial differential field equations and the integrodifferential radiation constraint equations. The introduction of radiation leads to five dimensionless parameters (heat flux ratio, Rayleigh number, aspect ratio, emissivity, and radiation number) which affect wall temperature and heat transfer performance. Radiation to the inlet-exit and the cooler opposing entrance wall significantly alters the nonradiation results by reducing the maximum wall temperature by as much as 50 percent. The nonradiation fully developed flow solution often could not be obtained with radiation present. Under certain conditions the Nusselt number actually becomes negative indicating a large radiative loss to the exit and a subsequent heating of the wall by the high local fluid temperature. The numerical results are verified experimentally.

Introduction

Developing free convection channel flow for a viscous fluid such as air is well understood [1–3].[1] The interaction of radiation and convection has been investigated [4, 5] for forced flow with high surface temperatures ($T > 2000°$ R). The radiation contribution is also important for low surface temperature if the fluid is flowing at reduced flow rates (free convection). The interaction of radiation and free convection does not seem to appear anywhere in the literature. The fluid under consideration, air, may be treated as a nonabsorbing gas for low temperatures (500–700° R) which is the range typically found for cooling electronic equipment.

The present study concerns a theoretical and numerical investigation of combined radiation free convection in air in a parallel plate vertical channel. The channel walls are uniformly heated but need not be at the same level (asymmetric heating). The walls may have a variable surface emissivity (gray surface) while the inlet and exit are treated as imaginary black surfaces at a uniform temperature. The channel walls are of low thermal conductivity to exclude the effects of axial conduction.

Governing Equations

The flow geometry for combined radiation-free convection is shown in Fig. 1. The channel walls are heated uniformly and as a result of heat transfer the local fluid temperature increases. The resultant change in density produces a buoyancy force causing the fluid to rise. The fluid entering the channel at a temperature T_∞ is assumed to have a uniform velocity U_0. Due to asymmetric heating the opposing wall is at a different temperature. For symmetric heating there exists radiation heat transfer to the cooler entrance wall of the opposing surface and to the inlet and exit. The degree of radiation is directly affected by the aspect ratio (spacing to flow length). For asymmetric heating there exists an additional radiation transfer across the channel to the cooler surface.

[1] Numbers in brackets designate References at end of paper.

Contributed by the Heat Transfer Division of THE AMERICAN SOCIETY OF MECHANICAL ENGINEERS and presented at the AIChE-ASME Heat Transfer Conference, San Francisco, Calif., August 10–13, 1975. Revised manuscript received by the Heat Transfer Division, November 21, 1975. Paper No. 75-HT-19.

The dimensionless field equations (conservation of mass, momentum, and energy) for laminar incompressible (except for the Boussinesq density variation in the buoyancy term) boundary layer flow [6] are:

$$\frac{\partial u}{\partial x} + \frac{\partial v}{\partial y} = 0 \tag{1}$$

$$u\frac{\partial u}{\partial x} + v\frac{\partial u}{\partial y} = \frac{\partial^2 u}{\partial y^2} - \frac{dp}{dx} + \theta \tag{2}$$

$$u\frac{\partial \theta}{\partial x} + v\frac{\partial \theta}{\partial y} = \frac{1}{\mathrm{Pr}}\frac{\partial^2 \theta}{\partial y^2} \tag{3}$$

In addition, the integral continuity equation may be applied at the inlet and any downstream position.

$$\int_0^1 u\, dy = u_0 \tag{4}$$

Specifying the heat flux on the cooler wall as q_2 and the hotter wall as q_1 a heat flux ratio may be defined:

$$r_H = \frac{q_2}{q_1} \qquad q_2 \le q_1 \tag{5}$$

The boundary conditions in dimensionless form using the geometry of Fig. 1 are:

At the Inlet. ($x = 0$ and $0 < y < 1$)

$$u = u_0 \quad v = 0 \quad \theta = 0 \quad p = 0 \tag{6a}$$

At the Exit. ($x = L$ and $0 < y < 1$). Note: $L = 1/\mathrm{Gr}$

$$\mathrm{p} = 0 \tag{6b}$$

At Surface 2. ($y = 0$ and $0 \le x \le L$)

$$u = 0 \qquad v = 0$$

$$r_H + \int_0^L \left\{\frac{1-\epsilon_1}{\epsilon_1}\left[\left.\frac{\partial\theta}{\partial y}\right|_{y=1} - 1\right] + N_{\mathrm{RAD}}\theta_{y=1}\right\} \times \frac{1}{2}\left[1 - r_a{}^2(x-x')^2\right]^{-3/2} r_a dx'$$

$$= \frac{1-\epsilon_2}{\epsilon_2}\left[-\left.\frac{\partial\theta}{\partial y}\right|_{y=0} - r_H\right] + N_{\mathrm{RAD}}\theta_{y=0} - \left.\frac{\partial\theta}{\partial y}\right|_{y=0} \tag{6c}$$

At Surface 1. ($y = 1$ and $0 \le x \le L$)

FLOW CONFIGURATION

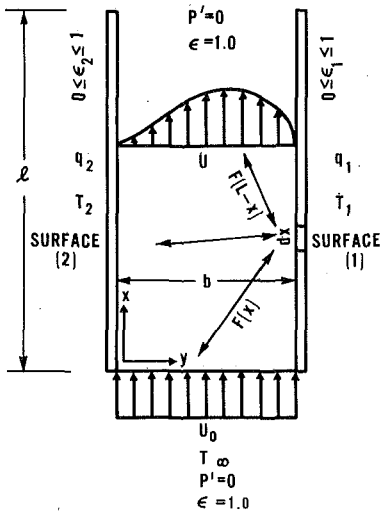

Fig. 1

$$u = 0 \qquad v = 0$$

$$1 + \int_0^L \left\{\frac{1-\epsilon_2}{\epsilon_2}\left[-\left.\frac{\partial\theta}{\partial y}\right|_{y=0} - r_H\right] + N_{\mathrm{RAD}}\theta_{y=0}\right\} \times \frac{1}{2}\left[1 + r_a{}^2(x-x')^2\right]^{-3/2} r_a dx'$$

$$= \frac{1-\epsilon_1}{\epsilon_1}\left[\left.\frac{\partial\theta}{\partial y}\right|_{y=1} - 1\right] + N_{\mathrm{RAD}}\theta_{y=1} \quad {}_{fr=1} + \left.\frac{\partial\theta}{\partial y}\right|_{y=1} \tag{6d}$$

where ϵ is the surface emissivity, N_{RAD} is the radiation number and r_a is the modified aspect ratio.

The radiation number appears due to the linearization of a fourth power temperature difference obtained from radiant interchange between a particular channel position and the channel inlet, exit and opposing surface. The radiation constraint equations (6*c*) and (6*d*), were derived for gray diffuse surfaces and small temperature differences. These constraint equations were

Nomenclature

b = channel width
c_p = specific heat J/Kg °C
Gr = Grashof number $(g\beta q_1 b^5)/(\nu^2 k\ell)$
Gr = average Grashof number $(g\beta(q_1 + q_2)b^5)/(2\nu^2 k\ell)$
k = thermal conductivity w/m·°C
ℓ = channel length
L = dimensionless channel length (1/Gr)
N_{RAD} = radiation number $4b\bar{T}^3\sigma/k$
Nu = Nusselt number (based on local wall temperature gradient)
$\overline{\mathrm{Nu}}$ = average Nusselt number (based on average temperature and gradient at channel midheight)
p = dimensionless pressure $(P - P_s)b^4/\rho\ell^2\nu^2\mathrm{Gr}^2$
P = local fluid pressure
P_s = hydrostatic pressure at uniform external ambient
Pr = Prandtl number (ν/α)
r_a = modified aspect ratio $\mathrm{Gr}/(b/\ell)$
r_b = aspect ratio (b/ℓ)
r_H = heat flux ratio $q_2/q_1 \quad q_2 \le q_1$
$\overline{\mathrm{Ra}}$ = Rayleigh number GrPr
$\bar{T}$ = average absolute surface-ambient temperature $1/2((T_1 + T_2/2) + T_\infty)$ K
$T_j{}^i$ = dimensionless numerical temperature at node $(i, j) - \theta$
u = dimensionless vertical velocity $Ub^2/(\nu\ell\mathrm{Gr})$
U = vertical velocity component
$U_j{}^i$ = dimensionless numerical velocity at $(i, j) - u$
v = dimensiolless horizontal velocity Vb/ν
V = horizontal velocity component
$V_j{}^i$ = dimensionless numerical velocity at $(i, j) - v$
x = dimensionless vertical coordinate $X/(\ell\mathrm{Gr})$
X = vertical coordinate
y = dimensionless horizontal coordinate Y/b
Y = horizontal coordinate
α = thermal diffusivity
β = volumetric expansivity
ϵ = wall emissivity
σ = Stefan-Boltzman constant 5.67×10^{-8} W/m² K⁴
μ = viscosity
ν = kinematic viscosity
θ = dimensionless temperature $T - T_\infty/q_1 b/k$
$\bar{\theta}$ = dimensionless temperature $T - T_\infty/(q_1 + q_2)/2k$

Subscripts

1 = surface 1
2 = surface 2
½ = channel midheight
∞ = external ambient
0 = inlet

Superscripts

— = based on $q_1 + q_2/2$
′ = opposing wall

developed by eliminating the irradiation from the radiosity and flux balance equations for one surface, solving for the radiosity, and substituting this into the integral expression for the irradiation upon the opposite surface. Next, the radiosity for that surface is eliminated and the resulting equation is linearized with respect to the fourth power temperature difference and then placed in dimensionless form. In the cooling of electronic equipment, external room ambients vary from 25 to 50° C while internal surface temperatures range from 100 to 150° C. For these temperatures, the linearization produces only a 2 percent error.

Numerical Solution

Marching techniques have been employed successfully [1, 7] to solve convective flow problems. To use a marching technique it is first necessary to treat a boundary value problem, BVP, as an initial value problem, IVP, so that the marching solution may be started. For the pure free convection problem this is accomplished by assuming a known inlet velocity, u_0, and marching downstream until the pressure defect returns to zero. At this point, the Grashof number is fixed and the solution restarted using a different u_0 until the desired Grashof number is determined. It is not possible to treat the combined radiation free convection problem as an IVP due to radiation transfer with unknown downstream positions. Because of this, a unique iterative-marching technique was developed [6] to solve the combined problem.

Before a marching technique can be utilized the governing equations and equations of constraint must be expanded in finite difference form. The four different finite difference methods investigated are implicit, semi-implicit or Crank-Nicholson [8], alternating direction explicit with two-point differencing [9] and alternating direction explicit with three-point differencing [10]. The implicit methods involve solving groups of simultaneous equations at each axial node while the ADE methods require sweeping from one boundary to the next and back using known values and then averaging the results. The ADE methods do not involve the solution of simultaneous equations.

The fastest FDE form of the governing field equations for the same accuracy are expanded below at node (i, j). The continuity and momentum equations are expanded in implicit form and the energy equation in ADE form. This was due to the coupling of the integral continuity and momentum equation which necessitates the solution of a set of simultaneous equations at each axial step.

Continuity.

$$\frac{(U_{j+1}{}^{i+1} + U_j{}^{i+1})}{2\Delta x} - \frac{(U_{j+1}{}^{i} + U_j{}^{i})}{2\Delta x} + \frac{(V_{j+1}{}^{i+1} - V_j{}^{i+1})}{\Delta y} = 0 \quad (7)$$

Momentum.

$$U_j{}^{i}\frac{(U_j{}^{i+1} - U_j{}^{i})}{\Delta x} + V_j{}^{i}\frac{(U_{j+1}{}^{i+1} - U_{j-1}{}^{i+1})}{2\Delta y} = \left[\frac{U_{j+1}{}^{i+1} - 2U_j{}^{i+1} + U_{j-1}{}^{i+1}}{\Delta y^2}\right] - \frac{[P^{i+1} - P^{i}]}{\Delta x} + T_j{}^{i+1} \quad (8)$$

Energy—Sweeping From Left to Right.

$$U_j{}^{i}\frac{(T_j{}^{i+1} - T_j{}^{i})}{\Delta x} + V_j{}^{i}\frac{T_{j+1}{}^{i} - T_{j-1}{}^{i+1}}{2\Delta y} = \frac{1}{\mathrm{Pr}}\left[\frac{T_{j+1}{}^{i} - T_j{}^{i} - T_j{}^{i+1} + T_{j-1}{}^{i+1}}{\Delta y^2}\right] \quad (9a)$$

Energy—Sweeping From Right to Left.

$$U_j{}^{i}\frac{(T_j{}^{i+1} - T_j{}^{i})}{\Delta x} + V_j{}^{i}\frac{(T_{j-1}{}^{i} - T_{j+1}{}^{i+1})}{2\Delta y} = \frac{1}{\mathrm{Pr}}\left[\frac{T_{j-1}{}^{i} - T_j{}^{i} - T_j{}^{i+1} + T_{j+1}{}^{i+1}}{\Delta y^2}\right] \quad (9b)$$

Integral Continuity. (Simpson's Rule)

$$4U_2{}^{i+1} + 2U_3{}^{i+1} + 4U_4{}^{i+1} + \cdots + 4U_{N-3}{}^{i+1} + 2U_{N-2}{}^{i+1} + 4U_{N-1}{}^{i+1} = \frac{3u_0}{\Delta y} \quad (10)$$

This system of finite difference equations has been shown to be a stable and convergent representation of the incompressible free convection equations [6].

The radiation constraint equation was expanded in finite difference form by using standard three point differencing for the wall temperature gradients and Simpson's rule for the integrals [6]. The implicit form of the momentum equation was chosen since at each axial node a set of simultaneous equation was generated due to coupling of the integral continuity and momentum equations.

The solution procedure may be stated as follows: As an initial guess for the iteration procedure, a wall temperature variation is calculated for a constant heat flux channel with no radiation. To do this, values for the inlet velocity, heat flux ratio and Prandtl must be selected. Using the inlet condition, the energy equation is solved for temperature using ADE technique with averaging. Next the combined momentum and integral continuity equations are solved for axial velocity and pressure using implicit techniques and a matrix reduction procedure [6]. This matrix reduction procedure tests for row diagonal dominance, converts to a upper triangular matrix and then uses Gaussian elimination to obtain a solution. Knowing the axial velocity, the transverse velocity can be calculated at each transverse node. The procedure is restarted until the pressure defect returns to zero which defines the channel length.

The iteration procedure may be started by using the constant wall heat flux temperature variation as an initial solution to the integrals in the radiation constraint equation. At this point values of the surface emissivity, aspect ratio, and radiation number must be specified. Since the radiation number involves absolute wall temperature, which is an unknown, an initial guess plus iteration procedure is used to determine its value. An average wall temperature for both surfaces from inlet to exit is calculated from the constant heat flux, no radiation results and used as an initial guess for the combined problem. After each iteration the new wall temperature is used to calculate a revised radiation number. As the wall temperature begins to equalize between surfaces and from the inlet to the exit the radiation number converges to a constant value. The finite difference field equations are resolved using a variable wall temperature boundary condition. This is obtained from the radiation constraint equation where the unknown downstream temperature and gradients are assumed to be those previously recorded from the constant heat flux solution. A solution is obtained when the wall temperature variation satisfies both the governing field equations and the radiation constraint equations to within some predetermined accuracy.

Results

With the interaction of radiation and free convection, five dimensionless parameters affect wall temperature and heat transfer performance. Because of this a complete parametric study is not possible and only trends will be discussed. Fig. 2 shows typical fluid temperature profiles for large Rayleigh number, asymmetric flow (one wall adiabatic). The surface emissivity is varied from 1.0 to 0.0 to show the maximum effect of radiation at a moderate aspect ratio ($b/\ell = 0.1$) and radiation number ($N_{\mathrm{RAD}} = 3.75$). Radiation serves to transfer a considerable amount of the convective heat flux from one wall to the opposing surface. This substantially reduces the wall temperature gradient and temperature on one surface while increasing it on the previously adiabatic surface. This decreases the maximum wall temperature by 40 percent.

A similar effect is shown in Fig. 3 for typical velocity profiles for asymmetric heating. Because of radiation transfer across the channel the velocity profile is not skewed as much towards the heated surface. This effect is important for a large channel spacing, i.e., large Rayleigh number because the assumption of a uniform inlet velocity in the numerical solution is not valid. However, this assumption is justified when radiation is present due to a more sym-

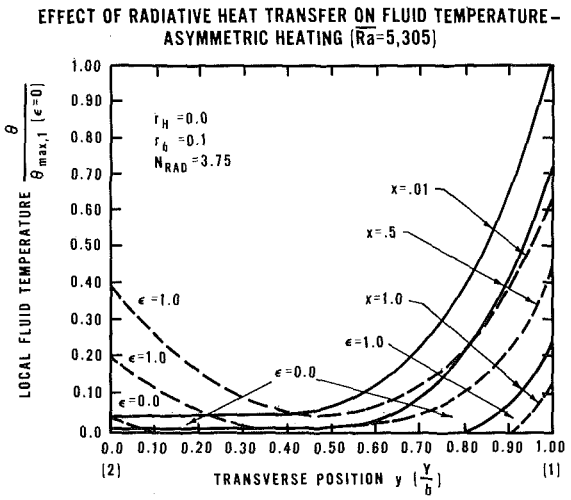

Fig. 2

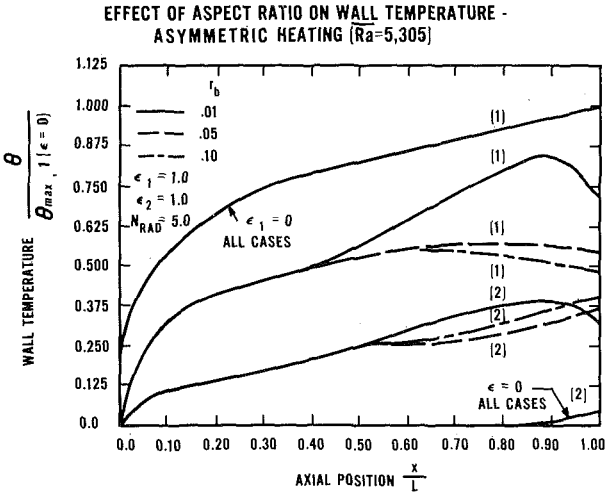

Fig. 5

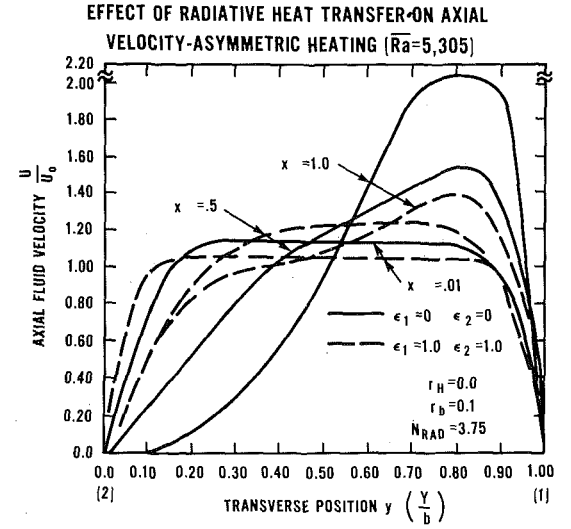

Fig. 3

metric velocity profile.

The thermal designer is primarily interested in wall temperature variation. Fig. 4 demonstrates the effect of radiation on wall temperatures for asymmetric flow. The wall temperature on the heated surface is reduced and the previously adiabatic wall temperature is increased due to radiation transfer across the channel. The dip in the wall temperature near the exit is due to radiation transfer directly to the exit. The most significant effect is the 40 percent reduction in maximum wall temperature when radiation is considered.

Figs. 5 and 6 show the effect of varying the radiation number and aspect ratio for asymmetric flow. Both tend to decrease the exit region temperature. Still the greatest effect in reducing wall temperature for asymmetric heating is the radiation transfer directly across the channel.

The percentage of radiation transfer of the total may be defined as the difference between the local power dissipation (constant) and the local convective heat flux. Fig. 7 shows the percentage radiation transfer for both symmetric and asymmetric heating. For symmetric heating, the wall temperature on opposing surfaces are equal which negates radiation transfer (except for large aspect ratio flow) near the midchannel height. There is still significant

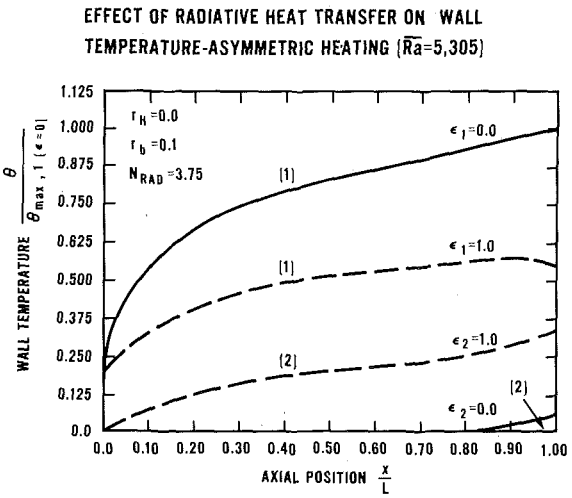

Fig. 4

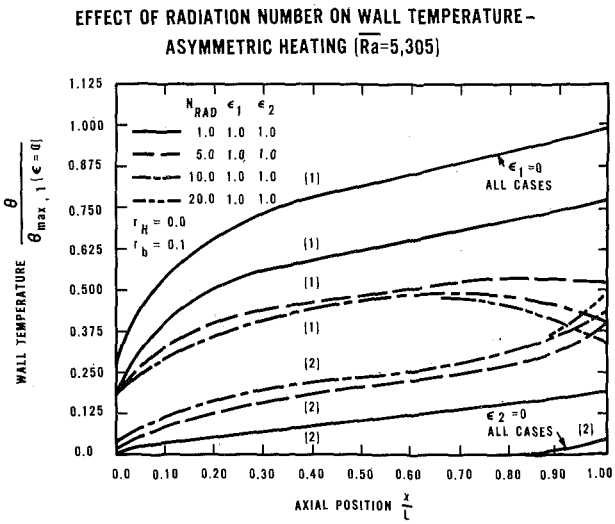

Fig. 6

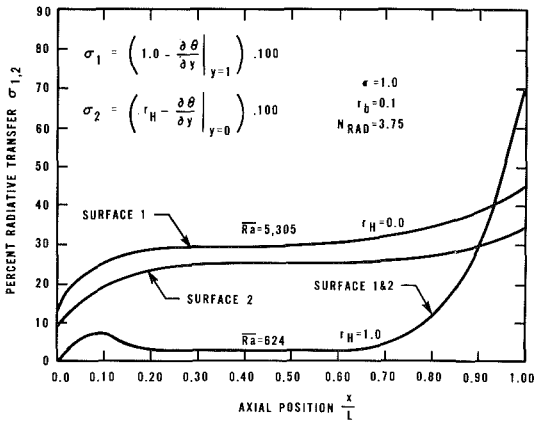

Fig. 7

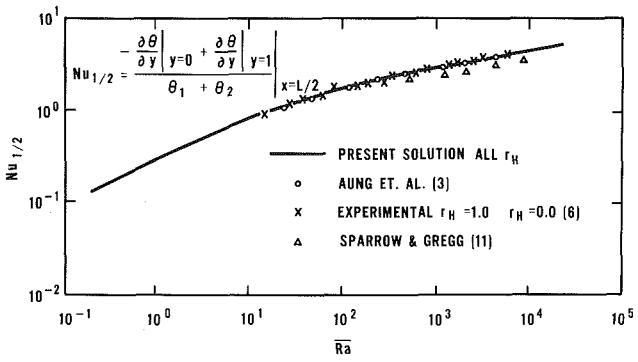

Fig. 8

end loss radiation which, for this example, accounts for 70 percent of the total dissipation. For asymmetric heating there is no region of the channel where radiation can be neglected.

For uniform heat flux, nonradiation flow, a universal Nusselt-Rayleigh number correlation has been found [3] where the Rayleigh number is defined using the average wall temperature and gradient evaluated at channel midheight. This also holds when radiation is present due to the averaging effect used in the definition. Verification has been accomplished numerically and experimentally (using a Wollaston prism interferometer [6] as shown in Fig. 8. The interferometer was used to measure local wall temperature gradients. The difference between the local convective heat flux, obtained from the interferometer, and the uniform power dissipation was an indirect measure of the radiative heat transfer. The large spacing, single vertical plate results are 10–15 percent lower than the channel flow results due to the difference in inlet boundary conditions. However, the assumption of a uniform velocity does not significantly affect the maximum wall temperature due to the dominance of radiation over free convection at the channel exit.

Fig. 9 summarizes the effect of radiation on maximum wall temperature over the Grashof number range tested ($10^{-1} < \overline{Gr} < 10^4$). As the spacing is reduced the fully developed, nonradiation free convection results may be used to predict maximum wall temperature. For large spacing ($\overline{Gr} > 10$) radiation cannot be neglected for either symmetric or asymmetric heating. The pure free convection results ($\epsilon = 0.0$) are also plotted to show the magnitude of the effect of radiation on wall temperature. The experimental results are in good agreement with the numerical results. The thermal designer may use these results for estimating maximum wall temperature at moderate aspect ratio and radiation number. For different values of aspect ratio and radiation number, Figs. 5 and 6 may be used for estimating the change and also for determining the location of the maximum wall temperature.

Conclusion

For symmetric heating with a Rayleigh number less than 10 or aspect ratio less than 0.01, radiation was found to have little effect. For this region radiation could be ignored and the fully developed free convection results applied. As the Rayleigh number and/or aspect ratio was increased radiative end losses were important which tended to reduce the maximum wall temperature. Also, the maximum wall temperature no longer occurred at the exit and the Nusselt number continued to decrease and in some cases became negative at the exit. As much as a 50 percent decrease in maximum wall temperature occurred when the aspect ratio was increased to $0.2(b/\ell = 0.2)$ or the radiation number was increased to $20(T > 700°\ R, b/\ell = 0.1)$. This occurred for *black* surfaces with a moderate Rayleigh number, $(10^2 < Ra < 10^3)$.

For asymmetric heating, one wall adiabatic with a Rayleigh number less than 2, radiation was also found to have little effect. This occurred for very small channel spacing where a rapidly heated fluid equalized the wall temperatures on both surfaces. For this region the pure free convection results also accurately predicted the value and location of maximum wall temperature.

As the Rayleigh number was increased for asymmetric heating, radiation serves to transfer the heat across the gap, increasing the convective heat flux from one surface while decreasing it on the opposite higher powered surface. This effect significantly reduces the maximum wall temperature on the powered surface while increasing it on the previously adiabatic surface. This trend was evidenced for an aspect ratio range of 0.05–0.2 and radiation numbers from 1.0 to 20.0. Increasing the aspect ratio serves to decrease the maximum wall temperature and move its location from the channel exit to channel midheight. Similar trends were evidenced while increasing the radiation number. However, the most important effect in reducing the maximum wall temperature for asymmetric heating was the radiative transfer across the gap with increased convection from one surface and decreased convection from the opposing one. This effect was even noted for surface emissivities as low as 0.3 with moderate aspect ratio $(b/\ell = 0.1)$ and radiation number $(N_{RAD} = 5.0)$.

The nonradiation numerical and experimental results agree with other published data. At high Rayleigh numbers $(\overline{Ra} > 10^4)$, the single vertical plate Nusselt number results were 10 percent higher than those previously published [11]. This was probably due to the assumption of a uniform inlet velocity, which is equivalent to superimposing forced convective flow on a single vertical flat plate. This effect was far less pronounced when radiation was considered at large Rayleigh numbers due to the dominance of radiation over free convection. Here the shape of the inlet velocity profile was insignificant when determining position and value of maximum wall temperature.

A universal correlation still existed between Nusselt number and Rayleigh number when evaluated at average wall temperature and temperature gradient at midheight for all heat flux ratios and radiation parameters. However, the maximum wall temperature was greatly affected by radiation and generally did not occur at the exit.

Acknowledgments

Acknowledgments are due from one of the authors (JRC) to the Bell Telephone Laboratories for its support of this investigation toward his doctoral dissertation at Rutgers University.

References

1 Bodoia, J. R., and Osterle, J. F., "The Development of Free Convection Between Heated Vertical Plates," JOURNAL OF HEAT TRANSFER, TRANS. ASME, Series C, Vol. 84, No. 1, Feb. 1962, pp. 40–44.

2 Elenbaas, W., "Heat Dissipation of Parallel Plates by Free Convection," *Physica*, Vol. 9, No. 1, 1942, pp. 1–28.

3 Aung, W., Fletcher, L. S., and Sernas, V., "Developing Laminar Free Convection Between Vertical Flat Plates With Asymmetric Heating," *International Journal of Heat and Mass Transfer*, Vol. 15, 1972, pp. 2293–2308.

4 Keshock, E. G., and Siegel, R., "Combined Radiation and Convection in a Asymmetrically Heated Parallel Plate Flow Channel,' JOURNAL OF HEAT TRANSFER, TRANS. ASME, Series C, Vol. 86, No. 3, Aug. 1964, pp. 341–350.

5 Liu, S. T., and Thorsen, R. S., "Combined Forced Convection and Radiation Heat Transfer in Asymmetrically Heated Parallel Plates," *Proceedings of the Heat Transfer and Fluid Mechanics Institute*, Stanford University Press, Palo Alto, Calif., 1970, pp. 32–44.

6 Carpenter, J. R., "An Analysis of Combined Radiation and Convective Heat Transfer to a Fluid Flowing Between Asymmetrically Heated, Vertical Parallel Plates Including Entrance Effects," PhD thesis, Rutgers University, New Brunswick, N. J., 1975.

7 Roache, P. J., *Computational Fluid Dynamics*, Hermosa Publishers, Albuquerque, N. Mex., 1972.

8 Isaacson, E., and Keller, H. B., *Analysis of Numerical Methods*, Wiley, New York, 1966.

9 Saul'yev, *Integration of Equations of Parabolic Type by the Method of Nets*, (Russian Translation) MacMillan, New York, 1964.

MAX. WALL TEMPERATURE VS GRASHOF NUMBER

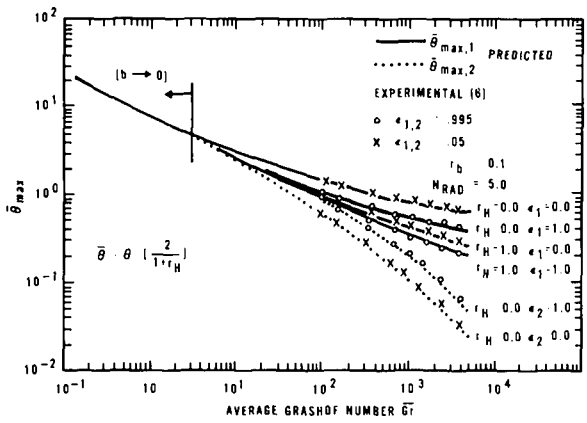

Fig. 9

10 Liu, S. L., "Stable Explicit Difference Approximations to Parabolic Partial Differential Equations," *AIChE Journal*, Vol. 15, No. 3, May 1968.

11 Sparrow, E. M., and Gregg, J. L., "Laminar Free Convection From a Vertical Plate With Uniform Surface Heat Flux," TRANS. ASME, Vol. 78, 1956, pp. 435–440.

A. T. Wassel[1]
D. K. Edwards
Professor.
Mem. ASME

School of Engineering and Applied Science,
University of California, Los Angeles, Calif.

Molecular Gas Radiation in a Laminar or Turbulent Pipe Flow

The temperature profile and the radiative and convective wall-heat fluxes for a hydrodynamically established flow of a nongray gas in a cylinder are calculated numerically for laminar or turbulent flow. Turbulent eddy viscosity is represented by a two-region model having a near-wall-region and a far-from-wall region. Gas properties are represented by the exponential-winged band model. The controlling parameters are N_{rm}, the ratio of radiation conductance to molecular conductance, $\tau_{R,i}$, the maximum spectral optical depth of the radius for the ith gas band, W_i, a measure of the importance of the ith band, and R_t, the turbulent Reynolds number. Qualitatively the results for a gas with a single major band agree with a previous solution for a cylinder with internal heat generation. Radiative Nusselt number Nu_R increases nearly linearly with N_{rm}. Radiative flux increases with τ_R rapidly at first and then only slowly. Increasing R_t increases markedly the convective Nusselt number Nu_C and appreciably Nu_R. The gas layer effective transmissivity was found to increase with increasing R_t and decrease with increasing τ_R. Quantitative comparisons with the constant-volume-heat-source case show discrepancies of up to 10 percent in Nu_R and up to 25 percent in Nu_C.

Introduction

Transfer of heat by simultaneous convection and radiation is of interest to the designer of combustion chambers and industrial furnaces. In some postulated nuclear reactor loss-of-coolant accident scenarios, the engineer wishes to predict heat transfer from heated walls to flowing water vapor, which is capable of absorbing and emitting thermal radiation. An element of intellectual curiosity also exists, for example, in wondering how much thermal radiation contributes to the heat transfer to steam flowing through heated tubes in the superheating section of a power plant steam generator. This paper addresses the question of how to calculate the simultaneous radiation and convection heat transfer to or from a molecular gas with infrared absorption bands flowing laminarly or turbulently within a pipe.

Viskanta [1][2] studied the interaction of conduction, laminar convection, and radiation in a plane layer of a radiating gas. Einstein [2] considered radiation heat transfer in an absorbing emitting gray gas flowing within a black-walled cylindrical pipe. Nichols [3] studied the influence of the absorption of radiation on the temperature profile and heat transfer to an absorbing medium flowing turbulently in an annulus. deSoto [4] investigated numerically the coupling of radiation with the conduction and convection mechanisms in a nonisothermal, nongray gas flowing in the entrance region of a black-walled tube. Pearce and Emery [5] treated the thermal entry region for laminar flow of a gray gas or a gas with gray bands. Kesten [6] presented the equations for the spectral radiant heat flux distribution in an absorbing-emitting gas contained in a long cylinder. Landram, Greif, and Habib [7] studied heat transfer in turbulent pipe flow with optically thin radiation. Tiwari and Cess [8] studied heat transfer to laminar flow of nongray gases through a circular tube. The analysis of [8] is based upon an approximation suitable only for the optically thick limit [9, 10]. Jeng, Lee, and DeWitt [11] also treated laminar flow of a radiating gas in a circular tube with constant wall temperature. They considered both gray and nongray media. In the nongray case, the Tien and Lowder [12] expression for band radiation was used together with the method of undetermined coefficients or discrete ordinates to solve the linearized energy equation. Edwards and Balakrishnan

[1] Presently at Science Applications Inc., El Segundo, Calif.

[2] Numbers in brackets designate References at end of paper.

Contributed by the Heat Transfer Division for publication in the JOURNAL OF HEAT TRANSFER. Manuscript received by the Heat Transfer Division August 5, 1975. Paper No. 76-HT-Q.

[13, 14] used the slab band absorptance function to investigate simultaneous radiation, turbulent transfer, and heat source in plane parallel ducts. Wassel and Edwards [15] formulated the radiative flux distribution in terms of an axial band absorptance function, for the exponential-winged band model [16] and Wassel, Edwards, and Catton [17] investigated the heat transfer for the thermally and hydrodynamically established flow of a gas with a hypothetical uniform volume heat source within a cylinder.

Coupling between the different modes of energy transfer is important unless radiation is either very strong or very weak. Under these extreme conditions, either the dominant mode only need be considered, or the minor flux can be superposed onto the major flux. It is the purpose of the present paper to establish a method by which interaction of radiation and laminar or turbulent convection can be treated in a black-walled tube subject to a constant wall heat flux.

Mathematical Formulation

Energy Equation and Boundary Conditions. The thermal energy equation describing a hydrodynamically established flow of a turbulent radiating gas flowing in a pipe is

$$\rho C_p u \frac{\partial T}{\partial z} = \frac{1}{r}\frac{\partial}{\partial r}\left[(k_m + \rho C_p \epsilon_H) r \frac{\partial T}{\partial r}\right] - \frac{1}{r}\frac{d}{dr}(rq_R) \tag{1}$$

Axial diffusion and radiation are neglected, as is viscous dissipation. This integro-differential equation is subject to the boundary conditions

$$r = R: T = T_w \text{ and } r = 0: \partial T/\partial r = 0 \tag{2}$$

For a fully developed temperature profile and constant wall heat flux there holds

$$\frac{\partial}{\partial z}\left(\frac{T_w - T}{T_w - T_b}\right) = 0, \frac{\partial T}{\partial z} = \frac{dT_w}{dz} = \frac{dT_b}{dz} = \frac{2\pi R q_w}{\dot{m} C_p} = \frac{4q_w}{\rho C_p \nu_m \mathrm{Re}_D} \tag{3}$$

where

$$\dot{m} = 2\pi\rho \int_0^R u(r) r dr,\ \mathrm{Re}_D = V2R/\nu_m,\ V = \frac{2}{R^2}\int_0^R u(r) r dr \tag{4}$$

and where T_w and T_b are the wall and bulk temperatures, respectively. Substituting equation (3) into the energy equation (1), integrating it with respect to the coordinate r, and making the use of the zero radiant and conductive fluxes condition at the center of the pipe gives

$$(4q_w/\nu_m \mathrm{Re}_D) \int_0^r u(r') r' dr' = (k_m + \rho C_p \epsilon_H) r \frac{\partial T}{\partial r} - r q_R \tag{5}$$

Formulation of the radiative flux follows.

Radiative Flux. For black walls with no temperature jump, the radial radiative flux can be written as follows [15]:

$$q_R(r^*) = \sum_{i=1}^{k} q_{R,i}(r^*) \tag{6}$$

$$\begin{aligned} q_{R,i}(r^*) = \omega_i \int_{\gamma=0}^{\pi/2} \cos\gamma \Bigg\{ & \int_{r^*}^{1} B'_{\nu_i}(r^{*\prime}) \\ & \times A^*_{a,i}(\tau_{R,i}[(r^{*\prime 2} - r^{*2}\sin^2\gamma)^{1/2} - r^*\cos\gamma]) dr^{*\prime} \\ & - \int_{r^*\sin\gamma}^{1} B'_{\nu_i}(r^{*\prime}) A^*_{a,i}(\tau_{R,i}[(r^{*\prime 2} - r^{*2}\sin^2\gamma)^{1/2} + r^*\cos\gamma]) dr^{*\prime} \\ & + \int_{r^*\sin\gamma}^{r^*} B'_{\nu_i}(r^{*\prime}) A^*_{a,i}(\tau_{R,i}[r^*\cos\gamma \\ & - (r^{*\prime 2} - r^{*2}\sin^2\gamma)^{1/2}]) dr^{*\prime} \Bigg\} d\gamma \end{aligned} \tag{7}$$

where

$$r^* = r/R,\ r^{*\prime} = r'/R,\ B'_{\nu_i}(r^{*\prime}) = \frac{d}{dr^{*\prime}}[B_{\nu_i}(r^{*\prime})],$$

$$B_{\nu_i}(r^{*\prime}) = \frac{2\pi_{hc}{}^2\nu^3}{e^{hc\nu/kT(r^{*\prime})} - 1}$$

Nomenclature

$A^\dagger$ = van Driest universal constant
A_a = axial band absorptance
a_n = Galerkin coefficient
B_ν = spectral black body radiosity
B'_ν = derivative of B_ν with respect to r
B_{nj} = matrix
c = speed of light
C_p = specific heat at constant pressure
C_f = coefficient of friction
D_j = vector
E_1 = exponential integral function
G^* = dimensionless radiant flux
h = Planck's constant
K = von Karman constant
k = number of bands
k_m = molecular conductivity
k_ν = spectral mass absorption coefficient
k = Boltzmann constant
$\dot{m}$ = mass flow rate
N = number of Galerkin terms
N_{rm} = radiation to molecular conductance ratio
Nu_C = convective Nusselt number
Nu_R = radiative Nusselt number
Nu_T = total Nusselt number
Pr = Prandtl number
Pr_t = turbulent Prandtl number
$\mathrm{Pr}_{\mathrm{eff}}$ = effective Prandtl number
q_C = convective heat flux
q_R = radiative heat flux
q_w = wall heat flux
r, r' = radial coordinate
R = cylinder radius
R_t = turbulent Reynolds number
Re_D = Reynolds number
T = temperature
u = local velocity
V = bulk velocity
W_i = dimensionless weighting parameter
x = argument
z = axial coordinate
α_i = integrated band intensity
α = absorptivity
α_m = thermal diffusivity
γ_e = Euler-Mascheroni constant = 0.5772156 . . .
ϵ = emissivity
ϵ_H = eddy diffusivity for heat
ϵ_M = eddy diffusivity for momentum
θ = dimensionless temperature
λ = empirical universal constant
ν_m = molecular kinematic viscosity
ν = wavenumber, reciprocal wavelength
π = 3.141592 . . .
ρ = gas density
σ = Stefan-Boltzmann constant
$\tau_{w\ell}$ = wall layer transmissivity
τ = shear stress
τ_R = optical depth of the tube radius at maximum absorption
ω = band wing decay width parameter

Subscripts

b = bulk
C = convective
cl = center line
H = heat
i = ith band, ith node point
M = momentum
m = molecular
R = radiative
T = total
t = turbulent, transition
w = wall
$w\ell$ = wall layer
ν = spectral

Superscripts

* = dimensionless quantity
+ = dimensionless turbulent quantity

The axial band absorption function, $A^*_{a,i}$ was defined as follows [15]:

$$A^*_{a,i}(x_i) = \ln(4x_i/\pi) + E_1(4x_i/\pi) + \gamma_e,\ x_i \le 0.38 \quad (8a)$$

$$A^*_{a,i}(x_i) = \ln x_i + E_1(3\pi x_i/8) + \gamma_e + \ln 2 - \tfrac{1}{2},\ x_i > 0.38 \quad (8b)$$

where

$$x_i = \tau_{R,i}\bar{r}^*,\ \tau_{R,i} = \frac{\alpha_i}{\omega_i}\rho R,\ \bar{r}^* = \eta r^* \cos\gamma + \xi(r^{*\prime 2} - r^{*2}\sin^2\gamma)^{1/2} \quad (9)$$

$$\gamma_e = \int_0^1 (1 - e^{-t})\frac{dt}{t} - \int_1^\infty e^{-t}\frac{dt}{t} = 0.5772156\ldots$$

$$E_1(x) = \int_0^1 e^{-x/t}\frac{dt}{t} = \int_1^\infty e^{-xt}\frac{dt}{t}$$

The parameters η and ξ take the values ± 1 as required by equation (7). The expression of the axial band absorptance, $A^*_{a,i}$, given by equation (8a and 8b) represent gases whose spectral absorption coefficient, k_ν, is represented by the exponential-winged band model. That is,

$$k_\nu = \sum_{i=1}^{k} k_{\nu_i},\ k_{\nu_i} = \frac{\alpha_i}{\omega_i}\exp[-(\nu_i - \nu)/\omega_i],\ \nu < \nu_i \quad (10)$$

where α_i is the integrated intensity of the ith band, ω_i is the band wing decay width and ν_i is the spectral location of the band head.

Dimensionless Form of Energy Equation. Introduce the following dimensionless quantities

$$T^* = (T_w - T)/(q_w R/k_m),$$

$$\epsilon^* = (1 + \epsilon_H/\alpha_m) = \mathrm{Pr}\mathrm{Pr}_{\mathrm{eff}}^{-1}(1 + \epsilon_M/\nu_m)$$

$$\mathrm{Pr}_{\mathrm{eff}} = (1 + \epsilon_M/\nu_m)/[\mathrm{Pr}^{-1} + \mathrm{Pr}_t{}^{-1}(\epsilon_M/\nu_m)],\ \mathrm{Pr}_t = \epsilon_M/\epsilon_H$$

$$q_R^* = q_R/q_w,\ u^* = u/V,\ r^* = r/R$$

into equation (5). There results

$$2\int_0^{r^*} u^*(r^{*\prime})r^{*\prime}dr^{*\prime} = -\epsilon^* r^*\frac{dT^*}{dr^*} - r^* q^*_R \quad (11)$$

where

$$q^*_R = -N_{rm}\sum_{i=1}^{k} W_i G^*_i\left(\tau_{R,i}, r^*, \frac{dT^*}{dr^*}\right),$$

$$N_{rm} = \sum_{i=1}^{k}\omega_i\,(dB_{\nu_i}/dT)/(k_m/R) \quad (12)$$

$$W_i = \omega_i(dB_{\nu_i}/dT)\Big/\sum_{i=1}^{k}\omega_i(dB_{\nu_i}/dT) \quad (13)$$

$$G_i^* = \int_{\gamma=0}^{\pi/2}\cos\gamma\left\{\int_{r^*}^{1}\frac{dT^*}{dr^{*\prime}}(r^{*\prime})\right.$$
$$\times A^*_{a,i}(\tau_{R,i}[(r^{*\prime 2} - r^{*2}\sin^2\gamma)^{1/2} - r^*\cos\gamma])dr^{*\prime}$$
$$- \int_{r^*\sin\gamma}^{1}\frac{dT^*}{dr^{*\prime}}(r^{*\prime})$$
$$\times A^*_{a,i}(\tau_{R,i}[(r^{*\prime 2} - r^{*2}\sin^2\gamma)^{1/2} + r^*\cos\gamma])dr^{*\prime}$$
$$+ \int_{r^*\sin\gamma}^{r^*}\frac{dT^*}{dr^{*\prime}}(r^{*\prime})$$
$$\left.\times A^*_{a,i}(\tau_{R,i}[r^*\cos\gamma - (r^{*\prime 2} - r^{*2}\sin^2\gamma)^{1/2}])\,dr^{*\prime}\right\}d\gamma \quad (14)$$

Equation (11) is subject to the boundary condition $T^* = 0$ at $r^* = 1$. In order to solve the energy equation, equation (11), the velocity field, $u^*(r^*)$, as well as the eddy diffusivity, $\epsilon^*(r^*)$, have to be specified by solving the equation of conservation of axial momentum.

For the laminar case, where $\epsilon^* = 1$, and $u^*(r^*) = 2(1 - r^{*2})$, the energy equation reduces to

$$\frac{dT^*}{dr^*} - N_{rm}\sum_{i=1}^{k} W_i G^*_i\left(\tau_{R,i}, r^*, \frac{dT^*}{dr^*}\right) + 2r^*(1 - r^{*2}/2) = 0 \quad (15)$$

For the turbulent case the momentum equation has to be solved numerically as explained in the next section.

Momentum Equation and Eddy Diffusivity Model. The equation of conservation of axial momentum for a hydrodynamically established flow can be written as

$$(\nu_m + \epsilon_M)\frac{du}{dr} = (\tau_w/\rho)(-r/R) \quad (16)$$

subject to $du/dr = 0$ at $r = 0$ and u = 0 at $r = R$. The eddy viscosity, ϵ_M, is described by a two-layer model. The wall region is described by the van Driest model [18] modified by Patankar and Spalding [19]. In the wake-like region a uniform mixing length is adopted. The momentum equation, equation (16), boundary condition, and the previously described viscosity model can be rewritten as follows:

$$(1 + \epsilon_M/\nu_m)\frac{du^+}{dr^+} = -r^+/\mathrm{R}_t \quad (17)$$

$$(\epsilon_M/\nu_m) = -K^2(\mathrm{R}_t - r^+)^2\{1 - \exp[-(\mathrm{R}_t - r^+)(r^+/\mathrm{R}_t)^{1/2}/A^+]\}^2 \times\frac{du^+}{dr^+} \quad \text{For } r_t{}^+ \le r^+ \le \mathrm{R}_t \quad (18a)$$

$$(\epsilon_M/\nu_m) = -(\lambda\mathrm{R}_t)^2\frac{du^+}{dr^+} \quad \text{For } 0 \le r^+ \le r_t{}^+ \quad (18b)$$

subject to $u^+ = 0$ at $r^+ = \mathrm{R}_t$, where $u^+ = u/\sqrt{\tau_w/\rho}$, $r^+ = r\sqrt{\tau_w/\rho}/\nu_m$ and $r_t{}^+$ is a transition radius at which the eddy viscosity given by equations (18a) and (18b) have the same value. The von Karman constant, K, the van Driest constant, A^+, and the empirical constant λ were taken to be 0.40, 30, and 0.075, respectively [18–22].

The turbulent Reynolds number, R_t, is related to the Reynolds number based on the cylinder diameter as follows:

$$\mathrm{R}_t = \sqrt{\mathrm{C}_f/8}\,\mathrm{Re}_D \quad (19a)$$

$$\mathrm{Re}_D = \frac{V2R}{\nu_m} = \frac{4}{\mathrm{R}_t}\int_0^{\mathrm{R}_t} u^+(r^+)r^+dr^+ \quad (19b)$$

$$C_f = (\tau_w/\rho)\Big/\frac{1}{2}V^2 \quad (19c)$$

It is necessary to extract the velocity in the (u^*, r^*) plane in order to solve the energy equation, equation (11), as follows:

$$r^* = r/R = r^+/\mathrm{R}_t \quad (20a)$$

$$u^* = u/V = 2u^+\mathrm{R}_t\Big/\left(\frac{4}{\mathrm{R}_t}\int_0^{\mathrm{R}_t} u^+(r^+)r^+dr^+\right) = 2u^+\mathrm{R}_t/\mathrm{Re}_D \quad (20b)$$

The system of equations (17) and (18a) and (18b) is solved first with R_t as a parameter, hence establishing the required $u^*(r^*)$ and $\epsilon^*(r^*)$ which enables one to solve the energy equation, equation (11), by an appropriate method.

Nusselt Numbers, Average Temperature, and Effective Transmissivity. Nusselt numbers are based on the bulk (mixing cup) temperature T_b, defined as

$$T_w - T_b = \int_0^R u(T_w - T)rdr\Big/\int_0^R urdr \quad (21)$$

From the definition of the dimensionless temperature T^*, the foregoing relation yields

$$T^*_b = 2\int_0^1 u^*T^*r^*dr^* \quad (22)$$

The convective, radiative, total Nusselt numbers and the peak or center-line to bulk temperature ratio can be written as follows:

$$\mathrm{Nu}_C = -q_{C,w}2R/k_m(T_w - T_b) = -\frac{2}{T^*_b}\frac{dT^*}{dr^*}(r^* = 1) \quad (23)$$

$$\mathrm{Nu}_R = -q_{R,w}2R/k_m(T_w - T_b) = \frac{-2}{T^*_b}q^*_R(r^* = 1) \quad (24)$$

$$\mathrm{Nu}_T = \mathrm{Nu}_C + \mathrm{Nu}_R \text{ (with mutual interaction)} \quad (25)$$

$$\theta = \frac{T_w - T_{c1}}{T_w - T_b} = \frac{T^*_{c1}}{T^*_b} \quad (26)$$

The wall layer effective transmissivity is defined as the actual radiant wall heat flux divided by the radiant heat flux which would occur if the gas were isothermal at the bulk temperature

$$\tau_{w\ell} = \frac{-q_{R,w}}{\alpha_g\sigma T_w^4 - \epsilon_g\sigma T_b^4} = \frac{-q_{R,w}}{\sum_{i=1}^{k}[\bar{A}_i B_{\nu_i}(T_w) - \bar{A}_i B_{\nu_i}(T_b)]} \quad (27)$$

where $\bar{A}_i = \omega_i \bar{A}^*_i$ is the mean band absorptance given by [15]

$$\bar{A}_i = \omega_i \int_{\gamma=0}^{\pi/2} A^*_{a,i}(2\tau_{R,i}\cos\gamma)\cos\gamma\, d\gamma \quad (28)$$

Linearizing equation (27) and introducing the radiative Nusselt number, allows one to rewrite equation (27) as follows, provided single major bands are considered

$$\tau_{w\ell} = \frac{1}{2}[\mathrm{Nu}_R/\bar{A}^*][(k_m/R)(\omega dB_\nu/dT)] = \frac{1}{2}\mathrm{Nu}_R/[\bar{A}^* N_{rm}] \quad (29)$$

Values of $\bar{A}^*$ as a function of τ_R are reported in reference [15].

Recall the classical limiting case, in which both radiation and turbulent diffusion are absent. The energy equation has the exact solution

$$T^* = (1 - r^{*2}) - (1/4)(1 - r^{*4}) \quad (30)$$

the bulk temperature and convective Nusselt number are $11/24$ and 4.364, respectively [20].

Methods of Solution

The laminar form of the energy equation, equation (15), is solved by the Galerkin technique for single major bands. For the turbulent case, equation (11) is solved by the numerical iteration procedure, provided $\epsilon^*(r^*)$ is established as described in the foregoing.

The Laminar Case. The temperature $T^*(r^*)$ is expanded in a series of the form

$$T^*(r^*) \doteq T^*_0(R^*) + \sum_{n=1}^{N} a_n T^*_n(r^*) \quad (31)$$

If the series is substituted into equation (15), multiplied by T^*_j and integrated over the volume of the tube, one obtains the following

$$\sum_{n=1}^{N} a_n B_{nj} = D_j \qquad j = 1, 2, \ldots, N \quad (32)$$

where

$$B_{nj} = \int_0^1 \left\{\frac{dT^*_n}{dr^*} - N_{rm}G^*_n\left(\tau_R, r^*, \frac{dT^*_n}{dr^*}\right)\right\} T^*_j r^* dr^*$$

$$D_j = -\int_0^1 \left\{2r^*\left(1 - \frac{1}{2}r^{*2}\right) + \frac{dT^*_0}{dr^*} - N_{rm}G^*_0\left(\tau_R, r^*, \frac{dT^*_0}{dr^*}\right)\right\} T^*_j r^* dr^*$$

and G^*_0 and G^*_n are the parts of the function G^* that depend on dT^*_0/dr^* and dT^*_n/dr^* respectively. The coefficients a_n are found by solving the set of simultaneous equations (32) through matrix inversion. By comparison with the exact solution, equation (30), it may be seen that the two-term approximation yields the solution to the laminar energy equation with no radiation.

The Turbulent Case. The domain (0, 1) is divided into N unequal steps where more node points are stacked near the wall in a logarithmic fashion appropriate to turbulent flows as follows

$$r^*_i = 1 - \frac{1}{K\mathrm{R}_t}(e^{z^*_i} - 1)$$

Equally spaced values of z^*_i between 0 and $\ln(1 + K\mathrm{R}_t)$ are used to fix r^*_i values. The momentum equation is solved together with the eddy viscosity model for a given value of R_t thereby establishing the $\epsilon^*(r^*)$ profile. The energy equation is then solved through an iterative procedure. Iterates are repeated until a prescribed convergence criterion is satisfied. Having established dT^*/dr^* profile, the temperature profile is extracted using the wall boundary condition, i.e., $T^*_{N+1}(r^* = 1) = 0$.

Results and Discussion

Results are obtained for a gas with a single major band for both the laminar and turbulent cases. A preliminary study to compare the Galerkin technique with the numerical iteration procedure applied to a radiating laminar flow showed that the former is more appropriate. The Galerkin method was found to be faster and requires less core storage in the machine. A maximum of seven terms were needed in the series representation of the dimensionless temperature T^*.

For the turbulent case, the numerical iteration method was found to be the appropriate one when compared with the Galerkin method. It is difficult to construct a continuous trial function that has a linear behavior in the viscous sublayer and logarithmic behavior in the core region. Also a large number of terms were needed in the series representation of T^*. Fifty-one node points were employed in the iteration scheme.

Established Turbulent Radiating Flow in a Pipe. Table 1 gives computed values of convective, radiative, and total Nusselt numbers, the center-line-to-bulk temperature ratio and the wall layer transmissivity factor for $\mathrm{R}_t = 500$ and 2000. The table covers a range of τ_R from 0.1 to 200 and N_{rm} from 0 to 30. Turbulent Prandtl number was assumed to be 0.9. A radially-varying turbulent Prandtl number was tested in preliminary studies, but the effect was found to be insignificant.

The radiative contribution to the total heat transfer grows very nearly linearly with N_{rm} as may be seen in the table. For engineering estimations one can predict values of Nu_R at high values of N_{rm} from values at low N_{rm}, simply by linear extrapolation. Increasing the optical depth, measured by τ_R, increases the radiative Nusselt number with a rate that decreases with increasing τ_R.

Increasing R_t increases appreciably the radiative Nusselt number as may be seen from the following short table that gives Nu_R for $\tau_R = 10$.

	Nu_R		
N_{rm}	$\mathrm{R}_t = 500$	$\mathrm{R}_t = 1000$	$\mathrm{R}_t = 2000$
1.0	5.58	5.82	5.99
10.0	55.1	57.7	59.6
30.0	163.0	170.9	177.0

The behavior is due to less blockage of radiation achieved by a thinner boundary layer, which results from increasing turbulence, measured by R_t. At low values of N_{rm} the convective transfer dominates, and R_t becomes the parameter that controls the total transfer of energy. For a transparent medium ($N_{rm} = 0$) and $\mathrm{Pr} = 0.7$, calculations show two features.

R_t	Re_D	Nu_C	$\mathrm{Nu}_C \doteq 0.022\,\mathrm{Pr}^{0.6}\mathrm{Re}^{0.8}$
500	16,900	44.8	42.8
1000	37,185	82.3	80.5
2000	80,650	151.2	149.5

First, increasing R_t increases markedly the convective transfer at the wall, and, second, the predicted values are in very good

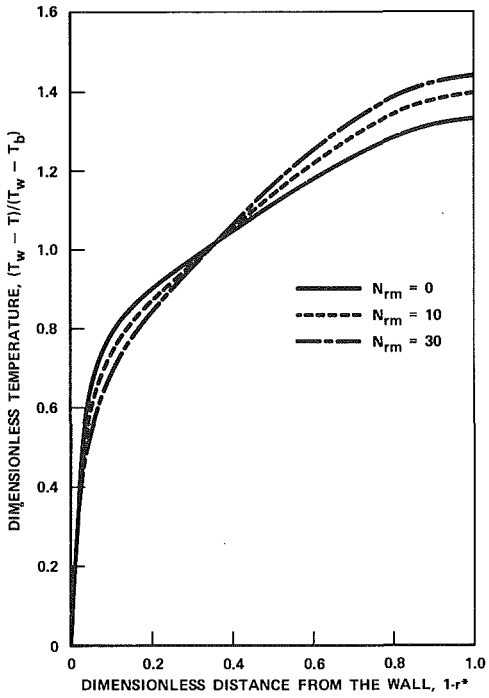

Fig. 1(*a*) $R_t = 500$

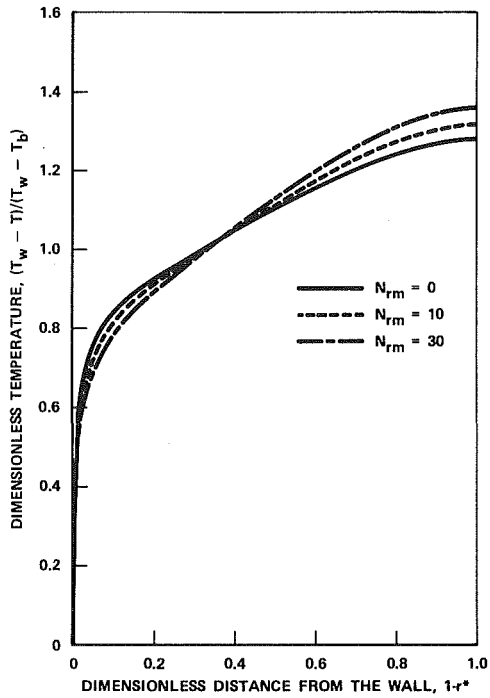

Fig. 1(*b*) $R_t = 2000$

Fig. 1 Dimensionless temperature profiles of an established turbulent flow, $\tau_R = 50$

agreement with the turbulent, constant-heat-flux, empirical formula [20]. Values of Nu_C are based on the bulk temperature.

Radiation does decrease the difference between the wall temperature and the centerline temperature, and the higher N_{rm}, the smaller this difference will be, because the gas is being heated by a constant wall heat flux. In other words, the gas in the core becomes hotter with increasing radiation, and the gas near the wall becomes colder in order to have the same bulk temperature. For the same mass flow rate, a given wall heat flux, and a given bulk temperature, the wall temperature becomes less with increasing radiation. The total Nusselt number increases with radiation, because it can be written as $(q_w 2R)/[k_m(T_w - T_b)]$, and the smaller is $(T_w - T_b)$, produced by higher N_{rm}, the higher Nu_T is, as can be seen from Table 1. Landram, Greif, and Habib [7] studied established turbu-

Table 1 Established turbulent pipe flow of a radiating gas $R_t = 500$ ($Re_D = 16{,}900$) and $R_t = 2000$ ($Re_D = 80{,}650$)

N_{rm}		τ_R=0.1		τ_R=1		τ_R=10		τ_R=50		τ_R=100		τ_R=200	
		R_t=500	R_t=2000	R_t=500	R_t=2000	R_t=500	R_t=2000	R_t=500	R_t=2000	R_t=500	R_t=2000	R_t=500	R_t=2000
0.0	Nu_C	44.774	151.758	44.774	151.758	44.774	151.758	44.774	151.758	44.774	151.758	44.774	151.758
	Nu_R	0.0	0.0	0.0	0.0	0.0	0.0	0.0	0.0	0.0	0.0	0.0	0.0
	Nu_T	44.774	151.758	44.774	151.758	44.774	151.758	44.774	151.758	44.774	151.758	44.774	151.758
	θ	1.327	1.277	1.327	1.277	1.327	1.277	1.327	1.277	1.327	1.277	1.327	1.277
0.1	Nu_C	44.775	151.758	44.777	151.759	44.767	151.735	44.751	151.698	44.749	151.685	44.749	151.675
	Nu_R	0.036	0.037	0.232	0.239	0.559	0.600	0.684	0.777	0.709	0.828	0.723	0.863
	Nu_T	44.811	151.795	45.009	151.998	45.326	152.335	45.435	152.475	45.458	152.513	45.472	152.538
	θ	1.327	1.277	1.327	1.277	1.327	1.277	1.328	1.278	1.328	1.278	1.328	1.278
	$\tau_{w\ell}$	0.9489	0.9752	0.9233	0.9511	0.8079	0.8670	0.6747	0.7665	0.6153	0.7185	0.5600	0.6685
1.0	Nu_C	44.778	151.760	44.803	151.763	44.711	151.532	44.561	151.165	44.538	151.034	44.539	150.944
	Nu_R	0.358	0.367	2.321	2.394	5.580	5.993	6.805	7.757	7.054	8.258	7.193	8.605
	Nu_T	45.136	152.127	47.124	154.157	50.291	157.525	51.366	158.922	51.592	159.292	51.732	159.548
	θ	1.327	1.277	1.326	1.277	1.332	1.279	1.337	1.281	1.337	1.281	1.337	1.282
	$\tau_{w\ell}$	0.9436	0.9673	0.9237	0.9527	0.8063	0.8660	0.6713	0.7652	0.6121	0.7166	0.5572	0.6665
10.0	Nu_C	44.807	151.776	45.059	151.813	44.544	149.674	43.787	146.432	43.773	145.336	43.901	144.614
	Nu_R	3.584	3.674	23.210	23.932	55.113	59.601	65.861	76.298	67.902	80.837	69.027	83.906
	Nu_T	48.391	155.450	68.269	175.745	99.657	209.275	109.648	222.730	111.675	226.173	112.927	228.520
	θ	1.326	1.277	1.323	1.277	1.365	1.296	1.392	1.311	1.395	1.315	1.394	1.317
	$\tau_{w\ell}$	0.9446	0.9684	0.9237	0.9524	0.7964	0.8613	0.6497	0.7526	0.5892	0.7015	0.5347	0.6499
30.0	Nu_C	44.872	151.812	45.598	151.926	45.500	146.436	45.278	138.839	45.662	136.517	46.179	135.131
	Nu_R	10.753	11.022	69.638	71.821	163.040	177.022	190.722	222.414	195.642	233.880	198.508	241.379
	Nu_T	55.625	162.834	115.236	223.747	208.540	323.458	236.000	361.253	241.304	370.397	244.687	376.510
	θ	1.324	1.277	1.318	1.277	1.396	1.323	1.436	1.357	1.437	1.364	1.434	1.367
	$\tau_{w\ell}$	0.9447	0.9684	0.9238	0.9527	0.7853	0.8527	0.6271	0.7313	0.5659	0.6765	0.5125	0.6232

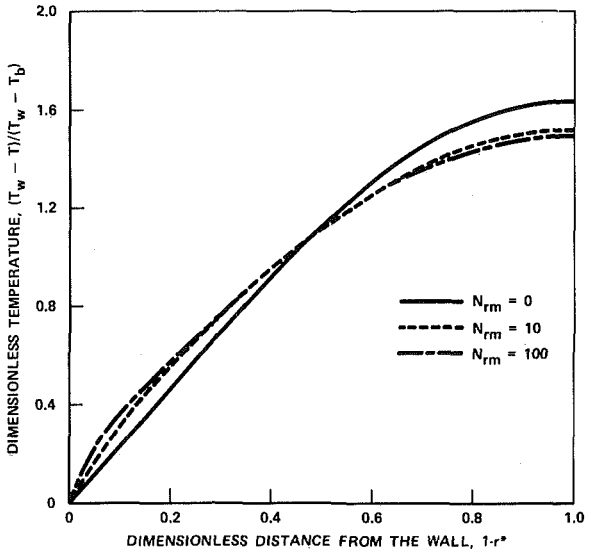

Fig. 2 Dimensionless temperature profiles of an established radiating laminar flow, $\tau_R = 50$

lent flows in a pipe with optically thin radiation and found that $(T_w - T)$ decreases and Nu_T increases with increase in radiation, which agrees with the present results.

Figs. 1(*a*) and 1(*b*) show plots of normalized dimensionless temperature profiles as function of N_{rm} for different R_t. The peak-to-mean temperature ratio θ is found to increase with N_{rm} except in thin limit of radiation where θ decreases slightly with N_{rm}, as can be seen in Table 1. It should be noted that both T^*_{c1} and T^*_b decrease with increasing N_{rm}, and the normalized dimensionless temperature profiles do intersect in such a way that the integrated T^*/T^*_b becomes unity for all cases.

The figures show that the action-at-a-distance effect of radiative transfer is to thicken the thermal wall layer in a highly turbulent flow. Thus, the convective contribution to the wall heat flux actually decreases while the total flux strongly increases with increasing radiation as measured by either N_{rm} or τ_R. This behavior was noted previously [13, 14].

The transmissivity factor is found to increase with increasing R_t due to the resulting thinner boundary layer, and decreases with increasing τ_R.

Table 2 Established laminar pipe flow of a radiating gas

N_{rm}		τ_R=0.1	τ_R=1	τ_R=10	τ_R=50	τ_R=100	τ_R=200
0.0	Nu_C	4.364	4.364	4.364	4.364	4.364	4.364
	Nu_R	0.0	0.0	0.0	0.0	0.0	0.0
	Nu_T	4.364	4.364	4.364	4.364	4.364	4.364
	θ	1.636	1.636	1.636	1.636	1.636	1.636
0.1	Nu_C	4.365	4.385	4.457	4.474	4.474	4.474
	Nu_R	0.027	0.172	0.341	0.368	0.374	0.378
	Nu_T	4.392	4.556	4.798	4.842	4.848	4.852
	θ	1.636	1.634	1.629	1.629	1.629	1.629
	$\tau_{w\ell}$	0.7116	0.6845	0.4928	0.363	0.3246	0.2928
1.0	Nu_C	4.376	4.562	5.186	5.309	5.303	5.295
	Nu_R	0.275	1.724	3.496	3.808	3.877	3.926
	Nu_T	4.651	6.286	8.682	9.117	9.180	9.220
	θ	1.634	1.614	1.584	1.585	1.585	1.585
	$\tau_{w\ell}$	0.7248	0.6861	0.5052	0.3756	0.3364	0.3041
10.0	Nu_C	4.481	5.765	9.052	8.998	8.741	8.555
	Nu_R	2.756	17.682	37.721	42.194	43.109	43.721
	Nu_T	7.236	23.447	46.773	51.192	51.850	52.276
	θ	1.617	1.528	1.501	1.515	1.517	1.517
	$\tau_{w\ell}$	0.7264	0.7037	0.5451	0.4162	0.3741	0.3386
100.0	Nu_C	5.057	10.054	16.066	12.741	11.838	11.283
	Nu_R	27.958	183.388	407.782	456.827	464.590	469.551
	Nu_T	33.015	193.442	423.848	469.568	476.428	480.834
	θ	1.545	1.464	1.473	1.494	1.497	1.498
	$\tau_{w\ell}$	0.7369	0.7298	0.5893	0.4506	0.4032	0.3637

Established Laminar Radiating Flow in a Pipe. Table 2 shows a list of convective, radiative, and total Nusselt numbers, center line to bulk temperature ratios, and transmissivity factors for τ_R from 0.1 to 200 and for N_{rm} from 0 to 100.

Similar to the turbulent case, the radiative Nusselt number grows nearly linearly with N_{rm}. Radiation transfer dominates the total transfer at high values of N_{rm}. The radiative contribution also increases with increasing τ_R at a rate that decreases with increasing τ_R.

Convective Nusselt number increases markedly with increasing N_{rm}, in contrast to the high turbulent case. For example, Nu_C increases from the well-known value of 4.364 to a value as high as 3 times that when N_{rm} increases from 0 to 100. This behavior is due to the fact that radiation tends to isothermalize the core of a laminar flow and thus steepens the temperature gradient near the wall as shown in Fig. 2. There is a decrease in the difference between the wall and center-line temperatures as well as the difference between the wall temperature and the bulk temperature. The quantity T^*/T^*_b near the wall becomes higher, and T^*/T^*_b in the core region must decrease in order to result in the same bulk temperature when increasing N_{rm}. The ratio T^*_{c1}/T^*_b decreases with increasing N_{rm}. The curve marked $N_{rm} = 0$ in Fig. 2 represents a plot of the exact solution of the energy equation, equation (30). The transmissivity factor increases with N_{rm} and decreases with increase in τ_R.

It remains now to compare the present established pipe flow case with the volume heat source case, presented in reference [17]. One can regard the comparison of Nusselt numbers as the comparing of wall to bulk temperature difference for a fixed wall heat flux. Consider the following table for $\tau_R = 50$.

		R_t = 500		R_t = 1000		R_t = 2000	
N_{rm}		$\dot{Q}_V$	q_w	$\dot{Q}_V$	q_w	$\dot{Q}_V$	q_w
1.0	Nu_C	50.0	44.6	88.8	81.8	160.8	151.2
	Nu_R	7.3	6.8	7.7	7.3	8.1	7.8
	Nu_T	57.3	51.4	96.5	89.1	168.9	159.0
10.0	Nu_C	51.8	43.8	87.8	78.8	157.7	146.4
	Nu_R	71.7	65.9	76.1	71.6	79.9	76.3
	Nu_T	123.5	109.7	163.9	150.4	237.6	222.7
30.0	Nu_C	57.3	45.3	88.0	75.7	153.1	138.8
	Nu_R	211.0	190.7	223.0	207.2	234.9	222.4
	Nu_T	268.3	236.0	311.0	282.9	388.0	361.2

where $\dot{Q}_V$ and q_w denote the volume heat source and established pipe flow cases, respectively. The foregoing table shows that Nu_C for the volume heat source case is higher than Nu_C for established pipe flow. For example, for R_t = 500, $Nu_C(\dot{Q}_V)$ is 11 and 26 per cent higher than $Nu_C(q_w)$ for N_{rm} = 1 and 30, respectively. For R_t = 2000, $Nu_C(Q_V)$ is only 6.4 and 10 per cent higher than $Nu_C(q_w)$ for N_{rm} = 1, 30, respectively. A radiative Nusselt number of an established turbulent flow is less than that of the volume heat source case: $Nu_R(\dot{Q}_V)$, at R_t = 500, is higher than $Nu_R(q_w)$ by approximately 7.4 –10.6 percent when N_{rm} increases from 1 to 30. However, this deviation becomes less with increasing R_t; for example, at R_t = 2000, $Nu_R(\dot{Q}_V)$ is only 3.8 and 5.6 percent higher than those of established flow for N_{rm} = 1, 30, respectively.

Summary and Conclusions

The results in Tables 1 and 2 permit one to estimate combined convective and radiative transfer rates rather simply for hydrodynamically and thermally established pipe flow. With the aid of a friction factor chart one uses equation (19*a*) to find the turbulent

parameter R_t. One computes τ_R according to equation (9) and N_{rm} according to equation (12). These latter two quantities are unambiguously found for a gas with a single strong absorption band, and reference [14] suggests how to estimate equivalent values for a multiband gas as well as giving guides as to where to find the requisite gas radiation property data. With these values Table 1 or 2 can be entered to find radiative and convective Nusselt numbers. Linear interpolation with N_{rm} can be made. Logarithmic interpolation with $\tau_R \geq 1.0$ and linear interpolation with $\tau_R < 0.1$ is appropriate. For a nonblack gray wall, a lower bound can be found by reducing the radiative Nusselt number by the wall emissivity, while the black wall result is clearly an upper bound.

References

1 Viskanta, R., "Interaction of Heat Transfer by Conduction, Convection, and Radiation in Radiating Fluids," JOURNAL OF HEAT TRANSFER, TRANS. ASME, Series C, Vol. 85, 1963, pp. 318–328.

2 Einstein, T. H., "Radiant Heat Transfer in Absorbing Gases Enclosed in a Circular Pipe With Conduction, Gas Flow and Internal Heat Generation," NASA TR R-156, 1963.

3 Nichols, L. D., "Temperature Profile in the Entrance Region of an Annular Passage Considering the Effects of Turbulent Convection and Radiation," *International Journal of Heat and Mass Transfer*, Vol. 8, 1965, pp. 589–607.

4 deSoto, S., "Coupled Radiation, Conduction and Convection in Entrance Region Flow," *International Journal of Heat and Mass Transfer*, Vol. 11, 1968, pp. 39–53.

5 Pearce, B. E., and Emery, A. F., "Heat Transfer by Thermal Radiation and Laminar Forced Convection to an Absorbing Fluid in the Entry Region of a Pipe," JOURNAL OF HEAT TRANSFER, TRANS. ASME, Series C, Vol. 92, 1970, pp. 221–230.

6 Kesten, A. S., "Radiant Heat Flux Distribution in a Cylindrically Symmetric Nonisothermal Gas With Temperature Dependent Absorption Coefficient," *J. Quant. Spectrosc. Radiat. Transfer*, Vol. 8, 1968, pp. 419–434.

7 Landram, C. S., Greif, R., and Habib, I. S., "Heat Transfer in Turbulent Pipe Flow With Optically Thin Radiation," JOURNAL OF HEAT TRANSFER, TRANS. ASME, Series C, Vol. 91, 1969, pp. 330–336.

8 Tiwari, S. N., and Cess, R. D., "Heat Transfer to Laminar Flow of Nongray Gases Through a Circular Tube," *Applied Sci. Res.*, Vol. 25, 1971, pp. 155–162.

9 Edwards, D. K., and Wassel, A. T., "The Radial Radiative Heat Flux in a Cylinder," JOURNAL OF HEAT TRANSFER, TRANS. ASME, Series C, Vol. 95, 1973, pp. 276–277.

10 Chiba, Z., and Greif, R., Discussion of "Nongray Radiative Transport in a Cylindrical Medium," JOURNAL OF HEAT TRANSFER, TRANS. ASME, Series C, 1973, p. 142.

11 Jeng, D. R., Lee, E. J. and DeWitt, K. J., "Simultaneous Conductive, Convective, and Radiative Heat Transfer for Laminar Flow in Circular Tubes With Constant Wall Temperature," *Heat Transfer 1974*, Vol. I, pp. 118–122, *Proceedings of the Fifth International Heat Transfer Conference*, Tokyo, Japan, Sept. 3–7, 1974.

12 Tien, C. L., and Lowder, J. E., "A Correlation for Total Band Absorptance of Radiating Gases," *International Journal of Heat and Mass Transfer*, Vol. 9, 1966, pp. 698–701.

13 Edwards, D. K., and Balakrishnan, A., "Nongray Radiative Transfer in a Turbulent Gas Layer," *International Journal of Heat and Mass Transfer*, Vol. 66, 1973, pp. 1003–1015.

14 Edwards, D. K., and Balakrishnan, A., "Self-Absorption of Radiation in Turbulent Molecular Gases," *Combustion and Flame*, Vol. 20, 1973, pp. 401–417.

15 Wassel, A. T., and Edwards, D. K., "Molecular Gas Band Radiation in Cylinders," JOURNAL OF HEAT TRANSFER, TRANS. ASME, Series C, 1974, pp. 21–26.

16 Edwards, D. K, and Menard, W. A., "Comparison of Models for Correlation of Total Band Absorption," *Applied Optics*, Vol. 3, 1964, pp. 621–625.

17 Wassel, A. T., Edwards, D. K., and Catton, I., "Molecular Gas Radiation and Laminar or Turbulent Heat Diffusion in a Cylinder With Internal Heat Generation," *International Journal of Heat and Mass Transfer*, Vol. 18, 1975, pp. 1267–1276.

18 van Driest, E. R., "On Turbulent Flow Near a Wall," *J. Aeronaut. Sci.*, Vol. 23, 1956, pp. 1007–1011.

19 Patankar, S. V., and Spalding, D. B., *Heat and Mass Transfer in Boundary Layers*, Morgan Grampian, London, 1967.

20 Kays, W. M., *Convective Heat and Mass Transfer*, McGraw-Hill, New York, 1966.

21 Blom, J., "An Experimental Determination of the Turbulent Prandtl Number in a Developing Temperature Boundary Layer," *Heat Transfer 1970*, Vol. II, Paper FC2.2, *Proceedings of the Fourth International Heat Transfer Conference*, Paris-Versailles, Aug. 1970.

22 Deissler, R. G., "Analytical and Experimental Investigation of Adiabatic Turbulent Flow in Smooth Tubes," NACA Tech. Note 2138, July 1950.

M. Epstein
D. H. Cho

Argonne National Laboratory, Reactor Analysis and Safety Division, Argonne, Ill.

Laminar Film Condensation on a Vertical Melting Surface

Laminar film condensation of a saturated vapor on a vertical melting surface is treated theoretically, with emphasis on departures from a previous treatment produced by: (a) arbitrary liquid Prandtl numbers and (b) condensation-melting systems involving two materials of immiscible liquids. An integral method is utilized which takes full account of the effects of both liquid film inertia and shear force at the condensing vapor-liquid film interface. For a one-component system accurate numerical results for the melting rates are displayed graphically and define the range of validity of a simple treatment of this problem based on Nusselt's method. For a two-component system, illustrative calculations are made for the condensation of a refrigerant vapor on melting ice.

Introduction

The heat transfer problem involved in simultaneous vapor condensation and melting of the condensing surface has been analyzed by Tien and Yen [1][1] and more recently by Yen, Zehnder, Zavoluk, and Tien [2]. The former study treats a pure vapor condensing on a vertical melting solid, while the latter study is concerned with the effect of noncondensable gases on film condensation-melting heat transfer. These workers assumed that the condensing vapor and the melting solid are of the same material and that the Prandtl number of the material is much greater than unity. The present analysis considers a gravity-flow, condensation-melting system involving two materials of immiscible liquids. In addition, the analysis accounts for the effects of arbitrary Prandtl number and the subcooling of the solid material below its melting temperature. These effects can be important in several applications of technical interest. For example, in the freeze-desalination process, ice is melted by direct contact with a refrigerant vapor that is insoluble in water [3, 4]. Also, the melting attack of structural materials (e.g., steel) by metal vapors or ceramic fuel vapors is of interest in safety studies of fast-breeder nuclear reactors [5].

The mathematical formulation of the problem is similar to the boundary-layer analysis developed by Koh, Sparrow, and Hartnett [6] in their classic paper on laminar film condensation, except that we allow for mass addition at the solid surface due to melting. Results are obtained from an integral solution of the boundary-layer equations. The reliability of the present integral method is established by comparing its predictions to available exact (similarity) solutions for laminar film condensation in the absence of melting [6] and for laminar film condensation with melting when only one material having a large liquid Prandtl number is considered [1]. The problem involves a large number of independent physical parameters. Accordingly, we propose to proceed by considering (i) a one-component problem for a wide range of Prandtl numbers and (ii) a two-component problem for physical parameter values that correspond roughly to the technologically important organic vapor-ice systems. Numerical results for the one-component system are displayed graphically and define the range of validity of a simple treatment of this problem based on Nusselt's method [7].

Physical Model

A schematic diagram of the physical model and coordinate system is presented in Fig. 1. A relatively cold vertical solid surface (material 2) is exposed to a large volume of pure hot vapor (material 1). The heat released due to vapor condensation on the solid surface is divided among energy convection by the falling condensate-melt film, melting of the solid, and heat conduction into the solid. The liquids from melting and condensation are assumed to flow side by side as a composite laminar falling film; i.e., dropwise condensation of the vapor onto the melt layer does not occur. The temperature at the melting surface is the melting temperature, T_{mp}, of the solid material. The temperature of the solid far from the melt interface is maintained at $T_0 (T_0 < T_{mp})$, while the vapor is saturated at its temperature $T_v (T_v > T_{mp})$. Phase transformations occur under steady-state conditions. In order to simplify the analysis, the coordinate system chosen is fixed to the vapor condensate-melt interface. In this coordinate system, the interior of the solid moves toward the stationary melting surface with constant velocity equal to the melting velocity. While the melting rate is a function of x, it is assumed here that the geometry change of the melting surface can be neglected. In addition, as is usual in theories of laminar film condensation, we neglect effects related to liquid film surface instabilities. Finally, physical properties that appear in the governing equations are considered to be constant.

[1] Numbers in brackets designate References at end of paper.

Contributed by the Heat Transfer Division for publication in the JOURNAL OF HEAT TRANSFER. Manuscript received by the Heat Transfer Division September 8, 1975. Paper No. 76-HT-AA.

Analysis

Governing Equations. The underlying boundary layer equations incorporating the aforementioned assumptions are similar to those developed in reference [6] and need not be repeated here. These partial differential equations can be transformed to ordinary differential equations by the following similarity transformations for the liquid condensate layer (material 1) and melt layer (material 2):

(i) Liquid condensate layer.

$$\eta_1 = \left(\frac{g}{4\nu_1^2 x}\right)^{1/4} y \tag{1}$$

$$u_1 = 2(gx)^{1/2}\frac{dF_1}{d\eta_1} \tag{2}$$

$$v_1 = \left(\frac{\nu_1^2 g}{4x}\right)^{1/4}\left(\eta_1\frac{dF_1}{d\eta_1} - 3F_1\right) \tag{3}$$

(ii) Melt layer.

$$\eta_2 = \left(\frac{g}{4\nu_2^2 x}\right)^{1/4} y \tag{4}$$

$$u_2 = 2(gx)^{1/2}\frac{dF_2}{d\eta_2} \tag{5}$$

$$v_2 = \left(\frac{\nu_2^2 g}{4x}\right)^{1/4}\left(\eta_2\frac{dF_2}{d\eta_2} - 3F_2\right) \tag{6}$$

The momentum and energy equations for the film-by-film flow then become:

$$F_1''' + 3F_1F_1'' - 2(F_1')^2 + 1 = 0 \tag{7}$$

$$\theta_1'' + 3\mathrm{Pr}_1F_1\theta_1' = 0 \tag{8}$$

$$F_2''' + 3F_2F_2'' - 2(F_2')^2 + 1 = 0 \tag{9}$$

$$\theta_2'' + 3\mathrm{Pr}_2F_2\theta_2' = 0 \tag{10}$$

where the superscript prime denotes differentiation with respect to η_1 or η_2 and θ_1 and θ_2 are dimensionless temperatures defined by

$$\theta_1(\eta_1) = \frac{T_1(\eta_1) - T_{mp}}{T_v - T_{mp}} \tag{11}$$

$$\theta_2(\eta_2) = \frac{T_2(\eta_2) - T_{mp}}{T_v - T_{mp}} \tag{12}$$

The boundary layer equations for each film are connected through compatability conditions at the liquid condensate-melt interface ($y = 0$). These conditions are

$$\mu_1\left(\frac{\partial u_1}{\partial y}\right)_{y=0} = \mu_2\left(\frac{\partial u_2}{\partial y}\right)_{y=0},\quad k_1\left(\frac{\partial T_1}{\partial y}\right)_{y=0} = k_2\left(\frac{\partial T_2}{\partial y}\right)_{y=0} \tag{13}$$

$$u_1(x, 0) = u_2(x, 0),\quad v_1(x, 0) = v_2(x, 0) = 0,\quad T_1(x, 0) = T_2(x, 0) \tag{14}$$

In terms of the transformed variables they become

$$F_1''(0) = aF_2''(0),\quad \theta_1'(0) = b\theta_2'(0) \tag{15}$$

$$F_1'(0) = F_2'(0),\quad F_1(0) = F_2(0) = 0,\quad \theta_1(0) = \theta_2(0) \tag{16}$$

where

$$a = \left(\frac{\rho_2\mu_2}{\rho_1\mu_1}\right)^{1/2} \tag{17}$$

$$b = \frac{k_2}{k_1}\left(\frac{\nu_1}{\nu_2}\right)^{1/2} \tag{18}$$

Koh, Sparrow, and Hartnett [6] have shown that the shear force at the liquid condensate-vapor interface ($y = \delta_1$) is not negligible at high rates of condensation of low Prandtl number liquids. Denny and Mills [8] have shown that for gravity-flow film condensation, the shear force at the vapor interface is equal to the momentum given up by the condensing vapor. Thus, the momentum balance at $y = \delta_1$ is

$$\nu_1\left(\frac{\partial u_1}{\partial y}\right)_{y=\delta_1} = \left[u_1\left(v_1 - u_1\frac{d\delta_1}{dx}\right)\right]_{y=\delta_1} \tag{19}$$

Energy conservation at the liquid condensate-vapor interface requires that

$$k_1\left(\frac{\partial T_1}{\partial y}\right)_{y=\delta_1} = -L_v\rho_1\left[v_1 - u_1\frac{d\delta_1}{dx}\right]_{y=\delta_1} \tag{20}$$

After introducing the transformed variables, equations (19) and (20) take the form

$$F_1''(\eta_{\delta_1}) + 3F_1(\eta_{\delta_1})F_1'(\eta_{\delta_1}) = 0 \tag{21}$$

$$-N_1\theta_1'(\eta_{\delta_1}) + 3\mathrm{Pr}_1F_1(\eta_{\delta_1}) = 0 \tag{22}$$

where N_1 is the condensation parameter defined by

$$N_1 = \frac{c_1(T_v - T_{mp})}{L_v} \tag{23}$$

The temperature condition $T_1 = T_v$ at $y = \delta_1$ results in

Nomenclature

a = dimensionless $\rho\mu$ ratio, equation (17)
b = dimensionless $k/\nu^{1/2}$ ratio, equation (18)
c = heat capacity
F_1, F_2 = dimensionless similarity velocity variables
g = acceleration due to gravity
k = thermal conductivity
L_f = latent heat of fusion for material 2
L_v = latent heat of vaporization for material 1
$\dot{m}_s$ = local rate of melting at the solid surface per unit area
$\dot{m}_v$ = local rate of vapor condensation per unit area
$\dot{m}_{s,\mathrm{Nu}}$ = local melting rate based on the Nusselt approximation
$\dot{m}_{v,\mathrm{Nu}}$ = local condensation rate based on the Nusselt approximation
N_1 = condensation parameter, equation (23)
N_2 = melting parameter, equation (27)
Pr = liquid Prandtl number
t_{ss} = time to achieve steady-state temperature profile in melting solid
T = temperature
u = velocity component in x-direction
v = velocity component in y-direction
x = coordinate in the direction of flow, Fig. 1
y = transverse coordinate measured from liquid condensate-melt interface, Fig. 1
α = thermal diffusivity of melting solid
$\beta = \eta_{\delta_1}/\eta_{\delta_2}$
δ_1 = condensate film thickness
δ_2 = melt film thickness
δ_T = thermal boundary layer thickness in melting solid
η_1, η_2 = dimensionless (similarity) coordinates, equations (1) and (4)
η_{δ_1} = dimensionless condensate film thickness, $(g/4\nu_1^2x)^{1/4}\delta_1$
η_{δ_2} = dimensionless melt film thickness, $(g/4\nu_2^2x)^{1/4}\delta_2$
θ_1, θ_2 = dimensionless temperatures, equations (11) and (12)
μ = absolute viscosity
ν = kinematic viscosity
ρ = density

Subscripts

1 = liquid condensate film (material 1)
2 = melt film (material 2)
2,s = solid (material 2)
mp = melting point (material 2)
0 = conditions in the solid at large distances from the melting surface
v = vapor

$$\theta_1(\eta_{\delta_1}) = 1 \tag{24}$$

The energy conservation condition at the melting surface ($y = \delta_2$)[2] is [9]

$$k_2 \left(\frac{\partial T_2}{\partial y}\right)_{y=\delta_2} = [L_f + c_{2,s}(T_{mp} - T_0)]\rho_2 v_2(\delta_2) \tag{25}$$

Since our coordinate system is fixed to the condensate-melt interface, the solid material appears to be moving toward the film with constant mass flux $\rho_2 v_2(\delta_2)$. Equation (25) states that the heat conducted to the melting surface is equal to the heat of melting plus the sensible heat required to raise the solid temperature to the melting point. In terms of the transformed variables, equation (25) becomes

$$N_2\theta_2'(\eta_{\delta_2}) + 3\mathrm{Pr}_2 F_2(\eta_{\delta_2}) = 0 \tag{26}$$

where N_2 is the melting parameter defined by

$$N_2 = \frac{c_2(T_v - T_{mp})}{L_f + c_{2,s}(T_{mp} - T_0)} \tag{27}$$

Two other boundary conditions to be satisfied at the melting surface are $T_2 = T_{mp}$ and $u_2 = 0$, or in terms of the new variables,

$$\theta_2(\eta_{\delta_2}) = 0 \tag{28}$$

and

$$F_2'(\eta_{\delta_2}) = 0 \tag{29}$$

The local condensation rate, $\dot{m}_v$, and melting rate, $\dot{m}_s$, are

$$-\dot{m}_v = \rho_1 \left[v_1 - u_1 \frac{d\delta_1}{dx}\right] \tag{30}$$

$$\dot{m}_s = \rho_2 v_2(\delta_2) \tag{31}$$

In terms of the transformed variables, they are given by

$$\frac{\mathrm{Pr}_1 \dot{m}_v}{\rho_1 N_1}\left(\frac{4x}{\nu_1^2 g}\right)^{1/4} = \theta_1'(\eta_{\delta_1}) \tag{32}$$

and

$$\frac{\mathrm{Pr}_2 \dot{m}_s}{\rho_2 N_2}\left(\frac{4x}{\nu_2^2 g}\right)^{1/4} = \theta_2'(\eta_{\delta_2}) \tag{33}$$

It is seen from the foregoing equations that once the dimensionless temperature gradients $\theta_1'(\eta_{\delta_1})$ and $\theta_2'(\eta_{\delta_2})$ are determined, the melting rate and vapor condensation rate follow immediately. The governing conservation equations (7)–(10) combined with the boundary conditions (15), (16), (21)–(24), and (26)–(29) suffice to determine $\theta_1'(\eta_{\delta_1})$ and $\theta_2'(\eta_{\delta_2})$.

Method of Solution. Accurate predictions of melting and condensation rates can be obtained by employing the integral technique (von Karman-Pohlhausen type). To solve the problem by this computational method the governing conservation equations (7)–(10) are replaced by their integral forms[3] and physically reasonable polynomial forms for the velocity and temperature fields are postulated, involving unknown constants ("shape" factors). In the present work, a second-degree polynomial in η_1(or η_2) was used for both the velocity and temperature profiles (a quadratic velocity profile corresponds to a cubic profile for F_1 or F_2). Upon substituting the assumed profiles into the integrated conservation equations, carrying out the integrations, and making use of the boundary conditions, there follows a system of algebraic equations relating the unknown constants to the dimensionless parameters a, b, N_1, N_2, Pr_1, and Pr_2. This algebraic system only involves equations of second degree and is easily solved by simple iteration techniques. Once the constants have been determined, one can then calculate condensation and melting rates from equations (32) and (33).

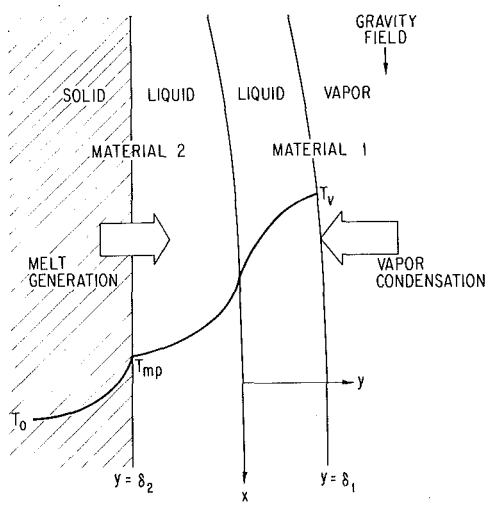

Fig. 1 Schematic diagram of composite melted solid-vapor condensate film flowing under gravity, with coordinates fixed to the liquid-liquid interface

Nusselt Approximation

In the Nusselt method, the nonlinear inertia terms in the liquid film momentum equations, the energy convection terms, and the shear forces at the vapor-liquid condensate interface are neglected. In this case, the momentum equations (7) and (9) are easily integrated to give quadratic velocity profiles in the falling composite film, and solution of the energy equations (8) and (10) results in linear temperature profiles in the film. The condensate and melt film thicknesses are determined from the following equations:

$$\eta_{\delta_1}^4 = \frac{\beta^3 N_1/\mathrm{Pr}_1}{3\left(\beta - \frac{1}{b}\right)\left(\frac{1}{3}\beta^2 - \frac{1}{a}\beta + \frac{1}{2}\right)} \tag{34}$$

and

$$\eta_{\delta_2} = \frac{\eta_{\delta_1}}{\beta} \tag{35}$$

where β is obtained by solving the cubic equation

$$\frac{1}{3}\beta^3 - \frac{1}{a}\beta^2 + \frac{1}{2}\left(1 - \frac{1}{a}\frac{bN_1\mathrm{Pr}_2}{N_2\mathrm{Pr}_1}\right)\beta + \frac{1}{3}\frac{bN_1\mathrm{Pr}_2}{N_2\mathrm{Pr}_1} = 0 \tag{36}$$

Note that the film thickness ratio β is a negative number since $\delta_1 > 0$ while $\delta_2 < 0$. The condensation and melting rates are then given by

$$\frac{\mathrm{Pr}_1 \dot{m}_{v,\mathrm{Nu}}}{\rho_1 N_1}\left(\frac{4x}{\nu_1^2 g}\right)^{1/4} = \frac{b\mathrm{Pr}_2 \dot{m}_{s,\mathrm{Nu}}}{\rho_2 N_2}\left(\frac{4x}{\nu_2^2 g}\right)^{1/4} = \frac{b}{b\eta_{\delta_1} - \eta_{\delta_2}} \tag{37}$$

Closed-form expressions can be obtained for the single material system. Setting $a = b = 1$ in the expressions (34)–(37) leads to the following form for the phase change rates:

$$\frac{\dot{m}_{v,\mathrm{Nu}}}{\rho N_1}\left(\frac{4x}{\nu^2 g}\right)^{1/4} = \frac{\dot{m}_{s,\mathrm{Nu}}}{\rho N_2}\left(\frac{4x}{\nu^2 g}\right)^{1/4} = \frac{1}{\mathrm{Pr}}\left(\frac{\mathrm{Pr}}{N_1 + N_2}\right)^{1/4} \tag{38}$$

which corresponds to equation (50) of reference [1].

The Nusselt approximations have been discussed in reference [6] for the case of gravity-flow film condensation. The conclusion is that the error in the heat transfer introduced by the Nusselt method is less than 10 percent for $\mathrm{Pr} > 1$ and the condensation parameter $N_1 < 0.5$. The validity of Nusselt's method when melting occurs may be determined by comparison with the integral-method calculations which are presented in the next section. If $\mathrm{Pr} > 1$ and $N_1 < 0.5$, the Nusselt solution is found to be accurate to within 10

[2] Note that in the coordinate system chosen here, δ_2 takes on negative values (see Fig. 1).

[3] A similar integral formulation has been used in reference [10].

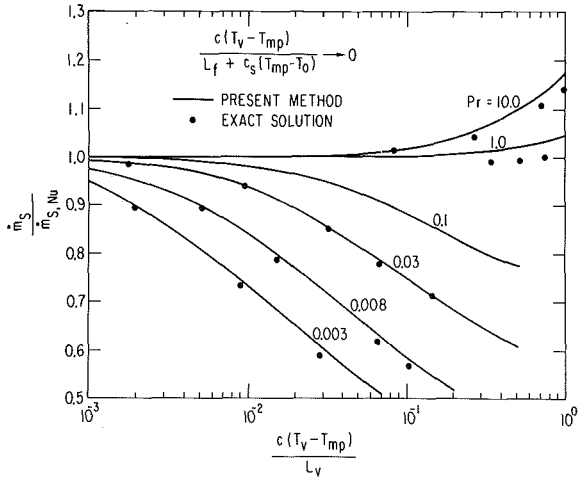

Fig. 2 Normalized melting rate in the limit $N_2/N_1 \to 0$; comparison of the present integral method with the exact (similar) solutions provided by Koh, Sparrow, and Hartnett (reference [6])

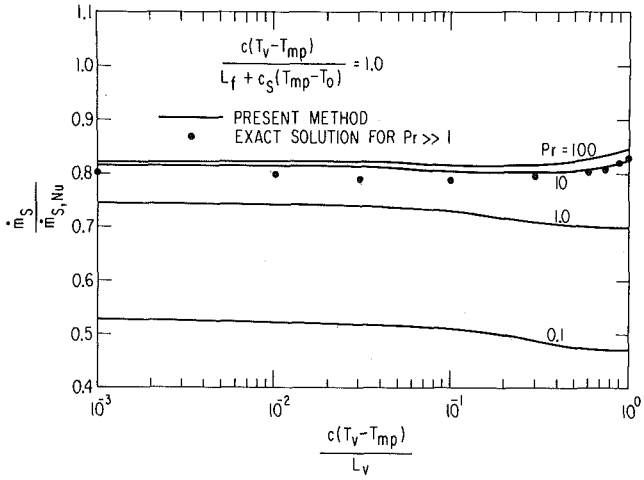

Fig. 4 Normalized melting rate for $N_2 = 1.0$; comparison of the present integral method with the exact (similar) solutions provided by Tien and Yen (reference [1])

percent providing that the melting parameter $N_2 < 0.2$. Values of N_1 less than 0.5 are quite common in terms of engineering or experimental practice. However, since L_f can be considerably less than L_v, values of N_2 as large as 10.0 are possible. This fact plus the need to consider liquid film inertia effects for low Prandtl numbers makes the usefulness of the Nusselt method rather limited.

Results and Discussion

Condensation-melting heat transfer results have been obtained via the integral method for the following cases: For the one-component system where the condensing vapor and the melting solid are of the same material, melting rates were obtained for Prandtl numbers between 0.1 and 100, for N_1 between 0.001 and 1.0, and for N_2 ranging from essentially zero to 10.0. For the two-component system, melting and condensation rates were obtained for $Pr_1 = Pr_2 = 4.0$, $a = 1.0$, and $b = 7.0$; for N_1 between 0.001 and 1.0 and for N_2 between 0.01 and 10.0. These physical parameter values are representative of organic vapors condensing on ice.

One-Component System. Melting rates are presented in Figs. 2–5, which correspond, respectively, to melting parameters (N_2) of essentially zero, 0.1, 1.0, and 10.0. Note that the melting rates are normalized by the rate predicted by the Nusselt method (equation (38)). In Fig. 2 for $N_2 \to 0$, the reliability of the present integral method is established by reproducing within 4 percent the exact (similar) solutions of Koh, Sparrow, and Hartnett [6] for gravity-flow film condensation in the absence of melting. Of course, these authors did not report a normalized melting rate but instead a heat flux to the condensing surface (normalized by the Nusselt heat flux). The two normalized quantities, however, are identical.

The effects of increasing the melting parameter N_2 are readily seen by comparing Figs. 3, 4, and 5 with Fig. 2. Turning first to Fig. 3, it is seen that, while the curves for the melting rate retain their shape, the melting rate decreases relative to the simple Nusselt value. For high Prandtl number liquids, this is due to the fact that melting creates a normal velocity at the melting surface. The interfacial velocity acts to reduce the steepness of the temperature gradient and, consequently, decrease the heat flux to the melting surface. This "self-shielding" mechanism is well-known from the study of mass transport phenomena [11]. We note that reductions in the normalized melting rate are most dramatic for the low Prandtl number liquids. This is expected, since for low Prandtl number liquids, inertia effects and liquid-vapor interfacial shear lead to reduced normalized heat fluxes, as has been established in reference [6]. These effects become more pronounced as the film

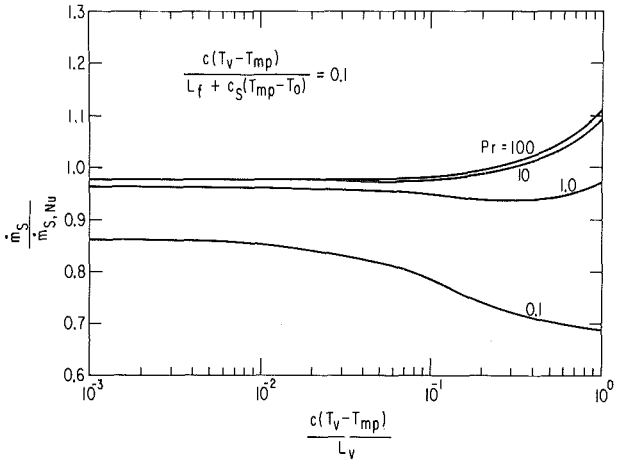

Fig. 3 Normalized melting rate; $N_2 = 0.1$

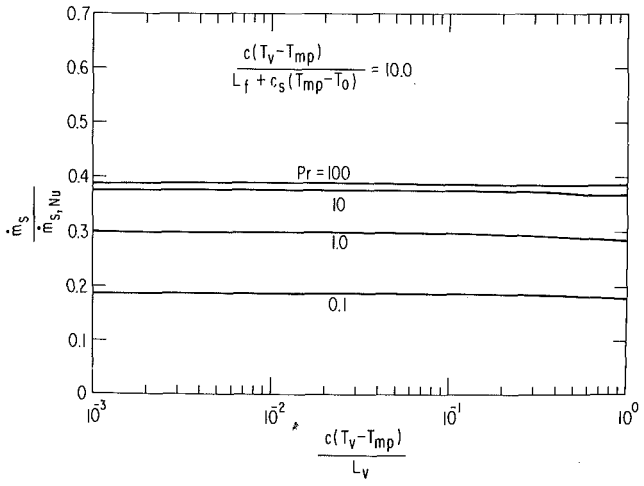

Fig. 5 Normalized melting rate; $N_2 = 10.0$

thickness increases with melting (i.e., as N_2 increases). Proceeding to Fig. 4 for $N_2 = 1.0$, we observe that increased melting causes even further reductions in the normalized melting rate; in fact, the melting rate falls below the Nusselt predictions even for high Prandtl number liquids. While increased melting tends to increase the heat flux at the melting surface due to energy convection when $Pr \gg 1$, the interfacial shielding effect appears to be large enough to dominate. The effects of melting are demonstrated even more dramatically in Fig. 5. It is seen that the melting rate is remarkably insensitive to the condensation parameter N_1. Since $N_2 \gg N_1$, the entire resistance to heat flow across the falling film is due to melting and hence the condensation parameter does not enter into the problem. In this limit, it can be shown that boundary conditions (21) and (22) simplify to $F''(\eta_{\delta_1}) = 0$ and $F(\eta_{\delta_1}) = 0$, making it relatively easy to integrate the governing equations numerically. Fig. 6 shows the results of such (exact) calculations and compares them with predictions based on the integral technique. The good agreement again demonstrates the correctness of the integral method approach.

Further indication of the reliability of the present integral method can be gained from Fig. 4, which compares melting rates as predicted by an exact (similarity) solution by Tien and Yen [1] for the case $Pr \gg 1$.[4] The maximum deviation between the present results and those of reference [1] is about 4 percent. Tien and Yen also reported an integral-method treatment of condensation-melting heat transfer. In their formulation, which is restricted to a one-component system, no distinction is made between the melt and vapor condensate components within the film. In the present formulation, the film is always treated as a two-component film-by-film flow, even if the condensing vapor and melting solid are of identical materials. This method has the advantage of properly accounting for the distortion in the temperature profile due to "blowing" effects within the film caused by simultaneous melting and condensation. The Tien-Yen method yields closed-form expressions for the melting and condensation rates; however, their results appear to be considerably less accurate than our integral solutions when the relative rate of melting to condensation is greater than unity ($N_2/N_1 > 1.0$).

It should be mentioned that since $L_v > L_f + c_s(T_{mp} - T_0)$ for most materials, the results in Figs. 3 and 4 for parameter values $N_1 > N_2$ would be of little practical significance.

Two-Component System. Here we present calculations for the case where the condensing vapor and the melting solid are of different materials of immiscible liquids. The calculations were made using physical parameter values which correspond approximately to the Freon 114-ice system (and which correspond roughly to most organic refrigerant vapor-ice systems).

The local melting rate is plotted in Fig. 7, and the local vapor condensation rate is plotted in Fig. 8. The dashed curves represent the results obtained from Nusselt's method. The increased rate of melting that accompanies increased melting parameter N_2 is illustrated in Fig. 7. It is seen that increased vapor condensation onto the melt layer (i.e., increasing N_1) decreases the rate of melting at the solid surface (for N_2 constant). This is obvious since the resistance to heat flow to the melt layer is proportional to the thickness of the liquid condensate layer. In Fig. 8, we observe a slowly increasing vapor condensation rate with increasing melting parameter N_2. This behavior differs from that of the one-component system[5] and is directly related to the large value assigned to the parameter b. Due to the relatively large thermal conductivity of the melt layer, the temperature difference across the liquid condensate film decreases slowly with increased melting rate. On the other hand, the thickness of the condensate film decreases relatively rapidly with increased melting (since it moves at a higher speed) and consequently tends to increase the vapor condensation rate.

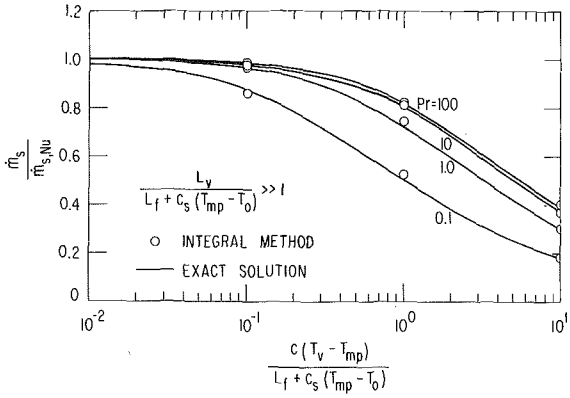

Fig. 6 Normalized melting rate for $N_2/N_1 \gg 1$; comparison of the present integral method with the exact (similar) solutions

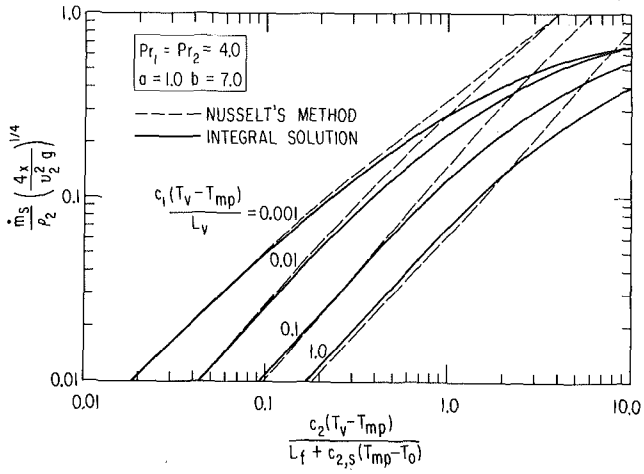

Fig. 7 Dimensionless melting rate in a two-component system; $Pr_1 = Pr_2 = 4.0$, $a = 1.0$, $b = 7.0$ (which correspond approximately to the condensation of Freon-114 vapor on melting ice)

Validity of the Model

We shall now consider some of the approximations exploited herein and examine their physical validity.

The assumption of a plane melting interface is a useful approximation when x is large enough to ensure that the film thickness and the melting rate vary slowly with x. Generally, one anticipates that the principal effect of geometry distortion in the leading edge region of the melting solid would be equivalent to some shift in the effective location of the leading edge ($x = 0$). This assumption was first exploited for solving steady-state film condensation-melting problems in references [1, 2]. It has been used extensively, however, for solving the problem of the steady melting of a flat plate in a warm laminar stream (see, e.g., [12, 13]).

As long as the melting solid is large compared with its thermal boundary layer thickness $\delta_T = \alpha/v_2(\delta_2)$, transient effects in the solid are negligible. The relaxation time to steady state, t_{ss}, is easily seen to be comparable to the time it takes the thermal wave thickness to span one steady-state boundary layer thickness, namely, $t_{ss} \sim \delta_T^2/\alpha = \alpha/[v_2(\delta_2)]^2$. Landau [14] in his classic paper

[4] Tien and Yen obtained exact similarity solutions only for melting parameters between 1.0 and 1.8. Our experience with vapor condensation problems seems to indicate that the case $Pr \gg 1$ constitutes the most stringent test of the accuracy of the integral method (see Fig. 2). This is probably due to the fact that energy convection effects are most important as $Pr \to \infty$.

[5] For the one-component system, the vapor condensation rate decreases with increasing melting parameter. This can readily be seen from the Nusselt solution, equation (38).

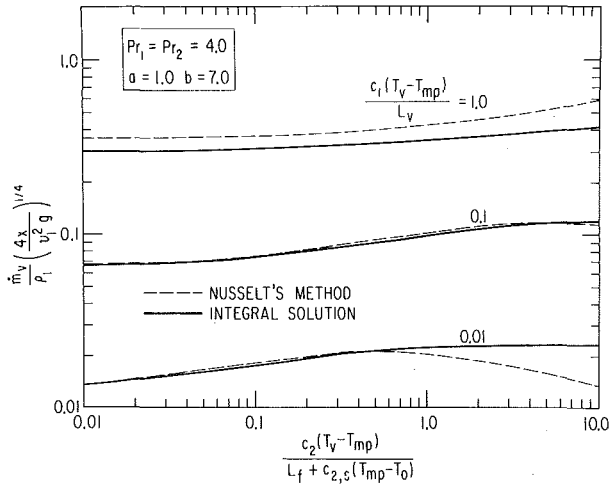

Fig. 8 Dimensionless condensation rate in a two-component system; $Pr_1 = Pr_2 = 4.0$, $a = 1.0$, $b = 7.0$ (which correspond approximately to the condensation of Freon-114 vapor on melting ice)

on heat conduction in a melting solid provides a more rigorous derivation of this criterion. In terms of the dimensionless parameters used here, we have for a single component system

$$t_{ss} \sim \frac{2(N_1 + N_2)^{1/2} x^{1/2}}{(\dot{m}_s/\dot{m}_{s,\mathrm{Nu}})^2 N_2^2 \mathrm{Pr} g^{1/2}} \tag{39}$$

As an example, we choose the typical conditions $N_2 \sim 1.0$, $N_1 \sim 0.1$, and $\mathrm{Pr} = 1.0$. For these conditions, the time required to achieve steady state is 0.07 s at $x = 1$ cm and 0.2 s at $x = 10$ cm. In steady-state melting, the effect of solid subcooling is simply to modify the heat of fusion, as indicated by equation (25) (see also references [12, 15]).

Our treatment of condensation-melting heat transfer involving two materials requires that the vapor condense as a film on the melt layer. At present, there is no direct experimental evidence to either verify or contradict the two-film description given here. However, it is reasonable to suppose that the criterion used to distinguish between film condensation and dropwise condensation on solid surfaces is applicable here [16, 17]. Namely, if the condensing material liquid spreads spontaneously on the melt layer (i.e., has a positive spreading coefficient) the vapor will condense as a film on the melt layer; if the spreading coefficient is negative, one expects the vapor to condense as drops on the melt layer. The film-by-film flow concept may still be applicable in the case of dropwise condensation, providing that the condensed drops moving on the melt layer flow together and cover large areas of the melt film below. From a consideration of spreading coefficients for organic liquids on water [18], it appears that the composite flowing film assumption is valid for many organic vapor-ice systems. We might remark that the use of a film-by-film model for immiscible liquid pairs is not without precedent. An identical approach has been used in reference [19] to treat condensation of binary vapor mixtures of immiscible liquids.

It is recognized that part of the N_1-N_2-Pr parameter space investigated here is physically unrealistic in certain condensation-melting systems. For low-viscosity liquids, values of N_1/Pr_1 and/or N_2/Pr_2 greater than unity would lead to turbulent flows beyond $x \sim 10$ cm. Nevertheless, laminar flow models can prove to be quite useful in correlating heat-transfer data for turbulent films.

Finally, it should be mentioned that in reference [2] theoretical predictions (based on a model of this type for $\mathrm{Pr} \gg 1$) of melting heat-transfer coefficients were found to be in good agreement with experiments involving steady-state steam condensation on a vertical ice plate in the presence of air.

Summary

An integral method of solution has been used for the calculation of phase-change rates during steady-state vapor condensation onto a vertical melting surface. The analysis allows for the possibility that the condensing vapor and melting solid are of different materials of immiscible liquids and accounts for the effects of both liquid film inertia and shear at the condensing vapor-liquid film interface.

The results show that for the one-component system, the parameters governing the condensation-melting process are Pr, $N_1 = c(T_v - T_{mp})/L_v$, and $N_2 = c(T_v - T_{mp})/[L_f + c_s(T_{mp} - T_0)]$. It is shown that when $N_1 \ll N_2$ the vapor condensation rate is negligibly small compared with the melting rate and hence only two parameters Pr and N_2 are important. A simple treatment of the problem based on Nusselt's method was found to overestimate the melting rates. Numerical results for the two-component system were limited to organic refrigerant vapor condensation onto melting ice. However, using the computational method presented here, other combinations of condensing vapor and melting solid may be treated with equal facility.

Acknowledgment

This work was performed under the auspices of the U. S. Energy Research and Development Administration.

References

1 Tien, C., and Yen, Y. C., "Condensation-Melting Heat Transfer," *Chem. Eng. Progr. Symposium Ser.*, Vol. 67, No. 113, 1971, pp. 1–9.

2 Yen, Y. C., Zehnder, A., Zavoluk, S., and Tien, C., "Condensation-Melting Heat Transfer in the Presence of Air," *Chem. Eng. Progr. Symposium Ser.*, Vol. 69, No. 131, 1973, pp. 23–29.

3 Weiss, P. A., "Desalination by Freezing," in *Practice of Desalination* R. Bakish, ed., Noyes Data Corp., N. J., 1973, pp. 260–270.

4 Smith, K. A., Petri, L. W., and Brian, P. L. T., "Melter-Condenser Operation: Theory and Experiment," *Ind. Eng. Chem. Process Des. Develop.*, Vol. 11, No. 4, 1972, pp. 485–490.

5 Epstein, M., and Cho, D. H., "Melting Rates for the Attack of Steel Structure by UO_2 Fuel or Steel Vapor," *Trans. Am. Nucl. Soc.*, Vol. 21, 1975, p. 311.

6 Koh, J. C. Y., Sparrow, E. M., and Hartnett, J. P., "The Two-Phase Boundary-Layer in Laminar Film Condensation," *International Journal of Heat and Mass Transfer*, Vol. 2, 1961, pp. 69–82.

7 Nusselt, W., "Die Oberflachen-Kondensation des Wasserdampfes," *Z. Ver. D-Ing.*, Vol. 60, 1916, pp. 541–546.

8 Denny, V. E., and Mills, A. F., "Nonsimilar Solutions for Laminar Film Condensation on a Vertical Surface," *International Journal of Heat and Mass Transfer*, Vol. 12, 1969, pp. 965–979.

9 Carslaw, H. S., and Jaeger, J. C., *Conduction of Heat in Solids*, Oxford University Press, Second ed., 1959, p. 292.

10 Sparrow, E. M., Minkowycz, W. J., and Saddy, M., "Forced Convection Condensation in the Presence of Noncondensables and Interfacial Resistance," *International Journal of Heat and Mass Transfer*, Vol. 10, 1967, pp. 1829–1845.

11 Spalding, D. B., *Some Fundamentals of Combustion*, Chapter 3, Buttersworths Scientific Publications, London, 1955.

12 Griffin, O. M., "Heat, Mass, and Momentum Transfer During the Melting of Glacial Ice in Sea Water," JOURNAL OF HEAT TRANSFER, TRANS. ASME, Series C, Vol. 95, 1973, pp. 317–323.

13 Pozvonkov, F. M., Shurgalskii, E. F., and Axselrod, L. S., "Heat Transfer at a Melting Flat Surface Under Conditions of Forced Convection and Laminar Boundary Layer," *International Journal of Heat and Mass Transfer*, Vol. 13, 1970, pp. 957–962.

14 Landau, H. G., "Heat Conduction in a Melting Solid," *Quart. Appl. Math.*, Vol. 8, 1950, pp. 81–94.

15 Roberts, A. L., "On the Melting of a Semi-Infinite Body Placed in a Warm Stream of Air," *J. Fluid Mech.*, Vol. 4, 1958, pp. 505–528.

16 Fox, H. W., and Zisman, W. A., "The Spreading of Liquids on Low Energy Surfaces, II. Modified Tetrafluoroethylene Polymers," *J. Colloid Sci.*, Vol. 7, 1952, p. 109.

17 Davies, G. A., and Ponter, A. B., "The Prediction of the Mechanism of Condensation on Condenser Tubes Coated With Tetrafluoroethylene," *International Journal of Heat and Mass Transfer*, Vol. 11, 1968, pp. 375–379.

18 Adam, N. K., *The Physics and Chemistry of Surfaces*, Dover, New York, 1968, pp. 209–212.

19 Marschall, E., and Hickman, R. S., "Laminar Gravity-Flow Film Condensation of Binary Vapor Mixtures of Immiscible Liquids," JOURNAL OF HEAT TRANSFER, TRANS. ASME, Series C, Vol. 95, 1973, pp. 1–5.

Y. Hayashi
Assoc. Professor.

A. Takimoto
Assistant.

M. Kanbe
Postgraduate Student.

Department of Mechanical Engineering,
Kanazawa University,
Kanazawa, Japan

Transport-Reaction Mechanism of Mist Formation Based on the Critical Supersaturation Model

The transport-reaction mechanism of mist formation in a convective field is discussed on the basis of a "critical supersaturation model." Analyses are performed for mist formation conditions, mist region, and vaporization rate, and are verified experimentally by using a naphthalene sublimation technique.

1 Introduction

Mist formation in the vaporization-condensation process is sometimes observed as "fog" or "mist" in meteorological aspects. Such a phenomenon usually should be avoided in industrial processes. For example, sodium mist formation in the Fast Breeder Reactor results in serious accidents due to the deposits of sodium inside the devices. In the case of cooler-condensers for vapors, "misting" or "throwing fog" is often associated with the loss of valuable or noxious materials in the condenser effluent.

When mist formation occurs, the concentration gradient becomes steep at the vaporizing surface, and the vaporization rate increases in comparison with the rate predicted under the assumption that vapor condensation does not occur. In this case, the critical conditions for mist formation are affected by many factors such as the presence of foreign nuclei, their characteristics, and the turbulence level in the flow field. With reference to the theoretical analysis, two basic models are suggested; a "saturation model" [1][1] and a "critical supersaturation model (C.S.M.)."

Turkdogan and Mills [2, 3] illustrated the enhancement of diffusion limited vaporization rates for the case of molten iron nickel alloys evaporating into helium, and suggested a transport-reaction mechanism based on the notion that the condition occurs where a "critical supersaturation" is achieved. Rosner [4] cast the critical supersaturation model into a more lucid and usable form with the help of several reasonable physical approximations. Epstein and Rosner [5] examined the validity of "C.S.M." for predicting mass transfer effects of nonequilibrium fog formation in a thermal boundary layer.

In this paper, the transport-reaction mechanism of mist formation in a convective field is discussed generally. Analyses are performed for mist formation conditions, mist region, and also vaporization rate for a given degree of supersaturation on the basis of the boundary layer theory, and are verified experimentally by using a naphthalene sublimation technique. Specifically this paper deals with the case of mist formation of subliming naphthalene vapor on foreign nuclei which are fully contained in the air field. This kind of mist formation is different from mist formation based on self-nucleation which is not dependent on foreign nuclei. But this condition is not unreasonable for discussing the mechanism of C.S.M., since it is considered that some degree of supersaturation must be necessary for solid state condensation on foreign nuclei. As for mist formation on foreign nuclei, several papers have been published in connection with aerosol generation. Davis and Liao [6] analyzed the aerosol growth with Poiseuille flow based on the studies of Nicolaon, et al. [7]. Davis and Nicolaon [8] examined the effect of foreign nuclei on aerosol nucleation and growth. This kind of mist formation is different from solid state condensation, which is discussed in our paper, and is treated on the basis of a saturation model.

In the present context the term "mist" is consistently employed instead of the expressions "dust" or "fume," although it is not strictly suitable in considering the fact that condensed naphthalene is solid under the experimetal temperature conditions.

2 Observations and Mechanism of Mist Formation

2.1 Experimental Apparatus and Observations. Experiments were carried out by using a vertical flat plate of solid naphthalene heated at uniform surface temperature around which laminar natural convection took place. A schematic diagram of the test setup is presented in Fig. 1. Construction of the flat plate is composed of an aluminum plate coated with naphthalene and heaters which are divided into four sections to control surface temperature. The surface temperature is measured at several fixed points by 0.1-mm copper-constantan thermocouples attached to the aluminum plate and are corrected by taking account of the tempera-

[1] Numbers in brackets designate References at end of paper.

Contributed by the Heat Transfer Division for publication in the JOURNAL OF HEAT TRANSFER. Manuscript received by the Heat Transfer Division August 20, 1975. Paper No. 76-HT-CC.

ture drop in the naphthalene layer. Velocity and temperature profiles are measured also at several positions above the plate in order to ascertain that the boundary layer is laminar. The naphthalene mist was observed by means of the scattering of a slit beam thrown parallel to the wall. Experiments were made under the condition of constant ambient temperature, $-10 \sim 20°C$, and the wall temperature was changed gradually by controlling each heater until mist had appeared. The photographs in Fig. 2 show the shape of the mist. Thus, at a certain wall temperature, a narrow mist strip appeared at some distance apart from the wall (Fig. 2 (a)). Furthermore, when the difference between wall and ambient temperature is increased, the width of the mist region tends to widen and its inner boundary (i.e., near to the wall) seems to be close to the wall (Fig. 2(b)). In any case, the inner boundary of the mist region represents a very definite profile, and therefore it would be justified to regard this boundary as the nucleation boundary. Then, the critical degree of supersaturation for naphthalene vapor crystallization on foreign nuclei is to be evaluated experimentally from the critical condition at which mist has appeared. Namely, the critical degree of supersaturation, which is defined as the ratio of partial pressure to saturation pressure at the critical mist formation point, is obtained with the help of the partial pressure profile, the temperature profile, and the Clausius-Clapeyron relation as follows:

$$S_{crit} = P_c/P_s \tag{1}$$

$$P/P_w = (1 - y/\delta'')^2 \tag{2}$$

$$\frac{T - T_\infty}{T_w - T_\infty} = (1 - y/\delta')^2 \tag{3}$$

$$P_s = \exp(A + B/T) \tag{4}$$

The partial pressure profile, equation (2), and the temperature profile, equation (3), are Squire's solutions for laminar natural convection over a vertical flat plate. A detailed discussion is found later (see Section 3.1).

Fig. 3 shows the plot of S_{crit} versus $1/T$ by experiments, and the following relation is obtained:

$$S_{crit} = \exp(-7.85 + 2795/T) = \exp(A' + B'/T) \tag{5}$$

This expression is equivalent to that suggested by Rosner [4] as $S_{crit} = \exp(A' + B'/T)$ where A' and B' are constants. The foregoing result is obtained under ordinary aerosol conditions assuming that sufficient foreign nuclei are present (i.e., number concentration of $10^4 \sim 10^5$ particles/cm^3), in the region of interest. It follows that a certain degree of supersaturation is required for naphthalene vapor crystallization on foreign nuclei, thus the analysis based on C.S.M. is justified.

2.2 Mechanism of Mist Formation in a Convective Field. Let us consider the mechanism of mist formation based on C.S.M. in the convective field. Fig. 4 shows a schematic diagram of suggested pressure profiles in the boundary layer. The solid line denotes the actual pressure profile of condensable gas, while the dotted line is for a saturation pressure profile corresponding to the temperature field, and the chained line is for the critical pressure profile required for mist formation. It can happen that the vapor pressure is much higher than the saturated vapor pressure in the boundary layer because of the pronounced decrease of vapor pressure with decreasing temperature and equilibrium condition at the vaporizing surface. In the case of (a) in Fig. 4, mist formation does not occur because the actual pressure is lower than the critical pressure at any point in boundary layer. On the other hand, when actual pressure exceeds the critical pressure at any point as shown in Fig. 4(b), the necessary condition for nucleation of the condensing phase is satisfied and mist formation occurs. With regard to the possibility of smaller steady-state fluxes, it seems reasonable to assume that once P_c has been achieved locally, the actual vapor pressure P can not exceed P_c in the cooler parts of the boundary layer. It follows that the maximum flux compatible with local attainment of P_c occurs when the actual vapor pressure profile is tangent to P_c as shown in Fig. 4(c). Here, we first confine our attention only to an arbitrary section of the flat plate ($x = x_0$) for the sake of illustration, Fig. 4(c). This tangency condition, expressed as equation (6), simultaneously defines the point N at which crystallization commences within the thermal boundary layer and thereby determines the actual steady-state vapor pressure gradient established in the presence of mist formation. Another condition for steady-state mist formation is represented as equation (7). This is a mass balance equation concerning the mist formation rate

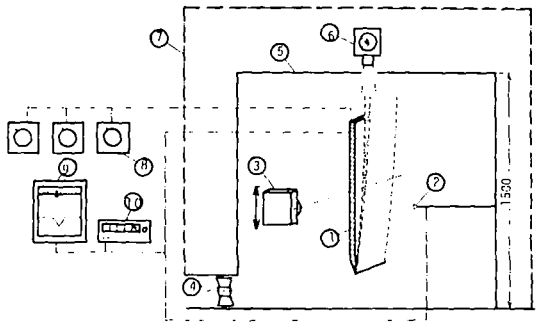

1. Heated Plate Coated with Naphthalene
2. Thermocouples
3. Camera
4. Ventilator
5. Light Chamber
6. Light Source with Collimation Slit
7. Constant Temperature Room
8. Slidac
9. Auto-Balancing Recorder
10. Digital mv-Recorder

Fig. 1 Schematic of experimental apparatus

Nomenclature

A,B = constants in equation (4)
A',B' = constants in equation (5)
C_1,C_2 = constants in equation (10)
D = diffusion coefficient
g = gravitational acceleration
Le = Lewis number
m = rate of mass flux
m_r = rate of mist formation
P = vapor pressure
P_c = critical vapor pressure
P_s = saturation vapor pressure
Pr = Prandtl number
R_v = gas constant
S_{crit} = critical degree of supersaturation
T = absolute temperature
t = temperature
u = velocity in the x-direction
v = velocity in the y-direction
x = vertical distance
y = horizontal (normal to vaporizing surface) distance
α = thermal diffusivity
β = coefficient of thermal expansion
δ = thickness of velocity boundary layer
δ' = thickness of thermal boundary layer
δ'' = thickness of vapor pressure boundary layer
δ_N = thickness of inner boundary of mist region
δ_0 = thickness of outer boundary of mist region
η = nondimensional boundary layer thickness, δ''/δ'
ξ = nondimensional thickness, δ_N/δ'
ν = kinematic viscosity

Subscripts

c = critical
N = inner boundary of mist region (nucleation point)
$-N$ = entering into point N
$+N$ = leaving from point N
0 = outer boundary of mist region
s = thermodynamic saturation
w = at wall
∞ = far from the vaporizing surface

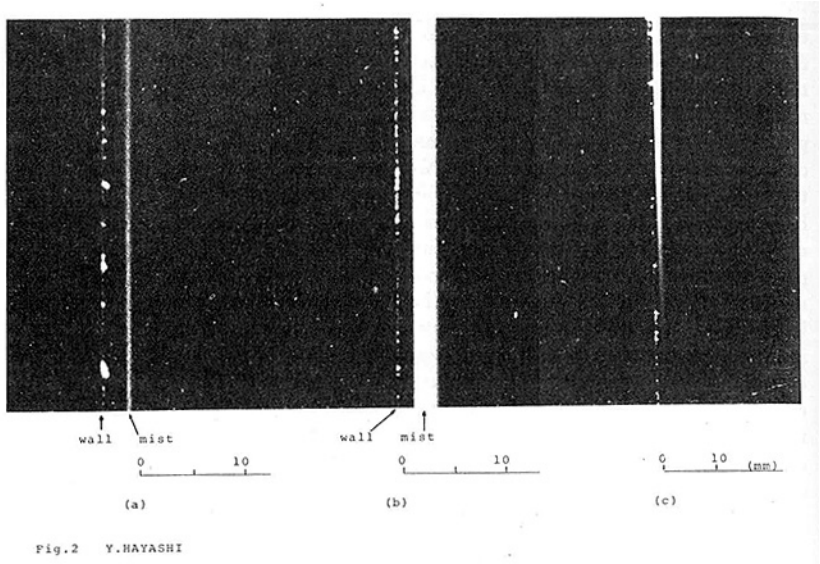

Fig. 2 Photographs of mist formation

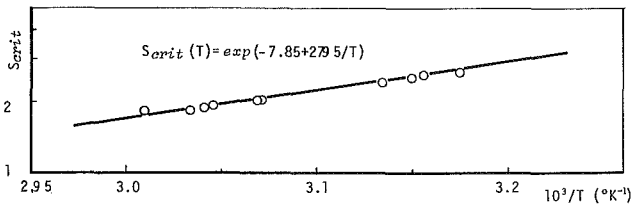

Fig. 3 Temperature dependence of the critical degree of supersaturation

m_r at point N. In steady state, m_r should not exceed the difference between the vapor flux entering into N, m_{-N} and that leaving from N, m_{+N} which is restricted by its minimum possible value corresponding to the gradient of saturation pressure profile. The mist formation rate m_r, which seems to be similar to a chemical reaction rate, depends on the concentration of foreign nuclei on which naphthalene vapor crystallizes, and on temperature of surrounding medium, etc., and thus it is expressed from the kinetic point of view as equation (10). From mass balance condition at N, the vapor flux leaving from N, m_{+N} is given as equation (11).

$$dP/dy|_N = dP_c/dy|_N,\ P_N = P_{c,N} \tag{6}$$

$$m_r \leqq m_{-N} - m'_{+N} \tag{7}$$

$$m_{-N} = -D/R_v T \cdot dP_c/dy|_N + V_N \cdot P_c/R_v T_N \tag{8}$$

$$m'_{+N} = -D/R_v T \cdot dP_s/dy|_N + V_N \cdot P_s/R_v T_N \tag{9}$$

$$m_r = C_1 \cdot \exp(-C_2/T) \tag{10}$$

$$m_{+N} = m_{-N} - m_r \tag{11}$$

The appearence of the narrow strip mist corresponds to the singular case for which the equality holds in equation (7). In this case, a sudden decrease of the actual vapor pressure occurs at point N, and drops to the saturation line corresponding to the temperature. On the other hand, in case that $m_r < m_{-N} - m'_{+N}$ also the actual vapor pressure suddenly decreases; however, a certain degree of supersaturation would be maintained at point N. This state of supersaturation continues from point N to point O, where the actual pressure line intersects the saturation pressure line. Thus, excessive vapor as shown $N'O$ should be served for growth of the mist which comes from the upper stream. It should be noted that solid line $N'O$ is a hypothetical vapor pressure profile in the absence of the upper stream contribution, thus the actual vapor pressure in this region may almost be equal to that of saturation. That is to say, the region between $N'O$ is a "mist stabilizing region" in which growth of the mist from the upper stream takes place, and beyond which the mist is re-evaporated and vanishes. The photograph in Fig. 2(*c*) was taken under the condition of a nonuniform wall temperature gradually rising in the positive x-direction. In this case, the mist originates at some distance from the leading edge within the boundary layer at which the critical supersaturation is attained. Therefore it seems reasonable that the inner boundary of the mist region is not the same trace which is drawn by the mist which originated at the leading edge of the flat plate, but all the points on the inner boundary can be considered as the nucleation boundary.

3 Theoretical Analysis

Based on the discussion in the preceeding section, the analysis of the mist formation condition in laminar natural convection over a vertical flat plate is presented as well as mist region and enhancement of mass transfer rate. The following assumption are introduced in the analysis:

1 The analysis is restricted to the laminar regime.

2 The fluid treated here is two-dimensional noncompressible steady flow.

3 A two-phase mixture of well dispersed mist, vapor, and air is treated, and its fluid properties are constant throughout the boundary layer.

4 The latent heat of mist formation and its effect on the veloci-

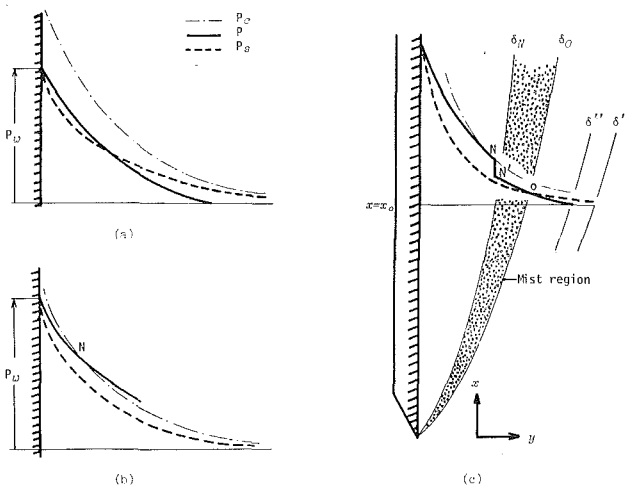

Fig. 4 Schematic diagram of the suggested pressure profiles in the boundary layer

ty and temperature fields are neglected.

5 The interfacial velocity at the wall is neglected.

6 The mass fraction of the vapor in the free-stream is zero.

7 Only the buoyancy force due to temperature differences is considered (i.e., the effect of density difference due to molecular weight difference is neglected).

8 Thermal and velocity boundary layer thicknesses are approximately equal.

Mist formation is one of the characteristic phenomena of simultaneous heat and mass transfer. It follows that consideration of the buoyancy force due to the concentration difference as well as the temperature difference and the velocity component of unidirectional diffusion directed away from the wall must be required in the analysis. In our experiment for the air-naphthalene system, the effect of density difference due to molecular weight difference on the buoyancy force turns out to be no greater than 5 percent, and the interfacial velocity is the order of 10^{-5} m/s even if the melting point of naphthalene, 80.6°C, is attained. Thus assumptions (7) and (5) are valid. The effect of latent heat of mist formation on the temperature field is about 3°C when the temperature difference between wall and ambient is in the range 50 ~ 80°C, and cannot be neglected in the strict sense. In particular, the vapor pressure of the condensing species is affected considerably by an error of 3°C. But, here, we ignore these effects for the sake of analytical simplicity and leave the detailed discussion for a future study. Other assumptions are traditionally accepted in this kind of analysis.

3.1 Conditions of Mist Formation. Because the argument was focused on the critical condition for mist formation, the temperature and concentration profile in the absence of mist formation could be adopted for equations (6) and (7). Fundamental equations for momentum, energy, and mass balance based on the assumptions are presented in integral form with appropriate boundary conditions.

$$\frac{d}{dx}\int_0^{\delta} u^2 dy = -\nu\left(\frac{du}{dy}\right)_{y=0} + g\beta\int_0^{\delta'}(T - T_\infty)\,dy \tag{12}$$

$$\frac{d}{dx}\int_0^{\delta'}(T_\infty - T)u dy = \alpha\left(\frac{dT}{dy}\right)_{y=0} \tag{13}$$

$$\frac{d}{dx}\int_0^{\delta''}(P_\infty - P)u dy = D\left(\frac{dP}{dy}\right)_{y=0} \tag{14}$$

(B. C.)

$$\text{at } y = 0;\ u = 0,\ v = 0,\ T = T_w,\ P = P_w$$

$$y \to \infty;\ u = 0,\ du/dy = 0,\ T = T_\infty,\ dT/dy = 0, \tag{15}$$

$$P = P_\infty = 0,\ dP/dy = 0$$

Squire has solved this set of equations by approximating each profile in polynomial form [9]. His solutions are as follows:

$$u = u_x\frac{y}{\delta}\left(1 - \frac{y}{\delta}\right)^2 \tag{16}$$

$$\frac{T - T_\infty}{T_w - T_\infty} = \left(1 - \frac{y}{\delta'}\right)^2 \tag{17}$$

$$\frac{P}{P_w} = \left(1 - \frac{y}{\delta''}\right)^2 \tag{18}$$

where

$$\delta = \delta' = 3.93\,\mathrm{Pr}^{-1/2}\left(\mathrm{Pr} + \frac{20}{21}\right)^{1/4}\left(\frac{g\beta\Delta T}{\nu^2}\right)^{-1/4} x^{1/4},\ \delta'' \simeq \delta'\mathrm{Le}^{1/2}$$

The critical vapor pressure distribution is obtained by substituting equations (4) and (5) into equation (1) together with equation (17).

$$P_c = P_s \cdot S_{crit} = \exp\left(A + A' + \frac{B + B'}{T}\right) \tag{19}$$

in which $A = 26.59$, $B = -8669$, $A' = -7.85$, $B' = 2795$.

Substituting the foregoing expression and equation (18) into equations (6) and (7), the mist formation conditions are obtained as follows:

$$\frac{T_N^2}{T_w - T_\infty} = (B + B')(1 - \mathrm{Le}^{1/2}\xi)(\xi - 1)\mathrm{Le}^{1/2} \tag{20}$$

$$\exp\left(A' + \frac{B + B'}{T_N} - \frac{B}{T_w}\right) = (1 - \mathrm{Le}^{1/2}\xi)^2 \tag{21}$$

$$C_1\exp(-C_2/T_N) \le \frac{2D(T_w - T_\infty)(\xi - 1)\{(B + B')P_{cN} - BP_{sN}\}}{R_v T_N{}^3\delta'} - \frac{(P_{cN} - P_{sN})V_N}{R_v T_N} \tag{22}$$

where $\xi = \delta_N/\delta'$.

That is to say, the nucleation boundary ξ and its temperature are given by the solution of equations (20) and (21) that satisfies equation (22).

3.2 Mist Region and Enhancement of Vaporization Rates. In the presence of mist formation, the concentration boundary layer is divided into three regions phenomenologically as seen in Figs. 2 and 4(*c*). The temperature and concentration distribution are also expressed by equations (16) and (17), respectively, so long as the latent heat of mist formation is neglected. The concentration distribution must be treated separately within and without the nucleation boundary, point N, at which sudden decrease of vapor pressure exists. In this case, the vapor pressure in the region beyond point N is analyzed on the assumption that the excessive vapor due to supersaturation in the mist region is not consumed for the growth of the mist which comes from the upper stream.

(*a*) *Region Between the Wall and the Mist Formation Boundary.* Supersaturation, although below the critical value, is achieved in this region. A mass balance equation accompanied by its boundary conditions is given as follows:

$$\frac{d}{dx}\int_0^{\delta_N} u(P - P_N)dy = D\left\{\left(\frac{dP}{dy}\right)_{y=\delta_N} - \left(\frac{dP}{dy}\right)_{y=0}\right\} \tag{23}$$

(B. C.)

$$\text{at } y = 0;\ P = P_w = P_s \tag{24a}$$

$$y = \delta_N;\ P = P_N = P_{cN} \tag{24b}$$

$$\frac{dP}{dy} = \frac{dP_c}{dy} \tag{24c}$$

The vapor pressure profile is assumed in polynomial form as follows:

$$\frac{P - P_N}{P_w - P_N} = a + b\left(\frac{y}{\delta_N}\right) + c\left(\frac{y}{\delta_N}\right)^2$$

By using the boundary conditions equations (24*a*), (24*b*), the foregoing equation is rewritten by

$$\frac{P - P_N}{P_w - P_N} = 1 + b\left(\frac{y}{\delta_N}\right) - (b + 1)\left(\frac{y}{\delta_N}\right)^2 \tag{25}$$

Substituting equation (25) and the velocity profile equation (16) into the basic equation (23), the following relation is obtained on the assumption that ξ is independent of x.

$$\frac{\xi^2}{60}\{(2b + 5)\xi^2 - 2(3b + 8)\xi + 5(b + 3)\}\frac{d}{dx}(u_x\delta) = \frac{2D(b + 1)}{\xi\delta} \tag{26}$$

On the other hand, the critical vapor pressure in the field is introduced by equations (17) and (19), and its gradient at point N is represented by

$$\left.\frac{dP_c}{dy}\right|_N = \left.\frac{dP_c}{dT}\cdot\frac{dT}{dy}\right|_N$$

$$= -\frac{2(B+B')(T_w - T_\infty)(\xi - 1)P_{cN}}{T_N{}^2\delta'} \quad (27)$$

Substituting this equation and equation (25) into the last boundary condition equation (24c), another relation between ξ and b is obtained as follows:

$$(P_N - P_w)\frac{b}{\xi} = \frac{2(B+B')\,P_{cN}(T_w - T_\infty)(1-\xi)}{T_N{}^2} \quad (28)$$

The position of the mist formation boundary ξ and b are given as the solution of the set of equations (26) and (28), and the vapor pressure profile is determined by equation (25). In this case, the rate of mass flux from the wall is given with the aid of equation (25) as follows:

$$m_w = -\frac{D}{R_v T_w}\cdot\frac{dP}{dy}\bigg|_N = D\frac{b(P_w - P_N)}{R_v T_w \delta_N} \quad (29)$$

(*b*) *Region Between the Mist Formation Boundary and the Outer Edge of Concentration Boundary Layer.* Though the region beyond point N is composed of two regions phenomenologically, analyses are performed at the same time throughout the region. Namely, the hypothetical vapor pressure profile is obtained by the analyses with the assumption that the excessive vapor in the mist region is not consumed for the growth of mist. Assuming the hypothetical vapor pressure P'_N at $y = \delta_N$, the fundamental equation and its boundary conditions are represented as follows:

$$\frac{d}{dx}\int_{\delta_N}^{\delta''} u(P - P_\infty)dy - P'_N\frac{d}{dx}\int_0^{\delta_N} Udy = -D\frac{dP}{dy}\bigg|_N \quad (30)$$

(B. C.)

$$\text{at } y = \delta_N;\ P = P'_N \quad (31a)$$

$$y = \delta'';\ P = P_\infty = 0 \quad (31b)$$

$$\frac{dP}{dy} = 0 \quad (31c)$$

The vapor pressure profile is assumed as

$$\frac{P}{P'_N} = a' + b'\left(\frac{y - \delta_N}{\delta'' - \delta_N}\right) + c'\left(\frac{y - \delta_N}{\delta'' - \delta_N}\right)^2 \quad (32)$$

where the constants a', b', and c' are determined by the boundary conditions described in the foregoing. Equation (32) is rewritten by

$$\frac{P}{P'_N} = 1 - 2\left(\frac{y - \delta_N}{\delta'' - \delta_N}\right) + \left(\frac{y - \delta_N}{\delta'' - \delta_N}\right)^2 \quad (33)$$

The hypothetical vapor pressure P'_N, which is included in the foregoing equation, is related by a mass balance at point N, equation (34).

$$-\frac{D}{R_v T}\cdot\frac{dP}{dy}\bigg|_N + \frac{v_N P'_N}{R_v T_N} = -\frac{D}{R_v T}\frac{dP_c}{dy}\bigg|_N + \frac{v_N P_{cN}}{R_v T_N} - m_r \quad (34)$$

Combining equation (33) with equations (30) and (34), the following relations are obtained,

$$\{\eta^6 - 4\eta^5 + 5\eta^4 - (6\xi^5 - 20\xi^4 + 20\xi^3)\eta + 15\xi^4 - 16\xi^5 + 5\xi^6\}\frac{d}{dx}(u_x\delta) = \frac{120\cdot D(\eta - \xi)}{\delta} \quad (35)$$

$$P'_N = \frac{P_{cN}\left\{\dfrac{2D(B+B')(T_w - T_\infty)(\xi - 1)}{T_N{}^2} - \dfrac{(3\xi^4 - 8\xi^3 + 6\xi^2)\delta}{12}\dfrac{d}{dx}(u_x\delta) - \dfrac{R_v T_N \delta}{P_{cN}}m_r\right\}}{\dfrac{2D}{\eta - \xi} - \dfrac{(3\xi^4 - 8\xi^3 + 6\xi^2)\delta}{12}\dfrac{d}{dx}(u_x\delta)} \quad (36)$$

where $\eta = \delta''/\delta'$, $\xi = \delta_N/\delta'$.

Substituting the solution of the set of equations (35) and (36) into equation (33), the vapor pressure profile in this region is obtained. The outer boundary of the mist region δ_0, which corresponds to the intersection of the saturation pressure profile and hypothetical vapor pressure, is obtained by equation (33) under the condition: $P = P_{s0}$ at $y = \delta_0$.

$$\frac{P_{s0}}{P'_N} = \left(\frac{\delta'' - \delta_0}{\delta'' - \delta_N}\right)^2 \quad (37)$$

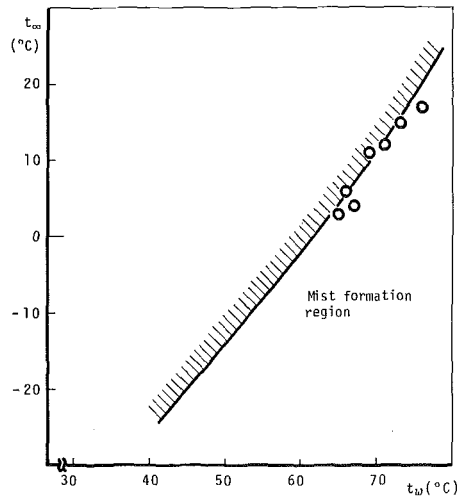

Fig. 5 Relation between the wall and ambient temperature at critical condition for mist formation

4 Results and Discussion

Fig. 5 indicates the relation between the wall and ambient temperature at the critical condition for mist formation with respect to naphthalene vapor, and the cross-hatched zone corresponds to the nonmist condition. Such was derived by solving the system of equations (20) and (21), together with the expression for S_{crit}, equation (5). Fig. 6 represents the calculated results of the pressure profile for the example case, $t_w = 79°C$, $t_\infty = 28°C$. The chained line and dotted line denote the critical supersaturation and the saturation pressure profile, respectively, corresponding to the temperature distribution (shown as a thin solid line in the same figure). The thick solid line from the wall to point N represents the actual vapor pressure profile, while the same line beyond point N' indicates the hypothetical vapor pressure profile which is obtained on the assumption that the excessive vapor in the mist region is not consumed for the growth of mist. Fig. 7 shows the variation of the mist region in nondimensional form with respect to the thermal boundary layer thickness. The experimental data are also plotted for comparison. Each solid curve drawn downward denotes the inner boundary at which the mist formation takes place, that is calculated by the system of equations (26) and (28). Each solid curve drawn upward denotes the outer boundary. Although the outer boundaries of the mist regions were determined with the intersection of the hypothetical vapor pressure and the saturation vapor pressure as shown in Fig. 6, they agree approximately with the experimental results. In order to realize the calculation, the mist formation rate at point N (i.e., represented by equation (10)) is required. A calculation was carried out by introducing the value inversely deduced from the experimental data for $t_w = 67°C$ and $70°C$, $t_\infty = 0°C$ (shown by ▲ in the figure).

$$m_r = 0.17\exp(-3840/T) \quad (38)$$

where the constants seem to depend on the concentration of for-

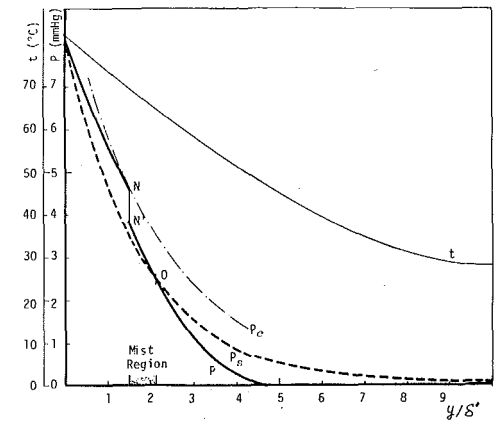

Fig. 6 Calculated results of the pressure profiles for the case, $t_w = 79°C$, $t_\infty = 28°C$

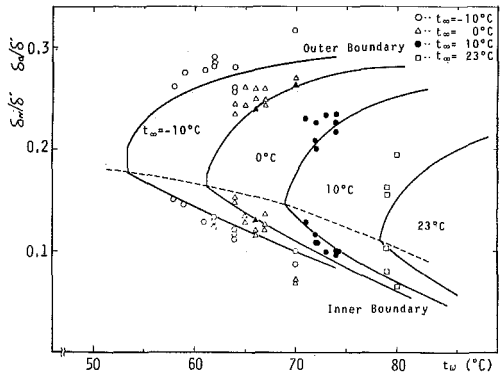

Fig. 7 Mist region in nondimentional form with respect to the thermal boundary layer thickness

eign nuclei, the interfacial property between the condensate and foreign nuclei, and the surrounding temperature. It is concluded that the inner boundary tends to widen inward and the outer boundary tends to widen outward as t_w increases while t_∞ remains constant, which is in agreement with the experiment. Fig. 8 indicates the enhancement of vaporization rate due to mist formation calculated by equation (29). The ordinate denotes the ratio of the actual outward mass flux from the wall with respect to that in the absence of mist formation. Hence the noticable enhancement of vaporization rate can be perceived with the increase of the mist region in accordance with Fig. 7.

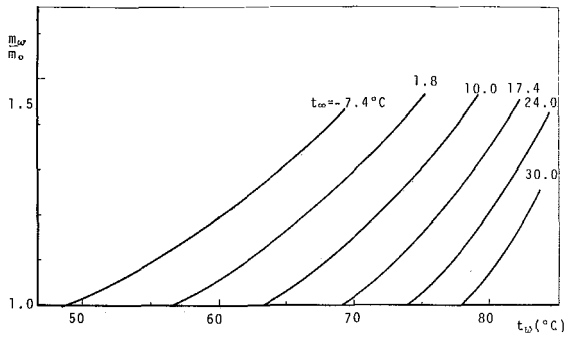

Fig. 8 Enhancement of vaporization rates due to mist formation

5 Conclusion

The transport-reaction mechanism of mist formation in a convective field was discussed on the basis of a critical supersaturation model. Experiments were performed using a naphthalene sublimation technique in order to obtain some degree of supersaturation of vapor pressure for mist formation on foreign nuclei.

Analytical results for mist formation condition, mist region, and enhancement of vaporization rate agreed approximately with the experimental results.

Acknowledgment

This work was supported by the Science Research Grants of the Ministry of Education and Matsunaga Foundation.

References

1 Hill, A. W. D., et al., "A Note on the Enhancement of the Diffusion Limited Vaporization Rates by Condensation Within the Thermal Boundary Layer," *International Journal of Heat and Mass Transfer*, Vol. 12, 1969, p. 111.

2 Turkdogan, E. T., "The Theory of Enhancement of Diffusion-Limited Vaporization Rates by a Convection-Condensation Process. Part I-Theoretical," *Trans. Met. Soc. AIME*, Vol. 230, 1964, p. 740.

3 Turkdogan, E. T., and Mills, K. C., "The Theory of Enhancement of Diffusion-Limited Vaporization Rates by a Convection. Part II-Experimental," *Trans. Met. Soc. AIME*, Vol. 230, 1964, p. 750.

4 Rosner, D. E., "Enhancement of Diffusion-Limited Vaporization Rates by Condensation Within the Thermal Boundary Layer," *International Journal of Heat and Mass Transfer*, Vol. 10, 1967, p. 1267.

5 Epstein, M., and Rosner, D. E., "Enhancement of Diffusion-Limited Vaporization Rates by Condensation Within the Thermal Boundary Layer," ibid., Vol. 13, 1970, p. 1393.

6 Davis, E. J., and Liao, S. C., "The Growth Kinetics and Polydispersity of Condensational Aerosols," *J. Colloid Interface Sci.*, Vol. 50., 1975, p. 488.

7 Nicolaon, G., et al., "A New Liquid Aerosol Generator. II. The Effect of Reheating and Studies on the Condensation Zone," ibid., Vol. 35, 1971, p. 490.

8 Davis, E. J., and Nicolaon, G., "A New Liquid Aerosol Generator. III. Operating Characteristics and Theoretical Analysis," ibid., Vol. 37, 1971, p. 768.

9 Goldstein, S., *Modern Developments in Fluid Dynamics*, 1938.

Shi-Chune Yao
Argonne National Laboratory,
Reactor Analysis and Safety Division,
Argonne, Ill.
Assoc. Mem. ASME

V. E. Schrock
Professor of Nuclear Engineering,
University of California,
Berkeley, Calif.
Mem. ASME

Heat and Mass Transfer From Freely Falling Drops

When a drop breaks free from a liquid film or feeding orifice and falls through an atmosphere of lower temperature it experiences a transient heat and mass transfer process involving acceleration, the development of hydrodynamic, thermal, and concentration boundary layers in the gas, oscillation of the drop shape, and the development of internal circulation within the drop. This problem, which is of importance in evaporative cooling systems, has been studied experimentally for water drops 3–6 mm in diameter falling through air. Study of a simplified set of governing equations indicates that similitude does not exist in this problem. However, it has been found that for this size range an approximate procedure based on the assumption of negligible internal thermal resistance and an empirical transient correction factor applied to the Ranz-Marshall [1][1] correlation could describe the data very well.

Introduction

Heat and mass transfer from drops has been studied extensively both theoretically and experimentally. In general the problems previously studied may be classified as steady state or transient and according to the importance of internal and external transport resistances.

For the case of resistance in the continuous phase only, the steady-state heat transfer from a sphere was solved by Acrivos and Taylor [2] who found for Stokes flow, for $Re < 1$, $Pe < 1$

$$Nu = 2 + 1/2\ Pe \tag{1}$$

while for $Re < 1$, $Pe \gg 1$, Acrivos and Goddard [3] obtained

$$Nu = 0.922 + 0.991\ Pe^{1/3} \tag{2}$$

Boussinesq [4] assumed steady potential flow around an isothermal sphere and obtained for $Re \gg 1$, $Pe \gg 1$

$$Nu = \frac{2}{\sqrt{\pi}} Pe^{1/2} \tag{3}$$

and for the same case Watt [5] obtained

$$Nu = 4.73 + 1.156\ Pe^{1/2} \tag{4}$$

Empirical correlations for the case of steady-state heat transfer from solid spheres of small internal resistance have been obtained by Ljachowski [6], Vyroubow [7], Gröber [8], and Kramer [9]. Correlations for liquid drops under the same conditions have been obtained by Frossling [10] and Hsu, et al. [11] and Ranz and Marshall [1] whose equations

$$Nu = 2 + 0.6\ Pr^{1/3}\ Re^{1/2} \tag{5a}$$

$$Sh = 2 + 0.6\ Sc^{1/3}\ Re^{1/2} \tag{5b}$$

have been widely used. Lee and Ryley [12] obtained a correlation for heat transfer from superheated steam to evaporating water drops.

The transient thermal problem has been treated by Konopliv and Sparrow [13] for an isothermal sphere in steady Stokes flow, $Re < 1$, subject to a step change in environmental temperature. The thermal boundary layer was solved for $Pr \gg 1$ for the cases of constant sphere temperature (infinite thermal capacity) and variable temperature (finite thermal capacity).

The case of negligible external resistance was analyzed by Kronig and Brink [14] who assumed that concentrations are uniform on stream surfaces within the drop. The transient conduction problem was solved for the initial condition of uniform concentration within the drop and a step change in the environmental concentration and compared with the result for a stationary fluid (no internal circulation) with the same initial and boundary conditions.

Problems involving resistances on both sides of the interface have been studied using boundary layer analysis. Levich [15] studied the steady-state problem for $Re < 1$ and $Pe \gg 1$, while Chao [16] solved this problem for $Re \gg 1$, $Pe \gg 1$. The transient thermal problem with steady hydrodynamic conditions, initially uniform drop temperature, and a step change in the temperature of the continuous phase was solved by Chao [16], Chao and Chen [17],

[1] Numbers in brackets designate References at end of paper.

Contributed by the Heat Transfer Division presented at the Winter Annual Meeting, November 30–December 5, 1975, of THE AMERICAN SOCIETY OF MECHANICAL ENGINEERS. Revised manuscript received at ASME Headquarters November 25, 1975. Paper No. 75-WA/HT-37.

and Ruckenstein [18] for extreme Reynolds numbers, both large and small.

Snyder [19] did experiments on freely falling drops immediately following release and during acceleration. He deduced a correlation by taking dT/dx from curves fit to the experimental data. However, the procedure is highly sensitive to error in temperature measurement, which in Snyder's work was a large percentage of the cooling range, e.g., ±0.5°C for 2°C. His correlation is

$$\mathrm{Nu} = 0.29\,\mathrm{Re}^{0.6} \tag{6}$$

In the present experiments more accurate temperature histories have been measured for drops in the size range 3–6 mm which is typical of cooling tower packing as reported by Okuno [20] and the transient aspect of the problem has been studied.

Description of the Problem

When the drop breaks away from the feeding system it may oscillate in shape and it may have some minor internal motion caused by the formation process. As it accelerates internal circulation is created by the shear stress on the surface and aerodynamic forces tend to distort the shape of the drop. A boundary layer is developed in the continuous phase surrounding the drop. If the distortion of the drop from a spherical shape is neglected the problem may be formulated as a set of axially symmetric equations expressing conservation of mass, momentum, and energy in the two regions with the appropriate initial and interface boundary conditions. Using a boundary layer formulation, the free stream velocity is found from potential flow theory in terms of the instantaneous drop velocity, which is in turn obtained from a total force balance on the drop using a quasi-steady empirical drag law. Boundary layer separation and formation of a wake further complicate the situation.

A more or less exact formulation of the problem was written [21] but because of the complexity no attempt was made to solve the equations. Instead they were used as the basis of a dimensional analysis. The dimensionless velocity, temperature, and water vapor concentration are seen to depend upon position and time in a prescribed way for a given set of the following dimensionless parameters:

$$\mathrm{Re},\ \mathrm{Pr},\ \mathrm{Sc},\ Su,\ \mathrm{Gr},\ A_c,\ \mathrm{Le}\frac{h_{fg}(C_{0,s}-C_\infty)}{\rho_c C_p(T_0-T_\infty)},$$

$$\frac{k_c}{k_d}\ \text{and}\ \frac{\mu_c}{\mu_d}$$

where these groups have the meanings defined in the Nomenclature. From this analysis it is seen that water drops of different sizes will not be similar in behavior because not all these parameters can be maintained constant as the size is varied.

Distortion and oscillation of drop shape is not accounted for and still there is a very large number of parameters required to describe the problem. A more approximate method was then developed in the hope that a simpler characterization could be found.

Approximate Models

Continuous Phase. When a sphere is accelerated impulsively in a fluid, the time for the hydrodynamic boundary layer to grow and reach steady state is on the order $tU_\infty/d = 1$ [22]. This means that the boundary layer growth is complete when the drop has moved a distance equal to its diameter. When the acceleration is continuous the boundary layer is approximately the same as the steady-state one at a velocity only a little lower than the instantaneous one and therefore a quasi-steady state approximation may be applied with little error for all but the first few diameters of fall. We are interested in the process over distances up to 500–1000 dia. Consequently the widely used Ranz-Marshall [1] steady-state correlation may reasonably substitute for all the governing equations for the external field.

The Ranz-Marshall experiments employed drops of diameter less than 1.1 mm and without oscillation. The larger drops used in the present investigation were observed to undergo damped oscillation after formation and these oscillations may influence the transport processes. Baxi and Ramachandran [23] found that in free convection the transverse vibration of a sphere strongly increases the heat transfer coefficient. Similarly Scanlan [24] observed an increase in the Nusselt number for forced convection on plates with normal vibration for $\mathrm{Re} \leq 2200$. However, in our first attempts to fit a simple model to the data the Ranz-Marshall equations were considered applicable.

Interior Field. *Complete Mixing Model.* There exist several different models for the transport processes in the interior of the drop. The simplest model is to assume that the internal motion of the drop is so vigorous that complete mixing is achieved. The temperature profile in the drop is essentially flat and resistance to heat and mass transfer exists only in the continuous phase. For the complete mixing model [19] the energy transport can be described by

$$-\frac{4}{3}\pi R^3 \rho_d C_{pd}\frac{dT_m}{dt} = 4\pi R^2[h(T_m - T_\infty) + h_{fg}h_D$$

Nomenclature

$A_c = \dfrac{d}{U_\infty{}^2}\left(\dfrac{dU_\infty}{dt}\right)$ = acceleration parameter
A_m = total amplitude of oscillation
C = vapor concentration
C_p = heat capacity, constant pressure
D = mass diffusivity of water vapor in air
d = diameter of drop
f = drop oscillation frequency
$\mathrm{Gr} = \dfrac{(1-(\rho_c/\rho_d))gd^3}{\nu_c{}^2}$ = Grashof type number
g = gravity; or correction factor for Ranz-Marshall equation
h_{fg} = latent heat of evaporation
h = heat transfer coefficient in forced convection
h_D = mass transfer coefficient in forced convection
k = thermal conductivity
$\mathrm{Le} = D/\alpha$ = Lewis number
$\mathrm{Nu} = h_c d/k_c$ = Nusselt number
$\mathrm{Pe} = \mathrm{Pr}\cdot\mathrm{Re}$ = Peclet number
$\mathrm{Pr} = \nu/\alpha$ = Prandtl number
R = radius of drop
$\mathrm{Re} = U_\infty d/\nu_c$ = Reynolds number
r = radial distance
$\mathrm{Sc} = \nu/D$ = Schmidt number
$\mathrm{Sh} = h_D d/D$ = Sherwood number
$Su = \sigma d/\rho_c \nu_c{}^2$ = surface tension number
S = a constant of proportionality
T = temperature
t = time
U_∞ = velocity at far upstream
$\mathrm{We} = d\rho_c U_\infty{}^2/\sigma$ = Weber number
x = falling distance measured from rest
α = thermal diffusivity
ϵ = emissivity for thermal radiation
μ = viscosity
ν = kinematic viscosity
ρ = density
σ = Stefan-Boltzmann constant for thermal radiation; or surface tension

Subscripts

c = continuous phase, e.g., air
d = dispersed phase, e.g., water
ic = internal circulation
m = mean value
max = maximum value
0 = initial value
osc = oscillation
s = saturation condition
w = water
∞ = at $r \gg R$, or at free stream of boundary layer

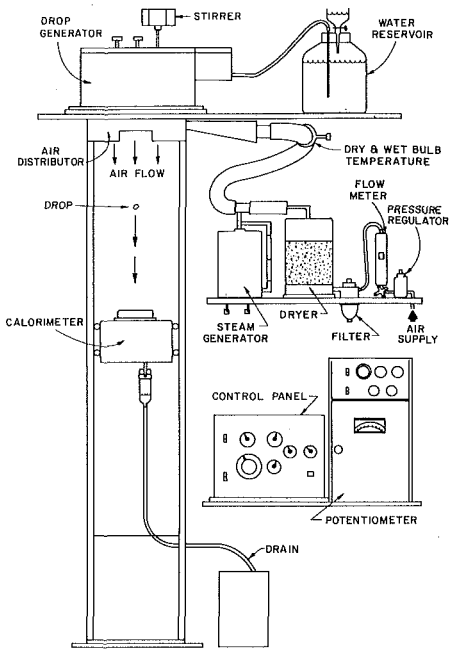

Fig. 1 Schematic of experimental setup

$$(C_s(T_m) - C_\infty) + \epsilon\sigma(T_m{}^4 - T_\infty{}^4)] \tag{7}$$

where both h and h_D are time dependent. With

$$\frac{dT_m}{dt} = U_\infty \frac{dT_m}{dx} \text{ and } \frac{h_D}{h} = \frac{\text{Le}}{\rho C_p}$$

the energy transport equation can be reduced to

$$\text{Nu} \equiv \frac{hd}{k_c}$$

$$= \frac{d}{k_c}\left[\frac{-\frac{1}{6}\frac{dT_m}{dx} d\rho_d C_{pd} U_\infty(x) - \epsilon\sigma(T_m{}^4 - T_\infty{}^4)}{(T_m - T_\infty) + \frac{\text{Le}\, h_{fg}}{\rho C_p}(C_s(T_m) - C_\infty)}\right] \tag{8}$$

Since the drop temperatures along the falling distances are known, the Nu can be evaluated.

Nonmixing Model. The nonmixing model assumes there is no internal motion and the energy equation is reduced to simply a transient heat conduction equation. The equations which describes the heat transport in the nonmixing drop are

$$\frac{\partial T}{\partial t} = \alpha_d\left(\frac{\partial^2 T}{\partial r^2} + \frac{2}{r}\frac{\partial T}{\partial r}\right) \text{ for } 0 < r \le R \tag{9}$$

with initial condition

$$T = T_0 \tag{10a}$$

and boundary conditions

$$\left.\frac{\partial T}{\partial r}\right|_{r\to 0} = 0 \tag{10b}$$

$$-k_d \left.\frac{\partial T}{\partial r}\right|_R = h(T(R) - T_\infty) + h_{fg} h_D (C_s(T(R)) - C_\infty) + \epsilon\sigma(T(R)^4 - T_\infty{}^4) \tag{10c}$$

Mixing Model. Neither the complete-mixing model nor the nonmixing model are realistic because they are based on the extreme situations of the drop internal motions. Therefore, a new model is proposed which considers both the effects of oscillation and internal circulation on the mixing in the drop.

The oscillations [25] of a drop contribute to the internal motion of the drop. This will be characterized by a maximum Reynolds number, based on surface radial velocity, which occurs on the surface at 45 deg latitude. This is

$$\text{Re}_{osc,max} = 3\sqrt{2}\left(\frac{A_m}{d}\right)_{\max}\left(\frac{\rho_d \sigma g_c d}{\mu_d{}^2}\right)^{1/2} \tag{11}$$

where A_m/d is the relative oscillation amplitude. Due to viscous damping, the oscillation decays [25] from its original value $A_{m,0}/d$ as

$$\left(\frac{A_m}{d}\right)_{\max} = \left(\frac{A_{m,0}}{d}\right)_{\max} e^{-20\nu_d t/d^2} \tag{12}$$

The maximum Reynolds number characterizing internal circulation was obtained from the Hadarmard solution [25]

$$\text{Re}_{ic,\max} = \frac{U_\infty d}{2\left(1 + \frac{\mu_d}{\mu_c}\right)\nu_d} \tag{13}$$

It is assumed that the effects of heat transport due to the internal motion can be represented by an increase of the heat diffusivity, and this increase of heat diffusivity is linear and proportional to the sum of the maximum Reynold numbers of oscillation and internal circulation. It is proposed that the effective diffusivity is given by

$$\alpha = \alpha_w[1 + S(\text{Re}_{\text{osc,max}} + \text{Re}_{ic,\max})] \tag{14}$$

where S is a constant which shows the significance of internal mixing. The equations of the mixing model are the same set of equations as the nonmixing model except that α_d is replaced by α in equation (9).

Experimental Equipment and Procedure

The experiment was designed to provide accurate data on the relationship between the mean temperature of the drop and its position in free fall for different drop size, initial drop temperature, and the temperature and humidity of the air through which it falls. The system used is shown in Fig. 1. It consists of a drop generator, a plastic column 3 m in height containing the conditioned air, air conditioning equipment, and a calorimeter that could be positioned at any elevation to catch and measure mean drop temperature. Fig. 2 shows the details of the drop generator which was designed to produce drops of consistent size and temperature. Fig. 3 shows the calorimeter detail. The drops were trapped in a small dewar and the water collected overflowed. The steady temperature was measured by a thermistor located in the dewar. Heat loss was minimized by surrounding the dewar with a bath adjusted to the drop temperature. Thermistors were calibrated to ±0.03°C. Con-

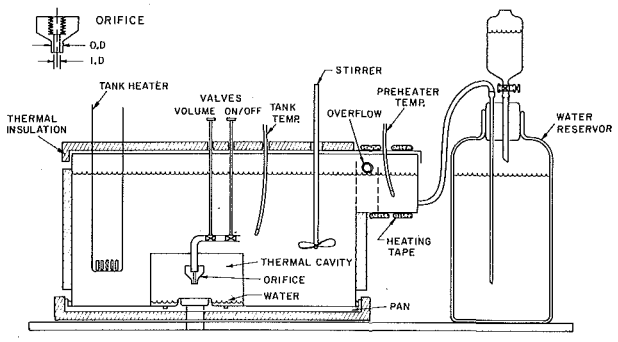

Fig. 2 Drop generation system details

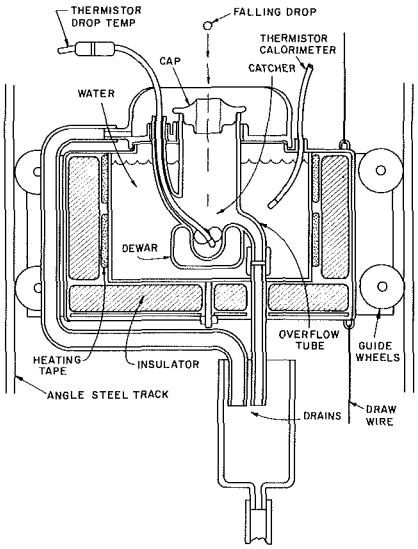

Fig. 3 Calorimeter detail

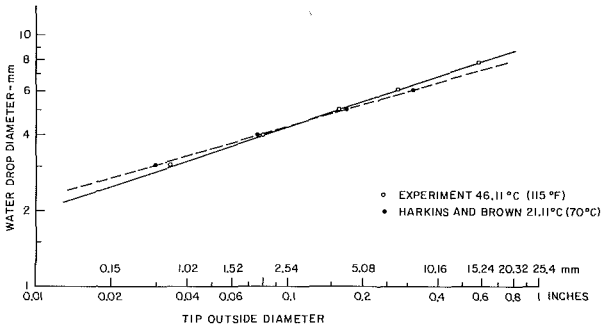

Fig. 4 Size of water drops generated from tips

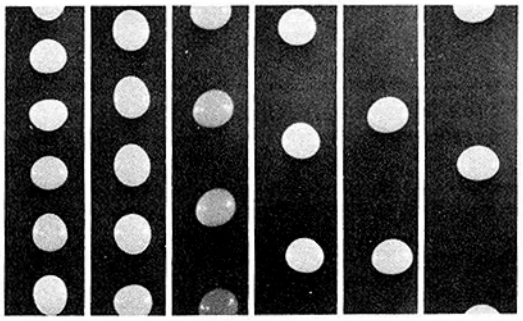

Fig. 5 Photographs of falling water drops—4 mm

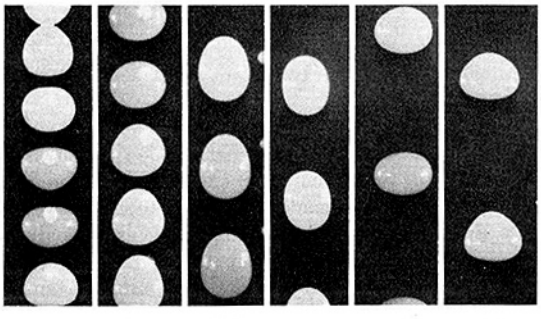

Fig. 6 Photographs of falling water drops—6 mm

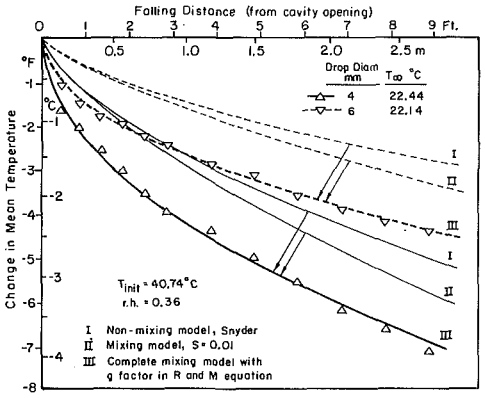

Fig. 7 Comparison of models with experimental data

sidering all sources of error the drop temperatures were estimated to measure within ±0.05°C at the generator and ±0.07°C in the calorimeter.

The air flowed downward in the column at a very low velocity (3 cm/s) to maintain a nearly constant environment. This rate assured that the rise in relative humidity was less than 3 percent. The inlet wet and dry bulk temperatures were controlled to ±0.05°C.

Drop sizes and oscillations were observed photographically. Drop sizes could be controlled precisely by the nozzle dimensions and the present results were very close to those of Harkins and Brown [26] (Fig. 4). For photographic measurements a small amount of oil-free white water color paint was added to the water. This had negligible effect on surface tension but produced good light scattering within the drops. Examples of the photographs obtained are shown in Figs. 5 and 6. A Nikon-F camera was used with an object field of 3 × 5 cm against a black background. Side lighting was provided by a General Radio 1513-A Strobotac with flash duration of about 0.8×10^{-6} s and flash rate of 15,000–24,000 flashes per second. With the camera set to an exposure time of 0.5 s several clear images of a single drop were recorded on the film as the drop passed the field of view. From these pictures the frequency and amplitudes of vibrations were measured.

Additional detail on the experimental equipment may be found in reference [21].

Results and Comparison With Models

The observed oscillations were found to be in two modes. Usually the drops underwent prolate-oblate oscillations about the spheroidal shape. But for drops larger than 4 mm and distances $x/d <$ 50 a distinct point was formed alternately on top and bottom. The oscillation frequency of drops along falling distances is shown in Fig. 8. The initial frequency was found to be about the same as predicted by Lamb [25] but the frequency decayed to negligible magnitude at $x/D \sim 150$. Fig. 9 shows the maximum relative deformation of the drops as a function of falling distances. At larger dis-

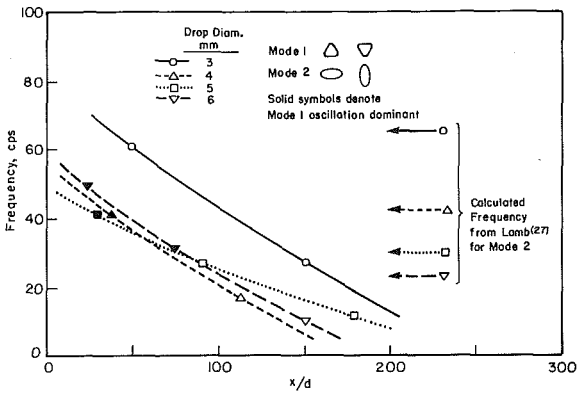

Fig. 8 Frequency of drop oscillations

tances the drops were in the form of oblate spheroids and the amount of deformation at the highest speeds (about 75 percent of terminal velocity) were consistent with measurements of Garner and Lane [27].

Drop cooling results are presented in Table 1. Typical comparisons of the data to the approximate models are given in Fig. 7 for the nonmixing model, curves I, and the mixing model, curves II. These models predict much less cooling than observed experimentally. Even for the complete mixing model as originally defined the cooling was underpredicted (not shown). This suggested that vibration and deformation of drops have an important effect upon the resistance of the external field. This is justified qualitatively as in Fig. 10 which shows the calculated ratio of the heat transfer coefficient with and without oscillation based on Figs. 8 and 9 according to Scanlan [24].

The computerized model and data reduction calculations were used to obtain a correction factor for the Ranz-Marshall correlation that would bring the complete mixing model prediction into agreement with the data. The correction factor was defined as

$$g \equiv \frac{\mathrm{Nu} - 2.0}{0.6\,\mathrm{Pr}^{1/3}\mathrm{Re}^{1/2}} = \frac{\mathrm{Sh} - 2.0}{0.6\,\mathrm{Sc}^{1/3}\mathrm{Re}^{1/2}} \tag{15}$$

In Fig. 11 the correction factor is plotted as a function of dimensionless position x/d and it is seen that it may be accurately described by a simple correlation equation

$$g = 25(x^*/d)^{-0.7} \tag{16}$$

In effect this is a transient correction factor that corrects the Ranz-Marshall equation for the effects of vibration and distortion of drop shape as it falls. The modified Ranz-Marshall equations are then

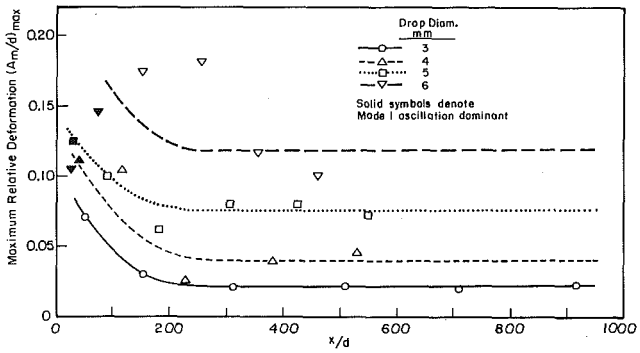

Fig. 9 Maximum relative deformation of drops

Table 1 Experimental data, temperature of drops falling in air

Drop size mm	3	3	3	4	4	4	5	5	5	6	6	6
Initial °C	40.70	40.73	40.69	40.74	40.64	40.79	40.68	40.72	40.74	40.74	40.66	40.70
T_∞ °C	23.29	22.32	23.33	22.44	21.33	23.33	22.88	22.56	23.61	22.14	21.33	23.33
r.h.	0.29	0.36	1.00	0.36	0.52	1.00	0.29	0.36	1.00	0.36	0.52	1.00
Falling distance	Cavity opining at 0.136 ft (4.15 cm)											
ft	cm					$T_{init} - T_m$ °C						
0.58	17.68	1.44	0.82	0.89	0.82	0.59	0.57	0.86	0.39	0.59	0.53	0.35
1.0	30.48	1.99	1.04	1.12	1.15	0.80	1.13	1.06	0.60	0.83	0.86	0.46
1.5	45.72	2.21	1.26	1.39		0.99	1.40	1.23	0.76	1.01		0.58
2.0	60.96	2.33	1.53	1.68	1.64	1.23	1.58	1.38	0.88	1.06	1.11	0.68
2.5	76.20	2.42	1.78	1.96		1.38	1.66	1.53	1.04	1.23		0.79
3.0	91.44	2.71	1.98	2.20	1.97	1.55	1.81	1.66	1.14	1.36	1.41	0.89
3.5	106.68	2.93					2.01					
4.0	121.92	3.31					2.19					
4.5	137.16	3.53					2.34					
5.0	152.40	3.71					2.47					
5.5	167.64	4.02					2.71					
6.0	182.88	4.22					2.78					
6.5	198.12	4.38					2.91					
7.0	213.36	4.62					3.06					
7.5	228.60						3.17					
8.0	243.84						3.27					
8.5	259.08						3.32					
9.0	274.32						3.43					
9.5	289.56						3.51					
	3	3	3	4	4	4	5	5	5	6	6	6

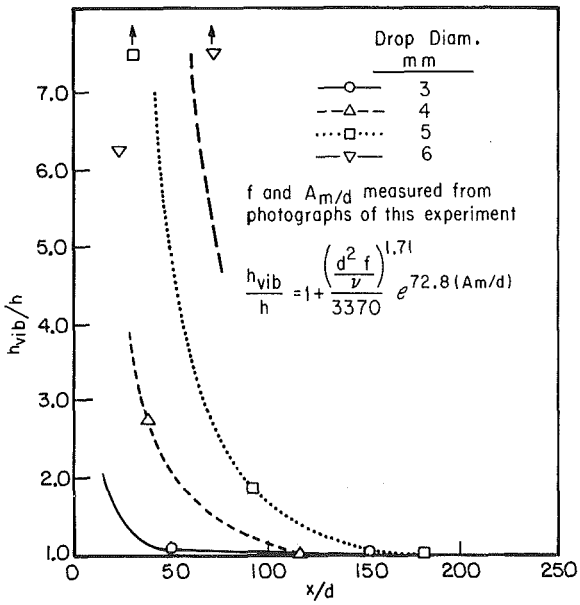

Fig. 10 Effect of surface vibration on heat transfer coefficient

$$\mathrm{Nu} = 2.0 + 15.0\,\mathrm{Pr}^{1/3}\mathrm{Re}^{1/2}\left(\frac{x}{d}\right)^{-0.7} \tag{17}$$

$$\mathrm{Sh} = 2.0 + 15.0\,\mathrm{Sc}^{1/3}\mathrm{Re}^{1/2}\left(\frac{x}{d}\right)^{-0.7} \tag{18}$$

$$\text{for } 3\text{ mm} \leq d \leq 6\text{ mm};\ 10 \leq \frac{x}{d} \leq 600$$

The predicted temperature histories based on these equations and the complete mixing model is then in close agreement with experimental data as shown by Fig. 12.

It may be noted that for $x/d < 100$ the effect of vibration is to enhance transport ($g > 1$) but for $x/d > 100$, $g < 1$ suggesting that the Ranz-Marshall equations overpredict Nu and Sh. This is probably not the case, however, and a better explanation is that the drops experience less than complete mixing for $x/d > 100$. It is very difficult to precisely account for contributions of drop distortion and internal resistance; however, the approximate empirical procedure developed in the present work does give accurate predictions for water drops of 3–6 mm dia for x/d up to 600.

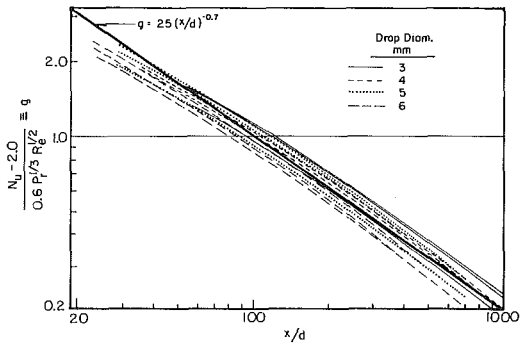

Fig. 11 The correction factor g for Ranz-Marshall equation

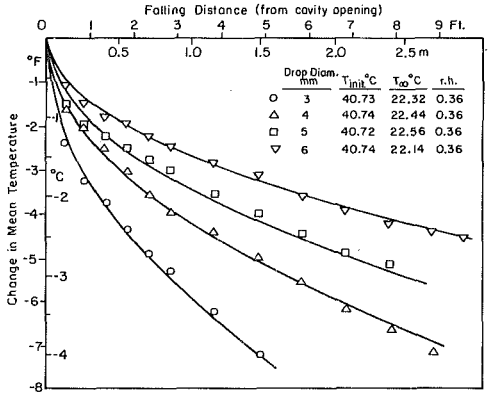

Fig. 12 Fit of data by complete mixing model with g factor in Ranz-Marshall equation

Acknowledgment

This work was supported by the National Science Foundation—RANN Grant GI34932.

References

1 Ranz, W., and Marshall, W., Jr., "Evaporation from Drops," *Chemical Engineering Progress,* Vol. 48, 1952, pp. 141–146, 137–180.

2 Acrivos, A., and Taylor, T. D., "Heat and Mass Transfer From Single Spheres in Stokes Flow," *The Physics of Fluids,* Vol. 5, No. 4, 1962, pp. 387–394.

3 Acrivos, A., and Goddard, J., "Asymptotic Expansion for Laminar Forced-Convection Heat and Mass Transfer, Part I," *Journal of Fluid Mechanics,* Vol. 23, 1965, p. 273.

4 Boussinesqy, M., "Calcul du pourvoir refroidissant des courant fluids," *J. Math. Pures Appl.,* Vol. 1, 1905, p. 285.

5 Watts, R., "The Effects of Curvature on Heat or Mass Transfer From an Isothermal Sphere," JOURNAL OF HEAT TRANSFER, TRANS. ASME, Series C, Vol. 94, Feb. 1972, pp. 1–6.

6 Ljachowski, D. N., *J. Techn. Phys.,* Leningrad, Vol. 10, 1940, p. 999.

7 Vyroubow, D., *J. Techn. Phys.,* Leningrad, Vol. 9, 1939, p. 1923.

8 Gröber, H., Erk, S., and Grigull, U., *Grundgesetze der Warmubertagung,* Springer–Verlag, Berlin, 1955.

9 Kramers, H., "Heat Transfer From Spheres to Flowing Media," *Physica,* Vol. XII, No. 2–3, 1946, pp. 61–80.

10 Frossling, N., "Uber die Verdungtung Fallenden Tropfen," *Gerlands Beitrage Zur Geophysik,* Vol. 52, 1938, pp. 170–216.

11 Hsu, N., Sato, K., and Sage, B., "Material Transfer in Turbulent Gas Stream," *Industrial and Engineering Chemistry,* Vol. 46, 1954, pp. 870–876.

12 Lee, K., and Ryley, D., "The Evaporation of Water Droplets in Superheated Steam," JOURNAL OF HEAT TRANSFER, TRANS. ASME, Series C, Vol. 90, No. 4, 1968, pp. 445–451.

13 Konopliv, N., and Sparrow, E., "Unsteady Heat Transfer and Temperature for Stokesian Flow About a Sphere," JOURNAL OF HEAT TRANSFER, TRANS. ASME, Series C, Vol. 94, Aug. 1972, pp. 266–272.

14 Kronig, R., and Brink, J., "On the Theory of Extraction From Falling Droplets," *Applied Scientific Research,* Vol. A2, 1950, pp. 142–154.

15 Levich, V., *Physicochemical Hydrodynamics,* Prentice-Hall, 1962, p. 406.

16 Chao, B. T., "Transient Heat and Mass Transfer to a Translating Droplet," JOURNAL OF HEAT TRANSFER, TRANS. ASME, Series C, Vol. 91, May 1969, pp. 273–281.

17 Chao, B. T., and Chen, L., "Series Solution of Unsteady Heat or Mass Transfer to a Translation Fluid Sphere," *International Journal of Heat and Mass Transfer,* Vol. 13, 1970, pp. 359–367.

18 Ruckenstein, E., "Mass Transfer Between a Single Drop and a Continuous Phase," *International Journal of Heat and Mass Transfer,* Vol. 10, 1967, pp. 1785–1792.

19 Snyder, N. W., "Cooling of a Freely Falling Water Drop," PhD thesis, University of California, Berkeley, 1947.

20 Okuno, A., "Drop Size Distribution in a Packed Cooling Tower," MS thesis, University of California, Berkeley, 1946.

21 Yao, S. C., Ph.D thesis, University of California, Berkeley, 1974; also University of California, Berkeley—NSF Waste Heat Management Report WHM-18, 1974.

22 Schlichting, H., *Boundary Layer Theory,* Sixth ed., McGraw-Hill, 1966, p. 403.

23 Baxi, C., and Ramachandran, A., "Effect of Vibration on Heat Transfer From Spheres," JOURNAL OF HEAT TRANSFER, TRANS. ASME, Series C, Vol. 91, Aug. 1969, pp. 337–344.

24 Scanlan, J., "Effects of Normal Surface Vibration on Laminar Forced Convective Heat Transfer," *Industrial and Engineering Chemistry,* Vol. 50,

No. 10, 1958, pp. 1565–1568.
25 Lamb, H., *Hydrodynamics*, Sixth ed., Cambridge University Press, 1932, pp. 450–475, 639–641.
26 Harkins, W., and Brown, F., "The Determination of Surface Tension (Free Surface Energy), and the Weight of Falling Drops: The Surface Tension of Water and Benzene by the Capillary Height Method," *Journal of American Chemical Society*, Vol. 41, 1919, p. 499.
27 Garner, F., and Lane, J., "Mass Transfer to Drops of Liquid Suspended in a Gas Stream, Part II: Experimental Work and Results," *Transaction Institution of Chemical Engineers*, Vol. 37, 1959, pp. 162–172.

Y. Jaluria

Engineering Research Center,
Western Electric Co.,
Princeton, N.J.

A Study of Transient Heat Transfer in Long Insulated Wires

This study concerns the transient thermal response of long insulated wires, a composite cylinder configuration, in which a highly conducting inner cylinder is sheathed in an outer cylinder of an insulating material. The study examines the heat transfer in such a cylindrical configuration and determines the parameters that govern its thermal response. A study of the transient behavior under various important surface boundary conditions, particularly the constant surface heat flux circumstance, is undertaken. The dependence of the transient response of the body, in terms of the characteristic surface and conductor temperatures, of the temperature distribution across the insulation and of other important physical aspects on the boundary conditions and on the governing parameters is investigated. The governing equation and boundary conditions are generalized and the solution obtained numerically to obtain the desired flexibility required for the variation in the boundary conditions. Several important and interesting results are obtained which indicate the nature of the thermal response and also the criteria for obtaining a desired variation in the transient behavior of this frequently encountered configuration.

Introduction

This study deals with the transient thermal behavior of a composite cylindrical body consisting of an outer insulation covering a highly conducting inner core. In manufacturing processes, this configuration encompasses a very wide range of problems frequently encountered. In the manufacture of insulated wires and cables, during and following the application of the insulation, the composite body invariably undergoes a thermal transient period. Similar considerations are of importance in insulated cables and pipes during start-up of energy transfer systems. Several other processes may similarly be mentioned which employ this configuration and this makes a study of the transient behavior of insulated wires, or the corresponding composite body, important. Such a study is of importance not only in the determination of the thermal response of the body for the evaluation of heat transfer rates and time involved, but also in providing the detailed information necessary in the selection of materials and in the design of the manufacturing facilities to obtain the required thermal process.

Much work has been done on the transient heat conduction in cylindrical bodies, a detailed collection of which has been given by Carslaw and Jaeger [1].[1] However, most of the analytical work has been on solid cylinders, Heisler [2], on hollow cylinders, Muskat [3], and under simplifying assumptions for the surface boundary conditions. Even with the assumption of a sudden step change in the surface temperature, which is not valid for most transients of interest, the analysis is very involved for the composite cylinder circumstance as discussed by Bowley and Koenig [4]. Some other solutions are given by Reid [5] and Jaeger [6]. These methods get even more involved for other surface boundary conditions, like the constant heat flux circumstance, and not much flexibility is obtained. In this regard, numerical methods allow a fast and simple determination of the transient response under varying boundary conditions. Recently, Beckett and Chu [7] have discussed a finite element method for heat conduction with nonlinear boundary conditions.

The composite cylindrical configuration studied here has a highly conducting inner cylinder sheathed in a cylinder of low thermal conductivity material. The temperature variation, therefore, is mainly in the outer insulation and the conducting core is essentially isothermal. This means that the problem centers on two characteristic temperatures—the outside surface temperature and the temperature of the core. This particular problem, though important and frequently encountered, has not been studied in any detail. The present work is a detailed study of its transient behavior under several surface boundary conditions of interest and with varying parameters that arise. The results are extended to include insulated pipes too.

The governing equation and boundary conditions are general-

[1] Numbers in brackets designate References at end of paper.

Contributed by the Heat Transfer Division for publication in the JOURNAL OF HEAT TRANSFER. Manuscript received by the Heat Transfer Division August 6, 1975. Paper No. 76-HT-U.

ized to determine the parameters that characterize the heat transfer in the composite body. This equation is solved numerically by finite-difference methods to determine the effect of these parameters on the transient response under various boundary conditions.

This study was undertaken in order to provide detailed transient heat transfer information on a configuration of considerable importance, under varying conditions and governing parameters. A simple numerical scheme was employed to obtain the desired flexibility and the important features in this problem are brought out from the results obtained. These considerations may relate to the temperature limitations of the insulation, to heat transfer characteristics or to the thermal process the body must undergo.

Method of Solution

The main purpose of this work is to study the transient heat transfer in long insulated wires, a configuration which, despite its importance, has not been studied in any detail heretofore. The important and interesting features in this work, therefore, concern the results which bring out several points of interest in this configuration. The method of solution employed is simple and allows the desired flexibility in order to obtain the results for varying conditions. However, it is quite straight forward and fairly well-documented and, therefore, not much need be said about it. In this section, an analysis of the problem is given in order to determine the governing parameters and to discuss the nature of the problem. Details of the numerical method may be obtained from Dusinberre [8].

The system under consideration consists of an inner cylinder of a highly conducting material and an outer one of an insulating material of low thermal conductivity k_0, Fig. 1. This implies that the temperature variation in the inner cylinder is small compared to the variation in the insulation and the core can, therefore, be taken as isothermal. However, it must be noted that for very short times, the penetration depth may be smaller than the dimensions of the core and in that case such a simplification is obviously not valid. For a step change in surface temperature of a semi-infinite body, the penetration depth is $\sqrt{12\alpha\tau}$, α being the thermal diffusivity and τ the time. The criterion for an isothermal core assumption is that the penetration depth be much greater than the core diameter, for radial heat transfer. For a material of large thermal diffusivity and for the time scales of interest in practical applications, the penetration depth is usually much larger than the dimensions of the core encountered and this assumption is quite valid. This study considers the case where there is essentially a uniform temperature in the core and the temperature variation occurs mainly in the insulation. For very short times, it might be more appropriate to approach the problem as a semi-infinite body. Analytical results for transients in a semi-infinite body are given by Gebhart [9] and Eckert and Drake [10]. This assumption of an isothermal core is not made for a simplification in the solution, since the numerical scheme allowing for temperature variation in the core can be easily obtained, but to facilitate an interpretation of the results and also because, in most applications of interest, the main concern is with the temperature distribution across the insulation and not with the slight variation in the core.

Employing the usual nondimensionalization in unsteady heat conduction, time τ' is generalized by R_0^2/α_0 to give the Fourier number $\alpha_0\tau'/R_0^2$ where R_0 is the outside radius of the composite body and α_0 the thermal diffusivity of the outer material. The absolute temperature T' is generalized by a reference temperature, taken as T_i' the initial temperature of the body. This allows a direct approach to a radiation boundary condition, though the temperature of the radiating source, if known, may also be employed, as done by Luikov [11]. The temperature, the radial distance, and time are denoted by T, r, and τ, respectively, in their nondimensional form.

The present problem is treated as a one-dimensional radial heat transfer problem. This requires that the cylindrical configuration be long, i.e., $L \gg R_0$, where L is the length subjected to the heat transfer, and that the heat transfer be uniform over the outer surface. Both these conditions are easily met in the case of insulated wires for most applications. The condition $L \gg R_0$ insures that the end effects are negligible. For a more rigourous evaluation of this condition, a study of the obtained results as a function of L/R_0 has to be made. The value of L/R_0 beyond which the axial heat flow could be neglected would depend on the material and heat transfer medium at the ends. For a higher thermal conductivity material, as the core, a greater temperature uniformity results and the criterion of employing this condition is restricted mainly to the insulation material. This study being for long insulated wires, which are usually encountered, the above condition is met satisfactorily.

With the foregoing nondimensionalization, the governing equation becomes:

$$\frac{\partial^2 T}{\partial r^2} + \frac{1}{r}\frac{\partial T}{\partial r} = \frac{\partial T}{\partial \tau} \tag{1}$$

For a constant heat transfer coefficient h at the surface, the boundary condition is given in terms of the Biot number, $\mathrm{Bi} = hR_0/k_0$:

$$\mathrm{Bi}(T_F - T_s) = \frac{\partial T}{\partial r}, \text{ at } r = 1 \tag{2}$$

Nomenclature

a = parameter defined in equation (4)
A = area of the interface between the core and the insulation
A_0 = outside surface area of the insulated wire
b = parameter defined in equation (5)
C = average specific heat of the insulated wire
C_0 = specific heat of the outer, or insulation, material
C_i = specific heat of the core material
G = thermal capacity ratio: $G = \rho_i C_i/\rho_0 C_0$
h = surface heat transfer coefficient
P = insulation thickness ratio: $P = \delta/R_0$
k_0 = thermal conductivity of insulation material
Q = heat flux input at the surface
Q_s = nondimensional heat flux input defined in equation (3)
R_0 = overall or outer radius of the composite body
R_i = radius of inner conductor or core
r' = radial distance from center of core
r = dimensionless radial distance: $r = r'/R_0$
T' = absolute temperature
T_i' = absolute initial temperature of the body
T = dimensionless absolute temperature: $T = T'/T_i'$
T_s = dimensionless surface temperature
T_F = dimensionless fluid temperature
Bi = Biot number
V = volume of the insulated wire-per-unit length
V_i = volume of the solid core-per-unit length
V' = volume of a hollow core-per-unit length
ΔT = nondimensional temperature difference across insulation
$\partial T/\partial \tau$ = nondimensional rate of temperature change with time
α_0 = thermal diffusivity of the outer, or insulation, material
ρ = average density of the insulated wire
ρ_0 = density of insulation material
ρ_i = density of inner conductor or core material
δ = insulation thickness
τ' = time from start of heat transfer process
τ = dimensionless time, $\alpha_0\tau'/R_0^2$

where T_s is the nondimensional surface temperature and T_F the fluid temperature. For the constant surface heat flux circumstance, the condition is:

$$\frac{\partial T}{\partial r} = \frac{QR_0}{k_0 T_i} = Q_s, \text{ at } r = 1 \tag{3}$$

where Q_s is a dimensionless parameter arising from Q, the constant heat flux absorbed at the surface. This is similar to that obtained by Luikov [11].

Similarly if the radiation emitted by the body is also incorporated, a time-dependent term is added due to the transient variation in surface temperature T_s. The resulting boundary condition is

$$\frac{\partial T}{\partial r} = Q_s[1 - a(T_s)^4], \text{ at } r = 1 \tag{4}$$

where a is the ratio of the radiant energy flux emitted by the body at the initial temperature to the constant flux absorbed Q. The ratio a would, obviously, depend on the radiation emissivities and angle factors involved. The dependence of the transient response on this parameter is studied. For combined convection and constant heat flux at the surface, the boundary condition is

$$\frac{\partial T}{\partial r} = Q_s[1 + b(T_F - T_s)], \text{ at } r = 1 \tag{5}$$

where b ($= hT_i/Q$) is the ratio of Bi and Q_s. Its effect is also studied.

With the assumption of an isothermal core, the boundary condition at the interface of the two materials is obtained by a balance of heat input and increase in thermal energy of the core. The resulting condition, with the nondimensionalization given earlier, is:

$$\frac{\rho_i C_i}{\rho_0 C_0} \cdot \frac{V_i}{AR_0} \cdot \frac{\partial T}{\partial \tau} = \frac{\partial T}{\partial r}, \text{ at } r = \frac{R_i}{R_0} \tag{6}$$

Therefore, this boundary condition gives rise to two parameters $\rho_i C_i/\rho_0 C_0$ and V_i/AR_0. The former is the ratio of the thermal capacity of the inner material to that of the outer. Let it be denoted by G. The other parameter V_i/AR_0 can be expressed in terms of the basic parameter δ/R_0, where δ is the thickness of the insulation. Denoting this insulation thickness ratio by P, the radius of the inner cylinder $R_i = (1 - P)R_0$. Also, $V_i/AR_0 = (1 - P)/2$ for a solid cylindrical core. Therefore,

$$G \cdot \frac{1 - P}{2} \frac{\partial T}{\partial \tau} = \frac{\partial T}{\partial r}, \text{ at } r = 1 - P \tag{7}$$

P and G would, therefore, be determined by the dimensions and materials in the problem. For a hollow inner cylindrical core, the above condition becomes simply:

$$G \cdot \frac{1 - P}{2} \cdot \frac{V'}{V_i} \cdot \frac{\partial T}{\partial \tau} = \frac{\partial T}{\partial r}, \text{ at } r = 1 - P \tag{8}$$

where V'/V_i is just the ratio of the volume of the hollow core to that of the solid one per unit length. This, therefore, in effect reduces the value of G and the results in this study can also be employed for determining the transient heat transfer in insulated pipes.

The governing equation was solved numerically for the appropriate boundary conditions at varying values of the important parameters discussed above. The insulation was divided into a large number of sections by nodal points. The number of nodal points was increased from 10 till the variation in the results by a further increase was less than 1 percent. On an average about 40 points were taken and the number was varied depending on the insulation thickness ratio P. Since the forward-difference method was employed, the results are obtained explicitly as one moves in time. Numerical stability, however, does pose a restriction on the time step size. Details on this are given in Dusinberre [8] and Gebhart [9]. The results obtained are presented and discussed in the following.

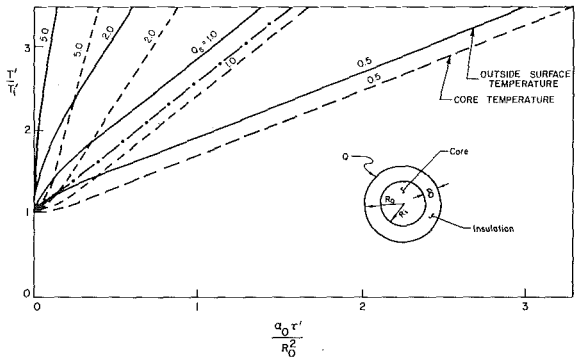

Fig. 1 The transient response of the surface and core temperatures at insulation thickness ratio $P = 0.5$ and thermal capacity ratio $G = 2.0$ for various values of the generalized heat flux Q_s. - • - • - •, Average temperature response for $Q_s = 1.0$.

Results and Discussion

Constant Surface Heat Flux. Results are first presented for the constant surface heat flux boundary condition. This circumstance is physically realized when in equation (4), $a(T_s)^4 \ll 1$, where T_s is the nondimensional surface temperature and a is the ratio of the radiant energy flux emitted by the body at the initial temperature T_i' to the constant heat flux absorbed Q. This condition is attained in several applications of interest in which the radiating source is at a temperature much higher than the transient body surface temperature, with the convective heat transfer negligible. These additional effects are considered separately later in this section.

Physically, a constant heat flux input at the surface implies a uniform increase in the energy content of the body which gives rise to a uniform increase in the average temperature. The transient response of the surface and core temperatures is shown in Fig. 1 for several values of the dimensionless heat flux Q_s. The ratio of the insulation thickness δ to the outer radius R_0, P, is kept constant at a value of 0.5, i.e., the case when the insulation extends to half the overall radius. The ratio G of the thermal capacity of the inner material to that of the outer is taken as 2.0. These values were chosen as they are close to typical average values encountered in practical applications and are physically easy to visualize. However, the effect of G and P on the thermal response is also considered separately later.

It is seen from Fig. 1 that all curves are essentially linear following an initial starting transient. Therefore, though the initial rate of temperature increase is very different for the surface as compared to that for the core, the starting effect dies out very fast and a constant rate of temperature rise is obtained beyond it. This gives rise to a constant temperature difference across the insulation. A similar result is discussed by Luikov [11] for a homogeneous cylinder. In this case too, the surface temperature rises very sharply at the beginning and then the difference between surface and centerline temperatures becomes constant. This is explained by an analysis which results in exponential terms that die out very rapidly with time and a linear rate of temperature increase is obtained when these terms become negligibly small. As expected, the rate of temperature rise increases as Q_s is increased, as does the temperature variation across the insulation.

The aforementioned interesting effects are seen more clearly in Fig. 2 in which the rate of temperature rise $\partial T/\partial \tau$ and the temperature difference across the outer cylinder ΔT are plotted against time τ for $Q_s = 1.0$, $G = 2.0$ and $P = 0.5$. The high rate of temperature rise at the surface decreases sharply with time and that in the core rises from its initial value of zero to attain a uniform rate of temperature rise throughout the body. The temperature difference ΔT similarly rises from its initial value of zero to attain a constant value. The dependence of these constant values of ΔT and $\partial T/\partial \tau$

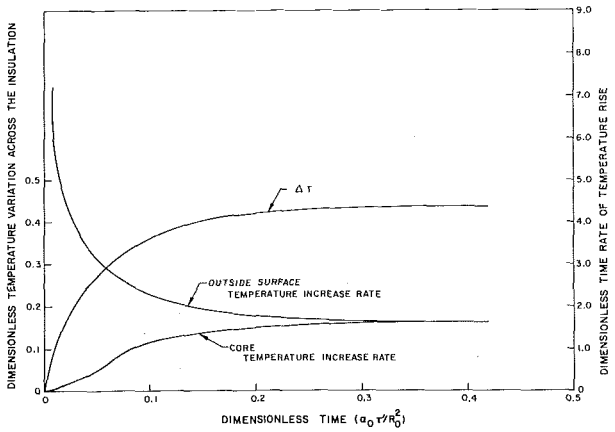

Fig. 2 Variation, with time, of the temperature difference across the insulation ΔT and of the rate of temperature rise $\partial T/\partial \tau$.

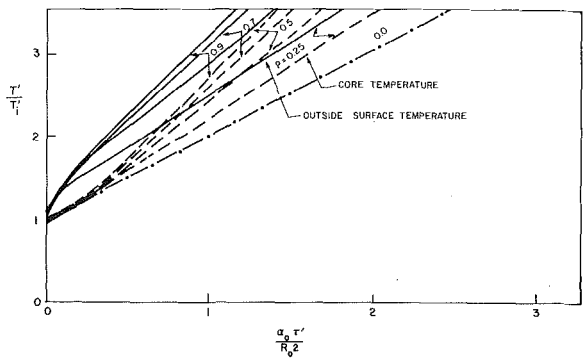

Fig. 3 Dependence of the transient temperature on the insulation thickness ratio P, surface flux being constant at $Q_s = 1.0$; $G = 2.0$

on P, G, and Q_s is discussed in detail in the following.

It is interesting to compare the foregoing results with the transient response of the average temperature of the composite body. For the constant surface heat flux case, the average temperature may be determined from an energy balance. Therefore,

$$\rho C V \frac{\partial T'}{\partial \tau'} = Q A_0 \tag{9}$$

where ρ, C, and T' are average values of density, specific heat, and physical temperature of the assembly, respectively. Nondimensionalization of the aforementioned equation gives, $\partial T/\partial \tau = Q_s \cdot A_0 R_0 \cdot \rho_0 C_0 / \rho C V$, where A_0 is the outside surface area and V the volume of the body per unit length. This clearly gives rise to a linear temperature increase with time and the curve corresponding to $Q_s = 1.0$, for $G = 2.0$ and $P = 0.5$, is shown in Fig. 1. The foregoing consideration indicates a very valuable result in that the time rate of temperature rise at any point in the composite body, following the initial starting transient discussed earlier, is given by its average temperature rise, obtained simply from the energy balance equation given in the foregoing.

The dependence of the transient response of the insulated wire on the parameter P, which determines the relative thickness of the insulation, for the surface heat flux $Q_s = 1.0$, and with $G = 2.0$, is shown in Fig. 3. $P = 0.0$ represents the case when the core occupies the entire volume and there is no insulation. The transient temperature of such an isothermal cylinder is calculated from equation (9) and shown in Fig. 3. Similarly, $P = 1.0$ is the case when only an homogeneous cylinder of the outer material is considered. For $P = 0.0$, equation (9) reduces to $\partial T/\partial \tau = Q_s$, at $G = 2.0$.

Fig. 3 shows that the rate of temperature rise $\partial T/\partial \tau$ decreases with a decreasing value of the insulation thickness ratio P, being lowest at 0.0. This is to be expected as a decrease in P implies a lowering of the relative insulation thickness which means that the insulation is replaced by a material of larger thermal capacity, being twice since $G = 2.0$. The effect of the insulation thickness ratio P on ΔT is determined by two factors. The first one is the total thermal capacity of the inner cylinder which decreases as P is increased. This increases the rate of temperature rise but at the same time holds the core temperature down less, tending to decrease the temperature variation across the insulation ΔT. However, an increase in P also increases the insulation thickness, which then tends to increase ΔT. These two effects act opposite to each other and the latter predominates over most of the variation of P. However, there is a slight drop beyond $P = 0.8$, Fig. 4, obviously due to the first effect being greater beyond this point.

Fig. 4 shows the dependence of the temperature variation across the insulation ΔT and Fig. 5 that of $\partial T/\partial \tau$ on the parameters P, G, and Q_s, for the constant surface heat flux boundary condition. A linear dependence on Q_s is obtained in both cases. This is not surprising considering the observed behavior of the transient temperature response due to which the rate of temperature increase is uniform throughout the body, and as Q_s linearly determines the gradient $\partial T/\partial r$ at the surface. The dependence on P is as discussed in the foregoing. With increasing G, $\Delta T'$ increases, implying that the core temperature is held lower due to the increase in energy required to raise it by a given amount. For a larger thermal capacity of the core, P being kept constant and the outer material unchanged so that Q_s and Fourier number $\alpha_0 \tau'/R_0^2$ remain unchanged, the rate of temperature increase $\partial T/\partial \tau$, following the starting transient, is obviously decreased due to increase in overall thermal capacity, equation (9). An increase in the thermal capacity of the core lowers the core temperature which then lowers the surface temperature. It is seen that this direct effect on the core temperature is greater and ΔT increases with an increase in G.

Effect of Radiative Loss. The foregoing considerations deal with the constant surface heat flux circumstance. The condition necessary for the validity of this assumption, besides negligible convection effects, is $(aT_s^4) \ll 1$ in equation (4). This condition is met in several applications of interest and the results obtained are important in a study of the transient response. In the manufacture of insulated cables, for instance, the radiating source may be at a temperature of around 2000 K and the cable surface temperature restricted to about 600 K, starting at room temperature. In this case, T_s is less than 2.0 and a is of the order of 10^{-3}. Clearly, the

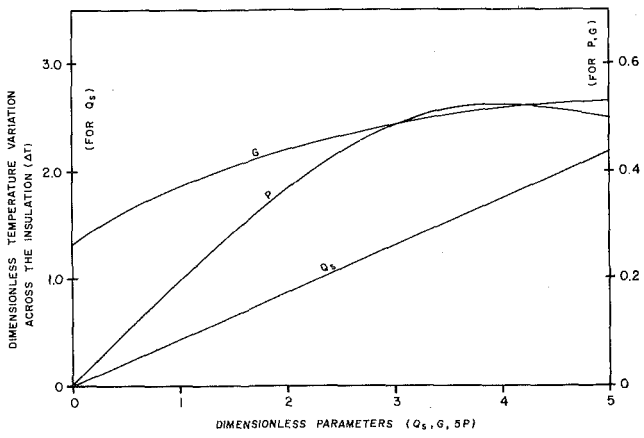

Fig. 4 Dependence of the constant temperature difference attained across the insulation ΔT beyond the starting transient, for the constant surface flux condition, on the parameters Q_s, G and P. For the variation of each, the other two are correspondingly held constant at the values of 1.0, 2.0 and 0.5 respectively.

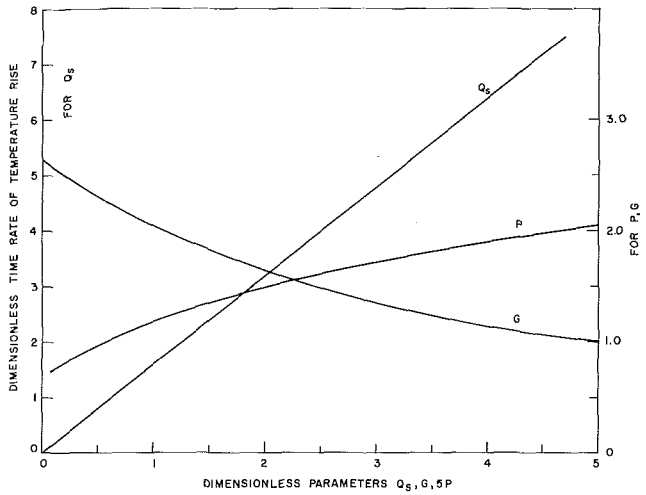

Fig. 5 Dependence of the constant rate of temperature rise $\partial T/\partial \tau$ attained beyond the starting transient, for the constant surface flux condition, on the parameters Q_s, G and P. For the variation of each, the other two are correspondingly held constant at the values of 1.0, 2.0 and 0.5 respectively.

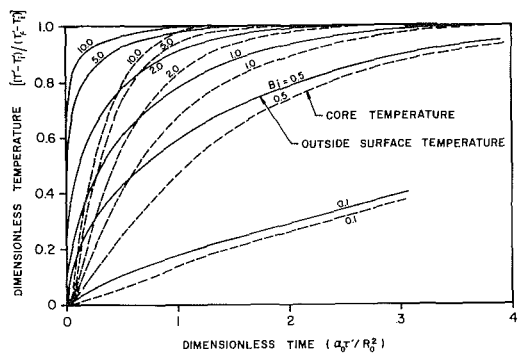

Fig. 7 Variation of the transient temperature with Bi, for immersion in fluid at temperature T_F; $G = 2.0$, $P = 0.5$.

assumption of constant surface heat flux is valid. However, in other cases, the radiation from the body and, possibly, convection may be important and must, therefore, be considered.

Fig. 6 shows the dependence of the transient response of the composite cylinder configuration on a, the parameter determining the importance of emitted radiation. The deviation from the constant heat flux case, $a = 0$, expectedly increases as the surface temperature increases, the deviation being larger at greater value of a. With increasing a, the temperature variation across the insulation and the rate of temperature rise, at a given time, are observed to decrease.

Addition of Convective Effects. The effect of an addition of convective heat loss, from the body, to the constant heat flux input at the surface is governed by equation (5), particularly by parameter b, the ratio of Bi to Q_s. However, first considering the pure convection mode, which occurs when the wire is immersed in a fluid, say at constant temperature, the boundary condition in equation (2) is employed. The transient response of the surface and core temperatures is shown in Fig. 7 as a function of Bi, for $P = 0.5$ and $G = 2.0$. The temperature is presented in the usual formulation, $(T^v - T_i')/(T_F' - T_i')$, so that it rises from 0 to 1.0, as the body temperature approaches the fluid temperature. The response is faster at higher Bi and a greater temperature uniformity in the wire is observed at low Bi. The effect, on the response, of variation in P and in G was found to be similar to that observed in the constant surface flux case.

The combined convection and constant surface heat flux circumstance is shown in Fig. 8. Keeping P and G fixed at 0.5 and 2.0, respectively, the parameter b is varied from 0.0 to 0.4, at $Q_s = 5.0$. This figure, therefore, indicates the dependence of the transient response of the body on the parameter b, where the mode of heat transfer at the surface goes from pure radiation towards pure convection as b increases. In the case shown, T_F is taken at T_i so that as the body heats up, the convective loss increases. If T_F were higher than T_i, the body initially gains heat from the ambient and then loses to it, when T_s is greater than T_F. The essential features of the heat transfer are seen in Fig. 8. With increasing b, the characteristic nature of the curves in Fig. 7 appear, wherein ΔT and $\partial T/\partial \tau$ decrease as the surface temperature approaches the fluid temperature. For each curve, there is a steady state temperature determined by the parameters of the problem. Radiative loss may similarly be added to the foregoing circumstance by a combination of equations (4) and (5).

When radiative and convective heat loss from the surface are added to the constant heat flux absorbed, the resulting boundary condition is:

$$\frac{\partial T}{\partial r} = Q_s[1 - a(T_s)^4 + b(T_F - T_s)], \text{ at } r = 1 \qquad (10)$$

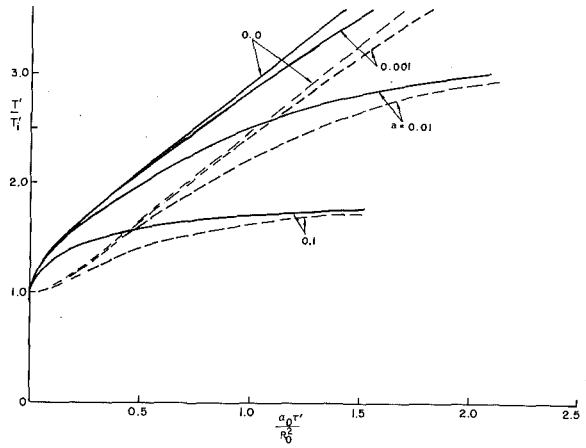

Fig. 6 Variation of the transient temperature with the parameter a, for $Q_s = 1.0$, $G = 2.0$ and $P = 0.5$, indicating the effect of radiative loss from the surface.

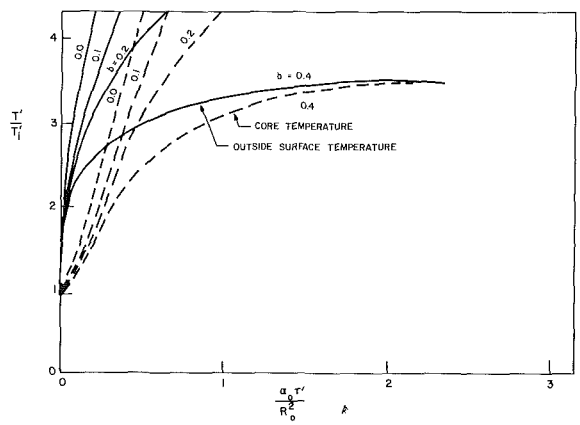

Fig. 8 Dependence of the transient temperature on parameter b, indicating the effect of convective heat loss from the surface, at $Q_s = 5.0$, $G = 2.0$ and $P = 0.5$.

The essential features of the results from this condition are already discussed in the foregoing and the problem may similarly be solved for given parameter values. This problem has been treated for a plate by Milton and Goss [12] for numerical stability considerations and by Crosbie and Viskanta [13] for the transient heat conduction. The foregoing equation (10) can also be employed in the determination of the appropriate boundary condition for an actual physical situation by evaluating the orders of magnitude of the various terms.

Conclusions

This work has considered the transient heat conduction in long insulated wires, in which the inner highly conducting core is assumed isothermal and the temperature variation exists only in the insulation. The parameters that govern the transient heat transfer are determined and their effect on important physical aspects of the transient response of this composite cylindrical body is considered in detail, under various surface boundary conditions of interest. Of particular interest was the constant surface heat flux circumstance, in which the temperature was found to increase linearly with time following an initial starting transient, and the variation in the response due to addition of radiative and convective heat loss from the surface was studied. Several important and interesting features concerning the heat transfer in such a configuration were obtained. The study provides detailed transient heat transfer information and determines important parameters and their effect on the thermal response for a problem of considerable importance in practical applications, on which no specific and detailed work has been done so far. These considerations are of importance in the determination of the thermal process for manufacture of insulated wires, and similar configurations, in the selection of materials and dimensions and in the determination of the transient temperatures in the body under various conditions of heat transfer at the surface.

References

1 Carslaw, H. S., and Jaeger, J. C., *Conduction of Heat in Solids*, Second ed., Oxford, 1959.

2 Heisler, M. P., "Temperature Charts for Induction and Constant Temperature Heating," TRANS. ASME, Vol. 69, 1947, p. 227.

3 Muskat, M., *Flow of Homogeneous Fluids Through Porous Media*, McGraw Hill, Chapter 10, 1937.

4 Bowley, W. W., and Koenig, H. A., "Charts for Thermal Transient in Composite Cylinders," JOURNAL OF HEAT TRANSFER, TRANS. ASME, Series C, Vol. 93, 1971, p. 248.

5 Reid, W. P., "Heat Flow in Composite Slab, Cylinder and Sphere," J. Franklin Inst., Vol. 274, 1962, p. 352.

6 Jaeger, J. C., "Heat Conduction in Composite Circular Cylinder," *Phil. Mag.*, Vol. 32, 1941, p. 324.

7 Beckett, R. E., and Chu, S. C., "Finite-Element Method Applied to Heat Conduction in Solids With Nonlinear Boundary Conditions," JOURNAL OF HEAT TRANSFER, TRANS. ASME, Series C, Vol. 95, 1973, p. 126.

8 Dusinberre, G. M. *Heat-Transfer Calculations by Finite Differences*, International Textbook Co., 1971.

9 Gebhart, B., *Heat Transfer*, Second ed., McGraw Hill, 1971.

10 Eckert, E. R. G., and Drake, R. M., *Analysis of Heat and Mass Transfer*, McGraw Hill, New York, 1972.

11 Luikov, A. V., *Analytical Heat Diffusion Theory*, Academic Press, McGraw Hill, 1968.

12 Milton, J. L., and Goss, W. P., "On Solving the Transient Conducting Slab With Radiating and Convecting Surfaces," JOURNAL OF HEAT TRANSFER, TRANS. ASME, Series C, Vol. 96, 1974, p. 547.

13 Crosbie, A. L., and Viskanta, R., "Transient Heating or Cooling of a Plate by Combined Convection and Radiation," *International Journal of Heat and Mass Transfer*, Vol. 11, 1968, p. 305.

A. Maewal
Research Assistant,
Department of A.M.E.S., University of California,
San Diego, Calif.

T. C. Bache
Staff Scientist, Systems,
Science & Software,
La Jolla, Calif.

G. A. Hegemier
Professor,
Department of A.M.E.S., University of California,
San Diego, Calif.

A Continuum Model for Diffusion in Laminated Composite Media[1]

Using a method developed for studying wave propagation problems, a continuum theory is developed for diffusion-type processes in a laminated composite with periodic microstructure. Construction is based upon an asymptotic scheme in which a typical macrodimension is assumed large compared to a microdimension. The order of truncation of the asymptotic sequence so obtained defines a hierarchy of models. Solutions are given for the lowest-order models and compared with the results from a finite difference code. For most cases the zeroth-order "effective conductivity" theory yields good results. For exceptional problems requiring a higher-order theory, a modified version of the first-order theory is shown to suffice. For many applications these elementary equations may offer an attractive alternative to other means for obtaining solutions.

Introduction

In recent years there has been much interest in the development of continuum models for composite materials; that is, models in which a single set (differential, differential-integral, etc.) of equations represent the material behavior. Such a continuum theory for elastic wave propagation in laminated composites has been presented by Hegemier, Bache, and Nayfeh [1–3][2] in a series of papers. These investigations are typical of work on this subject in that attention is focused on stress-wave propagation and the dominant phenomenon of dispersion. However, the work in [1, 2] is rather unique in that calculation of stress pulses and local (microstructure) quantities are given. The techniques developed may be applied as well to other composite material problems.

In this paper a continuum theory for the conduction of heat in laminated composite materials will be presented. It might be noted that a parallel analysis can be carried out for other physical processes characterized by the diffusion equation; for example, the slowing of neutrons governed by the Fermi age equation.

A general three-dimensional continuum theory of asymptotic character is developed. Based upon a small parameter ϵ which represents a ratio of typical composite micro- and macrodimensions, a consistent hierarchy of appropriate theories is defined. The lowest-order theory consists of a diffusion equation for a homogeneous, anisotropic material with material constants which are averages of the layer properties. Calculations comparing this lowest-order approximate theory to the exact show that it provides results sufficiently accurate for most problems of interest. For exceptional problems, a higher-order theory of elementary form is developed and an analytical solution obtained for a square wave input at the boundary. This latter theory contains microstructure information as is demonstrated by typical calculations.

Formulation

Consider a periodic array of homogeneous and isotropic laminates bonded at their interfaces. A plane view (for z = constant) of the geometry and coordinate system is shown in Fig. 1. Notations of the form $M_\alpha^{(k)}$ denote quantities in the kth layer of the αth material, $\alpha = 1, 2$; $k = 1, 2, \ldots$.

Each layer of the laminate is assumed to obey the diffusion equation

$$\gamma_\alpha \partial_t T_\alpha^{(k)} = \nabla^2 T_\alpha^{(k)}, \tag{1}$$

$\alpha = 1, 2$; $k = 1, 2, \ldots$

where $\nabla^2 = \partial_x{}^2 + \partial^2{}_{y_\alpha{}^{(k)}} + \partial_z{}^2$, and ∂_t represents partial differentiation with respect to time, etc. For heat conduction $T_\alpha^{(k)}(x, y_\alpha^{(k)}, z, t)$ represents the temperature of the α, k-layer, while t represents time. The constant γ_α is the reciprocal of the thermal diffusivity of the α-material defined by

$$\gamma_\alpha = \rho_\alpha c_\alpha / k_\alpha \tag{2}$$

where k_α, ρ_α, c_α are the thermal conductivity, mass density, and specific heat of the α-material [4].

Continuity of temperature across laminate interfaces requires

$$T_1^{(k)}(x, h_1, z, t) = T_2^{(k)}(x, -h_2, z, t),$$
$$T_1^{(k+1)}(x, -h_1, z, t) = T_2^{(k)}(x, h_2, z, t) \tag{3}$$

$k = 1, 2, \ldots$

Also, the heat flux normal to the laminates

[1] Research was sponsored by the Air Force Office of Scientific Research, Washington, D. C.

[2] Numbers in brackets designate References at end of paper.

Contributed by the Heat Transfer Division for publication in the JOURNAL OF HEAT TRANSFER. Manuscript received by the Heat Transfer Division June 30, 1975. Paper No. 76-HT-Z.

$$Q_\alpha{}^{(k)} = -k_\alpha \partial_{y_\alpha{}^{(k)}} T_\alpha{}^{(k)} \tag{4}$$

is required to be continuous at the interface (replace T by Q in equation (3)).

Equations (1)–(4) are the "exact" equations characterizing heat conduction in laminated materials. In the subsequent analysis, this infinite set of equations will be replaced by a set of four continuum equations of infinite order using the techniques developed in [1–3] for stress-wave propagation.

Equations of a Continuum Theory

Assume power series expansions of $T_\alpha{}^{(k)}$, $Q_\alpha{}^{(k)}$ about layer midplanes, i.e.,

$$g(x, y_\alpha{}^{(k)}, z, t) = g_{(0)}(x, z, t) + g_{(1)}(x, z, t) y_\alpha{}^{(k)} + \ldots + g_{(n)}(x, z, t) y_\alpha{}^{(k)n}/n! + \ldots \tag{5}$$

where g represents any of $T_\alpha{}^{(k)}$, $Q_\alpha{}^{(k)}$.

Substituting the expressions (5) into (1) and (4), and equating powers of $y_\alpha{}^{(k)}$ leads to differential-recurrence relations for the expansion coefficients. These are

$$T_{(\alpha)_{(n+2)}}{}^{(k)} = (\gamma_\alpha \partial_t - D^2) T_{\alpha_{(n)}}{}^{(k)},$$
$$Q_{\alpha_{(n)}}{}^{(k)} = -k_\alpha T_{(\alpha)_{(n+1)}}{}^{(k)} \tag{6}$$

where

$$D^2 \equiv \partial_x{}^2 + \partial_z{}^2 \text{ and } \alpha = 1, 2; k = 1, 2, n = 0, 1, 2, \ldots$$

The expansions (5) may then be reduced to

$$T_\alpha{}^{(k)}(x, y_\alpha{}^{(k)}, z, t) = C_\alpha{}^{(k)} T_{\alpha_{(0)}}{}^{(k)}(x, z, t) - y_\alpha{}^{(k)} k_\alpha{}^{-1} S_\alpha{}^{(k)} Q_{\alpha_{(0)}}{}^{(k)},$$
$$Q_\alpha{}^{(k)}(x, y_\alpha{}^{(k)}, z, t) = C_\alpha{}^{(k)} Q_{\alpha_{(0)}}{}^{(k)}(x, z, t) - y_\alpha{}^{(k)} k_\alpha L_\alpha{}^2 S_\alpha{}^{(k)} T_{\alpha_{(0)}}{}^{(k)} \tag{7}$$

where $C_\alpha{}^{(k)}$, $S_\alpha{}^{(k)}$, L_α are formal differential operators defined by

$$C_\alpha{}^{(k)} \equiv 1 + \frac{(y_\alpha{}^{(k)} L_\alpha)^2}{2!} + \frac{(y_\alpha{}^{(k)} L_\alpha)^4}{4!} + \ldots,$$
$$S_\alpha{}^{(k)} \equiv 1 + \frac{(y_\alpha{}^{(k)} L_\alpha)^2}{3!} + \frac{(y_\alpha{}^{(k)} L_\alpha)^4}{5!} + \ldots \tag{8}$$
$$L_\alpha{}^2 \equiv \gamma_\alpha \partial_t - D^2$$

Note that in equation (7), the temperature and heat flux throughout the laminated material are written in terms of their values ($T_{\alpha_{(0)}}{}^{(k)}$, $Q_{\alpha_{(0)}}{}^{(k)}$) at layer midplanes only.

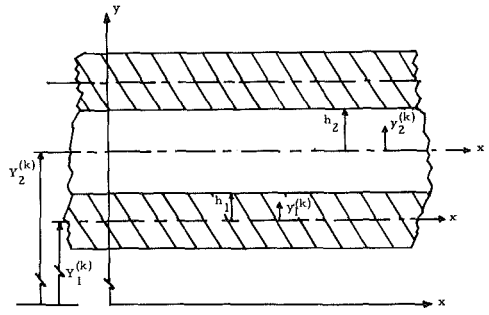

Fig. 1 Geometry and coordinate system

If the expansions (7) are substituted into the interface conditions (3) (and the analogous condition on $Q_\alpha{}^{(k)}$), the resulting four equations may be rearranged and written as

$$C_\alpha[Q_{\alpha_{(0)}}{}^{(k+1)} - Q_{\alpha_{(0)}}{}^{(k)}] + 2h_\beta k_\beta L_\beta{}^2 S_\beta T_{\beta_{(0)}}{}^{(k)} + h_\alpha k_\alpha L_\alpha{}^2 S_\alpha [T_{\alpha_{(0)}}{}^{(k+1)} + T_{\alpha_{(0)}}{}^{(k)}] = 0,$$
$$C_\alpha[T_{\alpha_{(0)}}{}^{(k+1)} - T_{\alpha_{(0)}}{}^{(k)}] + 2h_\beta k_\beta{}^{-1} S_\beta Q_{\beta_{(0)}}{}^{(k)} + h_\alpha k_\alpha{}^{-1} S_\alpha [Q_{\alpha_{(0)}}{}^{(k+1)} + Q_{\alpha_{(0)}}{}^{(k)}] = 0, \tag{9}$$
$$\alpha, \beta = 1, 2; \alpha \neq \beta; k = 1, 2, \ldots$$

The equations characterizing the problem have now been written as a set of differential-finite difference equations with dependent variables defined at discrete points (layer midplanes) along the y-axis. These will be converted to partial differential equations using the smoothing technique described in some detail in [1, 3]. In brief, $T_\alpha{}^{(k)}$, $Q_\alpha{}^{(k)}$ are replaced by the fields T_α, Q_α which are defined for all y and take on appropriate values when $y \epsilon (Y_\alpha{}^{(k)} - h_\alpha, Y_\alpha{}^{(k)} + h_\alpha)$; i.e., in the α, k layer (see Fig. 1). Since $Y_2{}^{(k)} = Y_1{}^{(k)} + \Delta$, where $\Delta \equiv h_1 + h_2$, equations (10) may be written with all dependent variables referred to $Y_\beta{}^{(k)}$. For example, $Q_{\alpha_{(0)}}{}^{(k+1)}$ is replaced by $Q_\alpha(Y_\beta{}^{(k)} + \Delta)$, $Q_{\beta_{(0)}}{}^{(k)}$ by $Q(Y_\beta{}^{(k)})$, $T_{\alpha_{(0)}}{}^{(k)}$ by $T_\alpha(Y_\beta{}^{(k)} - \Delta)$, etc. Here notations denoting functional dependence on x, z, t have been suppressed. Finally, the fields $T_\beta(x, Y_\beta{}^{(k)}, z, t)$, $Q_\alpha(x, Y_\alpha{}^{(k)} + \Delta, z, t)$, etc., are replaced by the smooth fields $T_\alpha(x, y, z, t)$, $Q_\alpha(x, y + \Delta, z, t)$, etc., defined throughout the domain by the problem, and all sums and differences are expanded about $\Delta = 0$. Thus, equations (9) are reduced to

Nomenclature

a_2, b_0, b_2, c_2, d_2 = nondimensional parameters, equation (22)
C_α, S_α = differential operators, equation (8)
$\mathcal{C}_\alpha$, $\mathcal{S}_\alpha$ = nondimensionalized operators corresponding to C_α and S_α
C_y, S_y = differential operators, equation (11)
$\mathcal{C}_\rho$, $\mathcal{S}_\rho$ = nondimensionalized operators corresponding to C_y and S_y
$D = \partial_x{}^2 + \partial_z{}^2$
$\mathcal{D} = \partial_\xi{}^2 + \partial_\zeta{}^2$
g = an arbitrary function
h_α = half length of α laminate
k = integer, denoting layer number from the origin
k_α = thermal conductivity of α material
k_M = mixture thermal conductivity normal to the laminates
k_D = mixture thermal conductivity parallel to laminates
L_α = differential operator, equation (8)
$\mathcal{L}_\alpha$ = nondimensionalized operator corresponding to L_α
ℓ = typical macrodimension
M_α, N_α = defined by equation (26b)
$n_a = h_\alpha/\Delta$
Q_0 = reference heat flux quantity
Q = heat flux normal to laminates
t = time
t_0 = reference time scale
T = temperature
T_0 = reference temperature
$-x, z$ = coordinate axes
$y_\alpha{}^{(k)}$ = local coordinate axis normal to laminates
y = global coordinate axis normal to laminates
α = 1 or 2, subscript denoting matrix or fiber material
β = 1 or 2, $\neq \alpha$
γ = reciprocal of thermal diffusivity
Γ = reciprocal of nondimensionalized thermal diffusivity
$\Delta = h_1 + h_2$
$\epsilon = \Delta/\ell$
$\zeta = z/\ell$
η = nondimensionalized temperature
μ = mixture heat capacity
$\xi = x/\ell$
$\rho = y/\ell$
$\rho_\alpha C_\alpha$ = heat capacity of α material
Σ = nondimensionalized heat flux normal to laminates
$\varkappa_\alpha$ = nondimensionalized thermal conductivity of α material

$$\Delta C_\alpha S_y \partial_y Q_\alpha + h_\beta k_\beta L_\beta{}^2 S_\beta T_\beta + h_\alpha k_\alpha L_\alpha{}^2 S_\alpha C_y T_\alpha = 0,$$

$$\Delta C_\alpha S_y \partial_y T_\alpha + h_\beta k_\beta{}^{-1} S_\beta Q_\beta + h_\alpha k_\alpha{}^{-1} S_\alpha C_y Q_\alpha = 0, \quad (10)$$

$$\alpha, \beta = 1, 2; \alpha \neq \beta$$

The operators C_y and S_y are defined by

$$C_y \equiv \cosh(\Delta\partial_y), \; S_y \equiv (\Delta\partial_y)^{-1} \sinh(\Delta\partial_y) \quad (11)$$

in analogy to equation (8).

Equations (10) are the equations of a continuum theory for heat conduction in a laminated composite material. The dependent variables T_α, Q_α have physical meaning at layer midplanes where they assume the appropriate exact values. Information on quantities within the layers is obtained from the microstructure equation (7).

Approximate Theories

A typical microdimension associated with the problem is the half bilaminate thickness Δ. Let ℓ represent a typical macrodimension and introduce the nondimensional quantities

$$\epsilon \equiv \Delta/\ell, \; \xi \equiv x/\ell, \; \rho \equiv y/\ell, \; \zeta \equiv z/\ell,$$

$$\eta_\alpha \equiv T_\alpha/T_0, \; \Sigma_\alpha \equiv Q_\alpha/Q_0, \; Q_0 \equiv k_M T_0/\ell,$$

$$\tau \equiv t/t_0, \; t_0 \equiv \gamma\ell^2 \quad (12)$$

where γ, k denote appropriate mixture diffusivity and conductivity to be defined subsequently. Note that characteristic time t_0 (such as that associated with heat input at the boundary) may be used to define the macrodimension ℓ. Using equation (12), equations (10) may be written as

$$\mathcal{C}_\alpha \mathcal{S}_\rho \partial_\rho \Sigma_\alpha + n_\beta \varkappa_\beta \mathcal{L}_\beta{}^2 \mathcal{S}_\beta \eta_\beta + n_\alpha \varkappa_\alpha \mathcal{L}_\alpha{}^2 \mathcal{S}_\alpha \mathcal{C}_\rho \eta_\alpha = 0,$$

$$\mathcal{C}_\alpha \mathcal{S}_\rho \partial_\rho \eta_\alpha + n_\beta \varkappa_\beta{}^{-1} \mathcal{S}_\beta \Sigma_\beta + n_\alpha \varkappa_\alpha{}^{-1} \mathcal{S}_\alpha \mathcal{C}_\rho \Sigma_\alpha = 0 \quad (13)$$

where $\mathcal{C}_\alpha$, $\mathcal{S}_\alpha$, $\mathcal{C}_\rho$, $\mathcal{S}_\rho$, $\mathcal{L}_\alpha$ are the scaled operators C_α, S_α, C_y, S_y, L_α. Also,

$$\Gamma_\alpha \equiv \gamma_\alpha/\gamma, \; n_\alpha \equiv h_\alpha/\Delta, \; \varkappa_\alpha \equiv k_\alpha/k_M, \; \mathcal{D} \equiv \partial_\xi{}^2 + \partial_\zeta{}^2 \quad (14)$$

From equations (13) and the (scaled) microstructure equations (7), a hierarchy of consistent approximate theories may be defined. A truncated system (13) of order N is obtained by truncating all $\mathcal{C}$ and $\mathcal{S}$ operators after terms of $O(\epsilon^{2N})$. A theory of order N is completed by truncating the scaled microstructure equations at the same level. The two lowest order cases ($N = 0, 1$) are of greatest practical interest. However, it might also be pointed out that the case $N = \infty$ represents an exact theory, as was demonstrated in [1–3] for the analogous equations governing stress wave propagation.

As equations (13) are a set of simultaneous, homogeneous, partial differential equations, it may be shown that the dependent variables all satisfy the same equation. That is, equations (13) may be reduced to

$$\{\cosh(2\epsilon\partial_\rho) - \cosh(2\epsilon n_1 \mathcal{L}_1)\cosh(2\epsilon n_2 \mathcal{L}_2)$$

$$- 2\epsilon^2 n_1 n_2 (\mathcal{H}\mathcal{L}_2{}^2 + \mathcal{H}^{-1}\mathcal{L}_1{}^2)\mathcal{S}_1\mathcal{S}_2\mathcal{C}_1\mathcal{C}_2\} \begin{Bmatrix} \eta_\alpha \\ \Sigma_\alpha \end{Bmatrix} = 0, \quad (15)$$

where $\mathcal{H} = \varkappa_2/\varkappa_1$. Of course, η_α and Σ_α, $\alpha = 1, 2$, do not satisfy equation (15) independently, but are related through equations (13) which serve as compatibility conditions.

In the limit as $\epsilon \to 0$, (15) reduces to

$$\{\partial_y{}^2 + (n_1{}^2 + n_2{}^2 + n_1 n_2(\mathcal{H} + \mathcal{H}^{-1}))D^2$$

$$- (n_1{}^2\gamma_1 + n_2{}^2\gamma_2 + n_1 n_2(\mathcal{H}^{-1}\gamma_1 + \mathcal{H}\gamma_2))\partial_t\} \begin{Bmatrix} T_\alpha \\ Q_\alpha \end{Bmatrix} = 0 \quad (16)$$

in dimensional form. Introduce the definitions

$$\mu \equiv n_1\gamma_1 k_1 + n_2\gamma_2 k_2, \; k_D \equiv n_1 k_1 + n_2 k_2,$$

$$k_M{}^{-1} = n_1 k_1{}^{-1} + n_2 k_2{}^{-1}, \; \gamma = \mu/k_M \quad (17)$$

and let γ^{-1} and k_M be the mixture diffusivity and conductivity for the scaling equation (12). (Alternately, define $\gamma_D = \mu/k_D$ and scale on k_D, γ_D. The choice is one of convenience.) With the definitions (17), equation (16) may be written

$$(k_M \partial_y{}^2 + k_D D^2 - \mu\partial_t) \begin{Bmatrix} T \\ Q \end{Bmatrix} = 0 \quad (18a)$$

where the dependent variables are now denoted by T and Q since the limiting $\epsilon \to 0$ approximation no longer distinguishes the two materials. Also, from equation (10) it may be deduced that heat flux normal to the laminates is

$$Q = -k_M \partial_y T \quad (18b)$$

Effective Conductivity Theory

Equations (18) are the equations of a truncated theory of order 0 as defined in the previous section. The first of these is seen to be the three-dimensional heat conduction equation for a homogeneous, anisotropic medium. The material constants appearing in the equation represent geometrically weighted averages of the properties of the individual layers. The zeroth-order theory may then be viewed as the heat conduction analog of the "effective modulus" theory of elasticity [5], which features averaged elastic constants similar in form to equation (17).

The heat conduction equation has been studied in great detail and solutions to many problems of interest may be found in the literature (see, for example, [4]). It will subsequently be shown that the "effective conductivity" equation (16) yields remarkably good agreement with an exact solution obtained via a finite difference numerical code for the particular case of heat conduction normal to the layers. Accepting the premise that the correlation remains substantially the same for two- or three-dimensional problems, in many applications the effective conductivity equations may offer an attractive alternative to other means for obtaining solutions.

Consider the case of heat propagating normal to the layers; e.g., assume that a given temperature field is applied to the boundary $y = 0$. For simplicity, assume a uniform temperature field of magnitude T_0 is applied to $y = 0$ from $t = 0$ to $t = t_0$ while the boundary temperature is zero for all other time. Then, using the nondimensionalization (12), the effective conductivity theory may be written[3]

$$(\partial_\rho{}^2 - \partial_\tau)\eta = 0,$$

$$\eta(0, \tau) = 1, \; \tau\epsilon(0, 1),$$

$$\eta(0, \tau) = 0, \; \tau\epsilon(0, 1),$$

$$\eta(\rho, 0) = 0 \quad (19)$$

Note that since $\ell = (t_0/\gamma)^{1/2}$, the parameter ϵ may be calculated. This parameter serves as a measure of the applicability of the effective conductivity theory since one expects good correlation with the exact when ϵ is small; that is, except for short temperature pulses input at the boundary.

The solution in equation (19) is

$$\eta = \operatorname{erfc}\left(\frac{\rho}{2\tau^{1/2}}\right), \; 0 < \tau \leq 1,$$

$$= \operatorname{erfc}\left(\frac{\rho}{2\tau^{1/2}}\right) - \operatorname{erfc}\left(\frac{\rho}{2(\tau-1)^{1/2}}\right), \; \tau > 1 \quad (20)$$

In Fig. 2, the solution equation (20) is compared to an exact solution for a typical problem. The exact solution was calculated by a finite difference code wherein the diffusion equation was differenced and solved by an implicit scheme. The figure depicts nondi-

[3] The effective conductivity equations for normal propagation can be derived in an elementary way using the analogy between the flow of heat and electrical current [6].

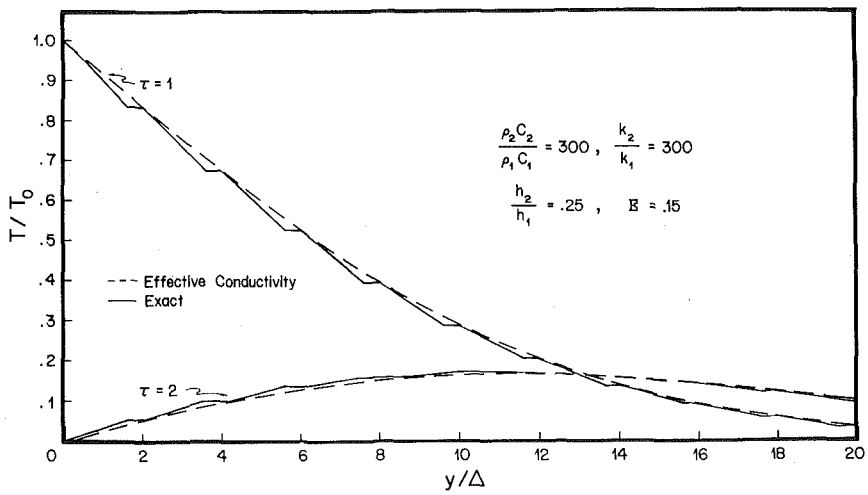

Fig. 2 Temperature distribution at $\tau = 1$ and 2 for widely differing material properties and large duration of input pulse t_0

mensionalized temperature η versus y/Δ for nondimensionalized time $\tau = 1$ and 2. The physical parameters characterizing the problem are listed on the figure. Here, despite the great variation in material properties between two layers, the agreement between exact and approximate theories is excellent, even with $\epsilon = 0.15$.

In Fig. 3, the exact and approximate theories are compared for a composite made up of similar materials but with $\epsilon = 0.5$. Once again, excellent agreement is obtained.

Higher Order Approximations

From Figs. 2 and 3, one infers that the 0th-order theory defined from equation (13) may differ appreciably from the exact only for problems with ϵ rather large, and even then only when the layer materials have substantially different heat conducting properties. For application to problems of the latter class, a higher-order theory of elementary form may be deduced from equation (13).

Expanding in powers of ϵ^2, equation (15) may be written

$$\{(1 + a_2\epsilon^2\partial_\rho{}^2)\partial_\rho{}^2 + (b_0 - b_2\epsilon^2\mathcal{D}^2 + d_2\epsilon^2\partial_\tau)\mathcal{D}^2 - (1 + c_2\epsilon^2\partial_\tau)\partial_\tau\}\begin{Bmatrix}\eta_\alpha\\ \Sigma_\alpha\end{Bmatrix} = 0, \alpha = 1, 2 \quad (21)$$

$$a_2 \equiv \tfrac{1}{3},\ b_0 \equiv k_D/k_M,$$

$$b_2 \equiv \frac{1}{3}(n_1{}^4 + n_2{}^4) + 2n_1{}^2n_2{}^2 + \frac{2}{3}n_1n_2(n_1{}^2 + n_2{}^2)(\mathcal{H} + \mathcal{H}^{-1}),$$

$$d_2 \equiv \frac{2}{3}(n_1{}^4\Gamma_1 + n_2{}^4\Gamma_2) + 2n_1{}^2n_2{}^2(\Gamma_1 + \Gamma_2) + \frac{2}{3}n_1n_2(n_1{}^2\Gamma_1 + n_2{}^2\Gamma_2)(\mathcal{H} + \mathcal{H}^{-1}) + \frac{2}{3}n_1{}^2(n_1{}^2 + n_2{}^2)(\mathcal{H}^{-1}\Gamma_1 + \mathcal{H}\Gamma_2),$$

$$c_2 \equiv \frac{1}{3}(n_1{}^4\Gamma_1{}^2 + n_2{}^4\Gamma_2{}^2) + 2n_1{}^2n_2{}^2\Gamma_1\Gamma_2 + \frac{2}{3}n_1n_2(\mathcal{H}^{-1}\Gamma_1 + \mathcal{H}\Gamma_2)(n_1{}^2\Gamma_1 + n_2{}^2\Gamma_2) \quad (22)$$

and where only terms of $O(\epsilon^2)$ have been retained in equation (21).

For heat flow normal to the layers, equation (21) reduces to

$$\{(1 + a_2\epsilon^2\partial_\rho{}^2)\partial_\rho{}^2 - (1 + c_2\epsilon^2\partial_\tau)\}\varphi = 0 \quad (23)$$

where φ represents any of η_α, Σ_α, $\alpha = 1, 2$. Expanding φ in a regular asymptotic expansion in powers of ϵ^2, substituting in equation (23), and collecting terms in the usual manner, equation (23) may be written, to the same order of accuracy as

$$\{\partial_\rho{}^2 - \partial_\tau + \epsilon^2(a_2 - c_2)\partial_\rho{}^2\partial_\tau\}\varphi = 0. \quad (24)$$

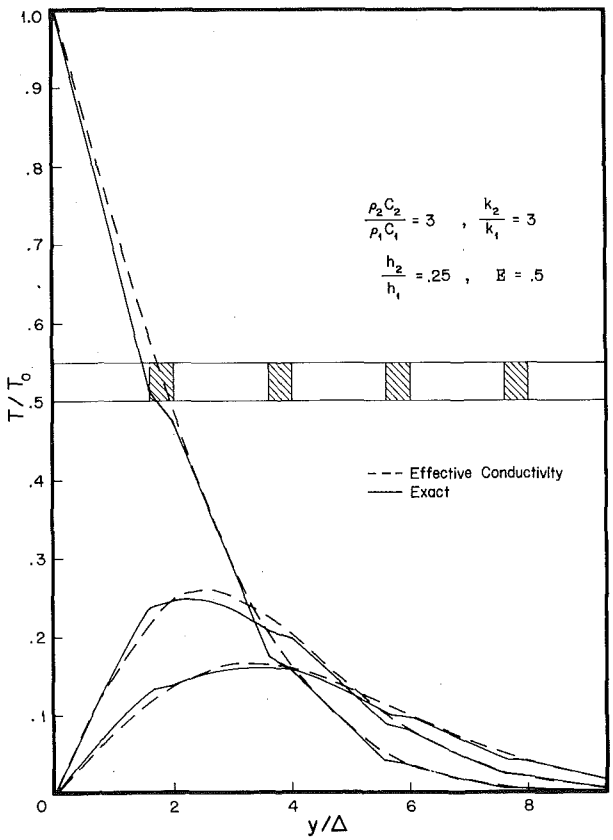

Fig. 3 Temperature distribution at $\tau = 1$, 1.5, and 2 for similar material properties and small duration of input pulse t_0

Also, it may be shown that $a_2 - c_2 > 0$ for any combination of material properties.

Equation (24) implies that

$$\partial_\rho{}^2 = \partial_\tau + O(\epsilon^2) \quad (25)$$

when operations are on any of the unknown functions. Using this property, equations (13) imply the following relations between the functions

$$\eta_\alpha = (1 + \epsilon^2 N_\alpha\partial_\tau)\eta_\beta,$$

$$\Sigma_\alpha = (1 + \epsilon^2 N_\beta \partial_\tau)\Sigma_\beta,$$

$$\Sigma_\alpha = -(1 + \epsilon^2 M_\alpha \partial_\tau)\partial_\rho \eta_\alpha, \alpha, \beta = 1, 2; \alpha \neq \beta \quad (26a)$$

where

$$N_\alpha = \frac{n_1 n_2}{2}\left(\frac{K_\beta \Gamma_\beta}{K_\alpha} - \frac{K_\alpha \Gamma_\alpha}{K_\beta}\right),$$

$$M_\alpha = \frac{1}{3}[n_1^2\Gamma_1 + n_2^2\Gamma_2 - 1 - n_1 n_2(n_1\Gamma_1/K_2 + n_2\Gamma_2/K_1) + 3n_1 n_2 K_\alpha \Gamma_\alpha / K_\beta]. \quad (26b)$$

Upon appending appropriate boundary conditions, equations (24) and (26) are the equations of the modified first-order theory. That is, given boundary conditions on one of the four dependent variables, solve equation (24) for that variable and use the relations (26) to obtain the remaining quantities. Recall from the derivation of equation (13) that the dependent variables η_α, Σ_α, $\alpha = 1, 2$, have physical meaning only at layer midplanes. Values of these functions at other points are given by the microstructure equations (7). For example,

$$\eta_\alpha^{(k)}(y_\alpha^{(k)}) = \eta_\alpha(Y_\alpha^{(k)}) + \epsilon \frac{\rho_\alpha^{(k)}}{K_\alpha}\partial_\rho \eta_\alpha(Y_\alpha^{(k)}) + \epsilon^2 \frac{\rho_\alpha^{(k)2}}{2}\Gamma_\alpha \partial_\tau \eta_\alpha(Y_\alpha^{(k)}) \quad (27)$$

where $\rho_\alpha^{(k)} \equiv y_\alpha^{(k)}/\Delta$ and $\eta_\alpha(Y_\alpha^{(k)})$ indicates η_α evaluated at $y = Y_\alpha^{(k)}$.

Addressing the difficult question of boundary conditions, one first observes that in truncating equation (13) or (15), terms involving higher-order space derivatives are dropped, a characteristic of singular perturbation problems. In this context the modified first-order theory must be viewed as an "outer" solution which should be extended to the boundary by matching with appropriate "inner" solutions. Rather than attempting this formidable task, we shall simply define the modified first-order theory to include the specification of the boundary conditions

$$\eta_1 = A(\tau) \text{ or } \Sigma_1 = B(\tau) \text{ on } \rho = 0 \quad (28)$$

where the origin $\rho = 0$ is defined to be at a distance $h_1 k_1/k_D$ from the free surface.

Given a square wave temperature input as specified in equation (19), an analytical solution to equation (24) may be obtained using the Laplace transform and contour integration. This is

$$\eta_1 = 1 - \frac{1}{\pi}\int_0^p \frac{e^{-r\tau}}{r}\sin\left(\left(\frac{pr}{p-r}\right)^{1/2}\rho\right)dr, \tau \leq 1,$$

$$= \frac{1}{\pi}\int_0^p \left(\frac{e^r}{r} - 1\right)\frac{e^{-r\tau}}{r}\sin\left(\left(\frac{pr}{p-r}\right)^{1/2}\rho\right)dr, \tau > 1 \quad (29)$$

where

$$p = [\epsilon^2(a_2 - c_2)]^{-1} \quad (30)$$

Then using the remaining equations (26) and (27) of the modified first-order theory, a complete solution may be obtained.

In Figs. 4 and 5, the results of two typical calculations are shown. As in the previous Figs. 2 and 3, the effective conductivity theory is compared to the exact results obtained from the finite difference code. For the modified first-order theory, equation (29) together with the first of equations (26a) and (27) give the temperature field for all ρ in terms of integrals like that in equation (29). Numerical value for the integrals were obtained using a standard Gaussian quadrature routine. In view of the close agreement between modified first-order and exact theories, investigation of still higher order analytical theories seems of little interest.[4]

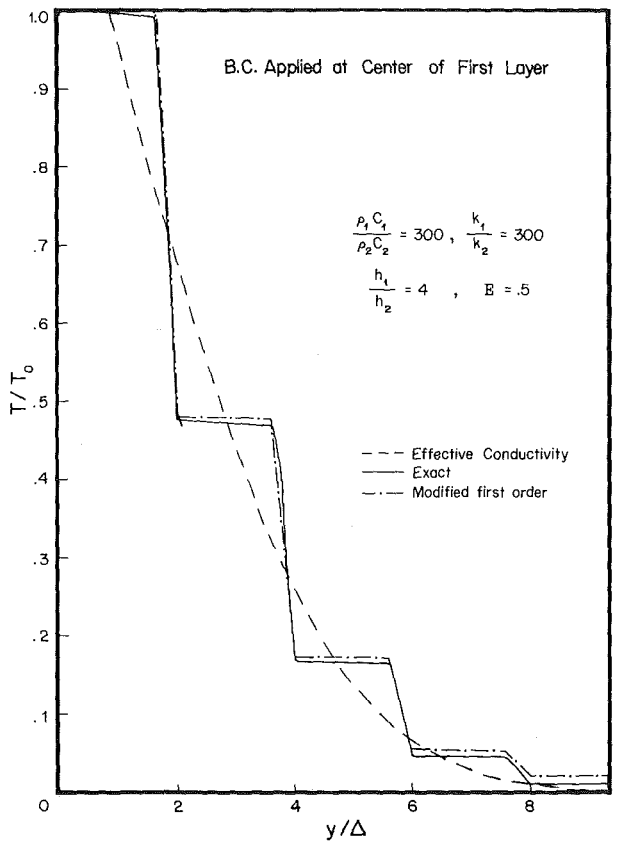

Fig. 4 Temperature distribution at $\tau = 1$ for widely differing material properties and small t_0

Concluding Remarks

The infinite set of equations (1)–(4) governing heat conduction in laminated composites was converted to a single set of equations (13) using a technique developed for studying wave propagation in composites. A hierarchy of continuum models was defined based upon a consistent truncation criterion. Of particular interest is the lowest-order theory called the "effective conductivity" theory. This theory is expected to correlate well with the exact for many problems of interest as is demonstrated by typical calculations (Figs. 2 and 3) for heat propagating normal to the layers. A higher-order approximate theory, the modified first-order theory, is discussed. For propagation normal to the layers the applicable equations are (24)–(28), and for a square-wave input at the boundary a closed form solution is given by equation (29). Typical calculations illustrating the ability of this theory to model microstructure details and thus closely match the exact are presented in Figs. 4 and 5.

It needs to be emphasized here that the basic set of equations (15) from which theories of various orders can be derived is valid for three-dimensional problems. The one-dimensional problem treated here was chosen mainly because the most important effects are expected when heat flow occurs normal to the laminates since the material properties are discontinuous in this direction. Hence a theory adequate for this situation will be satisfactory for three-dimensional problems also.

Since the equations of higher-order theories, e.g., equation (23), contain derivatives of orders higher than the second, there are some difficulties associated with prescribing proper boundary conditions. These difficulties can, however, be effectively avoided by

[4] Ben-Amoz [7] has suggested a continuum model for heat conduction in laminated composites which bears some similarity to that proposed here. For heat flow normal to the laminates and material properties such as those of Figs. 2, 4, 5 the lowest-order theory of Ben-Amoz is essentially identical to that of this paper. However, depicting numerical results for typical calculations in plots like Figs. 2–5, Ben-Amoz shows a significant deviation between his lowest-order and higher-order theories. It thus appears that either some error has been made or that the higher-order corrections of Ben-Amoz act to decrease the accuracy of his theory.

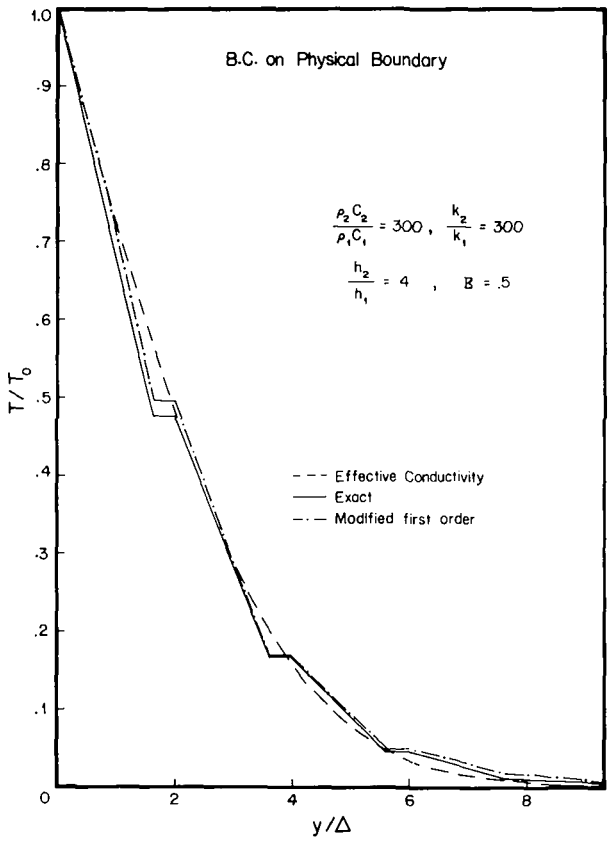

Fig. 5 Temperature distribution at $\tau = 1$ for widely differing material properties and small t_0

expanding the solution in powers of ϵ, as was done in the example problem.

There are some features of the theory that distinguish it from some other continuum models for heat conduction [7, 8]. First no a priori assumptions about the relative orders of magnitude of various field quantities are made. Moreover the zeroth order theory derived here is the "effective conductivity" theory which can also be constructed by simple averaging process. Finally the use of higher order theories allows the construction of local details (microstructure) of the field quantities. Because of these characteristics the model presented here appears to have greater usefulness.

Acknowledgment

The authors wish to thank Mike Gittings of Systems, Science and Software, Inc., for performing the finite difference calculations using his code CONDUCT.

References

1 Hegemier, G. A., and Nayfeh, Adnan, H., "A Continuum Theory for Wave Propagation in Laminated Composites Case 1: Propagation Normal to the Laminates," *Journal of Applied Mechanics*, Vol. 40, 1973, pp. 503–510.

2 Hegemier, G. A., and Bache, T. C., "A Continuum Theory for Wave Propagation in Laminated Composites Case 2: Propagation Parallel to the Laminates," *Journal of Elasticity*, Vol. 3, 1973, pp. 125–140.

3 Hegemier, G. A., and Bache, T. C., "A General Continuum Theory With Microstructure for Wave Propagation in Elastic Laminated Composites," *Journal of Applied Mechanics*, Vol. 41, 1974, pp. 101 105.

4 Sneddon, I. N., *Fourier Transforms*, McGraw-Hill, New York, Chapter 5, 1951.

5 Postma, G. W., "Wave Propagation in a Stratified Medium," *Geophysics*, Vol. 20, 1955, pp. 780–806.

6 Kreith, F., *Principles of Heat Transfer*, International Textbook Co., Scranton, Pa., 1958, p. 30.

7 Ben-Amoz, M., "Continuum Model of Heat Conduction in Laminated Composites," *Int. J. Engg. Sci.*, Vol. 9, 1971, pp. 1075 1085.

8 Ben-Amoz, M., "On Heat Conduction in Laminated Composites," *Int. J. Engg. Sci.*, Vol. 12, 1974, pp. 633–643.

K. Mastanaiah
Heat Transfer Group,
Propulsion Engineering Division,
Vikram Sarabhai Space Centre,
Trivandrum - 22, India

Correlation of Theoretical Analysis With Experimental Data on The Performance of Charring Ablators

Experimental data are obtained for surface recession, char depth, and temperatures in silica phenolic and carbon phenolic ablators from static test conducted on rocket nozzles. In an attempt to correlate the theoretical analysis with the experimental observations, it is found that the effective thermal conductivity of char is strongly dependent on the wall heat flux. An hypothesis is postulated that the char conductivity can best be correlated by cold wall heat flux treated as a generalized variable that includes the effects of other factors like temperature and chemical composition of the char. Exponential dependence of char conductivity on the cold wall heat flux is observed for both the ablators, and has offered excellent comparison between the theoretical and the experimental system response.

Introduction

Charring ablators have long been used in rocket nozzles and entry heat shields as an efficient insulation system to protect the structure from high heat flux and high temperature environment. While noncharring surface ablators like teflon do not block the incoming heat flux by transpiration, charring ablators like nylon, and silica phenolics have the advantage that the pyrolysis gases evolved due to decomposition tend to additionally cool the porous char as they pass through it, and simultaneously reduce the wall heat flux by transpiring into the main stream boundary layer.

Accurate prediction of char front and surface erosion in a charring ablator is essential for the thermal engineer to successfully carry out the design of an optimum thermal protection system that results in a minimum weight configuration. An excellent review of various mathematical models employed in the heat transfer analysis of charring ablation is recently given by Hurwicz and Rogan [1].[1] These models primarily differ from one another in the assumptions made to describe the mechanisms responsible for the char formation and its subsequent removal.

Rigorous numerical solution of the charring ablator problem has become a practical reality by the advent of the present day high speed digital computer. However, the theoretical analysis necessarily requires correct and reliable thermal properties to adequately describe the system response. There are about a dozen thermophysical-chemical properties of a charring ablator that go as input to the program which solves for the dynamics of the temperature field, char front, and surface regression. The determination of these properties over a wide temperature range by conventional experiments is often exhaustive and most difficult owing to the coupled phenomena involving heat and mass transfer. In such situations, nonlinear estimation [2] appears to be the only alternative procedure that serves as a simple, fast, powerful, and economic tool to simultaneously evaluate the property parameters and check the validity of the mathematical model used to describe the physical processes. The idea of the method is to minimize in the least squares sense the difference between the theoretical and the experimental system response, and has first been employed by Beck [3] for heat transfer problems.

Among the ablative properties the effective thermal conductivity of char is known to have a major influence on the performance of charring ablators [4]. Consequently considerable effort has been devoted to determine the char conductivity by conventional steady-state methods [4, 5]. It is widely recognized through experiments, as well as theoretical reasoning that the effective char conductivity is a function of several parameters like temperature, heating rate, char porosity and its radiative properties. It is concluded in references [4, 5] that the char thermal conductivity for nylon phenolic increases by nearly a factor of ten as the temperature is increased up to about 3000 K, and that radiation might be responsible for the significant rise in conductivity at high tempera-

[1] Numbers in brackets designate References at end of paper.

Contributed by the Heat Transfer Division for publication in the JOURNAL OF HEAT TRANSFER. Manuscript received by the Heat Transfer Division July 3, 1975. Paper No. 76-HT-P.

ture levels. It is also mentioned [6] that the conductivity of char made in an ordinary oven of low heating rate can differ markedly when made in an arc jet facility which simulates the intense heat flux encountered in rocket nozzles and entry heat shields.

It is surprising, however, to perceive that despite the importance of heating rate in controlling the char conductivity, a systematic study of the dependence of the effective char conductivity on the heating rate has been lacking in the literature. Fortunately, a simple and novel correlation of char conductivity with wall heat flux taken as a generalized variable is reported here in an attempt to compare the theory with the experimental data for estimating the thermal properties of ablators used in a rocket nozzle. As will be shown later in the paper, such a finding has rendered surprisingly good agreement between the theory and the experiment, thereby obviating the need for developing a complex expression for the char conductivity as a function of several variables.

Analysis

The physical assumptions employed for the present analysis are as follows:

1 Heat flow is one-dimensional.
2 Pyrolysis occurs in a single plane and at a fixed temperature.
3 The pyrolysis gases are in thermal equilibrium with the char.
4 Surface erosion is due to melting/sublimation of char at constant ablation temperature.
5 Linear ablation theory [7] is used to take into account the blocking effects due to mass transfer cooling in the main stream boundary layer.
6 The thermal properties are constant.
7 The effective thermal conductivity of char is dependent only on cold wall heat flux.
8 Reradiation from the exposed surface is neglected.

The calculation of the turbulent convective heat transfer coefficient h_g from combustion gases to the nozzle wall is based on the standard Bartz's equation [8] incorporating the effects of compressibility, throat curvature, and variation of transport properties in the boundary layer. The contribution of the radiative heat transfer is, however, ignored primarily since its magnitude is small compared to the total heat flux to the wall, and also due to the existing uncertainties in the prediction methods. Moreover, it is widely recognized that Bartz's equation would generally give conservative estimates for the convective heat transfer to the wall, thus compensating in some measure for the neglect of radiation from the gases to the nozzle wall.

A schematic of the system configuration for the ablative composite structure is shown in Fig. 1. Under the assumptions made, the mathematical description of transient heat conduction is given by:

Governing Equations.

$$K_1(\dot{q}_{cw})\frac{\partial^2 T_1}{\partial x^2} + \dot{m}_p \bar{C}_p \frac{\partial T_1}{\partial x} = \rho_1 C_{p_1}\frac{\partial T_1}{\partial t},\ \bar{X} < x < (\bar{X} + X_1) \quad (1)$$

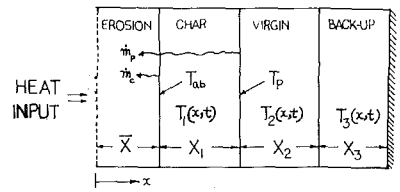

Fig. 1 Schematic of a Charring ablator

$$K_2\frac{\partial^2 T_2}{\partial x^2} = \rho_2 C_{p_2}\frac{\partial T_2}{\partial t},\ (\bar{X} + X_1) < x < (\bar{X} + X_1 + X_2) \quad (2)$$

$$K_3\frac{\partial^2 T_3}{\partial x^2} = \rho_3 C_{p_3}\frac{\partial T_3}{\partial t},\ (\bar{X} + X_1 + X_2) < x < (\bar{X} + X_1 + X_2 + X_3) \quad (3)$$

Boundary Conditions.

$$h_g(T_{aw} - T_1) = -K_1\frac{\partial T_1}{\partial x} + \dot{m}_p H_p + \dot{m}_c H_c,\ x = \bar{X} \quad (4)$$

$$-K_1\frac{\partial T_1}{\partial x} = -K_2\frac{\partial T_2}{\partial x} + \dot{m}_p \Delta H_p,\ x = (\bar{X} + X_1) \quad (5)$$

$$K_2\frac{\partial T_2}{\partial x} = K_3\frac{\partial T_3}{\partial x},\ x = (\bar{X} + X_1 + X_2) \quad (6)$$

$$\frac{\partial T_3}{\partial x} = 0,\ x = (\bar{X} + X_1 + X_2 + X_3) \quad (7)$$

Initial Condition.

$$T(x, 0) = T_0;\ \bar{X}_0 = X_{10} = 0 \quad (8)$$

Note that

$$\dot{m}_p = 0 \text{ if } (T_2)_{\max} < T_p$$
$$\text{and } \dot{m}_c = 0 \text{ if } (T_1)_{\max} < T_{ab} \quad (9)$$

The relations for the instantaneous surface locations are given by:

$$\bar{X} = \int_0^t \frac{\dot{m}_c}{\rho_1} dt$$
$$\bar{X} + X_1 = \int_0^t \frac{\dot{m}_p}{\rho_2 - \rho_1} dt$$
$$\bar{X} + X_1 + X_2 = \text{constant} \quad (10)$$

Numerical Solution.

The foregoing system of equations has been solved numerically by the finite difference explicit method. The solution procedure is similar to that employed by Swann and Pitman [7]. The method essentially utilizes the Murray-Landis scheme [9] which employs the substantial temperature-time derivative to take into account the moving boundaries of char front and surface erosion. Minor improvements have, however, been incorporated in the program. For example, the assumption of a small initial char for starting the

Nomenclature

C_p = specific heat
$\bar{C}_p$ = specific heat of pyrolysis gases
h_g = heat transfer coefficient
H_c = heat of ablation
H_p = blocking effectiveness of gaseous products of pyrolysis
K = thermal conductivity
$\dot{m}_c$ = rate of char loss
$\dot{m}_p$ = rate of loss of virgin material
$\dot{q}_{cw}$ = cold wall heat flux with no mass transfer, $h_g(T_{aw} - T_0)$
T = temperature
T_{ab} = ablation temperature
T_{aw} = adiabatic wall temperature
T_0 = uniform initial temperature
T_p = pyrolysis temperature
t = time
t_b = burning time
x = distance from the original inner surface
X = instantaneous thickness
$\bar{X}$ = surface erosion
ρ = density
ΔH_p = heat of pyrolysis

Subscripts

1, 2, 3 = refer to char, virgin, and back-up, respectively
0 = initial value

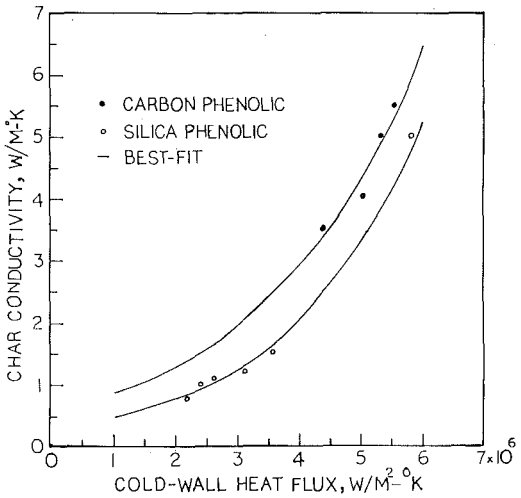

Fig. 2 Variation of char thermal conductivity with cold wall heat flux

solution is removed. Initially all the ablator is in virgin state and char begins to form only when the exposed surface reaches the decomposition temperature, and no starting difficulties have been observed. Uniform number of space intervals are taken both in the char and the virgin regions leading to a variable space net work. Different number of space divisions have been considered in the char and the virgin.

Experimental Data

A static test has been conducted on a rocket motor using silica phenolic and carbon phenolic ablators in different regions of the nozzle divergent. The temperature histories at the ablator-back-up interface have been recorded using 30 gauge insulated chromel-alumel thermocouples. The erosion and the char depth data along the nozzle divergent are measured by post test examination of the nozzles. Measured data on surface erosion and char depth at several axial locations in the divergent are depicted in Table 1. No correction has been applied to the post test values of char depth due to soak-back, and they are taken equal to the burn-out values, as the error in such an assumption is found to be insignificant [10]. In fact, sample calculations by the author have also indicated that the error due to soak-back in the char depth value is less than a fraction of a millimeter.

Correlation of Theory With Experiment

By a systematic correlation of the theoretical analysis with the test results of char depth and surface erosion, several thermophysical-chemical properties for both carbon phenolic and silica phenolic ablators have been estimated, and are found to lie within the band of the values reported in the literature. In particular, the properties evaluated for carbon phenolic appear to be in general agreement with those reported by Pfal and Mitchel [6] for the virgin and the char thermal conductivities, specific heat of char, heat of pyrolysis and pyrolysis temperature. They have used nonlinear regression for their estimation procedure, and considered the measured char interior surface temperature as a boundary condition for the analysis involving cylindrical coordinate system. Constant averaged properties are considered in their investigation. The detailed results of all the estimated thermal properties for both the ablators are not however reported here, as it is not the primary concern of this paper.

The results of this investigation have revealed an empirical relationship involving exponential dependence of the effective char conductivity on the cold wall heat flux. This explains the experimental observation that there is a pronounced increase in char depth and surface erosion in the near downstream region where heat fluxes are severe. The general correlation obtained is given by

$$K_1 = A \exp(B\dot{q}_{cw}) \tag{11}$$

where K_1 is expressed in W/(M − K) and $\dot{q}_{cw}$ in MW/(M² − K).

In equation (11), A and B are the two empirical constants which depend upon the type of material, and are to be established from the experimental data in conjunction with the theoretical model. It is found from the present results that the constants A and B for the two materials tested are given by:

$$A = 0.2884, B = 0.4845, \text{ for silica phenolic} \tag{12}$$

and

$$A = 0.5846, B = 0.3997, \text{ for carbon phenolic} \tag{13}$$

It would be worthwhile to mention here that in a preliminary attempt by the author to correlate the conductivity with temperature by first altering equation (1) to contain $\partial/\partial x(K_1 \partial T_1/\partial x)$, it is found that numerical instability has occurred at high heat flux values, and that even when stability is insured as in the case of a relatively low heat flux, the calculated char depth and erosion have not compared well with the experimental data. This clearly demonstrates the inadequacy of the correlation of conductivity with temperature alone.

On the other hand, an examination of the boundary condition equation (4) suggests that these mathematical instabilities that arise out of correlation with temperature can be in some sense representative of physical instabilities which bring to light the fact that the char conductivity should increase in relation to the cold wall heat flux. It is also known that the internal heat transfer depends on several variables like temperature, chemical reactions, porosity etc., all of which are in turn related to the wall heat flux. These arguments explain the basis of the present work for correlation of effective char conductivity with cold wall heat flux considered as a generalized variable. The mathematical model is accordingly followed in the present analysis, and this marks the important difference between the present model and the models employed by previous investigators.

Results and Comparison

The best-fit char thermal conductivity variation with cold wall heat flux is displayed in Fig. 2 both for carbon phenolic and silica phenolic. The conductivity for the silica phenolic char is estimated for a heat flux range of about 2–6 MW/M² and for carbon phenolic for about 4–6 MW/M². Extrapolation can, however, be made to determine the char conductivities outside this heat flux range, using the best-fit correlations. The correlation coefficient for silica phenolic is found to be 0.998 and is 0.966 for carbon phenolic. This high correlation is certainly indicative of the soundness of the mathematical model employed here regarding the effective char conductivity. The relatively low correlation for carbon phenolic is expected to be the result of small range of the cold wall heat flux for which the experimental data are available. It is interesting to note that the trend of the conductivity versus cold wall heat flux depicted in the figure is very similar to the trend obtained by conventional experiments [4, 5] for conductivity as a function of temperature. It is also found from Fig. 2 that for the same cold wall heat flux, the effective thermal conductivity of carbon phenolic char is higher than that of silica phenolic char. The increased conductivity for carbon phenolic char is attributed to its high carbon content. In general, the simple correlations obtained here for the effective thermal conductivity of chars are quite satisfactory for engineering design. It is expected that similar correlations may hold good for the chars of any other charring ablator, but the correlation constants A and B will be different and have to be established from experimental data in conjunction with theoretical analysis.

The calculated values of char depth, surface erosion, and temperatures using the best-fit thermal properties estimated here are now compared with the experimental data obtained from the test

Table 1 Comparison of calculated and experimental surface erosion and char depth at burn-out

Plane	$\dot{q}_{cw}$ (MW/M^2)	Ablator	Original thickness (mm)	Erosion (mm)		Char depth (mm)	
				Theory	Experiment	Theory	Experiment
1	5.82	Silica phenolic	30	4.7	5.5	16.1	17.5
2	5.53	Carbon phenolic	13	5.0	4.0	13.0	13.0
3	5.32	"	23	3.8	3.0	16.7	15.0
4	5.02	"	22	3.7	2.5	14.9	13.5
5	4.39	"	20	2.2	2.0	13.5	12.0
6	3.54	Silica phenolic	17	1.9	2.5	8.3	9.5
7	3.13	"	15	1.4	1.5	7.2	8.0
8	2.58	"	12	0.2	0.0	6.7	6.5
9	2.38	"	11	0.0	0.0	6.7	6.5
10	2.22	"	10	0.1	0.0	5.3	5.0

nozzle. Table 1 gives a summary of the comparison of char depth and surface erosion at burn-out at several planes located along the nozzle downstream. The values of cold wall heat flux and original ablator thickness have also been shown. The experimental char depth values at burnout are assumed equal to the post test values, since the error in such an assumption is known to be insignificant. The detailed theoretical histories of char depth, surface erosion, and temperature and comparison with test measurements are shown in Figs. 3–5.

Fig. 3 depicts the comparison of calculated char depth history with the experimental values. Good agreement is found between the theory and the experiment throughout the nozzle divergent. The maximum deviation in the predicted value of char depth is seen to be 1.7 mm. The calculated char depth increases very rapidly at the onset of pyrolysis and then gradually decreases, tending to reach a steady-state value. In all cases, char is found to form within a fraction of a second after firing starts. The char front appears nearly proportional to $\sqrt{t}$ like the penetration depth in a semi-infinite slab. The trend of the results is similar to that obtained by others.

The comparison for the surface erosion is shown in Fig. 4. The agreement between the calculated and the measured value is found to be very satisfactory, and the maximum error in the predicted erosion is about 1.2 mm. It is interesting to note that the trend of the theoretical surface erosion history is similar to that obtained for melt location history in a melting finite slab [11, 12], and also resembles the experimental trend of the ablation history measured using radioactive ablation sensors [13]. The measured surface erosions are generally slightly higher than the calculated values, revealing that some erosion due to mechanical shear and chemical oxidation is present.

A comparison of ablator-back-up interface temperature history at a particular location in the nozzle divergent is also displayed in Fig. 5. Excellent matching is observed between the calculated and the measured temperatures throughout the operating period.

The present theoretical analysis using the estimated thermal properties together with the correlations developed for the char thermal conductivities has compared favorably well with the experimental data of a few other test nozzles, thus demonstrating the consistency and the reliability of the correlations.

Conclusion

Comparison of the theoretical analysis with the experimental data on the performance of two charring ablators, namely carbon phenolic and silica phenolic, used in nozzle divergent has led to a postulation that the effective thermal conductivity of char can best be correlated by cold wall heat flux treated as a generalized variable to incorporate the effects of temperature and chemical composition of char. Simple exponential dependence of char conductivity is observed for both the ablators, and the corresponding correlation constants have been reported. The hypothesis postulated has permitted satisfactory agreement between the theoretical and the experimental system response. It is believed that a correlation of the type suggested here can be of considerable practical application in the design of efficient thermal protection systems as frequently demanded in space technology. The author hopes that fur-

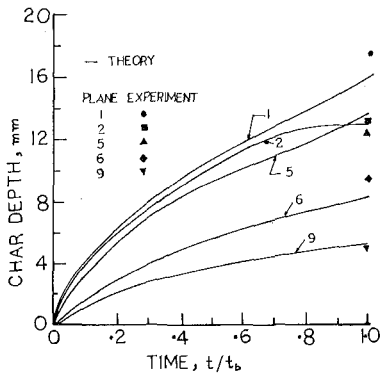

Fig. 3 Comparison of char depths

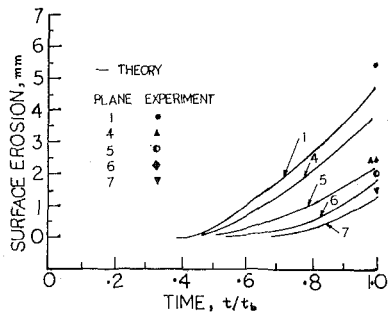

Fig. 4 Comparison of surface erosion

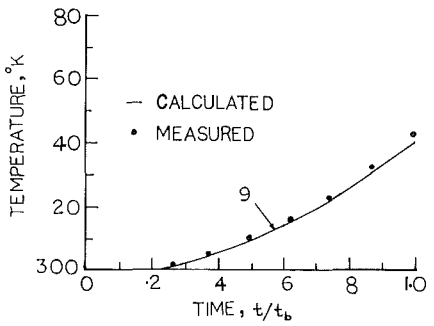

Fig. 5 Comparison of temperature history at the ablator-back-up interface

ther work in this direction will be carried out by other investigators to substantiate the applicability of the hypothesis.

References

1 Hurwicz, H., and Rogan, J. E., *"Ablation," Hand Book of Heat Transfer,* W. M. Rohsenow and J. P. Hartnett, eds., McGraw-Hill, New York, 1973, Section 16, pp. 16–1 to 16–.

2 Clark, B. L., "A Parametric Study of the Transient Ablation of Teflon," JOURNAL OF HEAT TRANSFER, TRANS. ASME, Series C, Vol. 94, No. 4, Nov. 1972, pp. 347–354.

3 Beck, J. V., "The Optimum Analytical Design of Transient Experiments for Simultaneous Determinations of Thermal Conductivity and Specific Heat," PhD thesis, Michigan State University, East Lansing, Mich., 1964.

4 Sanders, H. G., Smyly, E. D., and Pears, C. D., "An Investigation of Some Thermal and Mechanical Properties of a Low-Density Phenolic Nylon Ablation Material," NASA CR-66731, Feb. 1969.

5 Wilson, R., Gale, "Thermophysical Properties of Six Charring Ablators from 140° to 700°K and Two Chars from 800°K to 3000°K," NASA TN D-2291, Oct. 1965.

6 Pfal, R. C. Jr., and Mitchel, B. J., "Simultaneous Measurement of Six Thermal Properties of a Charring Ablator," *International Journal of Heat and Mass Transfer,* Vol. 13, 1970, pp. 275–281.

7 Swann, Robert T., and Pitman, Claud M., "Numerical Analysis of the Transient Response of Advanced Thermal Protection Systems for Atmospheric Entry," NASA TN D-1370.

8 Bartz, D. R., "A Simple Equation for Rapid Estimation of Rocket Nozzle Convective Heat Transfer Coefficients," *Jet Propulsion,* Vol. 27, No. 1, 1957, pp. 49–51.

9 Murray, W. D., and Landis, F., "Numerical and Machine Solutions of Transient Heat Conduction With Melting/Freezing," JOURNAL OF HEAT TRANSFER, TRANS. ASME, Series C, Vol. 81, No. 2, May 1959, pp. 106–112.

10 Barker, D. H., Kordig, J. W., Belnap, R. D., and Hall, A. F., "A Simplified Method of Predicting Char Formation in Ablating Rocket Exit Cones," *Heat Transfer-Cleveland, Chemical Engineering Progress Symposium Series,* Vol. 61, No. 59, 1965, pp. 108–114.

11 Citron, S. J., "Heat Conduction in a Melting Slab," *Journal of Aero/Space Sciences,* Vol. 27, 1960, pp. 219–228.

12 Mastanaiah, K., "On the Numerical Solution of Phase Change Problems in Transient Nonlinear Heat Conduction," to be published in the *International Journal for Numerical Methods in Engineering.*

13 Florentine, Robert, A., Schneider, J. F., and Gicking, D. S., "Radioactive Dispersions for Radioactive Ablation Sensors," *Journal of Spacecrafts and Rockets,* Vol. 4, No. 8, Aug. 1967, pp. 1083–1084.

ERRATUM

Erratum: W. Contreras and R. S. Thorsen, "Transient Melting of a Solid Heated by a Condensing Saturated Vapor—Case 1: Negligible Interface Curvature," published in the Nov. 1975 issue of the JOURNAL OF HEAT TRANSFER, pp. 570–575.

Equations (18) and (31*c*) should read:

$$\left.\frac{\partial \theta_L}{\partial \xi}\right|_{\xi=1} = \frac{\delta}{\alpha_L S_{LV}} [(\Delta_t + \delta_t) + \delta_x U_L - V_L]_{\xi=1} \tag{18}$$

$$c = 48\alpha_L \left\{ (1 + S_{LV}) - \left(1 + \frac{1}{2} S_{LV}\right) \frac{1}{S_{SL}} [(1 + 2S_{SL})^{1/2} - 1] \right\} \tag{31c}$$

journal of heat transfer

technical notes

Free Convection Heat Transfer To Non-Newtonian, Dilatant Fluids From a Horizontal Cylinder

C. B. Kim[1] and D. E. Wollersheim[2]

Nomenclature

C_p = specific heat, Btu/lbm-°F
g = gravitational acceleration, ft/s^2
g_c = gravitational constant, 32.2 lbm-ft/lbf-s^2
$G(n)$ = Gentry's flow behavior index-dependent coefficient
$K(n)$ = Kim's flow behavior index-dependent coefficient
K = consistency index, lbm/ft-(s)$^{2-n}$
k = thermal conductivity, Btu/hr-ft-°F
n = flow behavior index
N_{Gr_A} = Acrivos' Grashof number
N_{Pr_A} = Acrivos' Prandtl number
$N^+{}_{\mathrm{Gr}_K}$ = Kim's Grashof number
N_{Pr_K} = Kim's Prandtl number
$(N_{\mathrm{Nu}_r})_x$ = local Nusselt number based on radius
$(N_{\mathrm{Nu}_r})_{\mathrm{avg}}$ = average Nusselt number based on radius
q_0 = surface heat flux, Btu/hr-ft^2
r = radius, ft
T = temperature, °F
T_s = surface temperature, °F
T_∞ = bulk fluid temperature, °F
x = coordinate parallel to the surface
y = coordinate normal to the surface
β = coefficient of thermal expansion, 1/°F
ρ = density, lbm/ft^3
ϕ = circumferential angle
τ = shear stress, lbf/ft^2

Introduction

Theoretical studies on free convection to power-law fluids have been presented in the form of similarity solutions for an isothermal two-dimensional body [1],[3] similarity solutions for uniform heat flux-vertical flat plates [2], integral solutions for isothermal and uniform heat flux flat plates [3], and integral solutions for isothermal horizontal cylinders [4]. Experimental investigations have been reported in the cases of isothermal flat plates [5, 6], uniform heat flux-vertical flat plates [7], and isothermal horizontal cylinders [4]. The results of the experimental work generally seem to agree with the theoretical predictions.

Since only pseudoplastic test fluids were used in the previous studies, the present work was undertaken to obtain free convection data for rheological dilatant fluids using a horizontal cylinder. Surface boundary conditions considered were isothermal and uniform heat flux, and concentrated corn starch suspensions in aqueous sucrose solutions were utilized as dilatant fluids. The results of this investigation were analyzed and compared with the integral solutions presented in the Analysis.

Apparatus

The heat transfer apparatus employed in this investigation is essentially the same as that used earlier by Gentry and Wollersheim [4]. The cylindrical model is 2.034 in. in diameter and 8.018 in. in length, and consists of twenty aluminum segments each independently heated by resistance strips bonded to the interior surface. The local surface temperatures were measured by copper-constantan thermocouples embedded in the heated segments.

Analysis

For isothermal surface conditions, the integral solutions by Gentry and Wollersheim [4] are presented. These integral solutions compared well with Acrivos' similarity solutions. For uniform heat flux surface conditions, the integral solutions are provided by assuming proper dimensionless groups. In both cases the velocity and temperature profiles employed are those proposed by Fugii [8] and Tien [3] for a vertical plate.

Although the choice of velocity and temperature profiles used in the integral solutions is somewhat arbitrary, using Tien's profiles for a horizontal cylinder seems reasonable since these profiles satisfy well the imposed boundary conditions of the present investigation. With the assumption of high Prandtl number, inertial terms appearing in the momentum equation were neglected. The generalized Grashof and Prandtl numbers were defined, and the above velocity and temperature profile expressions were utilized to yield

[1] Graduate Student, Department of Mechanical and Aerospace Engineering, University of Missouri-Columbia, Columbia, Mo.
[2] Associate Professor, Department of Mechanical and Aerospace Engineering, University of Missouri-Columbia, Columbia, Mo.
Contributed by the Heat Transfer Division of THE AMERICAN SOCIETY OF MECHANICAL ENGINEERS. Manuscript received by the Heat Transfer Division July 24, 1975.

[3] Numbers in brackets designate References at end of technical note.

Table 1 Rheological properties of corn starch suspensions in aqueous sucrose solution

T	38% cs/ss Solution		39% cs/ss Solution		41% cs/ss Solution		42% cs/ss Solution	
°F	n	K	n	K	n	K	n	K
70	1.192	0.390	1.251	0.463	1.397	0.639	1.455	0.741
80	1.188	0.343	1.241	0.412	1.390	0.579	1.446	0.674
90	1.182	0.304	1.224	0.366	1.377	0.522	1.437	0.620
100	1.166	0.264	1.218	0.328	1.366	0.470	1.430	0.565

the solution for the local Nusselt number. The local Nusselt number based on the radius for both cases is expressed as follows:

Isothermal Conditions [4].

$$(N_{\mathrm{Nu}_r})_x = G(n)\left(\frac{2n+1}{3n+1}\right)^{\frac{n}{3n+1}} N_{\mathrm{Gr}_A}^{\frac{1}{2(n+1)}} N_{\mathrm{Pr}_A}^{\frac{n}{3n+1}} (\sin\phi)^{\frac{1}{2n+1}} \times \left[\int_{\phi=0}^{\phi} (\sin\phi)^{\frac{1}{2n+1}} d\phi\right]^{\frac{-n}{3n+1}} \quad (1)$$

where

$$N_{\mathrm{Gr}_A} = \left(\frac{\rho}{K}\right)^2 r^{n+2}[\beta g(T_s - T_\infty)]^{2-n} \quad (2)$$

$$N_{\mathrm{Pr}_A} = \frac{\rho C_p}{k}\left(\frac{K}{\rho}\right)^{\frac{2}{n+1}} r^{\frac{1-n}{n+1}}[r\beta g(T_s - T_\infty)]^{\frac{3(n-1)}{2(n+1)}} \quad (3)$$

Uniform Heat Flux Conditions.

$$(N_{\mathrm{Nu}_r})_x = K(n) N^{+}_{\mathrm{Gr}_K}{}^{\frac{3n+1}{2(n+1)(3n+2)}} N_{\mathrm{Pr}_K}^{\frac{n}{3n+2}} (\sin\phi)^{\frac{1}{2n+1}} \times \left[\int_{\phi=0}^{\phi} (\sin\phi)^{\frac{1}{2n+2}} d\phi\right]^{\frac{-n}{3n+2}} \quad (4)$$

where

$$N^{+}_{\mathrm{Gr}_K} = \left(\frac{\rho}{K}\right)^2 r^4 \left(\frac{g\beta q_0}{k}\right)^{2-n} \quad (5)$$

$$N_{\mathrm{Pr}_K} = \frac{\rho C_p}{k}\left(\frac{K}{\rho}\right)^{\frac{2}{n+1}} r^{\frac{2(n-1)}{n+1}} \left(\frac{g\beta q_0}{k}\right)^{\frac{3(n-1)}{2(n+1)}} \quad (6)$$

Test Fluids

Four volume concentrations (38, 39, 41, and 42 percent) of corn starch suspensions in an aqueous sucrose solution of 50 percent concentration by weight were used to represent rheological dilatant fluids. This sucrose solution had a viscosity of 8.4 centipoise at 85.2°F, and had a density of 1.23 gm/cc. The necessary concentration of sucrose solution was determined by making the density close to that of corn starch (1.24 gm/cc) in order to minimize settling problems in the suspension.

The viscometric tests showed that the dilatant behavior of the fluid, described by a power-law model (equation (7)), was restricted to particle concentrations of 36–44 percent by volume.

$$\tau = \frac{K}{g_c}\left(\frac{du}{dy}\right)^n \quad (7)$$

For the range lower than 36 percent, the fluid showed pseudoplastic behavior and for the range higher than 44 percent, the fluid was a Bingham plastic.

Rheological properties of the test fluids were obtained at four different temperatures (70, 80, 90, and 100°F) by using a Brookfield LVT viscometer, and these values were checked with a Weissenberg rheogoneometer at 88°F. Viscometric data were well represented by a power-law fluid model. The flow behavior index and consistency index of the fluids are presented in Table 1, and the actual Prandtl numbers of the test fluids were in the range from 6×10^3 to 2×10^4.

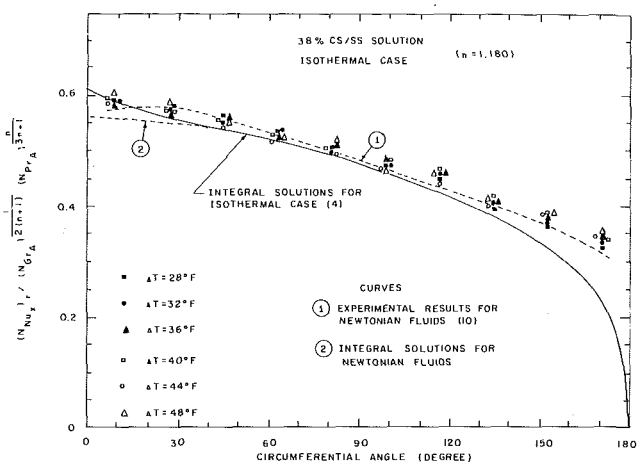

Fig. 1 Free convection results for isothermal surface conditions for 38 percent cs/ss solution

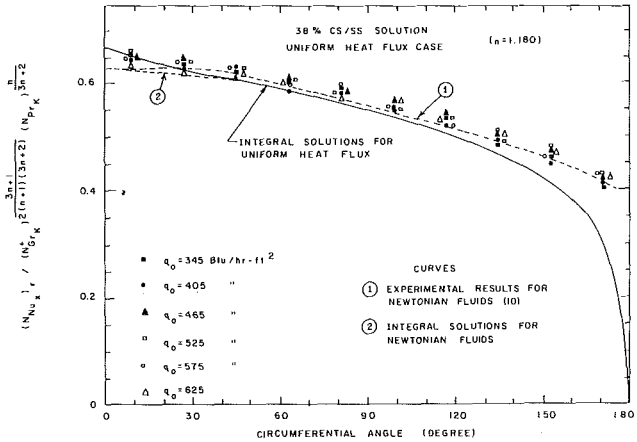

Fig. 2 Free convection results for uniform flux surface conditions for 38 percent cs/ss solution

Experimental Results

For uniform heat flux surface conditions, six different fluxes (255, 275, 295, 315, 335, and 355 Btu/hr-ft^2) were supplied to the cylinder surfaces and six temperature differences (28, 32, 36, 40, 44, and 48°F) were used for isothermal conditions.

A total of 24 runs was obtained for each of the boundary conditions. Local free convection data are expressed in terms of previously defined dimensionless groups for the 38 percent cs/ss solution in Fig. 1 for the isothermal case and in Fig. 2 for the uniform flux case. These results are typical for the four concentrations tested. The solid lines in the figures represent the integral solution predictions and experimental values are provided at angular positions of 9, 27, 45, 81, 99, 117, 135, 153, and 171 deg measured from the lower stagnation point.

In expressing the experimental property data, the dimensionless groups were evaluated at the local film temperature, which is the mean temperature of the cylinder surface and the bulk fluid temperature.

Experimental data for both isothermal and uniform heat flux conditions agree quite well with integral solutions for angles smaller than 140 deg. However, at angles higher than 140 deg, experimental values for the local free convection coefficients are significantly higher than the integral solutions.

Similar results were reported for pseudoplastic fluids for the isothermal case [4], and for mineral oil for both cases [10]. The results of mineral oil are shown in Figs. 1 and 2 for comparison. This phe-

nomenon is primarily attributable to boundary layer interaction in the upper stagnation region which is not accounted for in the integral solutions. At the upper stagnation region of the cylinder, the natural convection flow from one side of the cylinder interacts with the flow coming from the other side of the cylinder. As a result the integral solutions are not valid as the upper stagnation region is approached.

When comparing the integral solutions for different n values (including $n = 1$ for Newtonian fluids), it was found that the solutions were very close to each other when expressed in dimensionless form.

The expressions for average free convection were obtained by integrating local dimensionless groups over the test section surface. The average experimental Nusselt numbers for both cases are approximately 3–8 percent higher than the theoretical ones. The average Nusselt numbers for all experimental data were obtained from a least squares fit to be

$$(N_{\mathrm{Nu}_r})_{\mathrm{avg}} = 2.816\,(N_{\mathrm{Gr}_A} N_{\mathrm{Pr}_A})^{0.103}\text{: (isothermal)} \quad (8)$$

$$(N_{\mathrm{Nu}_r})_{\mathrm{avg}} = 3.544\,(N^{+}_{\mathrm{Gr}_K} N_{\mathrm{Pr}_K})^{0.071}\text{: (uniform heat flux)} \quad (9)$$

These expressions for the average Nusselt number for non-Newtonian, dilatant fluids should be useful for design purposes since their forms are relatively simple.

It was necessary to insure that the test fluids exhibited similar rheological behavior under natural flow conditions as those observed in the rotational viscometer since rheological properties determined by the viscometer were used for the actual flow conditions.

Due to the opaqueness of the test fluids, and the low velocity of the flow, the velocity profiles of the flow were not experimentally determined. However, the primary objective was to determine if shear rates under actual flow conditions were indeed within the range of the shear rates obtained by the viscometer. Therefore, Acrivos' expression [1] was employed to estimate the shear rates at the cylinder surface. The range of shear rates encountered under the actual flow conditions was approximately 0.100–2.00 l/s, while the shear rates produced in the rotational viscometer were in the range of 0.100–10.00 l/s. Therefore, it was assumed that the test fluids exhibited similar rheologically dilatant behavior. Further details regarding the present work may be found in reference [9].

References

1 Acrivos, A., "A Theoretical Analysis of Laminar Natural Convection Heat Transfer to Non-Newtonian Fluids," *AIChE Journal*, Vol. 6, Nov. 4, 1960, p. 584.

2 Chen, T. Y., and Wollersheim, D. E., "Free Convection at a Vertical Plate With Uniform Flux Condition in Non-Newtonian Power-Law Fluids," JOURNAL OF HEAT TRANSFER, TRANS. ASME, Series C, Vol. 95, No. 1, 1973, p. 123.

3 Tien, C., "Laminar Natural Convection Heat Transfer From Vertical Plate to Power-Law Fluid," *Appl. Sci. Res.*, Vol. 17, 1967, p. 233.

4 Gentry, C. C., and Wollersheim, D. E., "Local Free Convection to Non-Newtonian Fluids From a Horizontal Isothermal Cylinder," JOURNAL OF HEAT TRANSFER, TRANS. ASME, Series C, Vol. 96, No. 1, 1974, p. 3.

5 Reilly, I. G., Tien, C., and Adelman, M., "Experimental Study of Natural Convection Heat Transfer From a Vertical Plate in a Non-Newtonian Fluid," *Com. J. Ch.E.*, Vol. 43, 1965, p. 157.

6 Shanma, K. K., and Adelman, M., "Experimental Study of Natural Convection Heat Transfer From a Vertical Plate in a Non-Newtonian Fluid," *Com. J. Ch.E.*, Vol. 47, 1969, p. 553.

7 Dale, J. D., "Laminar Free Convection of Non-Newtonian Fluids From a Vertical Flat Plate With Uniform Surface Heat Flux," PhD thesis, University of Washington, Seattle, Wash., 1969.

8 Fujii, T., "Mathematical Analysis of Heat Transfer From a Vertical Flat Surface by Laminar Free Convection," *Bull. JSME*, Vol. 2, 1959, p. 363.

9 Kim, C. B., "Free Convection Heat Transfer to Non-Newtonian Rheological Dilatant Fluids From a Horizontal Cylinder," PhD thesis, University of Missouri-Columbia, Columbia, Mo., 1975.

10 Kim, C. B., Pontikes, T. J., and Wollershiem, D. E., "Free Convection From a Horizontal Cylinder With Isothermal and Constant Heat Flux Surface Conditions," JOURNAL OF HEAT TRANSFER, TRANS. ASME, Series C, Vol. 97, No. 1, 1975, p. 129.

Velocity Measurements for Buoyancy-Induced Flow in Mercury Adjacent to Vertical Single Cylinders

J. R. Welty[1] and D. R. Peinecke[2]

Nomenclature

f' = dimensionless velocity; = $xu/5\nu(\mathrm{Gr}_x{}^*/5)^{0.4}$

$\mathrm{Gr}_x{}^*$ = local modified Grashof number; = $\beta g q x^4/\nu^2 k$, evaluated at T_r

q = wall heat flux

T_r = reference temperature; = $0.7\,T_s + 0.3\,T_\infty$

u = local velocity in x-direction

x = axial coordinate measured from leading edge of heated section

y = coordinate normal to heated surface measured radially outward

β = coefficient of thermal expansion

η = dimensionless position; = $(y/x)(\mathrm{Gr}_x{}^*/5)^{0.2}$

Subscripts

∞ = value at distance far from heated surface

max = conditions representative of maximum value of u

s = evaluated at heated surface

x = evaluated at axial position, x

Introduction

It is the purpose of this note to present and characterize velocity profiles obtained from local measurements with mercury in buoyancy-induced flow adjacent to heated vertical cylinders. Experimentally determined velocity data for a liquid metal in natural convection and cylindrical geometry are reported here for the first time.

Velocity data have been previously reported with mercury adjacent to plane vertical surfaces [1, 2, 3];[3] analytical predictions are available for plane surfaces also [4, 5]. Heat transfer results and temperature profiles have been published with plane surfaces [1, 6, 3], single cylinders [7], and arrays of vertical cylinders [8]. A numerical solution for free convective heat transfer from slender cylinders has been reported recently by Cebeci, et al. [9]. The information presented herein supplements the heat transfer results of Wiles and Welty [7].

Measurement of local velocities in an opaque, highly conductive fluid such as mercury with relatively small temperature gradients existent presents a difficult experimental problem. A quartz-coated hot film anemometer probe was used for this purpose.

Experimental Apparatus and Procedure

Measurements were made with three different cylinder sizes; outside diameters were 5.354, 3.467, and 1.499 cm. Heated lengths were 9.779, 9.652, and 9.779 cm, respectively. Details of the heater construction and the constant temperature bath are available in [7].

The velocity probe was mounted to a two-dimensional traversing mechanism which provided positioning of the probe within ±0.00127 mm radially and 0.0127 mm axially (vertically). Calibra-

[1] Professor and Head, Department of Mechanical Engineering, Oregon State University, Corvallis, Ore. Mem. ASME.

[2] Aluminum Company of America, Wenatchee, Wash. Assoc. Mem. ASME.

[3] Numbers in brackets designate References at end of technical note.

Contributed by the Heat Transfer Division of THE AMERICAN SOCIETY OF MECHANICAL ENGINEERS. Manuscript received by the Heat Transfer Division August 29, 1975.

nomenon is primarily attributable to boundary layer interaction in the upper stagnation region which is not accounted for in the integral solutions. At the upper stagnation region of the cylinder, the natural convection flow from one side of the cylinder interacts with the flow coming from the other side of the cylinder. As a result the integral solutions are not valid as the upper stagnation region is approached.

When comparing the integral solutions for different n values (including $n = 1$ for Newtonian fluids), it was found that the solutions were very close to each other when expressed in dimensionless form.

The expressions for average free convection were obtained by integrating local dimensionless groups over the test section surface. The average experimental Nusselt numbers for both cases are approximately 3–8 percent higher than the theoretical ones. The average Nusselt numbers for all experimental data were obtained from a least squares fit to be

$$(N_{\mathrm{Nu}_r})_{\mathrm{avg}} = 2.816\,(N_{\mathrm{Gr}_A} N_{\mathrm{Pr}_A})^{0.103}\text{: (isothermal)} \quad (8)$$

$$(N_{\mathrm{Nu}_r})_{\mathrm{avg}} = 3.544\,(N^{+}_{\mathrm{Gr}_K} N_{\mathrm{Pr}_K})^{0.071}\text{: (uniform heat flux)} \quad (9)$$

These expressions for the average Nusselt number for non-Newtonian, dilatant fluids should be useful for design purposes since their forms are relatively simple.

It was necessary to insure that the test fluids exhibited similar rheological behavior under natural flow conditions as those observed in the rotational viscometer since rheological properties determined by the viscometer were used for the actual flow conditions.

Due to the opaqueness of the test fluids, and the low velocity of the flow, the velocity profiles of the flow were not experimentally determined. However, the primary objective was to determine if shear rates under actual flow conditions were indeed within the range of the shear rates obtained by the viscometer. Therefore, Acrivos' expression [1] was employed to estimate the shear rates at the cylinder surface. The range of shear rates encountered under the actual flow conditions was approximately 0.100–2.00 l/s, while the shear rates produced in the rotational viscometer were in the range of 0.100–10.00 l/s. Therefore, it was assumed that the test fluids exhibited similar rheologically dilatant behavior. Further details regarding the present work may be found in reference [9].

References

1 Acrivos, A., "A Theoretical Analysis of Laminar Natural Convection Heat Transfer to Non-Newtonian Fluids," *AIChE Journal*, Vol. 6, Nov. 4, 1960, p. 584.

2 Chen, T. Y., and Wollersheim, D. E., "Free Convection at a Vertical Plate With Uniform Flux Condition in Non-Newtonian Power-Law Fluids," JOURNAL OF HEAT TRANSFER, TRANS. ASME, Series C, Vol. 95, No. 1, 1973, p. 123.

3 Tien, C., "Laminar Natural Convection Heat Transfer From Vertical Plate to Power-Law Fluid," *Appl. Sci. Res.*, Vol. 17, 1967, p. 233.

4 Gentry, C. C., and Wollersheim, D. E., "Local Free Convection to Non-Newtonian Fluids From a Horizontal Isothermal Cylinder," JOURNAL OF HEAT TRANSFER, TRANS. ASME, Series C, Vol. 96, No. 1, 1974, p. 3.

5 Reilly, I. G., Tien, C., and Adelman, M., "Experimental Study of Natural Convection Heat Transfer From a Vertical Plate in a Non-Newtonian Fluid," *Com. J. Ch.E.*, Vol. 43, 1965, p. 157.

6 Shanma, K. K., and Adelman, M., "Experimental Study of Natural Convection Heat Transfer From a Vertical Plate in a Non-Newtonian Fluid," *Com. J. Ch.E.*, Vol. 47, 1969, p. 553.

7 Dale, J. D., "Laminar Free Convection of Non-Newtonian Fluids From a Vertical Flat Plate With Uniform Surface Heat Flux," PhD thesis, University of Washington, Seattle, Wash., 1969.

8 Fujii, T., "Mathematical Analysis of Heat Transfer From a Vertical Flat Surface by Laminar Free Convection," *Bull. JSME*, Vol. 2, 1959, p. 363.

9 Kim, C. B., "Free Convection Heat Transfer to Non-Newtonian Rheological Dilatant Fluids From a Horizontal Cylinder," PhD thesis, University of Missouri-Columbia, Columbia, Mo., 1975.

10 Kim, C. B., Pontikes, T. J., and Wollershiem, D. E., "Free Convection From a Horizontal Cylinder With Isothermal and Constant Heat Flux Surface Conditions," JOURNAL OF HEAT TRANSFER, TRANS. ASME, Series C, Vol. 97, No. 1, 1975, p. 129.

Velocity Measurements for Buoyancy-Induced Flow in Mercury Adjacent to Vertical Single Cylinders

J. R. Welty[1] and D. R. Peinecke[2]

Nomenclature

f' = dimensionless velocity; = $xu/5\nu(\mathrm{Gr}_x{}^*/5)^{0.4}$

$\mathrm{Gr}_x{}^*$ = local modified Grashof number; = $\beta g q x^4/\nu^2 k$, evaluated at T_r

q = wall heat flux

T_r = reference temperature; = $0.7\,T_s + 0.3\,T_\infty$

u = local velocity in x-direction

x = axial coordinate measured from leading edge of heated section

y = coordinate normal to heated surface measured radially outward

β = coefficient of thermal expansion

η = dimensionless position; = $(y/x)(\mathrm{Gr}_x{}^*/5)^{0.2}$

Subscripts

∞ = value at distance far from heated surface

max = conditions representative of maximum value of u

s = evaluated at heated surface

x = evaluated at axial position, x

Introduction

It is the purpose of this note to present and characterize velocity profiles obtained from local measurements with mercury in buoyancy-induced flow adjacent to heated vertical cylinders. Experimentally determined velocity data for a liquid metal in natural convection and cylindrical geometry are reported here for the first time.

Velocity data have been previously reported with mercury adjacent to plane vertical surfaces [1, 2, 3];[3] analytical predictions are available for plane surfaces also [4, 5]. Heat transfer results and temperature profiles have been published with plane surfaces [1, 6, 3], single cylinders [7], and arrays of vertical cylinders [8]. A numerical solution for free convective heat transfer from slender cylinders has been reported recently by Cebeci, et al. [9]. The information presented herein supplements the heat transfer results of Wiles and Welty [7].

Measurement of local velocities in an opaque, highly conductive fluid such as mercury with relatively small temperature gradients existent presents a difficult experimental problem. A quartz-coated hot film anemometer probe was used for this purpose.

Experimental Apparatus and Procedure

Measurements were made with three different cylinder sizes; outside diameters were 5.354, 3.467, and 1.499 cm. Heated lengths were 9.779, 9.652, and 9.779 cm, respectively. Details of the heater construction and the constant temperature bath are available in [7].

The velocity probe was mounted to a two-dimensional traversing mechanism which provided positioning of the probe within ±0.00127 mm radially and 0.0127 mm axially (vertically). Calibra-

[1] Professor and Head, Department of Mechanical Engineering, Oregon State University, Corvallis, Ore. Mem. ASME.

[2] Aluminum Company of America, Wenatchee, Wash. Assoc. Mem. ASME.

[3] Numbers in brackets designate References at end of technical note.

Contributed by the Heat Transfer Division of THE AMERICAN SOCIETY OF MECHANICAL ENGINEERS. Manuscript received by the Heat Transfer Division August 29, 1975.

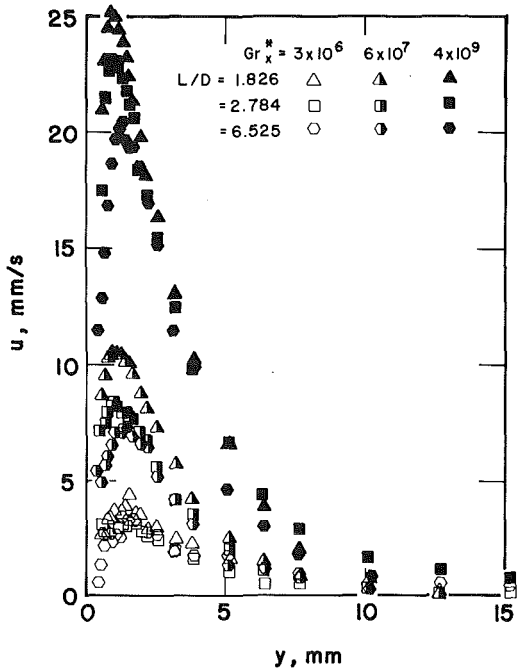

Fig. 1 Velocity data for three cylinders at three heat flux levels

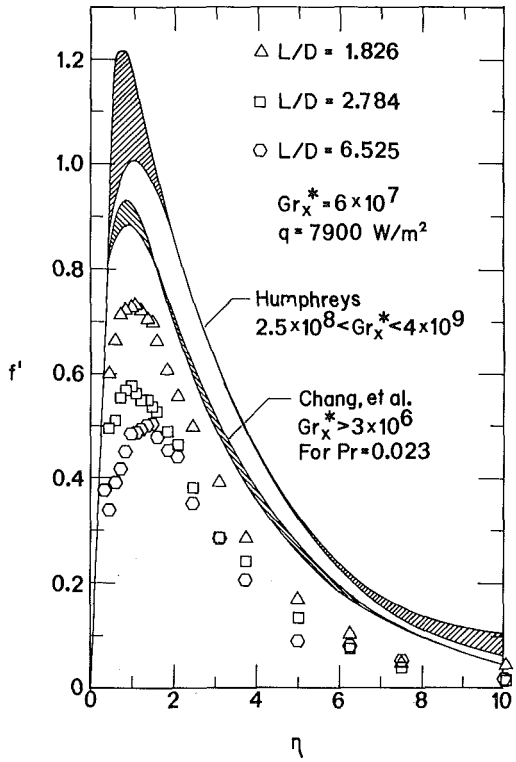

Fig. 3 Dimensionless velocity profiles, moderate heat flux

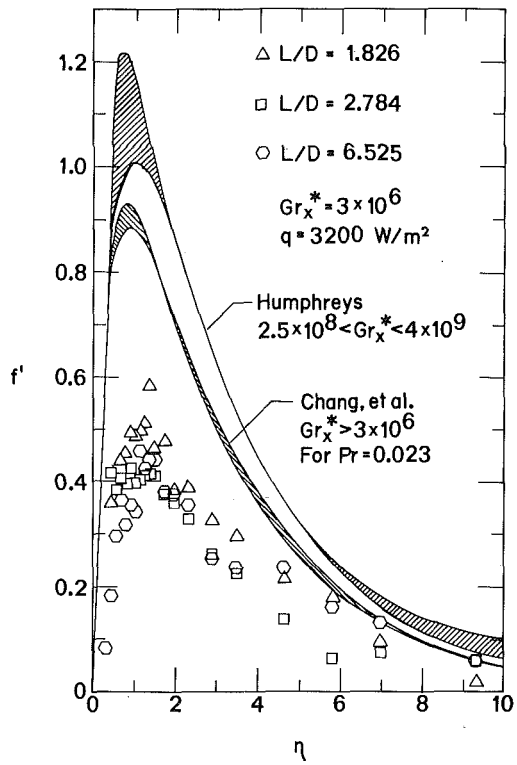

Fig. 2 Dimensionless velocity profiles, low heat flux

tion of the velocity probe was accomplished using procedures reported previously [10–12]. A miniature sheathed thermocouple, cemented to the anemometer probe support, permitted temperature and velocity data to be taken simultaneously.

The anemometer was calibrated before and after a series of velocity measurements with negligible change noted between them. The average correlation coefficient, for the more than 400 data points taken in this work, was 0.998.

Data were obtained with each test cylinder at heat flux levels of 3150, 7880, and 15760 W/m^2. For each heat flux, data were taken at axial positions, x, corresponding to values of Gr_x^* of 3×10^6, 6×10^7, and 4×10^9. Details of test procedures are discussed by Humphreys [12].

Results and Discussion

To characterize velocity profiles or to identify trends in the flow field as influenced by certain variables one would be interested in both the magnitude and location of the velocity maximum as well as the boundary layer thickness.

A priori one would reason that, for the same heat flux and location of observation relative to the surface, local velocity values would decrease with decreasing cylinder diameters, i.e., the effect of increased curvature would be to decrease local velocity, the plane-wall case being the maximum. Wiles [13] found that the effect of curvature on heat transfer was to increase local Nusselt numbers due to the greater radial temperature gradients present with smaller diameters.

Velocity profiles obtained for each of the three heat flux levels with each cylinder are of the typical shape for natural convection. Fig. 1 shows nine sets of velocity data, approximately one-third of the total data taken.

Trends in local velocity values and distribution are evident in Fig. 1. Hydrodynamic boundary layer thickness does not appear to change appreciably either with Gr_x^* or with cylinder diameter. Observable trends are present for both the magnitude and location of the maximum velocity.

Comparisons are shown in Figs. 2–4 with the flat plate data of Humphreys [11], and the perturbation results of Chang, et al. [5]. The parameters used are those suggested by Sparrow and Gregg [4], η being dimensionless position and f' being dimensionless velocity. The shaded areas in each figure represent the ranges in the results of each reference. It should be noted that both Humphreys

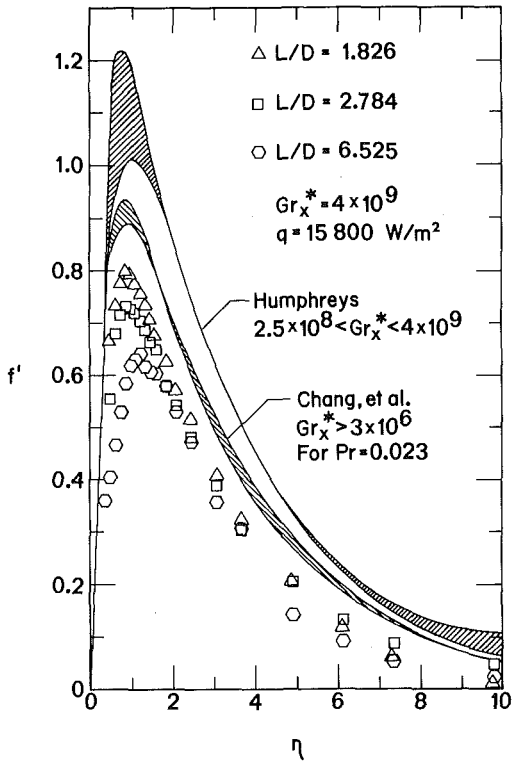

Fig. 4 Dimensionless velocity profiles, highest heat flux

and Chang, et al., observed a "crossing over" of their profiles, i.e., the Grashof number resulting in highest peak velocity yielded the lowest velocity far from the heated wall. Some evidence of this tendency is observable in these figures, particularly at $Gr_x^* = 3 \times 10^6$.

In each figure velocities adjacent to cylindrical surfaces are below those for a plane wall, the difference being less for increased values of Gr_x^*.

Experimental profiles display similar trends but do not coincide as would be true if the similarity parameters, η and f', were sufficient to describe the flow behavior. Definite variation is apparent with the amount of curvature and with Grashof number, variations with Gr_x^* due principally to a varying heat flux level. Since all measurements were accomplished in mercury no Prandtl number effect was investigated; the Prandtl number of mercury (Pr = 0.023) is representative of the liquid metals.

Conclusions that may be reached regarding natural convection in low Prandtl number fluids adjacent to heated vertical cylinders are the following:

1 Velocities adjacent to curved surfaces are below analytical results for flat plates, $L/D = 0$.

2 Velocity data, when reduced to f' versus η form, do not exhibit similarity. Differences are present both with heat flux level and with cylinder diameter.

3 Velocity profiles indicate the hydrodynamic boundary layer thickness to be only slightly affected by heat flux level or cylinder diameter.

4 The principal effect of heat flux and cylinder diameter is on magnitude and location of the velocity peak.

5 With increased heat flux the peak velocity increases and occurs nearer to the heated surface.

6 With decreasing diameter the peak velocity decreases in magnitude and occurs further away from the heated surface.

Indications from this work are that, with a given cylindrical surface oriented vertically, an increase in wall heat flux causes flow rates to increase in the near vicinity of the surface without appreciable effect on the extent of the flow field. This region is also where higher fluid temperatures exist. Thus, an increase in wall heat flux causes a significant increase in flow rate with an increase in energy concentration in the near-surface fluid layers.

Acknowledgment

This work was supported by the Energy Research and Development Administration, contract number AT(45-1)-2227.

References

1 White, D. H., Welty, J. R., and Hurt, J. C., "Experimental Study of Natural Convection Heat Transfer from Vertical Flat Plates in Mercury," *Progress in Heat Transfer*, Vol. 7, 1973, pp. 485–501.

2 Colwell, R. G., "Experimental Investigation of Natural Convection in Mercury in a Open Uniformly Heated Vertical Channel," PhD thesis, Department of Mechanical Engineering, Oregon State University, Corvallis, Ore., 1973.

3 Humphreys, W. W., and Welty, J. R., "Natural Convection With Mercury in a Uniformly Heated Vertical Channel During Unstable Laminar and Transition Flow," *AIChE Journal*, Vol. 21, Mar. 1975, pp. 268–274.

4. Sparrow, E. M., and Gregg, J. L., "Details of Exact Low Prandtl Number Boundary-Layer Solutions for Forced and Free Convection," NACA Memo 2-27-59E, 1959.

5 Chang, K. S., Akins, R. G., Burris, L., Jr., and Bankoff, S. G., "Free Convection of a Low Prandtl Number Fluid in Contact With a Uniformly Heated Vertical Plate," Argonne National Laboratory—6835, 1964.

6 Colwell, R. G., and Welty, J. R., "An Experimental Study of Natural Convection With Low Prandtl Number Fluids in a Vertical Channel With Uniform Wall Heat Flux," JOURNAL OF HEAT TRANSFER, TRANS. ASME, Series C, Vol. 96, Nov. 1974, pp. 448–454.

7 Wiles, L. E., and Welty, J. R., "An Experimental Investigation of Natural Convection With Vertical Cylinders in Mercury," JOURNAL OF HEAT TRANSFER, TRANS. ASME, Series C, Vol. 96, Nov. 1974, pp. 455–458.

8 Dutton, J. C., and Welty, J. R., "An Experimental Study of Low Prandtl Number Natural Convection in an Array of Uniformly Heated Vertical Cylinders," JOURNAL OF HEAT TRANSFER, TRANS. ASME, Series C, Vol. 97, Aug. 1975, pp. 372–377.

9 Cebeci, T., Quasim, J., Na, T. Y., "Free Convective Heat Transfer From Slender Cylinders Subject to Uniform Wall Heat Flux," Letters in *Heat and Mass Transfer*, Vol. 1, 1974, pp. 159–162.

10 White, D. H., "An Experimental Investigation of Natural Convection Heat Transfer From Vertical Flat Plates in Mercury," PhD thesis, Department of Mechanical Engineering, Oregon State University, Corvallis, Ore., 1971.

11 Hurt, J. C., and Welty, J. R., "The Use of a Hot Film Anemometer to Measure Velocities Below 5cm/sec in Mercury," JOURNAL OF HEAT TRANSFER, TRANS. ASME, Series C, Vol. 95, Nov. 1973, pp. 548–549.

12 Humphreys, W. W., "An Experimental Investigation of Heat Transfer in the Transition and Turbulent Regions for Natural Convection in Mercury in a Uniformly Heated Vertical Channel," MS thesis, Department of Mechanical Engineering, Oregon State University, Corvallis, Ore., 1975.

13 Wiles, L. E., "An Experimental Investigation of Laminar Natural Convection With a Uniformly Heated Vertical Cylinder in Mercury," MS thesis, Department of Mechanical Engineering, Oregon State University, Corvallis, Ore.

A Closed-Form Solution for the Radiosity at the Edge of a Rectangular Cavity

A. L. Crosbie[1]

Recently, Crosbie and Sawheny [1, 2][2] have applied Ambarzumian's method to the following integral equation describing the radiosity in a rectangular cavity:

[1] Thermal Radiative Transfer Group, Department of Mechanical and Aerospace Engineering, University of Missouri-Rolla, Mo.

[2] Numbers in brackets designate References at end of technical note.

Contributed by the Heat Transfer Division of THE AMERICAN SOCIETY OF MECHANICAL ENGINEERS. Manuscript received by the Heat Transfer Division July 24, 1975.

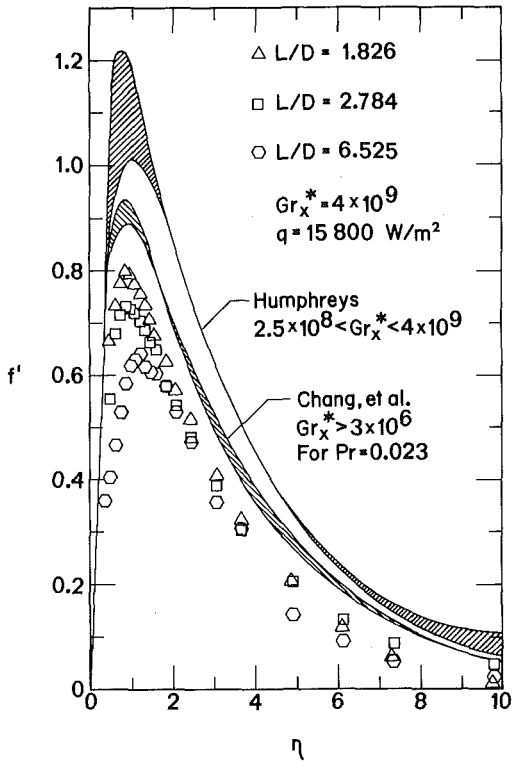

Fig. 4 Dimensionless velocity profiles, highest heat flux

and Chang, et al., observed a "crossing over" of their profiles, i.e., the Grashof number resulting in highest peak velocity yielded the lowest velocity far from the heated wall. Some evidence of this tendency is observable in these figures, particularly at $Gr_x^* = 3 \times 10^6$.

In each figure velocities adjacent to cylindrical surfaces are below those for a plane wall, the difference being less for increased values of Gr_x^*.

Experimental profiles display similar trends but do not coincide as would be true if the similarity parameters, η and f', were sufficient to describe the flow behavior. Definite variation is apparent with the amount of curvature and with Grashof number, variations with Gr_x^* due principally to a varying heat flux level. Since all measurements were accomplished in mercury no Prandtl number effect was investigated; the Prandtl number of mercury (Pr = 0.023) is representative of the liquid metals.

Conclusions that may be reached regarding natural convection in low Prandtl number fluids adjacent to heated vertical cylinders are the following:

1 Velocities adjacent to curved surfaces are below analytical results for flat plates, $L/D = 0$.

2 Velocity data, when reduced to f' versus η form, do not exhibit similarity. Differences are present both with heat flux level and with cylinder diameter.

3 Velocity profiles indicate the hydrodynamic boundary layer thickness to be only slightly affected by heat flux level or cylinder diameter.

4 The principal effect of heat flux and cylinder diameter is on magnitude and location of the velocity peak.

5 With increased heat flux the peak velocity increases and occurs nearer to the heated surface.

6 With decreasing diameter the peak velocity decreases in magnitude and occurs further away from the heated surface.

Indications from this work are that, with a given cylindrical surface oriented vertically, an increase in wall heat flux causes flow rates to increase in the near vicinity of the surface without appreciable effect on the extent of the flow field. This region is also where higher fluid temperatures exist. Thus, an increase in wall heat flux causes a significant increase in flow rate with an increase in energy concentration in the near-surface fluid layers.

Acknowledgment

This work was supported by the Energy Research and Development Administration, contract number AT(45-1)-2227.

References

1 White, D. H., Welty, J. R., and Hurt, J. C., "Experimental Study of Natural Convection Heat Transfer from Vertical Flat Plates in Mercury," *Progress in Heat Transfer*, Vol. 7, 1973, pp. 485–501.

2 Colwell, R. G., "Experimental Investigation of Natural Convection in Mercury in a Open Uniformly Heated Vertical Channel," PhD thesis, Department of Mechanical Engineering, Oregon State University, Corvallis, Ore., 1973.

3 Humphreys, W. W., and Welty, J. R., "Natural Convection With Mercury in a Uniformly Heated Vertical Channel During Unstable Laminar and Transition Flow," *AIChE Journal*, Vol. 21, Mar. 1975, pp. 268–274.

4. Sparrow, E. M., and Gregg, J. L., "Details of Exact Low Prandtl Number Boundary-Layer Solutions for Forced and Free Convection," NACA Memo 2-27-59E, 1959.

5 Chang, K. S., Akins, R. G., Burris, L., Jr., and Bankoff, S. G., "Free Convection of a Low Prandtl Number Fluid in Contact With a Uniformly Heated Vertical Plate," Argonne National Laboratory—6835, 1964.

6 Colwell, R. G., and Welty, J. R., "An Experimental Study of Natural Convection With Low Prandtl Number Fluids in a Vertical Channel With Uniform Wall Heat Flux," JOURNAL OF HEAT TRANSFER, TRANS. ASME, Series C, Vol. 96, Nov. 1974, pp. 448–454.

7 Wiles, L. E., and Welty, J. R., "An Experimental Investigation of Natural Convection With Vertical Cylinders in Mercury," JOURNAL OF HEAT TRANSFER, TRANS. ASME, Series C, Vol. 96, Nov. 1974, pp. 455–458.

8 Dutton, J. C., and Welty, J. R., "An Experimental Study of Low Prandtl Number Natural Convection in an Array of Uniformly Heated Vertical Cylinders," JOURNAL OF HEAT TRANSFER, TRANS. ASME, Series C, Vol. 97, Aug. 1975, pp. 372–377.

9 Cebeci, T., Quasim, J., Na, T. Y., "Free Convective Heat Transfer From Slender Cylinders Subject to Uniform Wall Heat Flux," Letters in *Heat and Mass Transfer*, Vol. 1, 1974, pp. 159–162.

10 White, D. H., "An Experimental Investigation of Natural Convection Heat Transfer From Vertical Flat Plates in Mercury," PhD thesis, Department of Mechanical Engineering, Oregon State University, Corvallis, Ore., 1971.

11 Hurt, J. C., and Welty, J. R., "The Use of a Hot Film Anemometer to Measure Velocities Below 5cm/sec in Mercury," JOURNAL OF HEAT TRANSFER, TRANS. ASME, Series C, Vol. 95, Nov. 1973, pp. 548–549.

12 Humphreys, W. W., "An Experimental Investigation of Heat Transfer in the Transition and Turbulent Regions for Natural Convection in Mercury in a Uniformly Heated Vertical Channel," MS thesis, Department of Mechanical Engineering, Oregon State University, Corvallis, Ore., 1975.

13 Wiles, L. E., "An Experimental Investigation of Laminar Natural Convection With a Uniformly Heated Vertical Cylinder in Mercury," MS thesis, Department of Mechanical Engineering, Oregon State University, Corvallis, Ore.

A Closed-Form Solution for the Radiosity at the Edge of a Rectangular Cavity

A. L. Crosbie[1]

Recently, Crosbie and Sawheny [1, 2][2] have applied Ambarzumian's method to the following integral equation describing the radiosity in a rectangular cavity:

[1] Thermal Radiative Transfer Group, Department of Mechanical and Aerospace Engineering, University of Missouri-Rolla, Mo.

[2] Numbers in brackets designate References at end of technical note.

Contributed by the Heat Transfer Division of THE AMERICAN SOCIETY OF MECHANICAL ENGINEERS. Manuscript received by the Heat Transfer Division July 24, 1975.

$$B(x, m) = e^{-mx} + \frac{\rho}{2}\int_0^\infty B(y, m)K(|x - y|)dy \quad (1)$$

with kernel

$$K(x) = \int_0^\infty ne^{-nx}J_1(n)dn = (1 + x^2)^{-3/2} \quad (2)$$

where $J_1(n)$ is the Bessel function of order one. The depth into the cavity is denoted by x. $\rho = 1$ corresponds to a cavity subject to exponentially decaying wall heat flux, i.e., $q_w(x) = q_0 \exp(-mx)$ [1], while $\rho < 1$ corresponds to a cavity subject to an exponentially decaying wall emissive power, i.e., $\sigma T_w^4(x) = \sigma T_0^4 \exp(-mx)$ [2]. The radiosity at the edge of the cavity satisfies either of the following two nonlinear integral equations:

$$B(0, m) = 1 + \frac{\rho}{2}B(0, m)\int_0^\infty \frac{nJ_1(n)B(0,n)}{n + m}dn \quad (3)$$

$$\overline{B(0,m)} = \sqrt{1 - \rho} + \frac{\rho}{2}\int_0^\infty \frac{mJ_1(n)B(0,n)}{n + m}dn \quad (4)$$

Inspection of equation (4) reveals that for $m = 0$

$$B(0, 0) = (1 - \rho)^{-1/2} \quad (5)$$

In the study of noncoherent scattering [3, p. 205] in a semiinfinite medium, the following integral equation for the source function arises:

$$S(\tau, z) = e^{-\tau/z} + \frac{\lambda}{2}\int_0^\infty S(t, z)K_1(|\tau - t|)dt \quad (6)$$

with kernel

$$K_1(\tau) = \int_0^\infty e^{-\tau/z'}G(z')dz'/z' \quad (7)$$

where τ is optical depth into the medium and λ is the albedo. The source function at the boundary, $S(0, z) = H(z)$ satisfies the following nonlinear integral equation [3, p. 212]:

$$H(z) = 1 + \frac{\lambda}{2}zH(z)\int_0^\infty \frac{H(z')G(z')}{z + z'}dz' \quad (8)$$

This equation can be solved [3, p. 216], i.e.,

$$H(z) = \exp\left\{-\frac{z}{\pi}\int_0^\infty \frac{\ln[1 - \lambda V(u)]}{1 + z^2u^2}du\right\} \quad (9)$$

where

$$V(u) = \int_0^\infty \frac{G(z)}{1 + u^2z^2}dz \quad (10)$$

Comparison of equations (1)–(3) with (6)–(8) reveals that $\lambda = \rho$, $z = 1/m$, $G(z) = J_1(1/z)/z^2$, and $B(0, m) = H(1/m)$. Thus,

$$V(u) = \int_0^\infty \frac{J_1(1/z)}{1 + u^2z^2}\frac{dz}{z^2} = \int_0^\infty \frac{m^2J_1(m)}{m^2 + u^2}dm = uK_1(u) \quad (11)$$

where $K_1(u)$ is the modified Bessel function of order one. The last integral was obtained from reference [4]; therefore, the radiosity at the edge of the cavity is given by

$$B(0, m) = \exp\left\{-\frac{m}{\pi}\int_0^\infty \frac{\ln[1 - \rho uK_1(u)]}{m^2 + u^2}du\right\} \quad (12)$$

This closed-form expression was evaluated numerically for a wide range of m and ρ values. The results agreed with the previous calculated values [1, 2] which were obtained from equation (4) by iteration.

Equation (12) is more suitable than equation (4) for investigating the nature of the edge singularity in the wall heat flux case ($\rho = 1$, $m \to 0$). When m is small, the main contribution to the integral in equation (12) occurs at small u. For small u

$$uK_1(u) \simeq 1 + \frac{1}{2}u^2\ln\frac{u}{2} + \frac{1}{4}u^2(2\gamma - 1) \quad (13)$$

with $\gamma = 0.5772156649\ldots$ Substitution of this approximation into equation (12) yields

$$B(0, m) \simeq \exp\left\{-\frac{m}{\pi}\int_0^\infty \ln\left[(1 - \rho) - \frac{1}{2}\rho u^2\ln\frac{u}{2} - \frac{1}{4}\rho u^2(2\gamma - 1)\right]\frac{du}{m^2 + u^2}\right\} \quad (14)$$

When $\rho < 1$ only the first term in equation (13) is required to yield equation (5). However, for the special case of $\rho = 1$, the next term is important. For this case the transformation $x = u/m$ yields

$$B(0, m) \simeq \exp\left\{-\frac{1}{\pi}\int_0^{2/m} \ln\left[-\frac{1}{2}m^2x^2\ln\frac{mx}{2} - \frac{1}{4}m^2x^2(2\gamma - 1)\right]\frac{dx}{1 + x^2}\right\} \quad (15)$$

or

$$B(0, m) \simeq \exp\left\{-\frac{1}{\pi}\int_0^{2/m}\left[2\ln x + \ln\left(\frac{1}{2}\Delta m^2\right) + \ln\left(1 - \frac{\ln x}{\Delta}\right)\right]\frac{dx}{1 + x^2}\right\} \quad (16)$$

with

$$\Delta = \ln(2/m) - \frac{1}{2}(2\gamma - 1)$$

Utilization of expansion

$$\ln(1 - \epsilon) = -\epsilon - \frac{1}{2}\epsilon^2 - \frac{1}{3}\epsilon^3 - \ldots \quad (17)$$

in the integrand of equation (16) gives

$$B(0, m) \simeq \exp\left\{-\frac{2}{\pi}\int_0^{2/m}\frac{\ln x}{1 + x^2}dx - \frac{1}{\pi}\ln\left(\frac{1}{2}m^2\Delta\right)\int_0^{2/m}\frac{dx}{1 + x^2} + \frac{1}{\pi\Delta}\int_0^{2/m}\frac{\ln x}{1 + x^2}dx + \frac{1}{2\pi\Delta^2}\int_0^{2/m}\frac{(\ln x)^2}{1 + x^2}dx + \ldots\right\} \quad (18)$$

Letting m become very small and introducing the following integrals:

$$\int_0^\infty \frac{\ln x}{1 + x^2}dx = 0, \quad \int_0^\infty \frac{dx}{1 + x^2} = \frac{\pi}{2}, \text{ and } \int_0^\infty \frac{(\ln x)^2}{1 + x^2}dx = \frac{\pi^3}{8} \quad (19)$$

into equation (18) yields

$$B(0, m) \simeq \exp\left[-\frac{1}{2}\ln\left(\frac{1}{2}m^2\Delta\right) + \frac{\pi^2}{16\Delta^2}\right] \quad (20)$$

or

$$B(0, m) \simeq \frac{\sqrt{2}}{m\sqrt{\Delta}}\exp(\pi^2/16\Delta^2) \quad (21)$$

Table 1 Comparison of various approximations of $B(0,m)$ with exact results for $\rho = 1$

m	$B(0,m)$	$\frac{\sqrt{2}}{m\sqrt{\Delta}}\exp\left(\frac{\pi^2}{16\Delta^2}\right)$	$\frac{\sqrt{2}}{m\sqrt{\Delta}}$	$\frac{\sqrt{2}}{m\sqrt{\ln(2/m)}}$
1.0	2.03112	9.16015	1.80198	1.69864
0.5	2.94387	3.54314	2.47208	2.40224
0.2	5.38909	5.36883	4.74006	4.65991
0.1	9.07591	8.89990	8.27816	8.17078
0.01	63.7895	63.3084	61.8919	61.4393
0.001	522.220	521.233	515.584	512.959
0.0001	4542.95	4540.41	4511.50	4493.87
0.00001	40786.7	40778.0	40607.4	40478.7

When m is very small, $\Delta = \ln(2/m)$ and equation (21) becomes

$$B(0, m) = \sqrt{2}/[m\sqrt{\ln(2/m)}] \quad (22)$$

Physically, equation (22) means the temperature at the edge of the cavity is inversely proportional to $[m \ln(2/m)]^{1/4}$. This behavior is somewhat unexpected since the overall heat transfer from the cavity is inversely proportional to m.

Approximations (21) and (22) are compared to the exact numerical results in Table 1. These approximations yield imaginary numbers when $m > 2$ and thus are not included. This behavior is due to the truncation of the series for $uK_1(u)$ to three terms. Inspection of Table 1 reveals that equation (21) is a more accurate approximation than equation (22) except when $m > 0.5$. For the range of m values reported in Table 1, approximation (22) underestimates the radiosity.

References

1 Crosbie, A. L., and Sawheny, T. R., "Application of Ambarzumian's Method to Radiant Interchange in a Rectangular Cavity," JOURNAL OF HEAT TRANSFER, TRANS. ASME, Series C, Vol. 96, 1974, pp. 191–196.

2 Crosbie, A. L., and Sawheny, T. R., "Radiant Interchange in a Nonisothermal Rectangular Cavity," *AIAA Journal*, Vol. 14, 1975, pp. 425–431.

3 Ivanov, V. V., *Transfer of Radiation in Spectral Lines*, National Bureau of Standards Special Publication 385, U. S. Government Printing Office, Washington, 1973.

4 Abromowitz, M., and Stegun, I. A., *Handbook of Mathematical Fnctions*, National Bureau of Standards, Applied Math. Series, 55, U. S. Government Printing Office, Washington, 1966, p. 488.

Critical Thickness of Insulation Accounting for Variable Convection Coefficient and Radiation Loss

L. D. Simmons[1]

Nomenclature

- F = shape factor, fraction of energy leaving the outside surface of the insulation which is incident on the portion of the environment having temperature T_∞
- h = mean convection heat transfer coefficient for the outside surface
- K = coefficient in the expression for variable convection heat transfer coefficient
- k = thermal conductivity of the insulation
- m = exponent of r_0 in the expression for variable convection heat transfer coefficient
- n = exponent of $(T_0 - T_\infty)$ in the expression for variable convection heat transfer coefficient
- q' = heat transfer rate per unit length of tube, wire, or cable
- r = radius of cylindrical insulation; r_i and r_0 are inside radius and outside radius, respectively; $r_{0_{crit}}$ is the outside radius which maximizes q'
- T = absolute temperature; T_i, T_0, and T_∞ are inside surface temperature, outside surface temperature, and temperature of the environment, respectively
- ϵ = total hemispherical emissivity of the outside surface of the insulation
- σ = Stefan-Boltzmann constant

[1] Department of Mechanical Engineering, University of Utah, Salt Lake City, Utah.

Contributed by the Heat Transfer Division of THE AMERICAN SOCIETY OF MECHANICAL ENGINEERS. Manuscript received by the Heat Transfer Division September 12, 1975.

Introduction

If the outside surface of a small diameter tube, wire, or cable has approximately constant temperature, there is a critical thickness of insulation which maximizes energy loss by heat transfer. This critical thickness of coating can be utilized when it is desired to cool the cylindrical tube, wire, or cable as effectively as possible. It is easily shown [1][2] that, if the insulation (with thermal conductivity k) around a long, slender cylinder has its inside radius r_i and its inside surface temperature T_i fixed, has an outside convection coefficient h which can be considered constant, and has negligible energy loss to its environment by radiation, the energy loss rate-per-unit length q' will be maximum when

$$r_0 = \frac{k}{h} \quad (1)$$

This maximizing radius is usually referred to as the critical radius $r_{0_{crit}}$ and $(r_{0_{crit}} - r_i)$ is referred to as the critical thickness of insulation. McAdams has shown [2] that if radiation is included in linearized form such that the radiation from the surface is given by $h_r A(T_0 - T_\infty)$, then the critical radius is given by

$$r_{0_{crit}} = \frac{k}{h + h_r}$$

However, both h (for convection) and h_r (for radiation) were considered constant, not varying with r_0 or T_0. Sparrow has shown [3] that if the variation of h with r_0 and outside surface temperature T_0 is considered in the form

$$h = K(T_0 - T_\infty)^n / r_0^m \quad (2)$$

and radiation neglected, then the critical radius is given by

$$r_{0_{crit}} = \left(\frac{1 - m}{1 + n}\right)\frac{k}{h} \quad (3)$$

Note, however, that now h on the right-hand side of equation (3) is a function of r_0 and T_0, which itself is a function of r_0, and so the value of $r_{0_{crit}}$ must be found by a trial-and-error or iterative procedure. In all three cases given in the foregoing the resulting expressions for $r_{0_{crit}}$ are simple in form (although not necessarily easily solved). However, none of the three could be expected to correctly predict the true critical radius because of simplifying assumptions. The purpose here is to develop an expression for $r_{0_{crit}}$ for insulation of cylinders with the variation of radiation and h with r_0 and T_0 accounted.

Analysis

The energy loss by conduction through the insulation is given by

$$q' = \frac{2\pi k(T_i - T_0)}{\ln(r_0/r_i)} = f[r_0, T_0(r_0)] \quad (4)$$

and the loss rate by convection and radiation from the surface is given by

$$q' = 2\pi h\, r_0(T_0 - T_\infty) + 2\pi r_0 \epsilon F \sigma(T_0^4 - T_\infty^4) \quad (5)$$

where h is given by equation (2). At steady state the energy loss rates will be equal so that

$$\frac{k(T_i - T_0)}{\ln(r_0/r_i)} = h r_0(T_0 - T_\infty) + r_0 \epsilon F \sigma(T_0^4 - T_\infty^4) \quad (6)$$

Now if dq'/dr_0 is found from equations (2), (4), and (6) by using chain rule and the result set to zero, the critical radius is found to be

$$r_{0_{crit}} = \frac{k[h(1 - m)(T_0 - T_\infty) + \epsilon F \sigma(T_0^4 - T_\infty^4)]}{[(n + 1)h + 4\epsilon F \sigma T_0^3][h(T_0 - T_\infty) + \epsilon F \sigma(T_0^4 - T_\infty^4)]} \quad (7)$$

[2] Numbers in brackets designate References at end of technical note.

When m is very small, $\Delta = \ln(2/m)$ and equation (21) becomes

$$B(0, m) = \sqrt{2}/[m\sqrt{\ln(2/m)}] \tag{22}$$

Physically, equation (22) means the temperature at the edge of the cavity is inversely proportional to $[m \ln(2/m)]^{1/4}$. This behavior is somewhat unexpected since the overall heat transfer from the cavity is inversely proportional to m.

Approximations (21) and (22) are compared to the exact numerical results in Table 1. These approximations yield imaginary numbers when $m > 2$ and thus are not included. This behavior is due to the truncation of the series for $uK_1(u)$ to three terms. Inspection of Table 1 reveals that equation (21) is a more accurate approximation than equation (22) except when $m > 0.5$. For the range of m values reported in Table 1, approximation (22) underestimates the radiosity.

References

1 Crosbie, A. L., and Sawheny, T. R., "Application of Ambarzumian's Method to Radiant Interchange in a Rectangular Cavity," JOURNAL OF HEAT TRANSFER, TRANS. ASME, Series C, Vol. 96, 1974, pp. 191–196.

2 Crosbie, A. L., and Sawheny, T. R., "Radiant Interchange in a Nonisothermal Rectangular Cavity," *AIAA Journal*, Vol. 14, 1975, pp. 425–431.

3 Ivanov, V. V., *Transfer of Radiation in Spectral Lines*, National Bureau of Standards Special Publication 385, U. S. Government Printing Office, Washington, 1973.

4 Abromowitz, M., and Stegun, I. A., *Handbook of Mathematical Fnctions*, National Bureau of Standards, Applied Math. Series, 55, U. S. Government Printing Office, Washington, 1966, p. 488.

Critical Thickness of Insulation Accounting for Variable Convection Coefficient and Radiation Loss

L. D. Simmons[1]

Nomenclature

- F = shape factor, fraction of energy leaving the outside surface of the insulation which is incident on the portion of the environment having temperature T_∞
- h = mean convection heat transfer coefficient for the outside surface
- K = coefficient in the expression for variable convection heat transfer coefficient
- k = thermal conductivity of the insulation
- m = exponent of r_0 in the expression for variable convection heat transfer coefficient
- n = exponent of $(T_0 - T_\infty)$ in the expression for variable convection heat transfer coefficient
- q' = heat transfer rate per unit length of tube, wire, or cable
- r = radius of cylindrical insulation; r_i and r_0 are inside radius and outside radius, respectively; $r_{0_{crit}}$ is the outside radius which maximizes q'
- T = absolute temperature; T_i, T_0, and T_∞ are inside surface temperature, outside surface temperature, and temperature of the environment, respectively
- ϵ = total hemispherical emissivity of the outside surface of the insulation
- σ = Stefan-Boltzmann constant

[1] Department of Mechanical Engineering, University of Utah, Salt Lake City, Utah.

Contributed by the Heat Transfer Division of THE AMERICAN SOCIETY OF MECHANICAL ENGINEERS. Manuscript received by the Heat Transfer Division September 12, 1975.

Introduction

If the outside surface of a small diameter tube, wire, or cable has approximately constant temperature, there is a critical thickness of insulation which maximizes energy loss by heat transfer. This critical thickness of coating can be utilized when it is desired to cool the cylindrical tube, wire, or cable as effectively as possible. It is easily shown [1][2] that, if the insulation (with thermal conductivity k) around a long, slender cylinder has its inside radius r_i and its inside surface temperature T_i fixed, has an outside convection coefficient h which can be considered constant, and has negligible energy loss to its environment by radiation, the energy loss rate-per-unit length q' will be maximum when

$$r_0 = \frac{k}{h} \tag{1}$$

This maximizing radius is usually referred to as the critical radius $r_{0_{crit}}$ and $(r_{0_{crit}} - r_i)$ is referred to as the critical thickness of insulation. McAdams has shown [2] that if radiation is included in linearized form such that the radiation from the surface is given by $h_r A(T_0 - T_\infty)$, then the critical radius is given by

$$r_{0_{crit}} = \frac{k}{h + h_r}$$

However, both h (for convection) and h_r (for radiation) were considered constant, not varying with r_0 or T_0. Sparrow has shown [3] that if the variation of h with r_0 and outside surface temperature T_0 is considered in the form

$$h = K(T_0 - T_\infty)^n / r_0^m \tag{2}$$

and radiation neglected, then the critical radius is given by

$$r_{0_{crit}} = \left(\frac{1 - m}{1 + n}\right)\frac{k}{h} \tag{3}$$

Note, however, that now h on the right-hand side of equation (3) is a function of r_0 and T_0, which itself is a function of r_0, and so the value of $r_{0_{crit}}$ must be found by a trial-and-error or iterative procedure. In all three cases given in the foregoing the resulting expressions for $r_{0_{crit}}$ are simple in form (although not necessarily easily solved). However, none of the three could be expected to correctly predict the true critical radius because of simplifying assumptions. The purpose here is to develop an expression for $r_{0_{crit}}$ for insulation of cylinders with the variation of radiation and h with r_0 and T_0 accounted.

Analysis

The energy loss by conduction through the insulation is given by

$$q' = \frac{2\pi k(T_i - T_0)}{\ln(r_0/r_i)} = f[r_0, T_0(r_0)] \tag{4}$$

and the loss rate by convection and radiation from the surface is given by

$$q' = 2\pi h\, r_0(T_0 - T_\infty) + 2\pi r_0 \epsilon F \sigma(T_0^4 - T_\infty^4) \tag{5}$$

where h is given by equation (2). At steady state the energy loss rates will be equal so that

$$\frac{k(T_i - T_0)}{\ln(r_0/r_i)} = h r_0(T_0 - T_\infty) + r_0 \epsilon F \sigma(T_0^4 - T_\infty^4) \tag{6}$$

Now if dq'/dr_0 is found from equations (2), (4), and (6) by using chain rule and the result set to zero, the critical radius is found to be

$$r_{0_{crit}} = \frac{k[h(1 - m)(T_0 - T_\infty) + \epsilon F \sigma(T_0^4 - T_\infty^4)]}{[(n + 1)h + 4\epsilon F \sigma T_0^3][h(T_0 - T_\infty) + \epsilon F \sigma(T_0^4 - T_\infty^4)]} \tag{7}$$

[2] Numbers in brackets designate References at end of technical note.

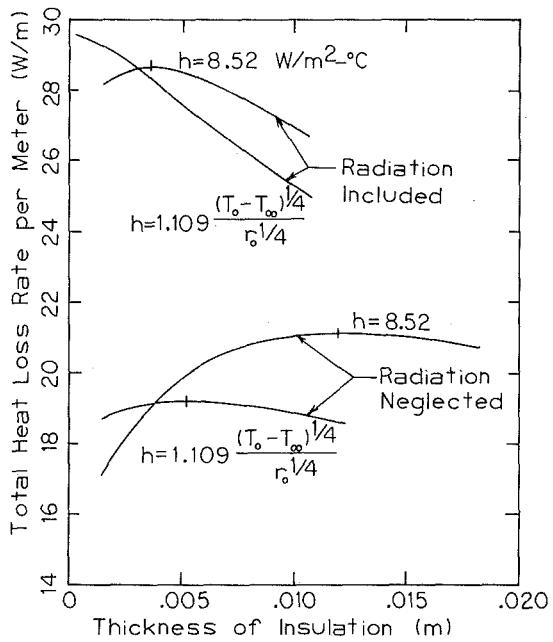

Fig. 1 Heat loss rate versus insulation thickness for Example 1 (rubber insulation on a 0.0127 m cable; natural convection)

If n, m, and ϵ are taken to be zero, this reduces to equation (1); if only ϵ is zero it reduces to equation (3). If only m and n are zero it reduces to

$$r_{0_{crit}} = \frac{k}{h + 4\epsilon F \sigma T_0^3} \tag{8}$$

which corresponds to the result derived by McAdams except that radiation has been exactly accounted rather than linearized with constant h_r.

In equation (7) the form of the expression for $r_{0_{crit}}$ is far from simple. It contains h and T_0 which both depend on r_0. Finding $r_{0_{crit}}$ requires simultaneous solution of equations (2), (6), and (7) for the three unknowns r_0 (which will be $r_{0_{crit}}$), h, and T_0.

Discussion and Examples

It was found that the easiest way to solve the three nonlinear equations in three unknowns is by using the Newton-Raphson iteration technique [4] on a digital computer. Three examples are given here to compare the critical radius as predicted by equations (1), (3), (8), and (7).

Example 1—(taken from [1]). An electrical cable, 0.0127 m (½ in.) OD, is to be insulated with rubber. The cable is located in air at 21.1°C (70°F) and has a surface temperature of 65.6°C (150°F). For the rubber insulation k = 0.159 W/m-°C (0.09 Btu/hr-ft-°F) and ϵ = 0.9. When h is constant it is taken as 8.52 W/m^2-°C (1.5 Btu/hr-ft^2-°F), and when its variation with r_0 and T_0 is considered then (for natural convection with Grashoff number based on diameter in the range 10^3–10^9)

$$h = 1.109 \frac{(T_0 - T_\infty)^{1/4}}{r_0^{1/4}} \text{ W/m}^2\text{-°C}$$

Example 2. Same as Example 1 except cable outside diameter is 0.003175 m (⅛ in.).

Example 3. Same as Example 2 except assume forced convection heat transfer. When h is constant it is taken as 22.7 W/m^2-°C (4 Btu/hr-ft^2-°F), and when it is variable then (for forced convection with Reynolds number based on diameter in the range 4000–40,000)

$$h = 3.246/r_0^{0.382} \text{ W/m}^2\text{-°C}$$

Figs. 1, 2, and 3 show the variation of q' with $(r_{0_{crit}} - r_i)$ for Examples 1, 2, and 3, respectively. Table 1 gives the critical radius and T_0, q', and h at the critical radius. For Example 1 equations (1), (3), and (8) do yield values for $r_{0_{crit}}$, but no solution exists for simultaneous equations (2), (6), and (7). For this example there is no critical radius in the most realistic case where both radiation and variation of h are taken into account, and Fig. 1 illustrates this fact. The cable size was taken smaller in Example 2 so that a criti-

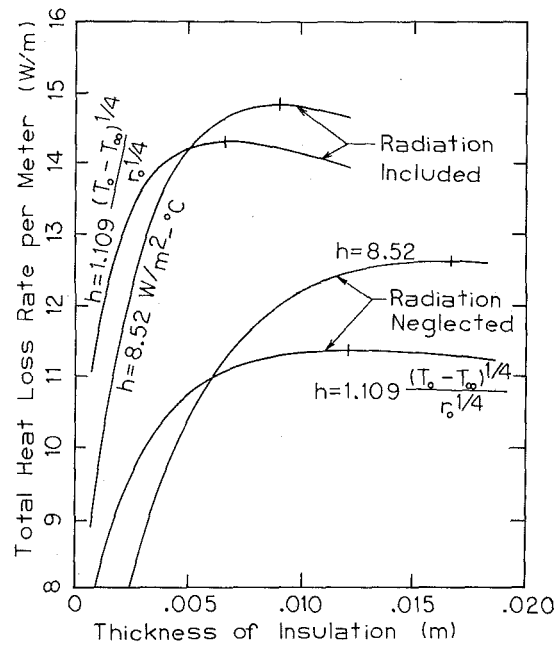

Fig. 2 Heat loss rate versus insulation thickness for Example 2 (rubber insulation on a 0.003175 m cable; natural convection)

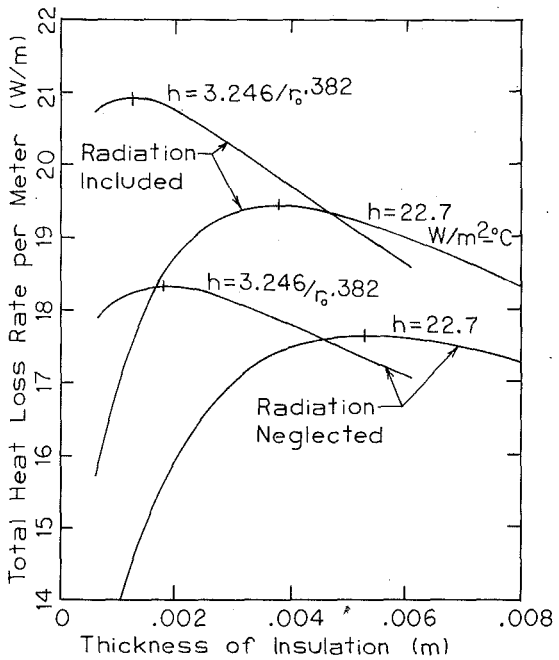

Fig. 3 Heat loss rate versus insulation thickness for Example 3 (rubber insulation on a 0.003175 m cable; forced convection)